

Gas-Solid Reactions for Energy Storage and Conversion

Habilitationsschrift

vorgelegt von

Dr.-Ing. Marc Linder

aus Ulm

Gutachter: Prof. Dr. André Thess
Prof. Dr.-Ing. Felix Ziegler
Prof. Dr. Henk Huinink

Tag des Habilitationskolloquiums: 29.06.2021

Institut für Gebäudeenergetik, Thermotechnik und Energiespeicherung der Universität Stuttgart

2022

Abstract

Reversible gas-solid reactions could offer relevant technological contributions to an energy system predominantly based on renewable energy. However, our current understanding of this technology is mainly based on fundamental material research and generic application concepts. Therefore, the first part of this work summarizes the current state of knowledge in order to identify unique advantages that could arise from reversible gas-solid reactions for energy storage and conversion. Starting with a technological differentiation between various reversible processes used for energy storage, a classification of different reactor designs and a generic approach for thermal integration and necessary reaction gas supply, three main directions are derived that currently seem most promising to transfer the specific properties of gas-solid reactions to technical systems: (1) open configurations to reduce system complexity, (2) utilization of available pressure differences to adjust the reaction temperature and (3) combination of abundant materials with the intrinsic possibility of lossless storage. Based on these considerations, the second part of this work summarizes our approach to transfer material properties to technical systems, e.g. by developing storages that utilize oxygen from air, by taking advantage of the pressure dependency of the reaction temperature of metal hydrides and salt hydrates or by combining the long-term energy storage possibility with abundant and cost-efficient reactants such as calcium oxide and water.

Zusammenfassung

Reversible Gas-Feststoff-Reaktionen könnten zentrale technologische Beiträge in einem zukünftigen erneuerbaren Energiesystem leisten. Unser aktuelles Verständnis basiert jedoch noch im Wesentlichen auf Materialuntersuchungen und generischen Anwendungskonzepten. Daher fasst der erste Teil der vorliegenden Arbeit den aktuellen Stand des Wissens zusammen und identifiziert dabei mögliche einzigartige Vorteile die aus der Nutzung von reversiblen Gas-Feststoff-Reaktionen zur Energiespeicherung und -wandlung entstehen können. Dabei werden, ausgehend von einer technologischen Unterscheidung der reversiblen chemischen Prozesse, einer Einteilung der unterschiedlichen Reaktorkonzepte sowie generischen Überlegungen zur notwendigen Gasversorgung, drei grundsätzliche Ansätze abgeleitet. Aus heutiger Sicht sind diese: (1) offene Systeme zur Reduktion der Anlagenkomplexität, (2) Nutzung vorhandener Druckdifferenzen zur Anpassung der Reaktionstemperatur und (3) die Kombination des intrinsischen Vorteils der verlustfreien Speicherung mit gut verfügbaren Materialien. Auf der Grundlage dieser Überlegungen, werden im zweiten Teil unsere Arbeiten zum Transfer spezifischer Materialeigenschaften in technische Systeme zusammengefasst. Diese basieren beispielsweise auf offenen Systemen die mit Luftsauerstoff reagieren, einer Ausnutzung der Druckabhängigkeit der Reaktionstemperatur von Metallhydriden und Salzhydraten oder einer Kombination aus Langzeit-Energiespeicherung mit den sehr gut verfügbaren und kostengünstigen Reaktanten Kalziumoxid und Wasser.

Contents

Abstract / Zusammenfassung

1.	Introduction and fundamentals	7
2.	Generic considerations.....	12
2.1.	Storage material: Thermochemical process.....	12
2.1.1.	Gas-Gas reactions: Mixture of reaction products and educts.....	13
2.1.2.	Ad- and Absorption processes: Graduate charging.....	14
2.1.3.	Gas-Solid reactions: Distinct equilibrium	16
2.2.	Thermochemical system: Process integration	18
2.2.1.	Closed systems	18
2.2.2.	Open systems	21
2.3.	Key component: Thermochemical reactor.....	23
2.3.1.	Rate of reaction and thermal power of the reactor.....	23
2.3.2.	Reactor concepts	25
3.	Own research and main results.....	29
3.1.	Utilizing available gases / Open operation.....	29
3.1.1.	Open to ambient	29
3.1.2.	Open to a technical system	32
3.2.	Utilizing pressure dependency / Thermal upgrade	37
3.2.1.	Open system to utilize existing pressure difference	38
3.2.2.	Closed system for waste heat utilization	40
3.3.	Utilizing abundantly available materials / Storage capacity at low cost.....	43
4.	Summary and conclusion	48
5.	References.....	50
6.	Own publications used for this work.....	57

1. Introduction and fundamentals

Our current energy system is able to cover basically all relevant aspects of energy demand. It is reliable, the consumption of energy is comparably cheap and it is resilient since the sources are reasonably diverse. However, our current concept of energy supply lacks of at least two important aspects in the context of sustainability: the first one is related to the eventual depletion of all fossil energy resources that currently form the backbone of our energy supply; the second one is related to the idea of utilizing the surrounding as allegedly infinite sink for e.g. exhaust gases from combustion processes, waste materials from mining or low grade thermal energy from power plants etc.

In this context, the reduction of primary energy consumption on one side and the transition to fossil-free energy supply on the other side are widely seen as key factors for a transformation into a sustainable energy system of the future where closed material cycles are basically driven by solar energy. The first factor is highly diverse and generally summarized as increase in efficiency. It aims for a combination of improving conversion processes, e.g. taking advantage of highly efficient traction in electrified vehicles, and minimizing unnecessary losses, e.g. reducing wasted thermal energy of industrial processes or improving building insulation. The second factor is comparably clear and is based on a subsequent reduction of energy generation based on fossil resources substituted by an increasing utilization of renewably available energies - if necessary in combination with storage technologies to preserve our reliable energy supply.

Consequently, besides the collection of renewable energy, its storage and efficient conversion to effective energy can be seen as main technological challenges for a sustainable energy system of the future. However, taking our effective energy needs into consideration and comparing them to our currently invested primary energy¹, it becomes obvious that a direct or linear transition from fossil to renewable energy supply seems at present unlikely leaving space - and need - for new, innovative emerging technologies.

Reversible chemical reactions between a solid and gaseous reactant, in the following abbreviated as gas-solid reactions, could form the basis for such emerging technologies. These systems are increasingly discussed and investigated not only in the context of energy storage but also in context of thermal energy conversion [e.g. 1-5]. However, since our understanding of these systems is so far mainly based on fundamental material research and generic concepts, their potential contribution to our future energy supply can be hardly evaluated. Therefore, this work aims to summarize the specific potential of gas-solid reactions for energy storage and conversion, analyze their limitations and finally tries to contribute to the transfer of specific and unique properties on material level to promising technical systems.

¹ Primary Energy Consumption in Germany, 2017: ca. 13.550 PJ, of which around 13 % was supplied by renewable energies (main fractions: biomass 54 %; wind energy 22 %; photovoltaic 10 %) [6]

The operation of a gas-solid reaction is based on the idea to use thermal energy as input to drive an endothermic decomposition reaction. Thereby a gaseous component is released and the thermal energy is transferred into a chemical potential. Figure 1 shows the schematic principle of this endothermic decomposition. In case of a subsequent separation of the reaction products (A and B) the chemical reaction allows directly for an – in principle – infinite storage time of the associated heat of reaction (ΔH).

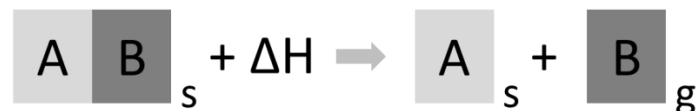


Figure 1: Schematic of an endothermic decomposition of a solid compound (AB) into a solid (A) and a gaseous (B) product

However, since the endothermic decomposition proceeds at a certain temperature, the fractions of thermal energy stored as sensible heat in the material masses have to be considered and depend mainly on the operation temperature and the heat capacity of the involved materials. For example, for low temperature thermochemical energy storage the sensible thermal losses can be very small and potentially neglected. So, in this case the reaction products can be cooled down and simply stored at ambient conditions. For higher storage temperatures however, the sensible thermal energy accounts for a higher fraction of the total energy and has to be taken into account – if a utilization is not possible, the storage products have to be insulated (comparable to thermophysical storages) in order to avoid respective thermal losses.

By recombining the reaction products, the exothermic backward reaction allows the release of the chemically stored thermal energy – basically on demand. This is schematically shown in Figure 2.



Figure 2: Schematic of an exothermic (re-)combination of a solid (A) and a gaseous (B) educt into the solid compound AB

Combining Figure 1 and Figure 2, it becomes clear that the gas-solid reaction can be either used as intermediate sink for thermal energy (Figure 1) or as sink for the gaseous reaction partner, e.g.

hydrogen (Figure 2). Due to the presupposed reversibility of this generic process, it is obvious that the exchange of thermal energy is directly linked to an exchange of the gaseous reaction partner. Various reactions that allow for this exchange are reported in recent literature, ranging from extensive material screenings [7-12] to experimental investigations on material and small laboratory scales [13-31].

Assuming a simplified theoretical set-up where the generic reaction of Figure 1 and 2 is contained within variable boundaries, four cases can be distinguished (compare Figure 3):

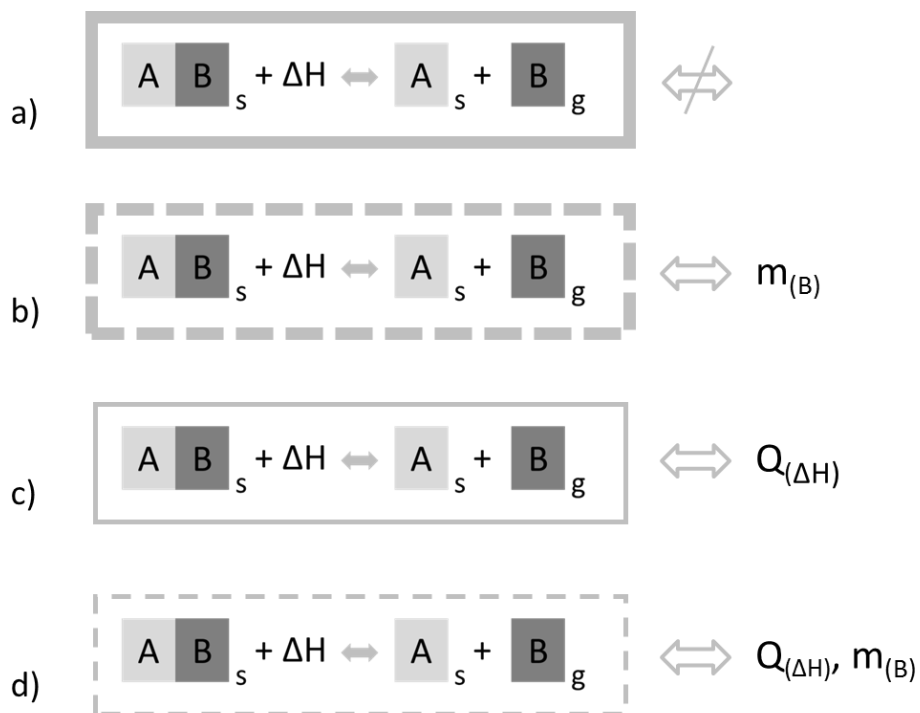


Figure 3: Schematic of a gas-solid reaction within four generic boundaries: a) adiabatic and closed, b) adiabatic and open, c) diathermic and closed, d) open boundaries

Case 1 – adiabatic and closed boundaries (Figure 3a, equilibrium): The system is in equilibrium which means that pressure and temperature are constant according to the thermodynamic characteristic of the reaction (details see chapter 2).

Case 2 – adiabatic, but open boundaries (Figure 3b, temperature change): The gaseous reaction partner can enter or leave the system. A supply of the gaseous reaction partner leads to an exothermal answer of the reaction and consequently to a temperature increase (or vice versa). The final (equilibrium) temperature is directly linked to the applied gas pressure and the thermodynamic characteristic of the reaction.

Case 3 – diathermic, but closed boundaries (Figure 3c, pressure change): Thermal energy can pass the boundaries which leads to a dissociation and consequently to a pressure increase. With increasing temperature of the solid, the pressure increases until the temperature of the material reaches the temperature of the external heat source.

Case 4 – open boundaries (Figure 3d, storage mode): In this case, reaction gas and thermal energy can be exchanged. Consequently, the reaction in Figure 1 (or Figure 2) is not self-limited and will continue until complete conversion is reached.

Following the schematic of Figure 3, a simplified reactor has to be partially open to utilize the full capacity of the reversible chemical reaction, compare case 4.² As a direct consequence, any thermochemical approach has to fit not only to a temperature but also to a pressure boundary condition. This clearly differentiates the thermochemical approaches from thermophysical approaches to store thermal energy. Up to now, a few demonstration systems with prototype character that are based on thermochemical gas-solid reactions have been reported in literature [32-37]. However, the associated supply (or removal) of the reaction gas – under realistic boundary conditions – might have a severe impact on the practicability and/or the efficiency of such thermochemical systems. Due to this generic reason, thermochemical energy storages or especially thermochemical systems dedicated to specific applications are more complex in comparison to thermophysical storages based on sensible or latent thermal energy.

Concluding above considerations and the state of the art of gas-solid reactions and related technical systems for energy storage and conversion, three major aspects can be identified that are crucial for the transition from a thermochemical process (basically the forward and backward reaction) to a thermochemical system.

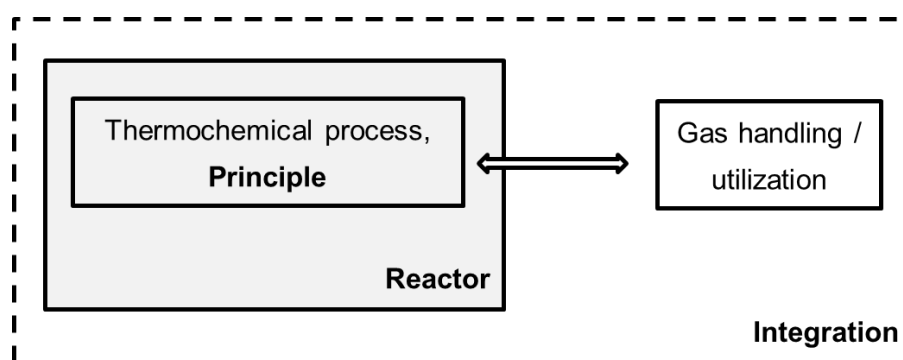


Figure 4: Schematic principle of a thermochemical system

² An exemption could be an artificial (chemical) heat capacity of a diathermic thermochemical system, e.g. as small spheres. Patent application (Linder, M. et al. (2015), DE102015108095A1, Germany)

Obviously, the thermochemical process has to be understood and taken into account. Different types of thermochemical processes (Fig. 4: principle) that are – in general – summarized as thermochemical heat storages possess important application relevant differences, such as e.g. storage temperature as a function of conversion. Besides that, the necessity of a gaseous reactant demands a proper integration and utilization of the reaction gas (Fig. 4: integration). Since the gas handling does not only affect the storage density of the system, but also its efficiency it is crucial and has to be adapted for any intended application. Finally, the component that connects the thermochemical process with the intended application is the thermochemical reactor (Fig. 4: reactor). The reactor defines, on one side, the dynamics of the thermochemical system as it has to ensure sufficient heat and mass transfer. On the other side, the reactor converts a gas supply into a release of thermal energy and vice versa.

Chapter 2 of this work (Generic considerations) focusses on these three major aspects of a thermochemical system in more detail. The main intention is to summarize the state of the art of gas-solid reactions for energy storage and conversion and derive specific aspects of reversible gas-solid reactions that could be transferred to and utilized in technical systems.

Some of these specific aspects – on material level – are:

- Long-term storage possibility; due to the separation of reactants and the associated storage at ambient temperature without thermal losses
- High storage densities; due to the involved thermochemical process
- Possibility to combine heat and/or cold storage
- Heat release ‘on-demand’; due to the controllability of the backward reaction
- Possibility to transform heat (thermal upgrade)
- Use of cheap and widely available materials

Chapter 3 of this work (Own research and main results) gives an overview of our approaches to transfer these specific aspects into technical systems and summarizes the main results. Besides open thermochemical systems that are able to utilize available gases and even pressure differences, the distinct correlation of reaction temperature and gas pressure opens new combinations of thermal energy storages and heat pumps, including heat transformation processes. And finally, abundantly available materials such as quick lime (based on natural lime stone) or some salt hydrates (e.g. based on Carnallite or CaCl_2) are available at low cost and with low environmental footprint and might be therefore promising candidates for e.g. future long-term storage solutions.

Chapter 4 (Summary and Outlook) concludes the main aspects of this work and aims to indicate future research directions for the transfer of specific material properties of gas-solid reactions to technical systems for energy storage and conversion.

2. Generic considerations

This chapter aims to introduce the three important aspects of gas-solid reactions. Since any potential specific advantage of a thermochemical system is based on material properties, the chapter starts with the definition of the thermochemical process itself. The second part refers to the integration of the thermochemical process into different generic systems, whereas the last part deals with the thermochemical reactor as crucial component.

2.1. Storage material: Thermochemical process

Gibb's free energy can be used to describe the necessity of a gaseous reactant for thermochemical energy storages - especially for reversible systems with associated high enthalpies per mol of reactant. The following equation states that for a given temperature (T), the chemical potential (Gibbs free energy) of the reversible reaction at equilibrium is zero:

$$0 = \Delta G = \Delta H - T\Delta S \quad (1)$$

However, as long as the system is in thermodynamic equilibrium, neither a charging nor a discharging of the storage is possible. According to Figure 1, for a thermal charging of the thermochemical storage, the equilibrium has to be disturbed in such a way that the dissociation reaction proceeds. This can be reached either by a supply of thermal energy or by reducing the concentration of the products (or one of the products). On the other hand, the thermal discharging of the thermochemical storage demands a supply of the educts and/or a removal of the heat of the thermochemical process (compare Figure 2).

Based on Equation (1), for a given temperature (T), the enthalpy change (ΔH) is directly proportional to the entropy change (ΔS). Thus, a large entropy change promises a high reaction enthalpy of the thermochemical process. Since volume changes are associated with a large change in entropy, a charging of a thermochemical system is generally combined with a release of a gaseous compound or product and vice versa. Even though a few potential applications exist that utilize the heat of involved thermochemical processes without a gaseous phase³, thermochemical reaction systems can be generally classified by the state of the second involved reaction partner – these are consequently gas-liquid, gas-gas or gas-solid thermochemical processes.

³ E.g. one way solid-liquid thermochemical systems for instantaneous heat release (www.barocook.eu)

A general introduction to thermochemical energy storage based on gas-solid reactions was given in the previous chapter. It was concluded that during an endothermic dissociation, thermal energy is transferred to a chemical potential and can be recovered by the exothermal backward process. Even though this generic description can be applied for gas-solid, gas-liquid and gas-gas reactions, it does not reflect the specific characteristics of each storage principle that can be utilized for thermochemical energy storage. Whereas the state of conversion of gas-gas reactions or sorption processes has a direct impact on the temperature of the reaction (due to different reasons), reversible gas-solid reactions follow an equilibrium line that allows for a complete conversion at a specific given pressure/temperature condition. Therefore, in the following chapter a general characterization is given that focuses briefly on the most important operation differences between the different thermochemical processes.

2.1.1. Gas-Gas reactions: Mixture of reaction products and educts

The main characteristic of gas-gas reactions for thermochemical heat storage is the mixture of gaseous reaction products and educts during the respective cycle. So, an easy separation of the reactants is not possible. This affects on one side the operation strategy of the storage system since a spontaneous recombination has to be avoided during the storage phase, e.g. by the absence of a catalyst and/or low storage temperatures. On the other side, it has also a crucial impact on the storage temperatures.

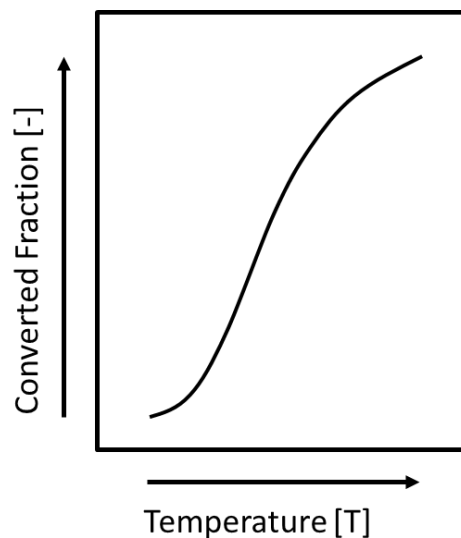


Figure 5: Schematic Gas-Gas Reaction: Reachable converted fraction depends on the available temperature level

The correlation between the converted fraction (concentration of the reaction product) and the equilibrium temperature of the reaction for a gas-gas reaction is schematically shown in Figure 5. It is obvious that the extent of converted fraction is equal to the stored thermal energy which – according to Figure 5 - depends directly on the maximum temperature that can be reached during the charging process. For the backward reaction the correlation is comparable – the lower the discharging temperature, the larger is the fraction of converted reaction partners. Therefore, in order to reach high converted fractions, a thermochemical heat storage based on gas-gas reactions requires a temperature operation range.

Examples of thermochemical systems based on a gas-gas reaction are reversible dissociations of ammonia or methane [38, 39]. For thermal energy storage, the ammonia-based thermochemical energy storage offers an intrinsic advantage: If the system is operated above the saturation pressure of ammonia, it is possible to easily separate a large fraction of ammonia from its dissociation products (nitrogen and hydrogen) by condensation [40]. Besides the application as thermal energy store, so-called ‘chemical heat pipe’ configurations of reversible gas-gas reaction offer the possibility of a long distance transfer of high temperature thermal energy with minimal losses [41]. A chemical heat pipe based on steam methane reforming was intensively investigated in the context of high temperature (nuclear) reactors [39].

2.1.2. Ad- and Absorption processes: Graduate charging

Even though ad- or absorption processes do not involve a chemical reaction, the systems that are based on these principles are often included in the expression ‘thermochemical energy storage’. Besides liquid sorption systems (such as e.g. LiBr-H₂O), the most prominent systems are based on silica gels or zeolites and use water vapor as gaseous reactant. Even though the reactants can be easily separated (supply or removal of water vapor), the storage density of a given system also increases with increased charging temperature and/or decreased discharging temperature. This is comparable to the gas-gas reactions mentioned above, even if the underlying reason is different.

The schematic of a sorption process is shown in Figure 6. The isosteres, shown as straight lines, refer to different states of charge that are characteristic for sorption processes since e.g. a thermal discharging corresponds to a gradual ‘filling’ of e.g. available surface area or pore volumes, respectively. Therefore, for a given pressure, the amount of adsorbed reaction gas increases with decreasing temperature. Thus, for a given gas pressure the ‘conversion’ of these thermochemical storage systems increases with increasing temperature differences between charging in discharging.

As a consequence, sorption based thermochemical energy storages demand a temperature (or pressure) difference between charging and discharging and - for a given system - its extend is directly correlated to the stored energy. The same coherences are valid for absorption processes of gas-liquid systems, in this case due to dilution effects.

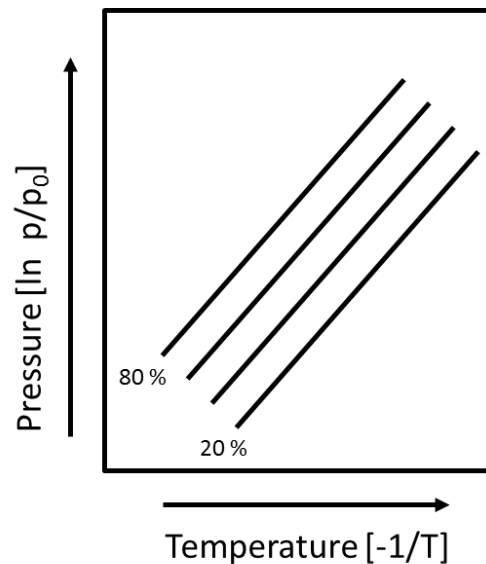


Figure 6: Schematic sorption processes: The state of charging depends for a given temperature on the available pressure or vice versa

Thermochemical systems based on ad- and absorption processes are commercially available, mainly as continuously operated thermally driven heat pumps. In these cases a temperature swing of the solid sorption material is externally induced which leads to a pressure swing of the gaseous reactant. If two processes are alternatingly coupled, a continuous mass flux of the reactant is obtained. Depending on the peak-to-peak amplitude of the temperature swing, the mass flux can be combined with a pressure increase – this process is comparable to conventional mechanical compression but with thermal energy as energy input. In state of the art sorption systems the gaseous reactant is condensable and used as working fluid for thermally driven heat pumps or cooling systems, e.g. for solar cooling or waste heat recovery [42, 43]. Gas-solid sorption systems for thermal energy storage are still in research state [44]⁴. As mentioned above, ideal conditions for this type of storages allow for a temperature difference between charging and discharging and require longer storage periods. This could be on side realized by the transport of thermal energy from a source (e.g. industrial waste heat) to a nearby sink [e.g. 45]. Additionally, a widely addressed potential application is the decentralized seasonal storage to cover the heat demand in winter. One major research and development aspect of this technology is related to the temperature difference between discharging in winter (as low as acceptable) and charging in summer (as high as possible with cost-effective solar thermal collectors). However, the environmental impact of manufacturing the material and the system has to be taken carefully into account – especially if the benchmark is sensible storage in non-pressurized water tanks [46].

⁴ Exemptions are based on unique features, e.g.: Dish washer (combination of drying and heating of air, <https://www.siemens-home.bsh-group.com.au/inspiration/innovation/highlights/zeolith>) and beer keg (cooling on demand, <http://www.tucher.de/unsere-biere/unser-sortiment/unser-coolkeg/>)

2.1.3. Gas-Solid reactions: Distinct equilibrium

Gas-solid reactions are in general comparable to adsorption processes since the reactants can also be easily separated. However, in contrast to the above described graduate filling, one distinct equilibrium line separates the charged state from the discharged one. This is due to a formation of a new chemical compound (e.g. formation of a metal hydroxide by the chemical reaction of a metal oxide and water vapor).

The schematic principle of such a gas-solid reaction is shown in Figure 7 using a specific phase diagram for a better visualization of the associated pressure. This so called van't Hoff plot separates the thermally charged state (below) from the discharged state (above the line). Therefore, for a given reaction gas pressure, a complete conversion corresponding to the maximum storage capacity of the respective stage is possible at one distinct temperature. Analogies can be drawn to the condensation of a gas (at a constant pressure) or to the solidification of a liquid.

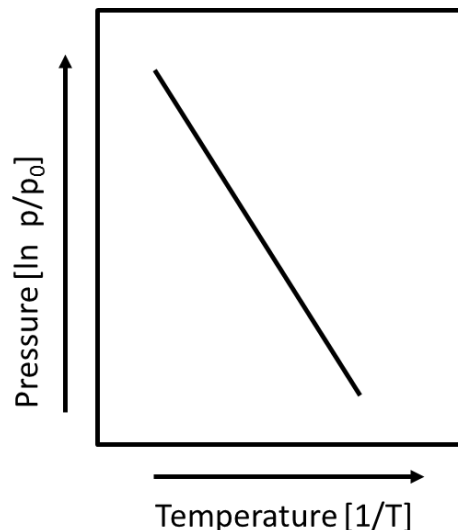


Figure 7: Schematic gas-solid reaction: Distinct equilibrium line separates the charged from the discharged state. As a consequence, for any given temperature/pressure combination above the line, the system is completely (thermally) discharged and vice versa

This theoretical coherence can be limited by effects like hysteresis (difference between formation and dissociation or kinetic limitations) or intermediate steps that can occur e.g. during hydration of some salts. However, due to this coherence, the discharging temperature for the full capacity of the thermochemical storage can be almost equal to the charging temperature. Gas-solid reactions are therefore especially interesting if e.g. distinct temperature levels are required or pressure differences can be used to upgrade thermal energy. This offers on one side promising applications such as combinations of heat pumps and thermal energy storage in one unit. On the other side, this distinct correlation is related to structural changes of the reacting solid. These might have direct impact on

the bulk structure and is one of the reasons why most of the thermochemical systems based on gas-solid reactions for energy storage and conversion are still in research state and have not left laboratory scales yet. Exemptions are chemisorption processes such as metal hydrides for e.g. hydrogen storage [47].

Additionally, the distinct equilibrium line imposes another challenge for the technical application of gas-solid reactions: The respective required temperature has to be reached in any case – in contrast to the above described systems, a gradual charging leading to a predictable lower performance (if the nominal temperature is not reached) is not possible. Either the temperature level is sufficiently high or the storage system doesn't work at all. Consequently, reversible gas-solid reactions have to perfectly match the required temperature condition of the intended application. According to Figure 8, this could be achieved by changing the pressure of the gaseous reactant. However, this option depends highly on the integration possibilities into the intended application. A logical approach to overcome this issue can be derived from Equation (1) and is shown in Figure 8. As the related equilibrium temperature for a given pressure increases with increasing specific reaction enthalpy, different reacting solids can be chosen for the same gaseous reactant (e.g. water vapor, forming hydroxide phases) [48]. Thereby the thermodynamic equilibrium of the gas-solid reaction based on a given reaction gas, e.g. water vapor, can be to a certain extent adapted to the intended application. One emerging research field in this context is the chemical modification of the reacting solid with the future goal to precisely tailor its thermodynamic equilibrium with the respective gaseous reactant [e.g. 24].

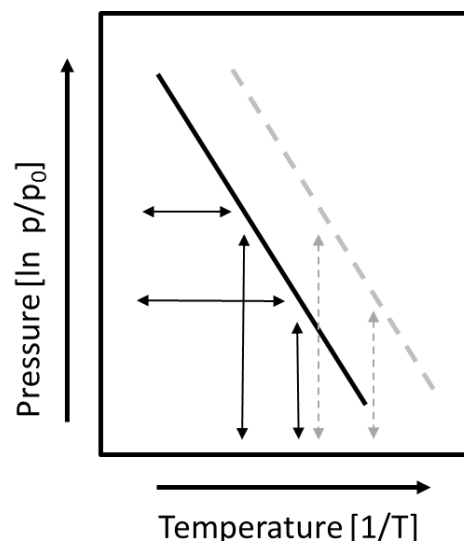


Figure 8: Adaptation possibilities of gas-solid reactions: Impact of a pressure change on the associated equilibrium temperature (arrows) and impact of the involved heat of reaction (dashed lines for solid reactant with lower ΔH)

It is rather obvious that above used general classification is only possible for the sake of certain impreciseness. For instance, in case of the above mentioned interstitial metal hydrides (chemisorption process), a strict classification is not possible since the reaction behavior depends highly on the chosen solid or alloy [49]. Moreover, by means of specifically tailored storage materials adapted to the respective gaseous reaction partner, the temperature dependency of the state of charge of sorption materials can be drastically reduced [50]. And finally, whether the specific differences of gas-solid processes to other thermochemical systems are important or not depends a lot on the intended application.

2.2. Thermochemical system: Process integration

The development of a thermochemical system does not only depend on the respective material properties, e.g. energy density, heat capacity or heat of reaction, but does also highly depend on the intended process. A proper integration strategy has to consider the supply and removal of the gaseous reactant and thereby finally defines whether a thermochemical system can offer some of the above mentioned advantages. In this context two general operation principles for thermochemical systems can be distinguished.

In a closed thermochemical system only thermal energy is exchanged with the respective process. Therefore, the released reaction partner has to be handled internally. In case the reactant(s) has to be stored in gaseous state, high storage densities can only be reached if the reactant is compressed. If a condensable gas (e.g. H₂O) is used as reaction partner, the required compression work can be substituted by thermal energy – which has to be available at the respective temperature level and during the process of thermal discharging. On the other hand, an open thermochemical system exchanges not only thermal energy but also its reaction partner – either with the ambient or with the respective process. In this case very high storage densities can be reached but challenges like e.g. potential side reactions with impurities or the ensured availability of the reaction partner have to be considered. In this chapter both options are briefly discussed.

2.2.1. Closed systems

The general schematics of closed thermochemical systems for thermal energy storage are shown in Figure 9. In this case both reaction partners need to be taken into account and a second container is necessary. However, since one reaction partner is gaseous and consequently possess a rather low density, additional measures are necessary to reach high storage densities of the system.

For this purpose, three different cases can be distinguished that are schematically given in Figure 9. The first option is the compression of the reaction partner (Figure 9a). The released reactant(s) from the charging process flows through a compression unit and is later stored in a vessel at a certain

pressure. For the compression, additional energy is required that has to be taken into account – especially since mechanical energy is necessary to operate the thermal energy storage.

Obviously, the compression work is partially available as potential energy in the storage vessel. Therefore, a re-utilization to a certain extent is possible – either by increasing the discharge temperature of the thermochemical storage (compare chapter 1.2) or by an expansion unit that partially recovers the mechanical energy.

Another option is to utilize a condensable gas, e.g. water vapor (Figure 9b). In this case, the gaseous reaction partner is released during the charging at the respective temperature and transferred to a connected condensation unit. If this condensation unit operates at temperatures below the condensation temperature the gaseous reaction partner automatically condenses, thereby drastically increasing its density. In order to operate at a constant pressure, the released enthalpy of condensation has to be removed. On the other hand, since the discharge process of the thermal energy storage demands a gaseous partner, the enthalpy of evaporation has to be supplied by an evaporation unit. So, the system operates actually between two temperature levels and both thermal energy fluxes have to be taken into account. Since this closed system can be in principle operated with all gases that are condensable at technically reasonable conditions, besides water vapor reactions e.g. also ammonia or CO₂ based reactions are possible if the operation pressure is adjusted to the respective temperature boundaries. Additionally, also systems combining approach (a) and (b) are possible.

Comparable to the condensation process, also a second reaction can be used to offer a sink for the gaseous reactant (Figure 9c). In this case, two reactors with two adapted reaction systems that operate at the same gas pressure but at different temperatures are necessary. This configuration is mainly investigated with coupled metal-hydrogen or salt-ammonia based reactions [51-53]. These concepts demand a couple of reacting solids with two different thermochemical properties that have to fit to the intended application. The occurring heat fluxes are comparable to case (b), but the systems complexity might be higher since at least two reactors are necessary.

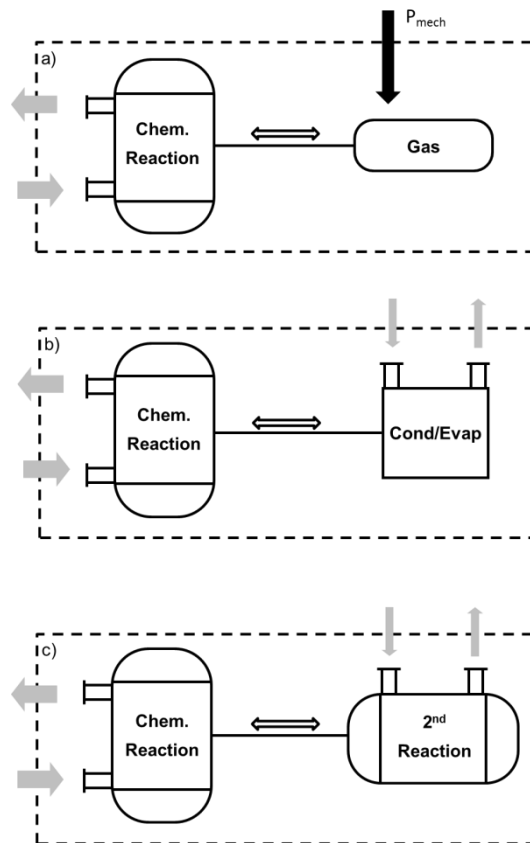


Figure 9: Schematics of closed thermochemical systems: a) compression of reaction gas, e.g. hydrogen or carbon dioxide; b) condensable reaction gases, e.g. water vapor or ammonia; c) coupled reactions, e.g. metal alloys and hydrogen or salts and ammonia. Greyish arrows indicate thermal energy, black arrow indicates mechanical energy

As mentioned above, case (b) and (c) are always operated between two heat fluxes (greyish lines). So, these thermochemical systems are also basic configurations for chemical heat pumps. The only difference might be related to the power and capacity level of the respective reactor. While a thermochemical energy store is rather operated as batch process which addresses a certain storage capacity, the chemical heat pump operates quasi-continuously by two alternating processes and has to reach a certain power level. However, the relevant similarity is the operation between two heat fluxes that occur at different temperature levels.

For closed thermochemical energy storages using a second heat flux (case (b) and case (c)), three operation strategies can be distinguished that are shown in Figure 10⁵.

⁵ In these examples the exothermic process during discharging is considered as 'useful' effect which is the case for thermochemical 'heat' storage. Obviously, in case of thermochemical 'cold' storage the respective endothermic process would be considered as useful effect. However, the integration aspects are comparable.

- (1) The second energy flux is used as additional benefit. In this case the endothermic process during discharge (e.g. evaporation of the reaction gas) is used as 'cold' storage. These systems therefore combine heat and cold storages and demand consequently a higher integration effort. The main challenge is to meet the actual required temperature level for both effects as well as for both cases – charging and discharging.
- (2) The ambient is used as basis. In this case thermochemical systems are designed to utilize the ambient as heat sink and heat source for condensation or evaporation, respectively. The main challenge is related to the variable temperature boundary condition (e.g. winter/summer).
- (3) The thermochemical system is designed to reuse the low grade thermal energy available within the process (e.g. generally released via cooling towers). In this case the thermal energy is not released to the ambient but used to supply the gaseous reaction partner (e.g. for evaporation). The thermochemical reaction then releases high grade thermal energy that can be used to generate mechanical energy (e.g. Honigmann process, details in [54]).

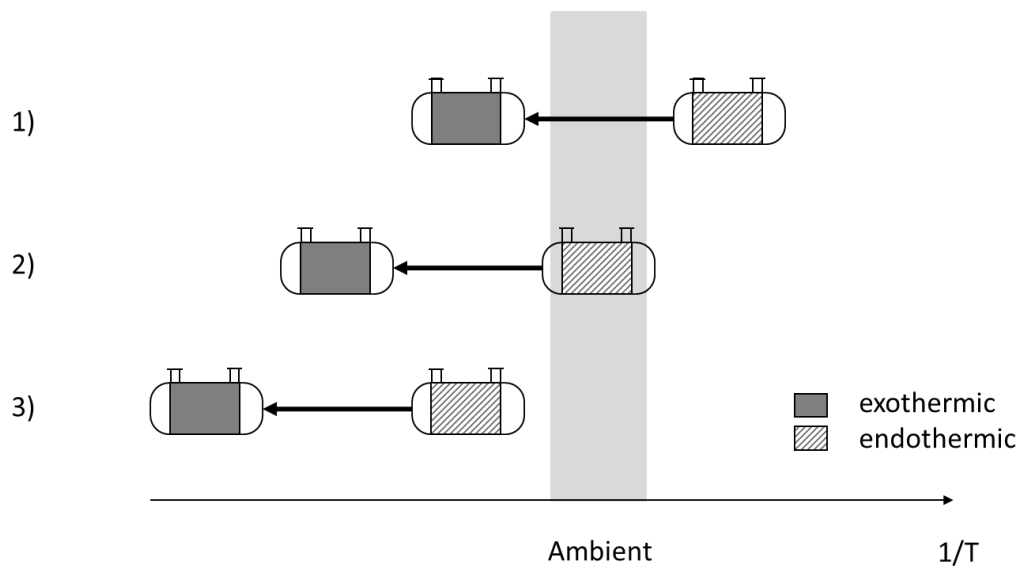


Figure 10: Operation principles of closed thermochemical energy storages (discharging case with exothermic process as primary 'useful' effect)

2.2.2. Open systems

Whereas closed systems do not exchange any mass with the process or the ambient, open reaction systems are based on the idea that the complexity of the system can be reduced if also an exchange of the reaction partner is possible.

Two general principles of open thermochemical systems are shown in Figure 11. In Figure 11a, the open thermochemical system is assumed as particular process that exchanges its gaseous reaction

partner e.g. with the ambient and additionally thermal energy with the respective application. In this case only systems based on water vapor (humidity) or oxygen are possible since the ambient is used as sink and source. Due to the very small concentration of CO_2 in ambient air, CO_2 based reactions are theoretically possible but might require additional measures to increase the availability, especially for the thermal discharging. Since the gaseous reaction partner does not have to be stored, the storage density of the thermochemical storage system is clearly increased. However, additional questions like poisoning of the storage material by side reactions (e.g. carbonation) or the guaranteed availability of a sufficient concentration of the gaseous reaction partner (e.g. water vapor in winter season) arise.

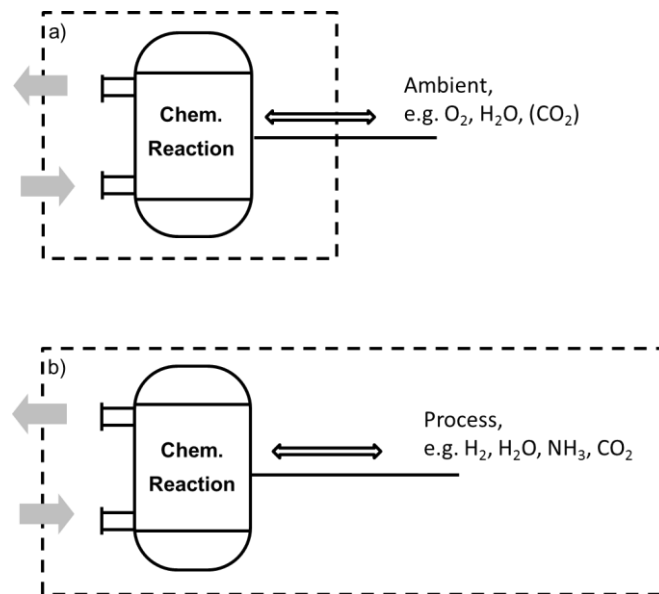


Figure 11: Schematics of open thermochemical systems: a) utilization of gases available in ambient air; b) utilization of gases already used in processes. Greyish arrows indicate thermal energy

The second option is only possible if the reaction system fits into the intended process since in this case the thermochemical system is directly integrated, compare Figure 11b. Obviously, again the storage density can be increased and also only one reactor is necessary. But additionally, even if the integration effort is higher, the quality of the reaction gas as well as its availability is known and projectable. One interesting advantage might be the utilization of available concentration or pressure differences that can be directly transferred into temperature differences, e.g. for cooling or thermal upgrading purposes. This type of system is only possible if the reaction gas is already available in the process, e.g. water vapor in industrial processes or hydrogen gas in hydrogen-fueled cars.

2.3.Key component: Thermochemical reactor

The thermochemical reactor is the crucial component of every thermochemical system since it connects the respective thermochemical process on one side and the intended application with its specific requirements on the other side.

The storage reactor has to ensure an excellent distribution of the gaseous reaction partner as well as an excellent heat transfer between the thermochemical process and the respective heat transfer fluid. In case of gas-solid or gas-liquid reactions, it has to guarantee a separation of the reactants in order to prevent, e.g. a discharge of the solid material. Additionally, depending on the chosen reaction system, also high pressures and/or temperatures can occur that might demand also certain measures. Finally, the respective application requirements such as charging or discharging power and capacity have to be reached and determine main design parameters of the reactor. But in contrast to thermophysical storages, like sensible or latent heat storage, the reachable thermal power does not only depend on the heat transfer from the heat transfer fluid to the storage material and the heat distribution inside, but also on the rate of reaction of the respective thermochemical process.

2.3.1. Rate of reaction and thermal power of the reactor

Thermodynamic data of the respective reaction systems can be found in literature and are in general reliable. Based on these data, theoretically suitable reactions for a specific application can be found and unsuitable systems can be excluded. However, the final applicability of any thermochemical system depends on the reachable rate of reaction of the material at the respective conditions.

Therefore, in order to identify possible reaction systems for thermochemical heat storage, a detailed analysis of the respective rate of reaction at application relevant temperatures and pressures is necessary. In general, the rate of reaction (dx / dt) can be described by following generic equation that takes three different dependencies into account:

$$dx/dt = f(T) \cdot f(p, p_{eq}) \cdot f(x) \quad (2)$$

(1) Temperature dependency: $f(T)$

For a given reaction system, a temperature increase leads in principle to an accelerated rate of reaction (Arrhenius' dependency).

(2) Equilibrium dependency: $f(p, p_{eq})$

The thermochemical process can only proceed until the equilibrium is reached. For gas-solid reactions, this equilibrium dependency can be described by an experimentally determined correlation between the locally available gas pressure (p) and the known equilibrium

pressure at the local temperature (p_{eq}). Due to this dependency on the equilibrium, thermochemical systems based on gas-solid reactions are self-limiting and the available pressure level directly determines the reaction temperature.

(3) Dependency on the reaction mechanism: $f(x)$

The third dependency summarizes possible reaction mechanisms and takes into account that the reached state of conversion has an additional impact on the further reaction. Examples are the deceleration of the chemical reaction towards full conversion, a slow but exponential rate of reaction at low conversion or the combination of both leading to a sigmoidal shape.

A proper determination of the rate of reaction and its mathematical description is generally complex. A practical approach in order to determine the application relevant rate of reaction is the experimental analysis at (almost) ideal conditions. For gas-solid reactions, these would be isothermal conditions with constant pressure that are not influenced by any transfer processes. Based on such an experimental configuration, a set of experiments in the relevant temperature and pressure boundaries can be performed to analyze main dependencies and a general applicability. Depending on the experimental set-up and the measurement principle, additional thermal ballast (inert material) can be used to decrease the thermal power density and thereby improve isothermal conditions.

In contrast to these experiments with (almost) ideal boundary conditions, the reactor of any later application is always limited by heat transfer and/or the distribution of the reaction gas. Both influence the reaction since they lead to a deviation between the values given by the application that are available at the reactor boundary and the local values where the reaction actually proceeds. This overlap of heat and mass transfer in combination with the respective rate of reaction of the material is schematically shown in Figure 12 for the exothermic reaction inside a gas-solid reactor and a schematic rate of reaction of the reacting material.

The heat transfer from the reacting solid (heat source marked as black rectangle) to the heat transfer fluid depends on thermophysical parameters, like thermal conductivity of the bulk material in combination with geometrical constraints like e.g. surface area or distance. Regarding the mass transfer, the heat source (black rectangle) actually 'consumes' the gaseous reaction partner and can consequently be seen as sink for the gaseous reactant. The respective mass transfer, in this case from the inlet on top, also depends on thermophysical parameters, mainly permeability of the respective gas through the powder bulk in combination with the distance to the rectangle.

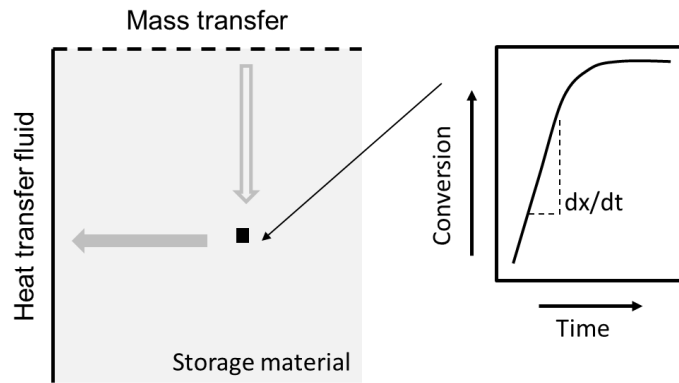


Figure 12: Schematic of transfer processes within the reactor. Shown example: gas-solid reaction (black rectangle) with schematic reaction mechanism (first order, right diagram), gas supply from top (unfilled arrow) and heat release to the left (greyish arrow)

Both transfer processes are driven by a gradient. The heat transfer demands a temperature difference between the reaction temperature (black rectangle) and the heat transfer fluid. Since this temperature gradient directly reduces the useful discharge temperature it has to be minimized. At the same time the mass transfer is driven by a pressure gradient. This gradient affects the required reaction gas pressure that has to be supplied by the process. As described above, the availability of a certain gas pressure is directly linked to the integration strategy of the storage and since it affects in most cases the storage efficiency it has to be minimized as well.

Therefore, the development of a reactor that is optimized with respect to the required thermal power, the required storage capacity, the necessary rate of reaction of the storage material, the required temperature level and the acceptable gradients for the transfer processes, requires excellent knowledge of all involved parameters.

2.3.2. Reactor concepts

In order to optimize thermochemical reactors, the above described correlation between specific rate of reaction, local availability of reaction partner and local temperature need to be addressed. Even though the variety of specific reactor designs is almost infinite, the following section aims to summaries generic concepts that have a direct impact on the operation of a thermochemical system.

Direct and indirect approaches

Comparable to sensible thermal energy storages, the heat transfer for gas-solid reactions can be realized by an internal heat exchanger that is surrounded by the storage material (compare e.g. storages based on concrete [55]) or without internal heat exchanger (compare regenerator type

storages, e.g. [56-58]). In contrast to these non-reacting storages, a direct concept of a thermochemical storage requires not only a direct contact with the heat transfer fluid but also with the gaseous reactant, compare Figure 13.

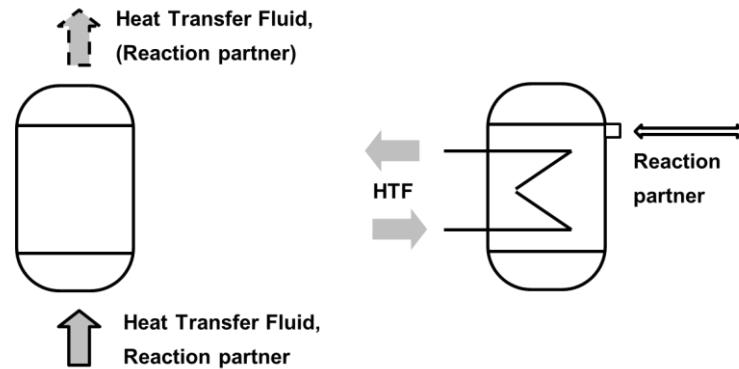


Figure 13: Schematic of direct (left) and indirect (right) concepts for gas-solid reactions. Greyish arrows indicate thermal energy; black outline indicates gaseous reaction partner

The main advantage of a direct concept is the possibility to avoid (or drastically reduce) limitations by heat conduction since the whole reaction material is in direct contact with the heat transfer fluid. Additionally, in case of a fluidization, the conditions for the thermochemical reaction are excellent leading to theoretically very high power densities. However, especially in case of gas-solid reactions, the bulk material is generally a fine powder which consequently leads to pressure drops along the length of the bed or tends to form agglomerates and channels that hinder a homogenous operation of the reactor. Additionally, the direct reactor concept demands either an excess of reaction gas or a gaseous heat transfer fluid that is mixed with the reaction gas. Therefore, a separate adjustment of the reaction gas pressure or high concentrations of reaction gas are difficult to realize. Especially if a surplus of reaction gas is required to serve as heat transfer fluid, the system integration becomes critical, since the reaction gas has to be supplied at the nominal operation pressure of the fluidized bed (e.g. evaporation at elevated temperatures).

On the other side, indirect concepts demand high efforts to support the heat transfer through the bulk of the reaction material. These additional measures can be internal fins, heat transfer matrices or foams to increase the effective thermal conductivity, a pelletizing of the reaction material with heat transporting additives, e.g. expanded natural graphite, or the utilization of a fluidized bed with internal heat exchanger. The main advantage of all indirect concepts is the possibility to separately adjust the reaction gas pressure and e.g. the flow rate of the heat transfer fluid.

The choice of a reactor concept therefore depends on the properties of the storage material, the possibility to modify the material but also to a large extend on the intended application.

Systems with fixed or moved thermochemical material

So far, it was assumed that the storage material remains inside of the reactor and the reactor for the discharging process is identical to the reactor for the charging process. This basic concept is shown in Figure 14 as case (a). The storage material is kept in one reactor that allows for a distribution of the reaction partner as well as for a sufficient heat transfer. In such a reactor, the capacity of the thermal storage is given by its volume and the amount of material that can be filled in. In order to minimize the dependency of the actual power level on the state of charge, the complete reactor volume has to show comparable heat and mass transfer capabilities. Consequently, any increase in capacity scales linearly with the effort for efficient heat transfer. Therefore, this class of reactors with a fixed storage material is reasonable for high power applications with rather small capacities.

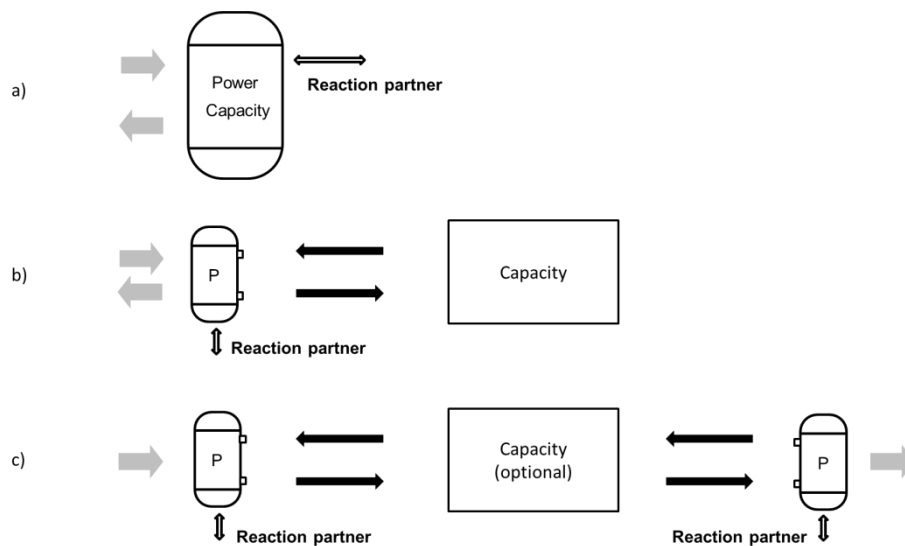


Figure 14: Schematic of thermochemical systems based on fixed (a) or moved solids (b and c): greyish arrows indicate heat fluxes, black arrows indicate mass transport of solid, unfilled arrows indicate connection for reaction partner

In contrast to the reactors based on fixed storage material, case (b) allows the detachment of power level and storage capacity. In this case the storage material has to be moved from the reaction zone to the storage volume and vice versa. The reaction zone is actually equipped with the necessary heat and mass transfer measures in order to reach the required power level of the process. The storage volume (capacity) however, can be a simple container that stores the inactive storage material. So, on one side, this concept allows for low-cost storage solutions if high capacities are required (e.g. long-term or seasonal storage) since the complex reaction part can be reduced to a minimum. On the other side the possibility to move the reaction material is mandatory.

The third case, shown in Figure 14c, is basically an extension of case (b). As soon as the storage material can be moved, it becomes possible to operate two different reaction zones. Consequently,

each reaction zone can be adapted to the respective boundary conditions. This is especially interesting if e.g. the heat transfer fluid of the heat source for charging is different to the heat transfer fluid of the indented heat sink. Case (c) also includes the transport of the material over longer distances. Even though these concepts are at present limited by the transportation efforts (driver, energy consumption, etc.), they could become an interesting alternative to couple heat sources (e.g. waste heat) with nearby heat sinks in the future.

In general it can be concluded that a thermochemical reactor is the crucial component for every thermochemical system. Even though the maximum volumetric and gravimetric energy densities are given by the reaction material, the practically reachable values for thermochemical systems are highly influenced by the reactor itself. As a direct consequence the thermochemical reactor can be seen as a compromise between mandatory aspects for the chemical reaction (local heat and mass transfer), mandatory aspects for the application (e.g. power and temperature level) and aspects that can be or have to be optimized (e.g. energy or power density and cost). Up to know, the basic concepts of thermochemical reactors are derived from analogies with thermophysical storages or heat exchangers based on established manufacturing methods (e.g. tube bundle or plate heat exchangers). However, additive manufacturing could help to design improved specific reactors that are not only optimized for heat exchange vs. energy density (thermophysical storages) or fluid transfer vs. pressure drop (heat exchangers) but take into account that thermochemical systems require all aspects together.

3. Own research and main results

The following chapter summarizes own published research on gas-solid reactions. The literature used for this part can be found in Chapter 6 and is therefore indicated by a different style of citation. As described above, this work is motivated by the idea of transferring specific characteristics of gas-solid reactions on material level to technical systems. Consequently, the first sub-chapter deals with the concept of open thermochemical systems that could offer high energy storage densities on system level since an internal gas handling is not necessary. In the second sub-chapter the distinct equilibrium line of gas-solid reactions described in Figure 7 is utilized to complement the storage option with an intrinsic heat pump effect. And finally, in order to address the discrepancy of long-term storage and economic constraints of technical systems, gas-solid reactions based on abundantly available and cheap materials are investigated. Each sub-chapter starts with a short description of the specific characteristic (that could turn into a unique selling point for the technical system) followed by an extended summary of own results and a brief outlook.

3.1. Utilizing available gases / Open operation

As described in chapter 1, a thermochemical system based on a gas-solid reaction is composed of at least two substances, a gaseous and a solid one. Even though this increases the system complexity in comparison to thermophysical energy storages, the pressure of the gaseous reactant offers one additional degree of freedom for the operation of the thermochemical system (compare Figure 8). One possibility to avoid additional gas handling components is based on an open operation principle. This open operation means that the gas-solid reaction exchanges the gaseous reaction partner, either with the ambient or with the technical system. In this case, some of the thermochemical characteristics (high energy density, lossless storage) could be utilized without the drawback of a rather complex system.

3.1.1. Open to ambient

Gas-solid reactions based on either a sorption process or a chemical reaction using water vapor as gaseous reactant are under investigation and development for seasonal storage since many years [59, 60]. As mentioned in Chapter 2.2.1, in closed systems the heat of evaporation to supply the system with water vapor has to be taken into account. Equation (1) indicates that the heat of reaction (or sorption) depends directly on the associated temperature. For technical systems that are designed for solar thermal collectors at charging temperatures of 100-160 °C, the heat of reaction (or sorption) can be assumed to around 60 kJ/mol – per mol H₂O. Even though this calculation is rather rough, one can conclude that without the possibility to utilize evaporated water (or low grade thermal energy for evaporation, ~ 40 kJ/mol_{H₂O}), the thermal energy released during discharging can

only be around 1/3 of the originally spent thermal energy for charging. However, if water vapor could be taken from the ambient, the full storage capacity of these reaction systems could be used. Consequently, technology development of seasonal energy storage based on a thermochemical process has to focus on very low water vapor pressures ($< 13 \text{ mbar}^6$) in order to be able to integrate low grade thermal energy.

Another substance useable for open gas-solid reactions and available in ambient air is oxygen. In contrast to water vapor, the concentration of oxygen in air is rather high and independent of the temperature. Therefore, we have worked on the identification of suitable reaction systems for open thermochemical energy storage based on the reaction partner oxygen. However, since reversible reactions with oxygen require temperatures above $700 \text{ }^\circ\text{C}$, these systems could only be used for applications operated at very high temperatures, e.g. power generation or high temperature process heat. Cobalt oxide (CoO) is one example that offers excellent thermochemical characteristics, like specific energy density, marginal hysteresis and good cycling stability. Therefore, it is investigated by research groups ranging from material characterization [14, 61, 62] to first prototypes [37, 63, 64].

Even though CoO seems to be an excellent material for open gas-solid reactions, for technical systems its health and environmental issues as well as its availability cannot be neglected. Therefore, we have focused on an alternative material based on Manganese. As pure MnO is not cycle stable, we worked with Mn-Fe-Oxides and could identify the thermodynamic and kinetic properties of $(\text{Mn}_{0.75}\text{Fe}_{0.25})_3\text{O}_4$ in the technical relevant range [65]. Additionally, we realized a lab-scale reaction bed and investigated its performance as open thermochemical energy storage with reactive granules of 1-3 mm particle size in a fixed bed (compare Figure 15).

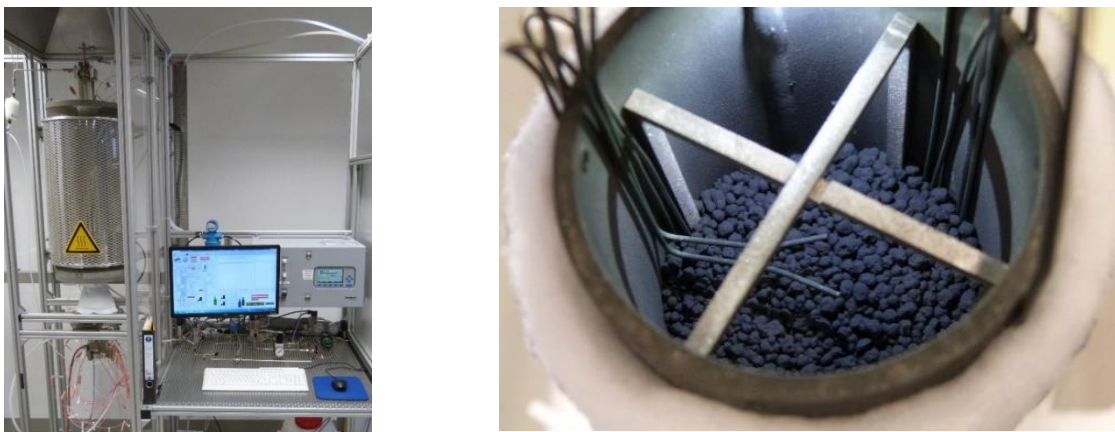


Figure 15: Lab-scale system for open thermochemical energy storage using Oxygen as reactant. Left: Lab-scale test-bench for investigation of gas-solid reaction based on oxygen; right: view into fixed bed reactor containing reactive granules of $(\text{Mn}_{0.75}\text{Fe}_{0.25})_3\text{O}_4$ [Wok_2017].

⁶ Vapor pressure of water at around 10°C

⁷ Different style of citation: a copy of this paper can be found in chapter 6.

Even though the small lab-scale system (ca. 500 g of solid material) was operated above 900 °C (with the associated challenge of thermal losses), it was possible to investigate its performance in detail and demonstrate its general suitability for high temperature thermal energy storage [Wok_2017]. Due to the high operation temperature in combination with a rather large hysteresis ($> 100 \text{ K} @ \sim 900 \text{ °C}$), the thermal charging of a fixed reaction bed with $(\text{Mn}_x\text{Fe}_{1-x})_3\text{O}_4$ in an open thermochemical system is crucial and in most cases the limiting factor. Figure 16 shows a comparison of relevant parameters for several charging (left) and discharging (right) cycles. During thermal charging (Figure 16, left), the chemical reaction proceeds at an almost constant temperature of around 980 °C which is close to the respective equilibrium temperature according to the local partial pressure of oxygen (compare temperature progression in Figure 16, left). Consequently, in order to reach a high heat flux from the heat transfer fluid to the chemically reacting solid, either a very high air temperature at the inlet or a very high mass flow is required (open system and direct reactor concept). Both hinders an efficient operation of this type of storage.

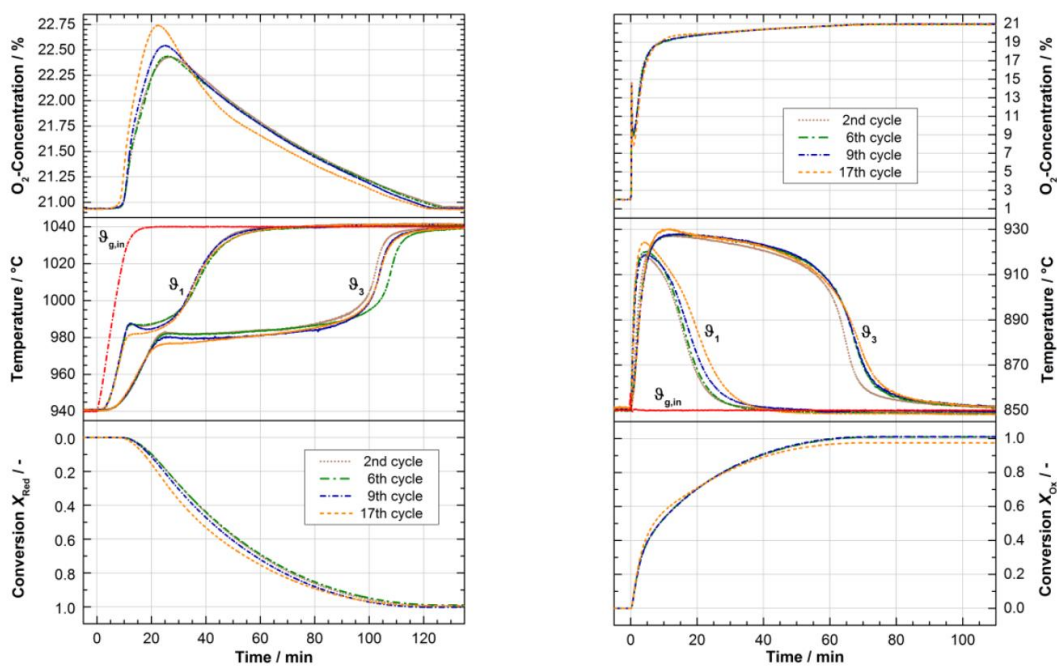


Figure 16: Exemplary results of the measurement campaign with reactive granules of $(\text{Mn}_{0.75}\text{Fe}_{0.25})_3\text{O}_4$; left: charging cycle; right: discharging cycle [Wok_2017]. (Further details can be found in the original publication attached in Chapter 6.)

As a consequence of these results, we currently work on a concept with two different reactors and a movement of the granules (compare Figure 14c), which could be used for CSP plants. In this case the energy for charging of the material is directly delivered from concentrated solar irradiation. The

material is then circulated between the receiver (thermal charging), a storage part and the discharging reactor. Due to the very high temperatures, the system does not only use the chemically stored thermal energy but also the sensible heat which could lead to high energy storage densities. We were able to show that the addition of ZrO to $(\text{Mn}_{0.7}\text{Fe}_{0.3})_2\text{O}_3$ granules drastically improves the material properties for such a system since this addition stabilizes the granules in terms of mechanical stress, agglomeration, thermal shock and cycling [66]. Utilizing these material improvements, we currently work on a lab-scale reactor based on a counter-current heat exchanger between air and reactive particles in order to analyze the temperature distribution, the necessary rate of reaction for different power levels as well as the maximum reachable conversion.

3.1.2. Open to a technical system

Besides the utilization of available reaction gases from the ambient to reduce system complexity, another approach is to utilize process gases (e.g. hydrogen or water vapor) for thermochemical systems (compare Figure 11b). During the last years, we have focused on two different concepts based on the reaction partner hydrogen with two different benefits. The first one addresses the preheating of components in hydrogen systems, e.g. to prevent a cold start of the fuel cell, and is based on interstitial metal hydrides. The second one utilizes the possibility to store hydrogen in a comparably compact system at moderate pressures and temperatures (solid state hydrogen storage).

Preheating of fuel cells

The necessity for preheating of fuel cells depends in general on the type of fuel cell and its nominal operating temperature. For PEM fuel cells degradation and consequently reduced life time can be a severe issue and could result from frost start of fuel cells at very low temperatures. However, as soon as the fuel cell has reached its nominal operating temperature, the fuel cell generates thermal energy that could be partially used for heating purposes but the majority has to be released to ambient as waste heat. This offers the possibility to integrate a thermochemical system based on metal hydrides that stores part of the thermal energy originally wasted during nominal operation. During thermal charging, hydrogen is released which can be immediately consumed by the fuel cell. So, the chemical potential can be stored – without losses – to support the subsequent cold-start. In order to pre-heat the fuel cell, hydrogen has to be delivered to the metal hydride which generates thermal energy and thereby closes the charging/discharging cycle.

As hydrogen is used as reaction partner of a reversible gas-solid reaction, it is not consumed and can be completely converted by the fuel cell. However, as the need for cold start support increases with decreasing ambient temperature, this mandatory request for technical application seems contradictory to Arrhenius' law that describes a tendency of decreasing reaction rates with decreasing temperature. We could show that the utilization of interstitial metal hydrides as reaction

material⁸ offers sufficient high reaction rates at technically relevant boundary conditions down to -20 °C [Koe_2019].

Based on these findings materials, we have developed a proof of concept in the laboratory demonstrating that currently a thermal power of up to 5 kW per kg of metal hydride can be reached and transferred to the heat transfer fluid [Die_2017]. This is only possible if an excellent heat transfer between metal hydride and heat transfer fluid is ensured which demands a sophisticated reactor design. As continuation of these results on material level, new design possibilities based on additive manufacturing technology might lead to further enhanced reactor designs especially regarding the internal distribution of reaction gas and thermal energy.

Hydrogen storage

The thermochemical storage of hydrogen offers – in principle – a compact and safe possibility to store hydrogen at moderate pressures and temperatures. However, according to Figure 1 and Figure 2, the chemical storage of hydrogen in a thermochemical system is always related to an exchange of thermal energy. Due to the associated heat of reaction, a release of hydrogen is only possible if the required thermal energy is supplied with sufficient heat flux and at the required temperature.

In case of interstitial metal hydrides operating close to ambient temperature, the thermal energy is in principle available from ambient. But in order to transfer the thermal energy efficiently to the reacting material, specific reactor concepts are necessary that offer sufficient hydrogen release, also at low state of charge. We developed a scalable hydrogen storage module based on an interstitial metal hydride that ensures excellent heat transfer due to the utilization of pellets with enhanced thermal conductivity (compare Figure 17 [Bue_2017]). This module does not require a thermal integration but can be operated in air at room temperature supported by small ventilators in the back. This is possible since the thermodynamic properties of the metal hydride fit to the respective boundary conditions and – at least equally important - the distribution of thermal energy inside the reactor is enhanced by means of graphite containing pellets. The respective pellets were developed together with the institute IFAM (Fraunhofer-Gesellschaft) and tested for more than 1000 cycles in a specifically designed and fully automated test rig [67].

Figure 18 gives exemplary measurement results for cycle 1 and 38. We could show that this design is scalable and can be charged and discharged with nominal hydrogen flow to an overall conversion of around 90 %.

⁸ Chemisorption as exemption of gas-solid reactions: Very fast conversion rates at low temperatures but – depending on the composition – a thermodynamic characteristic can be comparable to a chemical reaction (distinct correlation between gas pressure and reaction temperature) or to adsorption processes (reaction temperature depends additionally on state of charge)

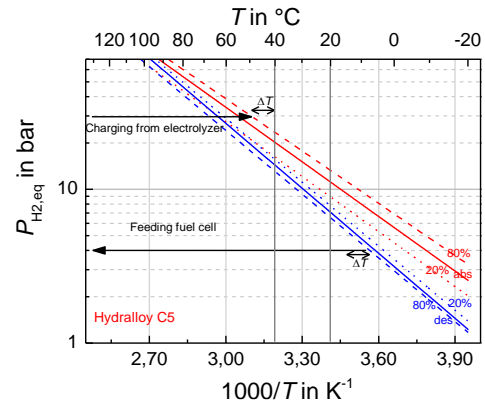


Figure 17: Solid state hydrogen storage with simplified thermal integration; left: Thermochemical reactor for hydrogen storage based on interstitial metal hydrides. Right: Due to specific material properties in combination with excellent heat transfer, ambient can be used as heat source and sink [Bue_2017]

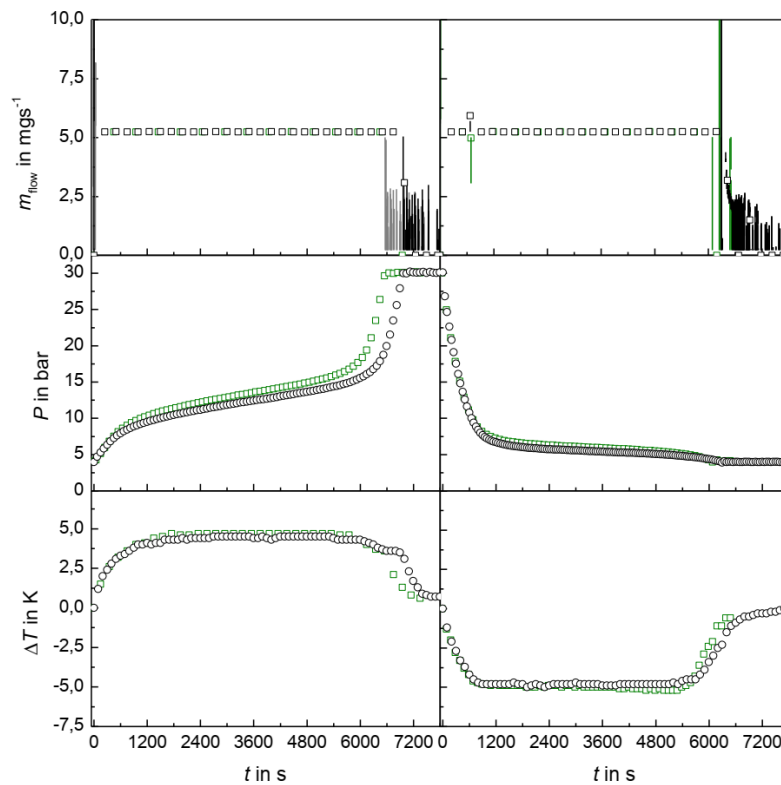


Figure 18: Mass flow rate (top), pressure (middle) and temperature difference (bottom) versus time for absorption (left) and desorption (right); Olive squares: 1st experiment, black circles: 38th experiment [Bue_2017]. (Further details can be found in the original publication attached in Chapter 6.)

One drawback of thermochemical hydrogen storage in technical systems is related to the mass (and volume) of the storage material. Interstitial metal hydrides reach storage capacities of less than 2 wt.-%. According to the current state of knowledge, the storage capacity of hydrogen storing materials seems to increase with increasing equilibrium temperature (compare e.g. [49]). So, on one side a high reaction temperature could be favorable for light-weight and compact storages. On the other side, the supply of thermal energy for discharging becomes difficult. Whereas for interstitial metal hydrides operating at ambient temperature the temperature level of waste heat of a PEM fuel cell is sufficiently high, at present, complex metal hydrides require higher temperatures. Therefore, we worked on ‘combination reactors’ with the idea of combining two thermochemical reactions in order to minimize technical drawbacks and limitations.

Especially for automotive systems, the application requirements differ with the driving cycle. After the critical cold start, sufficient thermal energy is available for discharging the solid state hydrogen storage. For HT-PEM fuel cells, operating at around 160-180 °C, we have demonstrated that a thermal coupling with a complex hydride (NaAlH₄) is possible [68]. However, even though, the complex hydride NaAlH₄ and a HT-PEM fuel cell can be thermally coupled, the storage material does not react at room temperature. Consequently, in order to be able to charge the thermochemical storage with hydrogen, a certain minimum temperature is required to initiate the exothermal chemical reaction. From this point on the generated thermal energy has to be released to the ambient. For this purpose, we developed an innovative storage module consisting of an interstitial and a complex metal hydride [Bue_2014a, Bue_2014_b]⁹. Its principle design is based on a tubular reactor concept with an internal gas permeable layer that forms an inner and outer part for the two different solids (compare Figure 19).

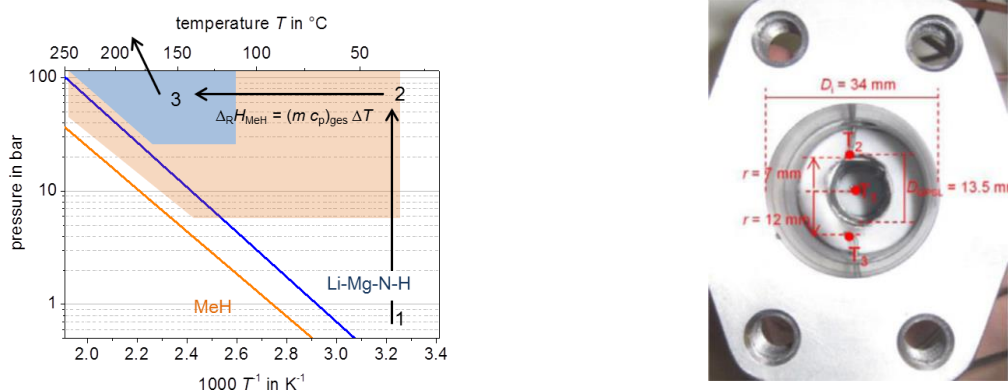


Figure 19: Combination reactor for hydrogen storage with internal preheater; left: schematic preheating process (orange area: high reactivity of metal hydride, blue area: high reactivity of complex hydride); right: picture of lab-scale reactor for model validation [Bue_2014a]. (Further details can be found in the original publication attached in Chapter 6.)

⁹ The material used in this case: 2 LiNH₂ – 1.1.MgH₂ – 0.1LiBH₄ – 3 wt.-% ZrCoH₃, supplied by KIT, Karlsruhe

Comparable to the above described preheating concept, for the inner part of the hydrogen store a specific interstitial metal hydride was chosen that releases its heat of reaction at a suitable temperature in order to preheat the surrounding complex hydride (Figure 19, left: Transition from point 1 to point 3) until a sufficiently high temperature is reached (point 3). From this point on the exothermic reaction of the complex hydride (outer part) proceeds and has to be cooled (tube wall) in order to reach maximum conversion. The effect of this internal preheater is shown in Figure 20: whereas the initiation of the charging reaction without metal hydride (left) takes around 10 min, the charging with metal hydride starts almost immediately (right). The simulation is based on an intensive study of specific material properties [Bue_2014c] and was used for the technical up-scaling. Starting from the proof of concept shown in Figure 19, this system has been realized within a European project¹⁰ in 1 kW scale (2 kWh), thermally coupled to a HT-PEM and operated in an IVECO Daily as auxiliary power unit (APU) [69].

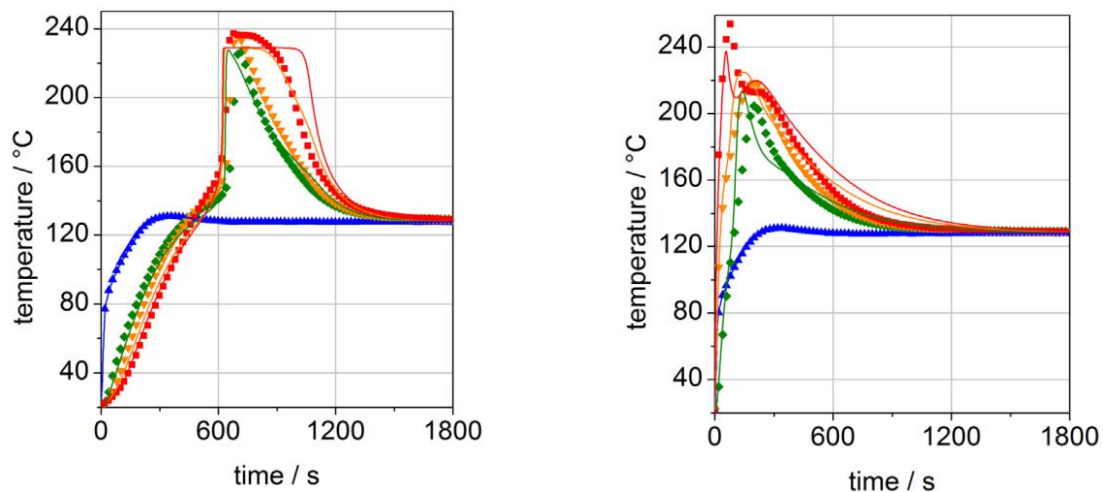


Figure 20: Exemplary results of combination reactor; left: Experiment without internal metal hydride. Experimental (symbols) and simulated (lines) temperature profiles; right: Experiment with internal metal hydride working as preheater [Bue_2014a]. (Further details can be found in the original publication attached in Chapter 6.)

This work shows that not all of the technical requirements have to be met on material level (in this case: slow reaction rates for charging and discharging at low temperatures), but that a proper integration and reactor design still could lead to technically relevant systems. Based on this first concept and the validated model, we worked on an optimum configuration including enhancement of thermal conductivity and internal heat exchangers [Bho_2015]. Even though the interstitial metal hydride also supports the dynamics of the hydrogen release [Bue_2015], as long as the thermal

¹⁰ SSH2S: Fuel Cell Coupled Solid State Hydrogen Storage Tank (Grant agreement no. 256653)

energy for hydrogen release has to be delivered by the connected fuel cell, the choice of solid hydrogen storage materials remains limited by thermodynamics [70].

In order to overcome this issue we started to work on a combination of a hydrogen storing material with a thermal energy storage material [Bho_2016]. In this case, the thermal energy released during the exothermic hydrogen uptake is transferred to an integrated thermochemical energy storage and stored by the endothermic dissociation, in our example dehydration of $\text{Mg}(\text{OH})_2$. The basic operation principle of such an adiabatic reactor is shown in Figure 21.

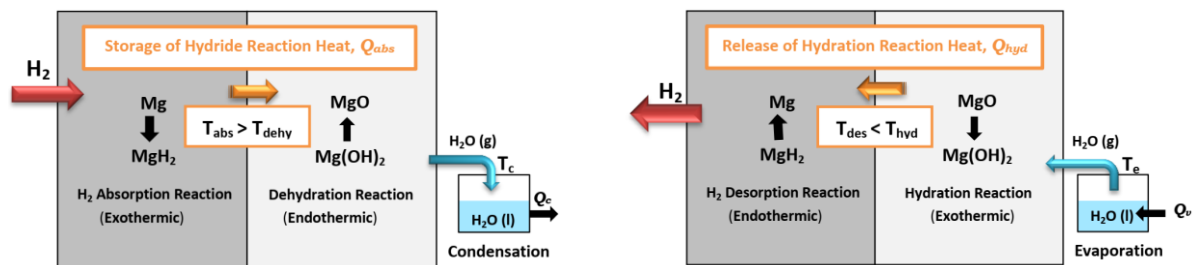


Figure 21: Schematic principle of adiabatic solid state hydrogen storage; left: Absorption of H_2 /Dehydration/Condensation; right: Desorption of H_2 /Hydration /Evaporation [Bho_2016]. (Further details and explanations can be found in the original publication attached in Chapter 6.)

This concept seems possible since both gas-solid reactions proceed at constant temperature (compare Figure 7). For the release of hydrogen, the required thermal energy at the required high temperature level can be delivered by the thermochemical energy storage. The thermal energy for evaporation of water could be taken from the exhaust of the fuel cell since the required temperature level for evaporation is low. We could show that this combination could offer high storage densities [71], especially favorable for e.g. long distance hauls or trains. Additionally, it might be interesting since abundantly available materials, e.g. Mg, could be used as reactants on both sides. Its technical realization as proof-of-principle in lab-scale is currently ongoing.

3.2. Utilizing pressure dependency / Thermal upgrade

The correlation of gas pressure and reaction (or sorption) temperature offers unique application possibilities. One approach of thermally driven compression that has been already commercialized is based on an adsorption process, e.g. of water vapor. Comparable to conventional compression heat

pumps, the useful effect is generated on the side of the physical phase change (evaporation/condensation) but the pressure difference is, in contrast to conventional mechanical compression, maintained by two alternating sorption processes. In this system, thermal energy at a certain temperature is used as input to desorb water vapor at a certain pressure - at the same time, a second reactor is cooled to ambient to absorb water vapor at a low pressure. Due to the dependency on the state of charge (compare Figure 6), the temperature of the sorption process cannot be constant if a certain gas pressure has to be maintained.

For gas-solid reaction this behavior is different: the distinct correlation between gas pressure and corresponding temperature – in principle independent of the state of conversion - offers an additional application possibility. Since the temperature of the reaction can be constant for the whole conversion, also the reaction side can be used to generate a useful thermal effect. Using coupled reactors with two different interstitial metal hydrides, thermally driven heat pumps, cooling systems or heat transformers have been realized. An overview of the technological development with interstitial metal hydrides can be found e.g. in [51]. Besides metal hydrides, also salts reacting with ammonia were used [52, 53]. However, the drawback of these systems is that for a continuous operation four reactors are required. Especially if the required piping is taken into account, the system's periphery becomes complex (valves and pumps) which - up to know - hinders a technical application.

Based on these considerations on the state of the art, we addressed two main approaches: The first one is based on the idea of utilizing an existing pressure difference of a gas stream in order to drive a heat pump effect (open system). The second one is based on the concept of adsorption heat pumps (coupling of reactor and evaporator/condenser) but uses the water side for thermally driven compression and the reaction side as useful thermal effect (closed system).

3.2.1. Open system to utilize existing pressure difference

In order to reach a sufficiently high energy density of the gaseous energy carrier hydrogen, it has to be compressed, up to 350 or 700 bar depending on the application. However, the compression work necessary to reach these pressures accounts for around 15 % of the energy content of the compressed hydrogen (referred to the lower heating value) [72]. As long as the hydrogen pressure is conventionally throttled down to the required supply pressure for the fuel cell the originally spent compression work is wasted. Consequently, by substituting the conventional throttle by a system that generates effective energy for onboard utilization not only the efficiency of the overall system would be increased. As a direct consequence also the onboard available energy for traction could be increased leading to longer driving ranges.

Following the considerations above, we developed a thermochemical system based on interstitial metal hydrides that utilizes this onboard available pressure difference to generate a temperature difference [73]. Consequently, as soon as hydrogen is consumed by the fuel cell (hydrogen mass flow), this system operates as heat pump for an associated heat flux that can support either the

cabin heating or its cooling. Figure 22 shows the basic idea of such a system operated at temperatures above ambient during hydrogen uptake from the tank and at a lower temperature for cooling purposes during hydrogen release to the fuel cell. For a continuous operation, two alternating reactors are necessary (analog to commercial pressure swing adsorption).

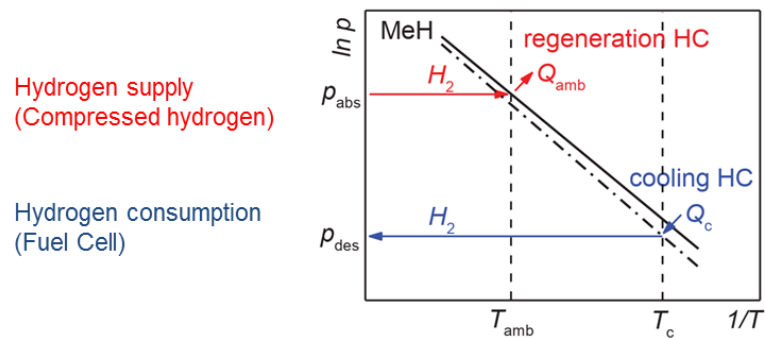


Figure 22: Schematic of an open thermochemical system to utilize the onboard available pressure difference of hydrogen, adapted from [Wec_2017]; HC = half cycle, MeH = metal hydride

In contrast to thermochemical energy storage, the main specific value to characterize this conversion system is its weight (or mass) specific thermal power. Consequently, the rather low storage capacity of interstitial metal hydrides can be compensated by their generally very fast reaction rates – if the reaction bed allows for fast conversion. Therefore, we developed and investigated a reactor design based on commercially available plate heat exchangers with excellent thermal contact between the reactive metal hydride bulk and a heat transfer fluid [Wec_2017]. The reactor and one exemplary result for its reaction dynamics is shown in Figure 23.

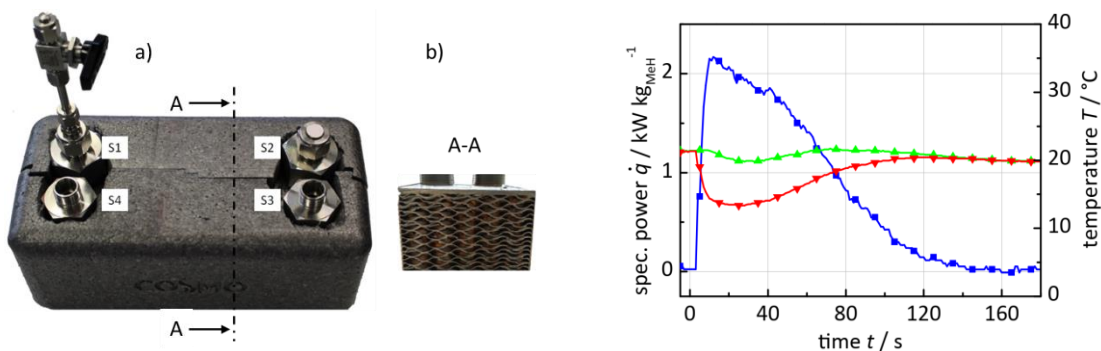


Figure 23: Plate reactor for open metal hydride cooling system; left: principle design based on modified plate heat exchanger; right: results of the reference experiment for endothermic desorption [Wec_2017]. (Further details can be found in the original publication attached in Chapter 6.)

Based on the plate reactor design, a complete conversion is possible within 120 s. Even if this value depends highly on the applied temperature condition, the respective process (ab- or desorption) and the intended conversion, we could show that for relevant operating conditions, an average specific power density of more than 1 kW per kg of metal hydride can be reached. Obviously, as indicated in Figure 22, a continuously operated system consists of two identical reactors that are alternately either connected to the hydrogen tank or to the fuel cell. So, according to Figure 23, right, the half-cycle time could be theoretically reduced to 60 s (or less) in order to increase the weight specific performance. However, since the whole reactor, including active metal hydride and passive reactor mass, has to change its temperature between every half-cycle, an incomplete conversion reduces the efficiency of the system. Consequently, any optimization of the reactor has to find a trade-off between the passive mass of the reactor (which is almost proportional to the heat exchanging surface) and the specific thermal power that can be reached at nominal operation conditions. In any case, due to thermodynamic limitations (compare Equation (1)), the thermal power that can be generated by the open thermochemical system is in the range of around 20 % of the electric power that is generated by the fuel cell. Consequently, such systems would have to be combined with additional measures to increase the efficiency of onboard thermal management.

An integrated system has to fulfill two mandatory boundaries: (1) the required supply pressure of the fuel cell has to be ensured and (2) at the same time the required cooling temperature has to be reached. Based on these considerations we are currently connecting a 2 kW_{th} module to a fuel cell system (including pressure tank) in order to investigate the performance of a coupled system in laboratory under realistic boundary conditions. One approach is to develop an integrated system that delivers electrical energy, hot thermal energy (fuel cell) as well as cold thermal energy from the open thermochemical system. This APU (auxiliary power unit) could be used as additional emission-free energy source for future e-mobility since it is able to deliver all relevant energy fluxes onboard including heat and cold for thermal comfort.

3.2.2. Closed system for waste heat utilization

Thermal energy that cannot be used is generally considered as waste heat (or wasted thermal energy). The generic reasons that lead to this waste of thermal energy are either related to time or to the quality of the thermal energy (temperature level). Whereas thermophysical energy storages can address the time dependency, a heat pump is required to increase the temperature of the heat flux. According to Figure 8, gas-solid reactions can address both issues in one system. In this case, a waste heat flux, e.g. a hot gas stream, is used to charge the thermochemical system. Due to the constant temperature of dehydration, the hot gas leaves the reactor at a temperature close to the reaction temperature. Consequently, the temperature of the gas stream is still high enough to be used in an evaporator connected in series to the reactor. Due to the cascading concept, thermal energy is available for charging of the gas-solid reaction and to supply the reaction partner at an elevated pressure. We have demonstrated this operation principle of a heat transformer based on CaCl₂ as

batch in 1 kW laboratory scale. The schematic flow sheet and the test bench without insulation are shown in Figure 24 [Ric_2016].

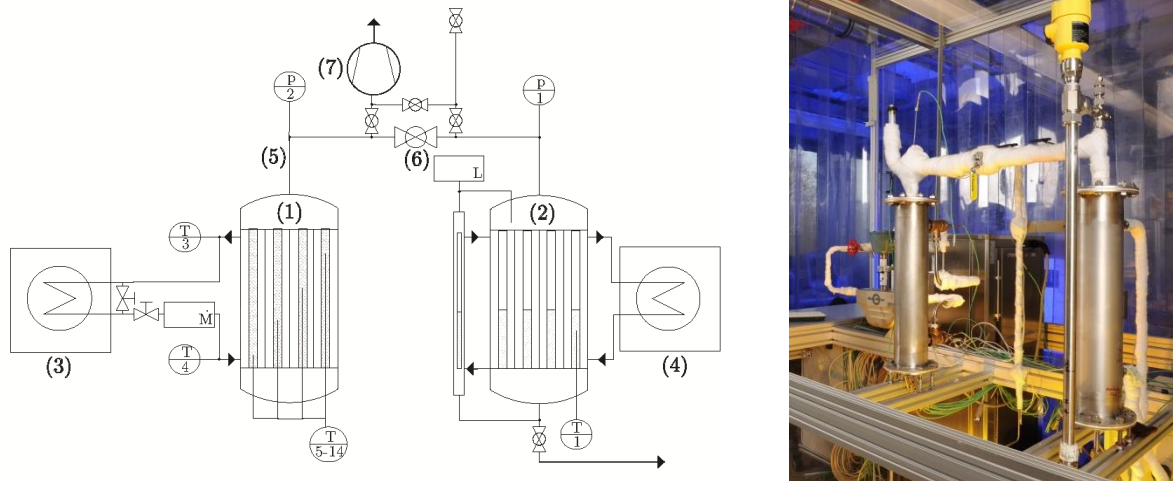


Figure 24: Thermochemical heat transformation; left: schematic of a closed heat transformer with evaporation/condensation [Ric_2016]; main components: (1) Reactor, (2) Evaporator/Condenser (Further instrumentation details can be found in in the original publication attached in Chapter 6.); right: the test bench without insulation of tube bundle heat exchanger/reactor

We could show that this operation principle based on salt hydrates is feasible and that depending on the design of the reactor, either thermal energy storage with integrated thermal upgrade (discontinuous operation) or a continuous operation (2 alternating couples) is possible. Besides the operation as closed system (compare Figure 24), we also developed an open operation that is based on the idea of utilizing waste steam [Bou_2016]. Depending on the integration, the reaction material CaCl_2 can be operated between $100\text{ }^\circ\text{C}$ and $180\text{ }^\circ\text{C}$ and is therefore in principle suitable for the temperature range most interesting for industrial waste heat. However, due to a three step reaction within this temperature range, either the temperature lift or the amount of conversion per cycle is limited [74]. This effect is shown in Figure 25 for both reactions. Especially during discharging (bottom), the three reaction steps (HI-HIII) can be clearly identified. An additional challenge we've identified in this work is related to the low permeability of the powder bulk that especially at low pressures (during charging) leads to significant pressure drops. Consequently, only short distances for mass transfer of the reaction partner can be allowed.

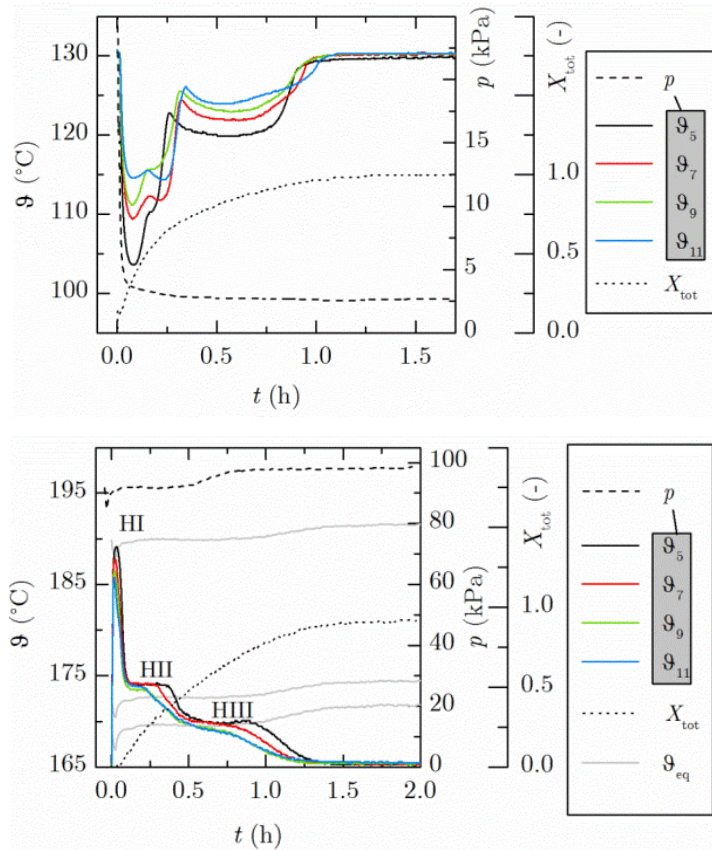


Figure 25: Exemplary results of heat transformation based on CaCl_2 ; top: Dehydration reaction of calcium chloride dihydrate at 130 °C with fixed gas channels; bottom: Hydration of calcium chloride at a temperature of 165 °C and a vapor pressure of 100 kPa [Ric_2016]. (Further details can be found in the original publication attached in Chapter 6.)

As shown in Figure 8, the described system configuration can be adapted to different materials that react with water vapor in order to meet certain application boundaries. We have performed an extensive screening of potentially available materials and have identified SrBr_2 as interesting reaction system for a slightly higher temperature range (150 °C – 250 °C) [Ric_2018]. In contrast to CaCl_2 , it possesses only one reaction step in the relevant temperature/pressure range. So, a complete conversion could be combined with a maximum temperature lift.

Ongoing material characterization is aimed to identify the apparent reaction rate of the reaction system at technical relevant boundary conditions and the investigation of the changes in bulk structure after continuous cycling. Besides material aspects, we currently work on a realization of a scalable reactor concept. This concept is adapted from thermophysical energy storage based on phase change materials (PCM) [75]. The main idea is to use extruded aluminum fins in order to enhance the heat transfer from the reaction bulk to the heat transfer fluid. Additionally, for gas-solid reactions, this finned tube is contained inside a filter material in order to prevent a discharge of reaction material. Based on these tubes a tube bundle reactor can be realized with gas distribution on the shell side for minimal gas transfer resistance.

3.3.Utilizing abundantly available materials / Storage capacity at low cost

In general a technical unit to characterize the capacity of a storage material is either specific in terms of weight or volume [e.g. kWh/m³ or Wh/g etc.]. As long as comparable boundary conditions (e.g. applied temperature, realistic porosity, etc.) are applied, this specific value can be used for a direct comparison between different materials. However, since in any case of a material related storage application (such as gas-solid reaction) the amount of stored energy scales linearly with the necessary mass of storage material, its availability, its cost as well as its environmental footprint are important parameters and have to be taken into account. Consequently, naturally available materials or materials currently treated as waste materials could offer interesting combined advantages, e.g. high storage capacity at low material cost. This chapter summarizes our work on the potential utilization of such materials for energy storage and currently identified limitations.

Some of our work was dedicated to analyze waste materials for a potential utilization in thermochemical systems. Whereas CaCl₂ is a byproduct of the production of sodium carbonate (Solvay process), potassium carnallite (KCl·MgCl₂) is one of the byproducts of inorganic mining. Both materials can be theoretically applied for thermochemical systems using water vapor as gaseous reactant. However, in case of potassium carnallite, the reaction process is complex and leads to a drastic degradation (decomposition) at temperatures above 150 °C. We could show that the decomposition can be clearly reduced at temperatures below 150 °C but so far the degradation mechanisms are not fully understood and consequently the material cannot be seen as cycle stable [Gut_2018]. CaCl₂ in contrast shows an excellent chemical reversibility in the applied temperature and pressure range [74]. The material was therefore chosen for the investigation of thermal upgrade driven by waste heat (compare Figure 25). However, due to the subsequent reaction steps during hydration and dehydration its applicability for thermal upgrade is reduced.

Even though its raw material cannot be seen as waste, in terms of availability and cost limestone (CaCO₃) and quick lime (CaO) are probably the most interesting materials. Consequently, experimental investigations in the context of thermal energy storage were already published in 1979 by Rosemary et al. [76]. Quick lime could be applied in thermochemical systems using CO₂ (forming CaCO₃) or using water vapor (forming Ca(OH)₂) as gaseous reactants. Our work focusses on the latter one due to the possibility to condense the reaction partner at moderate pressures in combination with a slightly lower reaction temperature of around 500 °C. Commercially available Ca(OH)₂ is generally a fine powder which tends to agglomerate during cycling. As a results, the bulk properties of unmodified Ca(OH)₂ are not stable over reaction cycles. Therefore, a crucial challenge for the technical utilization of Ca(OH)₂ is related to the changing bulk structure leading to two potential approaches: either the material has to be modified in order to stabilize its bulk structure or the reactor has to be able to handle changing bulk properties.

Following the first approach, we have investigated the addition of nanostructured additives in order to stabilize the particle size and prevent agglomeration [77]. These additives are generally used as flow aids to handle powder in pharmaceutical and food technology. We could show that by the addition of nanostructured SiO_2 the agglomeration tendency was clearly reduced [78]. Even if the SiO_2 is not stable with CaO and forms calcium silicate phases, these new compounds seem to serve as inhibitor for agglomeration and can therefore help to stabilize the bulk in its original fine grained form. Besides the approach of stabilizing the particle size, we currently also address the encapsulation of the material by gas-permeable clay.

Following the second approach we've developed an indirect reactor concept in 10 kW scale and brought it into operation to investigate and understand a technical scale storage based on $\text{Ca}(\text{OH})_2$ [79]. Due to the low thermal conductivity of the bulk (ca. 0.1 W/mK), the reactor design was based on a plate heat exchanger concept leaving a 20 mm distance for the reactive bulks (compare Figure 26, middle and right).



Figure 26: Plate heat exchanger for thermochemical energy storage based on $\text{Ca}(\text{OH})_2$ in 10 kW scale; left: integration and instrumentation with opened lid; middle: material as supplied [79]; right: material after 10 cycles [78]

As shown in Figure 26, left, water vapor could enter and leave from a connection in the lid and was distributed through a channel on top of the reaction bed. The reactor was connected to a condensing/evaporating unit and was heated/cooled by hot air (inside the plates, connection see Figure 26, left). Even though the material structure clearly changed (compare Figure 26, middle and right), the dynamics of the reactor was not affected with cycles. This can be explained as long as the reaction progress is dominated by heat transfer. Even if in this case the gas distribution is not homogenous inside the bulk, it is sufficient all over the bulk to transfer the required reaction partner. That might change with increasing power level (due to the associated higher demand of reactant).

The theoretical operation temperature of this material is in the range of 400 to 600 °C (and above, depending on the applied gas pressure). So, in principle the temperature is high enough to drive a steam cycle for power generation. As described above (compare Figure 10, c), an integration of the gaseous reactant is mandatory in order to realize a thermochemical system. In case of $\text{Ca}(\text{OH})_2$, the heat of reaction is around 105 kJ/mol, whereas the required thermal energy for evaporation of water is around 40 kJ/mol. Consequently, if the evaporation energy has to be delivered by the heat of reaction, the overall energetic efficiency of the thermochemical storage cannot exceed around 60 %. However, if the thermal energy for evaporation of water is supplied at 45 °C (0.1 bar water vapor pressures) the thermochemical reaction releases thermal energy at around 450 °C. Therefore, for power generation, the different temperature levels have to be taken into account and a purely energetic balance is misleading (compare Figure 10, c).

In order to understand the operational window of such thermochemical storages for power generation, we developed a second but smaller indirect reactor [Sch_2017a]. The main idea was to exclude – as far as possible - any limitation due the heat and mass transport but still operate it as technical system in the relevant temperature and pressure range. For this purpose the reactor was designed with large filter areas and consequently short penetration distances for water vapor. Additionally, this reactor was installed into a pressure vessel in order to allow for an investigation of the reaction in technical scale at high (up to 6 bar) as well as low pressures (less than 0.1 bar). A picture and a schematic drawing including instrumentation plan is shown in Figure 27.

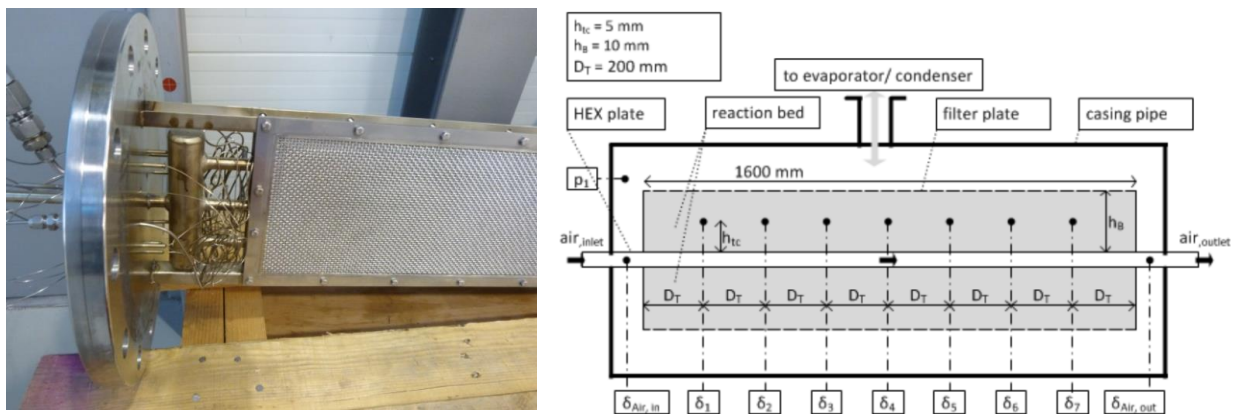


Figure 27: Closed reactor concept to investigate the operational window of $\text{Ca}(\text{OH})_2$; left: reaction bed with large filter surface; right: schematic drawing of the reactor including instrumentation [Sch_2017a]. (Further details can be found in the original publication attached in Chapter 6.)

Based on a series of experiments with this reactor varying temperature and pressure conditions, we were able to draw an operational window for unmodified quick lime (CaO) reacting with water vapor

at technically relevant time scales, technically reasonable pressures and corresponding temperatures. Two exemplary experimental results of these experiments are shown in Figure 28.

Whereas the discharging reaction reaches its theoretical equilibrium of 600 °C at the given pressure (Figure 28, right), a clear distance between the theoretical equilibrium and the temperature plateau during charging occurs (Figure 28, left). As a consequence, for the operation of such a thermochemical system not only the necessary temperature gradient for transport of thermal energy has to be taken into account but also the required distance from the equilibrium temperature. The second one seems to be an effect related to the reaction rate of the material that is especially relevant at pressures below 50 kPa.

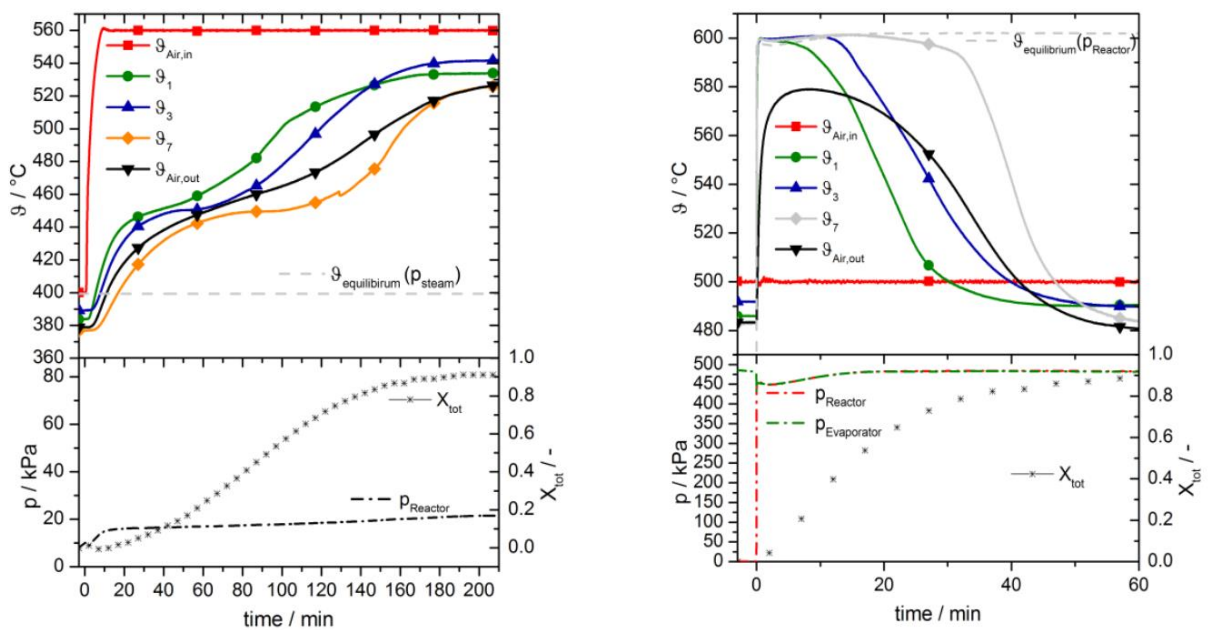


Figure 28: Exemplary experimental results of CaO reacting with water vapor at different boundary conditions; left: charging process (Dehydration experiment at 10 kPa and an air inlet temperature of 560 °C [Sch_2017a]; right: discharging process (Hydration experiment at 470 kPa and a starting temperature of 500 °C) [Sch_2017b]. (Further details can be found in the original publication attached in Chapter 6.)

As according to Figure 10c, gas-solid reactions can be used between an endothermic and exothermic process, we studied the combination of a thermochemical energy storage based on quick lime in combination with a Clausius-Rankine Cycle for power generation. We could show that an integration concept is possible that utilizes low pressure steam of the power block to drive the exothermic reaction. In this case, the thermochemical storage process reaches up to 87 % efficiency – without integrating the heat of condensation of water vapor during charging [Sch_2017b]. However, the

study also showed that an integration strategy leading to an efficient operation for power generation is technically complex.

Based on our research, we can conclude that hydration of quick lime offers high storage capacity at very low material cost. The reaction is fast and does not degrade with continuous cycling. As long as the reaction partners are separated and not exposed to CO_2 , the thermal energy is stored as chemical potential without time dependent losses. So, in general this gas-solid reaction offers the potential of cost efficient long-term storage, e.g. in order to address seasonal fluctuations.

Therefore we currently work on technical solutions for thermochemical energy storage based on quick lime to separate the complex and costly heat exchanger (reactor) from the simple storage (container), compare Figure 14. Especially in the context of an energy system that will be primarily based on renewable electricity, the dehydration of $\text{Ca}(\text{OH})_2$ could transfer surplus electricity, e.g. during summer, into winter periods for renewable heating. In contrast to reaction systems operated at lower temperature (resulting in lower heat of reaction, compare Equation (1)), also liquid water could be used as reactant for the discharging process which makes this thermochemical system independent of ambient condition (humidity and/or temperature). However, any detachment of power and storage capacity requires a movement of the reactive particles, so controlling or handling of changing bulk structures of quick lime during reaction remain the dominating challenges for this technology.

4. Summary and conclusion

The ongoing transition of our energy system from bankable but finite to fluctuating but renewable energy sources is challenging and leaves space – and need – for new, innovative storage technologies. This is especially relevant with increasing share of renewable energy supply and if besides electricity also thermal energy consumption and mobility are taken into account. In this context the utilization of gas-solid reactions offers various application possibilities for energy storage and conversion. However, as outlined in the first part of this work, thermochemical energy storage and specifically gas-solid reactions are also characterized by a complex and demanding reactor geometry as well as the need for proper system integration. Since the state of the art of gas-solid reactions is mainly based on principle material research and theoretical system description and analyses, we focused our work on the transition of specific material properties to lab-scale systems in order to better understand if and to what extent unique features of reversible gas-solid reactions could contribute to a future energy system.

Consequently, based on a generic analysis of the three dominating aspects for technical systems-reaction process, system integration and reactor design – we have derived following three approaches that offer the possibility to use specific properties of gas-solid reactions in technical applications for energy storage or conversion.

- 1) In order to minimize the complexity of the thermochemical system, especially the supply of gaseous reactant, open gas-solid reactions have been addressed. These systems could either utilize available reaction gases from air or any other available reaction gas in a technical system, e.g. hydrogen in fuel cell driven cars.
- 2) The distinct correlation of gas pressure and reaction temperature allows for an integrated heat pump effect. This additional effect was utilized in open systems to transfer an available pressure difference into a temperature difference or by means of thermal compression in closed systems. In both cases, it has been shown that the underlying principle can either be used for discontinuous thermal energy storage or for continuous systems, e.g. for thermal upgrade.
- 3) Some materials that can be used for thermochemical energy storage are abundantly available, e.g. CaO, or are even treated as waste materials (e.g. Carnallite or CaCl₂). This could lead to attractive synergies of specific properties, e.g. lossless energy storage in combination with low material cost. Especially the reaction system CaO with water vapor seems therefore be very promising for long-term decoupling of renewable energy supply and actual demand.

The main challenges and current technological obstacles that can be derived from our recent work are related to the intrinsic characteristic of the reversible gas-solid reactions themselves. Especially the structural changes of the primary particles related to the chemical phase transition during reaction propagate with cycles towards larger scales and end up in currently non-predictable anisotropic bulk properties. Whereas the impact of the transfer of the gaseous reactant through the

reaction bed depends highly on the used gases and pressure conditions, the thermal conductivity of the reacting bulk is generally low and in most of the cases determines the reachable power level. Depending on the intended application in combination with the related reactor design and chosen material, these structural changes during cycling can either be acceptable, could hinder a technological application or can even improve the performance of the thermochemical system – in any case, at present they cannot be controlled or predicted.

As a conclusion, future research and development aspects for reversible gas-solid reactions are on one side related to reactor designs that are adapted to the technical process and at the same time capable of handling the reactive bulks. In this context, the increased design flexibility offered by additive manufacturing processes might open new possibilities. Besides that, a better understanding of the fundamental and intrinsic mechanisms related to the structural changes of reactive bulks is equally important since it could lead to strategies to control or even adapt the reacting solid material. Combining both aspects, the transfer of promising material properties to technical systems could lead to new applications in the context of energy storage and conversion - of which some first steps might be discussed in this work.

5. References

- [1] Aydin, D., S.P. Casey, and S. Riffat: *The latest advancements on thermochemical heat storage systems*. *Renewable and Sustainable Energy Reviews*, 2015, 41: 356-367. DOI: <https://doi.org/10.1016/j.rser.2014.08.054>.
- [2] Carrillo, A.J., J. González-Aguilar, M. Romero, and J.M. Coronado: *Solar Energy on Demand: A Review on High Temperature Thermochemical Heat Storage Systems and Materials*. *Chemical Reviews*, 2019, 119(7): 4777-4816. DOI: <https://doi.org/10.1021/acs.chemrev.8b00315>.
- [3] Pardo, P., A. Deydier, Z. Anxionnaz-Minvielle, S. Rougé, M. Cabassud, and P. Cognet: *A review on high temperature thermochemical heat energy storage*. *Renewable and Sustainable Energy Reviews*, 2014, 32: 591-610. DOI: <https://doi.org/10.1016/j.rser.2013.12.014>.
- [4] Prieto, C., P. Cooper, A.I. Fernández, and L.F. Cabeza: *Review of technology: Thermochemical energy storage for concentrated solar power plants*. *Renewable and Sustainable Energy Reviews*, 2016, 60: 909-929. DOI: <https://doi.org/10.1016/j.rser.2015.12.364>.
- [5] Solé, A., I. Martorell, and L.F. Cabeza: *State of the art on gas–solid thermochemical energy storage systems and reactors for building applications*. *Renewable and Sustainable Energy Reviews*, 2015, 47: 386-398. DOI: <https://doi.org/10.1016/j.rser.2015.03.077>.
- [6] *Energy Consumption in Germany in 2017*. Working Group on Energy Balances (Energy Balances Group), Last Update: February 2018: www.ag-energiebilanzen.de.
- [7] Donkers, P.A.J., L.C. Sögütoglu, H.P. Huinink, H.R. Fischer, and O.C.G. Adan: *A review of salt hydrates for seasonal heat storage in domestic applications*. *Applied Energy*, 2017, 199: 45-68. DOI: <https://doi.org/10.1016/j.apenergy.2017.04.080>.
- [8] Deutsch, M., D. Müller, C. Aumeyr, C. Jordan, C. Gierl-Mayer, P. Weinberger, F. Winter, and A. Werner: *Systematic search algorithm for potential thermochemical energy storage systems*. *Applied Energy*, 2016, 183: 113-120. DOI: <https://doi.org/10.1016/j.apenergy.2016.08.142>.
- [9] Corgnale, C., B. Hardy, T. Motyka, R. Zidan, J. Teprovich, and B. Peters: *Screening analysis of metal hydride based thermal energy storage systems for concentrating solar power plants*. *Renewable and Sustainable Energy Reviews*, 2014, 38: 821-833. DOI: <https://doi.org/10.1016/j.rser.2014.07.049>.
- [10] N'Tsoukpoe, K.E., T. Schmidt, H.U. Rammelberg, B.A. Watts, and W.K.L. Ruck: *A systematic multi-step screening of numerous salt hydrates for low temperature thermochemical energy storage*. *Applied Energy*, 2014, 124: 1-16. DOI: <https://doi.org/10.1016/j.apenergy.2014.02.053>.
- [11] André, L., S. Abanades, and G. Flamant: *Screening of thermochemical systems based on solid-gas reversible reactions for high temperature solar thermal energy storage*. *Renewable and Sustainable Energy Reviews*, 2016, 64: 703-715. DOI: <https://doi.org/10.1016/j.rser.2016.06.043>.
- [12] Dizaji, H.B. and H. Hosseini: *A review of material screening in pure and mixed-metal oxide thermochemical energy storage (TCES) systems for concentrated solar power (CSP) applications*. *Renewable and Sustainable Energy Reviews*, 2018, 98: 9-26. DOI: <https://doi.org/10.1016/j.rser.2018.09.004>.

- [13] Angerer, M., M. Becker, S. Härzschel, K. Kröper, S. Gleis, A. Vandersickel, and H. Spliethoff: *Design of a MW-scale thermo-chemical energy storage reactor*. Energy Reports, 2018, 4: 507-519. DOI: <https://doi.org/10.1016/j.egy.2018.07.005>.
- [14] Agrafiotis, C., M. Roeb, M. Schmücker, and C. Sattler: *Exploitation of thermochemical cycles based on solid oxide redox systems for thermochemical storage of solar heat. Part 1: Testing of cobalt oxide-based powders*. Solar Energy, 2014, 102: 189-211. DOI: <https://doi.org/10.1016/j.solener.2013.12.032>.
- [15] Sögütöglu, L.C., P.A.J. Donkers, H.R. Fischer, H.P. Huinink, and O.C.G. Adan: *In-depth investigation of thermochemical performance in a heat battery: Cyclic analysis of K₂CO₃, MgCl₂ and Na₂S*. Applied Energy, 2018, 215: 159-173. DOI: <https://doi.org/10.1016/j.apenergy.2018.01.083>.
- [16] Schaube, F., L. Koch, A. Wörner, and H. Müller-Steinhagen: *A thermodynamic and kinetic study of the de- and rehydration of Ca(OH)₂ at high H₂O partial pressures for thermochemical heat storage*. Thermochemica Acta, 2012, 538: 9-20. DOI: <https://doi.org/10.1016/j.tca.2012.03.003>.
- [17] Schaube, F., A. Kohzer, J. Schütz, A. Wörner, and H. Müller-Steinhagen: *De- and rehydration of Ca(OH)₂ in a reactor with direct heat transfer for thermo-chemical heat storage. Part A: Experimental results*. Chemical Engineering Research and Design, 2013, 91(5): 856-864. DOI: <https://doi.org/10.1016/j.cherd.2012.09.020>.
- [18] Fujii, I., K. Tsuchiya, M. Higano, and J. Yamada: *Studies of an energy storage system by use of the reversible chemical reaction: CaO + H₂O ⇌ Ca(OH)₂*. Solar Energy, 1985, 34(4): 367-377. DOI: [https://doi.org/10.1016/0038-092X\(85\)90049-0](https://doi.org/10.1016/0038-092X(85)90049-0).
- [19] Rammelberg, H.U., T. Osterland, B. Priehs, O. Opel, and W.K.L. Ruck: *Thermochemical heat storage materials – Performance of mixed salt hydrates*. Solar Energy, 2016, 136: 571-589. DOI: <https://doi.org/10.1016/j.solener.2016.07.016>.
- [20] Fopah-Lele, A., C. Rohde, K. Neumann, T. Tietjen, T. Rönnebeck, K.E. N'Tsoukpoe, T. Osterland, O. Opel, and W.K.L. Ruck: *Lab-scale experiment of a closed thermochemical heat storage system including honeycomb heat exchanger*. Energy, 2016, 114: 225-238. DOI: <https://doi.org/10.1016/j.energy.2016.08.009>.
- [21] Mastronardo, E., L. Bonaccorsi, Y. Kato, E. Piperopoulos, and C. Milone: *Efficiency improvement of heat storage materials for MgO/H₂O/Mg(OH)₂ chemical heat pumps*. Applied Energy, 2016, 162: 31-39. DOI: <https://doi.org/10.1016/j.apenergy.2015.10.066>.
- [22] Funayama, S., H. Takasu, M. Zamengo, J. Kariya, S.T. Kim, and Y. Kato: *Performance of thermochemical energy storage of a packed bed of calcium hydroxide pellets*. Energy Storage, 2019, 1(2): e40. DOI: <https://doi.org/10.1002/est2.40>.
- [23] Shkatulov, A., J. Ryu, Y. Kato, and Y. Aristov: *Composite material “Mg(OH)₂/vermiculite”: A promising new candidate for storage of middle temperature heat*. Energy, 2012, 44(1): 1028-1034. DOI: <https://doi.org/10.1016/j.energy.2012.04.045>.
- [24] Shkatulov, A. and Y. Aristov: *Modification of magnesium and calcium hydroxides with salts: An efficient way to advanced materials for storage of middle-temperature heat*. Energy, 2015, 85: 667-676. DOI: <https://doi.org/10.1016/j.energy.2015.04.004>.

- [25] van der Pal, M. and R.E. Critoph: *Performance of CaCl₂-reactor for application in ammonia-salt based thermal transformers*. Applied Thermal Engineering, 2017, 126: 518-524. DOI: <https://doi.org/10.1016/j.applthermaleng.2017.07.086>.
- [26] Ward, P.A., C. Corngale, J.A. Teprovich, T. Motyka, B. Hardy, B. Peters, and R. Zidan: *High performance metal hydride based thermal energy storage systems for concentrating solar power applications*. Journal of Alloys and Compounds, 2015, 645: S374-S378. DOI: <https://doi.org/10.1016/j.jallcom.2014.12.106>.
- [27] Kato, Y., F.-u. Takahashi, A. Watanabe, and Y. Yoshizawa: *Thermal analysis of a magnesium oxide/water chemical heat pump for cogeneration*. Applied Thermal Engineering, 2001, 21(10): 1067-1081. DOI: [https://doi.org/10.1016/S1359-4311\(00\)00103-4](https://doi.org/10.1016/S1359-4311(00)00103-4).
- [28] Wang, C., P. Zhang, and R.Z. Wang: *Investigation of solid–gas reaction heat transformer system with the consideration of multistep reactions*. AIChE Journal, 2008, 54(9): 2464-2478. DOI: <https://doi.org/10.1002/aic.11560>.
- [29] Neises, M., S. Tescari, L. de Oliveira, M. Roeb, C. Sattler, and B. Wong: *Solar-heated rotary kiln for thermochemical energy storage*. Solar Energy, 2012, 86(10): 3040-3048. DOI: <https://doi.org/10.1016/j.solener.2012.07.012>.
- [30] Miguel, S.Á.d., J. Gonzalez-Aguilar, and M. Romero: *100-Wh Multi-purpose Particle Reactor for Thermochemical Heat Storage in Concentrating Solar Power Plants*. Energy Procedia, 2014, 49: 676-683. DOI: <https://doi.org/10.1016/j.egypro.2014.03.073>.
- [31] Zondag, H., B. Kikkert, S. Smeding, R.d. Boer, and M. Bakker: *Prototype thermochemical heat storage with open reactor system*. Applied Energy, 2013, 109: 360-365. DOI: <https://doi.org/10.1016/j.apenergy.2013.01.082>.
- [32] Mauran, S., H. Lahmidi, and V. Goetz: *Solar heating and cooling by a thermochemical process. First experiments of a prototype storing 60kWh by a solid/gas reaction*. Solar Energy, 2008, 82(7): 623-636. DOI: <https://doi.org/10.1016/j.solener.2008.01.002>.
- [33] Wenger, D., *Metallhydridspeicher zur Wasserstoffversorgung und Kühlung von Brennstoffzellenfahrzeugen*. 2009: VDI Verlag Düsseldorf.
- [34] Haije, W.G., J.B.J. Veldhuis, S.F. Smeding, and R.J.H. Grisel: *Solid/vapour sorption heat transformer: Design and performance*. Applied Thermal Engineering, 2007, 27(8): 1371-1376. DOI: <https://doi.org/10.1016/j.applthermaleng.2006.10.022>.
- [35] Wuerth, M., M. Becker, P. Ostermeier, S. Gleis, and H. Spliethoff: *Development of a Continuous Fluidized Bed Reactor for Thermochemical Energy Storage Application*. Journal of Energy Resources Technology, 2019, 141(7): 070710-070710-6. DOI: <https://doi.org/10.1115/1.4043629>.
- [36] Criado, Y.A., A. Huille, S. Rougé, and J.C. Abanades: *Experimental investigation and model validation of a CaO/Ca(OH)₂ fluidized bed reactor for thermochemical energy storage applications*. Chemical Engineering Journal, 2017, 313: 1194-1205. DOI: <https://doi.org/10.1016/j.cej.2016.11.010>.
- [37] Tescari, S., A. Singh, C. Agrafiotis, L. de Oliveira, S. Breuer, B. Schlögl-Knothe, M. Roeb, and C. Sattler: *Experimental evaluation of a pilot-scale thermochemical storage system for a concentrated solar power plant*. Applied Energy, 2017, 189: 66-75. DOI: <https://doi.org/10.1016/j.apenergy.2016.12.032>.

- [38] Lovegrove, K., A. Luzzi, I. Soldiani, and H. Kreetz: *Developing ammonia based thermochemical energy storage for dish power plants*. Solar Energy, 2004, 76(1): 331-337. DOI: <https://doi.org/10.1016/j.solener.2003.07.020>.
- [39] Fedders, H. and B. Höhle: *Operating a pilot plant circuit for energy transport with hydrogen-rich gas*. International Journal of Hydrogen Energy, 1982, 7(10): 793-800. DOI: [https://doi.org/10.1016/0360-3199\(82\)90070-2](https://doi.org/10.1016/0360-3199(82)90070-2).
- [40] Lovegrove, K.: *Thermodynamic limits on the performance of a solar thermochemical energy storage system*. International Journal of Energy Research, 1993, 17(9): 817-829. DOI: <https://doi.org/10.1002/er.4440170904>.
- [41] Ma, Q., L. Luo, R.Z. Wang, and G. Sauce: *A review on transportation of heat energy over long distance: Exploratory development*. Renewable and Sustainable Energy Reviews, 2009, 13(6): 1532-1540. DOI: <https://doi.org/10.1016/j.rser.2008.10.004>.
- [42] Maeda, S., K. Thu, T. Maruyama, and T. Miyazaki: *Critical Review on the Developments and Future Aspects of Adsorption Heat Pumps for Automobile Air Conditioning*. Applied Sciences, 2018, 8(11): 2061. DOI: <https://doi.org/10.3390/app8112061>.
- [43] Alahmer, A., S. Ajib, and X. Wang: *Comprehensive strategies for performance improvement of adsorption air conditioning systems: A review*. Renewable and Sustainable Energy Reviews, 2019, 99: 138-158. DOI: <https://doi.org/10.1016/j.rser.2018.10.004>.
- [44] Vasta, S., V. Brancato, D. La Rosa, V. Palomba, G. Restuccia, A. Sapienza, and A. Frazzica: *Adsorption Heat Storage: State-of-the-Art and Future Perspectives*. Nanomaterials, 2018, 8(7): 522. DOI: <https://doi.org/10.3390/nano8070522>.
- [45] Krönauer, A., E. Lävemann, S. Brückner, and A. Hauer: *Mobile Sorption Heat Storage in Industrial Waste Heat Recovery*. Energy Procedia, 2015, 73: 272-280. DOI: <https://doi.org/10.1016/j.egypro.2015.07.688>.
- [46] Nienborg, B., T. Helling, D. Fröhlich, R. Horn, G. Munz, and P. Schossig: *Closed Adsorption Heat Storage—A Life Cycle Assessment on Material and Component Levels*. Energies, 2018, 11(12): 3421. DOI: <https://doi.org/10.3390/en11123421>.
- [47] Bellosta von Colbe, J., J.-R. Ares, J. Barale, M. Baricco, C. Buckley, G. Capurso, N. Gallandat, D.M. Grant, M.N. Guzik, I. Jacob, E.H. Jensen, T. Jensen, J. Jepsen, T. Klassen, M.V. Lototsky, K. Manickam, A. Montone, J. Puszkil, S. Sartori, D.A. Sheppard, A. Stuart, G. Walker, C.J. Webb, H. Yang, V. Yartys, A. Züttel, and M. Dornheim: *Application of hydrides in hydrogen storage and compression: Achievements, outlook and perspectives*. International Journal of Hydrogen Energy, 2019, 44(15): 7780-7808. DOI: <https://doi.org/10.1016/j.ijhydene.2019.01.104>.
- [48] Kato, Y., R. Takahashi, T. Sekiguchi, and J. Ryu: *Study on medium-temperature chemical heat storage using mixed hydroxides*. International Journal of Refrigeration, 2009, 32(4): 661-666. DOI: <https://doi.org/10.1016/j.ijrefrig.2009.01.032>.
- [49] Rusman, N.A.A. and M. Dahari: *A review on the current progress of metal hydrides material for solid-state hydrogen storage applications*. International Journal of Hydrogen Energy, 2016, 41(28): 12108-12126. DOI: <https://doi.org/10.1016/j.ijhydene.2016.05.244>.
- [50] Henninger, S.K., S.-J. Ernst, L. Gordeeva, P. Bendix, D. Fröhlich, A.D. Grekova, L. Bonaccorsi, Y. Aristov, and J. Jaenchen: *New materials for adsorption heat transformation and storage*. Renewable Energy, 2017, 110: 59-68. DOI: <https://doi.org/10.1016/j.renene.2016.08.041>.

- [51] Muthukumar, P. and M. Groll: *Metal hydride based heating and cooling systems: A review*. International Journal of Hydrogen Energy, 2010, 35(8): 3817-3831. DOI: <https://doi.org/10.1016/j.ijhydene.2010.01.115>.
- [52] Spinner, B.: *Ammonia-based thermochemical transformers*. Heat Recovery Systems and CHP, 1993, 13(4): 301-307. DOI: [https://doi.org/10.1016/0890-4332\(93\)90053-X](https://doi.org/10.1016/0890-4332(93)90053-X).
- [53] Spoelstra, S., W.G. Haije, and J.W. Dijkstra: *Techno-economic feasibility of high-temperature high-lift chemical heat pumps for upgrading industrial waste heat*. Applied Thermal Engineering, 2002, 22(14): 1619-1630. DOI: [https://doi.org/10.1016/S1359-4311\(02\)00077-7](https://doi.org/10.1016/S1359-4311(02)00077-7).
- [54] Jahnke, A., L. Strenge, C. Fleßner, N. Wolf, T. Jungnickel, and F. Ziegler: *First cycle simulations of the Honigmann process with LiBr/H₂O and NaOH/H₂O as working fluid pairs as a thermochemical energy storage*. International Journal of Low-Carbon Technologies, 2013, 8(suppl_1): i55-i61. DOI: <https://doi.org/10.1093/ijlct/ctt022>.
- [55] Laing, D., D. Lehmann, M. Fiß, and C. Bahl: *Test Results of Concrete Thermal Energy Storage for Parabolic Trough Power Plants*. Journal of Solar Energy Engineering, 2009, 131(4): 041007-6. DOI: <https://doi.org/10.1115/1.3197844>.
- [56] Zunft, S., M. Hänel, M. Krüger, V. Dreißigacker, F. Göhring, and E. Wahl: *Jülich Solar Power Tower—Experimental Evaluation of the Storage Subsystem and Performance Calculation*. Journal of Solar Energy Engineering, 2011, 133(3): 031019-5. DOI: <https://doi.org/10.1115/1.4004358>.
- [57] Krüger, M., J. Haunstetter, P. Knödler, and S. Zunft: *Slag as an Inventory Material for Heat Storage in a Concentrated Solar Tower Power Plant: Design Studies and Systematic Comparative Assessment*. Applied Sciences, 2019, 9(9): 1833. DOI: <https://doi.org/10.3390/app9091833>.
- [58] Geissbühler, L., V. Becattini, G. Zanganeh, S. Zavattoni, M. Barbato, A. Haselbacher, and A. Steinfeld: *Pilot-scale demonstration of advanced adiabatic compressed air energy storage, Part 1: Plant description and tests with sensible thermal-energy storage*. Journal of Energy Storage, 2018, 17: 129-139. DOI: <https://doi.org/10.1016/j.est.2018.02.004>.
- [59] Frazzica, A., V. Brancato, V. Palomba, and S. Vasta, *Sorption Thermal Energy Storage*, in *Recent Advancements in Materials and Systems for Thermal Energy Storage: An Introduction to Experimental Characterization Methods*, A. Frazzica and L.F. Cabeza, Editors. 2019, Springer International Publishing: Cham. p. 33-54.
- [60] Lefebvre, D. and F.H. Tezel: *A review of energy storage technologies with a focus on adsorption thermal energy storage processes for heating applications*. Renewable and Sustainable Energy Reviews, 2017, 67: 116-125. DOI: <https://doi.org/10.1016/j.rser.2016.08.019>.
- [61] Block, T., N. Knoblauch, and M. Schmücker: *The cobalt-oxide/iron-oxide binary system for use as high temperature thermochemical energy storage material*. Thermochemica Acta, 2014, 577: 25-32. DOI: <https://doi.org/10.1016/j.tca.2013.11.025>.
- [62] Carrillo, A.J., J. Moya, A. Bayón, P. Jana, V.A. de la Peña O'Shea, M. Romero, J. Gonzalez-Aguilar, D.P. Serrano, P. Pizarro, and J.M. Coronado: *Thermochemical energy storage at high temperature via redox cycles of Mn and Co oxides: Pure oxides versus mixed ones*. Solar Energy Materials and Solar Cells, 2014, 123: 47-57. DOI: <https://doi.org/10.1016/j.solmat.2013.12.018>.

- [63] Agrafiotis, C., S. Tescari, M. Roeb, M. Schmücker, and C. Sattler: *Exploitation of thermochemical cycles based on solid oxide redox systems for thermochemical storage of solar heat. Part 3: Cobalt oxide monolithic porous structures as integrated thermochemical reactors/heat exchangers*. Solar Energy, 2015, 114: 459-475. DOI: <https://doi.org/10.1016/j.solener.2014.12.037>.
- [64] Karagiannakis, G., C. Pagkoura, E. Halevas, P. Baltzopoulou, and A.G. Konstandopoulos: *Cobalt/cobaltous oxide based honeycombs for thermochemical heat storage in future concentrated solar power installations: Multi-cyclic assessment and semi-quantitative heat effects estimations*. Solar Energy, 2016, 133: 394-407. DOI: <https://doi.org/10.1016/j.solener.2016.04.032>.
- [65] Wokon, M., T. Block, S. Nicolai, M. Linder, and M. Schmücker: *Thermodynamic and kinetic investigation of a technical grade manganese-iron binary oxide for thermochemical energy storage*. Solar Energy, 2017, 153: 471-485. DOI: <https://doi.org/10.1016/j.solener.2017.05.045>.
- [66] Preisner, N.C., T. Block, M. Linder, and H. Leion: *Stabilizing Particles of Manganese-Iron Oxide with Additives for Thermochemical Energy Storage*. Energy Technology, 2018, 6(11): 2154-2165. DOI: <https://doi.org/10.1002/ente.201800211>.
- [67] Dieterich, M., C. Pohlmann, I. Bürger, M. Linder, and L. Röntzsch: *Long-term cycle stability of metal hydride-graphite composites*. International Journal of Hydrogen Energy, 2015, 40(46): 16375-16382. DOI: <https://doi.org/10.1016/j.ijhydene.2015.09.013>.
- [68] Weiss-Ungethüm, J., I. Bürger, N. Schmidt, M. Linder, and J. Kallo: *Experimental investigation of a liquid cooled high temperature proton exchange membrane (HT-PEM) fuel cell coupled to a sodium alanate tank*. International Journal of Hydrogen Energy, 2014, 39(11): 5931-5941. DOI: <https://doi.org/10.1016/j.ijhydene.2014.01.127>.
- [69] Baricco, M., M. Bang, M. Fichtner, B. Hauback, M. Linder, C. Luetto, P. Moretto, and M. Sgroi: *SSH2S: Hydrogen storage in complex hydrides for an auxiliary power unit based on high temperature proton exchange membrane fuel cells*. Journal of Power Sources, 2017, 342: 853-860. DOI: <https://doi.org/10.1016/j.jpowsour.2016.12.107>.
- [70] Lototsky, M.V., I. Tolj, L. Pickering, C. Sita, F. Barbir, and V. Yartys: *The use of metal hydrides in fuel cell applications*. Progress in Natural Science: Materials International, 2017, 27(1): 3-20. DOI: <https://doi.org/10.1016/j.pnsc.2017.01.008>.
- [71] Lutz, M., M. Bhourri, M. Linder, and I. Bürger: *Adiabatic magnesium hydride system for hydrogen storage based on thermochemical heat storage: Numerical analysis of the dehydrogenation*. Applied Energy, 2019, 236: 1034-1048. DOI: <https://doi.org/10.1016/j.apenergy.2018.12.038>.
- [72] Jensen, J.O., A.P. Vestbø, Q. Li, and N.J. Bjerrum: *The energy efficiency of onboard hydrogen storage*. Journal of Alloys and Compounds, 2007, 446-447: 723-728. DOI: <https://doi.org/10.1016/j.jallcom.2007.04.051>.
- [73] Linder, M. and R. Kulenovic: *An energy-efficient air-conditioning system for hydrogen driven cars*. International Journal of Hydrogen Energy, 2011, 36(4): 3215-3221. DOI: <https://doi.org/10.1016/j.ijhydene.2010.11.101>.
- [74] Molenda, M., J. Stengler, M. Linder, and A. Wörner: *Reversible hydration behavior of CaCl₂ at high H₂O partial pressures for thermochemical energy storage*. Thermochemica Acta, 2013, 560: 76-81. DOI: <https://doi.org/10.1016/j.tca.2013.03.020>.

- [75] Johnson, M., S. Hübner, M. Braun, C. Martin, M. Fiß, B. Hachmann, M. Schönberger, and M. Eck: *Assembly and attachment methods for extended aluminum fins onto steel tubes for high temperature latent heat storage units*. Applied Thermal Engineering, 2018, 144: 96-105. DOI: <https://doi.org/10.1016/j.applthermaleng.2018.08.035>.
- [76] Rosemary, J.K., G.L. Bauerle, and T.H. Springer: *Solar Energy Storage Using Reversible Hydration-Dehydration of CaO-Ca(OH)₂*. Journal of Energy, 1979, 3(6): 321-322. DOI: <https://doi.org/10.2514/3.62440>
- [77] Roßkopf, C., M. Haas, A. Faik, M. Linder, and A. Wörner: *Improving powder bed properties for thermochemical storage by adding nanoparticles*. Energy Conversion and Management, 2014, 86: 93-98. DOI: <https://doi.org/10.1016/j.enconman.2014.05.017>.
- [78] Roßkopf, C., S. Afflerbach, M. Schmidt, B. Görtz, T. Kowald, M. Linder, and R. Trettin: *Investigations of nano coated calcium hydroxide cycled in a thermochemical heat storage*. Energy Conversion and Management, 2015, 97: 94-102. DOI: <https://doi.org/10.1016/j.enconman.2015.03.034>.
- [79] Schmidt, M., C. Szczukowski, C. Roßkopf, M. Linder, and A. Wörner: *Experimental results of a 10 kW high temperature thermochemical storage reactor based on calcium hydroxide*. Applied Thermal Engineering, 2014, 62(2): 553-559. DOI: <https://doi.org/10.1016/j.applthermaleng.2013.09.020>.

6. Own publications used for this work

Chapter 1 and 2 are partially reproduced from Marc Linder: *Thermochemical Energy Storage Devices*, In: *Thermal Energy Storage: Materials, Devices, Systems and Applications*, Ed. Yulong Ding, Royal Society of Chemistry, 2021. DOI <https://doi.org/10.1039/9781788019842> with permission from the Royal Society of Chemistry.

- Wok_2017: Michael Wokon, Andreas Kohzer, Marc Linder: *Investigations on thermochemical energy storage based on technical grade manganese-iron oxide in a lab-scale packed bed reactor*. *Solar Energy*, 2017, 153: 200-214. DOI: <https://doi.org/10.1016/j.solener.2017.05.034>
- Koe_2019: Mila Kölbig, Inga Bürger, Marc Linder: *Characterization of metal hydrides for thermal applications in vehicles below 0 °C*. *International Journal of Hydrogen Energy*, 2019, 44(10): 4878-4888. DOI: <https://doi.org/10.1016/j.ijhydene.2018.12.116>
- Die_2017: Mila Dieterich, Inga Bürger, Marc Linder: *Open and closed metal hydride system for high thermal power applications: Preheating vehicle components*. *International Journal of Hydrogen Energy*, 2017, 42(16): 11469-11481. DOI: <https://doi.org/10.1016/j.ijhydene.2017.03.024>
- Bue_2017: Inga Bürger, Mila Dieterich, Carsten Pohlmann, Lars Röntzsch, Marc Linder: *Standardized hydrogen storage module with high utilization factor based on metal hydride-graphite composites*. *Journal of Power Sources*, 2017, 342: 970-979. DOI: <https://doi.org/10.1016/j.jpowsour.2016.12.108>
- Bue_2014a: Inga Bürger, Lars Komogowski, Marc Linder: *Advanced reactor concept for complex hydrides: Hydrogen absorption from room temperature*. *International Journal of Hydrogen Energy*, 2014, 39(13): 7030–7041. DOI: <https://doi.org/10.1016/j.ijhydene.2014.02.070>
- Bue_2014b: Inga Bürger, Carlo Luetto, Marc Linder: *Advanced reactor concept for complex hydrides: Hydrogen desorption at fuel cell relevant boundary conditions*. *International Journal of Hydrogen Energy*, 2014, 39(14): 7346–7355. DOI: <https://doi.org/10.1016/j.ijhydene.2014.02.069>
- Bue_2014c: Inga Bürger, J.J. Hu, J.G. Vitillo, G.N. Kalantzopoulos, Stefano Deledda, Maximilian Fichtner, Marcello Baricco, Marc Linder: *Material properties and empirical rate equations for hydrogen sorption reactions in 2 LiNH₂–1.1 MgH₂–0.1 LiBH₄–3 wt.% ZrCoH₃*. *International Journal of Hydrogen Energy*, 2014, 39(16): 8283–8292. DOI: <https://doi.org/10.1016/j.ijhydene.2014.02.120>

- Bho_2015: Maha Bhour, Inga Bürger, Marc Linder: *Numerical investigation of hydrogen charging performance for a combination reactor with embedded metal hydride and coolant tubes*. International Journal of Hydrogen Energy, 2015, 40(20): 6626-6638. DOI: <https://doi.org/10.1016/j.ijhydene.2015.03.060>
- Bue_2015: Inga Bürger, Maha Bhour, Marc Linder: *Considerations on the H₂ desorption process for a combination reactor based on metal and complex hydrides*. International Journal of Hydrogen Energy, 2015, 40(22): 7072-7082. DOI: <https://doi.org/10.1016/j.ijhydene.2015.03.136>
- Bho_2016: Maha Bhour, Inga Bürger, Marc Linder: *Feasibility analysis of a novel solid-state H₂ storage reactor concept based on thermochemical heat storage: MgH₂ and Mg(OH)₂ as reference materials*. International Journal of Hydrogen Energy, 2016, 41(45): 20549-20561. DOI: <https://doi.org/10.1016/j.ijhydene.2016.09.125>
- Wec_2017: Christoph Weckerle, Inga Bürger, Marc Linder: *Novel reactor design for metal hydride cooling systems*. International Journal of Hydrogen Energy, 2017, 42(12): 8063-8074. DOI: <https://doi.org/10.1016/j.ijhydene.2017.01.066>
- Ric_2016: Margarethe Richter, Martin Bouché, Marc Linder: *Heat transformation based on CaCl₂/H₂O - Part A: Closed operation principle*. Applied Thermal Engineering, 2016, 102: 615-621. DOI: <https://doi.org/10.1016/j.applthermaleng.2016.03.076>
- Bou_2016: Martin Bouché, Margarethe Richter, Marc Linder: *Heat transformation based on CaCl₂/H₂O - Part B: Open operation principle*. Applied Thermal Engineering, 2016, 102: 641-647. DOI: <https://doi.org/10.1016/j.applthermaleng.2016.03.102>
- Ric_2018: Margarethe Richter, Eva-Maria Habermann, Eleonore Siebecke, Marc Linder: *A systematic screening of salt hydrates as materials for a thermochemical heat transformer*. Thermochemica Acta, 2017, 659: 136-150. DOI: <https://doi.org/10.1016/j.tca.2017.06.011>
- Gut_2018: Andrea Gutierrez, Svetlana Ushak, Marc Linder: *High Carnallite-Bearing Material for Thermochemical Energy Storage: Thermophysical Characterization*. ACS Sustainable Chemistry and Engineering, 2018, 6(5): 6135-6145. DOI: <https://doi.org/10.1021/acssuschemeng.7b04803>
- Sch_2017a: Matthias Schmidt, Andrea Gutierrez, Marc Linder: *Thermochemical Energy Storage with CaO/Ca(OH)₂ – Experimental investigation of the thermal capability at low vapor pressures in a lab scale reactor*. Applied Energy, 2017, 188(15): 672-681. DOI: <https://doi.org/10.1016/j.apenergy.2016.11.023>
- Sch_2017b: Matthias Schmidt, Marc Linder: *Power generation based on the Ca(OH)₂ / CaO thermochemical storage system – Experimental investigation of discharge operation modes in lab scale and corresponding conceptual process design*. Applied Energy, 2017, 203: 594-607. DOI: <https://doi.org/10.1016/j.apenergy.2017.06.063>



Investigations on thermochemical energy storage based on technical grade manganese-iron oxide in a lab-scale packed bed reactor



Michael Wokon^{a,*}, Andreas Kohzer^a, Marc Linder^b

^a German Aerospace Center (DLR e.V.), Institute of Engineering Thermodynamics, Linder Höhe, 51147 Cologne, Germany

^b German Aerospace Center (DLR e.V.), Institute of Engineering Thermodynamics, Pfaffenwaldring 38-40, 70569 Stuttgart, Germany

ARTICLE INFO

Article history:

Received 3 February 2017

Received in revised form 7 May 2017

Accepted 9 May 2017

Available online 29 May 2017

Keywords:

Thermochemical energy storage

Redox reaction

Manganese-iron oxide system

Packed bed reactor

Direct contact heat transfer

Thermal charging and discharging

ABSTRACT

Thermochemical energy storage (TCS) based on gas–solid reactions constitutes a promising concept to develop efficient storage solutions with higher energy densities compared to widely investigated sensible and latent thermal energy storage systems. Specifically for high temperature applications multivalent metal oxides represent an interesting storage material, undergoing a reversible redox reaction with oxygen. Due to the inherently high working temperatures such a TCS system could potentially be implemented in future generation concentrated solar power (CSP) plants with central receiver technology, in order to increase the total plant efficiency and ensure the dispatchability of power generation.

In this work an experimental test rig with a lab-scale tube reactor has been developed to analyze a packed bed of granular manganese-iron oxide storage material regarding heat and mass transport effects coupled with the chemical reaction. For this purpose manganese-iron oxide with a Fe/Mn molar ratio of 1:3 has been selected as a suitable reference material, which can be prepared from abundant, economical and nonhazardous raw materials. Consequently, in the context of this work the TCS technology is systematically approached based on the reference metal oxide in the temperature range between 800 °C and 1040 °C in order to derive the main influencing aspects of this storage concept.

Experimental results showed the development of characteristic temperature profiles along the bed height, which proved to be dependent on the thermodynamic properties as well as kinetic behavior of the redox reaction. It was demonstrated that bed temperatures could be stabilized due to the proceeding redox reaction in dynamic charging and discharging operation modes. Parametric studies have been carried out to examine the influence of different operating parameters on thermal charging and discharging and to analyze the main limitations affecting the reaction progress. Finally, cycling experiments of the material in the lab-scale reactor exhibited no reactivity degradation over 17 cycles, verifying the comparability of the experimental results obtained from the conducted parametric studies. Analysis and comparison of the raw and cycled material, however, indicated signs of material alterations due to sintering processes.

© 2017 Elsevier Ltd. All rights reserved.

1. Introduction

Thermal energy storage (TES) in high temperature applications becomes increasingly important with the expansion of renewable energy sources. The implementation of TES systems in concentrated solar power (CSP) plants for instance is crucial to facilitate the dispatchability of power generation. The unfavorable intermittency of solar energy can only be overcome by decoupling the solar energy supply during sunshine hours and the electricity demand, in order to bridge short-term deficiencies during cloud passage

and extend electricity production into the nighttime hours (Gil et al., 2010; Liu et al., 2016; Zhang et al., 2016).

The comparatively new concept of thermochemical energy storage (TCS) is based on the utilization of the enthalpy of reversible gas–solid reactions to convert thermal energy to chemical energy, which offers great potential for the development of efficient storage solutions with higher energy densities compared to sensible and latent TES systems (Kuravi et al., 2013; Pardo et al., 2014). Current research for high temperature storage applications from 600 °C up to even 1100 °C is focused on multivalent metal oxides, capable of undergoing reversible reduction–oxidation (redox) reactions to store thermal energy in the form of the reaction enthalpy $\Delta_R h$ according to the following pathway:

* Corresponding author.

E-mail address: michael.wokon@dlr.de (M. Wokon).

Nomenclature

Abbreviations

B	cubic bixbyite phase (Mn,Fe) ₂ O ₃
CLOU	chemical-looping with oxygen uncoupling
CSP	concentrated solar power
HTF	heat transfer fluid
Me	metal
MFC	mass flow controller
N ₂	nitrogen
O ₂	oxygen
redox reaction	reduction–oxidation reaction
S	cubic spinel phase β-(Mn,Fe) ₃ O ₄
SEM	scanning electron microscopy
STA	simultaneous thermal analysis
TCS	thermochemical energy storage
TES	thermal energy storage

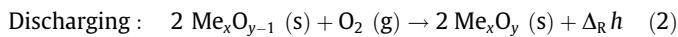
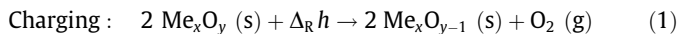
Symbols

$c_{p,g}$	specific heat capacity of gas phase (J/(kg K))
$C_{HTF} = c_{p,g} dm_g/dt$	heat capacity rate of HTF (W/K)
$\Delta H_{g,max}$	maximum possible enthalpy change of HTF flow (J)
$\Delta_R h$	specific reaction enthalpy (kJ/kg)

m	mass (kg)
n	molar amount (mol)
\dot{n}	molar reaction rate (mol/s)
p_{O_2}	oxygen partial pressure (kPa)
σ	volume concentration (%)
T	temperature (K)
ϑ	temperature, thermocouple (°C)
X	reaction conversion (mol/mol)

Subscripts

0	initial value
c	charging
d	discharging
g	gaseous
in	inlet
max	maximum
out	outlet
Ox	oxidation
Red	reduction
rxn	reaction
s	solid



Promising metal oxides exhibit the intrinsic advantage to react reversibly with oxygen (O₂) at high temperatures, which allows to employ ambient air simultaneously as heat transfer fluid (HTF) and carrier of the reaction gas O₂. Thermal energy supplied by the HTF is used to drive the endothermic reduction under the release of O₂, accounting for the thermal charging step of the storage material (1). Recombination of the reduced metal oxide and O₂ (from ambient air) leads to the exothermic oxidation, representing the thermal discharging step by the complete recovery of thermal energy (2). Consequently, there is no need for intermediate storage of the reactant gas, which is highly beneficial for future system integration. The implementation of a metal oxide storage reactor into a plant could thus be realized in the form of an open-loop system. In addition, the use of air as HTF allows to work with higher HTF temperatures up to and beyond 1000 °C, which renders redox reactions especially interesting for TCS in central receiver CSP plants, e.g. with a future generation of volumetric air receivers (Ávila-Marín, 2011; Ho, 2017).

High temperature thermochemical energy storage implicates a high degree of thermal energy stored as sensible heat due to the high working temperatures of the system, naturally temperatures above the reduction temperature in the charging stage. Correspondingly, this amount of thermal energy constitutes one of the most important intrinsic aspects of this TCS technology and cannot be neglected in the storage process and overall system examination. On this account also “hybrid storage” or “combined storage” concepts using sensible and thermochemical energy storage simultaneously have been suggested (Ströhle et al., 2016; Tescari et al., 2014). An experimental test of a small-scale cascaded configuration of cordierite honeycombs and foams coated with Co₃O₄ and Mn₂O₃ has been reported in this regard (Agrafiotis et al., 2016a).

Established high temperature regenerator-type storage systems merely based on sensible energy storage, working with a gaseous heat transfer medium and a stationary solid storage medium such

as ceramic or rocks, offer great potential to be adapted to the envisaged “hybrid storage” concepts. Implementing a high temperature TCS zone in a packed bed storage unit would favorably facilitate an increase in volumetric and gravimetric storage densities, whereas a low temperature cooling section employing low cost inert materials would result in cost savings (Ströhle et al., 2016). Fig. 1 illustrates the characteristic operating method of such a hybrid storage system.

During the charging process the HTF – hot air from the solar receiver – enters the storage tank from the top and flows downward (a), which leads to the formation of a characteristic temperature profile along the filling height. The direction of the flow is reversed in the subsequent stage of storage discharging to enter

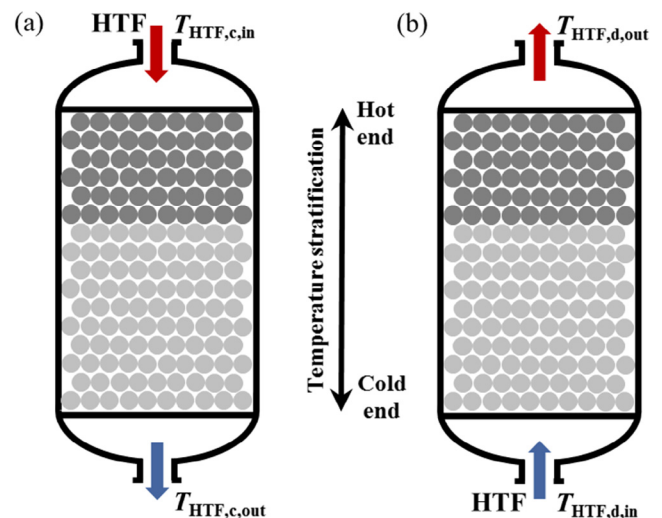


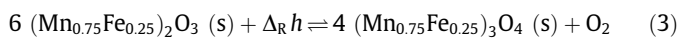
Fig. 1. Schematic description of a potential regenerator-type storage with thermochemical storage material, allowing the exploitation of the sensible heat and the heat of reaction due to a temperature stratification along the bed height: Thermal charging (a) and thermal discharging (b).

the tank at the bottom (b), being the cold end of the storage. This counter-flow mode generally provides to maintain an axial thermal stratification inside the packed bed, when thermal energy is transferred to and extracted from the storage (Zanganeh et al., 2012; Zunft et al., 2011). It is therefore comprehensible, that the positioning of the reactive TCS material is only reasonable in the hot upper part of the storage tank, where temperature operating conditions allow the reduction to take place. The integration of a potential hybrid TES system with a packed bed reactor into a CSP plant can be realized in the form of a parallel configuration of the TES system and the power block, taking advantage of the axial thermal stratification in the packed bed to exploit the stored sensible heat as well (Ströhle et al., 2016). The illustrated concept of a regenerator-type storage system with a metal oxide TCS topping serves as motivation for the fundamental research presented in this work. Our studies have a generic approach and are therefore independent of any assumed source of the HTF air or the operation principle.

The current state of the scientific knowledge shows that most examinations on redox reactions have been carried out by means of thermal analysis of small sample masses mostly on the mg-scale to survey the reversibility, cycling stability as well thermodynamic and kinetic behavior of storage materials. In consideration of the projected technical application the individual reaction steps – reduction and oxidation – need to be thermodynamically favored in the relevant temperature and pressure range depending on the prevailing process conditions. Several research groups focused on the screening of diverse redox couples regarding their TCS applicability, identifying BaO_2/BaO , $\text{Co}_3\text{O}_4/\text{CoO}$, $\text{Mn}_2\text{O}_3/\text{Mn}_3\text{O}_4$ and $\text{CuO}/\text{Cu}_2\text{O}$ as the most promising in the temperature range of 700–1100 °C at ambient pressure (Agrafiotis et al., 2014, 2016b, André et al., 2016; Block and Schmücker, 2016; Wong, 2011; Wong et al., 2010). Among those, pure manganese oxide with an energy density of ~ 202 J/g Mn_2O_3 constitutes a suitable storage material, which particularly fulfills the essential requirements on a storage material for large-scale applications to be nonhazardous, abundant in nature as well as low-priced, in contrast to other storage materials such as cobalt oxide (Carrillo et al., 2014; Karagiannakis et al., 2014; Wong, 2011). Even though the equilibrium temperature of 902 °C in air (Barin and Platzki, 1995) is favorable within the desired temperature range, the redox reaction of $\text{Mn}_2\text{O}_3/\text{Mn}_3\text{O}_4$ exhibits a distinctive thermal hysteresis. This characteristic behavior – most pronounced for manganese oxide – implies a strong disadvantageous decoupling of the forward and reverse reaction. Furthermore, cycling stability is not given, as re-oxidation rates appear to decrease continuously in the course of consecutive cycles (Block and Schmücker, 2016; Carrillo et al., 2014; Wong, 2011).

Recent studies have shown, that those drawbacks can be overcome by the incorporation of iron cations into manganese oxide. In particular binary oxides with molar ratios Fe/Mn of 1:4 (Carrillo et al., 2015, 2016) and 1:2 (Block and Schmücker, 2016) exhibit improved TCS properties, such as higher re-oxidation rates and better cycling stability (75 cycles carried out with molar ratio Fe/Mn of 1:4). Enthalpies of 219 J/g and 233 J/g were measured for the reduction step in air, respectively. Further, the pronounced thermal hysteresis measured for the redox pair $\text{Mn}_2\text{O}_3/\text{Mn}_3\text{O}_4$ could be narrowed (Block and Schmücker, 2016; Carrillo et al., 2015). Based on these data, a technical grade manganese-iron oxide with a Fe/Mn molar ratio of 1:3 has been selected as a suitable reference material for lab-scale experiments in the current work. In chemical-looping with oxygen uncoupling (CLOU) – a novel method for CO_2 capturing during combustion of fuels – spray-dried manganese-iron oxide with the same Fe/Mn molar ratio has been tested with respect to its oxygen carrier properties under CLOU conditions (Azimi et al., 2013). For this composition reported phase diagrams of the manganese oxide – iron oxide sys-

tem in air indicate the cubic bixbyite $(\text{Mn,Fe})_2\text{O}_3$ (B) to be the thermodynamically stable phase at low temperatures and the cubic spinel β - $(\text{Mn,Fe})_3\text{O}_4$ (S) to be the stable phase at high temperatures (Crum et al., 2009; Kjellqvist and Selleby, 2010; Wickham, 1969). Hence, the following redox reaction is expected upon changing the temperature and/or oxygen partial pressure ($p\text{O}_2$):



A detailed characterization of this redox reaction with respect to thermodynamic and kinetic properties was performed by means of thermal analysis in an associated paper (Wokon et al., 2017). Due to a thermal hysteresis yet present under practical dynamic measuring conditions, technically relevant $p\text{O}_2$ - T dependences have been experimentally derived by means of simultaneous thermal analysis (STA) measurements, giving temperature thresholds of ~ 981.8 °C for the reduction and ~ 920.4 °C for the oxidation onset in atmospheric air. It has to be noted, that particularly the oxidation step is subject to severe kinetic limitations, inhibiting the reaction in a temperature range nearby the equilibrium state (Wokon et al., 2017).

In contrast to thermal analysis a larger experiment is able to give information about the superimposed effects of heat and mass transport processes coupled with the chemical reaction. Up to date only few reactor types and storage concepts for high temperature TCS using metal oxides have been reported in the literature, mainly focusing on a principal demonstration of the storage feasibility.

In this context directly irradiated rotary kilns were investigated with regard to on-sun reduction and off-sun oxidation of the redox pairs $\text{Co}_3\text{O}_4/\text{CoO}$ (Neises et al., 2012) and $\text{CuO}/\text{Cu}_2\text{O}$ (Alonso et al., 2015) in a batch operation. It was concluded, that with the presented setups a measurement of the actual sample temperature during the reaction could not be performed inside the reaction chamber. This is why fundamental relationships between the reaction temperature and oxygen release/uptake under the prevailing conditions could not be assessed.

Furthermore, only few TCS concepts have been described, where air utilized as HTF directly flows through the bulk of the reactive metal oxide storage material both for thermal charging and discharging. Those range from a small quartz glass tube reactor using Co_3O_4 as well as MnO_2 -10% Fe_2O_3 in powder form (Wong, 2011; Wong et al., 2010), a lab-scale packed bed/fluidized bed reactor concept (Álvarez de Miguel et al., 2016, 2014), small-scale compact monolithic reactor/heat exchanger concepts using either extruded cobalt/cobaltous oxide honeycombs or cordierite honeycombs and foams coated with Co_3O_4 or Mn_2O_3 (Agrafiotis et al., 2016a; Karagiannakis et al., 2016), to a first pilot-scale thermochemical storage unit based on $\text{Co}_3\text{O}_4/\text{CoO}$ coated cordierite honeycomb structures as storage medium (Tescari et al., 2017). Although the concept could be validated in the latter case, the measurement of the O_2 concentration turned out to be unreliable in the pilot-scale system, which is why the reaction conversion could only be calculated based on the estimated thermal energy stored in the system.

It can be summarized that up to date little work has been done with respect to generic fundamental investigations on the understanding of the redox reaction behavior of metal oxides during charging and discharging, taking the arising change of the O_2 concentration in the gas phase (HTF) and observed reaction temperatures into account. The influence of essential operating parameters on the thermal behavior and performance of a directly permeated high temperature TCS reactor has not yet been addressed based on an experimental parametric study. Therefore, in this work a test rig with a lab-scale tube reactor has been designed to systematically analyze the redox reaction of granular metal oxides in a packed bed (~ 500 g of storage material) with direct contact heat transfer using air as HTF and carrier of

the reaction gas O_2 . The identification of determining aspects for the metal oxide based TCS technology in an appropriate scale represents the main focus of this work, in order to provide the technologically relevant directions for further storage material and storage system development.

2. Material and methods

2.1. Material

Granular manganese-iron oxide used in this study was prepared by means of a build-up granulation technique, which was performed by VITO (Mol, Belgium). In the process technical grade powders of Mn_3O_4 (Trimanox, Chemalloy) and Fe_2O_3 (98% metals basis, Alfa Aesar) were mixed with a Fe/Mn molar ratio of 1:3, which corresponds to a $Fe_2O_3:Mn_3O_4$ mass ratio of 25.9:74.1. The mixed material was sieved in the dry state to obtain a particle size fraction from 1.15 mm to 3.15 mm prior to calcination. Heat treatment for 4 h at 1025 °C and subsequent cooling down in air yielded the targeted combined manganese-iron oxide (solid state reaction), denoted $(Mn_{0.75}Fe_{0.25})_2O_3$ in the following. A second heat treatment step for 4 h at 1050 °C in air had the purpose to ensure adequate mechanical strength and increase the cycling stability of the material. Due to shrinkage of the granulated particles upon heat treatment a particle size range of about 1–3 mm was obtained for the experimental study. The detailed preparation method is described in an associated paper on a thermodynamic and kinetic analysis of this technical grade storage material (Wokon et al., 2017). The minimum particle size of ~1 mm was chosen to prevent fluidization under the applied measurement conditions as well as to minimize parasitic losses due to the occurrence of lower pressure drops over the bed in contrast to powder material. The maximum particle size of ~3 mm has been defined to minimize the influence of potential boundary effects on the fluid flow at the tube wall as well as to ensure comparable reactivity between small and large particles (exclusion of internal diffusion resistance within larger particles). An X-ray powder diffraction pattern of the binary oxide in the oxidized state is presented in Section 3.4, indicating the material to be of single phase cubic bixbyite structure $(Mn_{0.75}Fe_{0.25})_2O_3$.

Thermal analysis of the material revealed an average weight loss of about 3.181% in the reduction step, which is lower than the expected weight loss of 3.368% given by the stoichiometry of the reaction in Eq. (3). Based on this observation about 94.4% of the technical grade redox material is considered reactive, the remaining 5.6% inert. Consequently, for the examinations in this work a weight loss of ~3.181% is adopted as complete conversion of the reaction.

2.2. Reactor and test rig

A packed bed configuration has been chosen for the storage reactor, in order to analyze the main influencing facets and demonstrate the heat effect of the TCS concept based on redox reactions. In comparison to continuous concepts with a moving reaction material, a large impact of mechanical stress on the behavior of reactive particles can be widely excluded. Thus, a tube reactor for a directly permeated packed bed of granules has been designed and implemented in lab-scale. Air simultaneously serves as HTF and carrier of the reactant O_2 . In this regard a direct contact heat transfer between the gas phase and the solid metal oxide storage material is facilitated. This can be referred to as a directly heated (charging) and cooled (discharging) reactor concept for TCS. An additional high temperature heat exchanger is therefore not necessary. Typically, in the charging stage of a technical scale

regenerator-type storage system the HTF flow enters the storage from the top, whereas the direction of the flow is reversed in the discharging stage. It has to be noted, that charging as well as discharging in the current work is realized by means of an air flow passing through the reactor solely from the bottom to the top, so that a fairly uniform initial bed temperature serves as starting point and final point of each experiment, respectively. Consequently, an axial thermal stratification along the bed height is not formed and was also not in the focus of this study.

The reactor tube made of nickel-based alloy 2.4856 (Inconel 625) has an inner diameter of 54.3 mm with a wall thickness of 2.9 mm. The actual reaction chamber containing the reactive packed bed of metal oxide granules, as shown in Fig. 2 (left), has a total height of 195 mm. Sheath thermocouples (Nicrobell® sheath alloy) of type N with an insulated measuring point were implemented for all temperature measurements in the experimental setup. The tolerance of the class 1 thermocouples amounts to $\pm 0.004 \cdot |9|$ in the range of 375–1000 °C. Four thermocouples ($\varnothing = 1$ mm) are positioned in the center along the axis of the packed bed (Fig. 2, left) with a height of 10 mm (ϑ_1), 50 mm (ϑ_2), 90 mm (ϑ_3) and 130 mm (ϑ_4) above a gas distribution disc (fused silica frit, porosity P1), in order to measure the reaction progress in terms of a temperature front along the bed height. Along the axis the radial heat flows have the lowest influence on the reaction temperatures, owing to the intrinsically low thermal conductivity of the granular metal oxide bed. In order to measure the gas temperature at the inlet of the reactor ($\vartheta_{g,in}$), a thermocouple ($\varnothing = 1.5$ mm) was installed about 10 mm below the perforated plate holding the packed bed. The gas temperature at the outlet is monitored with a thermocouple ($\varnothing = 1$ mm) positioned approximately 10 mm above the packed bed ($\vartheta_{g,out}$). The reaction chamber is capped with a filter (fused silica frit, porosity P1) to retain possibly abraded metal oxide particles inside the chamber. The position of the reaction chamber within the experimental setup is shown in Fig. 2 (middle).

Fig. 3 illustrates the process flowsheet of the test rig, which has been designed to survey a TCS reactor based on metal oxides. An in-house developed electrical gas heater (2) is integrated into the reactor unit below the reaction chamber (1) in order to heat air or other compositions of O_2 and N_2 to the desired temperature for the experiments. The reactor tube is encased by a vertically arranged tube furnace (3), which is used to assist the gas heater and heat up the reaction bed as well as to minimize thermal losses to the ambience.

According to the prospective application oil-free, dry and filtered ambient air is used, which is provided by a bundle of compressed air (DIN EN 12021). Gas flow rates and the composition of mixtures of nitrogen 5.0 and oxygen 4.8 are adjusted by means of (4) three mass flow controllers (MFCs for Air/ N_2 in the range of 0.8–40 NL/min, MFC for O_2 in the range of 0.1–5 NL/min, all exhibiting an accuracy of $\pm 0.5\%$ of reading plus $\pm 0.1\%$ of full scale, Bronkhorst HI-TEC). A gas mixing chamber (5) provides homogeneous mixing of O_2 and N_2 in the case of cooling in atmospheres of reduced oxygen content. The maximum gas flow rate is restricted to 15 NL/min in the current experimental setup to ensure the attainment of the desired gas temperatures at the inlet of the packed bed.

Above the reactor tube the off-gas is cooled to about room temperature with an integrated HEPA filter (7). Subsequently, the gas is filtered by means of a HEPA filter. Five thermal shields consisting of nickel-based alloy 2.4856 (Inconel 625) disks and insulation layers, respectively, are arranged between the reactor unit and the water cooler to reduce the radiation of heat from the upper filter of the reaction chamber towards the cooler (see Fig. 2, middle).

A gas analysis (6) with a paramagnetic oxygen measurement (NGA-2000 MLT-2 multi-component gas analyzer with built-in



Fig. 2. Geometry of the reaction chamber with locations of thermocouples in the packed bed of metal oxide (left); position of the packed bed storage reactor integrated in a tube furnace with additional gas/air heater below the bed (middle); experimental setup of the test rig (right).

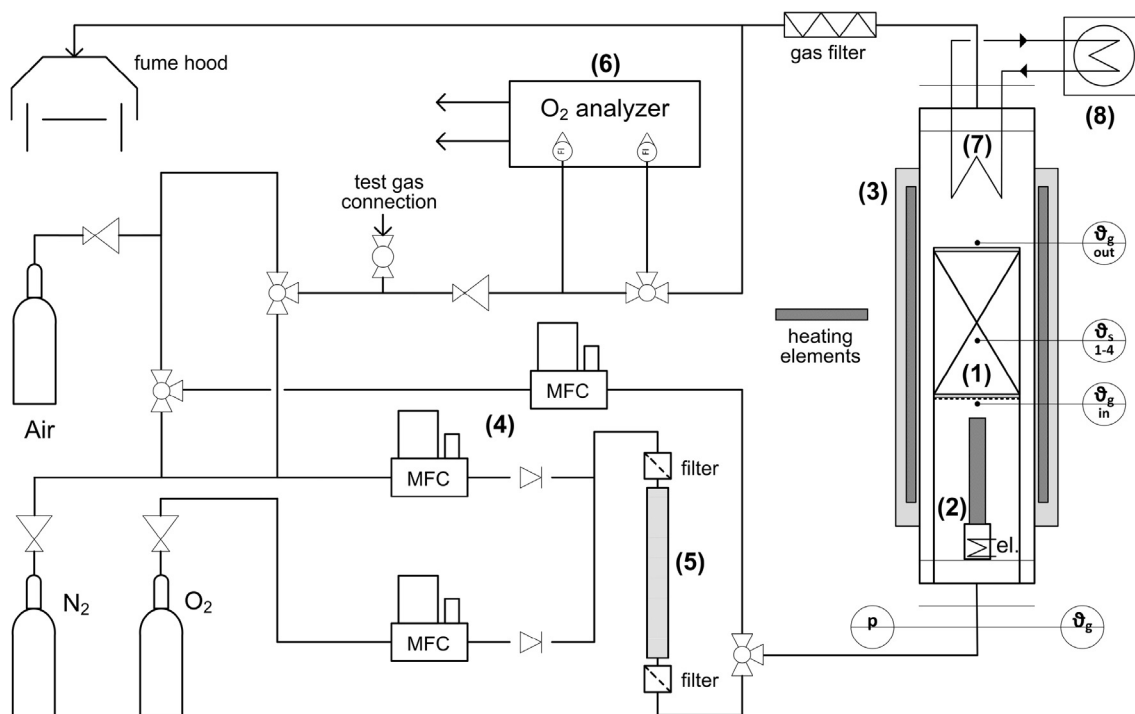


Fig. 3. Process flowsheet of the laboratory-scale test rig: Packed bed tube reactor (1), electrical gas/air heater (2), tube furnace (3), gas supply (4), gas mixing chamber (5), oxygen gas analyzer (6), gas cooler (7) and laboratory heat exchanger (8).

pressure and temperature compensation, Emerson Process Management | Rosemount Analytical) is used to record the O₂ concentration upstream ($\sigma_{O_2,in}$) and downstream the reactor unit ($\sigma_{O_2,out}$), in order to track the reaction progress and determine the reaction conversion. The test rig is open to the fume hood dismissing the off-gas stream, which is why all measurement series are conducted at atmospheric pressure.

The installation of a pressure transducer (Siemens SITRANS P200, 0–2.5 bar g) downstream the MFCs enables the determination of the pressure drop across the packed bed of metal oxide par-

ticles at room temperature or the entire setup during the experiments by indicating the present overpressure with a typical error of ± 6.25 mbar (± 12.5 mbar max). In addition, the absolute ambient pressure (Siemens SITRANS P200, 0–4 bar a) is monitored to determine the corresponding p_{O_2} at the gas outlet of the setup, calculated based on the product of the volume fraction of oxygen in the air flow (which equals the molar fraction of O₂ in air) and the ambient pressure in the laboratory. The entire test rig (Fig. 2, right) is controlled and regulated by the implementation of a programmable logic controller.

2.3. Experimental procedure for lab-scale experiments

The reaction chamber was filled with 471.2 g of granulated material in the oxidized state $(\text{Mn}_{0.75}\text{Fe}_{0.25})_2\text{O}_3$, resulting in a bed height of approximately 15.2 cm prior to gas flow and chemical reaction. Thermocouple ϑ_4 is located roughly 2 cm below the top layer of particles in the bed. The bulk density ρ_{bulk} of the loose $(\text{Mn}_{0.75}\text{Fe}_{0.25})_2\text{O}_3$ granule bed is around 1.353 g/cm^3 . Although the granulated material can be assigned to Geldart group D, the possibility of fluidization can be excluded under the applied measurement conditions working with granule sizes larger than 1 mm (Geldart, 1973).

Assuming full conversion in the course of the reduction reaction, a mass loss of 3.181% due to the release of oxygen can be taken into account (see Section 2.1). This correlates to an amount of 14.989 g ($m_{\text{O}_2, \text{max}}$) or 0.468 mol O_2 ($n_{\text{O}_2, \text{max}}$) correspondingly, which can be maximally released and taken up by the metal oxide in the course of the redox cycle. The mass balance for O_2 around the reactor unit allows to determine the molar reaction rate of the material in the reactor, expressed in terms of the rate of oxygen release or uptake $\dot{n}_{\text{O}_2, \text{rxn}}$. Integration of the molar rate of reacted oxygen over the reaction time gives the accumulative amount of oxygen $n_{\text{O}_2, \text{rxn}}$, released during the reduction step and taken up during the oxidation step, respectively. The corresponding reaction conversions X_{Red} and X_{Ox} can be derived from dividing the respective experimentally determined amount of reacted oxygen $n_{\text{O}_2, \text{rxn}}$ by the maximum amount of convertible oxygen $n_{\text{O}_2, \text{max}}$ to be transferred for complete conversion.

Overall, 17 cycles are performed with a single batch of storage material. A complete redox cycle consists of the endothermic reduction of $(\text{Mn}_{0.75}\text{Fe}_{0.25})_2\text{O}_3$ to $(\text{Mn}_{0.75}\text{Fe}_{0.25})_3\text{O}_4$ and the reverse exothermic oxidation step, also referred to as thermal charging and discharging of the storage thereafter. One redox cycle is carried out per day, cooling down the packed bed to room temperature under a flow of air after the performance of each cycle. The experimental procedure is described prior to the results of each measurement series. An overview of the experimental campaign is specified in Table 1.

In this work only selected experiments are discussed for the disclosure of the influencing effects on metal oxide based TCS with direct contact heat transfer between the HTF air and the solid inventory. Experimental conditions for a reference redox cycle (2nd, 6th, 9th and 17th) – denoted reference experiment below –

have been defined. This cycle is performed in between the individual series of measurements studying different parameter variations, in order to examine the material regarding its cycling stability and to ensure the comparability of the results obtained from parameter variations.

3. Experimental results and discussion

In the first part of the study the evolution of characteristic temperature profiles along the bed height is outlined and interpreted for a typical charging and discharging process of the storage reactor, respectively. In the second and third part, three parametric studies are conducted to examine different operating parameters influencing the behavior of a reactor with direct heat transfer, including the mass flow rate directed through the reactor as well as the gas inlet and initial bed temperature $\vartheta_{\text{g, in}} = \vartheta_0$. It is exemplarily referred to the bed temperatures ϑ_1 and ϑ_3 , located axially 1 cm and 9 cm above the gas distribution disc, for the representation of the temperature profiles in the granular packed bed. The cycling stability behavior of the material and packed bed properties are addressed in the last part of this work.

3.1. Characteristics of temperature driven thermal charging and discharging

Thermal charging is always performed by means of a temperature change to initiate the reduction. In this case the reaction can be considered temperature driven. At first the packed bed of granules is heated up to an initial temperature of 940 °C, using a constant air flow rate of 10 NL/min. The initial conditions of the experiment – prevalent $p\text{O}_2$ and initial temperature of the packed bed – do not allow the reduction reaction to take place. As soon as thermal equilibrium has been maintained for at least 20 min, the air temperature at the inlet of the reaction chamber as well as the tube furnace temperature are simultaneously raised to 1040 °C. The left part of Fig. 4 illustrates the reference experiment for thermal charging, showing the gas inlet temperature ($\vartheta_{\text{g, in}}$), the temperature profiles along the height of the packed bed (ϑ_1 – ϑ_4) and the O_2 concentration profile downstream the reaction chamber ($\sigma_{\text{O}_2, \text{out}}$). Point zero indicates the assignment of the temperature increase by 100 K.

In the beginning the solid storage material is heated up along the entire bed height due to the storage of sensible heat. The ther-

Table 1
Measuring plan for thermal charging (reduction) and discharging (oxidation) both performed in air.

Cycle No. ^a	\dot{V}_{Air} / (NL/min)	Reduction		Oxidation	
		$\vartheta_{\text{g, in}} = \vartheta_{\text{Furnace}}$ / °C	Initiation	$\vartheta_{\text{g, in}} = \vartheta_{\text{Furnace}}$ / °C	
(1)	10	940 → 1040	2% O_2 → Air	$\vartheta_0 = \vartheta_{\text{g, in}} = 850$	
2	10	940 → 1040	2% O_2 → Air	$\vartheta_0 = \vartheta_{\text{g, in}} = 850$	
3	10	940 → 1040	2% O_2 → Air	$\vartheta_0 = \vartheta_{\text{g, in}} = 825$	
4	10	940 → 1040	1% O_2 → Air	$\vartheta_0 = \vartheta_{\text{g, in}} = 800$	
5	10	940 → 1040	2% O_2 → Air	$\vartheta_0 = \vartheta_{\text{g, in}} = 875$	
6	10	940 → 1040	2% O_2 → Air	$\vartheta_0 = \vartheta_{\text{g, in}} = 850$	
7	15	940 → 1040	2% O_2 → Air	$\vartheta_0 = \vartheta_{\text{g, in}} = 825$	
8	5	940 → 1040	2% O_2 → Air	$\vartheta_0 = \vartheta_{\text{g, in}} = 825$	
9	10	940 → 1040	2% O_2 → Air	$\vartheta_0 = \vartheta_{\text{g, in}} = 850$	
(10)	10	940 → 1040	–	–5 K/min: 1040 → 400 ^b	
11	10	940 → 1040	–	–5 K/min: 1040 → 400	
(12)	10	940 → 1040	–	–3.5 K/min: 1040 → 400	
(13)	5	940 → 1040	–	–3.5 K/min: 1040 → 400	
(14)	15	940 → 1040	–	–3.5 K/min: 1040 → 400	
(15)	10	940 → 1040	–	–2 K/min: 1040 → 400	
(16)	10	940 → 1040	–	–2 K/min: 1040 → 400	
17	10	940 → 1040	2% O_2 → Air	$\vartheta_0 = \vartheta_{\text{g, in}} = 850$	

^a Cycles in brackets are not displayed and discussed in this paper.

^b Tube furnace turned off during cooling process.

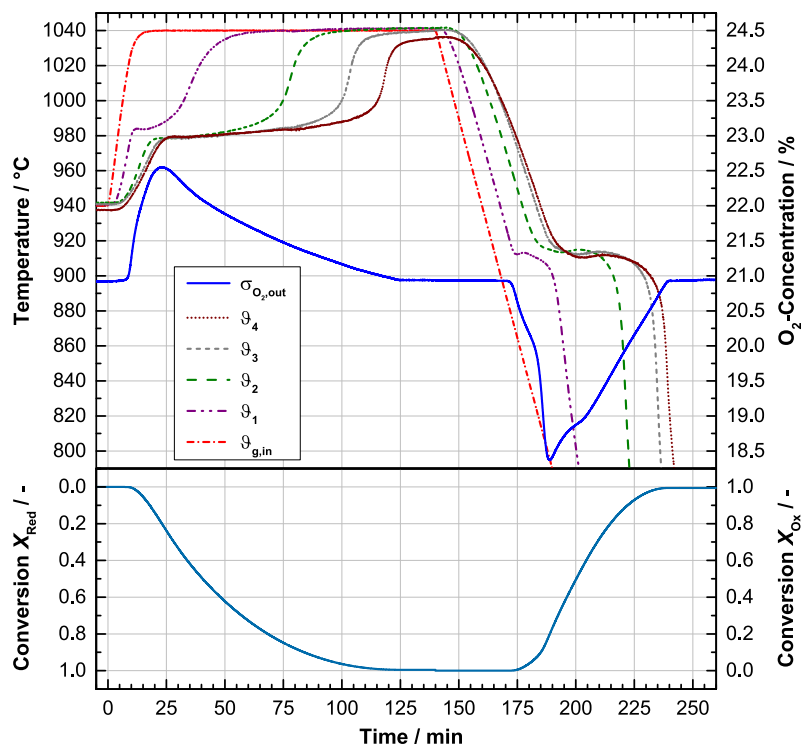


Fig. 4. Progress of the charging stage 6 ($\text{Mn}_{0.75}\text{Fe}_{0.25}\text{O}_3 \rightarrow 4(\text{Mn}_{0.75}\text{Fe}_{0.25})_3\text{O}_4 + \text{O}_2$) upon increase of air inlet and tube furnace temperature from 940 °C to 1040 °C (reference experiment) and excerpt of the discharging stage 4 ($(\text{Mn}_{0.75}\text{Fe}_{0.25})_3\text{O}_4 + \text{O}_2 \rightarrow 6(\text{Mn}_{0.75}\text{Fe}_{0.25})_2\text{O}_3$) with a cooling rate of air inlet and tube furnace temperature of 5 K/min, both at 10 NL/min air (11th redox cycle).

thermodynamic equilibrium of the redox reaction in air is being exceeded during this phase. Faster rates of heating in the lower part of the bed can be explained by the higher heat input via the HTF entering at the bottom, in comparison to the thermal energy which is introduced via the tube furnace across the tube wall along the entire height of the bed.

Approximately 5 min after assigning the temperature increase, the endothermic reduction of $(\text{Mn}_{0.75}\text{Fe}_{0.25})_2\text{O}_3$ particles is triggered in the lowest part of the bed, indicated by the beginning of oxygen release. As soon as the reaction zone has reached the position of the first thermocouple (ϑ_1) after about 12 min, a brief temperature drop to a level of about 983.5 °C can be observed due to the absorption of thermal energy. The short reaction time and comparatively high temperature in this region is due to the proximity of ϑ_1 to the bottom of the bed, where heat input by the entering air is more intense. As soon as $(\text{Mn}_{0.75}\text{Fe}_{0.25})_2\text{O}_3$ has been converted to $(\text{Mn}_{0.75}\text{Fe}_{0.25})_3\text{O}_4$ in the lower part, temperature ϑ_1 begins to rise up to 1040 °C owing to the storage of sensible heat. All bed temperatures show small signs of an initial overheating effect prior to the beginning of the reduction.

In contrast to the region of thermocouple ϑ_1 in the lower part, the storage material in the middle and upper part of the bed exhibits the formation of fairly constant temperature plateaus for longer periods. In the process thermal energy is absorbed due to the advance of the endothermic reduction, preventing the granules from further heating up. The lowest temperature plateaus are observed in the middle part for ϑ_2 and ϑ_3 , which amount to about 978.5 °C. This value is in good accordance with the experimentally determined (STA) temperature threshold for the reduction onset in air (Wokon et al., 2017), as described above. Overall, the reaction proceeds at temperature plateaus close to the equilibrium, where only slow reaction rates can be attained. Based on those low temperature levels and long duration of the reaction in this region, it

can be assumed, that the reduction step is mainly limited by heat transfer into the packed bed.

Input of thermal energy by means of the HTF entering at the bottom leads to the development of a pronounced temperature front gradually travelling in flow direction through the packed bed. The front indicates the termination of the reaction in a certain part of the bed, followed by sensible heating up to 1040 °C. The charging stage is completed after a total time of 124.7 min, once the O₂ concentration at the outlet has returned to the baseline level and temperatures along the bed height have reached constant values close to 1040 °C. As heat losses appear to be higher in the upper region of the bed, ϑ_4 has only reached a value somewhat lower than 1040 °C at the end of the experiment. The period of O₂-release accounts for only 120.9 min. The reaction reaches nearly complete conversion of about 99.5% (Fig. 4, bottom left), calculated based on the released amount of O₂.

A typical storage discharging experiment conducted with decreasing temperature is illustrated on the right hand side of Fig. 4. The packed bed is cooled down with a constant cooling rate of the gas inlet temperature of 5 K/min at 10 NL/min air. This mode is subsequently denoted dynamic operation mode for thermal discharging and allows to study the redox reactivity under fairly controlled conditions. In order to ascertain that consistent boundary conditions can be achieved, equal cooling rates are adjusted for the air inlet and tube furnace temperature. A rate of 5 K/min constitutes the maximum possible cooling rate to challenge the material appropriately, but still control the HTF inlet temperature at a constant rate in this work.

At first the sensible part of stored energy is extracted and the packed bed therefore cooled down along the bed height. The thermodynamic equilibrium of the redox reaction in air is being exceeded during this cooling phase. The reaction onset in the lowest part of the bed is indicated by the recorded oxygen uptake. It

can be observed, that the $(\text{Mn}_{0.75}\text{Fe}_{0.25})_3\text{O}_4$ oxidation is initiated in sequence along the axis throughout the discharging period. All bed temperatures show small signs of initial undercooling prior to the beginning of the oxidation, followed by a small temperature increase of 1.5–2 °C. This phenomenon can be ascribed to the energy necessary to overcome the activation energy barrier for nucleation, hence initiating nucleation and subsequent crystal growth. The rather short temperature plateau of ϑ_1 is again a consequence of the high cooling capacity of the entering HTF at this stage, while the granular particles above are still subject to sensible heat extraction. All temperature profiles exhibit steady temperatures over periods of up to 15 min. This clearly accentuates the possibility to stabilize bed temperatures due to the release of the heat of reaction, while the gas inlet and tube furnace temperature are constantly declining at 5 K/min. The levels of “self-adjusted” temperature plateaus are in the range of 912–915 °C, which are also fairly consistent with the experimentally determined (STA) temperature threshold for the oxidation onset in air (Wokon et al., 2017), as described above.

The oxidation reaction is completed after about 69.3 min, once the O_2 concentration at the outlet has risen to the baseline level. A total conversion of about 99.4% was identified based on the absorbed amount of O_2 (Fig. 4, bottom right). Overall, the duration of the oxidation step is significantly shorter than the corresponding reduction step. This can be explained by the evidently larger temperature gradient between the HTF at the inlet and the solid temperatures in the process of the oxidation reaction, eventually increasing the rate of heat removal.

Fig. 4 discloses the appearance of the above-mentioned thermal hysteresis, which amounts to roughly 63.5 °C in this case, thermally decoupling the reduction and oxidation step under technically relevant experimental conditions. Further assessment of the oxidation step via thermal analysis revealed, that the oxidation is primarily subject to kinetic limitations closer to the equilibrium, which distinctive behavior is further addressed in an associated paper on the thermodynamic and kinetic characteristics of this technical grade material (Wokon et al., 2017).

3.2. Temperature driven thermal charging: Flow rate variation

The utilization of air as HTF and purge gas to take up oxygen during the reduction has a strong impact on the chemical reaction in a directly permeated storage reactor. The heat capacity rate $C_{\text{HTF}} = c_{p,g} \cdot dm_g/dt$ resulting from the adjusted HTF flow rate generally constitutes the most important parameter to regulate the heat input and attainable thermal power level of a storage reactor. Therefore, the influence of different air flow rates on the reactor behavior is examined more closely. The packed bed is heated up to a 940 °C at an air flow rate of 5 NL/min, 10 NL/min or 15 NL/min, respectively. As soon as thermal equilibrium has been held for at least 20 min, the setpoints of the air inlet temperature ($\vartheta_{g,\text{in}}$) as well as the tube furnace temperature are simultaneously increased to 1040 °C. The $p\text{O}_2$ at ambient conditions amounts to ~21.2 kPa. Fig. 5 illustrates the experimental results of the charging experiments. Point zero marks the assignment of the temperature increase by 100 K. Generally, the rate of sensible heating turns out to be somewhat slower in the case of the lowest flow rate. About 4–6 min after assigning the temperature increase, the equilibrium condition of the redox reaction in air has already been exceeded for particles in the lowest part of the bed. Oxygen is released due to the initiation of the $(\text{Mn}_{0.75}\text{Fe}_{0.25})_2\text{O}_3$ reduction. According to the adjusted mass flow rates, the O_2 concentration profiles reflect the expected changes owing to the evolution of O_2 . The highest change with a maximum of ~23.8% O_2 was detected for 5 NL/min, whereas the flow rate of 15 NL/min yields the lowest change with a maximum of ~22.0% O_2 .

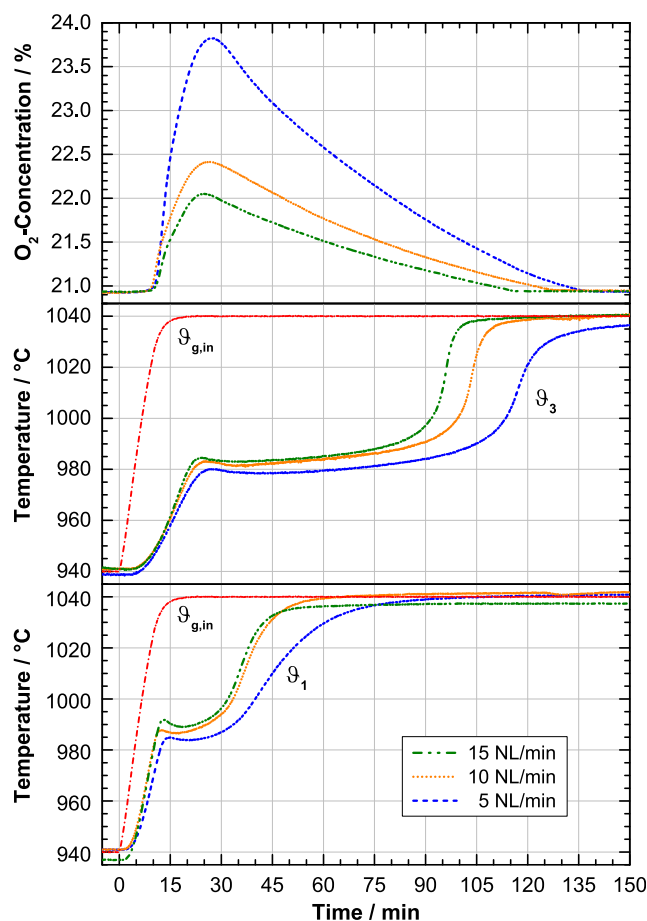


Fig. 5. Flow rate variation in storage charging step 6 ($\text{Mn}_{0.75}\text{Fe}_{0.25})_2\text{O}_3 \rightarrow 4(\text{Mn}_{0.75}\text{Fe}_{0.25})_3\text{O}_4 + \text{O}_2$ performed by increasing the air inlet and tube furnace temperature from 940 °C to 1040 °C: 5 NL/min, 10 NL/min and 15 NL/min air.

Temperatures ϑ_1 in the lower part of the bed are generally higher, as the incoming air flow at high temperature leads to a stronger heating effect. Since part of the thermal energy transported by the fluid flow has already been utilized to dissociate $(\text{Mn}_{0.75}\text{Fe}_{0.25})_2\text{O}_3$ and heat up the reduced material in the bottom part, only a lower temperature difference between fluid and solid is available in the upper part of the bed. Consequently, heat transfer in the upper part is lower, leading to higher reaction times and longer periods of fairly constant temperature plateaus, clarified by ϑ_3 in Fig. 5. With rising air flow rate this plateau becomes shorter. Higher gas velocities entail an enhancement of the heat transfer coefficient between gas and solid phase. Moreover, the adjustment of higher mass flow rates also implies higher heat capacity rates C_{HTF} , causing higher thermal power input. The transfer of thermal energy from the HTF to the solid hence increases, which provokes an accelerated reaction progress. All registered temperature levels (between ~978.5 °C and ~983 °C) during the proceeding reduction reaction are in the range of the technically relevant temperature threshold of ~981.7 °C for the reduction onset, calculated at a $p\text{O}_2$ of 21.2 kPa based on the experimentally determined $p\text{O}_2$ - T correlation, which has been briefly described in Section 1 (Wokon et al., 2017).

In summary, the variation of the adjusted mass flow rate has a significant impact on the charging time. This can be well distinguished by means of the O_2 evolution curves as well as the length of the temperature plateaus, also reflected in the offset of the respective sensible heating curves after completion of the reaction at the position of sensor ϑ_3 . Complete conversion within the feasi-

ble accuracy of the evaluation was achieved in all experiments. The total reaction time from the beginning of the temperature increase until the end of O_2 release amounts to ~ 138.0 min (5 NL/min), ~ 127.6 min (10 NL/min) and ~ 116.3 min (15 NL/min). As expected, the highest maximum reaction rate has been reached in the case of 15 NL/min. Correspondingly, the experiments at 10 NL/min and 5 NL/min yielded lower maximum reaction rates. For the charging stage the conclusion can be drawn, that thermal power input by means of the HTF as well as heat transferred from the tube wall to the solid storage material are the limiting factors under the applied operating conditions, the latter also attributed to the intrinsically poor thermal conductivity of metal oxides. Besides higher HTF mass flow rates, demonstrated in this section, a raise of the charging temperature generally leads to higher reaction rates and thus enhanced charging performance as well.

3.3. Thermal discharging at constant gas inlet temperature

Significant factors determining the reactor discharging behavior comprise the particle reaction rate, heat transfer, mass transport of O_2 as well as the maximum possible enthalpy difference $\Delta H_{g,max}$ of the HTF flow between reactor inlet and outlet. Compared to the dynamic mode of operation for thermal discharging, described in Section 3.1, an alternative approach enables to study the release of thermal energy at a constant gas inlet temperature (defined boundary condition), inducing the reaction by means of a sudden change of the pO_2 . In this case the reaction can be considered pressure driven. An operation mode with constant boundary conditions at the inlet of the packed bed – along with a uniform initial bed temperature as starting point – constitutes an effective way to investigate the influence of various gas inlet $\vartheta_{g,in}$ and initial bed temperatures ϑ_0 as well as different HTF mass flow rates on the specified macroscopic parameters.

3.3.1. Flow rate variation

According to the variation of the air flow rate in the preceding charging stage (see Section 3.2) the influence of different heat capacity rates C_{HTF} on the reaction performance along with heat and mass transfer effects is also surveyed in the exothermic oxidation step, adjusting the air flow rate through the reactor to 5 NL/min, 10 NL/min and 15 NL/min, respectively. After the reduction step the packed bed of granular $(Mn_{0.75}Fe_{0.25})_3O_4$ is cooled down to an arbitrarily chosen gas inlet and initial bed temperature of $825\text{ }^\circ\text{C}$ under a flow of 2% O_2 in N_2 at the respective flow rate for the reaction, since the atmosphere with reduced O_2 concentration inhibits the initiation of the oxidation. Once thermal equilibrium has been reached and maintained in the packed bed over a period of at least 20 min, the experiments are triggered by switching the gas flow to air, which corresponds to an abrupt elevation of the pO_2 from ~ 2.0 kPa to ~ 21.2 kPa (referred to ambient conditions at the gas outlet). The air inlet ($\vartheta_{g,in}$, not shown) as well as the tube furnace temperature are held at $825\text{ }^\circ\text{C}$ throughout the entire period of the corresponding experiment. Results of the thermal discharging of the storage are illustrated in Fig. 6, the gas change indicated by the point of origin. The experiments clearly reveal the superimposition of different phenomena in terms of the particle reaction rate as well as heat and mass transfer effects. In the following the impact of individual phenomenon on the discharging progression will be discussed.

The oxidation reactions are immediately initiated, since the prevailing conditions in the reactor thermodynamically favor the oxidized phase $(Mn_{0.75}Fe_{0.25})_2O_3$. Oxygen is taken up. At 10 NL/min and 15 NL/min all bed temperatures – indicated by ϑ_1 and ϑ_3 – show an instantaneous increase due to the release of the heat of reaction, causing a self-heating effect of the material. The presence of a strong driving force owing to the high degree of undercooling

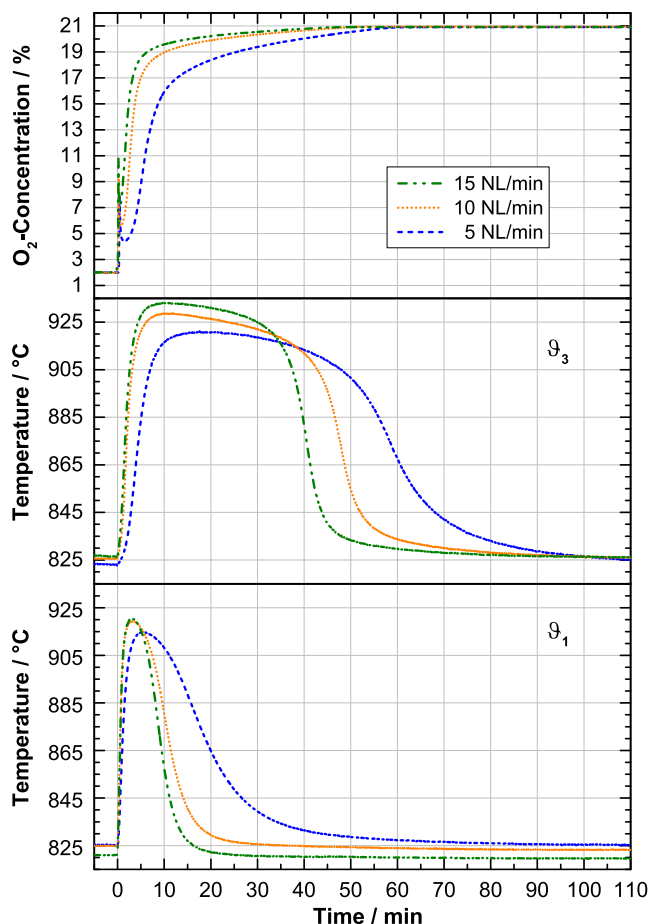


Fig. 6. Flow rate variation in storage discharging step 4 ($Mn_{0.75}Fe_{0.25})_3O_4 + O_2 \rightarrow 6(Mn_{0.75}Fe_{0.25})_2O_3$ with initial bed ϑ_0 and constant air inlet temperatures $\vartheta_{g,in}$ of $825\text{ }^\circ\text{C}$: 5 NL/min, 10 NL/min and 15 NL/min air.

of the granular particles becomes evident, when the gas flow is switched to air. Remarkably, 50% conversion has already been reached after ~ 4.2 min (15 NL/min) and ~ 5 min (10 NL/min), with the largest part of the released heat of reaction reflected in the sensible heating of the packed bed.

In accordance with the variation of air mass flow rates in the reduction step (see Section 3.2) similar results regarding heat transfer effects could be observed. Higher gas velocities due to rising gas flow rates generally lead to increased heat transfer coefficients between the solid particles and the gas phase. Moreover, higher mass flow rates imply enhanced heat capacity rates C_{HTF} , enabling to absorb a larger amount of thermal energy. This can be recognized by an acceleration of the reaction progress with higher air flow rates, as transfer of thermal energy from the reacting solid to the HTF is enhanced. At 15 NL/min the period of O_2 release is already over after ~ 48.2 min, whereas in the case of 5 NL/min the reaction proceeds only very slowly towards the end, reached at roughly 69.5 min. The maximum reaction rate, which can be derived from the O_2 concentration depicted in Fig. 6, decreases significantly with smaller flow rates. The overall discharging stage is completed, once the O_2 concentration at the outlet has reached a stable level – indicating the presence of pure air – and the initial thermal equilibrium within the packed bed has been resumed shortly after.

In all three cases the lowest temperature increase along with the fastest extraction of thermal energy via the HTF was registered by the sensor ϑ_1 for the material close to the inlet of the packed bed, where the granular material experiences the strongest initial

cooling effect due to the HTF entering the reactor at 825 °C. As expected, the most intense cooling effect emerges in the experiment with 15 NL/min. The conclusion can be drawn, that in the bottom part of the bed the reaction rate of the redox reaction poses the limiting factor.

In all experiments the temperatures in the middle and upper part of the bed reveal the largest temperature rise, reaching levels closer to the equilibrium, where the reaction rate decreases enormously. At this point the reaction mainly proceeds, as soon as the material experiences sufficient cooling by the HTF, slowly extracting the released thermal energy. This is reflected in the propagation of a temperature front from the bottom to the top. Maximum temperatures could always be observed within the initial 10–15 min of the reaction for ϑ_2 in the middle of the packed bed (ϑ_2 not shown). It can be assumed that in the region of ϑ_2 the HTF has already been heated up to its maximum possible temperature during the initial phase of the discharging step, which is why no more thermal energy can be transferred to and dissipated by the HTF in this case.

A maximum bed temperature of ~ 934 °C was registered for ϑ_2 in the case of 15 NL/min. In comparison, the technically relevant pO_2 - T correlation for the oxidation onset – experimentally derived by means of STA measurements in the cooling phase of the reduced material – gives a temperature threshold of ~ 920 °C at a pO_2 of 21.2 kPa (air) though (Wokon et al., 2017). Moreover, the “self-adjusted” temperature plateaus (912–915 °C) in the dynamic discharging mode described above turned out to be lower as well. As a particular degree of undercooling needs to be attained to initiate the reaction by thermal activation of nucleation, the oxidation reaction is generally subject to severe kinetic restrictions in those dynamic modes of continuous cooling down under air. This occurrence has been elaborately addressed in the associated paper (Wokon et al., 2017). In contrast, there seem to be no apparent limitations in the case of the strongly undercooled state of the reduced phase at 825 °C in the current runs. This is why in the presented study the reaction in air is able to reach temperatures closer to the equilibrium, therefore leading to packed bed temperatures somewhat higher than the temperatures calculated from the experimentally derived pO_2 - T dependency of the oxidation onset, irrespective of the locally lower O_2 concentration in the bed due to the O_2 uptake on the one hand as well as the somewhat increased local pO_2 due to the pressure drop over the entire experimental setup on the other hand.

It is particularly exceptional in this measurement series that the highest bed temperatures are reached for 15 NL/min, the experiment with the highest cooling capacity of the HTF. This occurrence can be directly ascribed to the open-loop storage operation with air as HTF, supplying the reactant O_2 : In general, the local minimum of the recorded O_2 concentration shortly after the initiation of the reaction denotes the point, where the highest reaction rate and thus the highest rate of heat release occurs, respectively. In the experiment applying a gas flow rate of 15 NL/min, providing the highest molar amount of O_2 for the reaction, the O_2 concentration shortly drops down to 7.1% due to the uptake of O_2 . A value of 5.6% O_2 is reached for 10 NL/min. At a flow rate of 5 NL/min, however, the O_2 concentration even drops down to 4.4%, held for the longest time in comparison to the experiments at higher flow rates. In this case the O_2 concentration in the bulk phase is not sufficient for the oxidation reaction to proceed with higher reaction rates. Thus, at a flow rate of 5 NL/min a spreading of the temperatures at different levels as well as different temperature maxima can be found along the bed height. The reaction does not take place immediately over the entire height of the packed bed, which becomes apparent in Fig. 6 (see ϑ_1 versus ϑ_3 within the initial 15 min). On the one hand, ϑ_1 close to the reactor inlet shows an abrupt increase, while on the other hand, temperature ϑ_3 towards the upper part exhibits a

delayed temperature rise. This might be attributed to an O_2 -depletion in the initial phase of the reaction, since most of the available O_2 is taken up in the bottom part of the packed bed, leading to the presence of a lower O_2 concentration in the upper region of the bed. As a result, at 5 NL/min reduced O_2 availability implies a reduced pO_2 and thus a decrease of the particle reaction rate according to the pO_2 - T dependency of the reaction.

In summary, the discharging performance at the lowest flow rate of 5 NL/min is mainly dominated by a decreased reaction rate due to a shortened availability of O_2 as well as by diminished heat transfer and heat transport capabilities, both effects eventually accounting for an elongated cooling process and longer reaction times at fairly constant temperature levels (see ϑ_3) compared to the experiments at higher flow rates. In contrast, higher thermal power output owing to the highest reaction performance can be accomplished in the experiment at 15 NL/min air (Fig. 6). As the HTF and source of O_2 are directly coupled in this open operation principle using air, the mutual interaction between the attainable thermal power level and the particle reaction rate has to be accounted for in future engineering and operation of a TCS reactor.

3.3.2. Temperature variation

A variation of the gas inlet temperature also represents a practical method to study the reaction performance in the discharging step, directly affecting the heat transfer and the maximum possible enthalpy change of the HTF flow from the inlet to the outlet of the packed bed. Four cycles at different air inlet $\vartheta_{g,in}$ and initial bed temperatures ϑ_0 were carried out, adjusting values between 800 °C and 875 °C in a step size of 25 °C, respectively. All experiments are performed under air at ~ 21.2 kPa (referred to ambient conditions) with a constant flow rate of 10 NL/min. In the case of 800 °C a cooling atmosphere of 1% O_2 ensures the prevention of a premature re-oxidation prior to the initiation of the oxidation by switching to air. A cooling atmosphere of 2% O_2 has been chosen for 825 °C, 850 °C and 875 °C. All temperatures can be assigned to the range closer to the equilibrium in air, which is characterized by decreasing reaction rates with rising temperature (Wokon et al., 2017). As soon as thermal equilibrium has been kept up for at least 20 min, the reactions are initiated by means of an increase of the pO_2 to ~ 21.2 kPa (referred to ambient conditions at the gas outlet). Fig. 7 shows the experimental results in terms of reaction conversion and temperatures. Rapid sensible heating of the packed bed indicates a fast self-heating effect ascribed to the release of chemically stored energy. Foremost, a large part of released energy is absorbed by the material itself, owing to the limitation by the C_{HTF} , respectively.

In all cases the most intense convective cooling could be observed in the bottom part of the packed bed close to the gas inlet, as ϑ_1 in Fig. 7 (bottom) shows the lowest temperature rise. This clarifies the influence of direct heat transfer from the solid particles to the HTF to dissipate the released heat of reaction. The evolution of the bed temperatures in the proximity to the gas inlet illustrates effectively, that higher temperatures closer to the equilibrium condition cannot emerge, if the rate of heat removal by the HTF is larger than the rate of heat release due to the chemical reaction. In other words, the heat of reaction cannot compensate for the maximum possible enthalpy change of the gas between the inlet condition and conditions closer to the equilibrium. Consequently, the lowest maximum temperature of ϑ_1 – moreover kept up for the shortest period – was recorded for a gas inlet temperature of 800 °C, as the corresponding gas flow exhibits the highest possible cooling capacity in this series of measurement. On that account, it can be stated that only for this comparatively more intense cooling conditions, the reaction rate of the granular material constitutes a limiting factor in the bottom area of the packed bed.

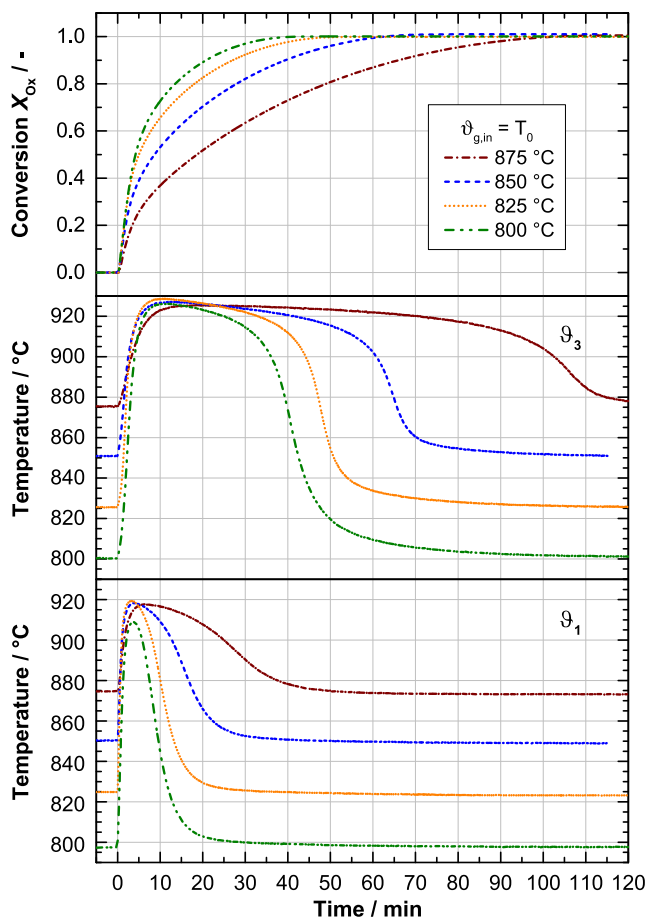


Fig. 7. Temperature variation in storage discharging step 4 ($\text{Mn}_{0.75}\text{Fe}_{0.25}\text{O}_3 + \text{O}_2 \rightarrow 6(\text{Mn}_{0.75}\text{Fe}_{0.25})_2\text{O}_3$) at 10 NL/min air: initial bed and constant air inlet temperatures $\vartheta_0 = \vartheta_{g,\text{in}}$ of 800 °C, 825 °C, 850 °C and 875 °C.

Different bed temperature maxima are attained depending on the air inlet and initial bed temperature. The experiment at 825 °C revealed the highest bed temperatures at every measuring point along the axis in comparison to the other measurement conditions. In the course of each experiment the reaction rate strongly decreases, once particle temperatures closer to the equilibrium of the reaction have been reached. As described in the previous section, the highest temperature in the bed was always observed for ϑ_2 (not displayed).

At the lowest air inlet and initial bed temperature of 800 °C the material experiences both the largest initial undercooling upon switching to air, implying a strong driving force for the phase transition, and the highest cooling effect via the HTF. Gas entering the reactor at lower temperatures has a higher potential capacity to absorb thermal energy due to a higher possible driving temperature gradient ΔT between the HTF, entering the reaction chamber at 800 °C in this case, and the solid temperatures reached during the reaction. Due to the initially high reaction rates at 800 °C the released thermal energy primarily leads to the sensible heating of the particles within the initial phase of the experiment, as the heat capacity rate of the HTF is limiting. Higher reaction conversion was observed in this phase compared to experiments at elevated temperatures. It can be viewed in Fig. 7 that 50% conversion has already been reached after ~ 4.2 min in the case of 800 °C, in contrast to a reaction period of 18.7 min in the case of 875 °C. The end of the O_2 uptake is thereby already registered after about 46.7 min at 800 °C, which marks the shortest period within all conducted experimental runs. For comparison the overall reaction

time at 875 °C amounts to about 117.9 min. Overall, full conversion has been reached in all cases.

In summary, a decrease of the air inlet temperature (and initial bed temperature) in the investigated range yields an accelerated reaction process owing to an enhanced cooling effect, which leads to a higher dissipation of the released heat of reaction by the HTF and therefore higher discharging performance. On this account the maximum possible enthalpy change of the adjusted gas flow between the inlet and outlet of the packed bed constitutes the limiting factor in the examined temperature operating range. Consequently, the thermal power output can generally be controlled by defining the HTF inlet temperature and mass flow rate.

3.4. Cycling test and material characterization

In general, a thermochemical storage material can only be implemented on a larger scale, if it exhibits the ability to maintain its integrity over repeated cycling, both physically and chemically. Cycling stability is considered a key feature of a TCS material, implying the progress of a reversible redox reaction over innumerable cycles without degradation of the material reactivity owing to microstructural changes, which could be caused by phase changes or sintering effects. Furthermore, the mechanical stability of the particles – characterized by low particle attrition and high crushing strength – should be sustained. Especially sintering effects can be more pronounced in larger sample masses and may influence the performance of a packed bed. Macroscopic effects, such as potential channeling, might also impair the redox behavior of the packed bed on the whole. However, cycling data on the basis of a packed bed of ~ 471 g of granular $(\text{Mn}_{0.75}\text{Fe}_{0.25})_2\text{O}_3$ material has not been available so far. For that purpose a total of 17 redox cycles have been performed on a larger scale. A reference redox cycle was repeated four times (2nd, 6th, 9th and 17th cycle) under identical experimental conditions in between the carrying out of different parameter studies, most of which have been presented above. In the scope of the parametric studies this allows to verify the comparability of the experiments among each other. Additionally, the cycled material can be further analyzed and compared to the original material.

The results of the temperature driven charging steps are displayed in Fig. 8 (left). We can assert that the heating-up period of the material – prior to the reaction onset – remained constant for all cycles, demonstrating good repeatability. During the course of the endothermic reaction a value of ~ 982 °C could be observed for the level of the temperature plateau ϑ_3 in the 2nd cycle, whereas the temperature dropped to ~ 979 °C in the 9th and to ~ 976 °C in the 17th cycle, closer to the equilibrium temperature. Temperature ϑ_1 indicates the same trend. Accordingly, the O_2 evolution onset was registered somewhat earlier in the 17th cycle. The progress of the O_2 evolution curves in the 9th and 17th cycle reveals a slight tendency towards faster reaction rates and somewhat shorter reaction times, also indicated by the conversion curves in Fig. 8 (left). The overall reaction time in terms of O_2 release took ~ 122.5 min in the 2nd cycle, whereas a duration of ~ 118.5 min could be determined for the 17th cycle.

In all reference charging experiments complete conversion has been achieved within the possible accuracy of the evaluation. Overall, the packed bed did not exhibit any reactivity deterioration during the reduction step, which is why the diffusion of O_2 out of the material during the phase transition does not seem to become a limiting factor.

The right hand side of Fig. 8 shows the experimental results of the subsequent discharging steps at a constant air inlet and initial bed temperature of 850 °C, assigning a change of the $p\text{O}_2$ to initiate the reaction. For simplification the preceding cooling phase in 2% O_2 atmosphere is not depicted. The highest O_2 uptake rate in the

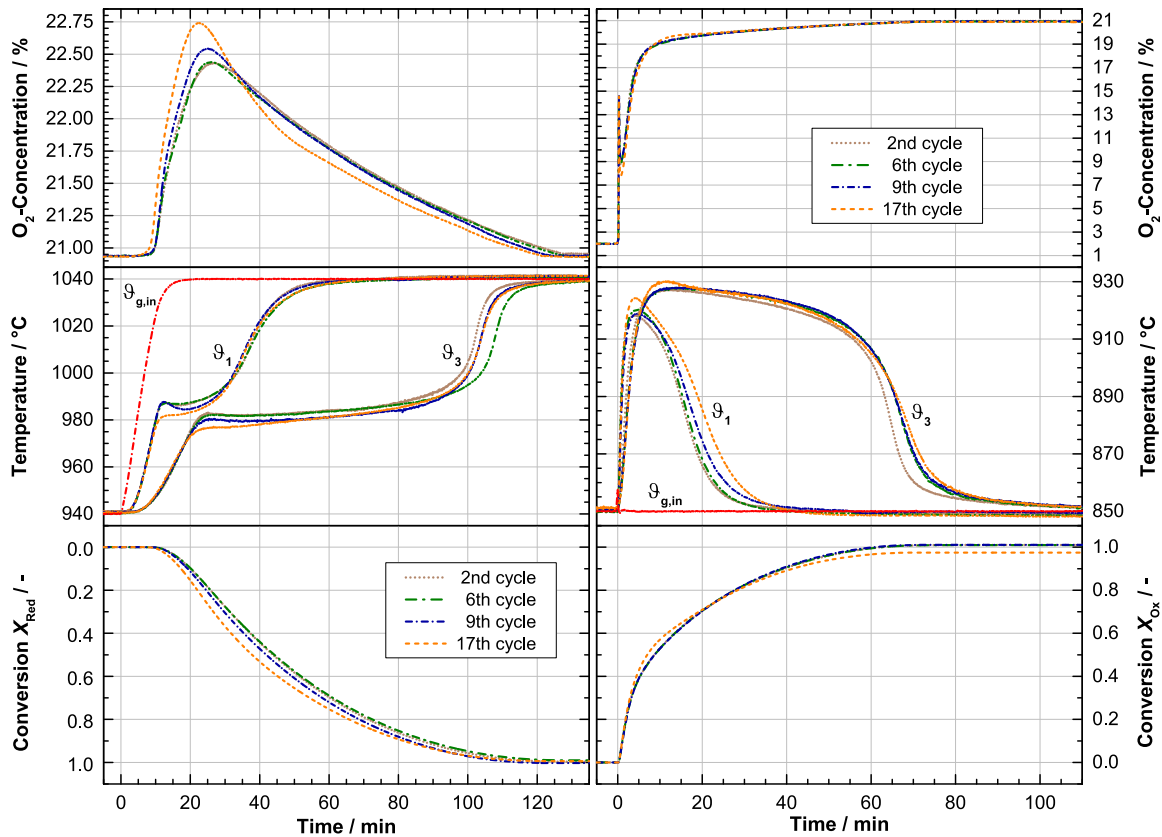


Fig. 8. Cycling test over 17 redox cycles at 10 NL/min air: Progress of thermal charging, $6 (\text{Mn}_{0.75}\text{Fe}_{0.25})_2\text{O}_3 \rightarrow 4 (\text{Mn}_{0.75}\text{Fe}_{0.25})_3\text{O}_4 + \text{O}_2$, conducted by means of an increase of the air inlet and tube furnace temperature from 940 °C to 1040 °C (left); progress of thermal discharging, $4 (\text{Mn}_{0.75}\text{Fe}_{0.25})_3\text{O}_4 + \text{O}_2 \rightarrow 6 (\text{Mn}_{0.75}\text{Fe}_{0.25})_2\text{O}_3$, conducted at a constant air inlet and tube furnace temperature of 850 °C (right).

initial phase of the reaction was observed for the 17th cycle, which also yielded the highest temperature values in the packed bed, depicted in Fig. 8 (right). ϑ_1 close to the gas inlet was about 6 °C and ϑ_3 in the middle of the packed bed about 3 °C higher compared to the fresh material in the 2nd cycle.

Analogous to the reduction step the temperature profiles occur to be slightly different in the last cycle, indicating potential changes in the packed bed behavior. The overall reaction time in terms of O_2 uptake amounts to ~ 78 min on average. As the reaction proceeds very slowly towards the end, 95% conversion has already been reached approximately ~ 49 min after initiation of the reaction, respectively. Within the accuracy of the evaluation complete conversion has been obtained throughout all reference discharging experiments. The low conversion of 97.5% calculated for the 17th cycle is considered a runaway value, since the storage material was recovered in the fully oxidized state upon emptying the reaction chamber.

We conclude that a continuance of the redox reactivity over several cycles can be verified for the packed bed of granular manganese-iron oxide. It is important to note, that the experiments do not allow conclusions to be drawn about the intrinsic cycling stability of the storage material though, owing to this relatively small number of total cycles conducted as well as the scale of ~ 500 g of storage material. However, the results constitute valuable data, as only scarce information can be found for the redox behavior of larger sample masses with regard to TCS.

When the reaction chamber was opened after 17 cycles, indications of channeling effects were not observed. For illustration purposes the view onto the loose packed bed of granulate just after filling of the reactor tube is presented in Fig. 9 (left), the view onto the bed after cycling looks alike. However, only granules in the

upper part of the packed bed showed free outflow upon turning the opened reactor tube. Material in the lower part of the bed formed larger agglomerates imbedding the sheath thermocouples. Hence, the granular material still tends to agglomerate due to occurring sintering effects. Agglomerated granules after cycling for 17 times are depicted on the right of Fig. 9.

The agglomerates are not hard and can thus easily be broken apart into single granules with the exertion of low force. In consequence of these sintering processes the gas flow behavior and present flow distribution within the packed bed cannot be precisely predicted. That is why a reasonably homogeneous gas flow through the packed bed might not have been thoroughly ensured throughout the series of experiments.

As described in Section 2.1 granular particles were prepared in the size range of 1–3 mm. However, the employed particles are irregularly shaped due to the preparation process, which can be clearly seen in Fig. 9. The mean particle size was evaluated by means of an image analysis based on the open source image processing program ImageJ. In the process two-dimensional particle images were recorded, so that the projected area of the particles can be determined for further analyses. For the determination of the mean particle size, only single granules – no agglomerates – have been taken into account. Therefore the existing agglomerates have been broken apart. The particle size distribution of the cycled material demonstrates a slight shift to smaller mean particle sizes in comparison to the raw material. The mean equivalent particle diameter of the raw material amounts to 2.13 ± 0.56 mm, whereas a value of 1.74 ± 0.51 mm was identified for the cycled material. This corroborates the physical impression of the granular particles, which seem to turn considerably more brittle and fracturable upon cycling. The slight change in granule size might be attributed to an

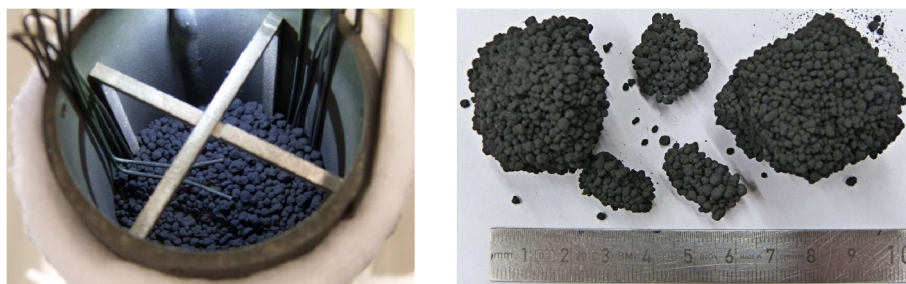


Fig. 9. View of manganese-iron oxide granulate in the reaction chamber prior to cycling, along with arrangement of thermocouples measuring the gas temperature above the packed bed (left); agglomerated material after cycling in air (17 redox cycles) upon cleanout of the reactor tube (right).

alteration of the physical material characteristics due to the high temperature exposition on the one hand, or even provoked by the chemical stress due to cycling on the other hand. A spalling of material has been observed, causing increased powder formation, which can be seen in the top right corner of Fig. 9 (right). The granules also experienced slight mechanical impacts during the emptying process of the reactor tube, which might have led to particle breakage as well. Consequently, it cannot be completely excluded, that the reason for the slight reduction in mean granule size was also attributed to the emptying of the reactor tube or the breakup of the agglomerates.

Prior to cycling, the pressure drop solely over the packed bed amounted to ~ 1.52 kPa measured at 30 NL/min of air at ambient temperature. However, after 17 redox cycles an air flow rate of 30 NL/min at room temperature yields a total pressure drop of ~ 3.97 kPa over the bed (typical accuracy of pressure transducer ± 0.625 kPa). The observed trend of a slight increase in pressure drop upon cycling might be explained by the above-mentioned appearance of some smaller particles, blocking open pathways for the fluid flow and eventually increasing the pressure drop over the packed bed somewhat. Consequently, although the change in pressure drop upon cycling is not significant, a modification of the granular particle arrangement and especially its interaction forces can be affirmed.

A phase analysis was performed by X-ray powder diffractometry (Bruker D8 Advance instrument using $\text{Cu-K}\alpha_{1,2}$ radiation) to identify the crystalline phase composition and compare the raw material with the cycled material, both present in the oxidized state. The diffraction patterns in Fig. 10 indicate a cubic Mn_2O_3 crystal phase (bixbyite phase; ICDD PDF-2, #41-1442) with the

crystal space group $\text{Ia}\bar{3}$ for both samples, which is consistent with phase diagrams in the literature (Crum et al., 2009; Kjellqvist and Selleby, 2010; Wickham, 1969). A hematite phase, which would still indicate the presence of the raw material Fe_2O_3 , cannot be observed.

In general, the cubic FeMnO_3 crystal structure (bimetallic bixbyite phase; ICDD PDF-2, #75-0894; space group $\text{Ia}\bar{3}$) exhibits virtually the same peak positions with a peak displacement by only $\sim 0.02^\circ$ (2Θ). Thus, it has to be noted that merely based on the lattice parameters a differentiation between the bixbyite phase Mn_2O_3 and bixbyite structure $(\text{Mn,Fe})_2\text{O}_3$ is not possible. X-ray fluorescence spectroscopy revealed the average elemental composition of the granules, yielding molar fractions of 30.13% Mn, 10.09% Fe, 0.37% Al, 0.36% Si, 0.07% Mg, 0.03% Ca, $<0.03\%$ Na, $<0.02\%$ K, $<0.01\%$ Ti, $<0.01\%$ Cr and 58.89% O. Thus, a Fe/Mn molar ratio of 1:3 can be verified. We can draw the conclusion that the X-ray diffraction patterns of the samples in Fig. 10 do not differ from each other, both disclosing a single phase crystal structure corresponding to a $(\text{Mn,Fe})_2\text{O}_3$ structure with molar fractions of 75% Mn and 25% Fe, referred to as $(\text{Mn}_{0.75}\text{Fe}_{0.25})_2\text{O}_3$ phase.

Scanning electron microscopy (SEM) was performed using a Zeiss Ultra 55 instrument in order to analyze the microstructure of the material. On the one hand, the performed redox cycles did not disclose a significant macroscopic effect on the cycling stability in terms of the reactivity in the lab-scale reactor. On the other hand, a comparison of the SEM images of the starting material and the cycled material in Fig. 11 (a) and (c), showing the topview of the granulate surface respectively, reveals a considerable change of the microstructural morphology over the course of the redox cycles. While the raw material features a finer structure with

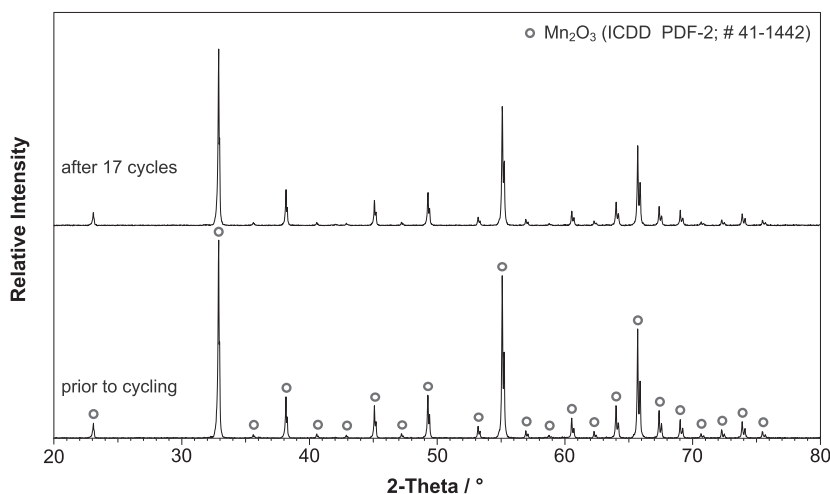


Fig. 10. X-ray diffraction patterns of manganese-iron oxide: raw material (bottom) and cycled material (top).

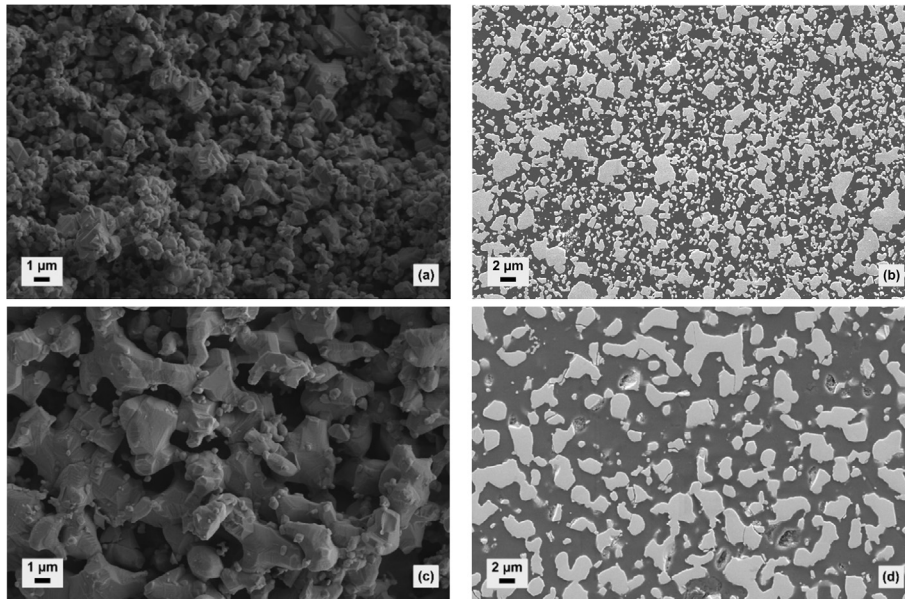


Fig. 11. Scanning electron micrographs: Granulate surface and microsection of manganese-iron oxide as prepared (a and b) as well as after 17 cycles (c and d), both samples being in the oxidized state; SEM images (b) and (d) show polished cross sections of the granules with epoxy glue (dark areas) and solid particle fraction (grey areas); working distances of 7.9 mm (a) 8.0 mm (b and c) and 7.8 mm (d); acceleration voltage of 5.0 kV.

irregularly shaped individual grains (a), the micrograph of the material cycled 17 times in the lab-scale reactor exhibits clearly larger, coherent bulk structures (c). Those can directly be attributed to strong sintering effects induced by the long exposition to high-temperature conditions up to 1040 °C during cycling. The formation of larger bulk structures and sintering necks upon cycling might have caused a more homogeneous temperature distribution inside the packed bed, eventually leading to the observed slight change in the reactivity of the packed bed (bulk reactivity), discussed above.

Moreover, Fig. 11 illustrates the polished granule cross sections of the raw material (b) and cycled material (d). The granular particles were infiltrated with epoxy glue to stabilize the structure. Dark areas (epoxy glue) represent the voidage of the granules. The image of the cycled material corroborates the formation of larger bulk structures over cycling. As the solid fraction (grey areas) per image section is fairly similar in both cases, the granulate porosity appears to be essentially unchanged after 17 redox cycles. Overall, the microstructural alterations seem to have an impact on the mechanical properties and integrity of the material, which supports the above-described indications of material embrittlement upon cycling in the reactor.

As the described reference cycles were performed for comparison over the course of merely 17 cycles in total, the information regarding the long-term trend of sustained reactivity of larger sample masses is only limited though. Extended studies over numerous cycles of $(\text{Mn}_{0.75}\text{Fe}_{0.25})_2\text{O}_3/(\text{Mn}_{0.75}\text{Fe}_{0.25})_3\text{O}_4$ need to be performed in the future. Furthermore, a preconditioning of the storage material in the form of repetitive thermal cycling in the furnace is recommended prior to use in lab-scale experiments, in order to reach stable conditions with regard to microstructure and reactivity.

In view of advanced reactor concepts continuous TCS reactors have the potential to facilitate an enhancement of the gravimetric energy storage density of the TES system in comparison to batch reactors with stationary storage material, since continuous concepts allow a larger amount of storage material to fully react. A moving bed reactor operated in a countercurrent flow of the metal oxide storage material and the HTF air represents a promising con-

cept (Ströhle et al., 2016). However, as the storage material has to withstand increased mechanical stress induced by the transportation, the preparation of mechanically more stable granules needs to be achieved. Moreover, a continuous reactor concept also allows a decoupling of the envisaged thermal power – determined by the size and operating conditions of the TCS reactor – from the energy storage capacity (amount of storage material), which approach would be essential for an efficient upscaling to industrial scale.

4. Conclusions

The reversible redox reaction of a granular technical grade manganese-iron oxide has been systematically investigated for TCS by means of a packed bed tube reactor on lab-scale. The experimental results successfully demonstrate the general feasibility of the redox reaction based storage concept with direct contact heat transfer and open-loop operation using air as HTF. The main attention is centered on the influence of essential operating parameters on the storage characteristics, which has been analyzed by means of several parametric studies, arriving at the following conclusions:

- The proceeding redox reactions disclosed the development of distinct temperature profiles with the formation of temperature plateaus and a temperature front travelling in flow direction through the packed bed, characteristic for exploiting the heat effect of reversible reactions for TCS, respectively. The temperature plateaus proved to be highly dependent on the thermodynamic properties as well as kinetic behavior of the redox reaction. The experiments revealed that the advancing reactions are mainly limited due to the rate of heat input (thermal charging) and the rate of heat dissipation (thermal discharging) by the HTF under the applied operating conditions in the lab-scale reactor.
- Thermal charging/discharging investigations under constantly increasing/decreasing air inlet temperature demonstrated the feasibility to stabilize bed temperatures due to the proceeding redox reaction with absorption/release of thermal energy. This characteristic TCS behavior leads to an extended charging/dis-

charging period in contrast to established sensible TES systems and allows the continuance of a fairly steady storage discharging temperature over an extended period.

- The dual function of air as HTF and O₂-carrier, removing or supplying the reactant O₂ respectively, has a direct impact on the prevailing O₂ concentration and therefore the oxygen partial pressure in the reactor. Changes of the O₂ concentration due to the proceeding reaction both influence the pO₂-dependent reaction rate as well as reaction temperature, and affect the heat capacity rate C_{HTF} of the HTF. Those phenomena need to be taken into account in the future design and operation of redox reaction based thermochemical storage reactors with direct contact heat transfer using air as HTF.
- The forward and reverse reaction has been examined by means of a reference cycle performed in between the outlined parametric studies, yielding no degradation of the material reactivity over 17 cycles. Hence, the material exhibits good cycling stability, which has been considered sufficient for the comparability of the experimental results obtained from the conducted parametric studies. On a microstructural level, though, sintering phenomena resulted in an alteration of the microstructure, in turn leading to a lack of mechanical strength of the granules upon cycling.

We can conclude from the current study, that heat transport poses the most essential factor for storage operation under the applied conditions in contrast to the reaction rate. In general, higher heat capacity rates are necessary to achieve high thermal power levels for a storage operation on a technically relevant scale. As the heat capacity rate C_{HTF} is rather low in the presented study, the influence of significantly higher heat capacity rates on the reaction rate and performance of a TCS reactor based on the redox reaction of metal oxides needs to be investigated in future work.

Acknowledgements

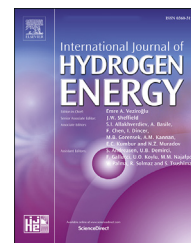
The authors wish to thank Tina Block (Institute of Materials Research, German Aerospace Center, Cologne, Germany) for performing the scanning electron microscopy and X-ray powder diffraction measurements as well as Sven Nicolai (VITO Flemish Institute for Technological Research, Mol, Belgium) for the preparation of the manganese-iron oxide granulate.

References

- Agrafiotis, C., Roeb, M., Schmücker, M., Sattler, C., 2014. Exploitation of thermochemical cycles based on solid oxide redox systems for thermochemical storage of solar heat. Part 1: Testing of cobalt oxide-based powders. *Sol. Energy* 102, 189–211.
- Agrafiotis, C., Becker, A., Roeb, M., Sattler, C., 2016a. Exploitation of thermochemical cycles based on solid oxide redox systems for thermochemical storage of solar heat. Part 5: Testing of porous ceramic honeycomb and foam cascades based on cobalt and manganese oxides for hybrid sensible/thermochemical heat storage. *Sol. Energy* 139, 676–694.
- Agrafiotis, C., Roeb, M., Sattler, C., 2016b. Exploitation of thermochemical cycles based on solid oxide redox systems for thermochemical storage of solar heat. Part 4: Screening of oxides for use in cascaded thermochemical storage concepts. *Sol. Energy* 139, 695–710.
- Alonso, E., Pérez-Rábago, C., Licurgo, J., Fuentealba, E., Estrada, C.A., 2015. First experimental studies of solar redox reactions of copper oxides for thermochemical energy storage. *Sol. Energy* 115, 297–305.
- Álvarez de Miguel, S., Bellan, S., García de María, J.M., González-Aguilar, J., Romero, M., 2016. Numerical modelling of a 100-Wh lab-scale thermochemical heat storage system for concentrating solar power plants. *AIP Conf. Proc.* 1734, 050005-1–050005-8.
- Álvarez de Miguel, S., Gonzalez-Aguilar, J., Romero, M., 2014. 100-Wh multipurpose particle reactor for thermochemical heat storage in concentrating solar power plants. *Energy Procedia* 49, 676–683.
- André, L., Abanades, S., Flamant, G., 2016. Screening of thermochemical systems based on solid-gas reversible reactions for high temperature solar thermal energy storage. *Renew. Sustain. Energy Rev.* 64, 703–715.
- Ávila-Marín, A.L., 2011. Volumetric receivers in Solar Thermal Power Plants with Central Receiver System technology: a review. *Sol. Energy* 85, 891–910.
- Azimi, G., Leion, H., Rydén, M., Mattisson, T., Lyngfelt, A., 2013. Investigation of different Mn-Fe oxides as oxygen carrier for chemical-looping with oxygen uncoupling (CLOU). *Energy Fuels* 27, 367–377.
- Barin, I., Platzki, G., 1995. Thermochemical Data of Pure Substances. VCH Verlagsgesellschaft mbH, Weinheim.
- Block, T., Schmücker, M., 2016. Metal oxides for thermochemical energy storage: A comparison of several metal oxide systems. *Sol. Energy* 126, 195–207.
- Carrillo, A.J., Serrano, D.P., Pizarro, P., Coronado, J.M., 2014. Thermochemical heat storage based on the Mn₂O₃/Mn₃O₄ redox couple: Influence of the initial particle size on the morphological evolution and cyclability. *J. Mater. Chem. A* 2, 19435–19443.
- Carrillo, A.J., Serrano, D.P., Pizarro, P., Coronado, J.M., 2015. Improving the thermochemical energy storage performance of the Mn₂O₃/Mn₃O₄ redox couple by the incorporation of iron. *Chemosuschem* 8, 1947–1954.
- Carrillo, A.J., Serrano, D.P., Pizarro, P., Coronado, J.M., 2016. Understanding redox kinetics of iron-doped manganese oxides for high temperature thermochemical energy storage. *J. Phys. Chem. C* 120, 27800–27812.
- Crum, J.V., Riley, B.J., Vienna, J.D., 2009. Binary phase diagram of the manganese oxide-iron oxide system. *J. Am. Ceram. Soc.* 92, 2378–2384.
- Geldart, D., 1973. Types of gas fluidization. *Powder Technol.* 7, 285–292.
- Gil, A., Medrano, M., Martorell, I., Lazaro, A., Dolado, P., Zalba, B., Cabeza, L.F., 2010. State of the art on high temperature thermal energy storage for power generation. Part 1 – Concepts, materials and modellization. *Renew. Sust. Energy Rev.* 14, 31–55.
- Ho, C.K., 2017. Advances in central receivers for concentrating solar applications. *Sol. Energy* 152, 38–56.
- Karagiannakis, G., Pagkoura, C., Halevas, E., Baltzopoulou, P., Konstandopoulos, A.G., 2016. Cobalt/cobaltous oxide based honeycombs for thermochemical heat storage in future concentrated solar power installations: multi-cyclic assessment and semi-quantitative heat effects estimations. *Sol. Energy* 133, 394–407.
- Karagiannakis, G., Pagkoura, C., Zygogianni, A., Lorentzou, S., Konstandopoulos, A.G., 2014. Monolithic ceramic redox materials for thermochemical heat storage applications in CSP plants. *Energy Procedia* 49, 820–829.
- Kjellqvist, L., Selleby, M., 2010. Thermodynamic assessment of the Fe-Mn-O system. *J. Phase Equil. Diffus.* 31, 113–134.
- Kuravi, S., Trahan, J., Goswami, D.Y., Rahman, M.M., Stefanakos, E.K., 2013. Thermal energy storage technologies and systems for concentrating solar power plants. *Prog. Energy Combust. Sci.* 39, 285–319.
- Liu, M., Steven Tay, N.H., Bell, S., Belusko, M., Jacob, R., Will, G., Saman, W., Bruno, F., 2016. Review on concentrating solar power plants and new developments in high temperature thermal energy storage technologies. *Renew. Sustain. Energy Rev.* 53, 1411–1432.
- Neises, M., Tescari, S., de Oliveira, L., Roeb, M., Sattler, C., Wong, B., 2012. Solar-heated rotary kiln for thermochemical energy storage. *Sol. Energy* 86, 3040–3048.
- Pardo, P., Deydier, A., Anxionnaz-Minvielle, Z., Rougé, S., Cabassud, M., Cognet, P., 2014. A review on high temperature thermochemical heat energy storage. *Renew. Sustain. Energy Rev.* 32, 591–610.
- Ströhle, S., Haselbacher, A., Jovanovic, Z.R., Steinfeld, A., 2016. The effect of the gas-solid contacting pattern in a high-temperature thermochemical energy storage on the performance of a concentrated solar power plant. *Energy Environ. Sci.* 9, 1375–1389.
- Tescari, S., Agrafiotis, C., Breuer, S., de Oliveira, L., Puttkamer, M.N.-V., Roeb, M., Sattler, C., 2014. Thermochemical solar energy storage via redox oxides: Materials and reactor/heat exchanger concepts. *Energy Procedia* 49, 1034–1043.
- Tescari, S., Singh, A., Agrafiotis, C., de Oliveira, L., Breuer, S., Schlögl-Knothe, B., Roeb, M., Sattler, C., 2017. Experimental evaluation of a pilot-scale thermochemical storage system for a concentrated solar power plant. *Appl. Energy* 189, 66–75.
- Wickham, D.G., 1969. The chemical composition of spinels in the system Fe₃O₄-Mn₃O₄. *J. Inorg. Nucl. Chem.* 31, 313–320.
- Wokon, M., Nicolai, S., Block, T., Linder, M., Schmücker, M., 2017. Thermodynamic and kinetic investigation of a technical grade manganese-iron binary oxide for thermochemical energy storage. *Sol. Energy* 153, 471–485.
- Wong, B., 2011. Thermochemical heat storage for concentrated solar power. Phase II Final Report GA-C27137 prepared for the U.S. Department of Energy, General Atomics, San Diego, CA, USA.
- Wong, B., Brown, L., Schaubé, F., Tamme, R., Sattler, C., 2010. Oxide based thermochemical heat storage, 16th SolarPACES Conference, Perpignan, France.
- Zanganeh, G., Pedretti, A., Zavattoni, S., Barbato, M., Steinfeld, A., 2012. Packed-bed thermal storage for concentrated solar power – Pilot-scale demonstration and industrial-scale design. *Sol. Energy* 86, 3084–3098.
- Zhang, H., Baeyens, J., Cáceres, G., Degrève, J., Lv, Y., 2016. Thermal energy storage: Recent developments and practical aspects. *Prog. Energy Combust. Sci.* 53, 1–40.
- Zunft, S., Hänel, M., Krüger, M., Dreißigacker, V., Göhring, F., Wahl, E., 2011. Jülich Solar Power Tower – Experimental evaluation of the storage subsystem and performance calculation. *J. Sol. Energy Eng.* 133, 031019-1–031019-5.

Available online at www.sciencedirect.com

ScienceDirect

journal homepage: www.elsevier.com/locate/hydro

Characterization of metal hydrides for thermal applications in vehicles below 0 °C

Mila Kölbig*, Inga Bürger, Marc Linder

German Aerospace Center (DLR), Institute of Engineering Thermodynamics, Thermal Process Technology, Pfaffenwaldring 38-40, 70569 Stuttgart, Germany

ARTICLE INFO

Article history:

Received 26 October 2018

Received in revised form

11 December 2018

Accepted 17 December 2018

Available online 18 January 2019

Keywords:

Metal hydride

Pressure concentration-isotherm

Reaction rate coefficient

LaNi_{4.85}Al_{0.15}

Hydralloy C5

ABSTRACT

Metal hydrides promise great potential for thermal applications in vehicles due to their fast reaction rates even at low temperature. However, almost no detailed data is known in literature about thermochemical equilibria and reaction rates of metal hydrides below 0 °C, which, though, is crucial for the low working temperature levels in vehicle applications.

Therefore, this work presents a precise experimental set-up to measure characteristics of metal hydrides in the temperature range of –30 to 200 °C and a pressure range of 0.1 mbar–100 bar. LaNi_{4.85}Al_{0.15} and Hydralloy C5 were characterized. The first pressure concentration-isotherms for both materials below 0 °C are published. LaNi_{4.85}Al_{0.15} shows an equilibrium pressure down to 55 mbar for desorption and 120 mbar for absorption at mid-plateau and –20 °C. C5 reacts between 580 mbar for desorption and 1.6 bar for absorption at –30 °C at mid-plateau.

For LaNi_{4.85}Al_{0.15}, additionally reaction rate coefficients down to –20 °C were measured and compared to values of LaNi₅ for the effect of Al-substitution. The reaction rate coefficient of LaNi_{4.85}Al_{0.15} at –20 °C is 0.0018 s⁻¹. The obtained data is discussed against the background of preheating applications in fuel cell and conventional vehicles.

© 2018 Hydrogen Energy Publications LLC. Published by Elsevier Ltd. All rights reserved.

Introduction

Cold start is a severe problem for vehicle drives such as internal combustion engines (ICE) or fuel cells (FC).

The challenge for ICEs are the emissions at low temperatures until the designated temperature of around 100 °C is reached. During the cold start phase neither the combustion process nor the exhaust gas treatment work sufficiently. Due to wall quenching in the cylinder and low combustion temperatures, the amount of pollutants is increased. Therefore, in these first couple of minutes, a great portion of all pollutants of the whole ride are produced. E.g. Cipollone et al. [2] state

that around 60% of harmful substances are produced during cold start. Even up to 80% of some pollutant species are associated with cold start according to Reiter and Kockelman [3]. Cold start emissions include mainly nitrogen oxides, hydrocarbons (CH₄ and other HC) and volatile organic compounds. Faster heat-up would reduce the emissions drastically [4–9].

Fuel cells face the challenge of degradation at temperatures below freezing point. If a proton exchange membrane fuel cell (PEMFC) is operated below 0 °C, the produced water might freeze and form an ice layer, which prevents gas flow and the expansion in volume can cause mechanical stress that leads to a shortened life time of the fuel cell. An

* Corresponding author.

E-mail addresses: mila.koelbig@dlr.de, mila.dieterich@dlr.de (M. Kölbig).

<https://doi.org/10.1016/j.ijhydene.2018.12.116>

0360-3199/© 2018 Hydrogen Energy Publications LLC. Published by Elsevier Ltd. All rights reserved.

Abbreviations

A	pre-exponential factor	s ⁻¹
d	diameter	mm
E _a	activation energy	kJ/mol
eq	equilibrium	
f	factor between end and equilibrium pressure	
f(p)	pressure dependence function	
f(x)	reaction mechanism function	
FC	fuel cell	
H ₂	hydrogen	
(Hydralloy) C5	investigated material (for hydrogen supply) (Ti _{0.95} Zr _{0.05} Mn _{1.46} V _{0.45} Fe _{0.09})	
ICE	internal combustion engine	
k	rate coefficient	s ⁻¹
LaNi _{4.85} Al _{0.15}	investigated material (for preheating)	
m	mass	g
MH	metal hydride	
m _{pl}	plateau slope of PCI	wt.-% ⁻¹
NPDM	normalized pressure dependence method [1]	
P	pressure	bar
PCI	pressure concentration-isotherm	
PEMFC	proton exchange membrane fuel cell	
R	gas constant, R = 8.314 J/(mol K)	J/(mol K)
S	Sieverts' volume	l
T	temperature	°C
t	time	s
tr	tube right	
V	volume	L
\dot{V}	volume flow	ml _N /min
VFC	volume flow control	
x	hydrogen conversion	
$\Delta_R H$	reaction enthalpy	kJ/mol
$\Delta_R S$	reaction entropy	J/(mol K)
ω	hydrogen conversion	wt.-%

application in vehicles therefore requires water management at low temperatures. Today, one state of the art start-up enhancement uses a positive temperature coefficient (PTC) heater run by electrical energy, which is itself very valuable at low temperatures and additionally might reduce the driving range. Preheating using surplus energy would increase the efficiency substantially [10–13].

In both cases, waste heat at operation temperature level is available later on in the driving cycle. This time shift is the point of application considered in this work. With the help of thermal energy storage, the surplus energy can be made available for preheating at cold start. This way, besides emission reduction and efficiency increase, the component operation life could be prolonged.

The challenge is the usage of low level waste heat in a small storage able to provide heat within seconds or few minutes. The thermochemical reaction of metal hydrides with hydrogen has the potential to meet these requirements. Metal hydrides are metal alloys reacting exo-/endothermally with hydrogen according to equation (1) [14]. Besides storage applications, they receive increasing attention for thermal applications due to their very fast reaction, even at low temperatures.



One important characteristic is the separation of hydrogen and the metal hydride, e.g. by a valve. This prevents the reverse reaction and the thermal energy can be stored as long as desired. The recombination generates heat and leads to a temperature increase of the solid material. Therefore, the storage can cool down to ambient temperature with no insulation required and generate the heat when needed. Another great advantage to sensible or phase change thermal storage is energy generation on demand and the higher energy density at a given temperature level.

In order to use metal hydrides for vehicle preheating, two characteristics of the reaction have to be known: the thermochemical equilibrium according to thermodynamics as well as the reaction rate that is dominated by intrinsic material properties. These terms are specified in the following.

The absorption of hydrogen in metal hydrides forms different phases. During the transition from α to the β -phase (called $\alpha+\beta$ -phase), much hydrogen can be absorbed by the solid metal leading to a comparatively low increase of the associated equilibrium pressure. This plateau represents the region which can be used most readily for metal hydride applications. This characteristic is described by pressure concentration-isotherms (PCIs). The pressure increases with increasing hydrogen conversion ($\omega = \frac{m_{H_2}}{m_{MH}} \cdot 100$). Real metal hydrides show a hysteresis between absorption and desorption. From these PCIs, the plateau region is used to describe the equilibrium between gas pressure and metal hydride temperature in a van't Hoff-plot.

The overall reaction rate is influenced by the reaction mechanism, the materials' rate coefficient as well as by the distance to the thermodynamic equilibrium. Besides valid descriptions of these influences, precise measurements allowing unimpeded gas flow and optimal heat transfer for almost isothermal conditions are essential to the determination of the reaction rate. Details on the reaction mechanism are given e.g. in Refs. [15,16]. Due to the very fast reaction of the materials considered here, precise measurements require a mature concept for the reactor and the experimental conditions. Details about the approach in this paper are given in the experimental section.

Two operation designs - an open system with single reaction in FC vehicles and a closed system with coupled reactions in ICES – can be considered, as presented and discussed in Refs. [17,18].

Since the reaction partner of metal hydrides is hydrogen, a metal hydride preheater for a FC vehicle consists of one reactor containing the heat generating material and can be directly integrated into the hydrogen infrastructure. Hydrogen is supplied for preheating from the vehicle's hydrogen tank and desorbed by waste heat during regeneration and converted into electricity in the FC. Hence, no hydrogen is consumed. Such a system is considered **open** and reacts in a single reaction of the heat generating material.

An ICE vehicle doesn't have a hydrogen infrastructure. Hence, the hydrogen has to be supplied by another hydrogen supplying metal hydride in a second reactor. During discharge, the hydrogen supplying material desorbs hydrogen

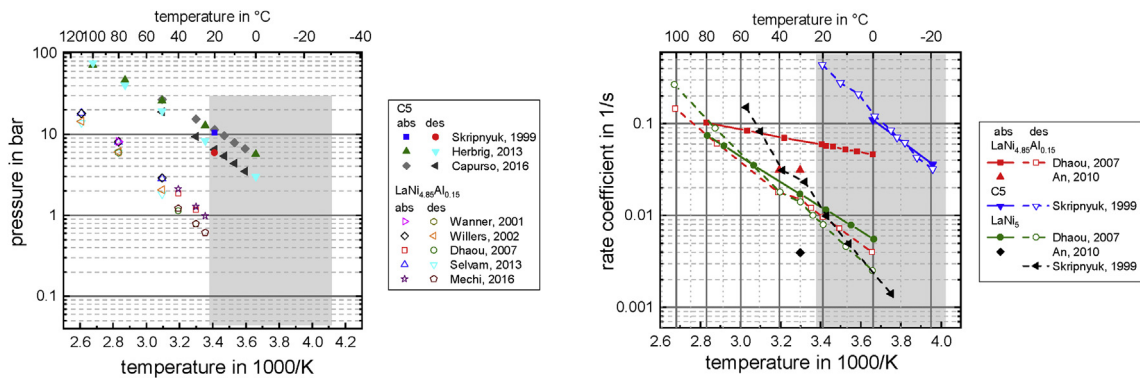


Fig. 1 – Available thermodynamic (left) [20–27] and kinetic data (right) [22,27,28] for LaNi_{4.85}Al_{0.15} and C5.

at a higher equilibrium pressure leading to an immediate absorption by the heat generating material. Waste heat during regeneration leads to a higher equilibrium pressure of the heat generating material and consequently recharges the hydrogen supplying material. This system is closed and consists of two strongly interdependent, coupled reactions of two different metal hydrides exchanging hydrogen.

The chosen materials are LaNi_{4.85}Al_{0.15} as heat generating material and Hydralloy C5¹ (Ti_{0.95}Zr_{0.05}Mn_{1.46}V_{0.45}Fe_{0.09}) as hydrogen supplying material for the coupled reactions in the closed system. The latter was also used by Weckerle et al. [19] for high thermal power air conditioning. Based on extrapolation of so far known PCI data to lower temperature, the materials should fit well the restricting boundary conditions of the preheating application at winter temperatures between –20 and 20 °C. Waste heat levels are considered to be between 90 and 130 °C for ICEs (closed system) and 60 °C for FCs (open system). The pressure level was limited to 30 bar due to mechanical stresses on potential reactor designs.

The knowledge of the thermochemical equilibrium and the reaction of the considered materials is crucial in order to predict the potential of the thermal power output in particular of the coupled reactions, understand the reactions responds and identify relevant influencing factors on both the reaction itself and design parameters for the system. However, little is known about the material properties of metal hydrides below 0 °C in general and almost nothing has been published for the selected materials.

Regarding the thermodynamic properties of LaNi_{4.85}Al_{0.15}, only five publications could be found on pressure concentration-isotherms in a temperature range between 25 and 110 °C [20–24]. This is also true for C5, for which only few publications in a temperature range between 0 and 100 °C are available [25–27]. The data is shown in a van't Hoff plot in Fig. 1, left, including in grey the range of interest for the presented application. A similar picture arises for kinetic properties. For LaNi_{4.85}Al_{0.15}, very little data exists [22,28]. Furthermore, the investigated temperature levels are far above the range considered here and little information about

the experiments and isothermal conditions is provided. More over even different equations have been used to derive the reaction rate. Therefore, this data can't be used for predictions of the material behavior down to –20 °C. In order to narrow the range for the characteristics of LaNi_{4.85}Al_{0.15}, literature data of a comparable alloy, LaNi₅, is also considered. However, the effect of aluminum substitution on the reaction rate is discussed controversy in literature. Whereas some authors state a decreasing effect on the intrinsic kinetics, such as [29–31], others suggest an increasing effect, e.g. Refs. [22,28,32,33]. The results of this work will be discussed against this background.

For C5, only one single publication could be found on kinetic investigations. The work of Skripnyuk and Ron [27] presented results down to a temperature of –20 °C and is used as a reference in this work. All kinetic data available is given Fig. 1, right.

As can be seen from this literature review, no data on the thermodynamic equilibrium below 0 °C exists for both materials and no reliable kinetic data for LaNi_{4.85}Al_{0.15} can be used. However, as this is crucial for the preheating application in vehicles, this data is obtained in this work.

For this purpose a precise experimental set-up is developed. Great care was taken to realize high precision and to exclude measurement errors and impacts of reactor or experimental design. Pressure concentration-isotherms (PCIs) are measured in a temperature range between –30 and 130 °C for both materials and reaction rate coefficients in the range between –20 and 40 °C are obtained for LaNi_{4.85}Al_{0.15}. Finally, the data is discussed regarding the suitability of the materials for the considered preheating application in vehicles.

Experimental

This section provides details about the methods of characterization, the test bench and the reactors as well as the analysis and the experimental design.

Method

PCI measurements require experiments very close to equilibrium. They can be measured either statically or dynamically.

¹ Hydralloy C-materials are AB₂ type hydride alloys numbered according to their percentage of other A-components than titanium. Therefore, Ti_{0.95}Zr_{0.05}Mn_{1.46}V_{0.45}Fe_{0.09} – the material used in this study – is called Hydralloy C5[®] and is referred to as 'C5' in this work.

The static measurement provides hydrogen to the material and allows sufficient time to reach equilibrium at the set temperature. These measurement steps are repeated several times, each step leading to one point of the PCI, until full conversion is reached. This type of measurement was performed extensively in literature, see e.g. Refs. [20,26,31,34,35]. Usually, little information is given about the testing procedure, such as the amount and pressure of hydrogen added or the resulting temperature peak inside the material. This, however, might influence the results, as mentioned by Friedlmeier et al. [36].

The dynamic method is rarely used in literature, e.g. by Muthukumar et al. [37]. During a dynamic measurement, hydrogen is supplied continuously resulting in continuous measurement values for the PCI. However, for such a measurement, the equilibrium state is disturbed at any time so the experimental variables have to be chosen with care [36]. This requires a considerable effort for the reactor design and experiment parameters. The heat management of the reactor has to be sufficient in order to ensure almost isothermal conditions and, thus, relate the results to the intended set temperature. The experiment has to be performed at such low hydrogen flow rates, that the material remains very close to equilibrium during reaction. If the flow rate is too high, the measurement is controlled by heat transfer rather than by the equilibrium of the reaction. This leads to pressure values presumably too high or low for absorption and desorption, respectively. Therefore, the mass flow and temperature change have to be examined intensively to ensure appropriate measurements.

This work uses the dynamic method. To ensure accurate results, the equilibrium state and (almost) isothermal conditions are considered carefully and the results are compared to literature values at available temperatures.

The measurement procedure to determine the reaction rate coefficient has to exclude limitations of the reaction other than the kinetics in order to yield correct results. In particular for the fast reaction rates of the materials considered in this work, careful considerations have to ensure correct measurements. If in particular heat flow limitations are underestimated, reported results can diverge greatly, as discussed e.g. by Goodell and Rudman [38]. The normalized pressure dependence method (NPDm) suggested by Ron [1] is used to determine the kinetic values. The following conditions are suggested there:

- Temperature change of the material should be limited to ± 1 K, e.g. by the thermal ballast method
- Mass transfer of hydrogen through the reaction bed should be high so the gas transport does not limit the reaction
- A reaction order or mechanism must be defined
- Within the considered temperature range, the reaction process has to obey the Arrhenius temperature dependence
- The hydrogen should be converted within the plateau region ($\alpha+\beta$ region)

The restriction on the maximal temperature change is strict compared to other work. Rudman [39], for example, discusses a temperature change of ± 10 K. In order to be able to

refer the derived rate coefficient to one temperature, the maximal temperature change allowed in this work is ± 3 K.

Test bench and reactor design

A test bench was designed and brought into operation as shown in Fig. 2. The left hand side depicts the layout of the bench with several hydrogen reservoirs (Sieverts' volumes, S1-S3) for flexible measurement of different probe masses. The range of the volume flow control (VFC) is small (0.5 ... 25 ml_N/min) to allow the approach of the equilibrium state during PCI measurements. A bypass (V_{tr2} and V_{tr3}) allows fast pressure change for measurements of the kinetic rate coefficient. The temperature of the material is set by a thermostatic bath (-30 ... 200 °C).

More details on the measurement equipment and accuracy are given in the [supplementary material in Table A-1](#) and in Ref. [18].

For near equilibrium PCI measurements, the reactor design has to allow sufficient heat and mass transfer in order to ensure reaction at constant temperature. Due to the small volume flow rates, an inner tube diameter of 9 mm satisfies this requirement, at the same time realizing enough sample mass to generate measurement values well above the measurement precision. The temperature change inside the reactor was measured by a thermocouple type K at the center of the tube, approx. 13 mm above the lower end of the reactor. The design limited the change of temperature of the material to less than 3 K at all times for all measurements, see details in Ref. [18]. The used reactor is shown in Fig. 3, left. The stainless steel tube ($d_{out} = 12$ mm) had a length of approx. 100 mm. A hand valve protects the material at installation. A filter with a pore size of 0.5 μ m was added to prevent the powder material from moving. A sample mass of 10.63 g of LaNi_{4.85}Al_{0.15} and 6.20 g of C5 has been used.

Due to the fast reaction, for the reaction rate measurements, aluminum powder with a particle diameter below 160 μ m is used as thermal ballast to disperse the heat of reaction quickly. The diameter, on the one hand, is considered to be small enough to mix well with the metal hydride of a diameter of approx. 5 μ m and, on the other hand, large enough for small pressure losses to allow good gas transfer ability through the bed. Additionally, relatively high pressure during the experiments of up to 20 bar further enhances the gas transport. This, however, might lead to the complete formation of the β -phase. This effect can be minimized by considering measurements only until 80% are transformed, related to the overall conversion. Different expressions for the reaction mechanism have been calculated for the experiments and the reaction of first order was found to fit all results [18].

Two charges were investigated, both prepared the same way. The total sample mass of 21 g contained a metal hydride mass of 0.38 g of LaNi_{4.85}Al_{0.15} and an aluminum mass of 20.62 g (factor of 55). The mixture was inserted into a stainless steel tube with an inner diameter of 9 mm ($d_{out} = 12$ mm). The temperature of the material was measured by a thermocouple type K at a height of approx. 10 mm from the bottom. A picture of the reactor is given on the right hand side of Fig. 3. This design allowed a small temperature change of below 3 K for all experiments, which is shown in the [supplementary material in Figure A-1](#).

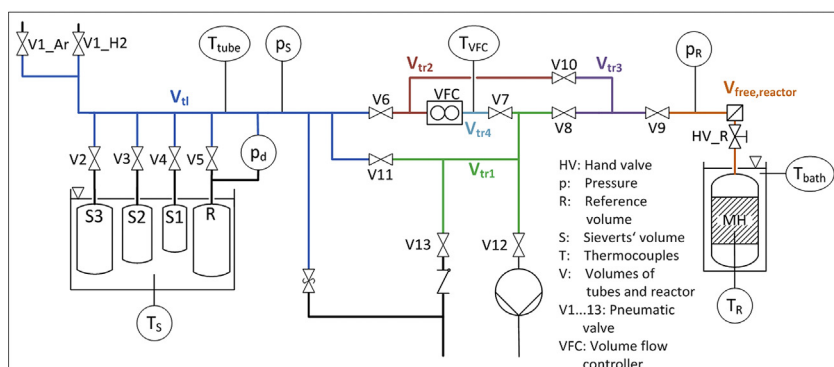


Fig. 2 – Layout and Picture of the characterization test bench.

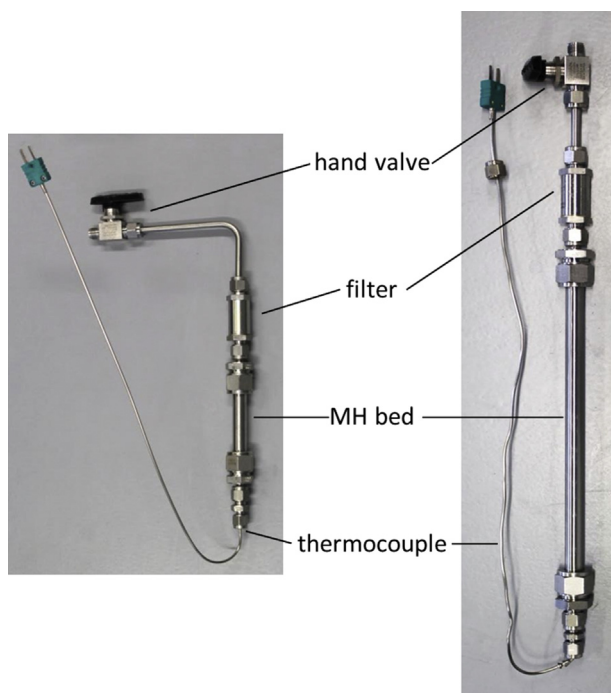


Fig. 3 – Reactor for dynamic pressure concentration-isotherm measurements (left) and reactor for reaction rate measurements (right).

Analysis

Pressure concentration-isotherm (PCI)

The value of interest for PCI measurements is the equilibrium pressure as function of hydrogen conversion and reaction temperature. The conversion of each measurement step is derived from the pressure drop in the Sieverts' volume. The yield conversion value is related to the measured equilibrium pressure in the metal hydride reactor. Due to the constant mass flow during the dynamic measurement, the pressure change in the reactor already shows the typical shape of a PCI. An exemplary measurement result is shown in the [supplementary material in Figure A-2](#).

For absorption, the hydrogen conversion is calculated from the pressure change in the Sieverts' volume, taking the temporal change of the temperatures in all volumes into account. Desorption is controlled and measured by the volume flow control. For balancing, the sum of its values every 0.5 s would lead to lower accuracy. However, the material has to desorb the same amount as was absorbed, because during the next absorption process, the same hydrogen conversion value was reached (without additional desorption). Therefore, the hydrogen conversion during desorption is normalized by fitting the overall released hydrogen to the value for the absorption. The ideal gas law was used, because the compressibility factor of hydrogen at the considered temperatures and pressures of below 1.03 [40] is negligible. Details on the calculations are given in the [supplementary material "Analysis"](#).

Only the plateau of the PCI is of importance when considering equilibrium properties for thermal applications, because here, the vast majority of hydrogen is converted and the pressure only changes slightly with conversion. The plateau slope m_{pl} for each PCI curve was determined by using equation (2).

$$m_{pl} = \left. \frac{d \left(\ln \frac{p_{eq}}{p_0} \right)}{d\omega} \right|_{\omega_{mid}} \quad (2)$$

The equilibrium states for each temperature and both absorption and desorption was determined from the PCI curves. The temperature dependent van't Hoff equation (3) can be fitted to these values resulting in values for the reaction enthalpy $\Delta_R H$ and entropy $\Delta_R S$ [14,41].

$$\ln \left(\frac{p_{eq}}{p_0} \right) = -\frac{\Delta_R H}{R T} + \frac{\Delta_R S}{R} \quad (3)$$

For $\text{LaNi}_{4.85}\text{Al}_{0.15}$, 11 experiments were conducted in a temperature range between -20 and 130 °C and 5 experiments were conducted for C5 in a temperature between -30 and 35 °C. The experiments were designed to find the maximal hydrogen flow rate for near equilibrium approach. For the large temperature range of the experiments with $\text{LaNi}_{4.85}\text{Al}_{0.15}$, here, a flow rate at a medium temperature level was additionally determined. More details on the experiments

conducted are given in detail in [Table A-3](#) of the [supplementary material](#).

Reaction rate coefficient

The measured value is the pressure drop, which correlates to the hydrogen conversion, over time. An exemplary measurement is shown in the [supplementary material in Figure A-3](#). The correlation between the hydrogen conversion over time $\frac{\partial x}{\partial t}$ during the measurement and the desired temperature dependent rate coefficient $k(T)$ is given in equation (4). The pressure dependence function $f(p)$ is interpreted differently in literature, leading to a large discrepancy between the results, as was pointed out by Ron in Ref. [1]. As a consequence, he proposes a normalization method (normalized pressure dependence method, NPDM), allowing good comparison of different experimental set-ups. Therefore, this work follows this method with the pressure dependence function as given in equation (5). The reaction mechanism $f(x)$ has to describe the rate controlling step correctly in order to yield a correct rate coefficient. Although there is no consensus in literature on the precise hydrogenation process [18], fortunately, for fast reactions, the measurement analysis of the reaction rate allows an approximation of the correctly reflected characteristics of the pressure dependence and mechanism functions. This can be ensured by using the ratio of their antiderivatives (cf. equation (7)). Here, all results have to coincide with one line and the slope corresponds to the rate coefficient. If this is the case, then the pressure dependence and mechanism are reflected correctly and the rate coefficient can be derived. Different expressions have been calculated for the experiments in this work and the reaction mechanism of first order as given in equation (6) [1,42], was found to be suitable for all results. [Figure A-4](#) of the [supplementary material](#) shows the fit of equation (7) to an exemplary experiment. With experimental results at varied temperatures, the explicit equation for the temperature dependent Arrhenius term for the rate coefficient can be derived. It is given in equation (8) and leads to the pre-exponential factor A in s^{-1} and the activation energy E_a in kJ/mol .

$$\frac{\partial x}{\partial t} = k(T) \cdot f(p) \cdot f(x) \quad (4)$$

$$f(p) = \frac{|p_{eq} - p|}{p_{eq}} \quad (5)$$

$$f(x) = 1 - x \quad (6)$$

$$\frac{F(x)}{f(p)} = \frac{-\ln(1-x) \cdot p_{eq}}{|p_{eq} - p|} = k(T) \cdot t \quad (7)$$

$$k(T) = A \exp\left(-\frac{E_a}{RT}\right) \quad (8)$$

For the calculation, the transformed fraction, the equilibrium pressure at material temperature and the pressure in the reactor over time are needed.

The following assumptions are made for the analysis:

- The temperature of the Sieverts' volume is assumed to stay constant for the whole reaction time

- Due to the very short reaction time, the hydrogen supplied from the Sieverts' volume is assumed to stay at its temperature rather than to adopt reactor temperature

The equilibrium pressure is calculated at the set temperature of the material using the results of the PCI measurements. Since the plateau slope of $LaNi_{4.85}Al_{0.15}$ is very small, it is neglected in this calculation.

With two different charges, 12 experiments were performed in total in a temperature range between -20 and 40 °C. Details are given in [Table 2](#) in the result section.

Experimental design and repeatability

The experiments were designed in order to fit the boundary conditions of the described preheating application in vehicles and to exclude errors due to the order of experiments. Several experiments were repeated during the experimental phase to exclude changes of the material or between the different charges. The results show no effect of these considered parameters. For all experiments, accurate pressure sensors for the according pressure ranges were used.

For the PCI measurements, different hydrogen flow rates were investigated in order to identify the conditions that allow for measurements as close as possible to the equilibrium while taking the least time possible. $LaNi_{4.85}Al_{0.15}$ was investigated between -20 and 130 °C and C5 between -30 and 35 °C. Details are given in [Table A-3](#) in the [supplementary material](#).

For the reaction rate measurements, $LaNi_{4.85}Al_{0.15}$ was investigated in a temperature range between -20 and 40 °C. For extensive measurements, different end pressures after full conversion were investigated. They relate to different factors f between end pressure and equilibrium pressure at the given temperature according to equation (9):

$$f = \frac{p_{end}(x_{end})}{p_{eq}(T_{MH})} \quad (9)$$

The investigated factors ranged between 2 and 57. For all factors, similar rate coefficients were obtained. Therefore we conclude that gas transport was sufficient for all investigated pressures. Details are given in [Table 2](#) in the result section.

The repeatability of all experiments was excellent. For the PCI measurements, repeated experiments as well as results for different hydrogen flow rates and the chosen values are given in the [supplementary material in Figure A-5](#). [Figure A-6](#) shows repeated experiments for the rate coefficient measurements and their agreement.

Results and discussion

The aim of this work was to develop a precise experimental set-up for metal hydride characterization and to provide thermodynamic and kinetic properties for two different metal hydrides suitable for vehicle applications below 0 °C. The presented test bench is able to characterize metal hydrides in a large temperature and pressure range at high precision.

In this section, first the results of the PCI measurements are presented. Comparison to literature at the same

temperature allows evaluation of the quality of the results. Then, the measurements can be extended to lower, previously not investigated temperatures. From the obtained PCIs, the van't Hoff-plots and the values for reaction enthalpy and entropy are derived.

The reaction rate measurements for $\text{LaNi}_{4.85}\text{Al}_{0.15}$ are presented and the pre-exponential factor and the activation energy are derived. The results are compared to measurement for LaNi_5 from literature in order to evaluate the effect of the Al-substitution.

Finally, the obtained properties are discussed regarding the considered vehicle application.

Results on PCI measurements

In Fig. 4, the PCI measurement results for both materials are compared to literature data at the respective temperature. As can be seen, there is good agreement between the data. Some deviations can be identified at the beginning of absorption and desorption, however, the largest variations occur between the different literature values for C5. Overall, all values show close agreement, in particular the level of the plateaus for both absorption and desorption agree well. Therefore, the expansion to lower temperatures and pressures promises reliable results.

The final PCI results for both materials are given in Fig. 5. To our knowledge, they represent the first publication of thermodynamic values at temperatures below 25 °C and 0 °C for $\text{LaNi}_{4.85}\text{Al}_{0.15}$ and C5, respectively. They allow precise description of the equilibrium state down to –20 °C for $\text{LaNi}_{4.85}\text{Al}_{0.15}$ and –30 °C for C5 and hence extend the available data for both absorption and desorption to lower temperatures. For details on the used experiments, refer to Table A-3 in the supplementary material. The upper part of Fig. 5 shows the results for $\text{LaNi}_{4.85}\text{Al}_{0.15}$. The PCIs are given on the left hand side. The van't Hoff-plot on the right hand side is derived for 10, 50 and 90% of hydrogen conversion for both absorption and desorption. It can be observed that the material exhibits a very small plateau slope and small hysteresis compared to other metal hydrides. At –20 °C, $\text{LaNi}_{4.85}\text{Al}_{0.15}$ shows an equilibrium pressure of 55 mbar for desorption and 120 mbar for absorption at mid-plateau.

The lower part of Fig. 5 shows the results for C5. Although the experiments have been conducted with great care and possible effects of the analysis were looked at intensively (see

Ref. [18]), the overall hydrogen conversion shows slightly smaller values for decreased temperatures. This behavior does not coincide with reported general metal hydride properties, from which one would expect an increase of the plateau at lower temperatures. The reason for this deviation is unclear. However, the resulting pressure level of the $\alpha+\beta$ -phase is not affected but allows precise description of the mid-plateau. Hence, the curves were aligned at 50% conversion and these values were used for the evaluation of the van't Hoff-plot. C5 reacts between 580 mbar for desorption and 1.6 bar for absorption at –30 °C at mid-plateau.

From the van't Hoff-plots on the right hand side of Fig. 5, the reaction enthalpy and entropy were derived. Additionally, the PCI plateau slope at the middle of the plateau α_{mid} is deduced. The values are given in Table 1. The very small value for the plateau slope of $\text{LaNi}_{4.85}\text{Al}_{0.15}$ of 0.004 wt.-%⁻¹ underlines the close horizontal shape of this plateau. For C5, the slope with values between 0.53 and 0.72 wt.-%⁻¹ shows a considerably steeper course, which is typical for many Ti-Zr-Mn alloys.

Results on reaction rate coefficient measurements

The reaction rate of $\text{LaNi}_{4.85}\text{Al}_{0.15}$ was investigated in the range of –20 to 40 °C. The resulting reaction rate coefficient are depicted in Fig. 6 and all values, together with measurement specifications, are given in Table 2. The rate coefficient values for C5 from Ref. [27] are also included in the figure. The

Table 2 – Results of all reaction rate experiments.

No. of exp.	T in °C	p-sensor	p_{end} in bar	factor f	k in 1/s		
I-4	–20	$p_{R,5}$	0.24	2	0.00148		
I-1			0.8	7	7.08861E-4		
II-7	0		3.5	10	7.16806E-4		
I-3					1.5	13	5.56077E-4
II-1					4.2	35	0.00159
II-5	0		3.5	10	0.00136		
II-6					0.00911		
II-2					$p_{R,40}$	20	57
I-2 ^a	20	$p_{R,5}$	4.2	5	–		
II-3					0.02057		
II-4	40	$p_{R,40}$	20	22	0.01828		
II-8					20	10	0.04887

^a Excluded due to unreasonable results.

Table 1 – Reaction enthalpy, entropy and plateau slope for $\text{LaNi}_{4.85}\text{Al}_{0.15}$ and C5.

$\text{LaNi}_{4.85}\text{Al}_{0.15}$							
	x in %	$\Delta_{\text{R}}H$ in kJ/mol	$\Delta_{\text{R}}H_{\text{mean}}$ in kJ/mol	$\Delta_{\text{R}}S$ in J/(mol K)	$\Delta_{\text{R}}S_{\text{mean}}$ in J/(mol K)	m_{pl} in wt.-% ⁻¹	Δ_{mid} in wt.-%
absorption	10	31.54	31.0	105.05	104.9	0.004	0.65
	50	31.08		105.10			
	90	30.47		104.66			
desorption	10	33.98	33.8	109.08	109.9		
	50	33.70		109.41			
	90	33.76		111.27			
C5							
	absorption	50	22.69		97.20	0.723	1.0
desorption	50	27.83		109.90	0.534		

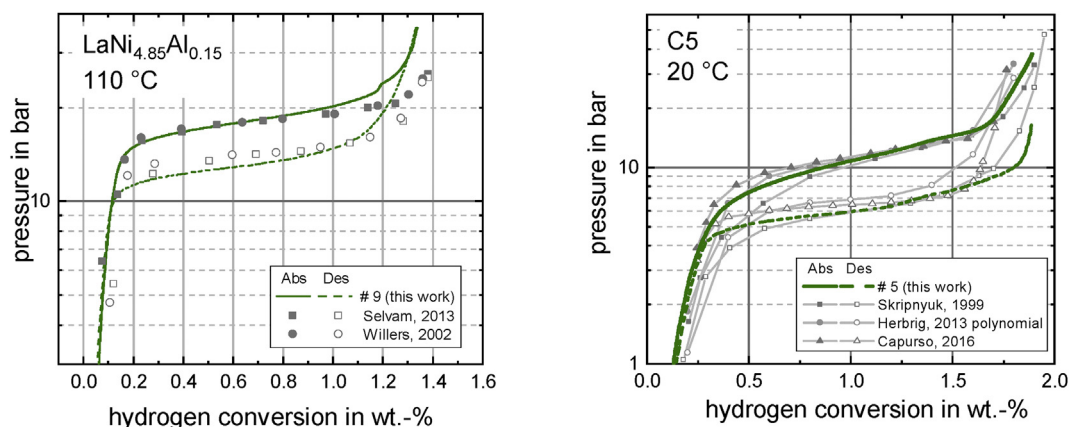


Fig. 4 – Comparison of results of $\text{LaNi}_{4.85}\text{Al}_{0.15}$ to literature [21,23] (left) and C5 to literature [25–27] (right).

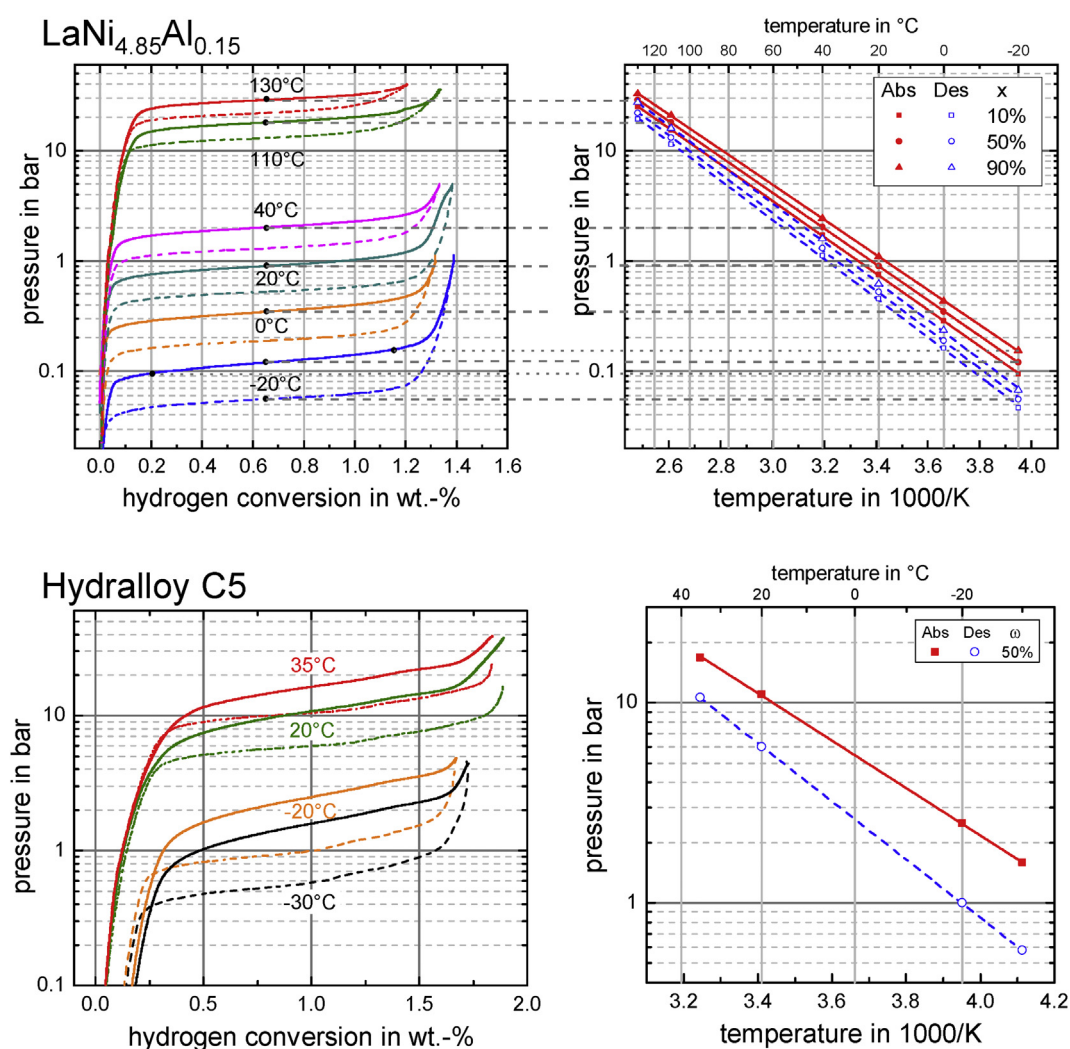


Fig. 5 – PCI measurements (left) and resulting Van't Hoff plot (right) for absorption (solid) and desorption (dashed) for $\text{LaNi}_{4.85}\text{Al}_{0.15}$ and for C5.

rate coefficients for $\text{LaNi}_{4.85}\text{Al}_{0.15}$ are clearly below the values for C5. However, they still show high values compared to other metal hydrides, e.g. the reaction rate coefficient of $\text{LaNi}_{4.85}\text{Al}_{0.15}$ at -20°C is 0.0018 s^{-1} . Hence hydrogen

conversion to a value of 90% would take around 8.5 min^2 . The

² At isothermal conditions and if only the reaction rate coefficient would determine the time.

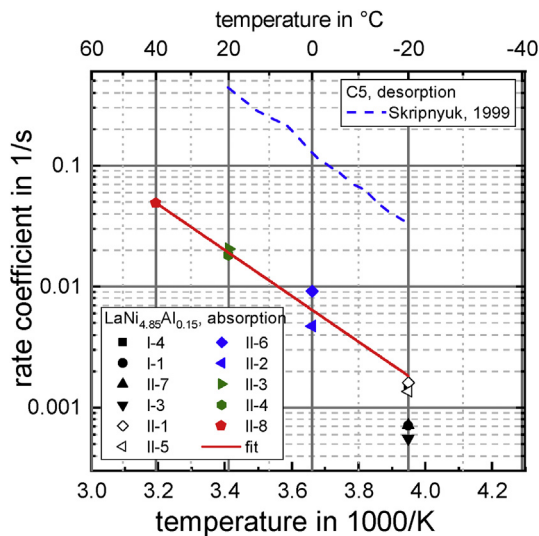


Fig. 6 – Rate coefficients for $\text{LaNi}_{4.85}\text{Al}_{0.15}$ for all performed experiments and for C5 [27].

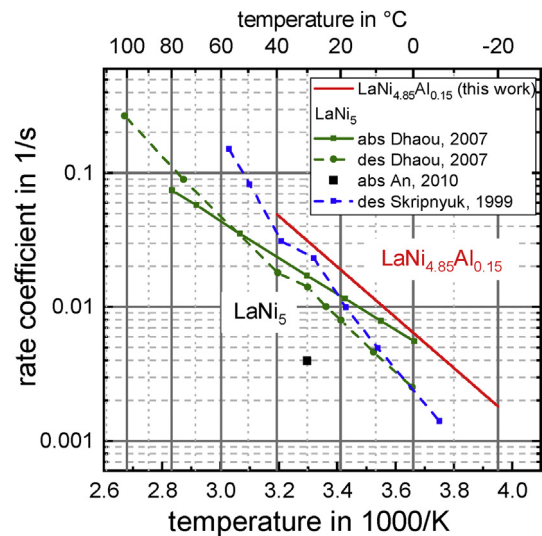


Fig. 7 – Rate coefficient for $\text{LaNi}_{4.85}\text{Al}_{0.15}$ compared to LaNi_5 [22,27,28].

reaction rate at 20 °C increases to 0.019 s^{-1} , leading to less than 1 min for complete conversion^b.

From the values for the reaction rate coefficient, the Arrhenius equation (8) can be used to derive the pre-exponential factor and the activation energy. For $\text{LaNi}_{4.85}\text{Al}_{0.15}$ the values are $A = 53,726 \text{ s}^{-1}$ and $E_a = 36,202 \frac{\text{J}}{\text{mol}}$. Therefore, the resulting Arrhenius term is as follows (10):

$$k(T) = 5.4 \cdot 10^4 \frac{1}{\text{s}} \cdot \exp\left(\frac{-36.2 \frac{\text{kJ}}{\text{mol}}}{RT}\right) \quad (10)$$

The effect of the substitution of nickel by aluminum on the reaction rates is discussed controversy in literature. Although, even for the well investigated LaNi_5 , publications don't agree on the exact rate coefficients for this material, showing the difficulty of these measurements such as isothermal conditions, a range can be defined and compared to the findings of this work for $\text{LaNi}_{4.85}\text{Al}_{0.15}$, see Fig. 7. As can be seen, the slope of the line for $\text{LaNi}_{4.85}\text{Al}_{0.15}$ is similar to the literature values for LaNi_5 , however, at a higher level. For example at 20 °C, the reaction rate of $\text{LaNi}_{4.85}\text{Al}_{0.15}$ is higher by a factor of around 2. Hence, it can be stated, at least for the investigated derivative, that the small aluminum content enhances the reaction rates.

Discussion in the context of vehicle application

In order to provide sufficient thermal energy for the vehicle component, of course much more material is required than for the characterization measurements. In order to provide sufficient thermal energy for preheating of e.g. 1 l of engine oil (in smaller circuit for cold start), 1 kg of material has to be considered for a temperature rise of 35 K. Therefore, large scale effects such as gas or heat transport limitations will occur. Hence, the chosen pair for the closed system and the heat generating material for the open system have to allow for temperature and pressure losses as well as for non-isothermal conditions and the system still has to work.

For the closed system in an ICE vehicle, the chosen material pair shows promising characteristics in this regard. In Fig. 8, the temperature boundary conditions are given together with the thermochemical equilibrium and reaction rates of the metal hydrides.

On the left hand side, the regeneration temperature level between 90 and 130 °C applied to $\text{LaNi}_{4.85}\text{Al}_{0.15}$ shows the resulting temperature level of absorption in C5 between 10 and 50 °C. According to the derived data, this absorption heat can always be released to the ambient. At elevated ambient temperatures, higher regeneration temperatures are required. This matches the experimental observation in Ref. [17], where, including temperature and pressure losses, a temperature difference between regeneration and ambient level of at least 110 K was necessary. During discharge, a theoretical temperature level between 20 and 70 °C can be reached for preheating.

Due to non-isothermal conditions, the materials will change their temperature during reaction, as indicated in Fig. 8, right. For the heat generating material, this leads to a temperature increase which is beneficial for the reaction rate. A temperature increase from –20 °C by 10 K leads to an increase in the reaction rate coefficient by a factor of around 2, leading to full conversion within 5 min instead of 9 min^b. In contrast, for the hydrogen supplying material, desorption will lead to temperature decrease. For example, a decrease of 10 K from –20 °C leads to a decrease of the reaction rate coefficient by a factor of 2 and the time for full conversion is prolonged from half a minute to around one minute^b. However, since this is still very fast, the temperature decrease will most likely allow for sufficiently fast reaction.

For the open system in a FC vehicle, the heat generating material $\text{LaNi}_{4.85}\text{Al}_{0.15}$ meets the requirements as well. Absorption at 1 bar and higher from the hydrogen storage tank leads to absorption temperature levels significantly above freezing point. Regeneration at 60 °C from FC waste heat leads to a desorption pressure above 2 bar and hence the hydrogen can be converted in the FC [17]. As for the closed

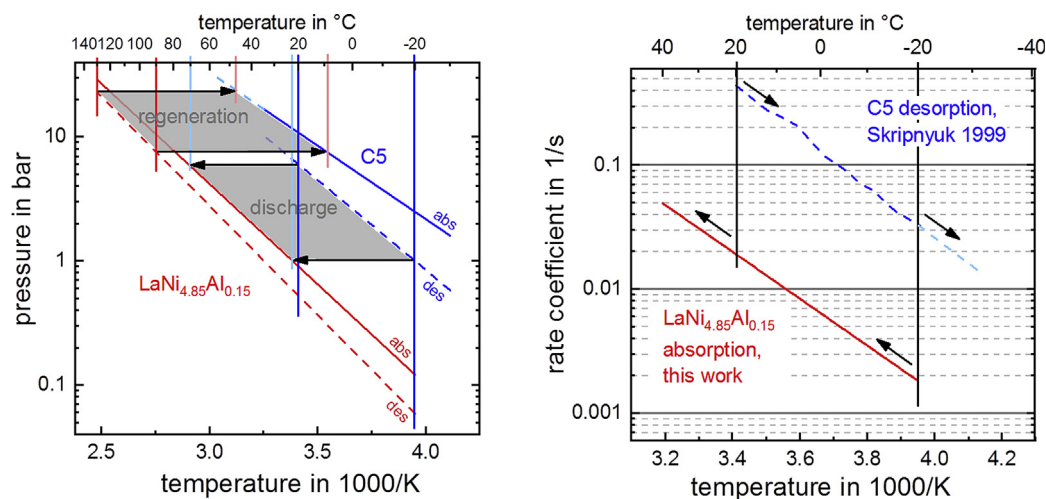


Fig. 8 – Material properties and vehicle boundary conditions.

system, the absorption heat also leads to a temperature increase and hence the reaction rate increases (self-acceleration). Higher pressures than in the closed system are possible and lead to even higher equilibrium temperatures and reaction rates.

Therefore, the material properties satisfy the vehicle requirements at the considered boundary conditions. However, in particular for the closed system, scale up effects might require higher temperature differences than suggest by the intrinsic material properties (PCI) and non-isothermal conditions might lead to limitations in extreme cases.

Conclusion

Almost no data is known in literature about equilibrium pressures and reaction rates of metal hydrides below 0 °C. However, for thermal applications in vehicles operated in winter conditions, this knowledge is crucial. This work presents a precise experimental set-up to measure characteristics of metal hydrides in the temperature range of –30 to 200 °C and a pressure range of 0.1 mbar–100 bar. Pressure concentration-isotherms for $\text{LaNi}_{4.85}\text{Al}_{0.15}$ and C5 ($\text{Ti}_{0.95}\text{Zr}_{0.05}\text{Mn}_{1.46}\text{V}_{0.45}\text{Fe}_{0.09}$) and reaction rate coefficients for $\text{LaNi}_{4.85}\text{Al}_{0.15}$ were measured in the temperature and pressure range necessary for vehicle preheating applications.

The first PCIs for both materials below 0 °C were published here. For $\text{LaNi}_{4.85}\text{Al}_{0.15}$, reaction rate coefficients down to –20 °C were measured for the first time and compared to values of LaNi_5 for the effect of nickel-substitution by aluminum. Only now, the characteristics of the material can be described in the necessary range for vehicle applications. $\text{LaNi}_{4.85}\text{Al}_{0.15}$ shows an equilibrium pressure down to 55 mbar for desorption and 120 mbar for absorption at mid-plateau at –20 °C. C5 reacts between 580 mbar for desorption and 1.6 bar for absorption at –30 °C at mid-plateau.

Beneficial for the application, the rate coefficient results for $\text{LaNi}_{4.85}\text{Al}_{0.15}$ show high values even at –20 °C of 0.0018 s^{–1}. Compared to LaNi_5 , the aluminum addition in $\text{LaNi}_{4.85}\text{Al}_{0.15}$

leads to increased reaction rates. C5 shows even higher values, namely by a factor of more than 10 even at –20 °C.

However, in vehicle applications a sufficient amount of heat needs to be stored. This required increase in mass of material will lead to gas and heat transport limitations. Hence, experiments in large scale have to show the up-scale limitation factors of the material pair in the considered applications. First measurements have been performed by the authors and published in Ref. [17]. Together with the complementary data presented here, preheating units that reduce automotive cold-start issues can be developed.

Appendix A. Supplementary data

Supplementary data to this article can be found online at <https://doi.org/10.1016/j.ijhydene.2018.12.116>.

REFERENCES

- [1] Ron M. The normalized pressure dependence method for the evaluation of kinetic rates of metal hydride formation/decomposition. *J Alloy Comp* 1999;283(1–2):178–91.
- [2] Cipollone R, Di Battista D, Mauriello M. Effects of oil warm up acceleration on the fuel consumption of reciprocating internal combustion engines. *Energy Proc* 2015;82:1–8.
- [3] Reiter MS, Kockelman KM. The problem of cold starts: a closer look at mobile source emissions levels. *Transport Res Transport Environ* 2016;43:123–32.
- [4] Di Battista D, Cipollone R. Experimental and numerical assessment of methods to reduce warm up time of engine lubricant oil. *Appl Energy* 2016;162:570–80.
- [5] Lee D-W, Johnson J, Lv J, Novak K, Zeitsman J. Comparisons between vehicular emissions from real-world in-use testing and epa moves estimation. 2012.
- [6] Deppenkemper DK, Günther M, Stefan P. Development of optimized exhaust gas heating strategies for passenger car Diesel engines by means of variable valve train applications. In: 17. Internationales stuttgarter symposium; 2017. p. 123–42.

- [7] Dardiotis C, Martini G, Marotta A, Manfredi U. Low-temperature cold-start gaseous emissions of late technology passenger cars. *Appl Energy* 2013;111:468–78.
- [8] Fan Q, Li L. Study on first-cycle combustion and emissions during cold start in a TSDI gasoline engine. *Fuel* 2013;103:473–9.
- [9] Rizvi SQA. A comprehensive review of lubricant chemistry, technology, selection, and design. West Conshohocken, PA: ASTM International; 2009.
- [10] Mishler J, Wang Y, Mukherjee PP, Mukundan R, Borup RL. Subfreezing operation of polymer electrolyte fuel cells: ice formation and cell performance loss. *Electrochim Acta* 2012;65:127–33.
- [11] Santamaria A, Tang HY, Park JW, Park GG, Sohn YJ. 3D neutron tomography of a polymer electrolyte membrane fuel cell under sub-zero conditions. *Int J Hydrogen Energy* 2012;37(14):10836–43.
- [12] Lim SJ, et al. Investigation of freeze/thaw durability in polymer electrolyte fuel cells. *Int J Hydrogen Energy* 2010;35(23):13111–7.
- [13] Lin R, Lin X, Weng Y, Ren Y. Evolution of thermal drifting during and after cold start of proton exchange membrane fuel cell by segmented cell technology. *Int J Hydrogen Energy* 2015;40(23):7370–81.
- [14] Dornheim M. Thermodynamics of metal hydrides: tailoring reaction enthalpies of hydrogen storage materials. In: Moreno Pirajan Juan Carlos, editor. *Thermodynamics - interaction studies - solids, liquids and gases*. Intech open science - open minds; 2011.
- [15] Bloch J, Mintz MH. Kinetics and mechanisms of metal hydrides formation—a review. *J Alloy Comp* 1997;253–254:529–41.
- [16] Muthukumar P, Satheesh A, Linder M, Mertz R, Groll M. Studies on hydriding kinetics of some La-based metal hydride alloys. *Int J Hydrogen Energy* 2009;34(17):7253–62.
- [17] Dieterich M, Bürger I, Linder M. Open and closed metal hydride system for high thermal power applications: preheating vehicle components. *Int J Hydrogen Energy* 2017;42(16):11469–81.
- [18] Kölbig M. Coupled metal hydride reactions for preheating vehicle components at low temperatures. University of Stuttgart; 2018.
- [19] Weckerle C, Buerger I, Linder M. Novel reactor design for metal hydride cooling systems. *Int J Hydrogen Energy* 2017;42(12):8063–74.
- [20] Mechi N, Ben Khemis I, Dhaou H, Knani S, Jemni A, Ben Lamine A. A macroscopic investigation to interpret the absorption and desorption of hydrogen in LaNi_{4.85}Al_{0.15} alloy using the grand canonical ensemble. *Fluid Phase Equil* 2016;427:56–71.
- [21] Selvam PK, Muthukumar P, Linder M, Mertz R, Kulenovic R. Measurement of thermochemical properties of some metal hydrides – titanium (Ti), mixed metal (Mm) and lanthanum (La) based alloys. *Int J Hydrogen Energy* 2013;38(13):5288–301.
- [22] Dhaou H, Askri F, Ben Salah M, Jemni A, Ben Nasrallah S, Lamoumi J. Measurement and modelling of kinetics of hydrogen sorption by LaNi₅ and two related pseudobinary compounds. *Int J Hydrogen Energy* 2007;32(5):576–87.
- [23] Willers E. Multi-Hybrid-Sorptionsanlage zur kombinierten Heizung und Kühlung. University of Stuttgart; 2002.
- [24] Wanner M. Untersuchung des Langzeitverhaltens der thermodynamischen Stabilität von Metallhydriden. University of Stuttgart; 2001.
- [25] Capurso G, et al. Development of a modular room-temperature hydride storage system for vehicular applications. *Appl Phys A* 2016;122(3):236.
- [26] Herbrig K, Röntzsch L, Pohlmann C, Weißgärber T, Kieback B. Hydrogen storage systems based on hydride–graphite composites: computer simulation and experimental validation. *Int J Hydrogen Energy* 2013;38(17):7026–36.
- [27] Skripnyuk VM, Ron M. Evaluation of kinetics by utilizing the normalized pressure dependence method for the alloy Ti_{0.95}Zr_{0.05}Mn_{1.48}V_{0.43}Fe_{0.08}Al_{0.01}. *J Alloy Comp* 1999;295:385–90.
- [28] An XH, Pan YB, Luo Q, Zhang X, Zhang JY, Li Q. Application of a new kinetic model for the hydriding kinetic of LaNi_{5-x}Al_x (0 ≤ x ≤ 1.0) alloys. *J Alloy Comp* 2010;506(1):63–9.
- [29] Sharma VK, Anil Kumar E. Measurement and analysis of reaction kinetics of La – based hydride pairs suitable for metal hydride – based cooling systems. *Int J Hydrogen Energy* 2014;39(33):19156–68.
- [30] Cao DL, Cheng HH, Ma L, Chen DM, Lue MQ, Yang K. Effects of Al partial substitution for Ni on properties of LaNi_{5-x}Al_x. *Trans Nonferrous Metals Soc China* 2007;17(50276063):S967–71.
- [31] Wang X-L, Suda S. Effects of Al-substitution on hydriding reaction rates of LaNi_{5-x}Al_x. *J Alloy Comp* 1993;191(1):5–7.
- [32] Park I-S, Kim J-K, Kim KJ, Zhang J, Park C, Gawlik K. Investigation of coupled AB₅ type high-power metal hydride reactors. *Int J Hydrogen Energy* 2009;34(14):5770–7.
- [33] Goudy AJ, Stokes DG, Gazzillo JA. The effect of heat transfer on the desorption kinetics of LaNi₅H₆. *J Less Common Met* 1983;91(1):149–58.
- [34] Wang X-L, Suda S. Study of the hydriding kinetics of LaNi_{4.7}Al_{0.3}-H system by a step-wise method. *J Less Common Met* 1990;159:109–19.
- [35] Feng F, Geng M, Northwood DO. Mathematical model for the plateau region of P–C-isotherms of hydrogen-absorbing alloys using hydrogen reaction kinetics. *Comput Mater Sci* 2002;23(1–4):291–9.
- [36] Friedlmeier G, Schaaf M, Groll M. How to measure pressure-concentration-isotherms representative for technical applications. *Z Phys Chem* 1994;183:185–95.
- [37] Muthukumar P, Linder M, Mertz R, Laurien E. Measurement of thermodynamic properties of some hydrogen absorbing alloys. *Int J Hydrogen Energy* 2009;34(4):1873–9.
- [38] Goodell PD, Rudman PS. Hydriding and dehydriding rates of the LaNi₅-H system. *J Less Common Met* 1983;89(1):117–25.
- [39] Rudman PS. Hydriding and dehydriding kinetics. *J Less Common Met* 1983;89(1):93–110.
- [40] Zhou L, Zhou Y. Determination of compressibility factor and fugacity coefficient of hydrogen in studies of adsorptive storage. *Int J Hydrogen Energy* 2001;26(6):597–601.
- [41] Huot J. Handbook of hydrogen storage. Weinheim: Wiley-VCH; 2010.
- [42] Jordan RB. Reaction mechanisms of inorganic and organometallic systems. Oxford: University Press; 1998.



ELSEVIER

Available online at www.sciencedirect.com

ScienceDirect

journal homepage: www.elsevier.com/locate/ijhe

Open and closed metal hydride system for high thermal power applications: Preheating vehicle components

Mila Dieterich*, Inga Bürger, Marc Linder

German Aerospace Center (DLR), Institute of Engineering Thermodynamics, Thermal Process Technology, Pfaffenwaldring 38 – 40, 70569 Stuttgart, Germany

ARTICLE INFO

Article history:

Received 22 December 2016
 Received in revised form
 10 February 2017
 Accepted 5 March 2017
 Available online 23 March 2017

Keywords:

Thermochemical energy storage
 Metal hydrides
 High power
 Cold start
 Coupled chemical reaction

ABSTRACT

Many vehicle components operate at temperatures above ambient conditions. At cold start, most of the pollutants are produced and lifespan is reduced. Thermochemical energy storage with high power density could prevent these disadvantages. In order to investigate achievable power densities of a thermochemical energy storage at technically relevant boundary conditions, a laboratory scale device using metal hydrides ($\text{LaNi}_{4.85}\text{Al}_{0.15}$ and $\text{C5}^{\text{®}}$) is designed and preheating operation modes (open and closed) are analyzed. The impact of the ambient temperature (from -20 to $+20$ °C), as well as other influencing factors on the thermal power output such as heat transfer flow rate, regeneration temperature and pressure conditions are investigated. The experiments proved the suitability of the reactor design and material selection for the considered application boundary conditions. For the coupled reaction (closed system), the ambient temperature has the greatest influence on the thermal power with decreasing values for lower temperatures. Here, values between $0.6 \text{ kW/kg}_{\text{MH}}$ at ambient temperature of -20 °C and $1.6 \text{ kW/kg}_{\text{MH}}$ at 20 °C, at otherwise same conditions, were reached. If hydrogen can be supplied from a pressure tank (open system), the supply pressure in relation to equilibrium pressure at the considered ambient temperature has to be large enough for high thermal power. At -20 °C, $1.4 \text{ kW/kg}_{\text{MH}}$ at a supply pressure of 1.5 bar and $5.4 \text{ kW/kg}_{\text{MH}}$ at a hydrogen pressure of 10 bar were reached.

© 2017 Hydrogen Energy Publications LLC. Published by Elsevier Ltd. All rights reserved.

Introduction

Many vehicle components operate at temperatures above ambient conditions. At cold start, especially at winter temperatures of -20 °C and below, most of the pollutants are produced and lifespan is reduced. This is described here in more detail for combustion drives and fuel cells.

Conventional engines are designed for temperatures around 100 °C. Starting at ambient temperatures neither the combustion process nor the exhaust gas treatment work sufficiently until operation temperature is reached. In these first couple of minutes, 60 – 80% of all pollutants of the whole driving cycle are produced [1,2]. As combustion engines become more and more efficient, waste heat is reduced and this leads to a prolonged cold start phase and more pollutants.

* Corresponding author. Fax: +49 711 6862 632.

E-mail address: mila.dieterich@dlr.de (M. Dieterich).

<http://dx.doi.org/10.1016/j.ijhydene.2017.03.024>

0360-3199/© 2017 Hydrogen Energy Publications LLC. Published by Elsevier Ltd. All rights reserved.

Nomenclature

c_p	heat capacity
\dot{m}	mass flow
P	thermal power
p	pressure
Q	overall heat
R	universal gas constant
T	temperature
x	hydrogen conversion
ΔH	reaction enthalpy
ΔS	reaction entropy

Subscripts

300 sec	after 300 s
600 sec	after 600 s
<i>amb</i>	at ambient level
<i>eq</i>	equilibrium state
<i>f_c</i>	fuel cell
H_2	hydrogen
<i>heat</i>	produced heat level
<i>HTF</i>	heat transfer fluid
<i>in</i>	at inlet of reactor
<i>MH</i>	metal hydride
<i>out</i>	at outlet of reactor
<i>reg</i>	regeneration level
<i>storage</i>	hydrogen storage material
<i>tank</i>	at tank level
<i>waste</i>	waste heat source

If the components are preheated, a large amount of the pollutants can be prevented.

Even in fuel cell driven vehicles, water produced in fuel cells would freeze below zero degrees. The ice layer prevents gas flow and the expansion in volume can cause mechanical destruction of the fuel cell [3–6]. Therefore, fuel cells are dried before shut down. When restarting, the membrane has to be wetted which requires temperatures above freezing point. So the fuel cell needs to be preheated to temperatures above 0 °C in order to avoid degradation and prolonging life time significantly.

Therefore, both combustion engines as well as fuel cells require preheating for long service life and reduced exhaust emissions. Since in both cases thermal energy is available later during the driving cycle, thermal energy storages are a suitable option to overcome the described problem. A high energy density of the application, including both storage material and containment, is of importance, because the thermal storage adds weight to the vehicle. A promising option is a thermochemical energy storage system, due to the high energy density at limited temperature conditions and its long-term storage possibility. Here, a gas reacts with a solid and absorption heat is released. If heat is supplied to the storage material, the gas is released while heat is absorbed. This relation between solid temperature and gas pressure is described in the Van't Hoff equation [7]:

$$\ln(p_{eq}) = -\frac{\Delta H}{RT} + \frac{\Delta S}{R} \quad (1)$$

Where p_{eq} is the equilibrium pressure of the gas, ΔH is the reaction enthalpy, R is the universal gas constant, T is the absolute temperature of the solid and ΔS is the reaction entropy. By controlling the chemical reaction, generating heat on demand and controlling the temperature and power of the released thermal energy is possible.

This study focuses on the investigation of metal hydrides for high power thermal energy storage systems. In this case, a metal alloy forms a hydride phase by chemisorption of hydrogen. Originally metal hydrides were investigated as hydrogen storage materials [8–10]. But because they release and absorb heat during reaction, more and more investigations deal with thermal applications such as e.g. thermally driven heat pumps [11–20]. Consequently, the available data in literature deals mainly with temperatures above freezing point. However, the intended application in this paper – the pre-heating of components – addresses also automotive applications with respective temperature conditions for both metal hydrides down to –20 °C. Since according to Arrhenius the reaction rate decreases at lower temperatures, the most important but so far hardly investigated aspect is related to the technically achievable power densities of metal hydrides at these boundary conditions. The systems developed in this work are designed for the following two generic applications:

- Combustion engines – coupled reaction as a closed system.** At nominal operation the combustion engine releases around 2/3 of the energy as heat [21] and consequently cooling is needed. This thermal energy can be stored in a thermochemical energy storage consisting of two reactors with different metal hydrides. The thermal energy leads to a desorption of hydrogen in one of the reactors. The released hydrogen is stored in the second reactor. This closed system doesn't require any exchange of hydrogen with the surrounding, but works only by absorbing and releasing heat. If the back reaction is prevented, e.g. by a separating valve, the chemically stored thermal energy can be released at the next cold start by opening the valve to preheat the respective component.
- Fuel cells – hydrogen supply from tank as an open system.** The potential energy stored in the hydrogen pressure tank, e.g. around 15% of the overall energy stored at 900 bar [22], is currently throttled on board and therefore lost. By conducting hydrogen at higher pressure onto a metal hydride, heat can be produced, e.g. to preheat the fuel cell. For regeneration, the waste heat of the fuel cell can be used to regenerate the thermochemical storage. In this open system, a combination of thermal energy from the fuel cell and the potential energy of the hydrogen tank is used to run the system. The hydrogen itself is not consumed since it is desorbed during regeneration and can be converted to electricity in the fuel cell.

Both applications (open and closed system) have in common that the chemical potential of the thermochemical energy storage is used to generate thermal energy when it is needed. Depending on the type of propulsion, the regeneration of the storages differs. However, the underlying challenge can be summarized to the requirement of high thermal power

densities at technically relevant boundary conditions. Even though it is generally assumed that the chemisorption of metal hydrides possess very fast reaction rates [23,24] until now, little data exists of metal hydride characteristics at very low temperatures. Moreover, experimental data of coupled reactions at relevant scale and at temperatures below freezing point is not available in literature. Therefore, this aspect is explicitly addressed and investigated in this work. For this purpose, a test bench is designed to investigate the influencing factors on high thermal power at vehicle temperature boundary conditions down to $-20\text{ }^{\circ}\text{C}$ for two different operation principles (combustion engines and fuel cells). Appropriate materials are selected and reactors are designed. In order to investigate the various influencing aspects, the mass flow of the heat transfer fluid (HTF), the ambient temperature, the regeneration conditions for the closed system as well as the supply pressure for the open system are varied. The experimental results are presented and discussed in the following.

Methodology and experimental details

The investigated systems are designed to produce heat at very low temperatures. Therefore, temperatures ranging from $-20\text{ }^{\circ}\text{C}$ to $+20\text{ }^{\circ}\text{C}$ were set as ambient conditions. Both systems are able to operate even at lower ambient temperatures, although this might affect the achievable temperature level of preheating. In the following section the two operation designs of the closed and open system are described as well as their possible application in vehicles including temperature and pressure boundary conditions for the material selection. Then, the test bench, the reactor design and the measured and calculated values are described. At the end, the experimental design and varied parameters are discussed.

Operation design

In the closed system hydrogen has to be stored in a second reactor containing a metal hydride with different thermodynamics. At the same (ambient) temperature, different equilibrium pressures result in the reactors separated by a valve. When the valve is opened, hydrogen flows from the “storage reactor” to the “heat generating reactor”. It is absorbed here, producing heat and maintaining the pressure difference between the reactors. Hence, the other metal hydride desorbs hydrogen. This process continues until the storing reactor cannot desorb or the heat reactor cannot absorb hydrogen anymore. To regenerate, waste heat is provided to the heat reactor causing the pressure to rise, while the storage reactor is maintained at ambient temperature. This causes a pressure difference in the other direction and hydrogen flows back into the storage reactor. Once all hydrogen is exchanged, the valve is closed and the heat reactor is allowed to cool to ambient temperature. No insulation is needed. When thermal energy is needed, the valve is opened and heat is produced from ambient temperature independent of the storage time without losses of the thermochemical energy.

The system design for this closed system is inspired by general vehicle applications to investigate the potential under

relevant boundary conditions. However, it doesn't claim to be a mature component considering all aspects for vehicle integration. Waste heat in combustion engines occurs for example in the cooling circuit or the engine lubricant. At cold start, increasing the temperature of the cooling circuit increases the temperature of the engine, too. This leads to less wall quenching in the cylinder and higher combustion temperatures which decreases the amount of pollutants like unburned hydrocarbons and carbon oxide [25,26]. This also leads to faster heating and functionality of the catalytic converter. Preheating of the engine lubricant has a similar effect. In addition, its viscosity decreases exponentially with temperature [27]. Every single Kelvin of increased temperature leads to less mechanical stress on the oil, leading to better lubrication properties and longer lifetime of the oil and the engine.

The assumed vehicle temperature boundary conditions for closed system in this work are as follows:

- $T_{amb} = -20\text{--}20\text{ }^{\circ}\text{C}$
- $T_{waste} = T_{reg} = 90\text{--}130\text{ }^{\circ}\text{C}$
- T_{heat} : subject of investigation

The equilibrium pressure boundary conditions for the reaction material are the following:

- $p_{storage} > p_{heat}$ at the same temperature
- $p_{heat}(T_{reg}) > p_{storage}(T_{amb})$

where $p_{storage}$ refers to the “storage reactor” and p_{heat} to the “heat producing reactor”.

In contrast to the closed system, the open system works with hydrogen from the infrastructure of the car. Heat is produced when hydrogen is conducted from the tank onto the metal hydride. To desorb the hydrogen and hence store thermal energy, the waste heat of the fuel cell is used. The released hydrogen is consumed by the fuel cell.

In order to be able to directly use the infrastructure of a fuel cell vehicle and to provide heat even at low tank level, the supply pressure was assumed to be at 10 bar and below. A polymer electrolyte fuel cell (PEFC, old: proton exchange membrane (PEM) fuel cell) works at hydrogen pressures of around 1–3 bar and temperatures between 60 and 80 $^{\circ}\text{C}$ [28] which can be used as regeneration heat for the thermal energy storage. Experimental constrains limited the release of hydrogen at pressures above 1 bar. However, this does not affect the general investigation, but needs to be taken into account for a later integration.

Consequently, the vehicle boundary conditions for the open system in this work are the following:

- $T_{amb} = -20\text{--}20\text{ }^{\circ}\text{C}$
- $T_{waste} = T_{reg} = 60\text{--}80\text{ }^{\circ}\text{C}$
- $T_{heat} \geq 20\text{ K}$ (to reach at least $0\text{ }^{\circ}\text{C}$)
- $p_{tank} = 1.5\text{--}10\text{ bar}$
- $p_{fc} = 1\text{ bar}$

The equilibrium pressure boundary conditions for the reaction material are:

- $p_{heat}(T_{reg}) > p_{fc}$
- $p_{heat} = 3–20$ bar
- $T_{heat} (p_{heat}) \geq 0$ °C

Material selection

For the material selection, the described boundary conditions are indicated in a Van't Hoff plot in Fig. 1. The suited materials are LaNi_{4.85}Al_{0.15} from WholeWin (China) for the heat producing side and Hydralloy C5® (Ti_{0.95}Zr_{0.05}Mn_{1.56}V_{0.46}Fe_{0.09}) from GfE Metalle und Materialien GmbH (Germany) for the hydrogen storage side in the closed system. Their thermodynamics are included in Fig. 1. This theoretical consideration does not take pressure losses etc. into account. The blue areas indicate the conditions for heat production (closed: ambient temperature, open: supply pressure from tank), the red areas the regeneration temperature and the orange areas show the temperature range of the produced heat. In the closed system (Fig. 1, left), the ambient temperature determines the hydrogen pressure for heat production. If C5 desorbs hydrogen at -20 °C the resulting pressure leads to heat production of around 25 °C if absorbed onto LaNi_{4.85}Al_{0.15} (indicated by the lower solid orange arrow). The desorption pressure of C5 at 20 °C leads to an absorption temperature of 75 °C of LaNi_{4.85}Al_{0.15} (upper solid orange arrow). Hence, heat can be produced theoretically between 25 and 75 °C. At regeneration temperature of 130 °C, the pressure of desorbed hydrogen from LaNi_{4.85}Al_{0.15} results in an absorption heat at 50 °C in the “storage reactor” (C5®) which can be dissipated to ambient (upper dotted orange arrow). At temperatures of 90 °C the absorption heat of C5 can only be dissipated at ambient temperatures below 10 °C (lower dotted orange arrow). Complete regeneration might therefore not be possible in all cases for the closed system which is investigated in 3.2.

The material in the open system (Fig. 1, right) can produce heat at a temperature level between 40 and 90 °C at the given supply pressure range. Since the hydrogen gas is taken from the hydrogen tank, this is independent of the ambient temperature. For desorbing hydrogen at pressures above 1 bar,

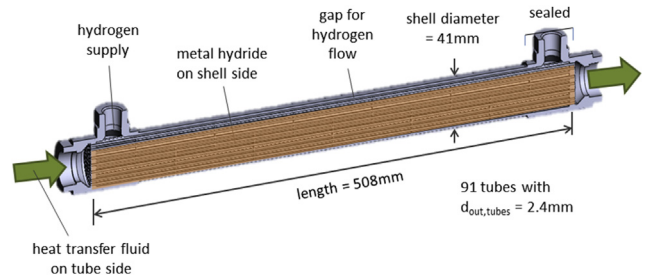


Fig. 2 – Metal hydride reactor in detail.

regeneration temperatures of above 30 °C are necessary. The selected materials have fast kinetics and in theory fit the boundary conditions quite well. The actual suitability is shown in the following results.

Test bench and experimental procedure

Micro tube bundle heat exchangers were chosen as reactors since they allow for high power applications due to the large surface area per volume. A drawing is given in Fig. 2. Metal hydride powder is located on the shell side, the heat transfer fluid (HTF) flows through the tubes. As the system works at pressures close to ambient or below, a gap at the top of the horizontal reactors is ensured to simplify the distribution of the hydrogen gas (clipped baffle plates). Commercially available heat exchangers by Exergy Heat Transfer Solutions (Model # 00256-06 with clipped baffles) are used to realize high thermal power. They consist of 91 tubes with an outer diameter of 2.4 mm and 508 mm of length, a total diameter of 41 mm and a maximal distance to the tubes of 1.15 mm. The reactors were filled with the corresponding amount of material so both can store about the same amount of hydrogen. The “heat generating reactor” (reactor 1) contains 960 g of LaNi_{4.85}Al_{0.15} (x ≈ 1.0 wt.-%) and the “storage reactor” (reactor 2) contains 615 g Hydralloy C5® (x ≈ 1.5 wt.-%).

A test bench is designed to investigate the system. It is able to mimic the required temperatures with the help of a heat

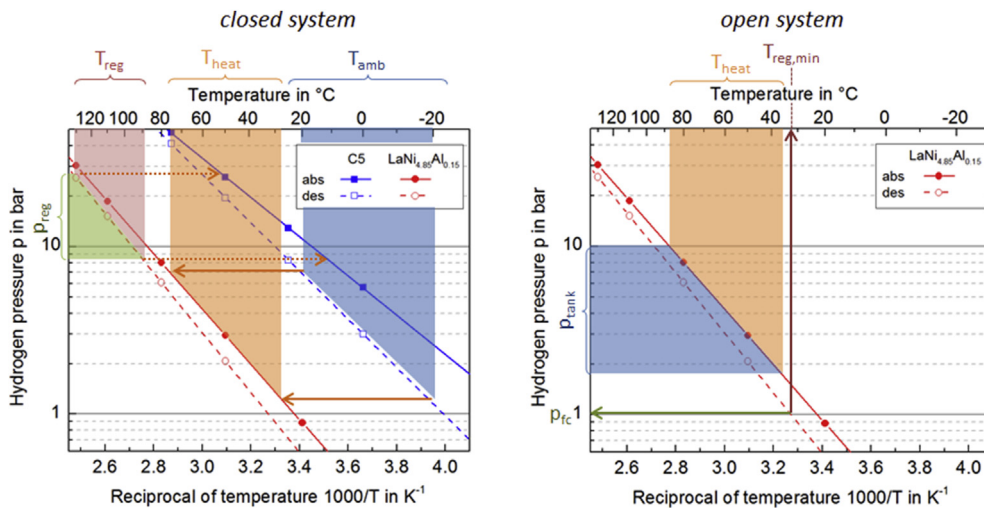


Fig. 1 – Van't Hoff Plot of LaNi_{4.85}Al_{0.15} [29] and Hydralloy C5® [30] including temperature and pressure boundary conditions for the closed (left) and open (right) system.

transfer fluid, supply hydrogen and measure and log the required data. Fig. 3 shows a picture of the two reactors integrated into the test bench (left) and a schematic drawing including thermostatic baths, measurement positions of the acquired data and valves (right). Both reactors are shown as in the closed system. For the open system, only reactor 1 was operated.

The temperatures of the HTF are measured by resistance thermometer (Pt100 according to DIN EN 60751), the mass flows are measured by Coriolis mass flow meters (measurement range set to 0–1000 kg/h, measurement uncertainty of $\pm 0.10/0.15\%$ RD for reactor 1/2, respectively) and the pressure is measured by a piezoresistive pressure sensor (measurement range of 0–40 bar_{abs}, measurement uncertainty of ± 0.4 bar). The hydrogen volume flow is measured by a gas flow meter (measurement range of 0–100 l_N/min extendable to 130 l_N/min, measurement uncertainty of $\pm (0.5\% \text{ Rd} + 0.1\% \text{ FS})$). The used heat transfer fluid is SilOil M40.165/220.10 by Huber Kältemaschinenbau AG (Germany). Its thermal capacity was measured at our institute with the differential scanning calorimetry method and is given as $c_{p,HTF} \left[\frac{\text{J}}{\text{gK}} \right] = 0.0013 T [^{\circ}\text{C}] + 1.6718$. The accuracy of the measurement is $\pm 10\%$. The most important value is the thermal power actually transferred to the heat transfer fluid. This is calculated by the temperature difference of the HTF before ($T_{HTF,in}$) and after ($T_{HTF,out}$) flowing through the reactor, the mass flow (\dot{m}_{HTF}) and the thermal capacity of the HTF ($c_{p,HTF}$). The thermal power in W is calculated according to the following equation:

$$P = \dot{m}_{HTF} c_{p,HTF} (T_{HTF,out} - T_{HTF,in}) \quad (2)$$

The overall heat in J released by the system is calculated by integrating the thermal power over time as given in Equation (3).

$$Q = \int_{t=0}^t P dt \quad (3)$$

By knowing the mass of metal hydride and the reaction enthalpy the hydrogen conversion can be calculated in wt.-% by Equation (4):

$$x = \frac{m_{H_2}}{m_{MH}} \cdot 100 \quad (4)$$

The absorption enthalpy of $\text{LaNi}_{4.85}\text{Al}_{0.15}$ is 31.6 kJ/mol_{H₂} [29].

An experiment consists of two half-cycles: regeneration and heat production. For regeneration, the thermostat tempering reactor 1 is set to the given regeneration temperature. The regeneration temperature of the open system was set to 130 °C in analogy to the reference experiment of the closed system for better comparison. While the regeneration pressure of the closed system is set by keeping reactor 2 to ambient temperature, reactor 1 in the open system desorbs against ambient pressure. As soon as all temperatures are at steady-state, the valve either to reactor 2 (closed system) or to the ambient at ambient pressure (open system) is opened. The regeneration is over as soon as the pressure value is at steady-state. Then the valve is closed and reactor 1 is also tempered to ambient temperature. The heat production experiment can start when all temperatures are at the simulated ambient temperature (e.g. –20 °C) in steady-state. The valve is opened to either reactor 2 (closed system) or the hydrogen gas cylinder via a mechanical pressure regulator (open system).

For the initial filling of the closed system with hydrogen, reactor 2 was tempered to 10 °C and provided with hydrogen at pressure of 20.8 bar until equilibrium was reached. Reactor 1 was evacuated at 50 °C for 0.5 h.

Different parameters were varied in order to investigate their influence on the thermal power output. The experiments were conducted in a mixed order and some were repeated to minimize systematic errors. The ambient temperature, the mass flow of the HTF and the supply pressure for the open system or regeneration temperature for the closed system, respectively, were varied. The variation ranges are given in Table 1 in the section “General discussion”.

Results and discussion

Repeatability

One reference experiment for both systems was repeated several times throughout the experimental period in order to

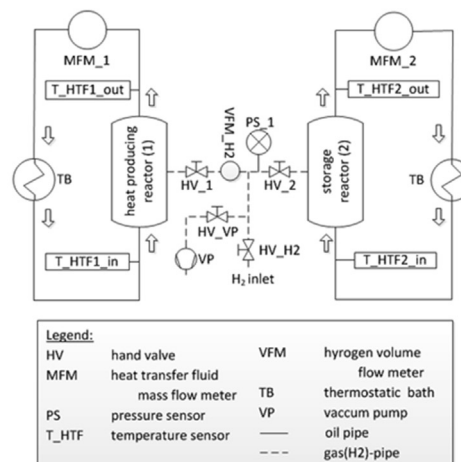
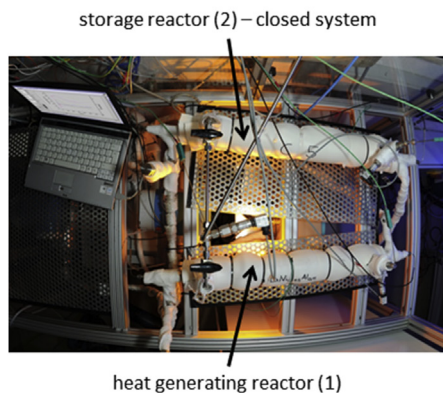


Fig. 3 – Test bench design with photo (left) and scheme (right).

check whether there are errors in the measurement itself or changes inside the material over time. The results in terms of pressure course, thermal power and hydrogen conversion are shown in Fig. 4.

For the closed system (Fig. 4, left) the reference experiment is performed at ambient temperature of $-20\text{ }^{\circ}\text{C}$, regenerated with at waste heat temperature of $130\text{ }^{\circ}\text{C}$ and a HTF mass flow of 250 kg/h . The course of the pressure and the thermal power are very similar. In experiment 2 (green solid line) a little higher peak value of 0.62 kW is reached compared to 0.58 and 0.56 kW of the other two experiments (10 and 16), but it is still within the same range. The integration of the reached power level over the measurement duration leads to similar courses and end values for the hydrogen conversion. Therefore, it can be stated that no changes occurred in the material and inside the reactor and thus the experiments are repeatable.

The reference experiment for the open system (Fig. 4, right) is conducted at $-20\text{ }^{\circ}\text{C}$, a HTF mass flow of 250 kg/h and supply pressure of 1.6 bar . Again, the pressure course is very similar

for each experiment. The measured peak thermal power values are between 1.34 and 1.43 kW . This variance is small and the curves still lie close together. Nevertheless, it causes a difference in the hydrogen conversion, which is obtained by integrating the thermal power over time. Since no general trend can be observed, it shows rather the sensitivity of the system to operation conditions. Still, since no significant changes in the material and the reactor are observed, the experiments with the open system are repeatable.

Closed system

For the closed system, the regeneration temperature, mass flow of the HTF and ambient temperature were varied in order to investigate their influence on the thermal peak and average power. The endothermal desorption in reactor 2 (storage reactor) causes a temperature decrease which leads to an additional cooling power. Its value is a little smaller than the one of the heating power due to the smaller desorption

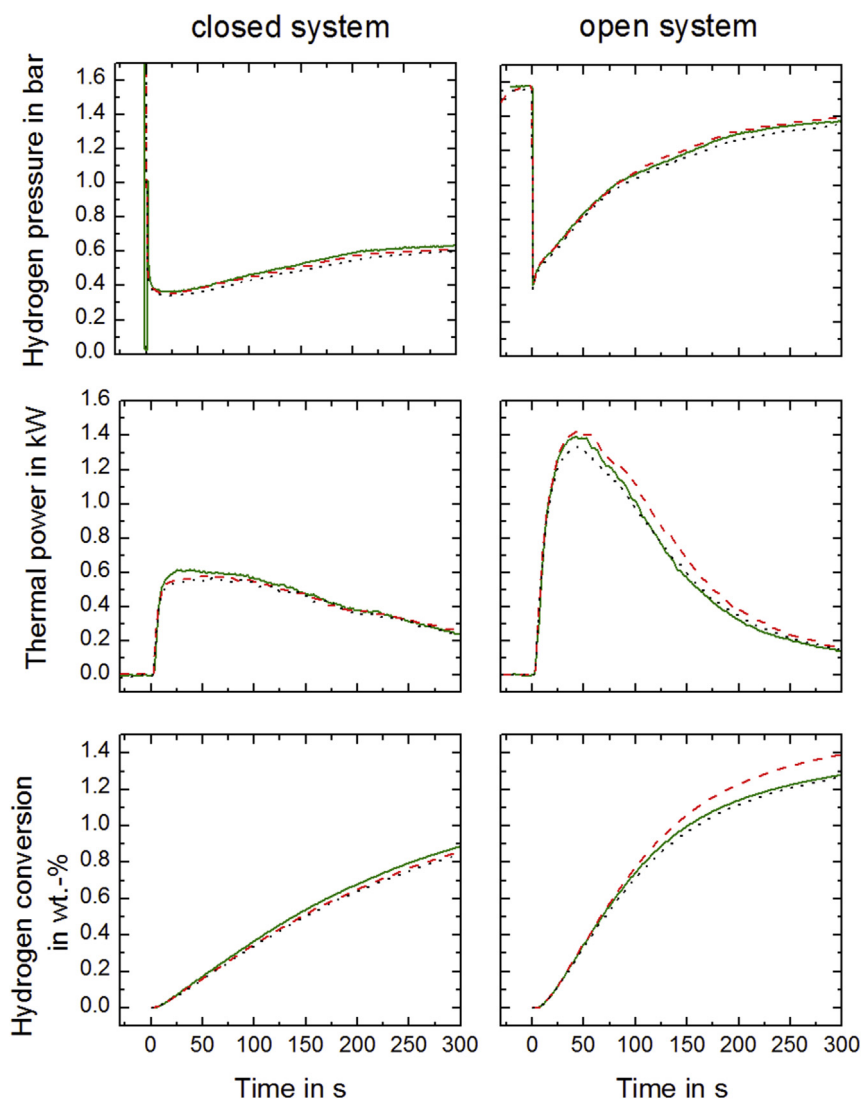


Fig. 4 – Repeatability for closed (left; green solid 2nd cycle, red dashed 10th cycle, black dotted 16th cycle) and open system (right; green solid 17th cycle, red dashed 24th cycle, black dotted 26th cycle). (For interpretation of the references to colour in this figure legend, the reader is referred to the web version of this article.)

enthalpy of $\text{C5}^{\text{®}}$ ($\Delta H = 28.4 \text{ kJ/mol}_{\text{H}_2}$ [30]). Nonetheless, this cooling power could probably be utilized for cooling purposes (e.g. air-conditioning) - in any case it needs to be taken into account for system integration.

For ambient temperature of -20°C and 0°C the regeneration temperature was varied between 90 and 130°C . In all cases the HTF mass flow was set to 250 kg/h . The resulting thermal power and hydrogen conversion are shown in Fig. 5. For ambient temperature of -20°C (Fig. 5 (a)), there is no significant difference evident in the course of both the thermal power and hydrogen conversion. The peak values for thermal power and hydrogen conversion at ambient temperature of -20°C are 0.58 kW and 1.06 wt.-% at regeneration temperature of 90°C and 0.58 kW and 1.10 wt.-% at 130°C . For ambient temperature of 0°C (Fig. 5 (b)) the course of thermal power and hydrogen conversion for regeneration temperatures of 110 and 130°C are very similar. The thermal power curves for regeneration temperature for 90°C reach lower peak values and decrease earlier and the hydrogen conversion reaches a smaller end value indicating the 90°C might not be sufficient for complete regeneration. For ambient temperature

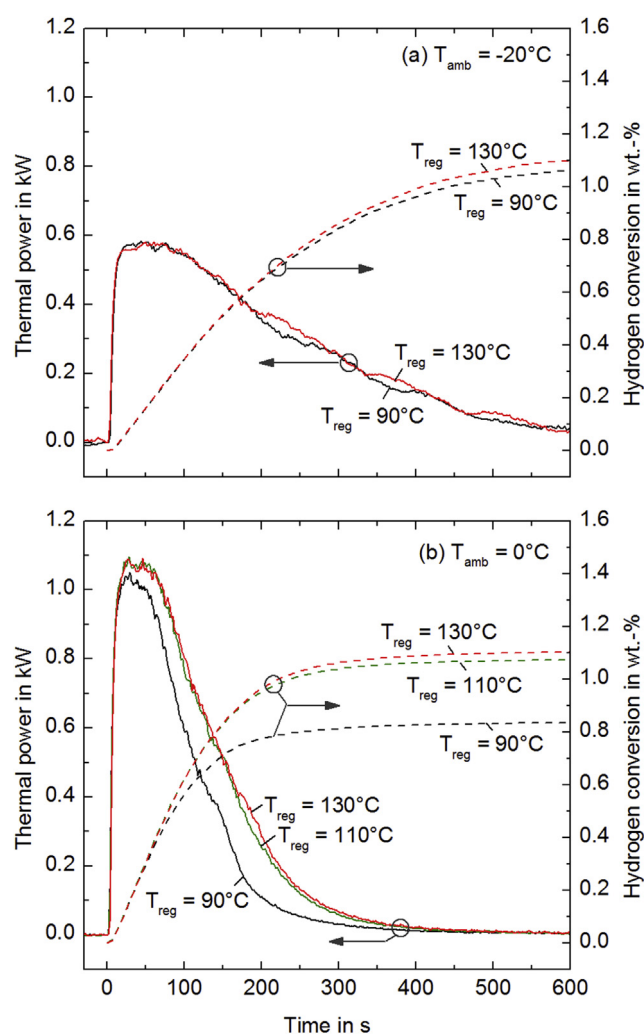


Fig. 5 – Closed system – Variation of regeneration temperature at ambient temperature of (a) -20°C and (b) 0°C .

of 0°C the peak values are 1.05 , 1.08 and 1.09 kW with 0.84 , 1.07 and 1.10 wt.-% of exchanged hydrogen at regeneration temperatures of 90 , 110 and 130°C , respectively.

The experimental results show the following. At -20°C , a regeneration temperature of 90°C or a temperature difference of 110 K is sufficient since increasing the regeneration temperature doesn't have an impact on the thermal power. At 0°C a regeneration temperature of 110°C is necessary to reach the highest thermal power values. Further increase doesn't improve thermal power. Therefore a certain temperature difference independent of ambient temperature has to be exceeded for complete regeneration, in the present case this value is around 110 K . A further increase doesn't have any positive impact on the performance of the storage. The required difference is actually determined by the chosen metal hydride pair. Their distance in the Van't Hoff-plot (see Fig. 1) defines the required temperature difference to reach a higher pressure in reactor 1 than in reactor 2 for regeneration. For the application in vehicles, this means that in winter, a lower waste heat temperature from the engine for regeneration is sufficient for a complete regeneration as compared to summer conditions.

Besides the regeneration temperature, the mass flow of the HTF was varied between 150 and 250 kg/h for ambient temperature of -20°C and between 150 and 425 kg/h for ambient temperature of 20°C . The resulting thermal power and hydrogen conversion are shown in Fig. 6. At an ambient temperature of -20°C (Fig. 6 (a)) no deviation is evident in thermal power or hydrogen conversion and the thermal power reaches peak values of about 0.6 kW . At ambient temperature of 20°C (Fig. 6 (b)) the peak thermal power of reactor 1 increases from 1.2 kW for 150 kg/h to 1.5 kW for 250 kg/h and reaches the highest values of 1.7 kW for a HTF flow of 425 kg/h . The hydrogen conversion curve is steeper for higher HTF mass flows but all reach the similar end value of about 1 wt.-% .

The following conclusions can be drawn from these experimental findings. The overall hydrogen conversion is independent of the HTF mass flow in the investigated ranges. Only the development over time at low mass flow rates and high ambient temperatures show small sensitivity. In general the mass flow seems to have an influence on the thermal power at higher ambient temperatures where thermal power values are comparably high (indicating a limitation due to the test facility). At -20°C the peak thermal power of 0.6 kW can be conducted sufficiently by HTF mass flow of 150 kg/h . At 20°C the power increases significantly with the mass flow, indicating an influence of the HTF mass flow on the overall heat transfer in the reactor at high thermal power values. Because the high thermal power is obviously ensured by the other influence factors (especially reaction rate), its value reached by the metal hydride couple operated at moderate temperatures might still be increased. However, for low temperature, the power density of the closed system seems to be intrinsically limited. This is discussed further in the section "Comparison of open and closed system".

In Fig. 7, the pressure gradient, the thermal power of reactor 1 and the hydrogen conversion is given for experiments with varying ambient temperature ($T_{\text{reg}} = 130^\circ\text{C}$, 250 kg/h mass flow of HTF). The pressure drops considerably with decreasing ambient temperature. At 20°C the peak

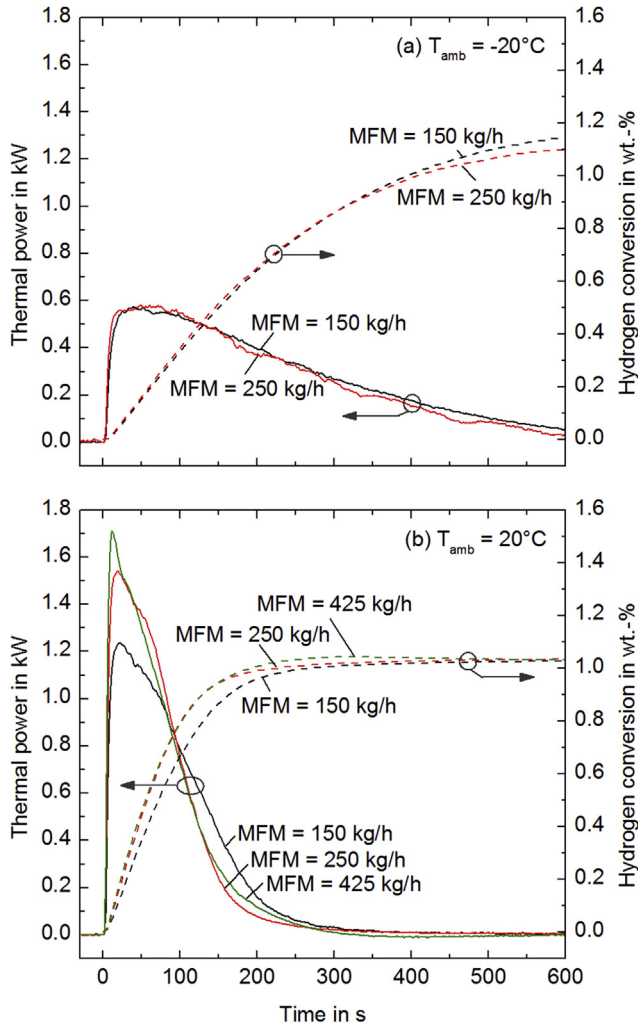


Fig. 6 – Closed system – Variation of mass flow of heat transfer fluid at ambient temperature of (a) $-20\text{ }^{\circ}\text{C}$ and (b) $20\text{ }^{\circ}\text{C}$.

pressure value is 2.5 bar, at $0\text{ }^{\circ}\text{C}$ it is around 1 bar and at $-20\text{ }^{\circ}\text{C}$ it is around 400 mbar with a peak value of 614 mbar after 321 s. A strong dependency on the ambient temperature is evident both in the thermal power and in the course of hydrogen conversion. Correspondingly, the peak values of thermal power increase from 0.58 kW for $-20\text{ }^{\circ}\text{C}$ ambient temperature to 1.1 kW at $0\text{ }^{\circ}\text{C}$ to 1.55 kW for $20\text{ }^{\circ}\text{C}$. The end value of hydrogen conversion at 600 s is comparable for all experiments (1.10, 1.10 and 1.03 wt.-% for -20 , 0 and $20\text{ }^{\circ}\text{C}$, respectively). The maximal temperature rise of the HTF was 5 K at $-20\text{ }^{\circ}\text{C}$ and 12 K at $20\text{ }^{\circ}\text{C}$. These experiments were additionally conducted for different values for regeneration temperature and HTF mass flow (see Table 1). In all cases the results follow the trend described here.

As in the closed system the same ambient temperature applies to reactor 1 and to reactor 2, the pressure of the provided hydrogen changes as well. Therefore, both equilibrium pressures in the reactors decrease with ambient temperature. Even though, the pressure difference between the reactors doesn't change much for the different ambient temperatures,

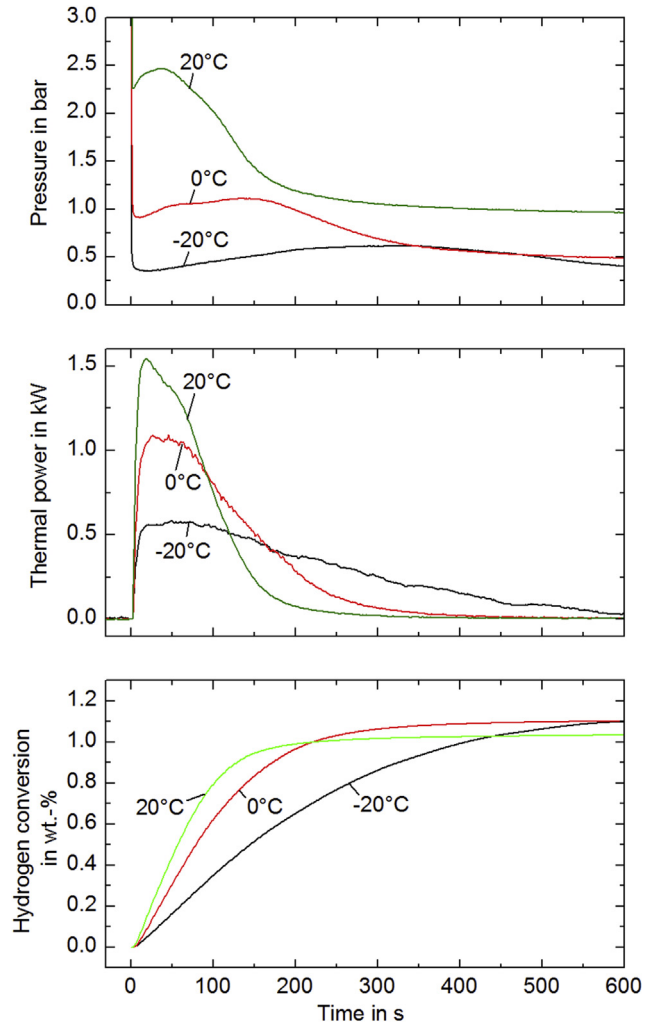


Fig. 7 – Closed System – Variation of ambient temperature.

the operation pressure of the system drops below 1 bar at $-20\text{ }^{\circ}\text{C}$. This might limit the mass transfer in the system and therefore the reaction. Another possibility might be reduced reaction kinetics of either one of the materials at lower temperatures. This point is discussed further in the section “Comparison of open and closed system” at the comparison of the open and the closed system.

In the following, the open system is investigated where – in contrary to the experiments with the closed system – the supply pressure is independent from the ambient temperature since it can be taken at a constant pressure from the hydrogen tank.

Open system

For the open system the influence of the supply pressure, the HTF mass flow and the ambient temperature on the thermal power were investigated by systematic variation of the experimental conditions.

The supply pressure was varied between 1.5 and 10.0 bar for an ambient temperature of $-20\text{ }^{\circ}\text{C}$ and between 1.5 and 2.9 bar for an ambient temperature of $0\text{ }^{\circ}\text{C}$. The resulting thermal power and hydrogen conversion are shown in Fig. 8.

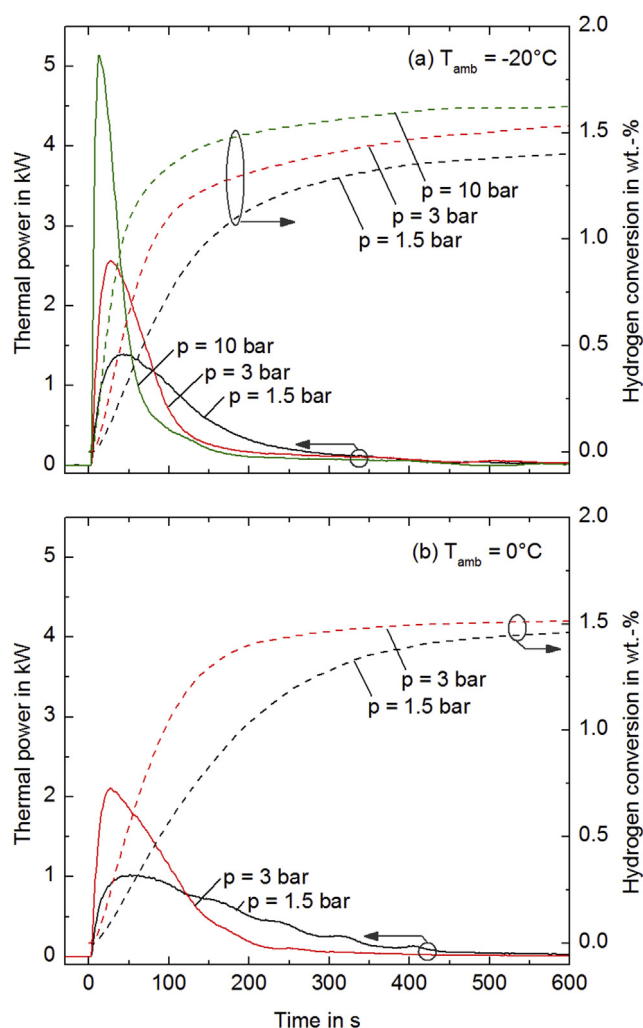


Fig. 8 – Open system – Variation of pressure for ambient temperature of (a) $-20\text{ }^{\circ}\text{C}$ and (b) $0\text{ }^{\circ}\text{C}$.

For both simulated ambient temperatures the thermal power increases significantly with supply pressure both in slope and peak value. The reached peak values for $-20\text{ }^{\circ}\text{C}$ are 1.39 kW at 1.5 bar, 2.56 kW at 3 bar and 5.14 kW at 10 bar, respectively. For $0\text{ }^{\circ}\text{C}$ they are 1.02 kW at 1.5 bar and 2.11 kW at 2.9 bar, respectively. The hydrogen conversion increases faster, reaches higher values and the heat production stops consequently earlier with increasing supply pressure. The maximal temperature increase of the HTF at $-20\text{ }^{\circ}\text{C}$ was 12 K at 1.5 bar and 43 K at 10 bar.

Since in the open system the supply pressure can be adjusted independently from the ambient temperature, an increasing supply pressure increases intrinsically the distance to the equilibrium pressure of the material in reactor 1. This explains the increase in thermal power. Another effect could be that the mass transfer limitation through the bed (as mentioned in 2.3) decreases with increasing pressure.

The mass flow of HTF was varied, too. Here, no significant trend was obvious. For peak values it is referred to Table 1 in the section “General discussion”.

The ambient temperature was varied between -20 and $20\text{ }^{\circ}\text{C}$ for a supply pressure of 3 bar and between -20 and $0\text{ }^{\circ}\text{C}$

for a supply pressure of 1.5 bar. For all experiments the HTF mass flow was 250 kg/h. The results of thermal power and hydrogen conversion are given in Fig. 9. The trends are the same for both supply pressures. The thermal power decreases with higher ambient temperature and the time of heat supply increases. The peak values for 3 bar are 2.56, 2.11 and 1.51 kW for -20 , 0 and $20\text{ }^{\circ}\text{C}$, respectively, and 1.39 and 1.02 kW for -20 and $0\text{ }^{\circ}\text{C}$, respectively, for 1.5 bar. A similar trend is evident in the hydrogen conversion. For higher ambient temperatures the slope decreases and it takes more time to reach the final value. Once the reaction is over, the final values of the hydrogen conversion are very similar for each supply pressure value.

At a first glance, these findings of decreasing thermal power at increasing temperature seem to be in contradiction to Arrhenius's law. However, since the supply pressure is fixed a decrease of the reaction temperature leads to a higher distance to the equilibrium pressure. Therefore, it can be stated for this set-up that the distance to the equilibrium has a stronger impact on thermal power than the ambient temperature itself.

Comparison of open and closed system

The comparison of open and closed system under same conditions is challenging due to the different courses of the system pressure. However, in order to be able to investigate the influence of reactor 2, a comparison of pressure, hydrogen flow into reactor 1 and thermal power are given in Fig. 10 as a function of the ambient temperature.

At an ambient temperature of $20\text{ }^{\circ}\text{C}$ (Fig. 10, left) the supply pressure for the open system was set to 3 bar which causes a similar pressure at 30 s as in the closed system (Even though the initial pressure in the closed system is 14 bar). The course of the pressure after 30 s is very different. However, the resulting thermal power is similar, at least at the beginning and reaches similar peak values with slightly higher value for the closed system (1.54 kW) than for the open system (1.51 kW). The thermal power of the closed system decreases slightly faster.

At ambient temperature of $0\text{ }^{\circ}\text{C}$ (Fig. 10, middle) the supply pressure for the open system was set to 1.5 bar (the initial pressure in the closed system was 7.9 bar). Even though the thermal power of the closed system increases faster the general trend is comparable between the open and closed system. The hydrogen volume flow is similar but decreases again slightly faster for the closed system.

At ambient temperature of $-20\text{ }^{\circ}\text{C}$ (Fig. 10, right) the supply pressure for the open system was set to 1.5 bar (the initial pressure in the closed system was 4.3 bar). The pressure increases faster for the open system and reaches its maximal value of 1.4 bar after 600 s not changing significantly after 300 s. In the closed system the pressure is rather constant with a slow increase to a maximal value of 0.6 bar after around 340 s before it drops again. The hydrogen flow increases steeply for both systems and reaches a peak value of 77 l_N/min for the closed and 65 l_N/min for the open system. The very sharp peak at the beginning of the experiment with the closed system is due to the equalization of the gas pressure inside the void fraction. The most interesting point of the comparison

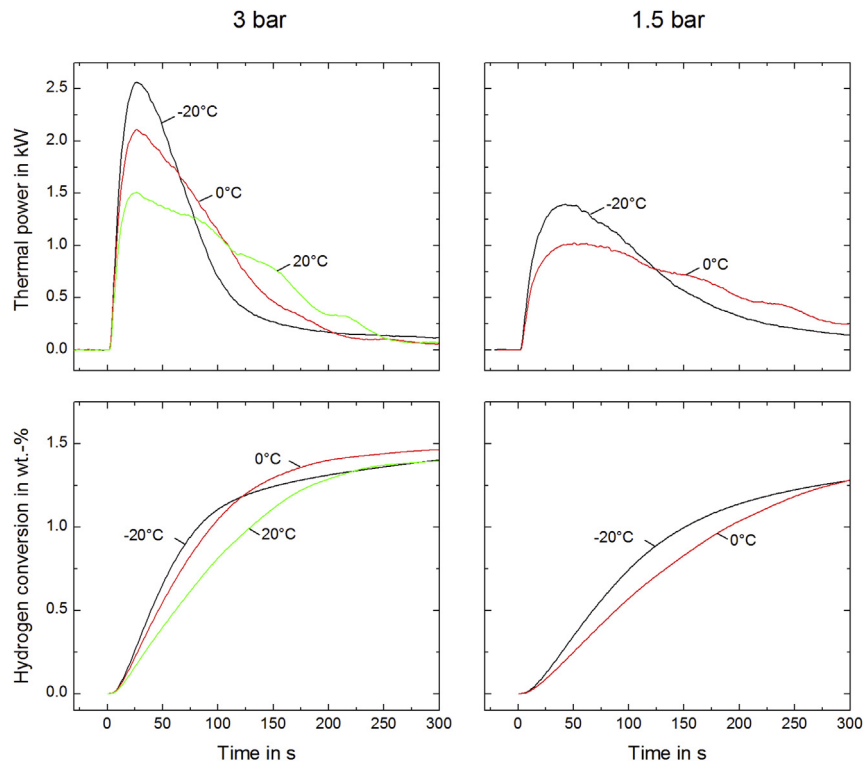


Fig. 9 – Open System – Variation of ambient temperature with supply pressure of 3 bar (left) and 1.5 bar (right).

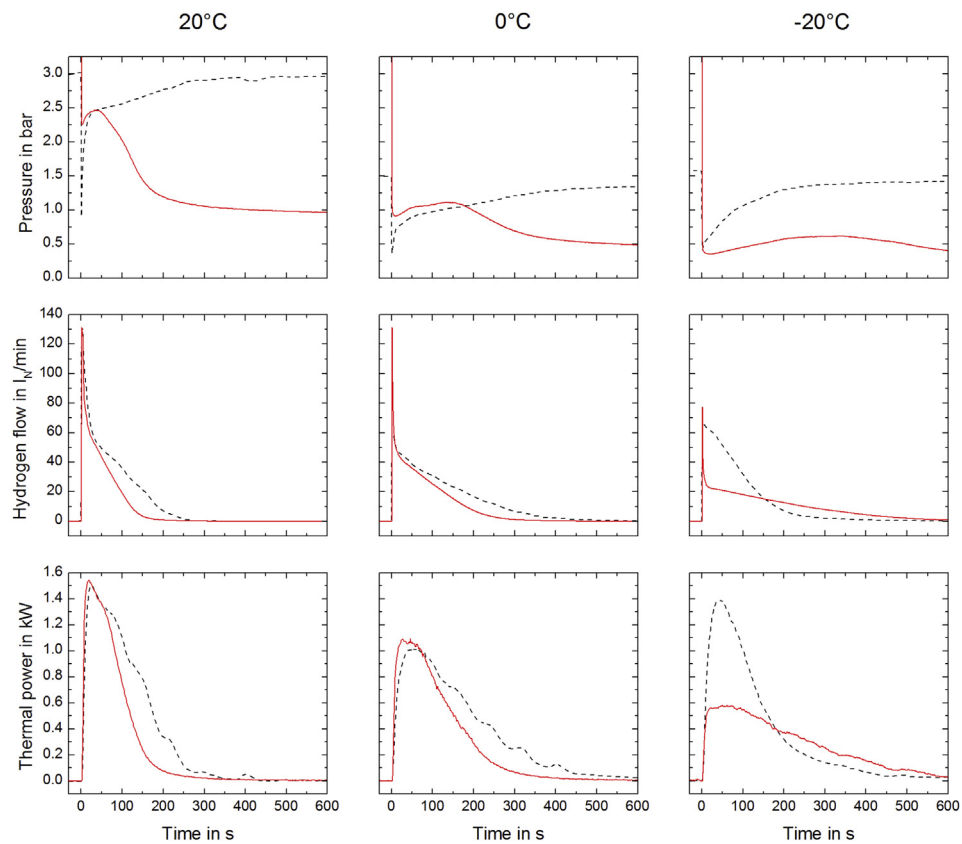


Fig. 10 – Comparison of open (dashed black) and closed (solid red) system for ambient temperature of 20 °C (left), 0 °C (middle) and –20 °C (right). (For interpretation of the references to colour in this figure legend, the reader is referred to the web version of this article.)

can be observed after this equalization when it decreases quickly to a value of only around 20 l_N/min and continues to decrease parallel to the thermal power until the end of the experiment.

From these comparisons it can be concluded that for temperatures of 20 °C and 0 °C similar hydrogen flow and pressure courses lead to similar thermal power generation. Obviously, the open system could be adjusted to even higher power levels – due to the additional degree of freedom that comes with the independency of the supply pressure from the ambient temperature. However, the results for –20 °C show totally different curves of hydrogen flow and thermal power. In the closed system after the first seconds the hydrogen flow is much lower, leading to smaller pressure and thermal power values. Therefore, the limited thermal power in the closed system seems to be caused by the limited reaction rate of the metal hydride in reactor 2 at –20 °C and low pressure. Since these types of metal hydrides are in general supposed to possess very fast reaction

kinetics [24] this finding has to be confirmed in future work on reaction rate measurements at these temperature and pressure conditions.

General discussion

A summary of all experiments, including the boundary conditions, thermal power, thermal energy and hydrogen conversion for the closed and open system is given in Table 1. The probable error for the thermal power was $\pm 10.6\%$ with a standard deviation of 0.5%. High thermal power could be shown for both systems even though the open system is able to reach clearly higher values. In order to generalize the findings, the values are normalized and given per kg metal hydride. The closed system reached values between 0.6 kW/kg_{MH} at ambient temperature of –20 °C and 1.6 kW/kg_{MH} at 20 °C, at otherwise same conditions. The open system reached 1.4 kW/kg_{MH} at –20 °C and supply pressure of 1.5 bar and 5.4 kW/kg_{MH} at –20 °C and 10 bar.

Table 1 – Thermal power, thermal energy and conversion for different boundary conditions.

Closed System						
No. of Experiment	T _{amb} in °C	T _{reg} in °C	\dot{m}_{HTF} in kg/h	P _{peak} in kW/kg	Q _{600sec} in kJ/kg	X _{600sec} in wt.-%
8	-20	130	150	0.57	179.15	1.13
12				0.60	181.20	1.15
15				0.60	184.61	1.17
2				0.64	178.52	1.13
10				0.61	173.79	1.10
16				0.60	167.17	1.06
7		90	250	0.61	167.91	1.06
14				0.61	169.64	1.07
6				1.14	174.22	1.10
4				1.14	169.61	1.07
13	0	110	1.11	169.11	1.07	
3			1.09	132.08	0.84	
5			1.29	162.18	1.03	
1	20	130	1.61	162.65	1.03	
11			1.58	164.23	1.04	
9			1.78	163.04	1.03	
Open System						
No. of Experiment	T _{amb} in °C	\dot{m}_{HTF} in kg/h	P _{supply} in bar	P _{peak} in kW/kg	Q _{300sec} in kJ/kg	X _{300sec} in wt.-%
18	-20	250	1.5	1.55	211.15	1.34
17				1.45	202.09	1.28
24				1.49	220.29	1.39
26				1.39	200.12	1.27
20				2.67	221.58	1.40
25				5.36	245.87	1.56
19	0	1.5	3	1.16	200.91	1.27
22				1.07	202.46	1.28
21				2.20	231.45	1.46
23	20	1.57	220.66	1.40		

It is obvious that the investigations were performed with comparably heavy reactors of 2.09 kg. The ratio of mass of metal hydride to mass of reactor are 1: 2.2 for reactor 1 and 1: 3.4 for reactor 2. However, the given experimental values include the thermal mass and temperature change of the materials, containing reactors and HTF. Still high values are achieved, because of the high thermal energy density of the material, therefore showing high potential especially for mobile applications. In general, due to the “switchable” operation principle, it can be suggested to integrate the reacting material directly into the respective component. In this case, the additional heat transfer with a HTF can be avoided and the full thermal power is available at the point of demand.

In order to compare the results with the state of the art, the best comparable work in literature to the best of our knowledge, is discussed in the following.

Little work is found in literature for preheating fuel cells with the help of metal hydrides. Docter et al. [31] published a patent considering metal hydrides to shorten cold-start phase. TiFe is proposed for the application at temperatures between $-30\text{ }^{\circ}\text{C}$ and $50\text{ }^{\circ}\text{C}$. Unfortunately no experimental data is provided. Brack [32] investigated $\text{LaNi}_{4.1}\text{Al}_{0.52}\text{Mn}_{0.38}$ designed for direct integration into a high temperature PEM fuel cell operating at clearly higher temperatures ($100\text{--}170\text{ }^{\circ}\text{C}$). The maximal thermal power output reached $5.7\text{ kW/kg}_{\text{MH}}$ which is comparable to the power density reached in this work.

Some work was presented in literature concerning coupled metal hydride reactions. Fang et al. [33] investigated coupled catalyzed $\text{MgH}_2 - \text{TiV}_{0.62}\text{Mn}_{1.5}$ for heating and cooling of cabins in electric vehicles. Some boundary conditions differ to the presented study (regeneration temperature level of $270\text{ }^{\circ}\text{C}$, material partly combined with expanded natural graphite, ambient temperature of $20\text{ }^{\circ}\text{C}$) which limits comparability. The resulting thermal peak power of 320 W occurs only after about 2 min which limits the applicability for quick ramp-up or start-up applications. Aswin et al. [16] considered coupled metal hydrides in the temperature range of $30\text{--}80\text{ }^{\circ}\text{C}$. The work focuses on the simulation of coupled reactions and shows the possible fast reaction rates but no experiments were conducted.

The present work could experimentally show high thermal power densities of metal hydrides under automotive boundary conditions both for the open and coupled reactions. Therefore, the presented principle can meet the requirements for the considered applications in vehicles. In order to understand the observed limitations in more detail, in particular for coupled chemical reaction at low temperatures and pressures, further research is necessary. Detailed material characterizations at these conditions are therefore planned as subsequent work.

Conclusions

In this paper metal hydrides as candidates for thermochemical energy storage were investigated with regard to providing their high thermal power for preheating e.g. vehicle components applications. To shorten the cold start phase considerably, high thermal power is needed. Operation designs for open and closed systems were

developed, materials selected and reactors and a test bench built to investigate influence factors on the thermal power. $\text{LaNi}_{4.85}\text{Al}_{0.15}$ was used for the heat producing side and Hydralloy C5[®] was used for the hydrogen storage side in the closed system. Main unique features are investigations of the closed system with coupled chemical reactions, temperatures down to $-20\text{ }^{\circ}\text{C}$ and relevant scale for vehicle applications. The mass flow of the heat transfer fluid (varied range $150\text{--}425\text{ kg/h}$), the regeneration conditions for the closed system ($90\text{--}130\text{ }^{\circ}\text{C}$) and the supply pressure for the open system ($1.5\text{--}10\text{ bar}$) as well as the ambient temperature ($-20\text{--}20\text{ }^{\circ}\text{C}$) were varied.

- It was found that for the closed system, a certain temperature difference has to be reached for complete regeneration. Since this might already limit the integration possibilities, further increase of the distance of the thermodynamic values of the metal hydrides (distance in Van't Hoff plot, see Fig. 1) is not advantageous. The closed system reached values between $0.6\text{ kW/kg}_{\text{MH}}$ at ambient temperature of $-20\text{ }^{\circ}\text{C}$ and $1.6\text{ kW/kg}_{\text{MH}}$ at $20\text{ }^{\circ}\text{C}$, at otherwise same conditions.
- In the open system, the ambient temperature is of importance only in relation to the available supply pressure. The distance of the supply pressure to the pressure equilibrium of the chosen material at the highest considered ambient temperature has to be large enough. The open system reached $1.4\text{ kW/kg}_{\text{MH}}$ at $-20\text{ }^{\circ}\text{C}$ and supply pressure of 1.5 bar and $5.4\text{ kW/kg}_{\text{MH}}$ at $-20\text{ }^{\circ}\text{C}$ and 10 bar . Therefore, for the open system, the material selection for the given boundary conditions is most important.
- For the heat production with thermochemical systems the ambient temperature has the biggest influence. For the closed system the thermal power directly correlates with the ambient temperature. This might be attributed to limitations of desorption kinetics at low temperatures, but need to be confirmed in subsequent analysis. The open system can bypass this restriction, because it has an additional degree of freedom in the hydrogen pressure. Hence, depending on the chosen material and supply pressure, higher thermal power can be reached.

Acknowledgments

Our thanks go to Christian Brack and Mei Chin Pang for their supportive work as well as to Alexander Bonk and Stephanie Kraft for the measurement of the heat capacity of the HTF.

REFERENCES

- [1] Reiter MS, Kockelman KM. The problem of cold starts: a closer look at mobile source emissions levels. *Transp Res Part D Transp Environ* 2016;43:123–32. <http://dx.doi.org/10.1016/j.trd.2015.12.012>.
- [2] Cipollone R, Di Battista D, Mauriello M. Effects of oil warm up acceleration on the fuel consumption of reciprocating internal combustion engines. *Energy Procedia* 2015;82:1–8. <http://dx.doi.org/10.1016/j.egypro.2015.11.870>.

- [3] Mishler J, Wang Y, Mukherjee PP, Mukundan R, Borup RL. Subfreezing operation of polymer electrolyte fuel cells: ice formation and cell performance loss. *Electrochim Acta* 2012;65:127–33. <http://dx.doi.org/10.1016/j.electacta.2012.01.020>.
- [4] Santamaria A, Tang HY, Park JW, Park GG, Sohn YJ. 3D neutron tomography of a polymer electrolyte membrane fuel cell under sub-zero conditions. *Int J Hydrogen Energy* 2012;37:10836–43. <http://dx.doi.org/10.1016/j.ijhydene.2012.04.093>.
- [5] Lim SJ, Park GG, Park JS, Sohn YJ, Yim SD, Yang TH, et al. Investigation of freeze/thaw durability in polymer electrolyte fuel cells. *Int J Hydrogen Energy* 2010;35:13111–7. <http://dx.doi.org/10.1016/j.ijhydene.2010.04.079>.
- [6] Lin R, Lin X, Weng Y, Ren Y. Evolution of thermal drifting during and after cold start of proton exchange membrane fuel cell by segmented cell technology. *Int J Hydrogen Energy* 2015;40:7370–81. <http://dx.doi.org/10.1016/j.ijhydene.2015.04.045>.
- [7] Neveu P, Castaing J. Solid-gas chemical heat pumps: field of application and performance of the internal heat of reaction recovery process. *Heat Recover Syst CHP* 1993;13.
- [8] Srinivasa Murthy S. Heat and mass transfer in solid state hydrogen storage: a review. *J Heat Transf* 2012;134:31020. <http://dx.doi.org/10.1115/1.4005156>.
- [9] Mazzucco A, Dornheim M, Sloth M, Jensen TR, Jensen JO, Rokni M. Bed geometries, fueling strategies and optimization of heat exchanger designs in metal hydride storage systems for automotive applications: a review. *Int J Hydrogen Energy* 2014;39:17054–74. <http://dx.doi.org/10.1016/j.ijhydene.2014.08.047>.
- [10] Zhang J, Fisher TS, Ramachandran PV, Gore JP, Mudawar I. A review of heat transfer issues in hydrogen storage technologies. *J Heat Transf* 2005;127:1391. <http://dx.doi.org/10.1115/1.2098875>.
- [11] Muthukumar P, Groll M. Metal hydride based heating and cooling systems: a review. *Int J Hydrogen Energy* 2010;35:3817–31. <http://dx.doi.org/10.1016/j.ijhydene.2010.01.115>.
- [12] Bhuiya MMH, Kumar A, Kim KJ. Metal hydrides in engineering systems, processes, and devices: a review of non-storage applications. *Int J Hydrogen Energy* 2015. <http://dx.doi.org/10.1016/j.ijhydene.2014.12.009>.
- [13] Linder M, Mertz R, Laurien E. Experimental results of a compact thermally driven cooling system based on metal hydrides. *Int J Hydrogen Energy* 2010;35:7623–32. <http://dx.doi.org/10.1016/j.ijhydene.2010.04.184>.
- [14] Park I-S, Kim J-K, Kim KJ, Zhang J, Park C, Gawlik K. Investigation of coupled AB5 type high-power metal hydride reactors. *Int J Hydrogen Energy* 2009;34:5770–7. <http://dx.doi.org/10.1016/j.ijhydene.2009.05.012>.
- [15] Imoto T, Yonesaki T, Fujitani S, Yonezu I, Hiro N, Nasako K, et al. Development of an F-class refrigeration system using hydrogen-absorbing alloys. *Int J Hydrogen Energy* 1996;21:451–5. [http://dx.doi.org/10.1016/0360-3199\(95\)00106-9](http://dx.doi.org/10.1016/0360-3199(95)00106-9).
- [16] Aswin N, Dutta P, Murthy SS. Screening of metal hydride pairs for closed thermal energy storage systems. *Appl Therm Eng* 2016. <http://dx.doi.org/10.1016/j.applthermaleng.2016.04.129>.
- [17] Sharma VK, Anil Kumar E, Srinivasa Murthy S. Influence of dynamic operating conditions on the performance of metal hydride based solid sorption cooling systems. *Int J Hydrogen Energy* 2015;40:1108–15. <http://dx.doi.org/10.1016/j.ijhydene.2014.11.084>.
- [18] Yasuda N, Tsuchiya T, Okinaka N, Akiyama T. Application of metal hydride sheet to thermally driven cooling system. *Int J Hydrogen Energy* 2013;1–8. <http://dx.doi.org/10.1016/j.ijhydene.2013.04.011>.
- [19] Ni J, Liu H. Experimental research on refrigeration characteristics of a metal hydride heat pump in auto air-conditioning. *Int J Hydrogen Energy* 2007;32:2567–72. <http://dx.doi.org/10.1016/j.ijhydene.2006.09.038>.
- [20] Dehouche Z, de Jong W, Willers E, Isselhorst A, Groll M. Modelling and simulation of heating/air-conditioning systems using the multi-hydride-thermal-wave concept. *Appl Therm Eng* 1998;18:457–80. [http://dx.doi.org/10.1016/S1359-4311\(97\)00043-4](http://dx.doi.org/10.1016/S1359-4311(97)00043-4).
- [21] Jadhao JS, Thombare DG. Review on exhaust gas heat recovery for I.C. Engine. *Certif Int J Eng Innov Technol* 2013;2:2277–3754.
- [22] Krell M. Handbook of hydrogen storage. Chapter 1 storage of hydrogen in the pure form. Wiley-VCH Verlag GmbH & Co. KGaA; 2010. <http://dx.doi.org/10.1002/9783527629800.ch1>.
- [23] Muthukumar P, Satheesh A, Linder M, Mertz R, Groll M. Studies on hydriding kinetics of some La-based metal hydride alloys. *Int J Hydrogen Energy* 2009;34:7253–62. <http://dx.doi.org/10.1016/j.ijhydene.2009.06.075>.
- [24] Skripnyuk V, Ron M. Hydrogen desorption kinetics in intermetallic compounds C2, C5 and C5 with Laves phase structure. *Int J Hydrogen Energy* 2003;28:303–9. [http://dx.doi.org/10.1016/S0360-3199\(02\)00081-2](http://dx.doi.org/10.1016/S0360-3199(02)00081-2).
- [25] Rizvi SQA. A comprehensive review of lubricant chemistry, technology, selection, and design. ASTM International; 2009.
- [26] Lee D-W, Johnson J, Lv J, Novak K, Zeitsman J. Comparisons between vehicular emissions from real-world in-use testing and EPA moves estimation 2012;7.
- [27] Klamann D. Lubricants and related products – synthesis, properties, applications, international standards. Verlag Chemie GmbH; 1984.
- [28] Mittel J, Gülzow E, Kabza A, Hunger J, Araya SS, Piela P, et al. Identification of critical parameters for PEMFC stack performance characterization and control strategies for reliable and comparable stack benchmarking. *Int J Hydrogen Energy* 2016;41:21415–26. <http://dx.doi.org/10.1016/j.ijhydene.2016.08.065>.
- [29] Selvam PK, Muthukumar P, Linder M, Mertz R, Kulenovic R. Measurement of thermochemical properties of some metal hydrides – titanium (Ti), misch metal (Mm) and lanthanum (La) based alloys. *Int J Hydrogen Energy* 2013;38:5288–301. <http://dx.doi.org/10.1016/j.ijhydene.2013.02.009>.
- [30] Herbrig K, Röntzsch L, Pohlmann C, Weißgärber T, Kieback B. Hydrogen storage systems based on hydride–graphite composites: computer simulation and experimental validation. *Int J Hydrogen Energy* 2013;38:7026–36. <http://dx.doi.org/10.1016/j.ijhydene.2013.03.104>.
- [31] Docter A, Frank G, Konrad G, Lamm A, Mueller JT. Fuel cell and method for cold-starting such a fuel cell. 2008. US 2008/0102327 A1.
- [32] Brack C. Entwicklung, Konstruktion und Fertigung eines Vorheizers für Hochtemperatur-Polymeralektrolytmembran-Brennstoffzellen-Systeme auf der Basis von Metallhydriden. Hochschule Zwickau; 2011.
- [33] Fang ZZ, Zhou C, Fan P, Udell KS, Bowman RC, Vajo JJ, et al. Metal hydrides based high energy density thermal battery. *J Alloys Compd* 2015. <http://dx.doi.org/10.1016/j.jallcom.2014.12.260>.



Standardized hydrogen storage module with high utilization factor based on metal hydride-graphite composites



Inga Bürger ^{a,*}, Mila Dieterich ^a, Carsten Pohlmann ^{b,1}, Lars Röntzsch ^b, Marc Linder ^a

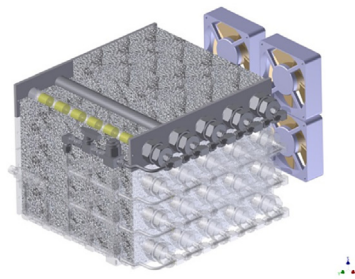
^a German Aerospace Center (DLR) - Institute of Engineering Thermodynamics, Thermal Process Technology, Pfaffenwaldring 38 – 40, 70569 Stuttgart, Germany

^b Fraunhofer Institute for Manufacturing Technology and Advanced Materials IFAM, Branch Lab Dresden, Winterbergstraße 28, 01277 Dresden, Germany

HIGHLIGHTS

- Standardized reactor design for stationary metal hydride hydrogen storage.
- Metal hydride-graphite composites for compact system with low temperature gradient.
- Utilization factor of 93% reached at relevant charging conditions.
- System scalability to higher loads.

GRAPHICAL ABSTRACT



ARTICLE INFO

Article history:

Received 2 November 2016
Received in revised form
21 December 2016
Accepted 26 December 2016

Keywords:

Metal hydride
Stationary application
Reactor design
Metal hydride-graphite composites

ABSTRACT

In view of hydrogen based backup power systems or small-scale power2gas units, hydrogen storages based on metal hydrides offer a safe and reliable solution. By using Hydralloy C5 as suitable hydride forming alloy, the present tank design guarantees very simple operating conditions: pressures between 4 bar and 30 bar, temperatures between 15 °C and 40 °C and minimal efforts for thermal management in combination with fast and constant charging and discharging capabilities. The modular tank consists of 4 layers with 5 reactor tubes each that are filled with metal hydride-graphite composites of a diameter of 21 mm. Experiments show that each layer of this tank is able to desorb the desired amount of hydrogen for a fuel cell operation at electrical power of 160 W_{el} for 100 min reaching a utilization factor of 93% of the stored hydrogen at RC. Furthermore, the experimental results of modularity, increasing loads and the electric air ventilation are presented.

© 2017 Elsevier B.V. All rights reserved.

1. Introduction

Increasing availability of devices that convert renewable energy into electricity like photovoltaic modules or wind turbines create the need for energy buffers in order to match energy availability

and energy needs. For remote or decentralized power supply, one promising option is to convert electricity to chemical energy in form of hydrogen gas [1]. This allows a separate dimensioning of power and capacity, immense cyclic use without degradation as well as different options to re-use the energy on demand. An example of such a system is depicted in Fig. 1. In this case, the surplus electricity converted from a fluctuating renewable energy source is used for hydrogen production by an electrolyzer. This hydrogen is then stored in a buffer tank and can be later used for

* Corresponding author.

E-mail address: inga.buerger@dlr.de (I. Bürger).

¹ Now at Aaqius & Aaqius, 12 Rue Vivienne, 75002 Paris, France.



Fig. 1. Scheme of a hydrogen-based power2gas system to store surplus electrical power.

different energy services such as electricity and heat via fuel cells, heat for cooking via catalytic burners and potentially also mobility.

Suitable electrolyzer and fuel cell demands for private domestic applications range between 600 W and 1.2 kW, and already exist on the market.² As hydrogen buffer tank for such systems usually either a high-pressure tank, which requires a hydrogen compressor, or a low-pressure tank is used, which requires a lot of free space.³ In addition, pressure tanks especially at high pressures bear safety risks when bursting. Metal hydrides can lower these risks dramatically due to the chemical absorption of hydrogen inside of the solid metal. Additionally, suitable metal hydrides prove cycling stabilities in the five-figure range [2,3]. Consequently, hydrogen can be stored with highest volumetric densities (up to 150 g-H₂ per liter) at rather low pressures and an inherent safety aspect: The corresponding exo-/endothermic storage reaction between the metal (Me) and the hydrogen (H₂) to a metal hydride (MeH) can be written as



As the desorption of hydrogen is an endothermal process, any unintentional release of hydrogen is immediately decelerated due to the heat demand for desorption. However, at the same time the involved heat of reaction is most challenging when designing a metal hydride hydrogen storage. Overcoming this drawback, a simple and standardized storage design combining the advantages of metal hydrides - safe, low volume, low pressure, little maintenance, no compressor - with improved thermal transfer is proposed in this paper.

In the literature, several studies have been published focusing on metal hydride buffer tanks for stationary applications.

For example, magnesium hydride-based storage tanks are intensively studied, as this material shows very high storage capacities of up to 7.7 wt% [4]. Due to their high operating temperature, these materials require a rather complex heat management based on a process integration [5] or e.g. the combination with a phase change material to preserve the associated thermal energy [6].

The advantages of metal hydrides working near ambient conditions for this buffer storage application is discussed by Hagstorm [7]. In this paper, it is emphasized that for the selection of a suitable material a small hysteresis as well as a flat plateau of the PCI curve are crucial, leading to the suggestion of LmNi(1)⁴ (JMC⁵) or Hydralloy C15 (GfE⁶).

Lototsky et al. also designed metal hydride reactors using an AB₂-type material as fuel cell supply tanks [8]. In that paper, the effect of different hydrogen desorption rates is discussed as well as

the influence of liquid or air heat transfer on the overall performance, and for the charging process very fast rates are assumed. A similar study has been performed by Capurso et al. using Hydralloy C5 powder material in 0.5 L containers as hydrogen storage for an urban concept car [9].

Bossi et al. tested a setup where a LaNi₅ based storage reactor for 6000 NL⁷ hydrogen is coupled to a fuel cell fluid for stationary backup systems [10], and Nakano et al. studied in the project THEUS a metal hydride tank that is integrated as buffer tank between an electrolyzer and a fuel cell [11]. In both cases, the hydride tank is integrated into a water based cooling/heating system, which leads to a rather complex tank design and overall system.

Furthermore, Liu et al. designed a new overall fuel cell -metal hydride hydrogen storage design for stationary applications [12]. This system show advantages for the air-cooled fuel cell due to a more direct heat management, however, in this case the capacity of the tank is linked to the size of the fuel cell.

Summarizing the experience of the given references, the focus of the present metal hydride tank has been on a standardized system design with a very low complexity of the thermal management. Therefore, the following points have been considered.

- A suitable low temperature metal hydride material with a low hysteresis has been chosen that can store and release hydrogen under the applying conditions of room temperature between 10 and 40 °C. Thus, no further system integration with e.g. fuel cell or water management was required.
- The power of the electrolyzer and the fuel cell were assumed to be in a similar range, thus, charging and discharging rates are similar with similar effects on the reactor design.
- The pure hydride material has been mixed with expanded natural graphite (ENG) and compressed to metal hydride-graphite composites (MHC) to improve the radial thermal conductivity. Thus, the final storage system is based on tubes with comparatively large diameter and aluminum foam on the outside to improve heat transfer and requires only simple air ventilation at low power.

For demonstration, a tank based on 4 layers with 5 tubes each, that are filled with in total 6 kg of Hydralloy C5[®] based MHC, has been built. The storage reactor has been designed in such a way that each layer is able to supply sufficient hydrogen to generate an electric power of 160 W by a fuel cell for more than 100 min. For the evaluation of the performance, a utilization factor has been defined that refers to the ratio between the “mass of hydrogen released/stored with relevant flow rates” and the “maximum mass of hydrogen that can be discharged/charged” at the corresponding operation conditions. The final goal was to show that with the presented reactor utilization factors of more than 90% can be reached.

In this paper, first, the general system layout based on Hydralloy

² E.g., www.actaspa.com.

³ E.g., www.heliocentris.com.

⁴ Lm = La-rich misch metal.

⁵ Japan Metals & Chemicals Co. Ltd.

⁶ Gesellschaft für Elektrometallurgie mbH.

⁷ NL = normal liter at 0 °C and 1.103 bar.

C5[®] is described and the effect of the usage of MHCs with enhanced heat conductivity is presented. Then, details on the final tank and the test rig are given before the experimental results are shown concluding that this system is able to store and provide hydrogen at the required rate. Finally, the results of varying flow rates and air ventilation are presented and a summary and evaluation of the total system is discussed.

2. System layout

As mentioned in the introduction, for hydrogen storage in metal hydride systems, usually an intense thermal management is required. For the present setup, the first measure to reduce the complexity of the system is the implementation of a material that can store (absorb) and release (desorb) hydrogen under ambient conditions (between 15 °C and 40 °C). Thus, in contrast to other proposed systems [11] no further heating or cooling integration is required.

The material that has been chosen is known as Hydralloy C5 (AB₂-type metal hydride) and has been widely studied in the literature. It is stable during cycling as powder [2,13] and in form of MHC [14,15]. Additionally, it can be filled into tanks in the unactivated state without inert-gas measures and can easily be activated inside the final tank [9]. Furthermore, the kinetics of the material are fast, i.e. absorption and desorption proceed in the relevant temperature and pressure range in less than 30 s [16], and its hysteresis as well as plateau slope are moderate [9,17]. Fig. 2 shows the Van't Hoff plot for this material indicating 20%, 50% and 80% transformed fraction for absorption and desorption, respectively. The arrows indicate the operational conditions for this system.

For absorption, a hydrogen supply pressure of 30 bar is assumed, as this corresponds to a reasonable pressure provided by an electrolyzer without a complementary compressor.⁸ Thus, if room temperature of 15 °C–40 °C is assumed, there is still a temperature difference of 10 K to the equilibrium of 80% transformed fraction for

absorption that can be used to remove the heat efficiently. As several typical fuel cells operate with back pressures between ambient and 200 mbar backpressure and as the expected pressure difference to the inlet pressure is only few 10s of mbar, for desorption [18], it is assumed that 4 bar correspond to a reasonable operation pressure. As can be seen in Fig. 2, the equilibrium temperature at 4 bar is 5 °C, thus in this case there is a temperature difference of 10 K to provide the heat to the storage tank.

In short, it can be stated that this material fulfills the thermodynamic requirements for a metal hydride hydrogen storage allowing for a quite simple thermal management as mentioned in the introduction.

Next to the selection of a suitable material, also for the reactor design two aspects were considered to keep the complexity of the system low: First, air was chosen as easy to handle heat transfer fluid that is also non-toxic and abundant. Second, the design of the reactor focused on a reduced amount of reactor wall material in comparison to the metal hydride material. Therefore, the applying loads and suitable heat transfer measures were analyzed for the design.

In most studies on metal hydride tanks, the thermal management of metal hydride reactions is difficult due to fast reaction rates and large amounts of thermal energy that have to be removed. E.g. in a recent study by Lototsky et al. on a hydrogen storage tank for forklifts [19], it is necessary to remove continuously ~ 9.2 kW during 15 min in order to fill the tank with 0.91 kg of hydrogen. Reducing the refueling time to the required values of less than 5 min for automotive applications will further increase the required cooling power. In order to handle these high heat fluxes – especially in combination with a relatively low thermal conductivity of metal hydride beds of only approximately 1 W(mK)⁻¹ [20] – several options to enhance the heat transfer have been discussed in the literature extending the heat transfer area with fins, foams etc. [21,22], or minimizing the distance to the heat transfer surface by reactor design [23] as well as introducing a heat transfer secondary phase, e.g. graphite, into the storage material [24].

Even though the thermal loads of the present application are lower, the utilization of one of these well-studied measures – metal hydride-graphite composites – can still contribute significantly to the simple system layout and a reduction in overall reactor mass. This will be shown in the following basic calculation for the temperature decrease in a tubular reactor for powdery and pelletized metal hydride material.

For this calculation it is necessary to know the thermal loads that will apply during operation. Furthermore, the maximum temperature decrease that still allows a continuous operation has to be considered. If these values are known, the maximum diameter of a tubular reactor using a given material can be calculated [25]. In Table 1, the basic conditions for the reference case as well as the layout of the present system are summarized. For the desired continuous electrical power of 160 W_{el} per layer, a hydrogen mass flow rate of 2.7 10⁻³ g s⁻¹ is required (assuming η_{fc} = 0.5). In order to release this amount of hydrogen, with a reaction enthalpy of Δ_RH = 28.4 kJ mol⁻¹, 38 W of thermal energy have to be provided to the material. Thus, for a continuous supply of 100 min, at least 1.35 kg of powdery Hydralloy material (corresponding to 1.42 kg of Hydralloy-based MHC including ENG) is required. Assuming an inner diameter of the tube of 21 mm, the total reactor length for the powder material is 1.95 m whereas only 1.05 m is required for the compacted MHC. As the resulting thermal power density of the MHC is about 2 times higher than the thermal power density of the powder, it is obvious that the MHC help to make the storage system more compact. However, for the MHC it is more difficult to supply the heat of reaction due to the smaller surface area. In order to show this for the present example, the temperature profile has

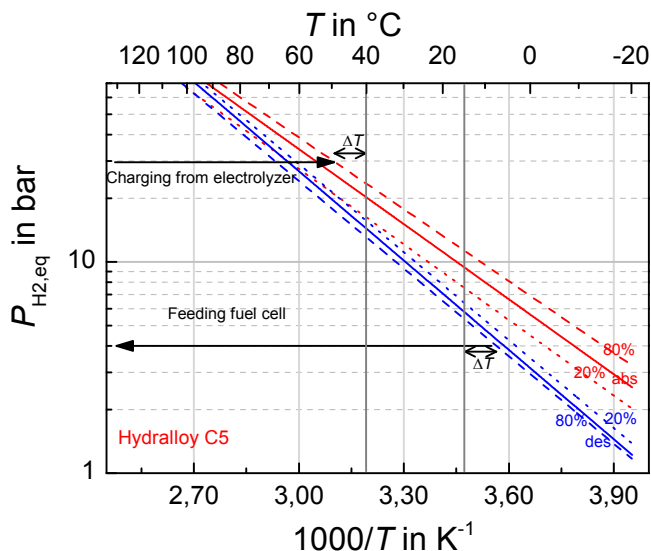


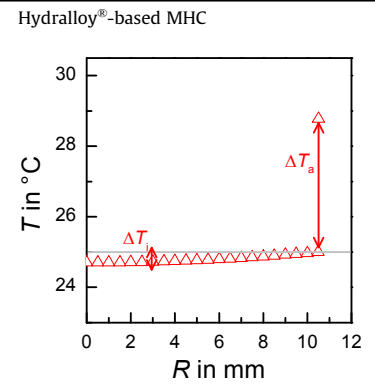
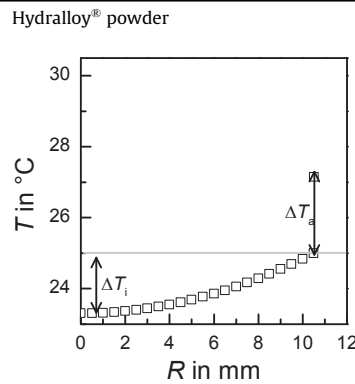
Fig. 2. Van't Hoff plot of Hydralloy C5 [17], and operation conditions for the present reactor design.

⁸ E.g., www.actaspa.com.

Table 1

Summary of properties for powder or MHC material as well as calculated design parameters (materials properties taken from Ref. [17]).

	Hydralloy [®] powder	Hydralloy [®] -based MHC
Req. power in W_{el} per layer	160	160
ρ in $kg\ m^{-3}$	2000	4040
λ in $W\ m^{-1}\ K^{-1}$	1	9.9
m in kg	1.35	1.42
L in m	1.95	1.01
Q/A in $W\ m^{-2}$	295	567
Q/V in $kW\ m^{-3}$	56.3	108.3
ΔT_i in K	1.55	0.30
ΔT_a in K	1.96	3.78



been calculated for MHC pellets and powder (Table 1).

Assuming a cylindrical shape with a constant temperature at the outside wall and a homogeneous heat sink due to the reaction (assumed to be independent of temperature), the occurring temperature decrease at the center of the tube can be calculated with:

$$\Delta T = \frac{1}{4\lambda} S \cdot R^2 \quad (2)$$

where S is the volumetric heat sink density during the desorption reaction in Wm^{-3} , λ is the heat conductivity of the material in $W(mK)^{-1}$ and R is the radius of the tube in m.

Due to the strong influence of the thermal conductivity, the temperature drop in the powder bed is a factor 5 higher than for the MHC material (see graph in Table 1) – despite the clearly higher power density in the MHC. Thus, the advantage of MHC for a compact system is based on three facts: The material is more compact, thus a smaller volume has to be covered by external steel walls. The increased thermal conductivity enables tubes with much larger diameters while still showing homogenous reaction, and a higher temperature gradient to a simple heat transfer fluid like air is acceptable. Especially the homogeneous reaction profile, that appears when pellets are used, is important as it also leads to a very homogeneous charging state of the material. Thus, basically all material in the reactor reacts at the same time and a high value of the utilization factor for the stored hydrogen can be achieved.

So far it has been shown that due to their high thermal conductivity, the MHC show a very homogeneous temperature profile inside of the tube although their power density is quite high (see also graph in Table 1). Thus, the performance during the desorption process is assumed to be very good although tubes with a diameter of 21 mm are used. However, even though the low ratio of outside surface to volume is good for the reduction of steel, this low ratio aggravates the heat transfer from the surface to the air. For the present setup, aluminum foam is used at the outside of the tubes resulting in a heat transfer coefficient of approximately $150\ W\ m^{-2}\ K^{-1}$. Thus, the temperature drop from the air to the center of the MHC is dominated by a $\Delta T_a = 3.78\ K$ from the air to the steel wall, while inside of the MHC the temperature gradient of ΔT_i

$\sim 0.33\ K$ can almost be neglected. This temperature difference of $\sim 4.1\ K$ is acceptable for the present system, as the distance of the operational temperature to the equilibrium temperature is more than 10 K, as mentioned above.

In summary it can be stated that with Hydralloy-based MHC a simple and compact hydrogen storage system could be designed as this material can operate at ambient conditions. Due to the utilization of MHC with a high thermal conductivity, the required homogeneous temperature and transformed fraction distribution can be achieved in tubes with an inner diameter of 21 mm.

3. Experimental details

In this Section, first details on the MHC are given, then the reactor design is shown and finally the test rig is presented.

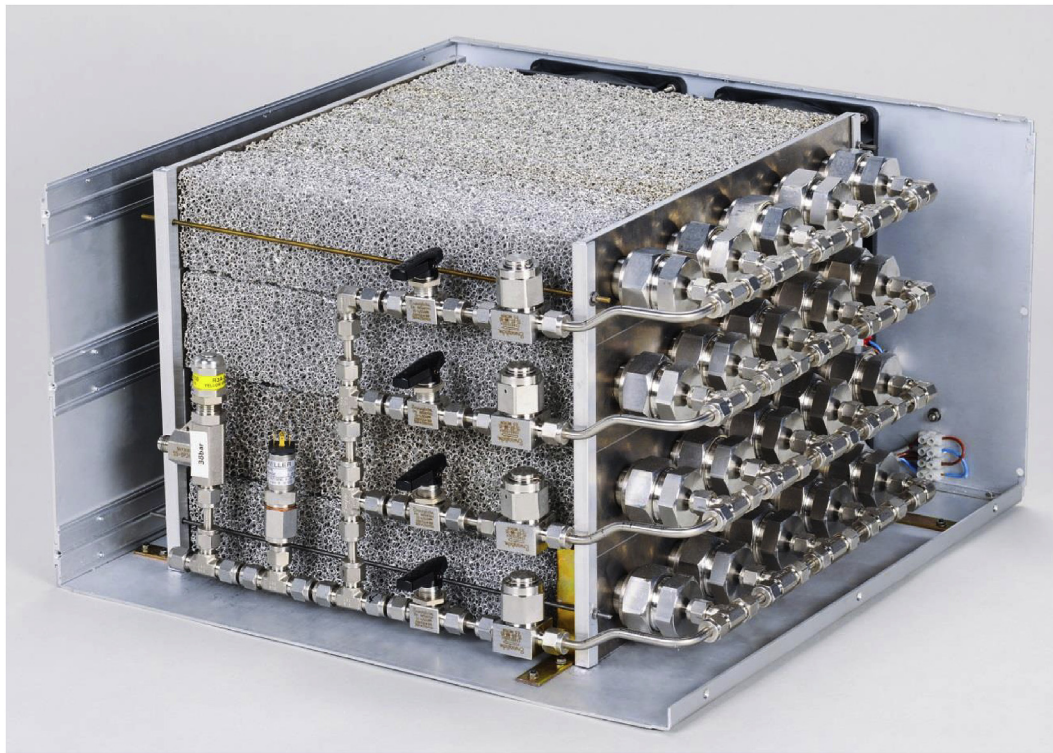
3.1. Metal hydride-graphite composites

The hydride material that has been used for the MHC is Hydralloy C5. To improve heat transfer properties, 5 wt% of ENG were added to Hydralloy powder particles of approx. 10 μm and the mixture was compressed to composites (so-called MHC) at a pressure of 75 MPa with a diameter (D) to height (H) ratio of approximately 1.5. After compaction, a hole was drilled in the center of each MHC pellet in order to enable sufficient gas transport in axial direction. Then, the MHC pellets were filled under ambient conditions into the reactor tubes using few pieces of polyurethane foam as spacer material between the pellets to buffer the volume expansion of the MHCs [26]. In our previous work [14], it has been shown that similar composites were geometrically stable for over 1000 cycles with a thermal conductivity of the cycled material in the range of $10\ W\ m^{-1}\ K^{-1}$.

3.2. Reactor design

Table 2 shows a picture of the final reactor consisting of 20 stainless steel tubes with an outer diameter of 25 mm, 2 mm wall thickness and a length of about 34 cm. For the overall design, the standardized dimensions of standard 19 inch rags have been

Table 2
Photograph of storage tank demonstrator and its main features.⁴



Mass MHC in kg	6
Total mass in kg	30
Stored volume of H ₂ in m ³	1
Designed load in W _{el} per layer	160 for 100 min, @ 4 bar back pressure
Dimensions in mm	261 × 444 × 458

considered according to the basic idea to combine a fuel cell, standardized modular hydrogen storage and optionally an electrolyzer in one rag. Thus, the outer dimensions of the storage tank were 261 × 444 × 458 mm.

In order to enhance the heat transfer to air at the outside surface of the tubes, aluminum foam has been attached to the tubes using an adhesive paste. In addition, four small ventilators with a required electric output of 8 W_{el} were used to blow air through the foam. This prototype consists of 4 layers with 5 tubes each that can be operated separately. Furthermore, gas filters, a pressure sensor, an overpressure valve and 3 thermocouples were integrated.

It is obvious that the weight of this system with approx. 30 kg was still too heavy for a 19 inch rack solution. However, it will be possible to reduce the weight by 50%, e.g. by replacing the fittings, as the mass of the hydride, the mass of the stainless steel tubes, and that of the foam is only 6 kg, 6.5 kg, and 1.5 kg, respectively.

3.3. Test rig set-up

The reactor was integrated into an existing test rig (see Fig. 3) that provides hydrogen at flow rates of up to 74.9 mg s⁻¹ at pressures up to 100 bar to simulate the electrolysis (MFC 1). Furthermore, hydrogen can be released at constant flow rates of up to 74.9 mg s⁻¹ at pressures >10 bar using MFC 2 and at pressures <10 bar using MFC 3, in order to simulate the hydrogen demand of a fuel cell. All mass flow controllers (MFC) have an accuracy of ± (0.5%

Rd + 0.1% FS⁹). The pressure sensor PS1 can measure pressures up to 160 ± 1.6 bar, and one thermocouple is integrated into the hydrogen supply tubes. Furthermore, another pressure sensor (PS) that is calibrated up to 40 ± 0.4 bar is integrated into the reactor. Thermocouples (Type K) have been integrated in three representative tubes. In case the pressure inside of the reactor exceeds 38 bar, an excess valve (EV) opens and the hydrogen is released to the hood. In order to fully desorb the reactor it is also possible to extract the hydrogen by a vacuum pump (VP) to decrease the pressures to 0.5 mbar.

4. Results and discussion

Preliminary to the results, in this section, the testing procedure as well as the list of experiments is presented.

The goal of the experiments was to evaluate the capability of the tank and to demonstrate that each layer of the reactor is able to store or provide sufficient hydrogen for 160 W_{el} by an electrolyzer or a fuel cell, over a time period of 100 min thereby utilizing about 90% of the storage capacity of the material at application relevant conditions. Using the dimensioning described in the previous section, this implies that - for the given charging and discharging loads - the developed storage system operates at steady state and the temperature at the center of the reactor tubes stays almost constant

⁹ Rd = Reading, FS = full scale.

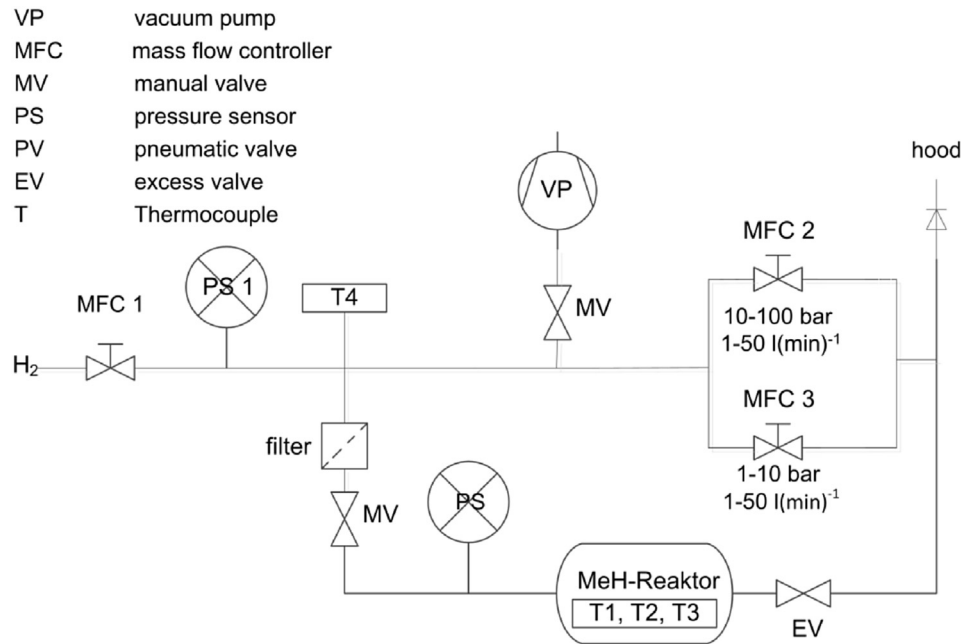


Fig. 3. Test rig layout.

during the experiment. In the reference experiment for absorption and desorption the pressure was changed between 4 and 30 bar at room temperature while keeping up a flow rate of 2.6 mg s^{-1} for at least 100 min per layer. For the complete storage (4 layers), these conditions refer to an electric fuel cell power of $640 \text{ W}_{\text{el}}$ for 100 min (efficiency of the fuel cell: $\eta_{\text{fc}} = 0.5$).

In addition to this experiment under *reference conditions* (indicated in the following as “RC”), experimental results for the following conditions will be presented: separately operated layers (modularity), increased flow rate (factor: 2, 4, 8, (16) *RC), and an experiment without fans (effect of outside heat transfer). The absorption experiments always refer to the charging process with hydrogen at constant flow rate from an electrolyzer, while the desorption experiments refer to the discharging process where hydrogen is provided to a fuel cell.

4.1. Reference conditions (RC)

The experiment for absorption and desorption at RC has been performed as first and last experiment of 38 experiments as well as several times in between. Fig. 4 shows the mass flow rate, the pressure as well as the temperature difference profile for one experiment at the beginning (olive) and the final experiment (black) for absorption (left) and desorption (right).

As it can be seen at the top, the mass flow rate for the studied two layers has been set to a constant value of $5.2 \times 10^{-3} \text{ g s}^{-1}$ in order to simulate the continuous operation of an electrolyzer or a fuel cell at $320 \text{ W}_{\text{el}}$. This flow rate could be absorbed or desorbed from the storage for the desired 100 min. The graphs at the center of Fig. 4 show the corresponding pressure profiles. In contrast to the temperature signal that is at steady state (Fig. 4, bottom), the pressure signal does not exhibit a perfectly flat plateau. This behavior has been expected as pressure-concentration-isotherms of the pure material also show a sloping plateau [17]. Furthermore, from Fig. 4, for absorption, the main fraction of hydrogen is absorbed at pressures between 10 and 15 bar and for desorption between 4 and 6.5 bar. The reason for this difference is the hysteresis of the material as well as the difference in the temperature. For both experiments the initial temperature was room

temperature. However, during the exothermal absorption reaction the temperature increases and reaches its steady state approximately 5 K above room temperature, while for the endothermal desorption the temperature decreases by 5 K (based on ambient temperature). Thus, according to the thermodynamics of the material, it is reasonable that for higher temperatures a higher pressure is required.

Overall it can be stated that during the reference experiment, the behavior of the tank showed the desired steady state behavior for 100 min, thus, the stored hydrogen can be used to a large extend (utilization factor 93%, see following section). Furthermore, during the 38 cycles the material did not show any degradation – in contrast – the material was rather continuously further activated.

4.2. Modularity – scale-up

After the proof of a continuous operation at steady state, for the presented reactor it is important to show that in the modular system the single layers operate independently. This implies that for higher or lower required powers of electrolyzer or fuel cell and the same operation time, the storage reactor can be scaled up or down by simply increasing or decreasing the number of layers. Fig. 5 presents the results for a continuous flow rate at 5.2 mg s^{-1} ($2 \times \text{RC}$) for layer 1 and layer 2 (triangles), furthermore the results for both layers at the double flow rate of 10.4 mg s^{-1} ($2 \times \text{RC} - 5.2 \text{ mg s}^{-1}/\text{layer}$, squares). As the pressure (A) as well as the temperature signals (B), show a very good agreement, it can be concluded that the single layers are independent of each other, thus the setup can be scaled up or down regarding the loads. The temperature difference between the signals for layer 1 (open symbols) and layer 2 (closed symbols) can be explained by a slightly different position of the thermocouples inside of the reactor tubes.

4.3. Increased load and hydrogen utilization factor

As shown before, each layer of the developed hydrogen storage reactor was able to operate at steady state for an electric load of 160 W and 100 min. Furthermore, it has been shown that the design is scalable, thus the number of layers can be adapted to the actual

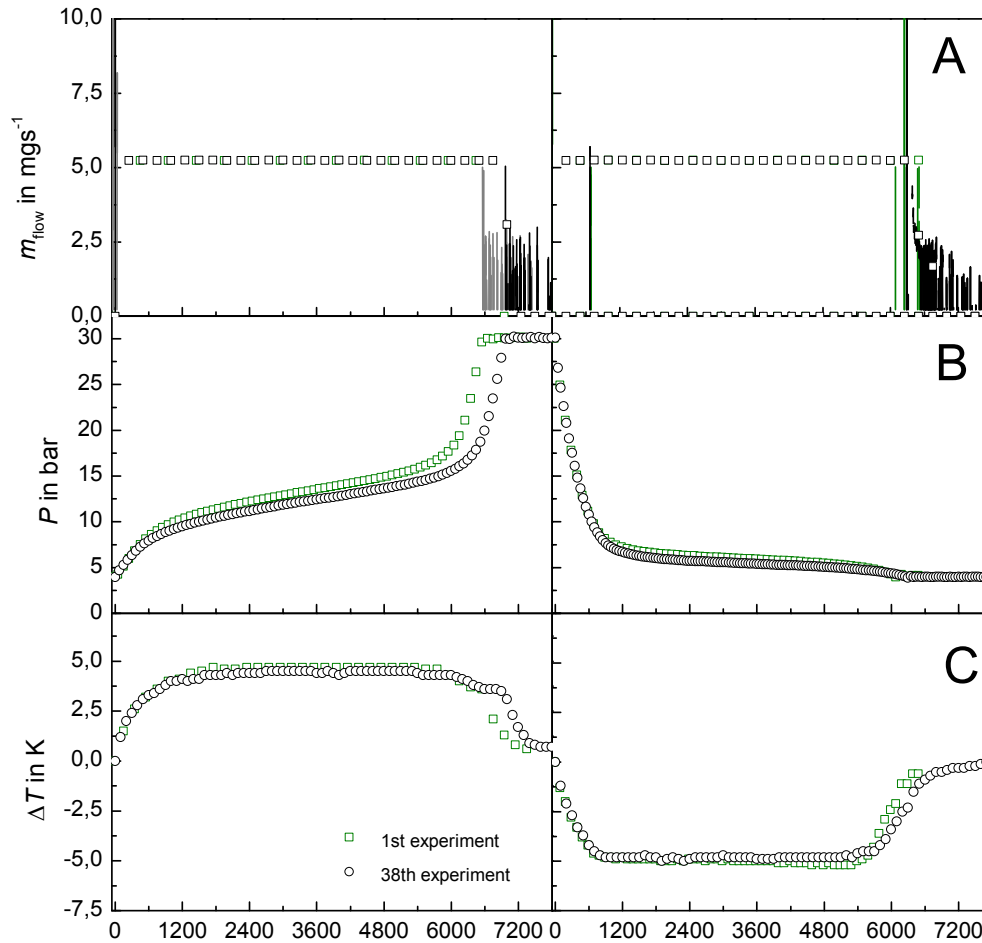


Fig. 4. Mass flow rate (A), pressure (B) and temperature difference (C) versus time for absorption (left) and desorption (right) under RC.

load without affecting the reachable discharge state.

In this section, the effect of an increased load of the present setup has been studied in order to reveal the limits of the present design. Furthermore, the utilization factor of the stored hydrogen is discussed. Fig. 6 shows the results for absorption and desorption of 2 layers with flow rates of 5.2 (RC), 10.5 ($2 \times$ RC), 21 ($4 \times$ RC), as well as 41.9 ($8 \times$ RC) mgs^{-1} .

For absorption (left), the trends are as expected: The time interval with constant flow rates (A) scales almost linearly with the applied flow rate. Thus, for $2 \times$ RC 50 min, for $4 \times$ RC 25 min and for $8 \times$ RC about 13 min are reached. However, in order to reach the corresponding power loads for flow rates above $2 \times$ RC, the temperature in the reactor does not reach a steady state anymore, but it continuously increases – indicating that heat transport is limiting even at $\Delta T > 25$ K. Corresponding to the thermodynamics of the material, not only the temperatures inside of the material, but also the pressures increase and for the higher rates basically no plateau is appearing.

For the desorption process (right), even for loads with $2 \times$ RC it was not possible to deliver sufficient hydrogen at pressures above 4 bar. As it can be seen in Fig. 6 (A, right), the time interval with a constant flow rate of hydrogen for $2 \times$ RC reaches less than the required 3000 s. This can be explained by the corresponding temperature and pressure plots. As the temperature decreases by more than 10 K (red circles), the equilibrium pressure decreases below the required 4 bar back pressure. For higher flow rates the behavior

is even more pronounced.

Next to the discussion of the experimental observations in Figs. 6 and 7 shows the calculated hydrogen mass absorbed (left) or desorbed (right) during the same experiments. Using these data, it is possible to discuss the actual utilization factor of the stored hydrogen that has been reached at the different flow rates. As long as the mass flow rate is constant, the evolution of the hydrogen mass is represented with straight lines, and as soon as the mass flow rate decreases the evolution of the absorbed/desorbed mass is shown with dots. All values are already reduced by the amount of hydrogen stored in the void volume of $0.90 \times 10^{-3} \text{ m}^3$ at the exact experimental conditions (on average this refers to about 2 g hydrogen).

For the experiment at RC, three repeated experiments are shown (light grey to black). All the corresponding graphs show exactly the same slope, and towards the end, for a higher cycling number a slightly higher mass of hydrogen can be absorbed. This indicates that the capacity is still slightly increasing with the cycles. In the last experiment at RC (black), a final value of 34.6 g absorbed hydrogen is reached at constant flow rate. This value refers to a very good utilization factor of 93%, when at the experimental conditions starting from 4 bar and reaching 30 bar at 25 °C a maximum hydrogen mass of 37.3 g (1.31 wt%, grey dashed line) is calculated. In case the experiment at RC conditions is extended starting from a pressure of 1 bar instead of 4 bar (turquoise), the absorption time is extended by 8.8% reaching a final mass of 36.6 g of hydrogen.

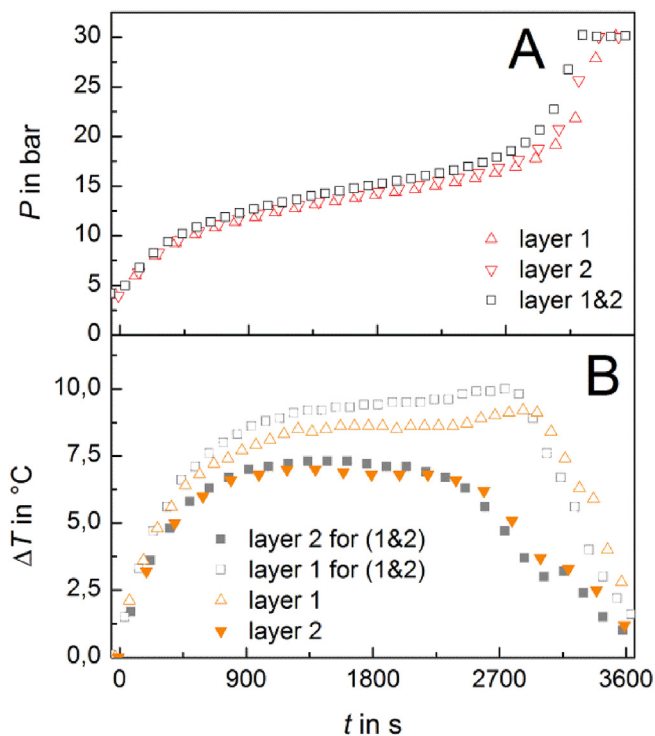


Fig. 5. Pressure (A) and temperature difference (T1: full and T2: open symbols, B) versus experimental time with $2 \times \text{RC}$ and 2 layers (squares) as well as with $2 \times \text{RC}$ and two single layers (triangles up and triangles down).

However, under these conditions a storage capacity of 1.55 wt% resulting in 44.2 g would theoretically be feasible leading to a utilization factor of 83%. As discussed before, for the experiments with $2 \times \text{RC}$ and $4 \times \text{RC}$, the absorption time at constant flow rate decreases - as expected - to times of almost $\frac{1}{2}$ and $\frac{1}{4}$. Therefore, it is clear that also the utilization factor for $4 \times \text{RC}$ is only reduced to 82% in comparison to 93% for RC.

For desorption, it could be observed that all final values are approx. 2 g lower than for absorption. The reason for this behavior is in the experimental setup, where in the first seconds starting at high pressure the mass flow meter is not able to measure the correct values. Therefore, the trends are still obvious, but for the utilization factor lower values are calculated. In the repeated experiments (grey to black) the same effects as for absorption can be observed: during cycling the amount of hydrogen increases and for the extension to 1 bar more hydrogen is released (turquoise). In case of an increasing flow rate of $2 \times \text{RC}$ (red) and $4 \times \text{RC}$ (green), however, it is obvious that the utilization factor of the stored hydrogen at constant flow rate is significantly decreasing and for $2 \times \text{RC}$ and $4 \times \text{RC}$ values of 74%, and 36%, respectively, are calculated compared to 83% at RC.

The reason in the strong decline of the utilization factor for higher flow rates during desorption in contrast to absorption can be explained by Fig. 2. As mentioned in the beginning, the temperature difference between the nominal operational temperature and the equilibrium temperature was 10 K for absorption and desorption. However, in this graph, the assumption for the nominal ambient temperature was between 15 $^{\circ}\text{C}$ and 40 $^{\circ}\text{C}$. Since the experiments were performed with ambient air at an ambient temperature of around 20 $^{\circ}\text{C}$, the absorption reaction was

thermodynamically favored at the current experimental conditions.

At this point it can be summarized that the modular tank design with a simple thermal management is able to combine constant mass flow rates with a high hydrogen utilization factor - at RC. If the load is increased to higher values, the temperature and pressure profiles get highly dynamic and especially for desorption the load cannot be provided until the storage reactor is fully depleted. Thus, in case higher loads are required, a modular scale-up of the reaction is necessary, e.g. the number of layers should be increased. However, this will not only increase the possible hydrogen loads, but also the total amount of hydrogen stored. In case, the total amount of hydrogen should stay constant while the loads should be increased, it is obvious that a different design with thinner tube diameters is required in order to decrease the heat load per surface area.

4.4. Effect of electric fan

The last effect that has been studied is the impact of the fan on the performance of the reactor. As mentioned in the section on the system layout, the external heat transfer is more important for the reactor design with thicker tubes and MHC inside.

Fig. 8 depicts the resulting temperature and pressure profiles for the reference absorption experiment with fan (black) and without fan (turquoise). The temperature clearly indicates that the heat transfer between air and the tube is significantly reduced when the fan is switched off, as the temperature continuously decreases to less than 10 $^{\circ}\text{C}$. After around 2400 s the pressure in the tank reaches 4 bar (indicated by arrow) and the required mass flow of hydrogen cannot be provided. At this time clearly no steady state has been reached and only 10.2 g of hydrogen are desorbed. Concluding, it can be stated that the fans are strictly required to guarantee the desired performance. However, with their electric power consumption of about 1.7 W per layer this effort seems reasonable.

5. Conclusion

In the present publication a standardized metal hydride buffer hydrogen storage reactor is presented that focusses on two aspects for a simple system: selection of a storage material able to operate near ambient conditions and a simple heat transfer design using MHC as well as air as heat transfer fluid. The main objective was to investigate the operational characteristics of such a tank with regard to the utilization factor of the stored hydrogen for given charging and discharging rates.

The reactor consists of 4 identical layers that are designed to provide sufficient hydrogen for 100 min of fuel cell operation at 160 W_{el} using MHC at ambient temperatures between 10 $^{\circ}\text{C}$ and 40 $^{\circ}\text{C}$. The experimental results demonstrate that it is possible to operate this reactor at the load of this reference case at steady state with a temperature difference between ambient and reaction of approximately 5 K. Furthermore, it has been shown that the modular system is scalable thus that single tube layers operate independently. The effect of an increased load on the present system for absorption and desorption is also presented using loads that are a factor of 2, 4 and 8 higher. It is shown that for absorption at RC a very high utilization factor of the stored hydrogen of 93% can be achieved, that is only reduced to 89% when the flow rate is increased to $4 \times \text{RC}$. For desorption at RC, a slightly lower utilization factor of 83% is calculated due to the measuring setup and due to the operating conditions this value is even reduced to 36% for $4 \times \text{RC}$. Finally, the experimental results reveal that electric fans are crucial for the overall performance as they significantly

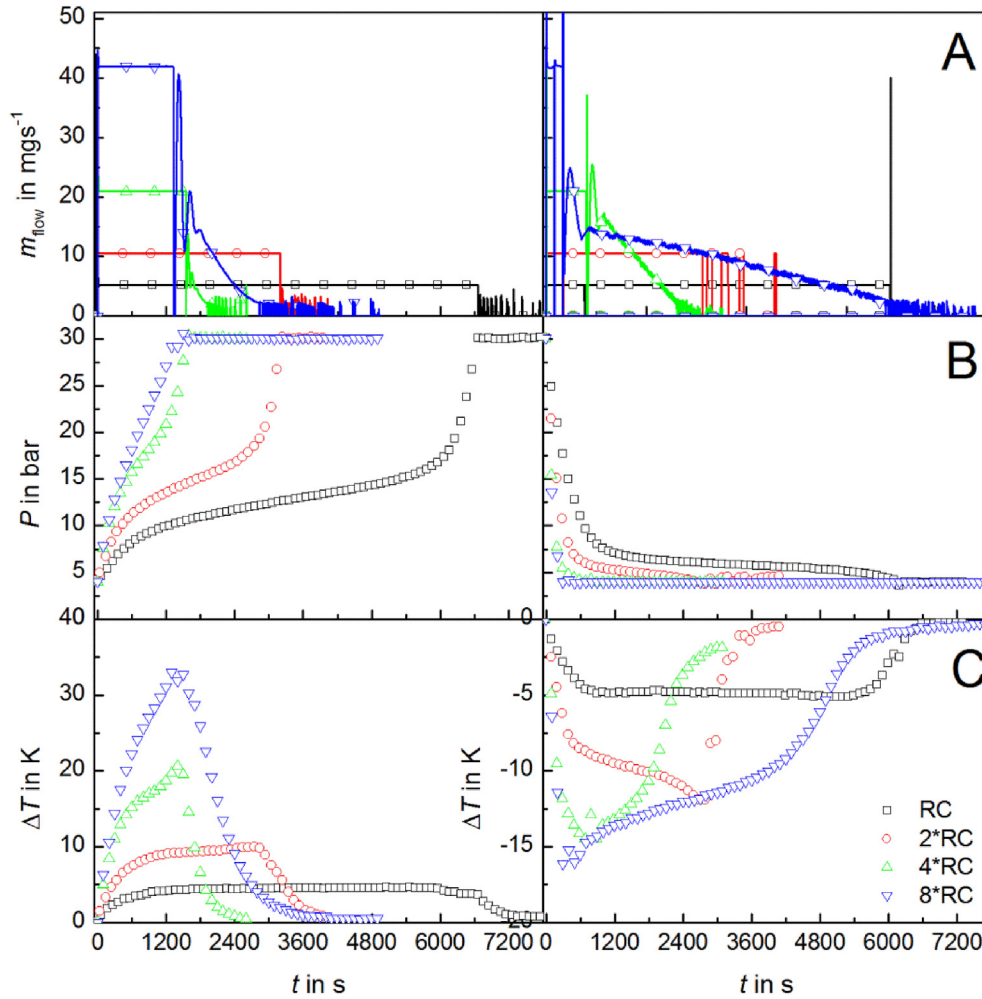


Fig. 6. Mass flow rate (A), pressure (B) and temperature difference (C) versus time for absorption (left) and desorption (right) under RC, 2 × RC, 4 × RC, and 8 × RC.

influence the heat transfer from the reactor tube to the air. With 30 kg the laboratory system is currently too heavy, however using improved assembly techniques it will be possible to reduce the weight by 50%.

Summarizing, a solid-state hydrogen storage tank with simple design and little heat transfer effort was presented that is able to reach high utilization factors of around 90%.

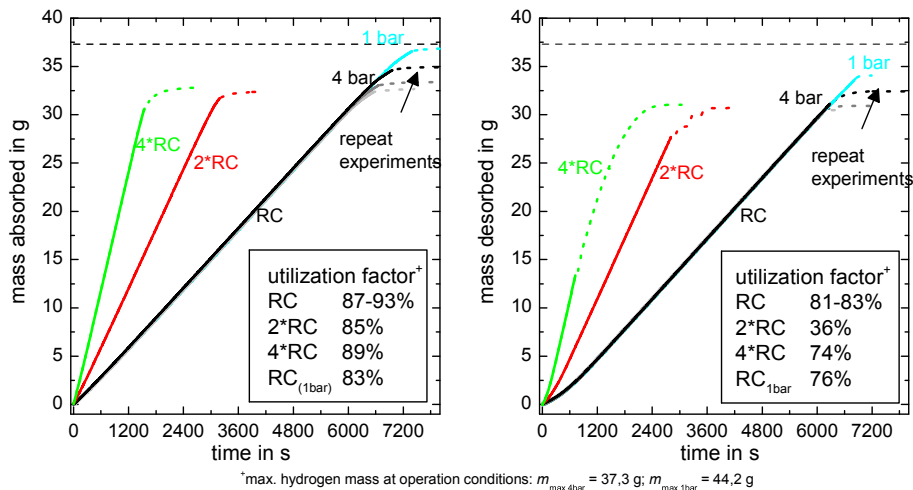


Fig. 7. Mass absorbed (left) and mass desorbed (right) versus time for repeated experiments at RC (light grey, grey, black), 2 × RC (red), 4 × RC (green), and RC starting/ending at 1 bar instead of 4 bar (turquoise). (For interpretation of the references to colour in this figure legend, the reader is referred to the web version of this article.)

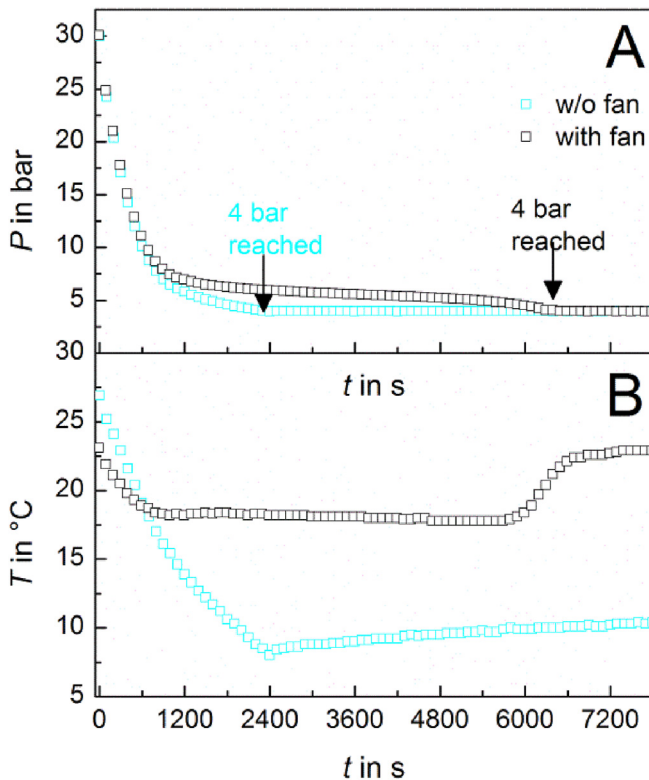


Fig. 8. Pressure (A) and temperature difference (B) versus time for desorption experiment at RC with fan and without fan.

Acknowledgements

This work is financially supported by the German Federal Ministry of Education and Research (BMBF) within the project Highly Dynamic Hydride-Graphite Composites (HD-HGV) (grant number 03EK3020). The authors want to thank Maximilian Marschall and Philipp Golebniak for their contributions to reactor design and measurements of the tank.

References

- [1] G. Saur, Wind-to-hydrogen Project: Electrolyzer Capital Cost Study, NREL/TP-550-44103, 2008, <http://dx.doi.org/10.2172/944892>.
- [2] G. Friedlmeier, A. Manthey, M. Wanner, M. Groll, Cyclic stability of various application-relevant metal hydrides, *J. Alloys Compd.* 231 (1995) 880–887, [http://dx.doi.org/10.1016/0925-8388\(95\)01776-3](http://dx.doi.org/10.1016/0925-8388(95)01776-3).
- [3] M. Wanner, G. Friedlmeier, G. Hoffmann, M. Groll, Thermodynamic and structural changes of various intermetallic compounds during extended cycling in closed systems, *J. Alloys Compd.* 253–254 (1997) 692–697, [http://dx.doi.org/10.1016/S0925-8388\(96\)03041-1](http://dx.doi.org/10.1016/S0925-8388(96)03041-1).
- [4] B. Sakintuna, F. Lamari-Darkrim, M. Hirscher, F. Lamaridarkrim, Metal hydride materials for solid hydrogen storage: a review, *Int. J. Hydrogen Energy* 32 (2007) 1121–1140, <http://dx.doi.org/10.1016/j.ijhydene.2006.11.022>.
- [5] B. Delhomme, A. Lanzini, G. a. Ortigoza-Villalba, S. Nachev, P. de Rango, M. Santarelli, P. Marty, P. Leone, Coupling and thermal integration of a solid oxide fuel cell with a magnesium hydride tank, *Int. J. Hydrogen Energy* 38 (2013) 4740–4747, <http://dx.doi.org/10.1016/j.ijhydene.2013.01.140>.
- [6] P. Marty, P. de Rango, B. Delhomme, S. Garrier, Various tools for optimizing large scale magnesium hydride storage, *J. Alloys Compd.* 8388 (2013), <http://dx.doi.org/10.1016/j.jallcom.2013.02.169>.
- [7] M. Hagstrom, Metal hydride hydrogen storage for near-ambient temperature and atmospheric pressure applications, a PDSC study, *Int. J. Hydrogen Energy* 20 (1995) 897–909, [http://dx.doi.org/10.1016/0360-3199\(95\)00025-9](http://dx.doi.org/10.1016/0360-3199(95)00025-9).
- [8] M.V. Lototsky, M.W. Davids, I. Tolj, Y.V. Klochko, B.S. Sekhar, S. Chidziva, F. Smith, D. Swanepoel, B.G. Pollet, Metal hydride systems for hydrogen storage and supply for stationary and automotive low temperature PEM fuel cell power modules, *Int. J. Hydrogen Energy* (2015), <http://dx.doi.org/10.1016/j.ijhydene.2015.01.095>.
- [9] G. Capurso, B. Schiavo, J. Jepsen, G. Lozano, T. Klassen, M. Dornheim, Development of a modular room-temperature hydride storage system for vehicular applications, *Appl. Phys. A* 236 (2016) 1–11, <http://dx.doi.org/10.1007/s00339-016-9771-x>.
- [10] C. Bossi, a. Del Corno, M. Scagliotti, C. Valli, Characterisation of a 3 kW PEFC power system coupled with a metal hydride H₂ storage, *J. Power Sources* 171 (2007) 122–129, <http://dx.doi.org/10.1016/j.jpowsour.2006.11.006>.
- [11] A. Nakano, H. Ito, T. Maeda, T. Munakata, T. Motyka, C. Cognale, S. Greenway, J.M. Perez-Berrios, Study on a metal hydride tank to support energy storage for renewable energy, *J. Alloys Compd.* 580 (2013) S418–S422, <http://dx.doi.org/10.1016/j.jallcom.2013.03.152>.
- [12] Z. Liu, Y. Li, Q. Bu, C.J. Guzy, Q. Li, W. Chen, C. Wang, Novel fuel cell stack with coupled metal hydride containers, *J. Power Sources* 328 (2016) 329–335, <http://dx.doi.org/10.1016/j.jpowsour.2016.07.096>.
- [13] T. Maeda, T. Fuura, I. Matsumoto, Y. Kawakami, M. Masuda, Cyclic stability test of AB₂ type (Ti, Zr)(Ni, Mn, V, Fe)₂ for stationary hydrogen storage in water contaminated hydrogen, *J. Alloys Compd.* 580 (2013) S255–S258, <http://dx.doi.org/10.1016/j.jallcom.2013.03.230>.
- [14] M. Dieterich, C. Pohlmann, I. Bürger, M. Linder, L. Röntzsch, Long-term cycle stability of metal hydride-graphite composites, *Int. J. Hydrogen Energy* (2015), <http://dx.doi.org/10.1016/j.ijhydene.2015.09.013>.
- [15] C. Pohlmann, L. Röntzsch, F. Heubner, T. Weißgärber, B. Kieback, Solid-state hydrogen storage in Hydralloy-graphite composites, *J. Power Sources* 231 (2013) 97–105, <http://dx.doi.org/10.1016/j.jpowsour.2012.12.044>.
- [16] M. Ron, The normalized pressure dependence method for the evaluation of kinetic rates of metal hydride formation/decomposition, *J. Alloys Compd.* 283 (1999) 178–191, [http://dx.doi.org/10.1016/S0925-8388\(98\)00859-7](http://dx.doi.org/10.1016/S0925-8388(98)00859-7).
- [17] K. Herbrig, L. Röntzsch, C. Pohlmann, T. Weißgärber, B. Kieback, Hydrogen storage systems based on hydride-graphite composites: computer simulation and experimental validation, *Int. J. Hydrogen Energy* (2013) 1–11, <http://dx.doi.org/10.1016/j.ijhydene.2013.03.104>.
- [18] J. Mitzel, E. Gülzow, A. Kabza, J. Hunger, S.S. Araya, P. Piela, I. Alecha, G. Tsoiridis, Identification of critical parameters for PEMFC stack performance characterization and control strategies for reliable and comparable stack benchmarking, *Int. J. Hydrogen Energy* 41 (2016) 21415–21426, <http://dx.doi.org/10.1016/j.ijhydene.2016.08.065>.
- [19] M.V. Lototsky, I. Tolj, A. Parsons, F. Smith, C. Sita, V. Linkov, Performance of electric forklift with low-temperature polymer exchange membrane fuel cell power module and metal hydride hydrogen storage extension tank, *J. Power Sources* 316 (2016) 239–250, <http://dx.doi.org/10.1016/j.jpowsour.2016.03.058>.
- [20] S. Suda, Y. Komazaki, N. Kobayashi, Effective thermal conductivity of metal hydride beds, *J. Less Common Met.* 89 (1983) 317–324, [http://dx.doi.org/10.1016/0022-5088\(83\)90340-5](http://dx.doi.org/10.1016/0022-5088(83)90340-5).
- [21] F.S. Yang, G.X. Wang, Z.X. Zhang, X.Y. Meng, V. Rudolph, Design of the metal hydride reactors - a review on the key technical issues, *Int. J. Hydrogen Energy* 35 (2010) 3832–3840, <http://dx.doi.org/10.1016/j.ijhydene.2010.01.053>.
- [22] P. Muthukumar, M. Groll, Metal hydride based heating and cooling systems: a review, *Int. J. Hydrogen Energy* 35 (2010) 3817–3831, <http://dx.doi.org/10.1016/j.ijhydene.2010.01.115>.
- [23] M. Linder, R. Mertz, E. Laurien, Experimental results of a compact thermally driven cooling system based on metal hydrides, *Int. J. Hydrogen Energy* 35 (2010) 7623–7632, <http://dx.doi.org/10.1016/j.ijhydene.2010.04.184>.
- [24] C. Pohlmann, L. Röntzsch, T. Weißgärber, B. Kieback, Heat and gas transport properties in pelletized hydride-graphite-composites for hydrogen storage applications, *Int. J. Hydrogen Energy* 38 (2012) 1685–1691, <http://dx.doi.org/10.1016/j.ijhydene.2012.09.159>.
- [25] I. Bürger, M. Bhouri, M. Linder, Considerations on the H₂ desorption process for a combination reactor based on metal and complex hydrides, *Int. J. Hydrogen Energy* 40 (2015) 7072–7082, <http://dx.doi.org/10.1016/j.ijhydene.2015.03.136>.
- [26] K. Herbrig, C. Pohlmann, L. Gondek, H. Fiegel, N. Kardjilov, A. Hilger, I. Manke, J. Banhart, B. Kieback, L. Röntzsch, Investigations of the structural stability of metal hydride composites by in-situ neutron imaging, *J. Power Sources* 293 (2015) 109–118, <http://dx.doi.org/10.1016/j.jpowsour.2015.05.039>.

Available online at www.sciencedirect.com

ScienceDirect

journal homepage: www.elsevier.com/locate/ije

Advanced reactor concept for complex hydrides: Hydrogen absorption from room temperature

I. Bürger*, L. Komogowski, M. Linder

Institute of Technical Thermodynamics, German Aerospace Center (DLR), D-70569 Stuttgart, Germany

ARTICLE INFO

Article history:

Received 18 December 2013

Received in revised form

7 February 2014

Accepted 12 February 2014

Available online 17 March 2014

Keywords:

Reactor concept

LaNi₅

Li–Mg–N–H

Hydrogen storage

Modelling

Combination of materials

Absorption

ABSTRACT

Complex hydride materials (CxH) are potential candidates for hydrogen storage in automotive applications due to their high hydrogen storage capacities. However, the reaction rates of these materials are rather low at temperatures below 100 °C implying negative effects on absorption performance e.g. at a fuelling station. In this paper simulated and experimental results of a new reactor concept that can improve the dynamic reactor performance are presented. This concept is based on the combination of a metal hydride (MeH) and a CxH in one reactor, separated by a gas permeable layer. The storage capacity of available MeH materials is just ~1 wt.%, however, they show very high reaction rates even at room temperature. Thus, the idea of this concept is to combine both: the high storage capacity of the CxH material and the high reaction rate of the MeH material. The two reference materials for this study are 2LiNH₂–1.1MgH₂–0.1LiBH₄–3 wt.%ZrCoH₃ (Li–Mg–N–H) and LaNi_{4.3}Al_{0.4}Mn_{0.3} (MeH). In the first part, 2D simulation results are presented showing the development of a reaction front from the core to the annulus of the tubular reactor caused by the fast exothermal absorption reaction of the MeH material. In the second part, experimental results of a 50 g lab-scale reactor and simulated scenarios are presented and used for model validation. In the present scenario it has been possible to reduce the time to initiate the absorption reaction from room temperature by approximately 500 s.

Copyright © 2014, Hydrogen Energy Publications, LLC. Published by Elsevier Ltd. All rights reserved.

1. Introduction

For future fuel cell driven cars hydrogen storage still poses a major challenge. The state of the art storage method for conventional vehicles is realized by a pressure tank. However, as the density of gaseous hydrogen is very low, high pressures of up to 700 bar are required accompanied by the corresponding accident risk potential [1]. One out of several alternative technologies to high pressure tanks is hydrogen storage

in solid state hydride materials. In these materials, gaseous hydrogen is bonded to a solid compound, e.g. a metal (M), by a reversible exothermic/endothermic reaction according to:



The advantages of such a solid state hydride material in comparison to the other storage options are the relatively low pressures (<100 bar), the possibility to store hydrogen at ambient temperatures and the reduced amount of free

* Corresponding author. Tel.: +49 711 6862492.

E-mail address: inga.buerger@dlr.de (I. Bürger).
<http://dx.doi.org/10.1016/j.ijhydene.2014.02.070>

0360-3199/Copyright © 2014, Hydrogen Energy Publications, LLC. Published by Elsevier Ltd. All rights reserved.

Table 1 – Summary of important characteristic properties for MeH and CxH materials [27,35].

	MeH	CxH
Type of reaction	Insertion	Conversion
Thermodynamics	Δ_{RH} from 30 to 40 kJ mol ⁻¹ possible	Δ_{RH} from 30 to 40 kJ mol ⁻¹ possible
Kinetics	Seconds at RT	Minutes/hours at $T < 100$ °C
Capacity	1–2 wt.%	2–18.4 wt.%
Availability	Commercial	Limited, only from research laboratories

hydrogen, as the gaseous hydrogen is bonded to the solid by a chemical reaction.

The existing hydride materials for this solid state hydrogen storage show large variations in their properties and can be classified in different ways. For the reactor concept that is presented in this paper, the following distinction between metal and complex hydride materials is most convenient (compare Table 1) [1].

- 1.) Metal hydride materials absorb hydrogen by an *insertion reaction*. These materials are very well studied in the literature and an important representative is e.g. LaNi₅ [2,3]. The absorption reaction of these materials takes place in the order of seconds even at room temperature and the materials show hydrogen storage capacities below 2 wt.%.
- 2.) Reversible complex hydride materials absorb hydrogen by a *chemical conversion reaction*. This reaction type enables high storage capacities of up to 18.4 wt.% [4], but causes low reaction rates at temperatures below 100 °C [1,5]. These materials have been studied since 1997, when Bogdanović proved the reversibility of NaAlH₄ which became a major representative material for complex hydrides [6] in the consecutive years.

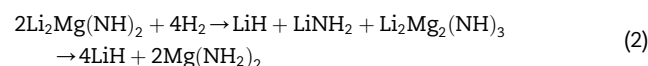
For hydrogen storage applications in automotive systems a high system gravimetric storage density of up to 0.075 kg_{H₂} kg_{system}⁻¹ is crucial (see DOE requirements in Ref. [7]). Therefore, the latter conversion reaction based materials with high theoretical storage capacities on a material level are suitable candidates. However, their low reaction rates at moderate temperatures and pressures will always lead to poor tank dynamics during absorption and desorption processes. Thus, a new reactor design for CxH materials for automotive applications has to focus on an improvement in the dynamic tank behaviour in order to reach the DOE goals for the filling time of 2.5 min for 5 kg_{H₂}. This is a new aspect in reactor design as for many applications and MeH materials the focus in the reactor design was on heat or mass transfer, leading to the development of numerous solutions, e.g. fins, foams, heating coils [8–13] or filters [10,14,15], etc.

In this paper, a new approach to solve this problem is presented that is based on the combination of a MeH material with a Li–Mg–N–H material in one storage reactor. With such a combination, the advantages of both material classes can be used: the high storage capacity of the Li–Mg–N–H material and the improved dynamic behaviour of the reactor due to the MeH material. In the literature, there is only one similar study using a low temperature metal hydride together with magnesium hydride [16]. However, in the present paper, such a combination reactor is studied for the first time using a novel

complex hydride material and a metal hydride material in the same reactor, thus applying the same hydrogen pressures on both materials.

1.1. Selection of representative materials

In order to study this new concept two suitable materials have been selected. As the amount of available, reversible complex hydride materials is limited, this material was defined first. One material that has already been studied on a reactor level is sodium Alanate [8,9,17–19]. This material theoretically absorbs 5.6 wt.% of hydrogen in two steps, however, approx. 4 wt.% reversible storage capacity are experimentally observed, e.g. Ref. [20]. Other materials that are also promising candidates are based on the basic Li–Mg–N–H system [21]. For example the material 2LiNH₂–1.1MgH₂–0.1LiBH₄–3 wt.% ZrCoH₃, that has been presented by Zhang et al., reversibly absorbs approx. 3.5–4 wt.% of hydrogen [22,23] at temperatures below 200 °C. The equation for the absorption reaction of the main Li–Mg-system of this material can be written according to [24] as



This material has been chosen as model material for reactor design in the present study, which is part of activities aiming at a coupling of a storage tank to a HT-PEM fuel cell in technically relevant scale – allowing for 2 h operation at 1 kW_{el}. In the following, the material will be abbreviated with Li–Mg–N–H material. The material has been synthesized by KIT¹ from 2LiNH₂ + MgH₂ requiring a 1st metathesis reaction to 2LiH + Mg(NH₂)₂, before it can reversibly absorb and desorb 3.2 wt.% of hydrogen in ~1 h. Details on this reaction, bulk properties and the reaction rates that are required for the model are published in Ref. [25] and summarized in Table 2.

For a suitable MeH material, the selection is much easier. For instance, there exists a variety of alloys based on LaNi₅ with different additives influencing the thermodynamics of the material [26,27]. For the present study, LaNi_{4.3}Al_{0.4}Mn_{0.3} has been chosen as it shows suitable material properties [28]. In the following, this material will be abbreviated as MeH. It has been purchased from Konik Industries Corporation with a particle size of 50 μm, and the first activation procedure has been performed at <10 bar and RT. The properties of this material have been adapted from LaNi₅ using several reaction rate experiments (not presented here), and all values are summarized in Table 2.

¹ KIT: Karlsruhe Institute of Technology, Institute of Nanotechnology.

Table 2 – Relevant material properties used for the simulation.

		Value	Units	Reference
General				
Temperature	T		K	
Pressure	P_g		Pa	
Universal gas constant	\mathcal{R}	8.314	$\text{J kg}^{-1} \text{K}$	
Mass change H_2 due to reaction	\dot{m}_R		$\text{kg m}^{-3} \text{s}^{-1}$	
Porosity	ϵ	0.55		
Gas density	ρ_g	Simplified van der Waals		
Heat capacity of gas	$c_{p,g}$	14,304	$\text{J kg}^{-1} \text{K}^{-1}$	[36] at 24.5 °C and 1 bar
Dynamic viscosity of gas	μ_g	$10^{-5} \cdot 9.05(T/293)^{0.68}$	Pa s	[34]
Molar mass of hydrogen	M	0.002	kg mol^{-1}	
MeH				
Solid density	$\rho_{\text{MeH},0}$	8200	kg m^{-3}	[37]
Max. gravimetric H_2 storage capacity	wt_{max}	1.2126–0.0003 $T[^\circ\text{C}] - 9 \cdot 10^{-6} T[^\circ\text{C}]^2$	$\text{kg}_{\text{H}_2} \text{kg}_{\text{MeH}}^{-1}$	exp. determined
Thermal conductivity	$\lambda_{\text{eff,MeH}}$	1.2	$\text{W m}^{-1} \text{K}^{-1}$	[33]
permeability	K_{MeH}	$1 \cdot 10^{-12}$	m^2	[38]
Specific heat capacity	$c_{p,\text{MeH}}$	420	$\text{J kg}^{-1} \text{K}^{-1}$	[33]
Enthalpy of absorption reaction	$\Delta_R H_{a,\text{MeH}}$	–35940	$\text{J mol}_{\text{H}_2}^{-1}$	[37]
Entropy of absorption reaction	$\Delta_R S_{a,\text{MeH}}$	–98.58	$\text{J mol}_{\text{H}_2}^{-1} \text{K}^{-1}$	[37]
Arrhenius parameter for abs	$A_{a,\text{MeH}}$	100	s^{-1}	adapted from Ref. [33]
Activation energy for abs	$E_{a,\text{MeH}}$	21,000	$\text{J mol}^{-1} \text{K}^{-1}$	[33]
Li–Mg–N–H				
Solid density	$\rho_{\text{LiMgNH},0}$	900	kg m^{-3}	[25]
Max. gravimetric H_2 storage capacity	wt_{max}	0.032	$\text{kg}_{\text{H}_2} \text{kg}_{\text{MeH}}^{-1}$	[25]
Max. gravimetric H_2 storage capacity, 1 st step	$wt_{\text{max}_1\text{step}}$	$0.33 wt_{\text{max}}$		[25]
Max. gravimetric H_2 storage capacity, 2 nd step	$wt_{\text{max}_2\text{step}}$	$0.67 wt_{\text{max}}$		[25]
Thermal conductivity	$\lambda_{\text{eff,LiMgNH}}$	0.35	$\text{W m}^{-1} \text{K}^{-1}$	In the range of [39]
Permeability	K_{LiMgNH}	$1 \cdot 10^{-12}$	m^2	Estimate
specific heat capacity	$c_{p,\text{LiMgNH}}$	1533	$\text{J kg}^{-1} \text{K}^{-1}$	[40]
Enthalpy of absorption reaction	$\Delta_R H_{a,\text{Li–Mg–N–H}}$	–38,000	$\text{J mol}_{\text{H}_2}^{-1}$	[25]
Entropy of absorption reaction	$\Delta_R S_{a,\text{Li–Mg–N–H}}$	–111	$\text{J mol}_{\text{H}_2}^{-1} \text{K}^{-1}$	[25]
Arrhenius parameter for abs, 1 st step	$A_{a,I,\text{Li–Mg–N–H}}$	$2.729 \cdot 10^{17}$	s^{-1}	[25]
Activation energy for abs, 1 st step	$E_{a,I,\text{Li–Mg–N–H}}$	164,800	$\text{J mol}^{-1} \text{K}^{-1}$	[25]
Arrhenius parameter for abs, 2 nd step	$A_{a,II,\text{Li–Mg–N–H}}$	$4.678 \cdot 10^{14}$	s^{-1}	[25]
Activation energy for abs, 2 nd step	$E_{a,II,\text{Li–Mg–N–H}}$	147,800	$\text{J mol}^{-1} \text{K}^{-1}$	[25]
Heat transfer				
Density of steel	ρ_{steel}	8000	kg m^{-3}	Thyssen Krupp, NIROSTA 4571
Thermal conductivity of steel	λ_{steel}	15	$\text{W m}^{-1} \text{K}^{-1}$	Thyssen Krupp, NIROSTA 4571
Heat capacity of steel	$c_{p,\text{steel}}$	500	$\text{J kg}^{-1} \text{K}^{-1}$	Thyssen Krupp, NIROSTA 4571
Heat transfer coefficient from steel wall to heat transfer fluid (HTF)	h_{HTF}	220	$\text{W m}^{-2} \text{K}^{-1}$	exp. determined

1.2. Concept

The combination reactor concept that is presented in this paper can be introduced based on thermodynamics and reaction rates for the different materials. In the following, the effects on the absorption process are discussed. For desorption, please refer to the affiliated publication [29].

Fig. 1 shows a van't Hoff diagram including the thermodynamic equilibrium line of the Li–Mg–N–H material with a high potential hydrogen storage capacity of up to 11.5 wt.% [30] (theoretical value). Furthermore, the equilibrium line of $\text{LaNi}_{4.3}\text{Al}_{0.4}\text{Mn}_{0.3}$ with a rather low hydrogen storage capacity of approx. 1 wt.% is plotted. In addition to the lines for the thermodynamic equilibrium of the two materials, Fig. 1 also shows two shaded areas that mark the temperature and pressure range which is required for a complete absorption reaction of each material in a technical time frame (<120 min).

The reaction of Li–Mg–N–H requires temperatures above 100 °C as well as pressures close to 100 bar to proceed at a reasonable rate (light blue area), whereas the metal hydride readily absorbs hydrogen at temperatures even as low as room temperature and 5 bar (dark orange area).

In order to show the advantages of a storage reactor with the combination of Li–Mg–N–H and the MeH material, first the absorption behaviour of a reactor based on a pure Li–Mg–N–H material is shown. At the beginning of the absorption reaction, the pressure in the reactor is about 1 bar and the temperature is room temperature (1). By applying a high charging pressure of approx. 70 bar the conditions for the material in the reactor are changed to the absorbed state. Thus the material should start to absorb hydrogen based on thermodynamics (2). However, the reaction rate is still negligible and the absorption will not proceed. Therefore, the reactor has to be preheated externally to temperatures

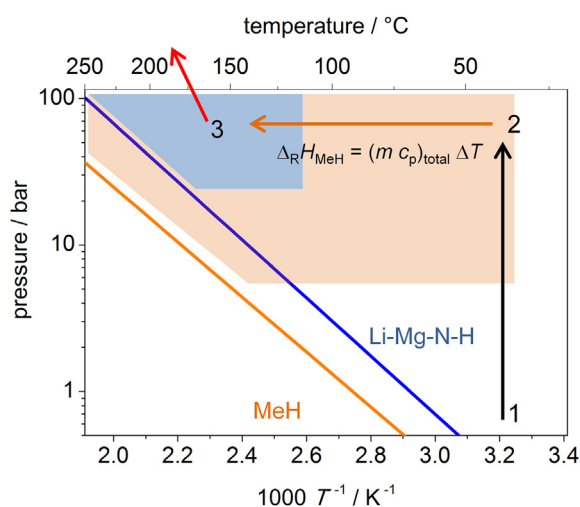


Fig. 1 – Schematic van't Hoff plot for MeH and Li–Mg–N–H material. The lines refer to the equilibrium lines of the reversible MeH (light orange) and Li–Mg–N–H (dark blue) sorption reaction. Shaded areas indicate temperature and pressure range where reaction rate proceeds in relevant time frames for absorption. Arrows indicate the absorption process in a reactor. (For interpretation of the references to colour in this figure legend, the reader is referred to the web version of this article.)

exceeding 100 °C in order to initiate the absorption reaction of the Li–Mg–N–H material (3).

This absorption behaviour will drastically change when the Li–Mg–N–H material is combined with a MeH material in the same reactor. In this case, a pressure increase will directly result in a strong temperature increase, as the exothermic reaction of the MeH material can already proceed at 20 °C, (1)→(2)→(3). Thus, after few seconds the MeH material has already absorbed hydrogen in the reactor based on the combination of materials. At the same time, the MeH releases thermal energy leading to temperatures of above 130 °C in the reactor. This temperature is sufficient to initiate the reaction of the Li–Mg–N–H, which is then able to absorb hydrogen using its high hydrogen storage capacity. In this case it is not necessary to provide heat externally in the beginning of the reaction. Furthermore, the heat can be removed at a temperature exceeding 100 °C, which is more convenient compared to the heat removal for a pure MeH reaction at room temperature. Thus, the thermal management of the reactor is clearly improved.

There are two options how the two materials can be combined in a reactor design. The first option is a direct mixture. In this case the two materials are mixed by shaking the two powders and filling both into the same compartment of a reactor. For this case, the temperature increase throughout the reactor bed is homogenous and defined by the ratio of the two materials as well as by their thermal properties according to

$$\Delta T = T - T_i = \frac{\Delta_R H^{\text{MeH}} x_{\text{MeH}} m_{\text{MeH}}}{m_{\text{Li-Mg-N-H}} c_{p,\text{Li-Mg-N-H}} + m_{\text{MeH}} c_{p,\text{MeH}}} \quad (3)$$

where T_i is the initial temperature in K, $\Delta_R H^{\text{MeH}}$ the reaction enthalpy of the MeH in $\text{J mol}_{\text{H}_2}^{-1}$, x the storage capacity in $\text{kg}_{\text{H}_2} \text{kg}_{\text{material}}^{-1}$, c_p the heat capacity in J kg^{-1} and m the mass of each material in kg. First experiments of this direct mixture showed that side reactions occur between the two materials leading to a significant decrease in the reaction rate of the MeH material (not shown here). Thus, for these materials the direct mixing option has been excluded.

The second option is an indirect mixture. In this case, the two materials are separated by a gas permeable separation layer (GPSL). This GPSL divides the reactor into the core that is filled with the MeH material, and into the annulus filled with Li–Mg–N–H material. Thus, the diameter of the GPSL defines the volumetric ratio of the two materials: $\epsilon_{\text{LiMgNH}} = V_{\text{LiMgNH}} / V_{\text{total}}$. In this case, the reaction of the Li–Mg–N–H material is initiated close to the MeH material, where very high temperatures can be reached. As just a very small fraction of MeH material can be sufficient to initiate the reaction of the Li–Mg–N–H material, it is possible to significantly reduce the amount of heavy and expensive MeH required, and thus reduce the overall weight and costs of the combination reactor.

The aim of this paper is to study such a reactor that is based on the combination of two materials. Therefore, first a mathematical model has been developed and simulations have been performed to gain insight into the thermal interaction of both materials. Then, an experimental setup has been designed and constructed that is used for model validation. Finally, the concept is validated by comparison of a pure Li–Mg–N–H reactor with a combination reactor.

2. Methodology

2.1. Experimental setup

For model validation, several experiments have been performed in a testing reactor. This reactor has an outer diameter of 42 mm and an integrated thin GPSL with a diameter of 13.5 mm inside the tube that is fixed with a 5 mm Teflon layer at the bottom and top of the reactor. Due to the thickness of less than 0.5 mm, the thermal mass as well as the gas transfer resistance of this GPSL have been neglected in the modelling. The Teflon layers at the bottom and the top are used to insulate the powder bed and avoid axial heat transfer effects in the tube. For model validation, three thermocouples (Type K) are integrated into the tube at the axial centre of the powder bed at three different radial positions. The corresponding thermocouple indices and positions are given in Fig. 2. The reactor is sealed by a 1" SAE flange using a Viton gasket as it has to withstand pressures of up to 100 bar.

This reactor is integrated into a testing setup where the inlet hydrogen mass flow can be varied from 0 to $30 \cdot 10^{-6} \text{ kg s}^{-1}$ and the outlet from 0 to $9 \cdot 10^{-6} \text{ kg s}^{-1}$. Furthermore, pressures up to 150 bar can be applied and the temperature can be controlled by a thermostatic bath to temperatures of up to 200 °C. In order to determine the absorbed mass of hydrogen, the mass of inflowing hydrogen is calculated by the integration of the mass flow signal by the inlet mass flow meter. This value is then reduced by the mass

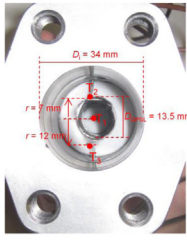


Fig. 2 – Left: radial positions of the three thermocouples in the reactor as well as inserted GPLS. T_{steel} is measured on the outer surface of the steel wall. Right: details of geometry and material masses for experiments.

		pure Li-Mg-N-H	combination reactor
D_i	in mm	34.0	34.0
D_{GPLS}	in mm	-	13.5
$\varepsilon_{\text{LiMgNH}}$	in 1	1.0	0.84
m_{LiMgNH}	in g	25.4	21.8
m_{MeH}	in g	0.0	26.9
m_{H_2}	in g	0.8	0.741+0.323
H_{COMSOL}	in m	0.069	0.07;0.051

of hydrogen that is stored in the defined void volume of the reactor at the present temperature and pressure.

The details on the masses of materials and the inner reactor geometry for the experiments are summarized in Fig. 2. The volumetric fraction in the combination reactor for the Li–Mg–N–H material, $\varepsilon_{\text{LiMgNH}} = V_{\text{LiMgNH}}/V_{\text{total}}$, is calculated to 0.84 and the measured gravimetric ratio $m_{\text{LiMgNH}}/m_{\text{total}} = 0.45$. Due to the higher volumetric H_2 storage density of the MeH material, the amount of hydrogen stored in the combination reactor is actually exceeding the mass H_2 stored in the pure Li–Mg–N–H reactor by a factor of 1.3. However, the focus of the present experiments is the validation of the reactor concept based on the combination of materials as well as the validation of the model equations.

2.2. Modelling

In the present paper, the software tool COMSOL Multiphysics has been used for modelling and the following assumptions have been applied:

- Similar to the assumptions in several models of metal hydride reactors, the gas and solid phase are *quasi-homogeneous*, the *bed porosity* and the *solid density* are constant, and all properties are independent of the transformed fraction [10,13,14,18,31,32].
- For the temperature of the gas and solid phase, the common assumption of *Local-Thermal-Equilibrium* (LTE) has been applied [10,13,14,18,31,32].
- *Darcy flow* in radial direction is implemented [14,33].
- The *simplified van der Waals equation* has been applied with $\rho_g = M P_g/[RT_g + (b-a/RT_g)P_g]$, and $a = 0.025 \text{ Pa m}^6 \text{ mol}^{-2}$, $b = 2.66 \cdot 10^{-5} \text{ m}^3 \text{ mol}^{-1}$.
- *Pressure work* is implemented into the model comparable to [10,13,31], due to significant pressure gradients in the beginning of the absorption experiments.
- The influence of *inflowing hydrogen* is neglected due to the modelled geometry.

2.2.1. Model equations

The complete set of model equations consists of the rate equations, the mass balance of the gas, and one single energy balance for gas and solid.

The rate equations can be written as

$$\frac{\partial x}{\partial t} = \dot{m}_R \quad (4)$$

and the according equations for \dot{m}_R (in s^{-1}) are determined in Ref. [25] for the Li–Mg–N–H material (compare Table 2). For the MeH material, 1st order rate equations from the literature have been adapted [33], and the resulting parameters are also summarized in Table 2.

In the mass balance of the hydrogen gas, Darcy flow is used for the description of the gas velocity $\nabla \vec{v}_g$ according to $\nabla P_g = -\mu_g/K \cdot \vec{v}_g$, where \vec{v}_g is the Darcy velocity that refers to the Seepage or actual velocity \vec{V}_g times the porosity: $\vec{v}_g = \varepsilon \cdot \vec{V}_g$. Furthermore, K refers to the permeability and μ_g to the dynamic viscosity that can be calculated as $\mu_g = c_1(T/293)^{c_2}$ [34]. Then, the mass balance for the gas phase, implementing the simplified van der Waals equation, can be written as

$$\varepsilon \frac{MRT_g}{\left(\Re T_g + \left(b - \frac{a}{\Re T_g}\right)P_g\right)^2} \frac{\partial P_g}{\partial t} - \varepsilon \frac{P_g M \left(\Re + \frac{aP_g}{\Re T_g^2}\right)}{\left(\Re T_g + \left(b - \frac{a}{\Re T_g}\right)P_g\right)^2} \frac{\partial T_g}{\partial t} - \nabla \left(\rho_g \frac{K}{\mu_g} \nabla P_g \right) = -(1 - \varepsilon) \dot{m}_R \omega t_{\text{max}} \rho_s \quad (5)$$

For the *energy balance of the system*, convective heat transfer of the gas phase, and heat transfer by thermal conduction in the gas and solid phase using the effective thermal conductivity $\lambda_{\text{eff}} = (1 - \varepsilon)\lambda_s + \varepsilon\lambda_g$ are considered. Additionally, a heat source due to the reaction as well as pressure work based on the general volumetric thermal expansion coefficient α_v^{real} for real gases according to

$$\alpha_v^{\text{real}} = \frac{1}{\rho_g} \frac{\partial \rho_g}{\partial T} \Big|_{P_g} = \frac{\Re + \frac{aP_g}{\Re T^2}}{\Re T + \left(b - \frac{a}{\Re T}\right)P_g} \quad (6)$$

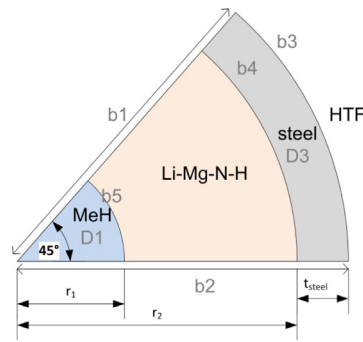
are implemented. Hence, assuming local thermal equilibrium (LTE $T = T_g = T_s$), and Darcy flow, the energy balance can be written as

$$\left[(1 - \varepsilon)c_{p,s}\rho_s + \varepsilon c_{p,g}\rho_g \right] \frac{\partial T}{\partial t} = c_{p,g}\rho_g \frac{K}{\mu_g} \nabla P_g \nabla T - \nabla \cdot (- (\lambda_{\text{eff}}) \nabla T) - (1 - \varepsilon) \dot{m}_R \rho_s \omega t_{\text{max}} \Delta_R H + \alpha_v T \cdot \left(\varepsilon \frac{\partial P_g}{\partial t} - \frac{K}{\mu_g} \nabla^2 P_g \right) \quad (7)$$

2.2.2. Geometry

The basic geometry used for the simulations in this paper is a segment of a circle (45°) that refers to a perpendicular cut of the reactor tube axis. Axial effects have been neglected as the radial temperature effects caused by the reaction of the two materials were in the focus of the present study.

The geometry used for the model validation as well as for the simulated scenarios is shown in Fig. 3. Three domains are modelled separately: the powder bed of the MeH (D1), the powder bed of the Li–Mg–N–H (D2) and the stainless steel wall (D3). For the stainless steel wall a simplified energy balance has been applied accounting just for heat conduction, and the influence of the GPLS on heat or mass transport has



rate equations	initial	D1,D2	$x = 0$	
	boundary	b4,b5 b1, b2	$-\bar{n} \left(\frac{x_i}{x_j} \right) = 0$	no flux, symmetry
MB gas	initial	D1,D2	$P = P_i$	
	boundary	D1,D2	\dot{m}_{in}	source term
		b1,b2,b4	$-\bar{n} \left(\frac{p}{p_{o,r}} \right) = 0$	no flux, symmetry
b5	$P_{g,MeH} = P_{g,Li-Mg-N-H}$	no mass transport limitation at GPSL		
EB	initial	D1,D2, D3	$T_{LiMgNH} = T_{Li-Mg-N-H} = T_{steel,i}$	
	boundary	b1,b2	$-\bar{n} \lambda_{eff} \left(\frac{T}{T_r} \right) = 0$	symmetry
		b3	$-\bar{n} \lambda_{eff} \left(\frac{T}{T_r} \right) = h_{HTF} (T_{HTF} - T_{steel})$	heat flux
	b4	$T_{steel} = T_{Li-Mg-N-H}$	no heat transfer limitation at GPSL and to steel wall	
	b5	$T_{Li-Mg-N-H} = T_{MeH}$		

Fig. 3 – Left: modelling geometry for combination reactor. Cut of tubular reactor and segment of circle with angle 45° including all domains and boundaries. Right: initial and boundary conditions.

been completely neglected. In all balances, b1 and b2 refer to symmetry boundary conditions. The mesh has been generated by the meshing function in COMSOL: 836 triangular elements have been used in the simulations for model validation. Further improvement in the mesh quality did not lead to an increase in quality, while the calculation time was approx. 40 s for 1800 s real time.

2.2.3. Initial and boundary conditions

The applied initial and boundary conditions for the model validation were derived from the experimental conditions that have been applied for the validation experiments and correspond to a later application in an automotive vehicle. The absorption scenario for the present simulation and the experiments are summarized in the following, and the corresponding initial and boundary conditions are shown in Fig. 3.

Before the absorption is initiated, both materials are fully desorbed and the temperature inside the reactor is 20 °C. When the fuelling process is initiated, the heat transfer fluid with a temperature of $T_{HTF,set}$, e.g., 130 °C is starting to circulate around the reactor filled with the two materials, hence the boundary condition is $T_{HTF} = T_{HTF,set}$ at $t = 1$ s. However, for the validation of the model, the experimentally applied flow rate \dot{m}_{in} of hydrogen in kg s^{-1} is implemented as a source term on the right hand side of the mass balance of the gas, Equation (5), in $\text{kg s}^{-1} \text{m}^{-3}$. As soon as the final pressure $P_{g,set}$ is reached, the flow rate is modified in order to model the pressure control mode of the reactor, hence a constant pressure $P_{g,set}$ is set. This switch in the boundary condition is implemented by a step-function (a smoothed if-condition) in the model equations. Applying these conditions, the reaction inside of the reactor is initiated and sufficient H_2 is supplied in order to control the pressure at P_{set} , while the temperature of the heat transfer fluid is kept at 130 °C.

3. Results and discussion

3.1. Simulations

In the first part of the result section, 2D simulations of the combination reactor are presented and discussed. These simulations can be used to show the operation principle in

more detail, especially the interaction of the MeH material with the Li–Mg–N–H material. For comparison, the initiation of the Li–Mg–N–H reaction is analysed in a reactor with pure Li–Mg–N–H as well as with the combination of both materials. For these simulations, the model described in Section 2.2 has been simplified with regards to gas pressure and a constant pressure of 70 bar has been assumed.

Fig. 4(a) shows the temperature distribution in the reactor tube at certain points in time for the pure Li–Mg–N–H material during the absorption scenario (see Section 2.2.3). In the first 550 s, the material is heated from the outside, where the temperature $T_{HTF} = 130$ °C is applied. During this period, heat is transferred from the wall to the core of the tube. Additionally the Li–Mg–N–H material slowly starts to absorb hydrogen by the exothermal reaction. At approx. 550 s, the temperature in the core of the reactor exceeds the temperature of the wall. This indicates that at this time, at the core of the tube, the heat developed by the reaction exceeds the heat that is removed by the heat transfer fluid. As a result, the temperature as well as the reaction rate continuously increase until at approx. 650 s the equilibrium temperature has been reached throughout the core of the tube. The development of the reaction of the Li–Mg–N–H reaction can also be observed in the transformed fraction plots in Fig. 4(b). While at 550 s the powder has barely absorbed, at 650 s an average transformed fraction of approx. 30% has been reached. At this point in time, the temperature in the bed is at equilibrium and the reaction is now dominated by heat transfer limitations: the material needs to be cooled to continue its absorption reaction which can be seen from both plots. In the temperature plots, the hottest region is in the core of the tube, while in the transformed fraction plot the reaction is not yet completed in the core. Finally, after about 900 s, the temperature in the tube has reached 130 °C. Summarizing, when a temperature of 130 °C is applied on the steel wall of a reactor with Geometry A, at a certain point the heat of reaction developing inside of the reactor exceeds the heat that is removed by the heat transfer fluid. Thus, the temperature is increasing and the reaction is accelerating. As soon as the reaction has reached equilibrium temperature, heat transfer limitations dominate the reaction and in this phase of the reaction, the temperature as well as the transformed fraction front move from the wall to the core of the tube. Therefore,

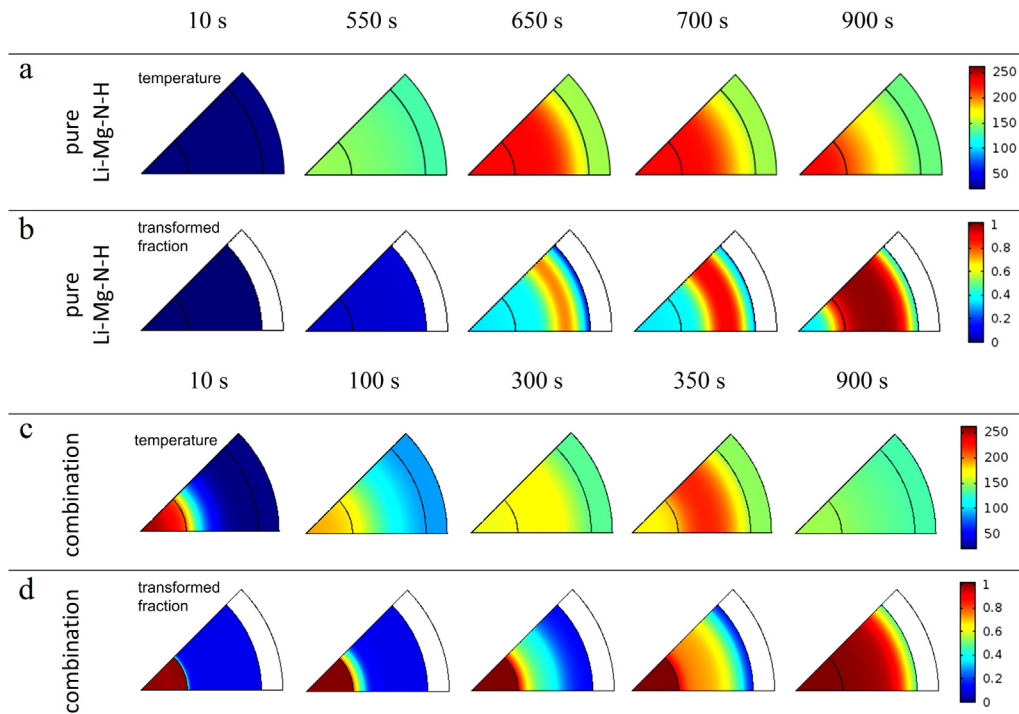


Fig. 4 – 2D simulation results of the modelled geometry at indicated points in time. Pure Li–Mg–N–H reactor: a) temperature T , b) transformed fraction x . Combination reactor: c) temperature T , d) transformed fraction x .

for a complete reaction, the innermost part of the tube needs to be cooled with a large thermal resistance through the powder bed at the end of reaction.

In Fig. 4(c) and (d), the behaviour in the reactor with the combination of materials and a volumetric ratio of $\epsilon_{\text{LiMgNH}} = 0.85$ is shown. In this case, already after 10 s, the MeH material reaches its equilibrium temperature of >200 °C and the heat is transferred to the Li–Mg–N–H material close to the MeH. In Fig. 4(d), it is also obvious that at this point in time, the MeH material has completely reacted. After 100 s, the reaction of the Li–Mg–N–H is initiated close to the GPSL and the reaction front moves from the core to the annulus (see 100 and 300 s). Similarly, the heat developed by the reaction at the core of the tube is transferred to the outer regions, where it initiates the reaction of the surrounding Li–Mg–N–H material. Finally, the heat transfer fluid can remove the excess heat of reaction close to the steel wall. After 900 s, the reaction is completed. Concluding, it can be stated that in this case, the reaction is internally initiated by the reaction of MeH that is simultaneously absorbing hydrogen. Furthermore, the developed heat of reaction is heating up the annulus filled with Li–Mg–N–H material, and the heat released by the last reacting fraction is released close to the heat transfer fluid. This implies that the temperature as well as reaction front move from the centre to the wall of the reactor tube facilitating the thermal management of such a reactor.

The presented 2D simulations show a significant difference between the absorption behaviour of a pure Li–Mg–N–H reactor and a combination reactor. In the 1st case, the dominating heat transfer processes take place at the surface of the heat transfer fluid (first heating than cooling). This implies that

for an improved performance the tube diameter should be reduced in order to increase the cooling/heating influence of the heat transfer fluid. However, considering the overall storage tank design this will lead to an increase in steel mass and consequently to a reduction in gravimetric storage density. In the beginning of the absorption in the combination reactor, on the other hand, the heat is released directly at the core where it is required. Then, it is transferred in radial direction and can be removed at the end of the reaction at the outer perimeter. Thus, the thermal performance of such a combination reactor allows even larger diameters and consequently less steel.

Concluding this section on simulations, it has to be mentioned that the evolution of this reaction front can vary significantly for materials with different properties. For example, an enhanced heat conductivity will increase heat transport from the core to the annulus. Thus, in case the reaction rate is not sufficiently high, the Li–Mg–N–H reaction will not be initiated due to too low temperatures. The diameter of the GPSL (D_{GPSL}) also influences the absorption performance. When D_{GPSL} is very small, the heat of reaction of the MeH is not sufficient to initiate the reaction. Thus, the temperature at the core increases and cools down again, and the reaction of the Li–Mg–N–H material is only initiated when sufficient heat is provided from the outside heat transfer fluid. In contrast, when D_{GPSL} is too large, the temperature at the core is too high and the reaction is limited by the thermodynamic equilibrium. Besides these two examples, also heat capacity, hydride density and heat of reaction can have a strong influence on the evolution of the reaction front. Thus, for a suitable reactor design, simulations based on validated models are essential.

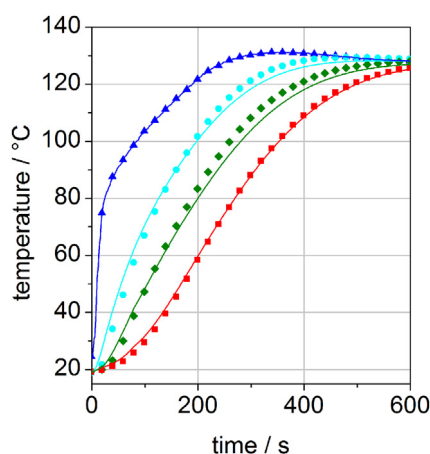


Fig. 5 – Experimental (symbols) and simulated (lines) temperature profiles with T_{HTF} (blue, \blacktriangle), T_{steel} (turquoise, \bullet), T_3 (green, \blacklozenge), T_1 (red, \blacksquare) during the heating-up procedure, (compare Fig. 2). (For interpretation of the references to colour in this figure legend, the reader is referred to the web version of this article.)

3.2. Model validation

In the second part of the results section, the presented model equations and properties of the materials are validated. Therefore, several experiments have been performed in the reactor with pure Li–Mg–N–H and in a reactor with the same dimensions, but including MeH material at the core. As mentioned in Section 2.2.3, during the scenario used for model validation of the absorption process, several processes occur simultaneously in the first 100–300 s. First, the external conditions are applied, hence the pressure is increased from vacuum to 70 bar in 90 s and the temperature of the heat transfer fluid is increased in the first 600 s from 20 to 130 °C. Additionally, the absorption reaction of both materials is initiated leading to a steep temperature increase in the first 10–90 s from 20 °C to 240 °C as well as to a gas absorption of approx. 1 g of H_2 . As all these processes superpose each other, a model validation is quite difficult and in order to achieve the best results the final scenario has been divided into different steps that have been validated individually.

3.2.1. Heating up and pressurizing procedure for pure inactive Li–Mg–N–H

In a first step, the reactor tube is completely filled with Li–Mg–N–H material. Then, a temperature increase in the heat transfer fluid is applied. From this experiment, the temperature difference between T_{oil} and T_{steel} has been used to determine the limiting outer heat transfer coefficient h_{HTF} to $220 \text{ W m}^{-1} \text{ K}^{-1}$. All remaining parameters have been taken from the literature. Then, in an extension to the previous experiment, not only the temperature is increased in the heat transfer fluid, but also the pressure is increased from 0 to 70 bar in 90 s. Fig. 5 shows the experimental (symbols) and simulated (lines) data for such a heating and pressurizing experiment, where the temperature of the outer heat transfer fluid (blue line, \blacktriangle) is implemented into the simulation. From

this plot it can be seen that the temperature at T_1 (centre of reaction bed) increases right from the first seconds of the experiment. This temperature increase can only be due to the influence of the steep pressure increase in the first 90 s of the experiment. The comparison with the experimental data shows that the model is able to capture the temperature behaviour already from the first seconds.

As the agreement between the experimental and simulated data of all three thermocouples in these plots is very good, the values for porosity, density, heat capacity and thermal conductivity of the pure Li–Mg–N–H material are confirmed. Furthermore, the agreement between simulation and experiment for an experiment with a pure heating up procedure in the combination reactor with both materials is also very good (not presented). Thus, the properties for the pure Li–Mg–N–H as well as for the complete reactor system including the MeH material are validated.

3.2.2. Pure Li–Mg–N–H absorption reaction

In a next experiment, the same scenario as before is applied but the Li–Mg–N–H material is in the desorbed state. Fig. 6 shows the experimental and simulated data for this case. In the beginning, the temperature inside of the reactor increases due to the temperature increase of the heat transfer fluid. At about 100 °C, the reaction of the Li–Mg–N–H material is initiated and quickly reaches equilibrium temperature. Then the reaction continues and finally the temperatures inside the tube cool down to the heat transfer fluid temperature. The comparison between simulation and experiment shows that there is a deviation between the data in the cooling process towards the end of the experiment. As the heating up procedure has been well captured, deviations in the thermal conductivity and the heat transfer resistance are not likely to cause this deviation. Furthermore, the temperature close to the wall is captured well, while the temperature at the centre shows the largest deviation, thus thermal losses are also not very likely. A possible explanation for this deviation is the accuracy of the thermodynamic data. As this data influences

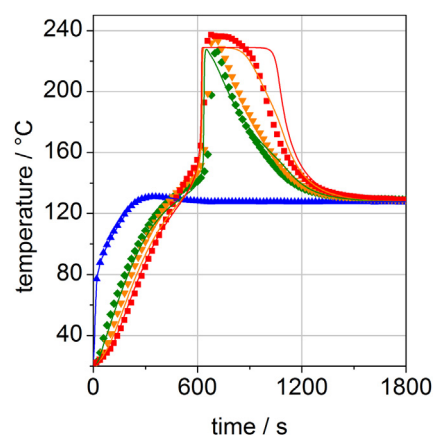


Fig. 6 – Experiment with pure Li–Mg–N–H reactor. Experimental (symbols) and simulated (lines) temperature profiles with T_{HTF} (blue, \blacktriangle), T_3 (green, \blacklozenge), T_2 (orange, \blacktriangledown), T_1 (red, \blacksquare), (compare Fig. 2). (For interpretation of the references to colour in this figure legend, the reader is referred to the web version of this article.)

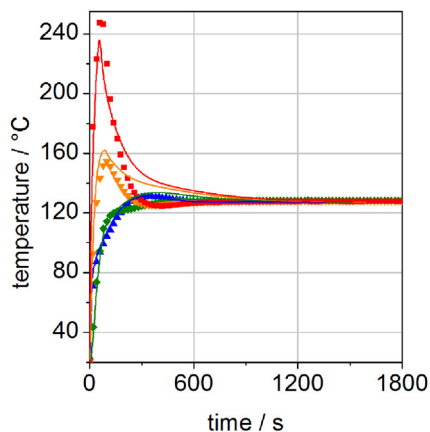


Fig. 7 – Experimental (symbols) and simulated (lines) temperature profiles with T_{HTF} (blue, \blacktriangle), T_3 (green, \blacklozenge), T_2 (orange, \blacktriangledown), T_1 (red, \blacksquare) in the reactor with the combination of materials, (compare Fig. 2). Experiment with inactive Li–Mg–N–H. (For interpretation of the references to colour in this figure legend, the reader is referred to the web version of this article.)

the equilibrium temperature as well as the enthalpy of reaction, small errors can cause the deviation in the temperature profile. However, focusing on the initial part of the experiment that is also most important during the following combination reactor experiments, the simulation results can be considered sufficiently accurate for this purpose.

3.2.3. Combination reactor

In a next step, the pure Li–Mg–N–H material has been removed from the reactor and the GPSL with a diameter of 13.5 mm separating the MeH material (inside) and the Li–Mg–N–H material (outside), has been integrated into the tube. When the two activated materials have been filled into the reactor, the following two limiting cases have been studied.

I) Combination reactor: Li–Mg–N–H inactive

In the first case, both materials have been fully absorbed and then cooled down to room temperature, where only the MeH material has been desorbed. This partial desorption of the reactor is possible, due to the kinetic limitations of the desorption reaction for the Li–Mg–N–H material at the applied conditions. Then, the absorption reaction is initiated by pressure and temperature increases and the MeH reaction at the core starts immediately. As the Li–Mg–N–H material is still fully absorbed no further reaction occurs and the temperatures decrease to the temperature of the heat transfer fluid. Fig. 7 shows the comparison of the experimental and simulated temperature behaviour in this case. The peak temperature in the simulation is slightly underestimated and during the cool-down at about 300 s the temperature decrease is faster in the experiment compared to the simulated results, which is analogue to the pure Li–Mg–N–H experiment. However, it can be stated that the experimental and simulated data are in good agreement.

II) Combination reactor: MeH inactive

In the next case, the MeH material is in the completely absorbed state before the reaction is initiated, thus only the Li–Mg–N–H is in the desorbed state. As soon as the temperature and pressure increase are applied, the temperatures in the reactor increase, and the temperature increase at the centre (red, \blacksquare) only due to the absorption of a small remaining fraction of MeH. When a temperature of 100 °C is reached, in this case, the reaction rate of the Li–Mg–N–H is insufficient to reach equilibrium temperature as the inner annulus filled with MeH acts as additional mass removing a large fraction of the heat of reaction. Therefore, the temperature just slightly exceeds the heat transfer fluid temperature and the reaction proceeds very slowly. As can be seen from Fig. 8, this case is also well captured by the model.

Therefore, besides the values for density, porosity, heat capacity and thermal conductivity, further properties of both materials like reaction enthalpy, storage capacity and kinetic parameters are confirmed.

III) Combination reactor: both materials active

Finally, the experiment for model and concept validation is shown in Fig. 9. In this case, the complete experiment is performed and both materials are fully desorbed in the beginning. As predicted by the simulation, the temperature at the centre increases very fast due to the absorption reaction of the MeH material at the core of the tube. Then, after about 100 s, the reaction of the Li–Mg–N–H material is initiated and already after about 600 s the reaction is completed. Similarly to the experimental cases before, the peak temperature is slightly underestimated and the cooling process in the experiment is faster than in the simulation. However, the accordance between simulated and experimental data is good, especially considering the difficult experimental

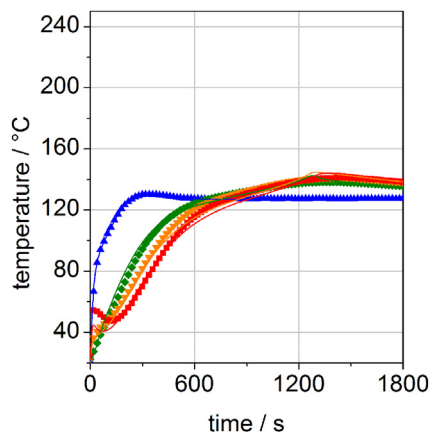


Fig. 8 – Experimental (symbols) and simulated (lines) temperature profiles with T_{HTF} (blue, \blacktriangle), T_3 (green, \blacklozenge), T_2 (orange, \blacktriangledown), T_1 (red, \blacksquare) in the reactor with the combination of materials, (compare Fig. 2). Experiment with inactive MeH. (For interpretation of the references to colour in this figure legend, the reader is referred to the web version of this article.)

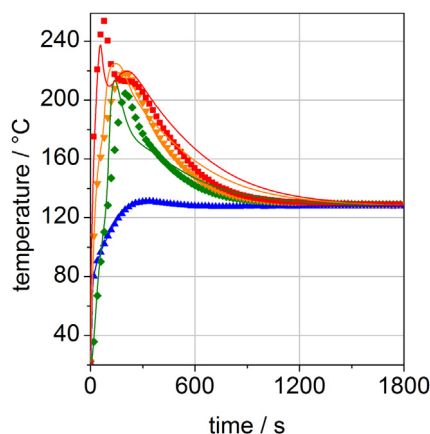


Fig. 9 – a) Experimental (symbols) and simulated (lines) temperature profiles with T_{HTF} (blue, \blacktriangle), T_3 (green, \blacklozenge), T_2 (orange, \blacktriangledown), T_1 (red, \blacksquare) for an absorption experiment in the combination reactor, (compare Fig. 2). (For interpretation of the references to colour in this figure legend, the reader is referred to the web version of this article.)

conditions: large temperature and pressure gradients are not just applied from outside, but also developing inside of the reactor.

So far, the experimental temperature profiles have been shown together with the simulated data for the different cases. In addition, Fig. 10 shows the simulated and experimental data for the mass of absorbed H_2 for all four cases. These masses have been calculated from the integral value of the cross-section geometry in COMSOL multiplied by a height with respect to the actual mass filled into the reactor H_{COMSOL} (compare Fig. 3). As seen from Fig. 10, this information is correctly predicted by the developed model. While the absorption reaction of the pure Li–Mg–N–H reactor starts at about 600 s and is completed after 800 s, the reaction in the combination reactor is already completed after 300 s (compact symbols). In addition to these two main experiments, Fig. 10 shows the two partial experiments in the combination reactor (open symbols). The pure MeH reaction is completed already after approx. 100 s, while the pure Li–Mg–N–H reacts just very slowly. From the comparison between simulation and experiment it is clear that not just the temperature profiles but also the masses of H_2 absorbed are well captured by the simulations.

3.2.4. Summary of model validation

One important result from the previously shown model validation steps is that the simulation and experimental data agree very well. This means that the basic equations used as well as the values for the properties are sufficiently accurate and the model can be used for future reactor design simulations. Furthermore, it can be emphasized that also the reactor concept in general has been proven to positively change the absorption performance of a pure Li–Mg–N–H reactor. In the tube filled with pure Li–Mg–N–H material it takes about 600 s to heat the material up and initiate the absorption reaction. In contrast, in the combination reactor with the same diameter the reaction is already initiated after 50 s. Thus, the concept

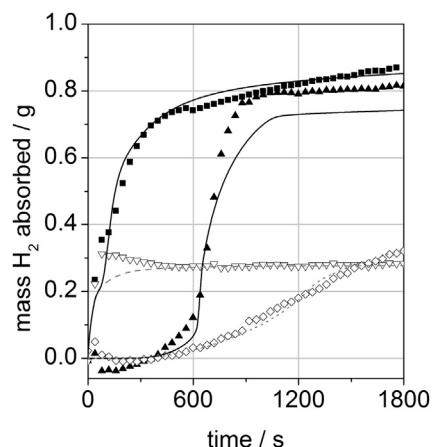


Fig. 10 – Experimental (symbols) and simulated (lines) mass H_2 absorbed lines vs. time. \blacksquare : combination reactor, \blacktriangle : pure Li–Mg–N–H reactor, \diamond : inactive MeH in combination reactor, \triangledown : inactive Li–Mg–N–H in combination reactor.

actually enables the application of such a complex hydride material, e.g., for future automotive applications using HT-PEM fuel cells.

3.3. Discussion of the combination reactor concept

Concluding this results section, the presented reactor concept will be discussed with respect to gravimetric and volumetric storage densities. However, the characteristics of the concept for the combination reactor design are summarized first:

- An indirect combination of both materials can reduce the required amount of MeH compared to a direct mixture.
- The additional MeH material is able to initiate a reaction of the Li–Mg–N–H material in few seconds by heating up the powder bed to the required temperature.
- While the MeH is initiating the reaction, it is already absorbing “reusable” hydrogen.
- The internal heat management of a reactor with two materials differs from a pure Li–Mg–N–H reactor: in the combination reactor heat is developed where it is needed and excess heat appears at the surface close to the heat transfer fluid.
- In the combination reactor large tube diameters can be realized without deterioration of the absorption performance. Therefore, the length of a reactors can be significantly reduced, while storing the same amount of hydrogen. This is leading to an improved system storage density as the amount of steel wall can be reduced.

These characteristics show a positive effect on the overall absorption behaviour of a storage reactor. However, besides the absorption performance of a storage reactor, the gravimetric and volumetric densities are very important properties with respect to an automotive application.

For the reference materials used in this manuscript, the storage capacity of the MeH material is lower than the storage

capacity of the Li–Mg–N–H material. Consequently, the addition of the MeH in the combination reactor will lead to a decrease in overall gravimetric storage density. In the present case, the storage capacity of the pure Li–Mg–N–H of 3.2 wt.% has been reduced by the MeH to an overall storage capacity of 2.0 wt.% (based on the total mass of both materials in the absorbed state). Looking at the volumetric hydrogen storage density, in the present reactor, the addition of MeH has improved the overall capacity of the Li–Mg–N–H material. This is due to the relatively low powder density of the Li–Mg–N–H material with just 450 kg m^{-3} compared to 4100 kg m^{-3} for the MeH. Therefore, in the present case 0.99 g of hydrogen can be stored when both materials are implemented in the reactor, while 0.81 g of hydrogen can be stored when the reactor is filled with the pure Li–Mg–N–H material.

However, the Li–Mg–N–H material can only be considered as reference material for future CxH materials, and it has been used for the present proof of concept due to availability. Thus, if this storage concept will be used for other complex hydride materials that actually show high storage capacities of up to 10 wt.% and powder material densities of over 1200 kg m^{-3} , the addition of MeH will always lead to a slight decrease in gravimetric as well as volumetric density on the material level. This decrease depends on the amount of MeH required for the given geometry as well as on the different material parameters, and can only be determined by detailed simulations. Considering the reactor on a system level, it is not clear how the MeH material affects the gravimetric density, as due to the larger diameters that are possible with the combination reactor concept, the steel mass for the system can also be reduced. However, a tank based on pure complex hydride material cannot simply be used in automotive applications at all, as the slow absorption performance at low temperatures due to the conversion reaction will not satisfy the requirements. Therefore, such a tank would require, e.g., the integration of an additional heater leading to an undesired increase in system complexity. Thus, even a slight decrease in storage capacity for the combination reactor might be acceptable with regard to the possible improvements in reactor dynamics and absorption as well as desorption performance.

4. Conclusion

In this paper a reactor concept with a combination of a complex hydride and a metal hydride has been presented. This new concept combines the advantages of both materials: the high storage capacities of complex hydride materials with the high reaction rates of metal hydride materials.

This concept has been studied using two reference materials: for the complex hydride, $2\text{LiNH}_2\text{--}1.1\text{MgH}_2\text{--}0.1\text{LiBH}_4\text{--}3 \text{ wt.}\% \text{ZrCoH}_3$ (Li–Mg–N–H) has been selected and for the metal hydride $\text{LaNi}_{4.3}\text{Al}_{0.4}\text{Mn}_{0.3}$ (MeH). The basic geometry for the simulations and experiments has been a tubular reactor, wherein the MeH material is placed at the core and the Li–Mg–N–H material in the annulus, separated by a thin gas permeable separation layer.

First, preliminary simulations of this setup showed a temperature front moving from the centre to the annulus and

initiating the reaction of the Li–Mg–N–H material. Then, a similar scenario has been studied by experiments in 50 g lab-scale. The results clearly showed that the reaction of the MeH material is initiating the reaction of the Li–Mg–N–H material and is thereby reducing the absorption time by 500 s. In several steps, the multiple modelled processes that take place simultaneously in the reactor have been validated and the final model can be used for future reactor design simulations.

Concluding, it can be stated that with this reactor concept, the feasibility of a CxH based hydrogen storage reactor has been significantly improved: The absorption reaction of the Li–Mg–N–H material has been initiated starting from room temperature although the reaction rate of the pure material is low at temperatures below $100 \text{ }^\circ\text{C}$ and pressures below 70 bar.

Acknowledgements

The research leading to these results has received funding from the European Union's Seventh Framework Programme (FP7/2007-2013) for the Fuel Cells and Hydrogen Joint Technology Initiative under grant agreement no. 256653.

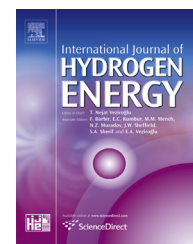
REFERENCES

- [1] Fichtner M. Conversion materials for hydrogen storage and electrochemical applications—Concepts and similarities. *J Alloys Compd* 2011;509:S529–34.
- [2] Huot J. Metal hydrides. In: Hirscher M, editor. *Handbook of hydrogen storage*. Weinheim: Wiley-VCH; 2010.
- [3] Schlapbach L, editor. *Hydrogen in intermetallic compounds I*. Berlin, Germany: Springer; 1988.
- [4] Züttel A, Wenger P, Rentsch S, Sudan P, Mauron P, Emmenegger C. LiBH_4 a new hydrogen storage material. *J Power Sources* 2003;118(1–2):1–7.
- [5] Yang J, Hirano S. Improving the hydrogen reaction kinetics of complex hydrides. *Adv Mater* 2009;21(29):3023–8.
- [6] Bogdanović B, Schwickardi M. Ti-doped alkali metal aluminium hydrides as potential novel reversible hydrogen storage materials. *J Alloys Compd* 1997;253–254:1–9.
- [7] Klebanoff LE, Keller JO. 5 Years of hydrogen storage research in the U.S. DOE Metal Hydride Center of Excellence (MHCoe). *Int J Hydrogen Energy* 2013;38(11):4533–76.
- [8] Mosher DA, Arsenault S, Tang X, Anton DLL. Design, fabrication and testing of NaAlH_4 based hydrogen storage systems. *J Alloys Compd* 2007;446–447:707–12.
- [9] Urbanczyk R, Peil S, Bathen D, Heßke C, Burfeind J, Hauschild K, et al. HT-PEM fuel cell system with integrated complex metal hydride storage tank. *Fuel Cells* 2011;11(6):911–20.
- [10] Bhourri M, Goyette J, Hardy BJ, Anton DL. Numerical modeling and performance evaluation of multi-tubular sodium alanate hydride finned reactor. *Int J Hydrogen Energy* 2012;37(2):1551–67.
- [11] Bhourri M, Goyette J, Hardy BJ, Anton DL. Honeycomb metallic structure for improving heat exchange in hydrogen storage system. *Int J Hydrogen Energy* 2011;36(11):6723–38.
- [12] Garrier S, Chaise A, de Rango P, Marty P, Delhomme B, Fruchart D, et al. MgH_2 intermediate scale tank tests under various experimental conditions. *Int J Hydrogen Energy* 2011;36(16):9719–26.

- [13] Garrison SL, Hardy BJ, Gorbounov MB, Tamburello DA, Corgnale C, VanHassel BA, et al. Optimization of internal heat exchangers for hydrogen storage tanks utilizing metal hydrides. *Int J Hydrogen Energy* 2012;37(3):2850–61.
- [14] Na Ranong C, Höhne M, Franzen J, Hapke J, Fieg G, Dornheim M, et al. Concept, design and manufacture of a prototype hydrogen storage tank based on sodium alanate. *Chem Eng Technol* 2009;32(8):1154–63.
- [15] Utz I, Schmidt N, Wörner A, Hu JJ, Zabara O, Fichtner M. Experimental results of an air-cooled lab-scale H₂ storage tank based on sodium alanate. *Int J Hydrogen Energy* 2011;36(5):3556–65.
- [16] Kapischke J. *Entwicklung und Untersuchung einer Startvorrichtung zur Aktivierung eines Hochtemperaturhydridreaktors*. Düsseldorf: VDI Verlag; 1996, ISBN 3-18-335106-4; 1996.
- [17] Utz I, Linder M, Schmidt N, Hu JJ, Fichtner M, Wörner A. Experimental study of powder bed behavior of sodium alanate in a lab-scale H₂ storage tank with flow-through mode. *Int J Hydrogen Energy* 2012;37(9):7645–53.
- [18] Johnson TA, Kanouff MP, Dedrick DE, Evans GH, Jorgensen SW. Model-based design of an automotive-scale, metal hydride hydrogen storage system. *Int J Hydrogen Energy* 2012;37(3):2835–49.
- [19] Bellosta von Colbe JM, Metz O, Lozano GA, Pranzas PK, Schmitz HW, Beckmann F, et al. Behavior of scaled-up sodium alanate hydrogen storage tanks during sorption. *Int J Hydrogen Energy* 2012;37(3):2807–11.
- [20] Lozano GA, Ranong CN, Bellosta von Colbe JM, Bormann R, Fieg G, Hapke J, et al. Empirical kinetic model of sodium alanate reacting system (I). Hydrogen absorption. *Int J Hydrogen Energy* 2010;35(13):6763–72.
- [21] Corgnale C, Hardy BJ, Tamburello DA, Garrison SL, Anton DL. Acceptability envelope for metal hydride-based hydrogen storage systems. *Int J Hydrogen Energy* 2012;37(3):2812–24.
- [22] Zhang X, Li Z, Lv F, Li H, Mi J, Wang S, et al. Improved hydrogen storage performance of the LiNH₂ MgH₂ LiBH₄ system by addition of ZrCo hydride. *Int J Hydrogen Energy* 2010;35(15):7809–14.
- [23] Ulmer U, Hu J, Franzreb M, Fichtner M. Preparation, scale-up and testing of nanoscale, doped amide systems for hydrogen storage. *Int J Hydrogen Energy* 2012;38(3):1439–49.
- [24] Weidner E, Dolci F, Hu J, Lohstroh W, Hansen T, Bull DJ, et al. Hydrogenation reaction pathway in Li₂Mg(NH)₂. *J Phys Chem C* 2009;113(35):15772–7.
- [25] Bürger I, Hu J, Vitillo JG, Kalantzopoulos GN, Deledda S, Fichtner M, et al. Material properties and empirical rate equations for hydrogen sorption reactions in 2 LiNH₂–1.1 MgH₂–0.1 LiBH₄–3 wt.% ZrCoH₃. *Int J Hydrogen Energy*; 2014. in press.
- [26] Dantzer P, Orgaz E. Thermodynamics of hydride chemical heat pump—II. How to select a pair of alloys. *Int J Hydrogen Energy* 1986;11(12):797–806.
- [27] Dornheim M. Tailoring reaction enthalpies of hydrides. In: Hirscher M, editor. *Handbook of hydrogen storage*. Weinheim: Wiley-VCH; 2010.
- [28] Willers E, Wanner M, Groll M. A multi-hydride thermal wave device for simultaneous heating and cooling. *J Alloys Compd* 1999;293–295:915–8.
- [29] Bürger I, Luetto C, Linder M. Advanced reactor concept for complex hydrides: hydrogen desorption at fuel cell relevant boundary conditions. *Int J Hydrogen Energy*; 2014. in press.
- [30] Chen P, Xiong Z, Luo J, Lin J, Tan KL. Interaction of hydrogen with metal nitrides and imides. *Nature* 2002;420(6913):302–4.
- [31] Hardy BJ, Anton DL. Hierarchical methodology for modeling hydrogen storage systems. Part II: detailed models. *Int J Hydrogen Energy* 2009;34(7):2992–3004.
- [32] Mohan G, Prakash Maiya M, Srinivasa Murthy S. Performance simulation of metal hydride hydrogen storage device with embedded filters and heat exchanger tubes. *Int J Hydrogen Energy* 2007;32(18):4978–87.
- [33] Jemni A, Nasrallah SB. Study of two-dimensional heat and mass transfer during absorption in a metal-hydrogen reactor. *Int J Hydrogen Energy* 1995;20(1):43–52.
- [34] White FM. *Fluid mechanics*. 4th ed. McGraw-Hill; 1999.
- [35] Eberle U, Felderhoff M, Schüth F. Chemical and physical solutions for hydrogen storage. *Angew Chem Int Ed* 2009;48(36):6608–30.
- [36] *Thermophysical properties of fluid systems*. In: Lemmon EW, McLinden MO, Friend DG, editors. *Nist chemistry webbook, nist standard reference database number 69*. Gaithersburg MD: National Institute of Standards and Technology; 2008.
- [37] Willers E. *Multi-Hydrid-Sorptionsanlage zur kombinierten Heizung und Kühlung*. University of Stuttgart; 2002. <http://elib.uni-stuttgart.de/opus/volltexte/2002/1073/>.
- [38] Nakagawa T, Inomata A, Aoki H, Miura T. Numerical analysis of heat and mass transfer characteristics in the metal hydride bed. *Int J Hydrogen Energy* 2000;25(4):339–50.
- [39] Wang J, Keller J, Gross KJ. DOE metal hydride center of excellence. *Annual Progress Report VI Storage*; 2005. pp. 487–527.
- [40] Xu F, Sun LX, Chen P, Qi YN, Zhang J, Zhao JN, et al. Studies on heat capacities and thermal analysis of Li–Mg–N–H hydrogen storage system. *J Therm Anal* 2009;100(2):701–6.

Available online at www.sciencedirect.com

ScienceDirect

journal homepage: www.elsevier.com/locate/ije

Advanced reactor concept for complex hydrides: Hydrogen desorption at fuel cell relevant boundary conditions

I. Bürger^{a,*}, C. Luetto^b, M. Linder^a^aInstitute of Technical Thermodynamics, German Aerospace Center (DLR), D-70569 Stuttgart, Germany^bTECNODELTA S.r.l. IT, Via Francesco Parigi 5/h, 10034 Chivasso, TO, Italy

ARTICLE INFO

Article history:

Received 18 December 2013

Received in revised form

7 February 2014

Accepted 12 February 2014

Available online 3 April 2014

Keywords:

Reactor concept

LaNi₅

Li–Mg–N–H

Hydrogen storage

Modelling

Combination of materials

Desorption

ABSTRACT

Hydrogen storage in complex hydrides can be a storage option in automotive applications due to the high theoretical hydrogen storage capacities. As hydrogen is bonded by a chemical reaction to the solid state storage material, it is just released when heat is provided. In an automotive application for complex hydrides, this heat source can possibly be provided by the waste heat of a high temperature PEM fuel cell. However, for the application of existing complex hydride materials the temperature level of the fuel cell at 180 °C is still quite low leading to low desorption rates. A new reactor concept based on the addition of a metal hydride (MeH) to a complex hydride (CxH) reactor, separated by a gas permeable separation layer, can improve the desorption performance. In this paper, the effects of this reactor concept on desorption performance are studied using the two reference materials 2LiNH₂–1.1MgH₂–0.1LiBH₄–3 wt.%ZrCoH₃ and LaNi_{4.3}Al_{0.4}Mn_{0.3}. First, a model is developed and 2D simulations are performed using a driving scenario. Then, the model is validated by experimental data that has been obtained using a ~600 g lab scale reactor. Concluding, there exist two main advantages of the combination reactor concept: The desorption time at a pressure above the fuel cell supply pressure is extended by a factor of 1.2, and 94 instead of 84% of the max. mass of hydrogen stored in the material can be desorbed at technically relevant boundary conditions.

Copyright © 2014, Hydrogen Energy Publications, LLC. Published by Elsevier Ltd. All rights reserved.

1. Introduction

State of the art fuel cell driven cars are equipped with high pressure hydrogen storage tanks. However, the accident risk potential of these tanks is still discussed encouraging the research for alternative and more safe hydrogen storage solutions [1]. Besides liquid hydrogen storage and cryo-adsorption, hydrogen storage in solid state hydride materials

can be an option [2]. In these materials, the following chemical reaction takes place between gaseous hydrogen and a solid metal (M) compound:



Due to this reversible chemical reaction, the amount of free hydrogen in a solid state storage tank is small, and the stored hydrogen is just released when heat ($\Delta_R H$) is provided. In future

* Corresponding author. Tel.: +49 711 6862492.

E-mail address: inga.buerger@dlr.de (I. Bürger).
<http://dx.doi.org/10.1016/j.ijhydene.2014.02.069>

0360-3199/Copyright © 2014, Hydrogen Energy Publications, LLC. Published by Elsevier Ltd. All rights reserved.

automotive applications a possible heat source for the release of hydrogen is the waste heat of a fuel cell. For instance, for complex hydride materials this can be a high temperature polymer electrolyte membrane (HT-PEM) in order to supply heat at the required temperature level. Several simulated studies already showed that the amount of heat released by the fuel cell is sufficient to desorb the required amount of hydrogen. However, experimental studies indicated that heat losses can pose problems [3–5]. As the fuel cell defines the constraints of such a coupling, a suitable storage material has to desorb sufficient hydrogen at pressures above ambient and temperatures below 180 °C. These conditions are quite challenging for the existing complex hydride materials, especially as the reaction rates are very low at pressures above ambient. If these materials are then integrated into a reactor, the overall performance mainly depends on the intrinsic reaction rates and in contrast to heat transfer limited metal hydride storage designs, the addition of fins, foams, heating coils, etc. is not able to solve this fundamental problem for the complex hydride materials.

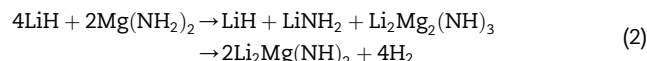
However, the reactor concept that is presented in this paper and that is based on the addition of a metal hydride to a complex hydride reactor separated by a gas permeable layer, can improve the overall desorption performance of the tank. The basic assumption of this concept is that on the one hand complex hydrides in general show high storage capacities, but rather low desorption reaction rates due to the conversion type of the absorption/desorption reaction [1]. Metal hydrides, on the other hand, have rather low hydrogen storage capacities (~1 wt.%), however, their reaction rates are very high even at room temperature or at pressures close to equilibrium. Thus, in a combination reactor, both advantages are combined: high storage capacities of the CxH material and high reaction rates of the MeH material. This concept has been developed in the framework of activities focussing on the design and construction of a prototype reactor that can be coupled to an HT-PEM fuel cell at technically relevant conditions, i.e. allowing for 2 h operation of 1 kW_{el}. For the absorption process of this prototype reactor, positive effects for the charging from room temperature are presented in [6].

In the present paper, this concept is for the first time studied for the desorption process. The focus is on the reactor pressure during desorption and on the improved desorption performance of the complex hydride when a metal hydride is present in the same storage tank.

1.1. Selection of reference materials

In analogy to the study on the absorption [6], 2LiNH₂–1.1MgH₂–0.1LiBH₄–3wt.% ZrCoH₃ has been used as CxH material in the present study on desorption. In this paper, this material will be abbreviated as Li–Mg–N–H material. The material has been synthesized by KIT¹ from lithium amide and magnesium hydride and it is able to absorb ~3.2 wt.% of hydrogen within 1 h at temperatures below 200 °C and desorb at pressures above 1 bar. Thus, it is possible to desorb hydrogen from this material below the fuel cell operating temperature of 180 °C and at a pressure above ambient (here

1.7 bar). The desorption equation for the main Li–Mg-system of this material can be written according to [7] as



Details on the determination of required material properties as well as on the required 1st metathesis reaction are summarized in [8].

As reference MeH material, LaNi_{4.3}Al_{0.4}Mn_{0.3} has been used as the equilibrium pressure of this material at room temperature is below the equilibrium pressure of the Li–Mg–N–H material. The material has been commercially available from Konik Industries Corporation. For the relevant properties, values from LaNi₅ have been adapted and they are summarized in Table 1.

1.2. Concept

In this section, the basic working principle of this reactor concept is explained by thermodynamic and kinetic information of the two materials that are plotted in Fig. 1. In this figure, the equilibrium line of the MeH (dark orange) and the reference complex hydride material, the Li–Mg–N–H (light blue) material, are given. Furthermore, the temperature and pressure regimes that are required for a technically feasible reaction rate of both materials are shaded in the respective colours.

The desorption procedure in a reactor with pure Li–Mg–N–H proceeds as follows: In the beginning, due to the previous charging, the pressure in the reactor is higher than the equilibrium pressure of the material, see (1) in Fig. 1. Then hydrogen is removed from the system and delivered by a constant mass flow rate to, e.g., a fuel cell. As soon as the pressure drops below the equilibrium pressure, the desorption reaction starts and the decrease in pressure is decelerated (2). However, as the reaction rate of the Li–Mg–N–H material even at 160 °C is rather low, the material cannot be discharged completely before the system pressure drops below 1.7 bar – which is the minimum supply pressure for the used FC.

The addition of some MeH material can improve this performance. As the rate of desorption for the MeH material is high at temperatures of 160 °C, the pressure in the system will not significantly drop below the equilibrium pressure of the MeH material before this is completely discharged. Thus, the system is kept at a pressure between the supply and the Li–Mg–N–H equilibrium pressure for a longer time, and the Li–Mg–N–H material can continue to desorb hydrogen at a low reaction rate. In this case, the required hydrogen mass flow can be supplied by both, the complex as well as the metal hydride. Since the equilibrium pressure of the complex hydride is higher, this material desorbs always at full rate. In contrast, the metal hydride only releases sufficient H₂ to compensate if the technically required flow rate exceeds the desorption capabilities of the Li–Mg–N–H material. Furthermore, in case the power of the fuel cell is significantly reduced, it is possible that the pressure in the system increases due to desorption of the Li–Mg–N–H material and the MeH material can even be recharged during these points in a driving cycle, see (3) in Fig. 1.

In analogy to the absorption study [6], there exist two options to combine the two materials in one storage reactor. The first is a

¹ KIT: Karlsruhe Institute of Technology, Institute of Nanotechnology.

Table 1 – Relevant material properties used for the simulation.

		Value	Units	Reference
General				
Temperature	T		K	
Pressure	P_g		Pa	
Universal gas constant	\mathfrak{R}	8.314	$\text{J kg}^{-1} \text{K}$	
Mass change H_2 due to reaction	\dot{m}_R		$\text{kg m}^{-3} \text{s}^{-1}$	
Porosity	ε	0.55		
Gas density	ρ_g	Simplified van der waals		
Heat capacity of gas	$c_{p,g}$	14,304	$\text{J kg}^{-1} \text{K}^{-1}$	[17] at 24.5 °C and 1 bar
Dynamic viscosity of gas	μ_g	$10^{-5} \cdot 9.05(T/293)^{0.68}$	Pa s	[18]
Molar mass of hydrogen	M	0.002	kg mol^{-1}	
MeH				
Solid density	$\rho_{\text{MeH},0}$	8200	kg m^{-3}	[19]
Max. gravimetric H_2 storage capacity	$w_{t,\text{max}}$	$1.2126 - 0.0003 T[^\circ\text{C}] - 9 \cdot 10^{-6} T[^\circ\text{C}]^2$	$\text{kg}_{\text{H}_2} \text{kg}_{\text{MeH}}^{-1}$	Exp. determined
Thermal conductivity	$\lambda_{\text{eff,MeH}}$	1.2	$\text{W m}^{-1} \text{K}^{-1}$	[15]
Permeability	K_{MeH}	$1 \cdot 10^{-12}$	m^2	[20]
Specific heat capacity	$c_{p,\text{MeH}}$	420	$\text{J kg}^{-1} \text{K}^{-1}$	[15]
Enthalpy of desorption reaction	$\Delta_R H_{d,\text{MeH}}$	42,360	$\text{J mol}_{\text{H}_2}^{-1}$	[19]
Entropy of desorption reaction	$\Delta_R S_{d,\text{MeH}}$	110.69	$\text{J mol}_{\text{H}_2}^{-1} \text{K}^{-1}$	[19]
Arrhenius parameter for desorption	$A_{d,\text{MeH}}$	20	s^{-1}	Adapted from [16]
Activation energy for desorption	$E_{d,\text{MeH}}$	16,500	$\text{J mol}^{-1} \text{K}^{-1}$	[16]
Li–Mg–N–H				
Solid density	$\rho_{\text{LiMgNH},0}$	900	kg m^{-3}	[8]
Max. gravimetric H_2 storage capacity	$w_{t,\text{max}}$	0.032	$\text{kg}_{\text{H}_2} \text{kg}_{\text{MeH}}^{-1}$	[8]
Max. gravimetric H_2 storage capacity, 1 st step	$w_{t,\text{max}_1\text{step}}$	$0.33 \cdot w_{t,\text{max}}$		[8]
Max. gravimetric H_2 storage capacity, 2 nd step	$w_{t,\text{max}_2\text{step}}$	$0.67 \cdot w_{t,\text{max}}$		[8]
Thermal conductivity	$\lambda_{\text{eff,LiMgNH}}$	0.35	$\text{W m}^{-1} \text{K}^{-1}$	In the range of [21]
Permeability	K_{LiMgNH}	$1 \cdot 10^{-12}$	m^2	Estimate
Specific heat capacity	$c_{p,\text{LiMgNH}}$	1533	$\text{J kg}^{-1} \text{K}^{-1}$	[22]
Enthalpy of desorption reaction	$\Delta_R H_{d,\text{Li–Mg–N–H}}$	45,100	$\text{J mol}_{\text{H}_2}^{-1}$	[8]
Entropy of desorption reaction	$\Delta_R S_{d,\text{Li–Mg–N–H}}$	123.9	$\text{J mol}_{\text{H}_2}^{-1} \text{K}^{-1}$	[8]
Arrhenius parameter for desorption, 1 st step	$A_{d,I,\text{Li–Mg–N–H}}$	$2.35 \cdot 10^{12}$	s^{-1}	[8]
Activation energy for desorption, 1 st step	$E_{d,I,\text{Li–Mg–N–H}}$	131,800	$\text{J mol}^{-1} \text{K}^{-1}$	[8]
Arrhenius parameter for desorption, 2 nd step	$A_{d,II,\text{Li–Mg–N–H}}$	$3.044 \cdot 10^{15}$	s^{-1}	[8]
Activation energy for desorption, 2 nd step	$E_{d,II,\text{Li–Mg–N–H}}$	161,400	$\text{J mol}^{-1} \text{K}^{-1}$	[8]
Heat transfer				
Density of steel	ρ_{steel}	8000	kg m^{-3}	Thyssen Krupp, NIROSTA 4571
Thermal conductivity of steel	λ_{steel}	15	$\text{W m}^{-1} \text{K}^{-1}$	Thyssen Krupp, NIROSTA 4571
Heat capacity of steel	$c_{p,\text{steel}}$	500	$\text{J kg}^{-1} \text{K}^{-1}$	Thyssen Krupp, NIROSTA 4571
Heat transfer coefficient from steel wall to heat transfer fluid (HTF)	h_{HTF}	600	$\text{W m}^{-2} \text{K}^{-1}$	Exp. determined

direct mixture where the two powders are mixed by shaking. The second option is an indirect mixture where the materials are separated by a gas permeable layer (GPSL). In order to avoid potential side reactions between the two materials, the second option has been selected for the present study and the MeH material has been placed at the core of a tubular reactor, while the Li–Mg–N–H material is placed in the annulus.

The aim of this paper is to study the behaviour of the new combination reactor concept in comparison to a pure Li–Mg–N–H reactor for the desorption process. Therefore, first, simulations are performed based on simplified scenarios

for an automotive application. Then, the presented model equations and parameters are validated by several lab-scale experiments.

2. Methodology

2.1. Experimental details

For the model validation of the desorption experiments, a prototype tank module has been designed. The outer diameter

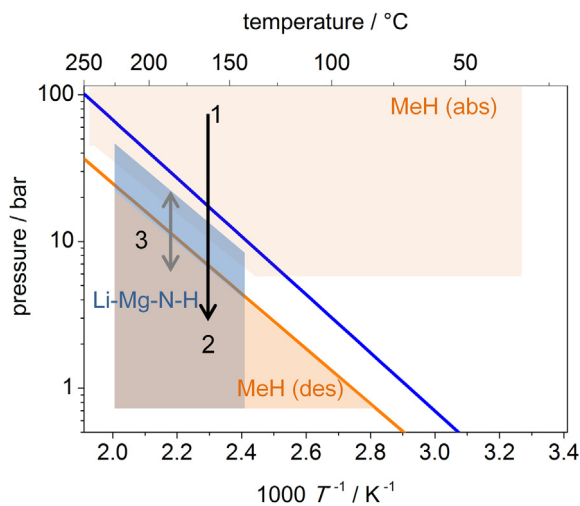


Fig. 1 – Schematic van't Hoff plot for MeH and Li–Mg–N–H material. Lines refer to thermodynamic equilibrium lines for the reversible sorption reaction of MeH (light orange) and Li–Mg–N–H (dark blue). Shaded areas show temperature and pressure range where the absorption and desorption reaction of MeH and Li–Mg–N–H proceed in relevant time frames. Arrows indicate desorption process in a reactor. (For interpretation of the references to colour in this figure legend, the reader is referred to the web version of this article.)

of the reactor tube is 42.2 mm with a wall thickness of 1.65 mm and a total length of 0.7 m. In order to avoid additional weight due to flange sealing, the tube has been welded after filling under argon atmosphere. The inner copper tube, that is stabilizing the GPSL, has an outer diameter of 14 mm and a thickness of 1 mm (see Fig. 2). In order to monitor the temperature inside of the tube, one thermocouple (Type K) is integrated at the outside of the copper tube at a distance of 40 cm from the bottom. In this module 283 g of MeH ($\text{LaNi}_{4.3}\text{Al}_{0.4}\text{Mn}_{0.3}$) and 283 g of Li–Mg–N–H ($2\text{LiNH}_2 \cdot 1.1\text{MgH}_2 \cdot 0.1\text{LiBH}_4 \cdot 3 \text{ wt. \%ZrCoH}_3$) have been filled as powdered material. The final tank that will be used for coupling with a fuel cell consists of 12 identical modules and is therefore able to provide sufficient H_2 for 2 h operation of a 1 kW_{el} HT-PEM fuel cell.

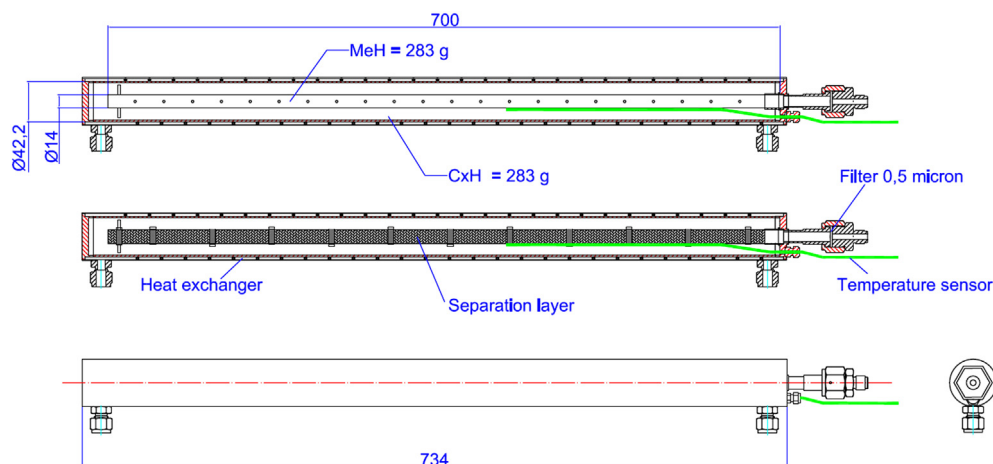


Fig. 2 – Drawing of complete reactor tube.

For the present study, the single module has been integrated into a testing setup where pressures of up to 150 bar can be applied and the heat transfer fluid (HTF) can be controlled at temperatures up to 200 °C. For detailed measurements, 40 thermocouples can be connected and the hydrogen can be supplied and released by pressure or mass-flow control (up to $30 \cdot 10^{-6} \text{ kg s}^{-1}$). The mass of hydrogen that is desorbed from the material is calculated by the difference in the mass of hydrogen released from the setup and the mass of hydrogen released due to a pressure decrease in the known void volume of the reactor.

2.2. Modelling

The model equations used for the simulation of the storage reactor apply the following common assumptions from different literature models:

- The gas and the solid phase are *quasi-homogeneous*, the *bed porosity* and the *solid density* are constant, and all properties are independent of the transformed fraction [9–14].
- *Local-Thermal-Equilibrium* (LTE) is assumed [9–14].
- *Darcy flow* in radial direction is implemented for all simulations and convective heat transport is considered in the energy balance, accordingly [10,15].
- *Ideal gas* is assumed for all simulations [9,11,13–15].
- *Pressure work* has been explicitly neglected due to small pressure gradients during the scenarios [12,14].
- No dependence on pressure, temperature or transformed fraction has been considered for the *properties of the materials* and the *hydrogen gas* [9–15].

2.2.1. Model equations

Analogous to [6], the model is implemented into the software COMSOL Multiphysics and rate equations, the mass balance of the gas as well as a total energy balance are considered.

The rate equations can be written as

$$\frac{\partial x}{\partial t} = \dot{m}_R \quad (3)$$

where \dot{m}_R is given in s^{-1} . The expressions for the two-step desorption reaction of the Li–Mg–N–H material have been

determined in [8], and are summarized in Table 1. For the MeH material, rate equations from a 1st order literature model ([16]) have been adapted and the according parameters are also summarized in Table 1.

The mass balance for the gas phase is

$$\varepsilon \frac{M}{RT} \frac{\partial P_g}{\partial t} - \varepsilon \frac{P_g M}{RT^2} \frac{\partial T}{\partial t} - \nabla \cdot \left(\rho_g \frac{K}{\mu_g} \nabla P_g \right) = -(1 - \varepsilon) \dot{m}_R w t_{\max} \rho_s \quad (4)$$

where Darcy flow is used for the description of the gas velocity $\nabla \vec{v}_g$ according to

$$\nabla P_g = -\frac{\mu_g}{K} \cdot \vec{v}_g \quad (5)$$

For the energy balance of the system, local thermal equilibrium (LTE) $T = T_g = T_s$, is assumed leading to

$$\left[(1 - \varepsilon) c_{p,s} \rho_s + \varepsilon c_{p,g} \rho_g \right] \frac{\partial T}{\partial t} = c_{p,g} \rho_g \frac{K}{\mu_g} \nabla P_g \nabla T - \nabla \cdot (\lambda_{\text{eff}} \nabla T) - (1 - \varepsilon) \dot{m}_R w t_{\max} \rho_s \Delta_R H \quad (6)$$

The expression on the left hand side of this equation refers to the accumulation of enthalpy in the gas as well as in the solid phase. On the right hand side, convective heat transfer of the gas phase, heat transfer by thermal conduction in the gas and solid phase and a heat source due to the reaction are accounted for. The expression for the effective heat conductivity can be calculated as

$$\lambda_{\text{eff}} = (1 - \varepsilon) \lambda_s + \varepsilon \lambda_g \quad (7)$$

or determined experimentally as the heat conductivity of the hydride powder.

2.2.2. Geometry

For modelling of the geometry (see Fig. 3), axial effects have been neglected and just a segment of a circle (45°) has been modelled leading to symmetry conditions on b1 and b2. The reactor is modelled using four domains: the stainless steel wall (D4), the powder bed of the Li–Mg–N–H (D3), the copper tube that is stabilizing the GPLS (D2), and the powder bed of the MeH (D1), (see Fig. 3). In order to model simplified gas transport holes in the copper tube, a porosity of 1% has been assumed.

2.2.3. Initial and boundary conditions

For the desorption experiments as well as for the simulated scenario, the boundary conditions have been set with respect

to a driving cycle in a car (compare Fig. 3). Thus, the initial pressure is equal to the charging pressure of the system (70 bar in the experiments, 20 bar in the basic scenario). Then, the pressure in the reactor decreases, as H₂ is released by a constant mass flow rate

$$\dot{m} = \rho_s w t_{\max} (1 - \varepsilon) \cdot r_{\text{req}} \cdot A_{\text{tube}} \cdot H \quad (8)$$

where the required H₂ flow rate r_{req} is given in s⁻¹. A_{tube} refers to the perpendicular cut to the tube axis that is modelled and the height H is 1 m. Using this definition, the pure Li–Mg–N–H reactor and the combination reactor can be directly compared with respect to the same possible operation time for the amount of hydrogen stored in each case. A maximum operation time of 2 h is assumed and in all experiments, the desorption process is interrupted as soon as the pressure falls below 1.7 bar, as this is the minimum working pressure to supply the fuel cell. During the total experiment, the temperature of the HTF is kept at a constant fuel cell operating temperature.

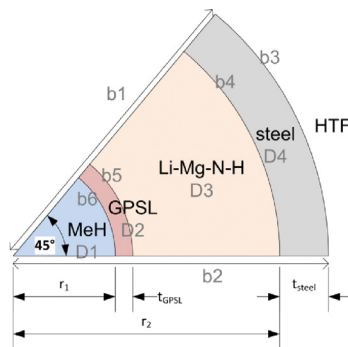
In the desorption experiments used for the model validation, the temperature has been varied by 5 K (165 and 170 °C) and the mass flow rate of H₂ has been changed from 0.75 to 1.5 and 3 · 10⁻⁶ kg s⁻¹. Furthermore, one experiment with a periodic mass flow rate between 0 and 3 · 10⁻⁶ kg s⁻¹ has been performed.

3. Results and discussion

3.1. Simulations

In this first part of the results, simulations of the desorption process are presented. Using these simulations, the interaction of both materials during the desorption process can be clarified, moreover information on the desorption progress of the two single materials, that is not experimentally available, can be derived.

As mentioned in Section 2.2.3, in the applied scenario the initial pressure is 20 bar, then hydrogen is released with a constant flow rate and the simulation is terminated as soon as a pressure of 1.7 bar is reached. In order to discuss the influence of the MeH material on the overall reactor performance, this scenario is calculated for pure Li–Mg–N–H and for the combination reactor using the same outer tube geometry: The



rate equations	initial boundary	D1,D3 b4,b5,b6 b1, b2	$x = 0$ $-\tilde{n} \left(\frac{\partial x}{\partial x} \right) = 0$	no flux, symmetry
MB gas	initial boundary	D1,D2,D3 D1,D3 b1,b2 b4	$P = P_i$ \dot{m}_{out} $-\tilde{n} \left(\frac{\partial x}{\partial x} \right) = 0$	source term no flux, symmetry
		b5,b6	$P_{\text{MeH}} = P_{\text{copper}}$ $P_{\text{copper}} = P_{\text{Li-Mg-N-H}}$	no mass transport limitation
EB	initial boundary	D1,D2,D3,D4 b1,b2 b3 b4 b5 b6	$T_{\text{Li-Mg-N-H}} = T_{\text{copper}} = T_{\text{steel}}$ $-\tilde{n} \lambda_{\text{eff}} \left(\frac{\partial T}{\partial x} \right) = 0$ $-\tilde{n} \lambda_{\text{eff}} \left(\frac{\partial T}{\partial x} \right) = h_{\text{HTF}} (T_{\text{HTF}} - T_{\text{out}})$ $T_{\text{out}} = T_{\text{Li-Mg-N-H}}$ $T_{\text{Li-Mg-N-H}} = T_{\text{copper}}$ $T_{\text{copper}} = T_{\text{MeH}}$	symmetry heat flux no heat transfer limitation

Fig. 3 – Left: modelling geometry of reactor with all 4 domains. Right: summary of initial and boundary conditions during desorption.

diameter of the GPSL is 13.5 mm and the diameter of the Li–Mg–N–H powder bed is 34 mm corresponding to a volume fraction of $\epsilon_{\text{LiMgNH}} = V_{\text{LiMgNH}}/V_{\text{total}} = 0.85$ for the Li–Mg–N–H material. For simplification, in the respective simulations, any resistance of the GPSL is neglected (only in this section). In the following, the calculated results of pressure, temperature and mass H_2 desorbed versus time for the simulations of both reactors are presented.

3.1.1. Pressure versus time

Fig. 4 shows the pressure versus time evolution for the simulation of the pure Li–Mg–N–H reactor, including the information of the actual equilibrium pressure of the material (depending on the average temperature). In the beginning, the pressure is decreasing linearly due to the H_2 release from the free volume inside of the reactor (red, solid line). As soon as the pressure falls below the equilibrium pressure of the Li–Mg–N–H (grey, dashed line), the desorption reaction can start. However, close to the equilibrium, the reaction rate of the Li–Mg–N–H material is still very low due to kinetic limitations. Therefore, the pressure inside the reactor cannot follow the equilibrium pressure instantaneously. At a pressure of approx. 5 bar, a plateau is formed indicating that the desorption reaction can supply the required amount of hydrogen. At this point in time, the driving pressure difference between the gas pressure and the equilibrium pressure of the Li–Mg–N–H material is approx. 3 bar. The slight increase in pressure in the beginning is due to the reaction mechanism of the Li–Mg–N–H material, that shows a sigmoidal shape for isothermal and isobaric conditions (compare [8]). At about 6000 s, the desorption scenario for the pure Li–Mg–N–H reactor is terminated as the pressure reaches 1.7 bar.

In contrast, Fig. 5 shows a pressure plot for the same scenario, but with the combination reactor. In this case, the pressure (solid, red line) decreases to the equilibrium pressure of the MeH material (dotted, grey line), and then follows this value instantaneously. This behaviour is due to the high reaction rates of the MeH material at the present temperatures

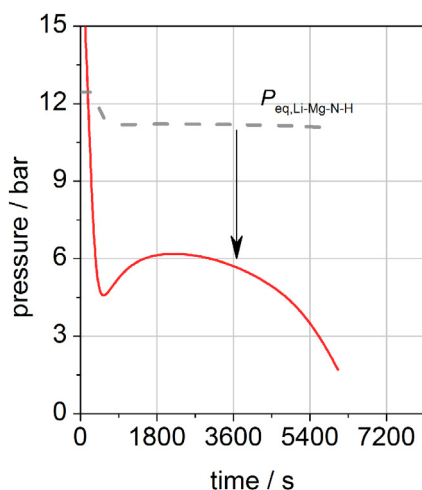


Fig. 4 – Gas pressure versus time for simulations with pure Li–Mg–N–H. Red solid line: P_g , grey dashed line: $P_{\text{eq, Li-Mg-N-H}}$.

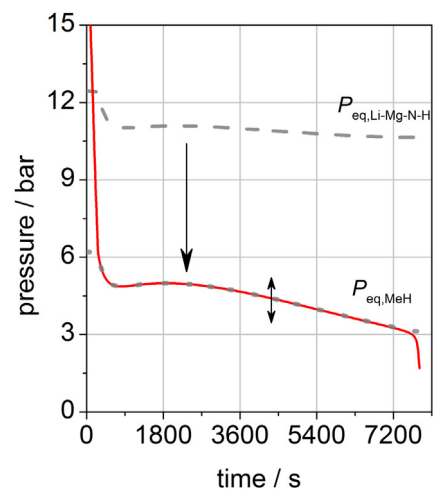


Fig. 5 – Gas pressure versus time for simulations with combination reactor at 165 °C. Red solid line: P_g , black dashed line: $P_{\text{eq, Li-Mg-N-H}}$, grey dotted line: $P_{\text{eq, MeH}}$.

that are approx. two orders of magnitude higher than the reaction rates of the Li–Mg–N–H material: On a material basis the metal hydride reaction proceeds in less than 20 s, at 165 °C and 1 bar, while the Li–Mg–N–H material requires 3600 s for a complete desorption, at 165 °C and static vacuum. Hence, both materials are desorbing very close to the equilibrium pressure of the MeH material. The Li–Mg–N–H desorbs H_2 with a rate possible at this pressure and temperature, and the MeH is releasing the additionally required amount of hydrogen to keep the pressure at the equilibrium pressure plateau. As soon as the MeH material is fully desorbed, the pressure in the system decreases and the desorption process is terminated. Thus, the MeH material is able to significantly improve the overall dynamic desorption performance of a pure Li–Mg–N–H reactor as it can provide a hydrogen buffer during peak loads due to reaction rates that are two orders of magnitude higher than for the Li–Mg–N–H material.

3.1.2. Mass desorbed and temperature versus time

Fig. 6 shows the mass of H_2 that is desorbed from the reactor per m length of model reactor. The overall mass (solid line) is linear, as H_2 is removed from the system by a constant flow rate. This value can also be calculated based on experimental results. However, using the simulation, it is additionally possible to determine how much hydrogen has been desorbed by each material at each point in time. From this plot it is obvious that the Li–Mg–N–H material is able to desorb a large fraction of the required amount of H_2 up to 3600 s (dashed line). However, in the following seconds the amount desorbed by the MeH material increases (dotted line), thus compensates the decreasing amount of H_2 that can be desorbed by the Li–Mg–N–H material. In the end, the Li–Mg–N–H material has released 94% of its max. H_2 capacity (indicated by symbol) in the combination reactor, while in the pure reactor just 84% of the H_2 are desorbed before the pressure falls below the fuel cell supply pressure (not shown here).

In Fig. 7, the temperature profile inside of the reactor is shown: T_{GPSL} is shown as dashed line, and T_1 as solid line for

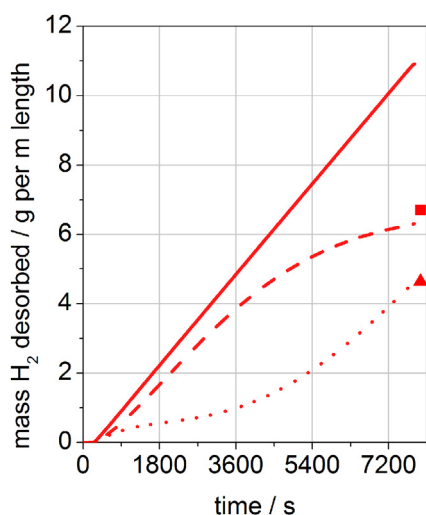


Fig. 6 – Mass H_2 desorbed in g per m of reactor length in a simulated desorption scenario in the combination reactor. **Solid line:** total desorbed H_2 mass, **dashed line:** H_2 desorbed by Li–Mg–N–H, **dotted line:** H_2 desorbed by MeH, **■:** max. H_2 mass of Li–Mg–N–H, **▲:** max. H_2 mass of MeH.

the combination reactor. During the first 3600 s of the reaction, the temperature in the reactor reaches a homogeneous, approx. constant temperature and shows only a small temperature difference between T_1 and T_{GPSL} . This indicates that the Li–Mg–N–H material is desorbing a sufficient amount of H_2 for the required hydrogen mass flow rate. In the following seconds, a significant temperature decrease can be observed and T_1 starts to deviate from T_{GPSL} . This decrease as well as the deviation in temperature is due to an increasing fraction of the MeH material, which is additionally desorbing hydrogen at the centre of the reactor tube. Thus, the simulated temperature profiles support the observations in the pressure and mass desorbed versus time plots, indicating that the MeH material compensates the low reaction rate of the Li–Mg–N–H material.

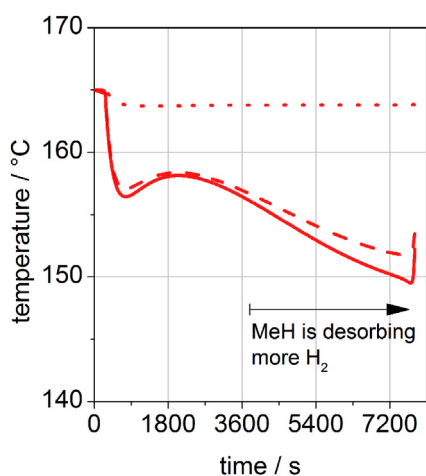


Fig. 7 – Temperature versus time for a simulated desorption scenario in the combination reactor. **Solid line:** T_1 , **dashed line:** T_{GPSL} , **dotted line:** T_{HTF} .

3.1.3. Discussion

From the simulation results, it is obvious that for the present reference materials the desorption performance in the combination reactor is advantageous in comparison to the pure Li–Mg–N–H reactor. In case of a constant mass flow rate of hydrogen to the fuel cell, the length of the pressure plateau is significantly extended (from approx. 6000 s–7400 s), as the fast desorbing MeH material is stabilizing the plateau pressure and therefore extends the desorption time for the Li–Mg–N–H material. Thus, the Li–Mg–N–H material is actually able to desorb H_2 to a higher extend at technically relevant conditions in the combination reactor in comparison to the pure reactor (94–84%).

At this point it has to be mentioned that the observed effects are not only influenced by the reaction rates of the two materials, but also by the remaining material properties as enthalpy of reaction, thermal conductivity, heat capacity, etc. Furthermore, the total diameter of the reactor tube as well as the diameter of the GPSL will influence the performance. Thus, for the design of a suitable combination reactor, information on the properties of the materials as well as parameter studies using validated model equations are essential.

3.2. Model validation

In this second part of the result section, the model equations and parameters are experimentally validated using the reactor described in Section 2.1. Therefore, several desorption experiments have been performed at 165 and 170 °C and applying hydrogen mass flow rates of 0.75, 2 and $3 \cdot 10^{-6} \text{ kg s}^{-1}$. A flow rate of $1.5 \cdot 10^{-6} \text{ kg s}^{-1}$ corresponds to the amount of H_2 required for 2 h operation of a 1 kWel fuel cell (50% efficiency), if all 12 modules are used in parallel. Furthermore, one experiment with a periodic mass flow rate between 0 and $3 \cdot 10^{-6} \text{ kg s}^{-1}$ has been performed.

3.2.1. Varying hydrogen mass flow rate

Fig. 8 shows the simulated and experimental desorption results for the experiments at 170 °C and three different hydrogen mass flow rates. As expected, the pressure almost linearly decreases due to the constant mass flow rate of hydrogen in the beginning of the procedure. Then, the desorption reaction starts and a plateau in pressure is formed. Corresponding to the different mass flow rates the level of the plateau pressure varies – for low flow rates the plateau pressure is higher. This effect is very well captured by the model. As soon as the pressure falls below 1.7 bar, the experiment and the simulation are terminated since the pressure is too low for a coupling to the fuel cell. Also this behaviour is well captured by the simulation. However, there is a significant deviation between the model and the simulation in the first seconds of the experiment, where the pressure is in theory linearly decreasing. While in the simulation, no hydrogen is released by the material above the equilibrium pressure of the Li–Mg–N–H material, in the experiment some hydrogen is already released slowly, indicated by the deviation of the pressure signal from a solid line.

In addition to the pressure versus time plots, in Fig. 9, the temperature evolution at the position of the thermocouple is

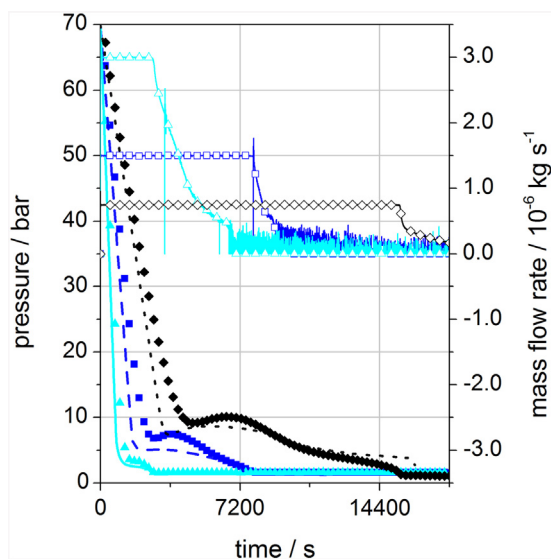


Fig. 8 – Pressure (open symbols) and mass flow rate (compact symbols) of hydrogen versus time for experiments at three different required mass flow rates. Turquoise, Δ : $3 \cdot 10^{-6} \text{ kg s}^{-1}$, blue, \square : $1.5 \cdot 10^{-6} \text{ kg s}^{-1}$ and black, \blacklozenge : $0.75 \cdot 10^{-6} \text{ kg s}^{-1}$. Lines: pressure simulations. (For interpretation of the references to colour in this figure legend, the reader is referred to the web version of this article.)

shown. From this plot it is also obvious that in the experiment the reaction is initiated at much higher pressures in comparison to the simulation. Furthermore, the level of the temperatures in the simulation is slightly lower than in the experiment. This can be for instance due to the incorrect modelling of the exact position of the thermocouple. However, similarly to the experiment, the simulated temperature evolution first shows a plateau, before the reaction of the MeH is increasingly desorbing H_2 which leads to an enhanced temperature decrease at about 4000 s.

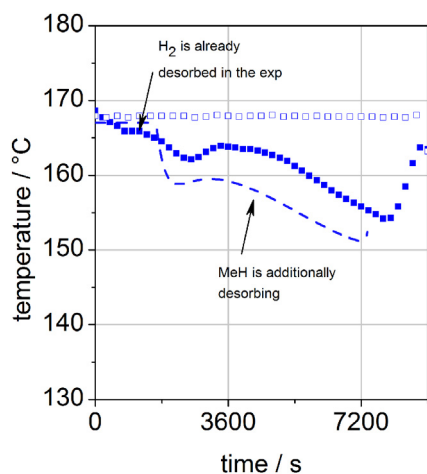


Fig. 9 – Temperature versus time for the desorption experiment at 170 °C and $1.5 \cdot 10^{-6} \text{ kg s}^{-1}$. \square : temperature of the HTF, \blacksquare : temperature at $r = 0.007 \text{ mm}$. Line: simulation.

The fact that in the simulation the reaction is initiated at lower pressures than observed experimentally can only be explained if the thermodynamic equilibrium of the reaction appears actually at a higher pressure than it is assumed for high weight fractions of hydrogen. However, for the modelling of the reaction rate, just desorption experiments at pressures below 6 bar have been available and for the fitting procedure an average equilibrium pressure for the complete hydrogen storage capacity has been assumed [8]. Hence, these model equations cannot capture any desorption reaction at pressures that are higher than the assumed average equilibrium pressure. In order to improve these model equations, more studies on the reaction rates even at higher pressures would be necessary. However, as the general behaviour of the reactor concept with the two materials is captured quite well, especially in the – for the coupling – important low pressure regimes, the available data seems to be sufficient.

3.2.2. Periodic mass flow rate

In addition to the experiments with constant mass flow rate, Fig. 10 shows the pressure and mass flow rate versus time for the experiment at $1.5 \cdot 10^{-6} \text{ kg s}^{-1}$ and for an experiment with a periodic hydrogen flow rate of 0 and $3 \cdot 10^{-6} \text{ kg s}^{-1}$ at 170 °C . Analogous to the previous pressure plots, in the first seconds of the experiments, where the pressure is slowly decreasing, there is a constant deviation in the reaction rate between the experiment and the simulation leading to an increasing deviation between the two signals. However, at pressures below the equilibrium pressure, the simulation is capturing the experimental behaviour very well. This is even the case for the experiment with the periodic flow rate, where the resulting pressure changes can be captured by the model. Furthermore,

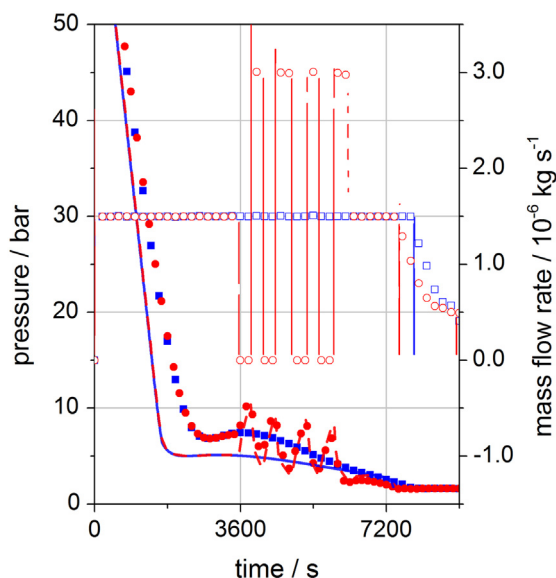


Fig. 10 – Pressure (compact symbols) and mass flow rate (open symbols) of two desorption experiments at 170 °C . Blue, \blacksquare : constant flow rate of $1.5 \cdot 10^{-6} \text{ kg s}^{-1}$, red, \bullet : periodic hydrogen flow rate. Lines: pressure simulation. (For interpretation of the references to colour in this figure legend, the reader is referred to the web version of this article.)

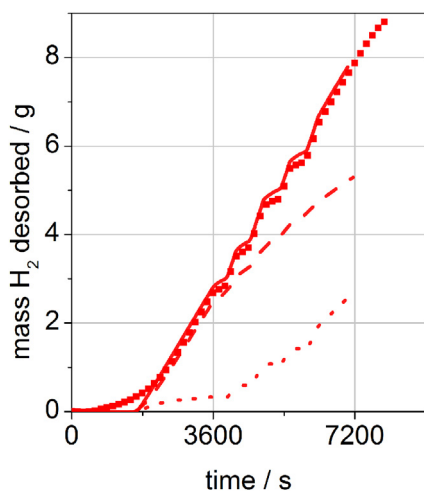


Fig. 11 – Mass of H₂ desorbed by the reactor in the experiment with periodic flow rate at 170 °C. ■: experimental data, solid line: simulated desorbed H₂ mass, dashes: simulated H₂ mass desorbed by MeH, dash-dots: simulated H₂ mass desorbed by Li–Mg–N–H.

in Fig. 11, the desorbed mass of hydrogen versus time is calculated for the desorption experiment and the simulation with the periodic hydrogen mass flow rate. In this plot it can be seen that the mass of hydrogen that is actually desorbing in the first seconds before the plateau is reached is quite small: at 2000 s less than 1 g of hydrogen has been desorbed from the 283 g of Li–Mg–N–H, corresponding to approx. 10% of the total 9.1 g of hydrogen that can be stored in the Li–Mg–N–H material.

Overall, the accordance between the simulated and experimental results of the desorbed mass of hydrogen is very good. Thus, this model can be used to provide further information on the desorption state of the materials that cannot be extracted from the experimental results. E.g. from the two additionally simulated graphs in Fig. 11, corresponding to the mass desorbed by the MeH and desorbed by the Li–Mg–N–H, it is obvious that in the first 4000 s the Li–Mg–N–H material is desorbing the main part of the released hydrogen. Then, the reaction rate is not sufficient anymore and the fraction of hydrogen desorbed by the MeH material is increasing. As soon as the MeH material is fully depleted, the pressure in the system cannot be stabilized anymore and the experiment is terminated. Thus, from this information it is clear that the addition of the MeH material is actually improving the performance of a pure Li–Mg–N–H reactor during the desorption process.

3.3. Discussion of the combination reactor concept

From the preliminary simulation as well as the experimental results presented in this paper, two important points that are characterizing the new concept for the desorption process can be summarized:

- The desorption time in the simulated scenario is extended from the pure Li–Mg–N–H scenario to the combination

reactor as the system pressure is stabilized above the fuel cell supply pressure. In the presented case, the desorption time is increased by a factor of 1.2.

- The transformed fraction of Li–Mg–N–H material is actually higher in the combination reactor than in the pure Li–Mg–N–H reactor as 94 instead of 84% can be reached.

Thus, it is clear that in the present case, the influence of the combination has positive effects on the overall desorption performance of the reactor.

For future combination reactors with new CxH materials, it can be recommended to choose a MeH material with an even lower equilibrium pressure than the present material. This can be advantageous as the gas pressure of the system will always instantaneously follow this equilibrium pressure, due to the very high reaction rates of the MeH material. Therefore the desorption rate of the CxH material is also improved when this pressure is very low, and as a result the desorption efficiency of the CxH material will increase. Furthermore, the potential recharging of the MeH material is facilitated.

Finally, it has to be mentioned that the addition of a MeH to a future CxH material will always lead to a slight decrease in the overall volumetric and gravimetric storage density. However, for absorption [6] as well as desorption, the combination reactor concept has a positive effect on the dynamic reactor performance. For example, the charging time is reduced and the desorption time at pressures above the fuel cell supply pressure is extended. Thus, it enables the technical application and the utilization of the high H₂ storage capacities characterizing conversion materials.

4. Conclusions

In the present paper, the effects of a combination reactor concept based on the addition of a MeH material to a complex hydride material reactor have been studied for the desorption process. Preliminary 2D simulations showed that the MeH material is improving the overall desorption performance of the Li–Mg–N–H system at fuel cell relevant boundary conditions. This is mainly due to the fact that the fast desorption reaction of the MeH stabilizes the pressure in the reactor at the equilibrium pressure of the material. Furthermore, several experiments have been performed in a lab scale reactor with 283 g of each material. There is a deviation between model and experiment, as in the experiments the material already desorbs about 10% of the hydrogen at pressures well above the assumed equilibrium pressure. However, the general accordance between the simulation and the experiment has been good, thus the model and the parameters can be considered validated.

Finally, it can be concluded that a combination reactor concept based on the addition of a MeH material to a CxH material is a promising option to improve the overall desorption performance of a pure complex hydride reactor: The MeH material stabilizes the desorption system pressure above the fuel cell supply pressure and hence improves tank dynamics.

Acknowledgements

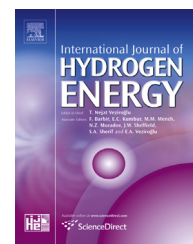
The research leading to these results has received funding from the European Union's Seventh Framework Programme (FP7/2007-2013) for the Fuel Cells and Hydrogen Joint Technology Initiative under grant agreement no. 256653.

REFERENCES

- [1] Fichtner M. Conversion materials for hydrogen storage and electrochemical applications—concepts and similarities. *J Alloys Compd* 2011;509:S529–34.
- [2] Eberle U, Felderhoff M, Schüth F. Chemical and physical solutions for hydrogen storage. *Angew Chem Int Ed* 2009;48(36):6608–30.
- [3] Urbanczyk R, Peil S, Bathen D, Heßke C, Burfeind J, Hauschild K, et al. HT-PEM fuel cell system with integrated complex metal hydride storage tank. *Fuel Cells* 2011;11(6):911–20.
- [4] Pfeifer P, Wall C, Jensen O, Hahn H, Fichtner M. Thermal coupling of a high temperature PEM fuel cell with a complex hydride tank. *Int J Hydrogen Energy* 2009;34(8):3457–66.
- [5] Weiß-Ungethüm J, Bürger I, Schmidt N, Linder M, Kallo J. Experimental investigation of a liquid cooled high temperature proton exchange membrane (HT-PEM) fuel cell coupled to a sodium-alanate tank. *Int J Hydrogen Energy*; 2013 [published online 25 Feb. 2014].
- [6] Bürger I, Komogowski L, Linder M. Advanced reactor concept for complex hydrides: hydrogen absorption from room temperature. *Int J Hydrogen Energy* 2014;39(14):7346–55.
- [7] Weidner E, Dolci F, Hu J, Lohstroh W, Hansen T, Bull DJ, et al. Hydrogenation reaction pathway in $\text{Li}_2\text{Mg}(\text{NH})_2$. *J Phys Chem C* 2009;113(35):15772–7.
- [8] Bürger I, Hu J, Vitillo JG, Kalantzopoulos GN, Deledda S, Fichtner M, et al. Material properties and empirical rate equations for hydrogen sorption reactions in $2\text{LiNH}_2\text{--}1.1\text{MgH}_2\text{--}0.1\text{LiBH}_2\text{--}3\text{ wt.}\% \text{ZrCoH}_3$. *Int J Hydrogen Energy*; Feb. 2014 [in press].
- [9] Bhouri M, Goyette J, Hardy BJ, Anton DL. Numerical modeling and performance evaluation of multi-tubular sodium alanate hydride finned reactor. *Int J Hydrogen Energy* 2012;37(2):1551–67.
- [10] Na Ranong C, Höhne M, Franzen J, Hapke J, Fieg G, Dornheim M, et al. Concept, design and manufacture of a prototype hydrogen storage tank based on sodium alanate. *Chem Eng Technol* 2009;32(8):1154–63.
- [11] Hardy BJ, Anton DL. Hierarchical methodology for modeling hydrogen storage systems. Part II: detailed models. *Int J Hydrogen Energy* 2009;34(7):2992–3004.
- [12] Johnson TA, Kanouff MP, Dedrick DE, Evans GH, Jorgensen SW. Model-based design of an automotive-scale, metal hydride hydrogen storage system. *Int J Hydrogen Energy* 2012;37(3):2835–49.
- [13] Garrison SL, Hardy BJ, Gorbounov MB, Tamburello DA, Corngale C, VanHassel BA, et al. Optimization of internal heat exchangers for hydrogen storage tanks utilizing metal hydrides. *Int J Hydrogen Energy* 2012;37(3):2850–61.
- [14] Mohan G, Prakash Maiya M, Srinivasa Murthy S. Performance simulation of metal hydride hydrogen storage device with embedded filters and heat exchanger tubes. *Int J Hydrogen Energy* 2007;32(18):4978–87.
- [15] Jemni A, Nasrallah SB. Study of two-dimensional heat and mass transfer during absorption in a metal-hydrogen reactor. *Int J Hydrogen Energy* 1995;20(1):43–52.
- [16] Jemni A, Nasrallah SB. Study of two-dimensional heat and mass transfer desorption in a metal-hydrogen reactor. *Int J Hydrogen Energy* 1995;20(11):881–91.
- [17] Thermophysical properties of fluid systems. In: Lemmon EW, McLinden MO, Friend DG, editors. Nist chemistry webbook, nist standard reference database number 69. Gaithersburg MD: National Institute of Standards and Technology; 2008.
- [18] White FM. Fluid mechanics. 4th ed. McGraw-Hill; 1999.
- [19] Willers E. Multi-hybrid-sorptionsanlage zur kombinierten heizung und kühlung. University of Stuttgart; 2002. <http://elib.uni-stuttgart.de/opus/volltexte/2002/1073/>.
- [20] Nakagawa T, Inomata A, Aoki H, Miura T. Numerical analysis of heat and mass transfer characteristics in the metal hydride bed. *Int J Hydrogen Energy* 2000;25(4):339–50.
- [21] Wang J, Keller J, Gross KJ. DOE metal hydride Center of Excellence. 2005 Annual Progress Report VI Storage, 487–417.
- [22] Xu F, Sun LX, Chen P, Qi YN, Zhang J, Zhao JN, et al. Studies on heat capacities and thermal analysis of Li–Mg–N–H hydrogen storage system. *J Therm Anal* 2009;100(2):701–6.

Available online at www.sciencedirect.com

ScienceDirect

journal homepage: www.elsevier.com/locate/he

Material properties and empirical rate equations for hydrogen sorption reactions in 2 LiNH₂–1.1 MgH₂–0.1 LiBH₄–3 wt.% ZrCoH₃

I. Bürger^{a,*}, J.J. Hu^b, J.G. Vitillo^c, G.N. Kalantzopoulos^d, S. Deledda^d, M. Fichtner^b, M. Baricco^c, M. Linder^a

^aInstitute of Technical Thermodynamics, German Aerospace Center (DLR), Pfaffenwaldring 38-40, D-70569 Stuttgart, Germany

^bInstitute of Nanotechnology, Karlsruhe Institute of Technology (KIT), D-76021 Karlsruhe, Germany

^cDipartimento di Chimica and NIS, Università di Torino, Via P. Giuria 7-9, I-10125 Torino, Italy

^dInstitute for Energy Technology, Physics Department, P.O. Box 40, NO-2027 Kjeller, Norway

ARTICLE INFO

Article history:

Received 10 December 2013

Received in revised form

10 February 2014

Accepted 19 February 2014

Available online 3 April 2014

Keywords:

Li–Mg–N–H hydride

Reaction rate

Model equations

Hydrogen storage

ABSTRACT

2 LiNH₂–1.1 MgH₂–0.1 LiBH₄–3 wt.% ZrCoH₃ is a solid state hydrogen storage material with a hydrogen storage capacity of up to 5.3 wt.%. As the material shows sufficiently high desorption rates at temperatures below 200 °C, it is used for a prototype solid state hydrogen storage tank with a hydrogen capacity of 2 kWh_{el} that is coupled to a high temperature proton exchange membrane fuel cell. In order to design an appropriate prototype reactor, model equations for the rate of hydrogen sorption reactions are required. Therefore in the present study, several material properties, like bulk density and thermodynamic data, are measured. Furthermore, isothermal absorption and desorption experiments are performed in a temperature and pressure range that is in the focus of the coupling system. Using experimental data, two-step model equations have been fitted for the hydrogen absorption and desorption reactions. These empirical model equations are able to capture the experimentally measured reaction rates and can be used for model validation of the design simulations.

Copyright © 2014, Hydrogen Energy Publications, LLC. Published by Elsevier Ltd. All rights reserved.

Introduction

Due to high theoretical storage densities, complex hydrides show the potential to improve the present state of the art of hydrogen storage for automotive applications [1]. As the hydrogen is strongly bonded to the powdered material, the amount of free gaseous hydrogen in equilibrium at room temperature and pressure is small and hydrogen is just

released when external heat is provided for the endothermal desorption reactions. In case the storage reactor is coupled to a fuel cell (FC), the required amount of hydrogen can be released by transfer of waste heat from the FC. This kind of coupled system has already been studied by several simulations and experiments for conventional metal hydrides, as well as for NaAlH₄ [2–4].

The present work has been developed within a framework of activities aiming to realize a hydrogen storage tank that is

* Corresponding author. Tel.: +49 711 6862 492.

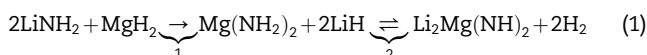
E-mail address: inga.buerger@dlr.de (I. Bürger).
<http://dx.doi.org/10.1016/j.ijhydene.2014.02.120>

0360-3199/Copyright © 2014, Hydrogen Energy Publications, LLC. Published by Elsevier Ltd. All rights reserved.

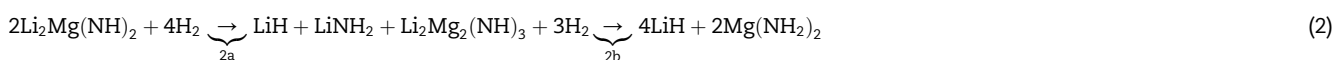
studied in technically relevant scale, i.e. allowing for 2 h coupled operation with a 1 kW_{el} high temperature proton-exchange membrane (HT-PEM) fuel cell. As for an appropriate tank design modelling simulation tools are used, reliable information on the properties of the selected storage material is required, e.g., bulk density, storage capacity, thermodynamic properties and reaction rate equations. In the present paper, these values are summarized for the selected material.

The material that has been chosen for the prototype system is based on the Li–Mg–N–H system, as these materials release significant amounts of H₂ at temperatures below the HT-PEM fuel cell operating temperature, i.e. max. 200 °C [5]. Hence, it is possible to maintain the tank at a temperature sufficiently high for the required hydrogen delivering rates by simply using waste heat of the fuel cell. Although the Li–Mg–N–H system has been suggested for hydrogen storage in automotive applications previously [6], to our knowledge, applications have not been reported yet.

While pure Li–N–H stores theoretically 11.5 wt.% [7], the partial substitution of LiH with MgH₂ reduces the amount of H₂ to 5.4 wt.% [8,9]. However, this substitution significantly reduces the thermodynamic barriers [10,11], and an experimental gravimetric density of 4.6 wt.% below 200 °C can be reached [8]. In the basic system for this study, the ratio of lithium amide to magnesium hydride is 2:1.1, and the reaction of this system is reported as [8]



The first step (1) is an irreversible exothermic metathesis reaction that just takes place during the first “activation” procedure. The corresponding reaction enthalpy has been estimated by Araújo et al. as 68.8 kJ mol⁻¹ [12] and experimentally verified by Luo [13]. The storing process corresponds to the second reaction (2), that reversibly absorbs/desorbs hydrogen in two steps (2a and 2b). These steps have been verified by in-situ neutron diffraction [14] and can be written as



PCI curves of this system show that the first step (2a) appears as a sloping region, while the second step (2b) corresponds to a plateau [8].

In order to improve this basic system, different additives have been investigated in the literature. LiBH₄ seemed to improve reaction rates and thermodynamics, when added in small ratios [15,16]. In 2010, Zhang et al. presented a system with 2–1.1–0.1 LiNH₂–MgH₂–LiBH₄ and 3 wt.% ZrCoH₃, showing a theoretical hydrogen capacity of 5.6 wt.% and experimentally observed capacities of 5.3 and 3.75 wt.% for absorption and desorption, respectively [17]. Ulmer et al. studied the same system resulting in capacities of 3.5–4.2 wt.% [18]. According to Hu et al. [19], the effects of the two additives in this basic system are different. While the addition of LiBH₄ facilitates the metathesis reaction for the first cycle and

furthermore generally enhances kinetics via the formation of a liquid intermediate phase, ZrCoH₃ leads to powder pulverizing effects. For the development of the prototype reactor, this material has been chosen due to the acceptable storage capacity and sufficient reaction rates below 200 °C. In the following, this material will be abbreviated as Li–Mg–N–H.

So far, in literature there are no model equations describing the reaction rates of this material for absorption and desorption, but rather qualitative comparative studies on the reaction rates using different dopants [15,19,20]. Therefore, in the present paper, the focus is on the determination of simple but satisfying mathematical equations describing the reaction rate of the absorption and desorption process of the material in the desired pressure and temperature range. Furthermore, thermodynamic data, as well as bulk density, will be determined.

Experimental

Material preparation

LiNH₂ (95%, Sigma–Aldrich), MgH₂ and LiBH₄ (95%, Alfa Aesar) were purchased, stored in the glove box and used as received without pretreatment. ZrCoH₃ was prepared from ZrCo ingot (SAES Getters S.p.A., Italy) by exposing to 1 MPa H₂ at ambient temperature and milled before use.

The starting chemicals with a composition of 2 LiNH₂–1.1 MgH₂–0.1 LiBH₄–3 wt.% ZrCoH₃ were loaded into a 500 ml milling vial made of stainless steel and sealed inside the glove box. Ball milling was conducted on a Retsch PM-400 planetary ball mill that can accommodate 4 milling vials in one run. Each vial contained 103 g of material, so that in total 412 g material was prepared in a single batch. The milling was operated at 250 rpm in a reverse mode at the interval of 10 min/1 min for 100 h with a ball-to-powder ratio of 5.

Activation procedure

After synthesis, the material is still present in the basic form as Lithium Amide and Magnesium Hydride with only a small fraction reacted to Li₂Mg(NH)₂. Therefore, before the material is studied for hydrogen sorption, the powder needs to be transformed by an exothermic metathesis reaction (see Equation (1)) that causes a visible change in material colour from dark black to light grey.

For small amounts of material this is usually done by applying a slow heating ramp (2–5 K min⁻¹) or just by cycling the powder in an isothermal measurement setup. However, for larger amounts (2 g or even kg scale for the final prototype), it is not possible to keep the reaction bed at isothermal conditions. In contrast, the reaction of the material is accelerating

due to the heat evolution of this metathesis reaction. Therefore, the activation of the material needs to be performed very carefully for larger volumes of materials and heat removal needs to be addressed by, e.g. heating the material up in isothermal steps of several hours for every 10 K.

Density

As He pycnometry is a suitable method to obtain the density of powder samples at room temperature [21], this method has been applied to the selected Li–Mg–N–H material. The He pycnometry measurements have been performed in a home-made, well-calibrated Sieverts apparatus. Expansions of He (purity 6.0) from a reservoir volume to the sample holder took place five times, and the maximum pressure was kept under 4 bar to minimize the effect of the gas compressibility.

PCI measurements

Hydrogen sorption experiments were performed in the 0–100 bar pressure range using a volumetric instrument (PCI instrument by Advanced Materials Corporation, Pittsburgh PA). Ultra-pure 6.0 grade H_2 was used and the powders (about 500 mg) were transferred under nitrogen atmosphere in the measurement cell. For all PCI measurements (performed at 170, 180 and 200 °C), the sample was previously activated by three cycles of absorption (100 bar)/desorption (vacuum) at 150 °C. For each PCI run, new sample material has been used.

Testing setup for measurement of reaction rates

For the measurements of the reaction rates, a reactor has been designed for approx. 2 g of material. The main requirement for this reactor has been to guarantee isothermal and isobaric

reaction conditions over the powder bed. Thus, any heat or mass transport limitations that could affect the measured reaction rate have been avoided. This has been realized by the following three points [22]:

- The contact surface with the surrounding stainless steel has been designed to be as large as possible to enhance heat removal and avoid hot spots inside the powder bed.
- The stainless steel mass of the reactor is big enough to limit the temperature increase to a maximum of $\Delta T = 2$ K inside the stainless steel material, while taking up the total heat of reaction of the powder.
- The amount of material inserted into the reactor has to be adapted to absorb 0.1 g H_2 , leading to a sufficient measurement accuracy for evaluation of conversion.

As shown in Fig. 1, the final geometry of the reactor is a spindle with a gap of 0.5 mm. The reactor can then be filled by screwing the spindle into the powder material. In order to control the temperature, one thermocouple is integrated into the reactor and placed close to the powder.

For the hydrogen sorption experiments, this reactor has been integrated into the setup shown in Fig. 1. The general principle of this setup is a volumetric measurement based on the measured pressure difference in a defined reference volume before and after the experiment (Sieverts type) [23]. Before the experiment starts, in the Sieverts volume ($V_s + V_{abs} + V_{des}$) a certain pressure (PS4) is applied. Furthermore, the temperature in the reactor is controlled by a thermostatic bath at the defined set temperature. Then, for absorption the manual valve HV-3 is closed in order to maintain the set pressure in the small volume V_{abs} . After opening the pneumatic valve PV-2, the gas is flowing into the reactor (V_R) and the absorption reaction is initiated: On one side of the differential pressure sensor (in $V_s + V_{des} + V_R$), the pressure decreases due to the void volume of the reactor and

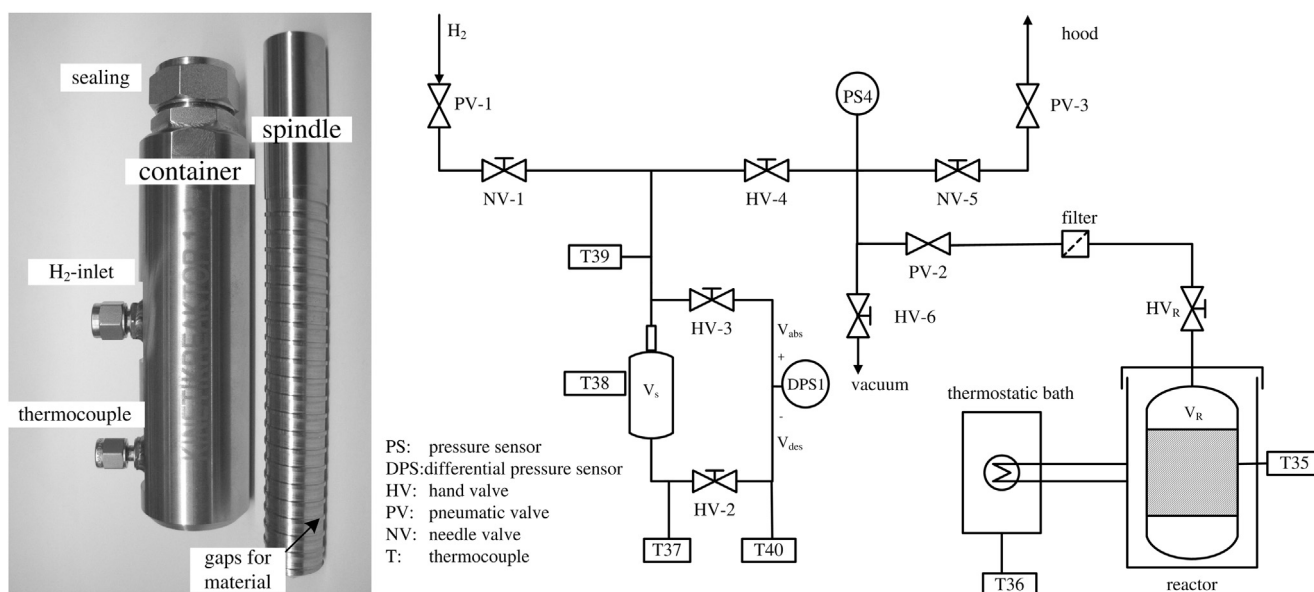


Fig. 1 – Left: photo of the reactor used for the reaction rate measurements consisting of container and spindle. Right: scheme of the Sieverts type testing setup.

Table 1 – Model parameters for 1st and 2nd reaction step of Li–Mg–N–H absorption (abs) and desorption (des) with according error values as well as the R² value for the quality of the fit.

		Value	Accuracy
1 st step abs $\left(\frac{P-P_{eq,abs}}{P_{eq,abs}}\right)$	$E_{a,abs,I}$ in kJ mol ⁻¹	164.8	±4.6
	$A_{abs,I}$ in kJ mol ⁻¹	$2.729 \cdot 10^{17}$	$\cdot e^{1.31} = 3.71,$ $\cdot e^{-1.31} = 0.27$
2 nd step abs $\left(\frac{P-P_{eq,abs}}{P_{eq,abs}}\right)$	$E_{a,abs,II}$ in kJ mol ⁻¹	147.8	±7.9
	$A_{a,II}$ in kJ mol ⁻¹	$4.678 \cdot 10^{14}$	$\cdot e^{0.95} = 2.59,$ $\cdot e^{-0.95} = 0.39$
1 st step des $\ln\left(\frac{P_{eq,des}}{P}\right)$	$E_{a,des,I}$ in kJ mol ⁻¹	131.8	±7.1
	$A_{des,I}$ in kJ mol ⁻¹	$2.35 \cdot 10^{12}$	$\cdot e^{1.92} = 6.82,$ $\cdot e^{-1.92} = 0.15$
2 nd step des	$E_{a,des,II}$ in kJ mol ⁻¹	161.4	–
	$A_{des,II}$ in kJ mol ⁻¹	$3.044 \cdot 10^{15}$	–

due to the absorption reaction inside of the reactor until the reaction is complete. While on the other side of the sensor in V_{abs} the pressure is constant. Hence, the pressure difference between these two volumes can be measured and it corresponds to the absorbed mass of hydrogen. This pressure difference reached maximum values of 1 bar in the present experiments, while the pressure variation between two experiments was 15 bar for absorption and 3 bar for desorption. Thus, the present experiments can be considered reasonably isobaric. In case of desorption, the same procedure is inverted: HV-2 is closed and the pressure is increasing in $V_S + V_{abs}$.

Results and discussion

In the following, the results of the important properties of the Li–Mg–N–H material for reactor design simulations are presented and summarized. The corresponding nomenclature is given in Table 2.

Bulk properties

The material density is a very important property in order to estimate the volume the material occupies in the reactor and thus an important input parameter for the reactor design simulations. Using the setup described in Section 2, the density of the as-milled sample has been determined to be

Table 2 – Nomenclature.

A	Pre-exponential factor	s ⁻¹
E_a	Activation energy	kJ mol ⁻¹
k	Rate coefficient	s ⁻¹
P	Gas pressure	bar
P_0	Standard pressure	bar
P_{eq}	Gas pressure at equilibrium conditions	bar
\mathfrak{R}	Gas constant (8.314)	J kg ⁻¹ K ⁻¹
s.v.	Static vacuum (here: 5 mbar)	
t	Time	s
T	Temperature	K
x	Transformed fraction	1
X_I	Transformed fraction of 1 st step	1
X_{II}	Transformed fraction of 2 nd step	1

$1.00 \cdot 10^3$ kg m⁻³. The sample was afterwards heated up to 500 °C at 2 °C min⁻¹ and was kept isothermally for 8 h under dynamic vacuum. Then, it was let to cool down to room temperature where pycnometry measurements took place. Its density in the desorbed state was $0.79 \cdot 10^3$ kg m⁻³. These values are in accordance with literature values of $0.54 \cdot 10^3$ kg m⁻³ for the bulk density, when an open porosity of 50–60% is assumed [24].

Thermodynamic properties

As during lab-scale experiments high equilibrium temperatures (220–250 °C) have been reached at pressures of 70 or 85 bar, experimental PCT measurements as well as results from experimental lab-scale reactor have been used for the determination of the thermodynamic parameters. PCT isotherms were characterized by two regions, as previously reported for LiNH₂–MgH₂ based material see Equation (2), [8,14]: (i) the first one, at low pressures, assigned to complex solid state transformations from Li₂Mg(NH)₂ to Li₂MgN_xH_y phases and (ii) the second one, at higher pressures, characterized by the gradual transformation of the previous species to Mg(NH₂)₂ + 2LiH (for more details see Ref. [25]). From the corresponding van't Hoff plot, the enthalpies ($\Delta_R H$) of the sorption reactions are $\Delta_R H_{abs} = -38$ kJ mol_{H₂}⁻¹ and $\Delta_R H_{des} = 45$ kJ mol_{H₂}⁻¹, and the entropies ($\Delta_R S$) of the reactions are $\Delta_R S_{abs} = -111$ J mol_{H₂}⁻¹ K⁻¹ and $\Delta_R S_{des} = 124$ J mol_{H₂}⁻¹ K⁻¹ for absorption and desorption, respectively. These values are in good agreement with those reported in Ref. [26].

Reaction rates

In order to simulate basic absorption or desorption scenarios in a reactor, the reaction rate of the material is necessary. Therefore, empirical equations for the absorption and desorption of the present Li–Mg–N–H material have been developed and the according results are summarized in this section.

The procedure that is used for the fitting of all rate equations is based on the assumption that the effective reaction rate can be described by the following equation

$$\frac{\partial x}{\partial t} = -A \cdot \exp\left(-\frac{E_a}{\mathfrak{R}T}\right) \cdot \underbrace{f(P)}_k \cdot f(x), \quad (3)$$

where x is the transformed fraction, t is the time and P is the gas pressure. The first factor on the right hand side refers to the Arrhenius equation describing the *temperature dependency* of the reaction rate, where A is the pre-exponential factor, E_a is the effective activation energy and \mathfrak{R} is the gas constant. The second factor represents the *thermodynamic information* by a dependency of the rate on the distance to the equilibrium pressure. For this factor, two basic mechanisms which are common for metal hydrides according to Refs. [27,28] or [29,30]

$$f(P) = \left(\frac{P - P_{eq}}{P_{eq}}\right), \quad \text{or} \quad f(P) = \ln\left(\frac{P}{P_{eq}}\right) \quad (4)$$

have been used, where P_{eq} is the equilibrium hydrogen pressure. As indicated in Equation (3), the product of the Arrhenius and the pressure factor is also referred to as rate coefficient k.

The last factor on the right hand side of Equation (3) is a function representing the reaction mechanism according to a suitable model. Several different functions are possible that represent according model concepts, e.g., reaction order, diffusion, 2D or 3D growth, etc. [31]. In the present paper, the focus is not on the determination of the actual mechanisms behind the reactions as this requires more detailed information on e.g. intermediate reaction steps or particle size. The goal of this study is rather to find suitable mathematical descriptions for the absorption and desorption reaction rate that can be used for modelling of suitable reactors. Hence, the following three basic mechanisms are used corresponding to the observed decelerating, linear or sigmoidal behaviour in the transformed fraction versus time plots:

$$1^{\text{st}} \text{ order (decelerating)} \quad f(x) = (1 - x). \quad (5)$$

$$0^{\text{th}} \text{ order (linear)} \quad f(x) = 1. \quad (6)$$

$$\text{general Avrami–Erofeev (sigmoidal)} \quad f(x) = n(1 - x) \times [-\ln(1 - x)]^{\frac{n-1}{n}}. \quad (7)$$

For the determination of the different factors and parameters in Equation (3), isothermal reaction rate measurements are performed, and the following four fitting steps summarize the applied procedure [32]:

- i. The thermodynamics of the reaction step is described by the van't Hoff equation.
- ii. The correct reaction mechanism for the reaction rate $f(x) = \frac{1}{k} \frac{dx}{dt}$ is determined. The mechanism is correct when the integral value versus the time follows a straight line, $g(x) = k \cdot t$. Then, the slope refers to the rate coefficient k .
- iii. In the next step, a correct pressure factor is determined: For each temperature and pressure, the associated rate coefficient k is divided by the values calculated for different pressure terms (see Equation (4)). A sufficient fit is achieved when the values for experiments at the same temperature but different pressures match each other.
- iv. In the last step, the activation energy E_a as well as the pre-exponential factor A are determined. According to $\ln\left(\frac{k}{f(P)}\right) = \ln A - \frac{E_a}{R} \frac{1}{T}$, A refers to the exponent of the value of the intersection with the ordinate, while E_a refers to the slope times R when $\ln\left(\frac{k}{f(P)}\right)$ is plotted versus $1/T$.

This scheme is applied for the fitting procedure of all reaction rate equations presented in the following for absorption and desorption of the Li–Mg–N–H material. For all fitting procedures of the absorption and desorption data, the minimum and maximum range of fitted values for the transformed fraction has been set between 10 and 80%, respectively.

Absorption reaction

The absorption experiments have been performed at three different pressures and up to five different temperatures

- 100 bar: (100), 125, 160 °C
- 85 bar: 125, 150, 160, 170 °C
- 70 bar: (100), 125, 150 – repeat, 160, 170 °C

The first absorption experiments show good reproducibility. However, after the last experiment at 170 °C, the reaction rate decreased significantly, probably due to material degradation effects while the capacity remained constant. For the determination of model equations, the experiments after the degradation process have been excluded. The experiments at 100 °C have also been removed from the fitting procedure, as the measurements of the pressure signal have not been significant due to very low reaction rates. For all remaining experiments, the experimental data have been fitted with reaction rate equations for the first 1800 s. Furthermore, the data have been normalized referring to a maximum H₂ fraction of 3.2 wt.%. For longer timescales, the material is still absorbing some H₂. However, the reaction rate is very low and in scale-up experiments, longer reaction times exceed the appropriate timeframe for an absorption experiment (e.g. automotive fuelling).

Fig. 2 shows all experiments performed in one plot. Different colours indicate different pressures. It can be clearly seen that the reaction is rather slow below 150 °C. However, above this temperature, the rates increase rapidly with increasing temperatures. At the highest temperature of 170 °C, the absorption of the material can be completed in less than 5 min. It is very important to capture this strong temperature dependency of the reaction rate correctly, as the temperature behaviour in a lab-scale tank can be strongly non-isothermal due to heat transfer resistance of the powder material. Furthermore, Fig. 2 indicates that besides the strong temperature dependency, the reaction rate also increases with increasing hydrogen pressure.

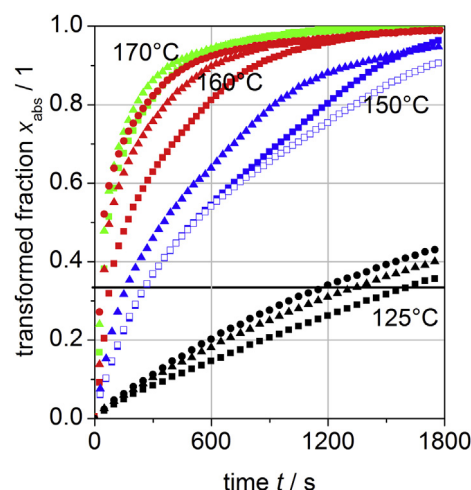


Fig. 2 – Transformed fraction versus time for all absorption experiments. ■, □ (repro): 70 bar, ▲: 85 bar, ●: 100 bar. Temperatures as indicated by numbers and colours (black: 125 °C, blue: 150 °C, red: 160 °C, green: 170 °C). The horizontal line refers to the transition between 1st and 2nd reaction step. (For interpretation of the references to colour in this figure legend, the reader is referred to the web version of this article.)

As it has been mentioned in Section 3.2 as well as in the literature, the reaction of the present material proceeds in two steps [8,14,25], (compare Equation (2)). The corresponding transition zone between the two steps is indicated by the horizontal line Fig. 2 and marks the bend in the curves, e.g. for the experiments at 150 °C. The normalized transformed fraction of the first step of absorption ($X_{abs,I}$) here refers to the first 33% of transformed fraction x_{abs} , for the second step ($X_{abs,II}$) to the following 67%, respectively. The mathematical formulation of the normalization is $X_{abs,I} = \frac{x_{abs}}{0.33}$ for $0 \leq x_{abs} \leq 0.33$ and $X_{abs,II} = \frac{x_{abs}-0.33}{0.67}$ for $0.33 \leq x_{abs} \leq 1$.

In order to follow the 4-step procedure described in Section 3.3, a description of reaction thermodynamics is required. In the present case, it is assumed that the thermodynamic data of both steps can be described by a single van't Hoff equation, as experimental data are not available for a more detailed description. Even though this is a rather strong assumption, the resulting fits show a sufficient accuracy in the required temperature and pressure range. This is mainly due to the fact that all application relevant conditions are far from the thermodynamic equilibrium ($P_{set} = 70$ bar $P_{eq,abs} < 20$ bar for $T < 170$ °C). Thus, this empirical approach can be used in order to sufficiently describe the thermodynamic information in the reaction rate equations required for reactor design simulations. The according values refer to Section 3.2

$$\ln\left(\frac{P_{eq}}{P_0}\right) = \frac{\Delta_R H}{RT} - \frac{\Delta_R S}{R}, \quad (8)$$

where P_0 is the reference pressure (1 bar). Using this information, the last three steps to fit the parameters for the empirical rate equations can be performed for both absorption steps.

1st Absorption step

In the first step, just one reagent (i.e. gaseous hydrogen) that is very abundant is involved in the reaction, and the measured transformed fraction versus time data show a linear behaviour (see Fig. 2). Therefore, a model with 0th reaction order has been chosen indicated by the factor of "1". Furthermore, an Arrhenius-type temperature dependency as well as a dependency on the thermodynamic equilibrium have been included

$$\frac{\partial X_{abs,I}}{\partial t} = A_{abs,I} \cdot \exp\left(-\frac{E_{a,abs,I}}{RT}\right) \cdot f(P, P_{eq,abs}) \cdot 1. \quad (9)$$

Due to the 0th order characteristic of the reaction, the integral equation for the transformed fraction can be written as

$$g(X_{abs,I}) = X_{abs,I}(t) = k \cdot t, \quad (10)$$

where k refers to the rate coefficient

$$k = A_{abs,I} \cdot \exp\left(-\frac{E_{a,abs,I}}{RT}\right) \cdot \left(\frac{P - P_{eq,abs}}{P_{eq,abs}}\right) \quad (11)$$

By fitting a straight line to the transformed fraction versus time plot (Fig. 2), this coefficient k can be determined as the corresponding slope. Additionally, using the second fitting step the pressure dependency of the reaction rate is determined. In this case, the best fit can be achieved, when the expression $f(P) = \left(\frac{P - P_{eq,abs}}{P_{eq,abs}}\right)$ is used. The corresponding

Arrhenius plot, with the 95% confidence intervals (dotted lines), is shown in Fig. 3. Finally, by fitting a straight line to this data, the kinetic parameters can be determined: the slope refers to the effective activation energy $E_{a,abs,I}$, and the intersection with the ordinate to the pre-exponential parameter $A_{abs,I}$.

2nd Absorption step

The determination of the rate equation for the 2nd reaction step is performed analogously. Fig. 2, clearly indicates that the evolution of the transformed fraction of this reaction step shows a decelerating behaviour. Therefore, a 1st order reaction has been assumed for the mathematical description of the reaction rate in this reaction step.

Complementing this term for the mechanism, again an Arrhenius-type temperature behaviour and a dependency on the thermodynamic equilibrium are included into the rate equation

$$\frac{\partial X_{abs,II}}{\partial t} = A_{abs,II} \cdot \exp\left(-\frac{E_{a,abs,II}}{RT}\right) \cdot f(P, P_{eq,abs}) \cdot (1 - X_{abs,II}). \quad (12)$$

According to the 1st order mechanism, the experimental data follow a straight line, when plotted according to the integrated rate equation

$$g(X_{abs,II}) = -\ln(1 - X_{abs,II}) = k \cdot t, \quad (13)$$

The slopes of these lines again refer to the rate coefficients k . The best fit for the pressure factor has been determined to $f(P) = \left(\frac{P - P_{eq,abs}}{P_{eq,abs}}\right)$, and the according Arrhenius plot with the 95% confidence intervals (dotted lines) is shown in Fig. 3.

The final full set of parameters for the rate equations of the two reaction steps is given in Table 1.

Discussion

The values for the activation energy presented in Table 1 are in the same range as literature values for the same reaction

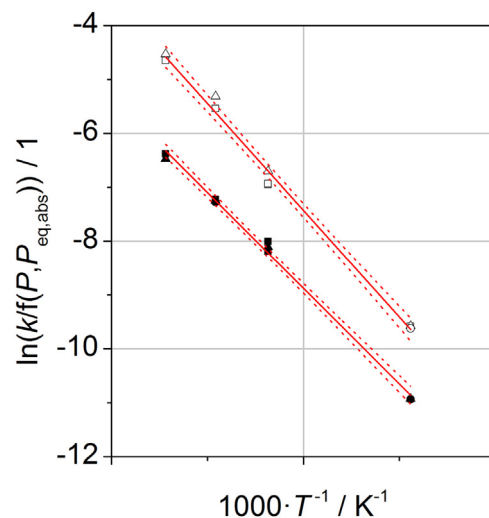


Fig. 3 – Arrhenius plots with experimental data (symbols) and fit with 95% confidence intervals (straight and dashed line, respectively) for 1st and 2nd reaction step. 1st reaction step: open symbols, 2nd reaction step: full symbols, 70 bar: ■, 85 bar: ▲, 100 bar: ●.

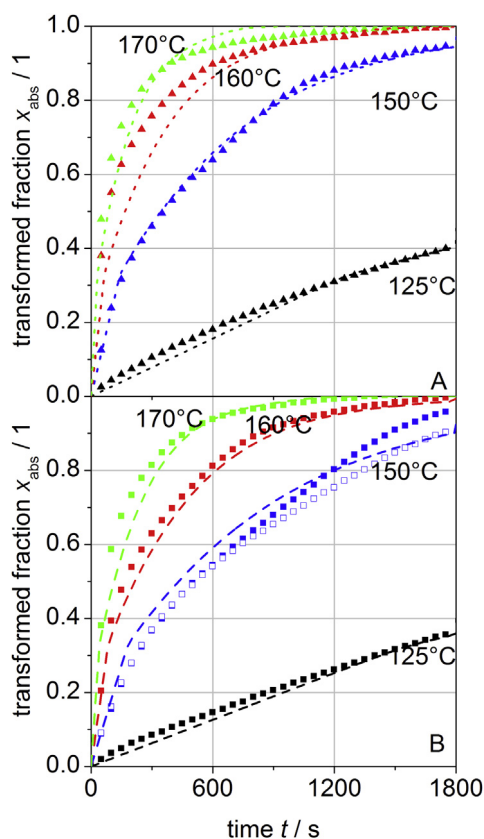


Fig. 4 – Experimental (symbols) and model (lines) data for transformed fraction in both steps versus time at indicated temperatures. (A) at 85 bar (B) at 70 bar.

(128 kJ mol⁻¹ [19]). However, the errors in the pre-exponential factor, which refer to the exponent of the error in the slope of the straight lines, are rather large. Therefore, all values presented in Table 1 should not be referred to the actual physical properties, but to apparent values for a sufficient fit of the effective reaction rate. Furthermore, these values are only valid in the measured temperature and pressure range and should therefore not be extrapolated.

Fig. 4(A) and (B) show the comparison between experimental and model data for the experiments at different temperatures and pressures of 70 and 85 bar, respectively. Changes in the slope of calculated curves for $x_{\text{abs}} = 0.33$ are related to the selected two-step model. Obviously, the empirical two-step model is able to capture the temperature and pressure behaviour very well from 125 to 170 °C. Only in the first range of the 2nd reaction step for the experiments at temperatures above 150 °C, the model equations underestimate the experimental effects. This behaviour can be explained by very fast reactions leading to non-perfect isothermal conditions in the reactor and thus overestimated reaction rates in the experiment. As a conclusion, it can be stated that the model equations can capture the temperature and pressure dependency of the absorption reaction rate. Therefore, they can be implemented into models that are used for tank design development, e.g. Ref. [33].

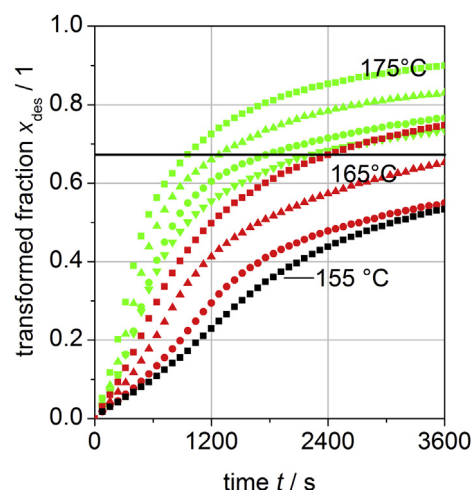


Fig. 5 – Transformed fraction versus time plot for all experimental measurements at temperatures indicated by values and colours. s.v.: ■, 1.4 bar: ▲, 3 bar: ●, 4.5 bar: ▼. (For interpretation of the references to colour in this figure legend, the reader is referred to the web version of this article.)

Desorption reaction

For desorption characterization, experiments have been performed at three different temperatures and up to four different starting pressures. The lowest starting pressures are indicated with “s.v.” for static vacuum at 5 mbar.

- 155 °C: s.v. (1.33 bar)
- 165 °C: s.v. (1.14), 1.4 (2.43), 3 (4.3) bar
- 175 °C: s.v. (1.35), 1.4 (2.42), 3 (4.24), 4.5 (5.55) bar.

Resulting transformed fraction versus time plots of these experiments are shown in Fig. 5 for the first 3600 s. For experiments with very low rates, or experiments at high desorption pressures, at the end of an experiment the temperature has been set to 180 °C and the pressure to static vacuum (5 mbar) in order to guarantee full conversion. As the experiments have been performed in the Sieverts type apparatus described in Section 2, the pressures, which have been set in the beginning, increased by the additional hydrogen released during the experiment due to the compressed gas in the void fraction and due to the reaction, corresponding to approximately 1 bar and 0.9 bar, respectively. Therefore, the pressures set in parentheses indicate the pressure present in the system at 0.25 transformed fraction. These values are also used for the fit of the pressure dependency. Analogous to the absorption experiments, the maximum gravimetric capacity is 3.2 wt.% ($w_{\text{t,max}} = 0.032 \text{ g}_{\text{H}_2} \text{ g}_{\text{LiMgNH}}^{-1}$).

A summary of all measured transformed fraction as a function of time is given in Fig. 5. From this plot, a clear sigmoidal shape of the curves can be observed as well as a very low reaction rate above 0.6–0.7 of transformed fraction. In accordance with the modelling of the absorption reaction, the desorption reaction is divided into two steps, where the

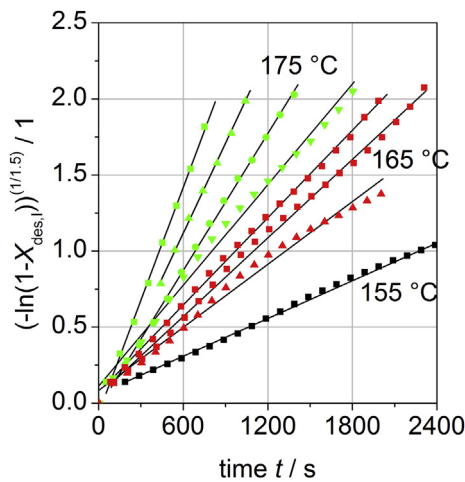


Fig. 6 – Experimental data and fit for reaction mechanism of 1st desorption step at varying temperatures and pressures. Initial pressures at s.v.: ■, 1.4 bar: ▲, 3 bar: ●, 4.5 bar: ▼. Temperatures at 175 °C: green, 165 °C: red, 155 °C: black. (For interpretation of the references to colour in this figure legend, the reader is referred to the web version of this article.)

transformed fraction of the first step $X_{des,I}$ refers to $0 \leq x_{des} \leq 0.67$ and for the second step $X_{des,II}$ refers to $0.67 \leq x_{des} \leq 1$, respectively.

Similar to the procedure for the determination of the rate equations for the absorption reaction, first a description of the thermodynamic equilibrium is necessary. These values differ from absorption due to a hysteresis behaviour of the reaction system and are summarized in Section 3.2.

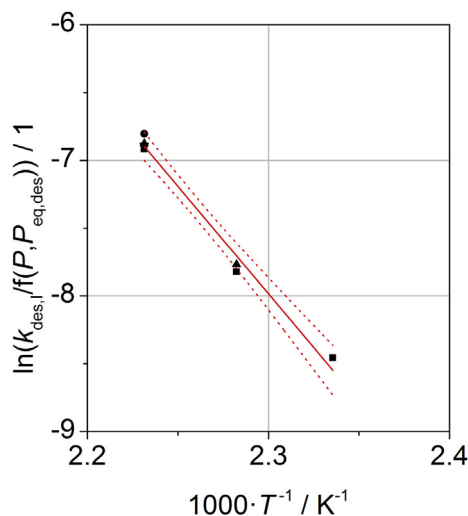


Fig. 7 – Arrhenius plot for 1st desorption step with experimental data (symbols) and fit (line) as well as 95% confidence intervals (dashed line), s.v.: ■, 1.4 bar: ▲, 3 bar: ●, 4.5 bar: ▼.

1st Desorption step

Due to the sigmoidal shape of the 1st reaction step, a model with a general Avrami–Erofeev mechanism is used for the mathematical description of the reaction rate in the present publication. For the variable n the best value has been determined to 1.5. Hence, the following equation describes the Arrhenius-type temperature dependency, the pressure factor as well as the mechanism

$$\frac{\partial X_{des,I}}{\partial t} = A_{des,I} \cdot \exp\left(-\frac{E_{a,des,I}}{RT}\right) \cdot f(P, P_{eq,des}) \cdot n(1 - X_{des,I}) \cdot [-\ln(1 - X_{des,I})]^{\frac{n-1}{n}} \quad (14)$$

The integrated form of this equation is

$$g(X_{des,I}) = [-\ln(1 - X_{des,I})]^{\frac{1}{n}} = k \cdot t, \quad (15)$$

which is plotted in Fig. 6 as a function of time. As the plotted data follows straight lines, the chosen mechanism sufficiently captures this reaction step, and the according slopes refer to the rate coefficients k . In this case, the thermodynamic contribution to the reaction rate is well described by a logarithmic pressure expression $f(P) = \ln\left(\frac{P_{eq,des}}{P}\right)$. The corresponding Arrhenius plot is shown in Fig. 7.

2nd Desorption step

For the second desorption step, the fitting procedure is difficult as the reaction rates are very low leading to unsatisfying accuracies in the experiments. Therefore, the focus for the empirical rate equations has been to capture the behaviour in a very small temperature and pressure range that is most interesting for the coupling to an HT-PEM fuel cell, i.e. 165 °C and <3 bar.

Analogous to the 1st absorption step, for the 2nd desorption step, a 0th order mechanism has been chosen resulting in a factor of “1” for the mechanism

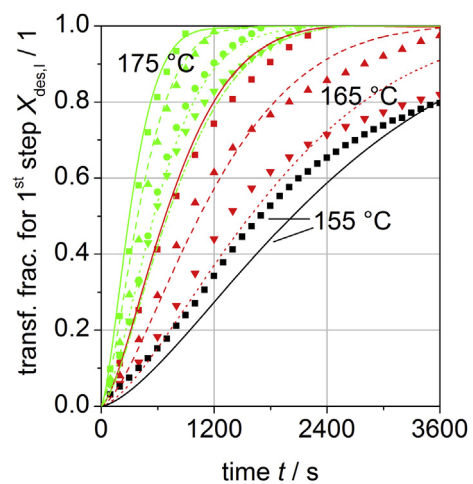


Fig. 8 – Transformed fraction versus time for the 1st reaction step of desorption. Symbols refer to experiments, lines to model equations. Black: 155 °C, red: 165 °C, green: 175 °C. s.v.: ■, 1.4 bar: ▲, 3 bar: ●, 4.5 bar: ▼. (For interpretation of the references to colour in this figure legend, the reader is referred to the web version of this article.)

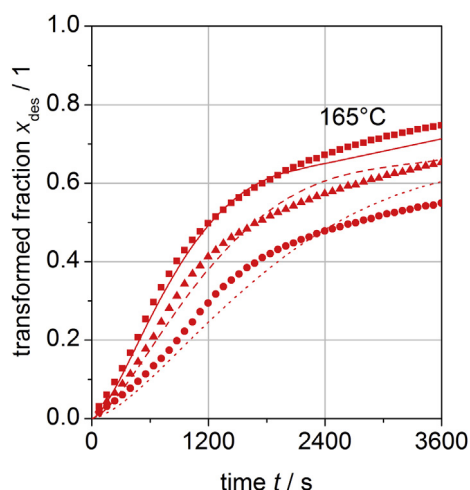


Fig. 9 – Transformed fraction versus time for complete desorption experiments at 165 °C. Symbols refer to experiments, lines to model equations. s.v.: ■, 1.4 bar: ▲, 3 bar: ●.

$$\frac{\partial X_{\text{des,II}}}{\partial t} = A_{\text{des,II}} \cdot \exp\left(-\frac{E_{a,\text{des,II}}}{RT}\right) \cdot f(P) \cdot 1. \quad (16)$$

As mentioned in Section 3.2, the PCI diagrams of the present material show a strong sloping region [25], similarly to [8]. Therefore, the pressure factor for the 2nd desorption step represents a dependency of the maximum weight fraction on the final back pressure applied. With lower desorption pressures, higher storage capacities can be reached. Hence, the implemented function is

$$f(P) = \left(1 - \frac{0.001515}{wt_{\text{max}} \cdot 0.33} (P - 1.1 [\text{bar}])\right), \quad (17)$$

which is only valid for the technically relevant boundary condition of $P < 8$ bar. The according parameters for the Arrhenius-type temperature dependency have been determined in analogy to the previous rate equations using only the experiments starting from static vacuum (5 mbar).

The final set of parameters for both steps is shown in Table 1.

Discussion

Fig. 8 shows the experimental and simulated data for the 1st desorption step. From this plot it can be stated that the model is able to capture the measured data in the relevant range of transformed fraction quite well. Furthermore, Fig. 9 shows experimental and simulated data for the complete desorption reaction at 165 °C with various back pressures. These parameters refer to the technically relevant conditions during a coupling procedure with an HT-PEM fuel cell. The agreement between the experimental data and the simulation using the empirical model equations is acceptable. However, it has to be emphasized, that the experimental data especially for the 2nd desorption step have been scarce. Therefore, any extrapolation to other temperatures should be avoided or checked carefully.

Finally, it can be concluded that the given desorption model equations are able to sufficiently describe the temperature, pressure and transformed fraction behaviour of the material in an application relevant range. Thus, the desorption model equations can be used for solid state hydrogen storage tank design simulations, see e.g. Ref. [34].

Conclusions

Important parameters for the modelling of a hydrogen storage reactor based on 2 LiNH₂–1.1 MgH₂–0.1 LiBH₄–3 wt.% ZrCoH₃ have been determined. For the bulk density in the absorbed state a value of $1.00 \cdot 10^3 \text{ kg m}^{-3}$ has been measured for the as-milled sample and $0.79 \cdot 10^3 \text{ kg m}^{-3}$ for the desorbed state. Furthermore, the enthalpy and entropy of the absorption reaction have been determined to $\Delta_{\text{R}}H_{\text{abs}} = -38 \text{ kJ mol}_{\text{H}_2}^{-1}$ and $\Delta_{\text{R}}S_{\text{abs}} = -111 \text{ J mol}_{\text{H}_2}^{-1} \text{ K}^{-1}$, and for desorption to $\Delta_{\text{R}}H_{\text{des}} = 45 \text{ kJ mol}_{\text{H}_2}^{-1}$ and $\Delta_{\text{R}}S_{\text{des}} = 124 \text{ J mol}_{\text{H}_2}^{-1} \text{ K}^{-1}$, respectively.

Regarding the rate of reactions, for absorption, a 2-step model has been fitted to experimental data using a 0th order model for the first and a 1st order model for the second reaction step. The comparison between simulated and experimental data shows a good agreement, especially for the temperature dependence that is very important for the simulation of strongly non-isothermal solid state hydrogen storage tanks.

The desorption behaviour is best captured with an Avrami–Erofeev model using $n = 1.5$ for the first step, while for the second step a dependency of the transformed fraction on the equilibrium pressure has been included. Using these empirical equations, the first reaction step can be captured by the model equations over the experimentally determined temperature and pressure range. However, for the second step, the determined equations are just valid for the boundary conditions (~ 165 °C and < 3 bar) that occur during the coupling to a fuel cell.

In general, the given material data enables a complete mathematical description for the conversion of the reaction system 2 LiNH₂–1.1 MgH₂–0.1 LiBH₄–3 wt.% ZrCoH₃ at technically relevant boundary conditions that can be used for future tank simulation and development.

Acknowledgements

The research leading to these results has received funding from the European Union's Seventh Framework Programme (FP7/2007-2013) for the Fuel Cells and Hydrogen Joint Technology Initiative under grant agreement n. 256653 (SSH2S).

REFERENCES

- [1] Eberle U, Felderhoff M, Schüth F. Chemical and physical solutions for hydrogen storage. *Angew Chem Int Ed* 2009;48(36):6608–30.

- [2] Pfeifer P, Wall C, Jensen O, Hahn H, Fichtner M. Thermal coupling of a high temperature PEM fuel cell with a complex hydride tank. *Int J Hydrogen Energy* 2009;34(8):3457–66.
- [3] Urbanczyk R, Peil S, Bathen D, Heßke C, Burfeind J, Hauschild K, et al. HT-PEM fuel cell system with integrated complex metal hydride storage tank. *Fuel Cells* 2011;11(6):911–20.
- [4] Weiß-Ungethüm J, Bürger I, Schmidt N, Linder M, Kallo J. Experimental investigation of a liquid cooled high temperature proton exchange membrane (HT-PEM) fuel cell coupled to a sodium-alanate tank. *Int J Hydrogen Energy* 2014;39(11):5931–41.
- [5] Zhang JJ, Xie Z, Tang Y, Song C, Navessin T, Shi Z, et al. High temperature PEM fuel cells. *J Power Sources* 2006;160(2):872–91.
- [6] Corgnale C, Hardy BJ, Tamburello DA, Garrison SL, Anton DL. Acceptability envelope for metal hydride-based hydrogen storage systems. *Int J Hydrogen Energy* 2012;37(3):2812–24.
- [7] Chen P, Xiong Z, Luo J, Lin J, Tan KL. Interaction of hydrogen with metal nitrides and imides. *Nature* 2002;420(6913):302–4.
- [8] Luo W. (LiNH₂–MgH₂): a viable hydrogen storage system. *J Alloys Compd* 2004;381(1–2):284–7.
- [9] Luo W. Corrigendum to “(LiNH₂–MgH₂): a viable hydrogen storage system”. *J Alloys Compd* 2004;385(1–2):316.
- [10] Nakamori Y, Orimo S. Li–N based hydrogen storage materials. *Mater Sci Eng B* 2004;108(1–2):48–50.
- [11] Aoki M, Noritake T, Nakamori Y, Towata S, Orimo S. Dehydrating and rehydrating properties of Mg(NH₂)₂–LiH systems. *J Alloys Compd* 2007;446–447:328–31.
- [12] Moysés Araújo C, Scheicher RH, Ahuja R. Hydrogen storage materials. *Appl Phys Lett* 2008;92(2):021907.
- [13] Luo W, Stavila V, Klebanoff LE. New insights into the mechanism of activation and hydrogen absorption of (2LiNH₂–MgH₂). *Int J Hydrogen Energy* 2012;37:6646–52.
- [14] Weidner E, Dolci F, Hu J, Lohstroh W, Hansen T, Bull DJ, et al. Hydrogenation reaction pathway in Li₂Mg(NH)₂. *J Phys Chem C* 2009;113(35):15772–7.
- [15] Hu JJ, Liu Y, Wu G, Xiong Z, Chua YS, Chen P. Improvement of hydrogen storage properties of the Li–Mg–N–H system by addition of LiBH₄. *Chem Mater* 2008;20(13):4398–402.
- [16] Yang J, Sudik A, Siegel DJ, Halliday D, Drews A, Carter RO, et al. Hydrogen storage properties of 2LiNH₂+LiBH₄+MgH₂. *J Alloys Compd* 2007;446–447:345–9.
- [17] Zhang X, Li Z, Lv F, Li H, Mi J, Wang S, et al. Improved hydrogen storage performance of the LiNH₂ MgH₂ LiBH₄ system by addition of ZrCo hydride. *Int J Hydrogen Energy* 2010;35(15):7809–14.
- [18] Ulmer U, Hu J, Franzreb M, Fichtner M. Preparation, scale-up and testing of nanoscale, doped amide systems for hydrogen storage. *Int J Hydrogen Energy* 2012;38(3):1439–49.
- [19] Hu JJ, Pohl A, Wang S, Fichtner M. Additive effects of LiBH₄ and ZrCoH₃ on the hydrogen sorption of the Li–Mg–NH hydrogen storage system. *J Phys Chem C* 2012;116:20246–53.
- [20] Janot R, Eymery J-B, Tarascon J-M. Investigation of the processes for reversible hydrogen storage in the Li–Mg–N–H system. *J Power Sources* 2007;164(2):496–502.
- [21] Gross KJ, Carrington KR. Recommended best practices for the characterization of storage properties of hydrogen storage materials; 2008. Berkeley, California.
- [22] Entwicklung Ruprecht D. Konstruktion und Fertigung eines Reaktors zur Untersuchung der Kinetik von Metallhydriden; 2011. Bachelor thesis.
- [23] Blach TPP, Gray EMM. Sieverts apparatus and methodology for accurate determination of hydrogen uptake by light-atom hosts. *J Alloys Compd* 2007;446–447:692–7.
- [24] Wang J, Keller J, Gross KJ. VI. A. 5 DOE metal hydride center of excellence. DOE Hydrogen Program; 2005. pp. 487–527.
- [25] Vitillo JG, Masala A, Hu JJ, Napolitano E, Dolci F, Bordiga S, et al. manuscript under preparation, 2014.
- [26] Wang J, Liu T, Wu G, Li W, Liu Y, Araújo CM, et al. Potassium-modified Mg(NH₂)₂/2 LiH system for hydrogen storage. *Angew Chem Int Ed* 2009;48(32):5828–32.
- [27] Vyazovkin S, Burnham AK, Criado JM, Pérez-Maqueda LA, Popescu C, Sbirrazzuoli N. ICTAC Kinetics Committee recommendations for performing kinetic computations on thermal analysis data. *Thermochim Acta* 2011;520:1–19.
- [28] Ron M. The normalized pressure dependence method for the evaluation of kinetic rates of metal hydride formation/decomposition. *J Alloys Compd* 1999;283(1–2):178–91.
- [29] Luo W, Gross KJ. A kinetics model of hydrogen absorption and desorption in Ti-doped NaAlH₄. *J Alloys Compd* 2004;385(1–2):224–31.
- [30] Mayer U, Groll M, Supper W. Heat and mass transfer in metal hydride reaction beds: experimental and theoretical results. *J Less Common Met* 1987;131:235–44.
- [31] Galwey AK, Brown ME. Thermal decomposition of ionic solids. 1st ed. Amsterdam: Elsevier; 1999.
- [32] Lozano GA, Ranong CN, Bellosta von Colbe JM, Bormann R, Fieg G, Hapke J, et al. Empirical kinetic model of sodium alanate reacting system (I). Hydrogen absorption. *Int J Hydrogen Energy* 2010;35(13):6763–72.
- [33] Bürger I, Komogowski L, Linder M. Advanced reactor concept for complex hydrides: hydrogen absorption from room temperature. *Int J Hydrogen Energy* 2014;39(13):7030–41.
- [34] Bürger I, Luetto C, Linder M. Advanced reactor concept for complex hydrides: hydrogen desorption at fuel cell relevant boundary conditions. *Int J Hydrogen Energy* 2014;39(14):7346–55.

Available online at www.sciencedirect.com

ScienceDirect

journal homepage: www.elsevier.com/locate/hydro

Numerical investigation of hydrogen charging performance for a combination reactor with embedded metal hydride and coolant tubes

Maha Bhourⁱ*, Inga Bürger, Marc Linder

Institute of Technical Thermodynamics, German Aerospace Center (DLR), D-70569 Stuttgart, Germany

ARTICLE INFO

Article history:

Received 20 October 2014

Received in revised form

16 January 2015

Accepted 12 March 2015

Available online 16 April 2015

Keywords:

Complex hydride

Metal hydride

Combination reactor

Embedded coolant tubes

Refueling time

2D simulation

ABSTRACT

A two-dimensional model investigating the hydrogen charging process in a combination reactor filled with both $\text{LaNi}_{4.3}\text{Al}_{0.4}\text{Mn}_{0.3}$ and $2\text{LiNH}_2\text{-}1.1\text{MgH}_2\text{-}0.1\text{LiBH}_4\text{-}3 \text{ wt.}\% \text{ZrCoH}_3$ materials has been developed. The selected configuration is a cylindrical reactor of 32 cm of diameter where the MeH is filled in annular tubes separated from the complex hydride bed by a gas permeable layer. The diffusion of hydrogen towards the two storage media is ensured by filters embedded in the middle of the MeH tubes whereas the coolant tubes are placed in the centre of their triangular arrangement. Simulation results have shown that the charging process depends on the MeH reaction heat required for the initiation of the CxH reaction as well as the heat management once the complex hydride starts to store hydrogen. High hydrogen storage rates and short refueling times can be obtained by increasing the number of MeH and coolant tubes and ensuring an efficient heat removal at the peripheral area of the CxH media. A refueling time of 3 min is achieved for an optimum configuration of 49 MeH tubes and 96 coolant tubes while increasing the thermal conductivity of the CxH media to 3.5 W/(m K). Such a result could make the identified optimum configuration as a suitable hydrogen storage system for fuel cell forklift trucks since it meets the requirements of this application in terms of weight and size.

Copyright © 2015, Hydrogen Energy Publications, LLC. Published by Elsevier Ltd. All rights reserved.

Introduction

As the international community raises its ambitions to tackle climatic and economic issues related to the use of fossil fuels, serious efforts are devoted to the building of the hydrogen economy. Firstly, research and development programs have been directed to the hydrogen-fueled light duty vehicles market. This was supported by the technical advances in fuel cell area. Nevertheless, there remain multiple challenges to be

overcome before the deployment of hydrogen fuel cell cars at a commercial scale [1].

As a second step along this path, the U.S. Department of Energy (DOE), in collaboration with the National Renewable Energy Laboratory (NREL) and Sandia National Laboratory (SNL) has worked to identify early adoption markets with less stringent technical challenges than automobile sector. It has been found that specialty vehicles, stationary back-up power and portable applications present a huge market potential for the near-term development of the hydrogen technology [2,3].

* Corresponding author. Tel.: +49 711 6862 531; fax: +49 711 6862 632.

E-mail address: maha.bhour@dlr.de (M. Bhour).

<http://dx.doi.org/10.1016/j.ijhydene.2015.03.060>

0360-3199/Copyright © 2015, Hydrogen Energy Publications, LLC. Published by Elsevier Ltd. All rights reserved.

For specialty vehicles, hydrogen powered fuel cell forklifts have significant benefits over existing technologies such as fossil fuel powered trucks and battery electric forklifts [4,5].

The most common battery used in the materials handling applications is the lead acid battery. The related electric forklifts are primarily designed for indoor use in order to minimize exhausts and noise, which is mandatory in such working environment. However, the long refueling time is the major issue of this technology. Indeed, the time required to change the battery is from 5 to 15 min for an automatic operation and up to 45 min for a manual one. Then, it takes 8 h to charge the battery and the same time interval to cool it down. This implies that a 24 h/7 days operation will require three batteries for each forklift. Furthermore, these operations involve the move of very heavy elements and require large battery rooms under controlled atmosphere, with the risk of hazardous materials presence. In addition, battery electric forklifts suffer from a loss of productivity as the battery discharges and show low performance under freezing conditions. Such problems could be addressed by the transition to the hydrogen powered fuel cell forklifts. Consequently, several demonstration projects have been undertaken to bring fuel cell forklifts to a commercial stage and to implement the necessary infrastructure [6–11].

The cost of the hydrogen storage and the saving in the refueling time are among the performance parameters being considered during these projects. For the majority of fuel cell forklifts tested under North American and European pilot programs, the hydrogen is supplied at pressures of 350 and 700 bar [7,10]. This corresponds to a refueling time of less than 5 min and eliminates the time consumed by the battery change-out. The choice of the pressurized hydrogen storage technique is supported by the development of the related hydrogen refueling equipment, although the infrastructure is still expensive. Furthermore, the use of compressed gaseous tank results in lighter hydrogen component system compared to the lead acid battery. Hence, additional ballast is incorporated to compensate this weight loss [7].

Solid-state hydrogen storage systems, showing poor gravimetric capacities in the case of light duty vehicles could be a suitable choice for applications such as forklift trucks since they provide weight, safety and low pressure-cost benefits over compressed gaseous storage systems. In this context, some models of fuel cell forklifts based on solid-state hydrogen storage have already been tested or are under development [7,11]. One of the first forklift trucks carrying hydrogen in a metal hydride tank has been introduced in Germany in 2000, as part of a joint project between Linde Group and Siemens AG's Power Generation Group [7]. The selected storage material is a titanium-based hydride with a charging time of 10 min. Over the past few months, researchers from Sandia National Laboratories and Hawaii Hydrogen Carriers are working together on the design of a solid-state hydrogen storage system filled with a Mischmetal-nickel-aluminium alloy [11]. The developed reactor will be integrated into the forklift fuel cell pack with the goal to show the potential storage time, cost and market growth advantages. Similarly, a wide variety of low-temperature metal hydrides extensively studied in hydrogen light duty vehicles projects could find their applications on-board forklift trucks.

Complex hydrides have high hydrogen storage capacities up to 10 wt.% and could be cost competitive compared to some metal hydrides [12]. However, their use is hindered by their slow kinetics at practical operating conditions. Recently, a new complex hydride reactor concept has been developed to overcome this weakness. It is based on the combination of $\text{LaNi}_{4.3}\text{Al}_{0.4}\text{Mn}_{0.3}$ and Li–Mg–N–H materials. The investigation of the charging process has proven the possibility to reduce the time required for the initiation of the complex hydride reaction by 600 s while starting the loading of hydrogen at room temperature [13]. In this paper, we investigate the capability of such a complex hydride reactor concept to meet the requirements of fuel cell forklift applications in terms of refueling time and system weight and size. In the first part, the charging performance of a hydrogen storage system with embedded filters, metal hydride and heat exchanger tubes is assessed through the numerical study of different reactor configurations. Thereafter, the weight and volume of the final selected reservoir design are determined in function of the fuel cell forklifts energy requirements.

Model formulation

Description of the studied configuration

In previous studies [13], the possibility of accelerating the charging process of the complex hydride, $2\text{LiNH}_2\text{-}1.1\text{MgH}_2\text{-}0.1\text{LiBH}_4\text{-}3$ wt.% ZrCoH_3 through its combination with the metal hydride, $\text{LaNi}_{4.3}\text{Al}_{0.4}\text{Mn}_{0.3}$ has been proven. The studied configuration is a 50 g tubular reactor where a gas permeable separation layer (GPSL) ensures the indirect contact between the two storage media: the metal hydride at the centre of the tube, surrounded by the complex hydride. The combination reactor, initially at room temperature, is filled with hydrogen at 70 bar. Since the AB_5 material, $\text{LaNi}_{4.3}\text{Al}_{0.4}\text{Mn}_{0.3}$ is able to absorb hydrogen very quickly at these ranges of temperature and pressure, its reaction heat ensures the heat up of the complex hydride bed to temperatures above 130 °C. Furthermore, based on the kinetics measurements of the Li–Mg–N–H material at 70 bar, it has been shown that temperatures above 130 °C are required for achieving high hydrogen loading rates [14]. Accordingly, in a combination reactor, the complex hydride charging process is initiated without the need of external heat source integration. The numerical investigation of the combination reactor charging process [13] has shown that the metal hydride, $\text{LaNi}_{4.3}\text{Al}_{0.4}\text{Mn}_{0.3}$ reaches its saturated state after only 10 s transferring then its reaction heat towards the complex hydride media. As a result, the Li–Mg–N–H material starts to absorb hydrogen in the region close to the GPSL and a reaction front is developed from the core to the annulus of the reactor. As the reaction proceeds, the complex hydride reaction heat is removed by the heat transfer fluid circulating through the reactor wall. Overall, the time required for the initiation of the complex hydride reaction is reduced by 600 s although the combination reactor charging process starts from room temperature.

A subsequent study of the same configuration with different thicknesses of the MeH and CxH materials has

proven that the dimensions of the two storage media should be chosen carefully in order to avoid slow CxH hydrogen charging process due to kinetics or heat transfer limitations [15]. A hydrogen charging time of 387 s has been achieved for a combination reactor of 10 mm and 12.5 mm for the metal hydride and complex hydride bed thicknesses, respectively. The scale up of such a configuration for the storage of higher amount of hydrogen (≥ 1 kg H_2) will result in a multi-tubular reactor design.

In this paper, we discuss the capability of a large cylindrical solid hydrogen storage system based on the advanced reactor concept described above to achieve fast hydrogen loading rate and short charging time. The motivation to select such a configuration is to present a comparison with the large pressurized hydrogen cylinders used for vehicles applications, in particular forklift trucks, in terms of refueling time as well as weight and size requirements. Accordingly, the dimensions (a diameter of 32 cm) of the studied reactor have been chosen comparable to those of gaseous storage tanks studied in Refs. [16,17].

In this context, the extensively studied configuration of the cylindrical reactor with embedded multiple filters and heat exchanger tubes has been selected [18–20]. Similar to the previous studies [13], [15], the two storage media, $2LiNH_2 \cdot 1.1MgH_2 \cdot 0.1LiBH_4 \cdot 3 \text{ wt.\%ZrCoH}_3$ and $LaNi_{4.3}Al_{0.4}Mn_{0.3}$, have been selected as reference materials and are abbreviated in the following text as CxH and MeH. Three different designs of the hydrogen storage system have been considered as shown in Fig. 1.

To adapt the multiple tubes and filters configuration to the present, the MeH material is filled into annular tubes distributed uniformly through the complex hydride bed in an octagonal arrangement. Since the AB_5 material should react first, the hydrogen injection tubes are at the centre of the MeH media and the hydrogen diffuses towards the complex hydride material through the gas permeable layer separating the two storage media. The coolant tubes are placed at the centre of the triangle arrangement formed by the three connected hydrogen injection tubes to remove the released CxH reaction heat since the CxH material starts to react mainly at the region close to the MeH media.

The optimization of the hydrogen charging process depends on the amount of the metal hydride required to initiate the CxH reaction as well as the thermal management of the CxH reaction heat. Therefore, two alternatives are examined in this study.

- Increasing the thickness of the MeH media, d_{MeH} while keeping the same number of coolant tubes, as shown in Case 1, Fig. 1.
- Increasing the number of the MeH annular tubes while keeping constant their thickness, d_{MeH} . Accordingly, the number of hydrogen injection tubes and coolant tubes is increased as illustrated in Cases 1–3, Fig. 1.

For all the studied cases, the diameters of the large combination reactor and the hydrogen injection tubes are set constant whereas the one of the coolant tubes decreases with their increasing number. The details of the corresponding combination reactor geometries are summarized in Table 1.

Governing equations

The mathematical model describing the heat and mass transfer in the combination reactor includes the kinetics equations, the hydrogen mass balance and the energy balance of the two storage media. It is developed based on the following assumptions.

- There is a local thermal equilibrium (LTE) between the MeH material, the CxH material and the hydrogen gas.
- The porosities of the complex and metal hydrides are constant.
- The thermo-physical properties of the two hydride beds are independent of the transformed fractions, the pressure and the temperature.
- The influence of the GPLS on heat and mass transport is neglected.
- The thermal contact resistance is neglected between the MeH bed and the hydrogen injection tubes and the CxH bed and the coolant tubes.

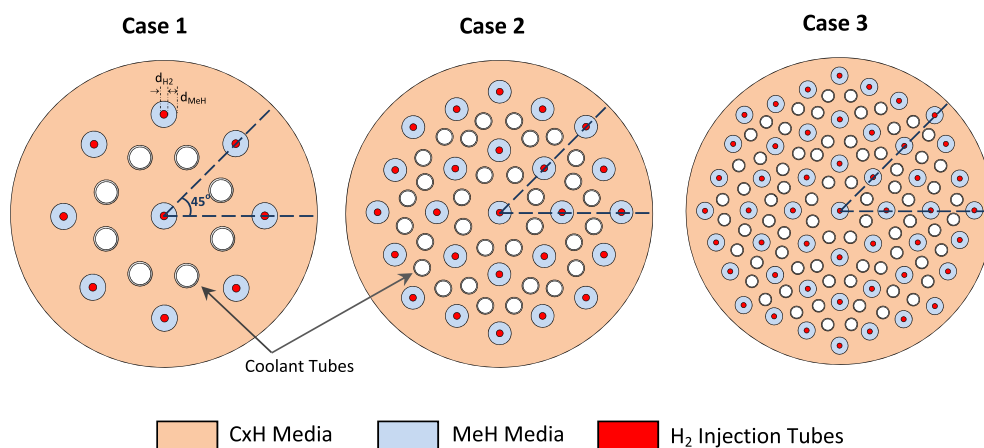


Fig. 1 – Geometries of the three studied configurations of the combination reactor with different numbers of MeH and coolant tubes.

Table 1 – Details of the combination reactor geometries.

	Case 1			Case 2	Case 3
	a	b	c		
Inner diameter of combination reactor (cm)				32	
Diameter of H ₂ injection tubes (cm)				0.6	
Metal hydride thickness (cm)	0.7	1.7	2.7	0.7	0.7
Diameter of coolant tubes (cm)		1.8		1.6	1.4
Coolant tube wall thickness (cm)				0.1	
Number of H ₂ injection tubes	9			25	49
Number of coolant tubes		16		32/41	72/96

- The bulk temperatures of the heat transfer fluid and the hydrogen supplied to the bed are constant and uniform.
- The equation of state for hydrogen is given by the simplified van der Waals equation.

Kinetics equations

Reaction kinetics of both, metal and complex hydrides are determined based on their measured hydrogen charging rates under different conditions of temperature and pressure as described in Ref. [14].

The transformed fractions x_{MeH} and x_{CxH} for the two storage media are defined in function of the bed weight fractions of stored hydrogen, $w_{f,\text{CxH}}$ and $w_{f,\text{MeH}}$ as

$$x_{\text{MeH}} = \frac{w_{f,\text{MeH}}}{w_{f,\text{MeH},\text{max}}} \quad (1)$$

$$x_{\text{CxH}} = \frac{w_{f,\text{CxH}}}{w_{f,\text{CxH},\text{max}}} \quad (2)$$

and their temporal evolutions are expressed by the following equations:

- MeH material

$$\frac{\partial x_{\text{MeH}}}{\partial t} = A_{a,\text{MeH}} \exp\left(-\frac{E_{A,\text{MeH}}}{RT}\right) \log\left(\frac{P}{\text{Peq}_{a,\text{MeH}}}\right) \times (1 - x_{\text{MeH}}) \quad (3)$$

- CxH material

$$\frac{\partial x_{\text{CxH}}}{\partial t} = \begin{cases} A_{a,\text{CxH},1} \exp\left(-\frac{E_{A,\text{CxH},1}}{RT}\right) \frac{(P - \text{Peq}_{a,\text{CxH}})}{\text{Peq}_{a,\text{CxH}}} \times 0.33 & 0 \leq x_{\text{CxH}} \leq 33\% \\ A_{a,\text{CxH},2} \exp\left(-\frac{E_{A,\text{CxH},2}}{RT}\right) \frac{(P - \text{Peq}_{a,\text{CxH}})}{\text{Peq}_{a,\text{CxH}}} \times (1 - x_{\text{CxH}}) & 33\% \leq x_{\text{CxH}} \leq 100\% \end{cases} \quad (4)$$

The equilibrium pressures $\text{Peq}_{a,\text{CxH}}$ and $\text{Peq}_{a,\text{MeH}}$ are based on the van't Hoff equation

$$\text{Peq}_{a,\text{CxH}} = P_0 \exp\left(\frac{\Delta H_{a,\text{CxH}}}{RT} - \frac{\Delta S_{a,\text{CxH}}}{R}\right) \quad (5)$$

$$\text{Peq}_{a,\text{MeH}} = P_0 \exp\left(\frac{\Delta H_{a,\text{MeH}}}{RT} - \frac{\Delta S_{a,\text{MeH}}}{R}\right) \quad (6)$$

Hydrogen mass balance

The density of the hydrogen gas is calculated based on the simplified van der Waals equation

$$\rho_g = \frac{PM_{\text{H}_2}}{[RT + (b - a/RT)P]} \quad (7)$$

and the Darcy's law is used for the description of the hydrogen gas velocity

$$\vec{v} = -\frac{K}{\mu_g} \nabla P \quad (8)$$

The hydrogen mass balance is given by

$$\frac{\partial(\epsilon \rho_g)}{\partial t} + \nabla \cdot (\rho_g \vec{v}) = -(1 - \epsilon) \dot{m}_R \quad (9)$$

Bed energy balance

During the charging process of the two storage media, the convective heat transfer of the gas phase, the heat transfer by thermal conduction in gas and solid phases, the reaction heat source and the pressure work are considered. Accordingly, the energy equation can be written as

$$\begin{aligned} \left[(1 - \epsilon) C_{p,\text{bed}} \rho_{\text{bed}} + \epsilon C_{p,g} \rho_g \right] \frac{\partial T}{\partial t} = & -C_{p,g} \rho_g \vec{v} \cdot \nabla T - \nabla \cdot (-k_{\text{bed}} \nabla T) \\ & - (1 - \epsilon) \dot{m}_R \Delta H_R + \alpha_v T \left(\epsilon \frac{\partial P}{\partial t} \right. \\ & \left. + \vec{v} \cdot \nabla P \right) \end{aligned} \quad (10)$$

\dot{m}_R and α_v are the mass change of hydrogen and the general volumetric thermal expansion coefficient for real gases, respectively. They are expressed as

$$\dot{m}_R = \rho_{\text{bed}} w_{f,s,\text{max}} \frac{\partial x}{\partial t} \quad (11)$$

$$\alpha_v = -\frac{1}{\rho_g} \left. \frac{\partial \rho_g}{\partial T} \right|_P \quad (12)$$

Wall tube energy balance

The energy equation for the stainless steel wall tube is

$$C_{p,s,s} \rho_{s,s} \frac{\partial T_{s,s}}{\partial t} = -\nabla \cdot (-k_{s,s} \nabla T_{s,s}) \quad (13)$$

Initial and boundary conditions

Initially, the MeH and CxH storage media are at a fully desorbed state. Their initial temperature and pressure are set to 22 °C and 1 bar.

To initiate the MeH charging process, the hydrogen pressure in the injection tubes increases exponentially to 70 bar, resulting in a pressure gradient which allows the gas to flow from the tubes into the metal and complex hydride beds.

At the same time, a heat transfer fluid flows through the stainless steel tubes at 130 °C. This leads first to a temperature increase in the surrounding CxH media which promotes the initiation of the complex hydride reaction. Thereafter, the heat transfer fluid acts as a coolant once the CxH starts to absorb hydrogen. It should be noted here that the coolant temperature of 130 °C has been carefully chosen by taking into account the compromise between the efficient cooling of the CxH bed due to its exothermic reaction nature and the need to maintain it at a temperature above 130 °C in order to ensure high hydrogen loading rates as discussed in Ref. [14].

In most studies, an adiabatic boundary condition is applied at the wall of the hydrogen injection tube [18], [21]. However, an analysis conducted by Na Ranong et al. [22] revealed that applying such a boundary condition is not appropriate since it does not predict the cooling effect of the inlet hydrogen on the loading behavior. In this study, this aspect is described by applying a heat flux boundary condition at the H₂ injection tubes wall

$$-\vec{n} \cdot (-k_{\text{MeH}} \nabla T_{\text{MeH}}) = h_{\text{H}_2} (T_{\text{H}_2} - T_{\text{MeH}}) \quad (14)$$

The reaction heat released during the charging process of the CxH material is transferred towards the heat transfer fluid through the lateral stainless steel tube surface, whereas the external reactor wall is thermally insulated. Thus, a heat flux boundary condition is applied at each coolant tube wall

$$-\vec{n} \cdot (-k_{\text{S,S}} \nabla T_{\text{S,S}}) = h_{\text{cool}} (T_{\text{cool}} - T_{\text{S,S}}) \quad (15)$$

The metal and complex hydrides properties as well as the coolant conditions used in the mathematical model are summarized in Table 2.

Numerical procedure

The mathematical model presented above has been validated for a 50 g lab-scale tubular reactor [13]. Here, it is applied to the cylindrical reactor configurations depicted in Fig. 1. The modeled domains are taken as one-eighth of the cross sections due to symmetry considerations (45°). The commercial finite element software, COMSOL Multiphysics®, version 4.4, has been used to carry out the numerical study and mesh sensitivity tests have been performed for all the studied configurations especially at the complex hydride/metal hydride

Table 2 – Input data for simulations [13].

Parameter	Symbol	Value
LaNi_{4.3}Al_{0.4}Mn_{0.3} material (MeH)		
Arrhenius parameter for abs (s ⁻¹)	A _{a,MeH}	100
Activation energy for abs (J mol ⁻¹ K ⁻¹)	E _{A,MeH}	21,000
Enthalpy of absorption reaction (J mol ⁻¹)	ΔH _{a,MeH}	-35,940
Entropy of absorption reaction (J mol ⁻¹ K ⁻¹)	ΔS _{a,MeH}	-98.58
Specific heat capacity (J kg ⁻¹ K ⁻¹)	C _{p,MeH}	420
Material density (kg m ⁻³)	ρ _{MeH}	8,200
Thermal conductivity (W m ⁻¹ K ⁻¹)	k _{MeH}	1.2
Permeability (m ²)	K	1 × 10 ⁻¹²
Max. gravimetric H ₂ storage capacity (wt.%)	w _{f,MeH,max}	(1.2126 - 0.0003T[°C] - 9.10 ⁻⁶ T ² [°C ²])/100
Li-Mg-N-H material (CxH)		
Arrhenius parameter for abs, 1st step (s ⁻¹)	A _{a,CxH,1}	2.729 × 10 ¹⁷
Arrhenius parameter for abs, 2nd step (s ⁻¹)	A _{a,CxH,2}	4.678 × 10 ¹⁴
Activation energy for abs, 1st step (J mol ⁻¹ K ⁻¹)	E _{A,CxH,1}	164,800
Activation energy for abs, 2nd step (J mol ⁻¹ K ⁻¹)	E _{A,CxH,2}	147,800
Enthalpy of absorption reaction (J mol ⁻¹)	ΔH _{a,CxH}	-38,000
Entropy of absorption reaction (J mol ⁻¹ K ⁻¹)	ΔS _{a,CxH}	-111
Specific heat capacity (J kg ⁻¹ K ⁻¹)	C _{p,CxH}	1,533
Material density (kg m ⁻³)	ρ _{CxH}	900
Thermal conductivity (W m ⁻¹ K ⁻¹)	k _{CxH}	0.35
Permeability (m ²)	K	1 × 10 ⁻¹²
Max. gravimetric H ₂ storage capacity (wt.%)	w _{f,CxH,max}	3.2
Porosity (MeH, CxH)	ε	0.55
Heat transfer		
Specific heat capacity of steel (J kg ⁻¹ K ⁻¹)	C _{p,S,S}	500
Density of steel (kg m ⁻³)	ρ _{S,S}	8,000
Thermal conductivity of steel (W m ⁻¹ K ⁻¹)	k _{S,S}	15
Coolant temperature (°C)	T _{cool}	130
Heat transfer coefficient for coolant (W m ⁻² K ⁻¹)	h _{cool}	220
Hydrogen temperature in the injection tube (°C)	T _{H₂}	22
Heat transfer coefficient for H ₂ in injection tubes (W m ⁻² K ⁻¹)	h _{H₂}	50
Hydrogen gas		
Coefficient, van der Waals equation (Pa m ⁶ mol ⁻²)	a	0.025
Coefficient, van der Waals equation (m ³ mol ⁻¹)	b	2.66 × 10 ⁻⁵
Molecular weight of gas (g mol ⁻¹)	M _{H₂}	2.016
Gas constant (J mol ⁻¹ K ⁻¹)	R	8.314
Dynamic viscosity (Pa s)	μ _g	10 ⁻⁵ × 9.05 × (T/293) ^{0.68}
Heat capacity (J kg ⁻¹ K ⁻¹)	C _{p,g}	14,304

boundaries to accommodate high spatial temperature gradients during the initiation stage of the CxH reaction. As a result, the temporal evolution of temperature and amount of stored hydrogen related to the different selected configurations are compared in order to assess the charging performance of the combination reactor.

Results and discussion

Effect of the MeH bed thickness

As a first attempt to study the dependence of the charging process on the amount of the metal hydride that should be used, the configuration of a combination reactor equipped with 9 MeH tubes and 8 coolant tubes has been selected. The thickness of the MeH bed, d_{MeH} is varied from 0.7 cm to 1.7 and 2.7 cm (Cases 1.a–c, Table 1). The spatial evolutions of temperature and transformed fraction of hydrogen at different selected times are shown in Fig. 2.

For both metal and complex hydrides, the exothermic charging processes are controlled by the driving forces defined as the ratio and the difference between the charging pressure and their equilibrium pressures, respectively (see Eqs. (3)–(6)). If the heat of reaction is not efficiently removed, the equilibrium temperature can be reached implying that the equilibrium pressure is almost equal to the hydride bed pressure and the uptake of hydrogen can be delayed or even stopped. In such case, the hydriding process is thermally limited. Consequently, for a charging pressure of 70 bar, the MeH and CxH beds temperatures should not exceed the equilibrium temperatures of 295 °C and 230 °C, respectively in order to ensure fast hydrogen loading rates.

For the metal hydride bed, this thermal limitation is not observed. Indeed, for the three studied cases, the metal hydride reacts very fast, so that after 60 s, the MeH media is the hottest region of the reactor with a temperature up to 250 °C and it is already saturated ($x_{\text{MeH}} = 1$). The MeH reaction heat is then transferred to the CxH material initiating its loading process, and a reaction front growing from

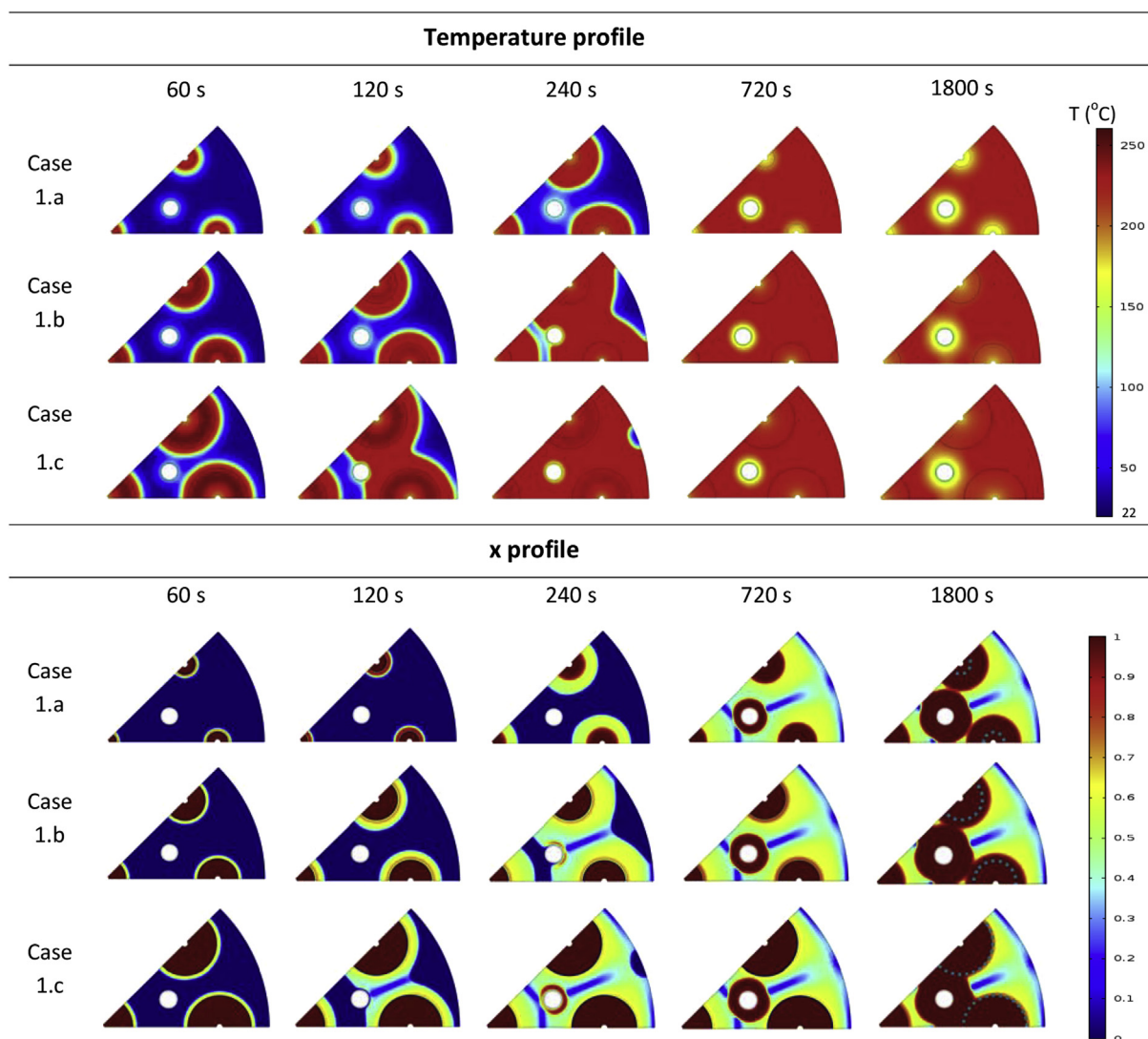


Fig. 2 – Evolution of temperature and transformed fraction of hydrogen for the first configuration with different thicknesses of MeH tubes at selected times.

the MeH annular tubes to the surrounding CxH area can be observed ($t = 120$ s).

The MeH reaction heat released during the absorption of hydrogen is proportional to the mass of the metal hydride introduced in the annular tubes. Thus, more heat is generated in Case 1.c ($d_{\text{MeH}} = 2.7$ cm) and a larger complex hydride area reaches or even exceeds the required kinetics temperature (130 °C) which promotes the CxH charging process. Indeed, at $t = 240$ s, the hydrogen uptake is almost occurring throughout the entire zone of the complex hydride while for Cases 1.a, b, the temperature and the fraction of stored hydrogen continue their slow increase mainly close to the MeH annular tubes.

At $t = 720$ s, the CxH material reaches its equilibrium temperature (230 °C at 70 bar) and the charging process of this material becomes thermally limited for the three studied cases. The hydrogen uptake is mainly occurring around the coolant tube where the temperature is the lowest whereas it has not even begun at the outer periphery of the reactor.

As time progresses from 720 s to 1800 s, more CxH reaction heat is removed by the coolant and larger CxH saturated area can be observed around the heat exchanger tube. Furthermore, there is more hydrogen uptake by the CxH material around the injection tubes in Cases 1.a, b compared to Case 1.c as it can be noted from the transformed fraction profile, x at $t = 1800$ s: a blue dashed line is added to distinguish between the two saturated areas (x_{MeH} and $x_{\text{CxH}} = 1$). This is due to the fact that there is less MeH material introduced in the annular tubes when d_{MeH} decreases (0.7 cm and 1.7 cm in Cases 1.a, b compared to 2.7 cm in Cases 1.c). Therefore, the cooling effect of the hydrogen flowing through the injection tubes is more pronounced in the CxH area around the MeH tubes. As a result, the CxH temperature in this region falls below the equilibrium temperature which promotes the CxH reaction. For the rest of the CxH media, the large conduction path towards the cooling media inhibits a fast hydriding reaction.

The time evolution of weight fractions of stored hydrogen, $w_{f,\text{CxH}}$ and $w_{f,\text{MeH}}$ for Cases 1.a-c is presented in Fig. 3a. As described above, the increase of the MeH bed thickness improves the hydrogen storage rate at the beginning of the CxH charging process. Thereafter, the CxH reaction rate slows down due to the heat transfer limitation since the complex hydride bed reaches its equilibrium temperature as seen in Fig. 2 for the three studied cases. Thus, the peripheral area of the complex hydride is equipped with another coolant tube and the resulting CxH reaction rate is determined for the three cases as shown in Fig. 3b. Cooling the peripheral area of the complex hydride bed does not affect the initiation of its charging process. It rather improves the thermal management of the complex hydride bed. Accordingly, a slight increase of $w_{f,\text{CxH}}$ can be observed over time. The hydrogen loading rates of the three studied cases are almost overlapping at 1800 s, corresponding to 81% of the maximum CxH hydrogen storage capacity, $w_{f,\text{CxH},\text{max}}$.

For the metal hydride, it is clear from the time evolution of $w_{f,\text{MeH}}$ (Fig. 3a) that the material reaches its saturated state after a few seconds of starting the absorption process. The difference between the maximum capacities, $w_{f,\text{CxH},\text{max}}$ reached for the three studied cases is due to its dependence on the metal hydride bed temperature (See the expression of $w_{f,\text{CxH},\text{max}}$ in Table 2).

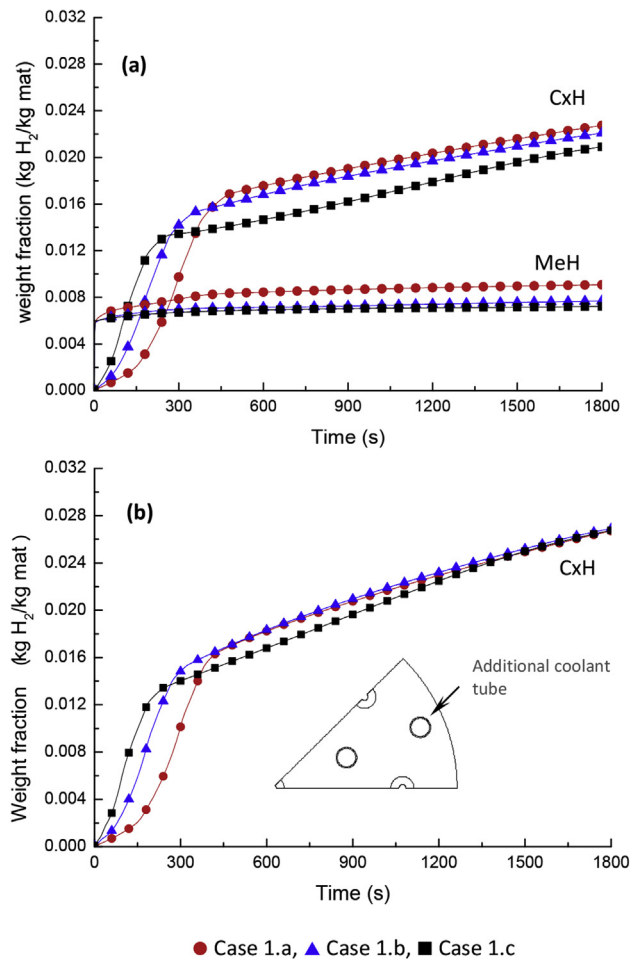


Fig. 3 – Effect of the thickness of MeH tubes on the charging process (a) without and (b) with additional coolant tube for the first configuration.

Concluding, it can be stated that for the studied configuration, the increase of the MeH bed thickness does not significantly improve the CxH charging process, in particular at the initiation stage where the reaction is not yet thermally limited. On the other hand, it is worth noting that the idea of the combination reactor concept is to use the minimum of the metal hydride material necessary for the fast initiation of the CxH reaction. Therefore, it would be better to keep thin the thickness of the MeH annular tubes while increasing their number throughout the CxH media. This is the subject of the next section.

Effect of the number and the arrangement of MeH and coolant tubes

As described above, the hydrogen charging process in the combination reactor proceeds in two stages. First, the metal hydride starts to absorb hydrogen while releasing reaction heat which is used to initiate the charging process of the CxH. Then, in the second stage, the uptake of H₂ by the complex hydride continues to proceed. In this case, the CxH reaction heat should be efficiently dissipated by the cooling media.

Otherwise, the temperature will reach the equilibrium, lowering then the CxH reaction rate.

Increasing the number of MeH and coolant tubes results in shorter conduction paths for both, metal and complex hydrides reaction heats. Therefore, a faster initiation stage of the CxH reaction and a better thermal management of the CxH bed could be expected. This is confirmed by the spatial evolution of temperature and transformed fraction of hydrogen shown in Fig. 4. The studied configurations and their geometrical parameters are presented in Fig. 1 and Table 1, respectively.

At 60 s in Case 3, the MeH reaction heat is distributed almost uniformly through the CxH media that has consequently reached almost everywhere the required 130 °C minimum temperature. As a result, faster CxH reaction rate can be observed in comparison with Cases 1.a and 2. Therefore, it takes in this case only 120 s for the hydrogen uptake to proceed overall the CxH media while the reaction still

continues to occur slowly for the two other cases, mainly close to the MeH tubes.

As time progresses from 240 s to 720 s, the generated thermal energy in Case 3 is continuously transferred towards the cooling media. Accordingly, more CxH material is transformed and reaches the saturated state. Therefore, the CxH temperature drops back to the coolant temperature, T_{cool} except for the peripheral region, where it is still close to 230 °C. This reflects the poor heat management in this area. Cases 1.a and 2 continue to show a poor hydrogen uptake even after 1800 s due to the heat transfer limitation.

The behavior of the combination reactor described above is supported by the temporal evolution of the hydrogen loading rates presented in Fig. 5. At $t = 120$ s, the weight fraction of stored hydrogen, $w_{f,CxH}$ represents 46.87%, 18.12% and 4.68% of the maximum CxH hydrogen storage capacity, $w_{f,CxH,max}$ for Cases 1.a, 2 and 3, respectively. This is almost twice the stored fraction for Case 1.c ($d_{MeH} = 2.7$ cm) at the same time (see

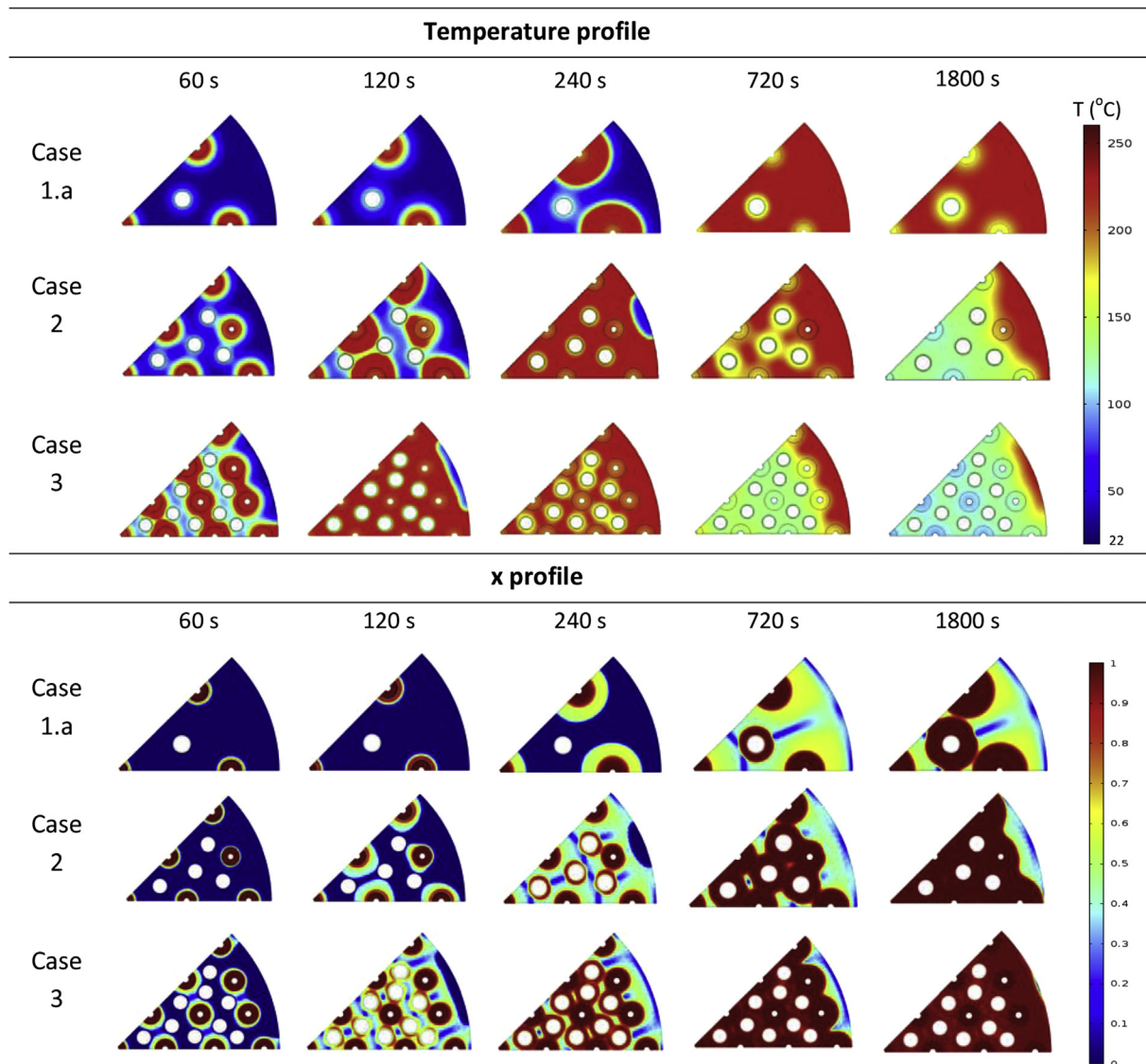


Fig. 4 – Evolution of temperature and transformed fraction of hydrogen for the three studied configurations with different numbers of MeH and coolant tubes at selected times.

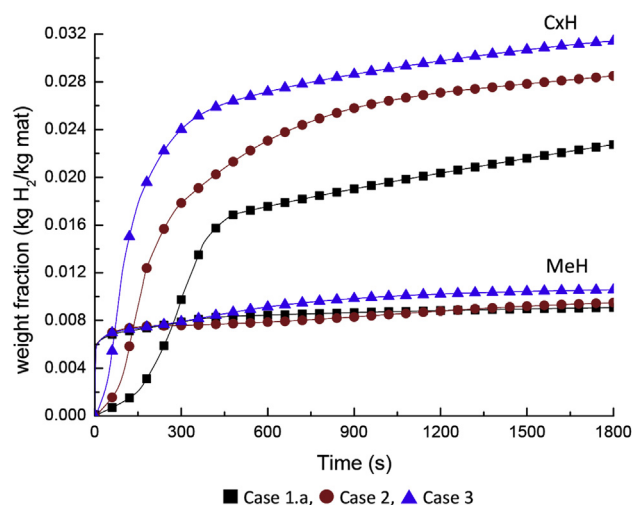


Fig. 5 – Effect of the number of MeH and coolant tubes on the charging process for the three studied configurations.

Fig. 3). Thus, it is clear that the third configuration is the most advantageous for the initiation stage of the CxH charging process. However, after 120 s, the hydrogen uptake becomes limited by the heat transfer, which explains the slow hydrogen loading rate and the long-time interval to fully charge the complex hydride (1800 s). For Cases 1.a and 2, only 71% and 89% of $w_{f,CxH,max}$ are reached after the same time interval due to the combined effect of kinetics and heat transfer limitations.

The large length scale for heat transfer within the peripheral area of the complex hydride coupled with its low thermal conductivity contributes to the inefficient use of the storage media. Such problem could be addressed by cooling efficiently the external CxH zone or/and increasing the material thermal conductivity.

Improvement of the combination reactor charging performance

Since the metal hydride reaches its saturated state within few seconds of the charging process, this section is devoted to the optimization of the hydrogen uptake by the complex hydride and only results of CxH temperature and the related hydrogen loading rate are presented.

Effect of adding coolant tubes in the peripheral CxH area

As a first attempt to improve the charging performance of the combination reactor, Cases 2 and 3 (see Fig. 1) are selected and their peripheral CxH area is equipped with coolant tubes as shown in Fig. 6. The temporal evolution of the average CxH bed temperature and the weight fraction of stored hydrogen, $w_{f,CxH}$ are presented in the same graph.

For both cases, with and without addition of coolant tubes in the peripheral area, the peak of the average CxH temperature is reached at the same time. From that moment, the charging process is driven by the heat transfer and the role of the added heat exchanger tubes comes into play to cool faster the complex hydride. As a result, the time required to fill the CxH media to 90% of its maximum hydrogen storage capacity

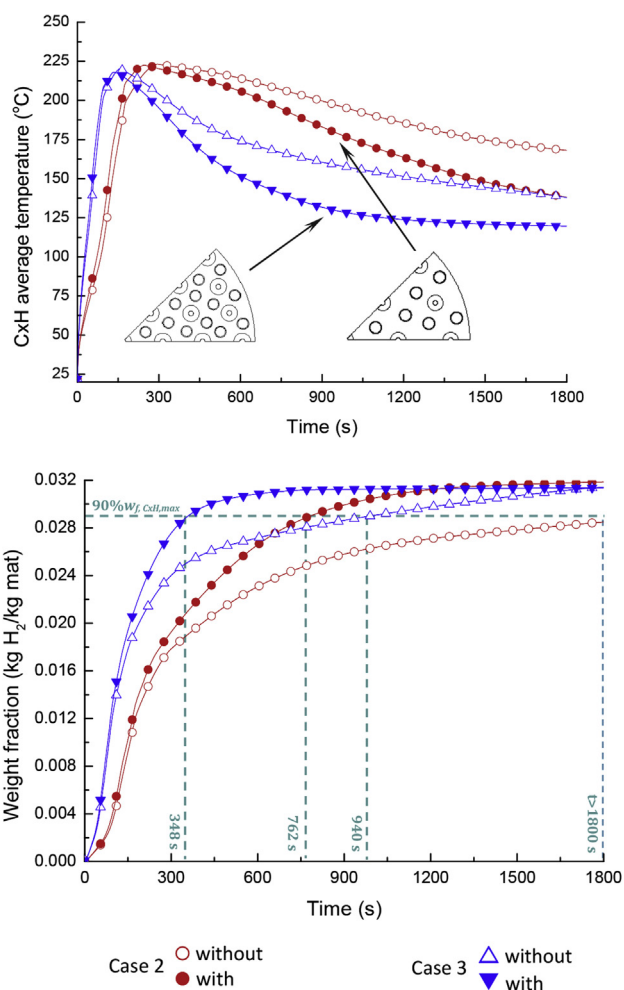


Fig. 6 – Effect of the addition of coolant tubes in the CxH peripheral area on its charging process for the second and third configurations.

decreases from more than 1800 s to 762 s in Case 2, and from 940 s to 348 s in Case 3, respectively.

Effect of the CxH thermal conductivity

In this study, a value of 0.35 W/(m K) is used for the thermal conductivity of the complex hydride bed. However, higher values of k_{CxH} (>10 W/(m K)) can be achieved by mixing the material with expanded natural graphite and compacting it in pellets as described in Ref. [23]. Thus, the dependence of the CxH charging process on the thermal conductivity is assessed and results are illustrated in Fig. 7 for the three studied configurations (Fig. 1). Based on the temporal evolution of the average CxH bed temperature and its hydrogen loading rate, three different behaviors of the CxH media are reported.

In Case 1, a slight increase of the CxH thermal conductivity, k_{CxH} delays the initiation of the CxH reaction by approximately 900 s. This is due to the fact that the amount of the MeH reaction heat is not enough to bring the CxH media to the optimum temperature for the reaction kinetics. Indeed, kinetics measurements have shown that temperatures above 130 °C are required to reach high hydrogen loading rates [14].

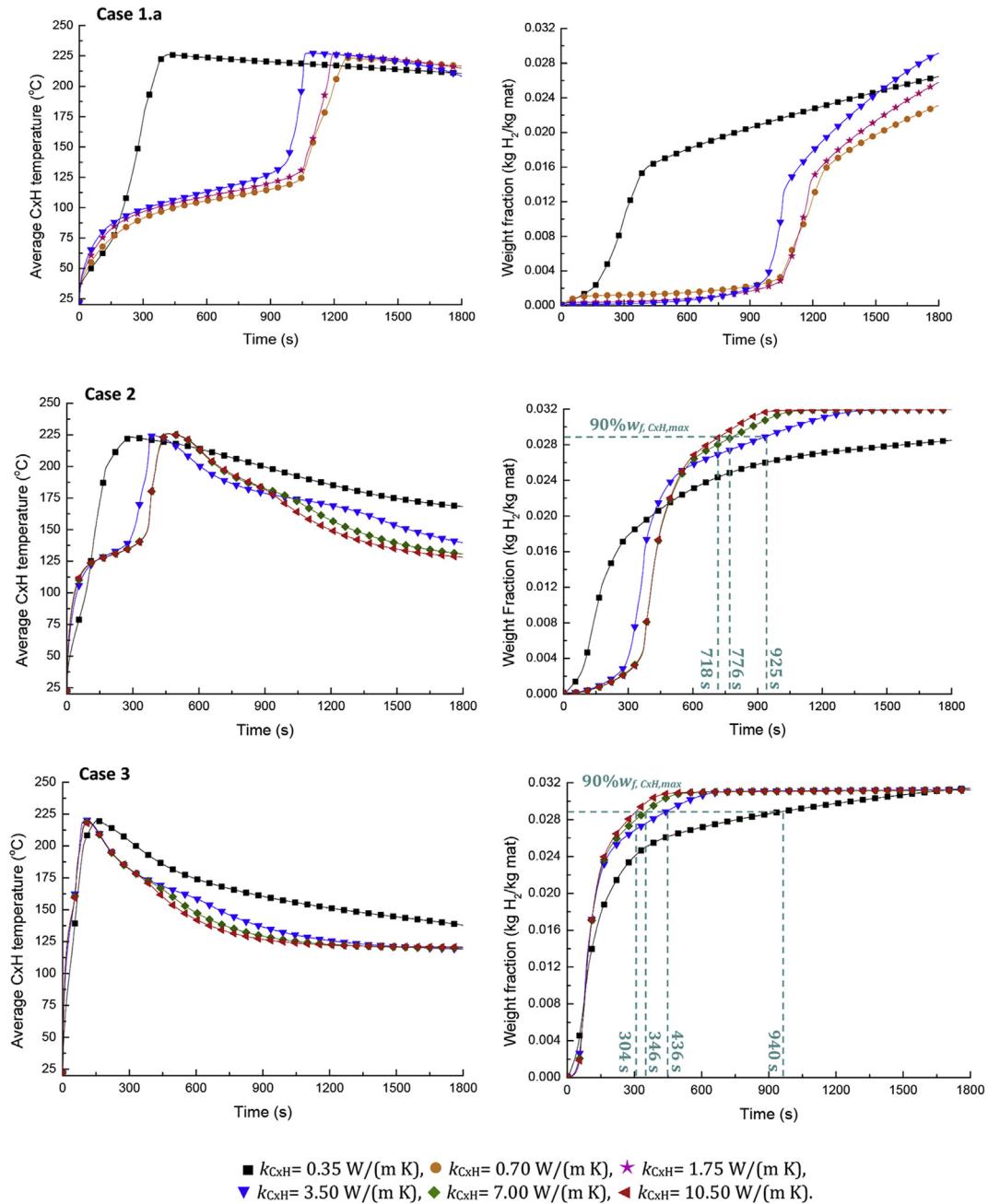


Fig. 7 – Effect of the complex hydride thermal conductivity on the CxH charging process for the three studied configurations.

Accordingly, an increase of the CxH thermal conductivity results in an overcooling of the CxH storage media since the MeH reaction heat is mainly conducted to the cooling media rather than heating the CxH media up to 130 °C and the charging process becomes limited by the kinetics.

The same trend is observed in Case 2 for higher values of k_{CxH} ; however the initiation of the CxH charging process is only delayed by 300 s. Thereafter, the increase of k_{CxH} leads to better heat management of the CxH media and the time required to reach 90% of the maximum hydrogen storage capacity, $w_{f,\text{CxH,max}}$ is decreased to 718 s for $k_{\text{CxH}} = 10.5 \text{ W/(m K)}$. This result is comparable to the one obtained by the addition of the coolant tubes in the CxH peripheral region

(Fig. 6). In this case, it is obvious that the CxH charging process is compromised by both, kinetics and heat transfer limitations.

In Case 3, the initiation of the CxH reaction is not affected anymore by the increase of k_{CxH} since a huge amount of MeH reaction heat is released due to the increase of the MeH annular tubes (49 MeH tubes in this case comparable to 9 in Case 1 and 25 in Case 2, see Table 1) and the charging process is only thermally limited. Therefore, the increase of k_{CxH} promotes an efficient use of the CxH storage media and it takes about 300 s to fill the complex hydride to 90% of its maximum hydrogen storage capacity for $k_{\text{CxH}} = 10.5 \text{ W/(m K)}$.

Combination of the two effects

Based on the results presented above, it is clear that there is no need for further improvement of the heat management in Cases 1 and 2 since this leads to kinetics limitation of the CxH charging process. Thus, the third configuration is selected here to combine the effects of equipping the CxH peripheral area with coolant tubes and increasing the CxH thermal conductivity. The temporal evolution of the hydrogen loading rate resulting from such a combination reactor is shown in Fig. 8.

The main result is that in this case, the CxH media can be filled to 90% of its maximum hydrogen storage capacity after only 200 s, a time interval competitive with the one achieved by a compressed gaseous storage system. It is interesting to note also that there is no need to increase the thermal conductivity, k_{CxH} more than 3.5 W/(m K) and that the initiation stage of the CxH reaction is only slightly affected by the increase of this parameter.

Impact on weight and volume constraints based on the forklift energy requirement

In order to determine the equivalence between electricity and hydrogen, most studies covered electric forklifts including Classes I, II and III with lift capacities ranging from 3000 lb to 20,000 lb [5]. The energy use by a forklift is evaluated considering 8 h of use per shift and a maximum of 3 shifts per day. Results vary depending on the efficiency of the fuel cell and the battery energy capacity used in calculations. Renquist et al. [24] reported a hydrogen consumption of 1.75 kg/shift/ forklift as an equivalence of 35 kWh DC battery energy content/shift. Elgowainy et al. [4] used the equivalency of 15 kWh at the wheels/fork to the consumption of 1 kg H₂ per fuel cell. Larriba et al. [5] based their calculation on a discharge battery capacity of 80% per shift and determined the hydrogen tank capacity to be equal to 1.8 kg H₂, 1.2 kg H₂ and 0.72 kg H₂ for Classes I, II and III forklifts, respectively.

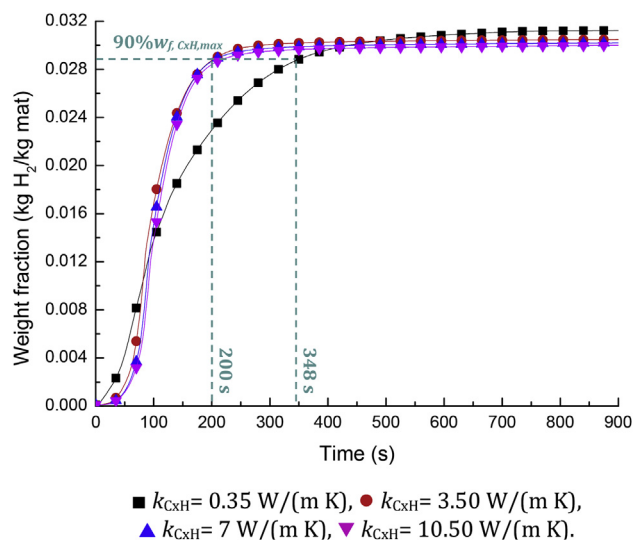


Fig. 8 – Combined effects of increasing the CxH thermal conductivity and adding coolant tubes in the CxH peripheral area for the third configuration.

In this study, the weight and volume of the hydrogen storage system, including the metal and complex hydrides, the hydrogen injection tubes and the stainless steel tubes, are calculated for the three classes of the forklift trucks based on the hydrogen tank capacities reported in Ref. [5]. Calculations are performed for the third configuration with and without addition of coolant tubes in the CxH peripheral area (Fig. 1 and Table 1, Case 3). Simulation results presented in the previous section have proven the charging performance of those configurations, resulting in refueling times close or even less than 5 min. Fig. 9 illustrates their related weights and volumes depending on the energy fuel cell forklift requirement.

McWhorter et al. [25] reported that a hydrogen system component with a H₂ fuel capacity of 2.5 kg will require a minimum weight of 200 kg and a volume less than 230 l to support a 10 kW fuel cell forklift vehicle. The calculated weights and volumes of the selected configurations presented in Fig. 9 are in line with those expectations. It should be noted here that the mass of the lids and the external tank wall as well as the material that could be used to improve the CxH thermal conductivity are not included in the calculations.

Nonetheless, it is relevant to note that for the selected configurations, the mass of the metal hydride is almost twice the mass of the complex hydride and the latter represents 66% of the total volume of the storage system, suggesting less interest to the combination of the two storage media. However, given the refueling time of 3 min achieved by the optimum configuration, such a complex reactor concept is attractive. Indeed, the simulation of the sorption process for the third configuration filled with pure LaNi_{4.3}Al_{0.4}Mn_{0.3} material and equipped with 96 coolant tubes has shown that it takes 452 s to reach 90% of the MeH maximum storage capacity (the result is not shown here), compared to 348 s and 200 s in the case of the combination reactor with the same number of coolant tubes, without and with improvement of the CxH thermal conductivity ($k_{\text{CxH}} = 0.35$ and 3.5 W/(m K) respectively). This loading time is achieved when the MeH reactor, initially at room temperature of 22 °C, is charged at 70 bar and the heat transfer fluid is flowing through the coolant tubes at 22 °C with a convective heat transfer coefficient, h_{cool} of 220 W/(m² K). The thermal conductivity of the MeH material is set at 1.2 W/(m K). Although shorter loading times for both, pure MeH and combination reactors could be expected by increasing h_{cool} which means the increase of the coolant mass flux, this might be an issue since more energy will be required to pump the coolant through the heat exchanger tubes.

A better performance of the studied combination reactor could be achieved by using the complex hydride material in pellets form which will improve its thermal conductivity, its density and its volumetric hydrogen capacity as discussed in Ref. [23].

It should also be emphasized that despite the increase of the CxH thermal conductivity (10.5 W/(m K) in Case 3 (Fig. 7) and 3.5 W/(m K) in Case 3 with the addition of coolant tubes in the CxH peripheral area (Fig. 8)), a big number of coolant tubes is used to ensure the efficient heat management of the CxH bed (72 and 96 coolant tubes for the two selected cases, respectively). As a result, the mass of the CxH material is decreased compared to the MeH as shown in Fig. 9. The use of radial fins could improve both, the mass and volumetric ratios

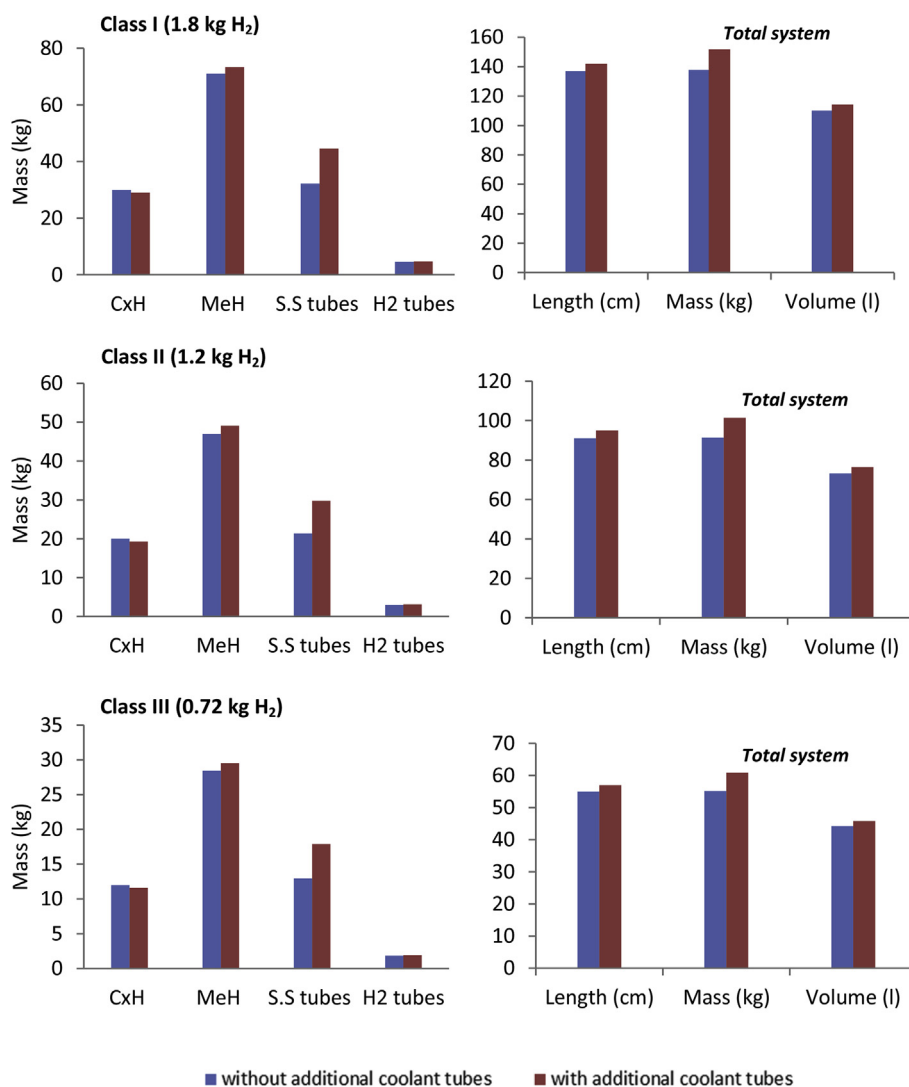


Fig. 9 – Weights and volumes of the optimum configurations of the combination reactor depending on the fuel cell forklifts energy requirements.

of the CxH media by reducing the number of coolant tubes for the same range of CxH thermal conductivity. Such a behavior has been observed in the case of sodium alanate storage systems [20] [26], and a configuration of a combination reactor equipped with smaller number of coolant tubes and radial fins would be the object of a future study.

In addition, considering the growing interest to the high temperature proton exchange fuel cells (HT-PEMFCs) operating at a temperature range of 100–200 °C [27], the proposed complex hydride reactor concept is suitable since it allows the use of the high thermal energy produced from HT-PEMFCs.

Conclusion

In this paper, the commercial finite element software, COMSOL Multiphysics has been used to optimize the charging process of a hydrogen storage system based on the combination of $\text{LaNi}_{4.3}\text{Al}_{0.4}\text{Mn}_{0.3}$ and Li–Mg–N–H materials. The

studied configuration is a large cylindrical reactor embedded with a variable number of MeH and coolant tubes. Simulation results have shown that increasing the number of MeH and coolant tubes leads to better use of the storage media since it results:

- First, in more MeH reaction heat distributed uniformly through the CxH media which promotes the initiation stage of the CxH reaction.
- Second, in shorter heat conduction path towards the heat transfer fluid, ensuring an efficient heat management during the CxH reaction.

A refueling time of 15 min has been achieved for the configuration with 49 MeH annular tubes of 0.7 cm of thickness and 72 coolant tubes of 1.4 cm of diameter. However, the spatial distribution of the corresponding CxH temperature has shown that the inefficient heat removal at the peripheral region of the complex hydride is responsible for the slow CxH

hydriding process. Accordingly, two effects are considered, increasing the number of coolant tubes in this area or/and increasing the thermal conductivity of the complex hydride. Comparable refueling times of 5 min are obtained by considering these two effects separately whereas a charging time of almost 3 min is achieved by combining the two effects with a total number of 96 coolant tubes and a CxH thermal conductivity of 3.5 W/(m K).

The optimum configuration of the combination reactor would be suitable for integration in fuel cell forklifts applications. In addition to the competitive refueling time compared to the high pressure hydrogen storage technology, the mass and volume of the optimum configuration are in line with the forklift trucks requirements in terms of weight and size.

Acknowledgments

The research leading to these results has received funding from the European Union's Seventh Framework Programme (FP7/2007–2013) for the Fuel Cells and Hydrogen Joint Technology Initiative under grant agreement no. 256653.

M.B. would like to thank the German Academic Exchange Service (DAAD) for the DLR-DAAD Research Fellowship.

REFERENCES

- [1] Ahluwalia RK, Hua TQ, Peng JK. On-board and off-board performance of hydrogen storage options for light-duty vehicles. *Int J Hydrogen Energy* 2012;37:2891–910.
- [2] Kurtz J, Ainscough C, Simpson L, Caton M. Hydrogen storage needs for early motive fuel cell markets. 2012.
- [3] Klebanoff L, Pratt J, Johnson T, Moreno M, Arienti M. Analysis of H₂ storage needs for early market non-motive fuel cell applications. 2011.
- [4] Elgowainy A, Gaines L, Wang M. Fuel-cycle analysis of early market applications of fuel cells: forklift propulsion systems and distributed power generation. *Int J Hydrogen Energy* 2009;34:3557–70.
- [5] Larriba T, Garde R, Santarelli M. Fuel cell early markets: techno-economic feasibility study of PEMFC-based drivetrains in materials handling vehicles. *Int J Hydrogen Energy* 2013;38:2009–19.
- [6] Oorja launches Model 1 DMFC as onboard battery charger for forklifts. *Fuel Cells Bull* 2010;2010:3.
- [7] McConnell VP. Rapid refill, high uptime: running forklifts with fuel cells. *Fuel Cells Bull* 2010;2010:12–9.
- [8] Lucas L. H₂ Logic, Dantruck launch fuel cells for heavy-duty forklifts. *Fuel Cells Bull* 2011;2011:2–3.
- [9] Power B. BMW, Linde MH and TUM to trial hydrogen forklifts, tow tractors. *Fuel Cells Bull* 2013;2013:3.
- [10] Office M, Fuel Cell D. Air liquide starts up hydrogen station for IKEA France forklifts. *Fuel Cells Bull* 2014;2014:7–8.
- [11] Sandia project to speed up refueling of hydrogen forklifts. *Fuel Cells Bull* 2014;2014:6.
- [12] Jain IP, Jain P, Jain A. Novel hydrogen storage materials: a review of lightweight complex hydrides. *J Alloys Compd* 2010;503:303–39.
- [13] Bürger I, Komogowski L, Linder M. Advanced reactor concept for complex hydrides: hydrogen absorption from room temperature. *Int J Hydrogen Energy* 2014;39:7030–41.
- [14] Bürger I, Hu JJ, Vitillo JG, Kalantzopoulos GN, Deledda S, Fichtner M, et al. Material properties and empirical rate equations for hydrogen sorption reactions in 2 LiNH₂–1.1 MgH₂–0.1 LiBH₄–3 wt.% ZrCoH₃. *Int J Hydrogen Energy* 2014;39:8283–92.
- [15] Bhouri M, Bürger I, Linder M. Optimization of hydrogen charging process parameters for an advanced complex hydride reactor concept. *Int J Hydrogen Energy* 2014:1–14.
- [16] Guo J, Yang J, Zhao Y, Pan X, Zhang L, Zhao L, et al. Investigations on temperature variation within a type III cylinder during the hydrogen gas cycling test. *Int J Hydrogen Energy* 2014;39:13926–34.
- [17] Wang G, Zhou J, Hu S, Dong S, Wei P. Investigations of filling mass with the dependence of heat transfer during fast filling of hydrogen cylinders. *Int J Hydrogen Energy* 2014;39:4380–8.
- [18] Mohan G, Prakash Maiya M, Srinivasa Murthy S. Performance simulation of metal hydride hydrogen storage device with embedded filters and heat exchanger tubes. *Int J Hydrogen Energy* 2007;32:4978–87.
- [19] Freni a, Cipiti F, Cacciola G. Finite element-based simulation of a metal hydride-based hydrogen storage tank. *Int J Hydrogen Energy* 2009;34:8574–82.
- [20] Bhouri M, Goyette J, Hardy BJ, Anton DL. Sensitivity study of alanate hydride storage system. *Int J Hydrogen Energy* 2011;36:621–33.
- [21] Bao Z, Wu Z, Nyamsi SN, Yang F, Zhang Z. Three-dimensional modeling and sensitivity analysis of multi-tubular metal hydride reactors. *Appl Therm Eng* 2013;52:97–108.
- [22] Na Ranong C, Lozano G, Hapke J, Roetzel W, Fieg G, Bellosta von Colbe J. Application of Danckwerts-type boundary conditions to the modeling of the thermal behavior of metal hydride reactors. *Chem Eng Sci* 2011;66:4654–62.
- [23] Pohlmann C, Röntzsch L, Weißgärber T, Kieback B. Heat and gas transport properties in pelletized hydride–graphite-composites for hydrogen storage applications. *Int J Hydrogen Energy* 2013;38:1685–91.
- [24] Renquist JV, Dickman B, Bradley TH. Economic comparison of fuel cell powered forklifts to battery powered forklifts. *Int J Hydrogen Energy* 2012;37:12054–9.
- [25] McWhorter S, Read C, Ordaz G, Stetson N. Materials-based hydrogen storage: attributes for near-term, early market PEM fuel cells. *Curr Opin Solid State Mater Sci* 2011;15:29–38.
- [26] Hardy BJ, Anton DL. Hierarchical methodology for modeling hydrogen storage systems. Part II: detailed models. *Int J Hydrogen Energy* 2009;34:2992–3004.
- [27] Chandan A, Hattenberger M, El-kharouf A, Du S, Dhir A, Self V, et al. High temperature (HT) polymer electrolyte membrane fuel cells (PEMFC) – a review. *J Power Sources* 2013;231:264–78.

Available online at www.sciencedirect.com

ScienceDirect

journal homepage: www.elsevier.com/locate/hydro

Considerations on the H₂ desorption process for a combination reactor based on metal and complex hydrides

I. Bürger*, M. Bhourri, M. Linder

Institute of Technical Thermodynamics, German Aerospace Center (DLR), D-70569 Stuttgart, Germany

ARTICLE INFO

Article history:

Received 20 October 2014

Received in revised form

16 January 2015

Accepted 26 March 2015

Available online 24 April 2015

Keywords:

Complex hydride

Metal hydride

Combination multi./tubular reactor

Modelling

Desorption

ABSTRACT

Hydrogen storage systems based on the combination reactor concept are promising for application of future complex hydride materials with high storage capacities and low reaction kinetics at moderate operating temperatures. In such reactors, a fast reacting metal hydride is added to a complex hydride material in a separate compartment of the tank combining the advantages of the high storage capacity of the complex hydride with the high reaction rate of the metal hydride. In the present publication, three issues regarding the desorption performance of such a reactor are discussed based on analytical considerations and 1D simulations. First, it is studied whether the optimal reactor design based on a tubular geometry that has been previously determined for the absorption reaction also enables satisfying desorption performances. It can be concluded from the corresponding simulations that based on the properties of the present reference materials LaNi_{4.3}Al_{0.4}Mn_{0.7} and 2 LiNH₂–1.1 MgH₂–0.1LiBH₄–3 wt.% ZrCoH₃, the hydrogen desorption performance of the materials in this reaction geometry is good. Second, it is shown that besides the geometry of the reactor, also its module size is important, as it can be crucial for the thermal management during the desorption. A methodology was developed that allows to analytically determine a first estimate for the best minimum module size configuration – only based on the desorption rate of the basic material. This approach is confirmed by time dependent 1D simulations applying a validated model for the reference materials. Third, the influence of a realistic periodic desorption load on the performance of a combination reactor is studied. The results clearly show that since the addition of a MeH material enables much smaller module sizes, it is advantageous for the thermal management of complex hydride based reactors and increases their flexibility.

Copyright © 2015, Hydrogen Energy Publications, LLC. Published by Elsevier Ltd. All rights reserved.

Introduction

It is discussed in several scenarios of our future energy system that hydrogen can play an important role as environmental

friendly energy carrier [1,2]. However, one bottleneck for a closed hydrogen cycle is still the efficient storage of this lightweight gas. Amongst others, one possibility is the utilization of solid state storage materials, which is a rather safe and long-term storage option. However, so far suitable

* Corresponding author.

E-mail address: inga.buerger@dlr.de (I. Bürger).
<http://dx.doi.org/10.1016/j.ijhydene.2015.03.136>

0360-3199/Copyright © 2015, Hydrogen Energy Publications, LLC. Published by Elsevier Ltd. All rights reserved.

materials still lead to quite heavy systems [3]. Thus, recently the focus of the application of these materials has been shifted from passenger cars to heavy duty vehicles, e.g. forklifts [4,5].

Besides classical metal hydrides (MeH) that are already considered for real-life applications, promising solutions based on complex hydrides (CxH) are still under investigation. These kind of materials show improved H₂ storage capacities, thus they are in principle able to overcome the obstacle of poor gravimetric storage density common for metal hydrides [6,7]. However, these materials usually show low reaction rates at temperatures below 100 °C due to kinetic limitations of their conversion reaction with hydrogen [8,9]. One possibility to use the high storage capacities of these materials and to overcome their limitation in reaction dynamics is a combination reactor concept that has been presented by the authors before [10,11]. The idea of this concept is the combination of a fast reacting metal hydride material with a slowly reacting complex hydride material that shows a very high storage capacity. In these previous works, this concept has been presented and discussed including a model validation for the absorption and the desorption processes. Based on the validated model for two reference materials, it is now possible to investigate various suitable tank designs. E.g., in a recent study, the absorption process has been investigated and an optimal geometry for the reference materials has been defined [12]. As for motive applications the fuelling of the gas has to be very fast, the absorption process is very sensitive towards reactor geometry and material properties. Thus, it is likely that the absorption requirements will define the overall geometry of a corresponding tank. However, for technical applications, not only the absorption process, but also the desorption process has to be considered. The most common scenario for a desorption process in mobile applications is the coupling to a HT-PEM fuel cell, where the exhaust heat of the fuel cell is used in order to supply the required heat for the desorption reaction to the hydride storage material [13–15]. For complex hydrides the desorption rates at fuel cell relevant pressures >1.7 bar and temperatures (HT-PEM, 170 °C) are usually quite low. Therefore, it is not trivial to combine high storage efficiencies (full capacity) with fast discharging dynamics in a practical application, e.g. due to heat management problems.

In the present paper, the main characteristics of a desorption process as well as the resulting challenges are discussed considering the two reference materials that have previously been used for model validation: LaNi_{4.3}Al_{0.4}Mn_{0.7}, in the following abbreviated as MeH material, and 2LiNH₂–1.1MgH₂–0.1LiBH₄–3wt.% ZrCoH₃, in the following abbreviated as CxH. It is obvious that with the effective storage capacities of 1.2 wt.% and 3.2 wt.% for the MeH and CxH material, a final reactor design will still not be sufficient to fulfil the system target values of the DOE for gravimetric and volumetric densities. However, for these two materials, validated models exist and the general principle of the combination reactor concept has been proven. Thus, these materials are chosen as reference materials for the present publication.

The design of the basic reactor geometry for this study has been taken from the previously published optimization process of the absorption reaction [12]. Starting from this publication, it will be first checked whether this geometry is also suitable for a generalized desorption scenario. Then in the

second part, a new aspect – the module size of a modular hydride reactor – is discussed, since it influences the thermal management of the reactor and thus highly affects the desorption process (e.g. coupling to a fuel cell). In order to clarify the wording in this manuscript, the size of a module always refers to the mass of hydride that desorbs hydrogen at the same time. Furthermore, when the desorption rate is mentioned it corresponds to the effective desorption reaction rate of the pure material, while the discharging rate corresponds to the discharging process of the overall tank.

Finally, in the third part, more realistic dynamic operation scenarios are discussed. Therefore, the basic model is extended to capture the MeH reabsorption process of hydrogen during low load conditions.

Model formulation

Geometry

For modelling purposes, in this paper a simple axisymmetric 1D geometry has been applied that represents the cylindrical shape of a tube-shaped reactor, compare Fig. 1 and [12]. The metal hydride material is located in the center with a radius $r_{\text{MeH}} = d_{\text{MeH}}/2$. In the annulus of the tube, the complex hydride is inserted and the thickness of this layer can be varied corresponding to the ratio $\xi = d_{\text{CxH}}/d_{\text{MeH}}$. The resulting volumetric fraction of the CxH material is referred to as $\varepsilon_{\text{CxH}} = V_{\text{CxH}}/V_{\text{total}}$. Both materials are separated by a gas permeable separation layer (GPSL). As this layer consists of a thin stainless steel mesh, the heat and mass transfer resistances at this boundary are negligible. The thickness of the stainless steel wall $d_{\text{s,s}}$ separating the hydride container from the heat transfer fluid is considered according to the following equation [12]

$$d_{\text{s,s}} = \frac{2r_o}{1 + \frac{20}{S} \frac{K}{P} v}, \quad (1)$$

where r_o is the external diameter of the stainless steel tube and P is the maximum applied pressure. The remaining parameters have been taken for stainless steel 1.4571 at a maximum temperature of 250 °C: design strength $K = 186 \text{ Nmm}^{-2}$, safety factor $S = 1.5$ and the utilization factor of the allowable design stress $v = 0.065$. The geometries used for simulations in this study are summarized in Table 1.

Model equations

For the presented simulations, the model is implemented into the FEM software COMSOL Multiphysics and rate equations, the mass balance of the gas as well as the total energy balance are considered for the metal hydride and the complex hydride domains. For the steel wall, only an energy balance of the solid is considered. The values for the respective properties as well as all assumptions can be taken from the previous publication, where this model has been validated [11].

The rate equations can be written as

$$\frac{\partial X}{\partial t} = r_{\text{R}}, \quad (2)$$

where X is the transformed fraction and r_{R} is the effective reaction rate for the materials as function of temperature and

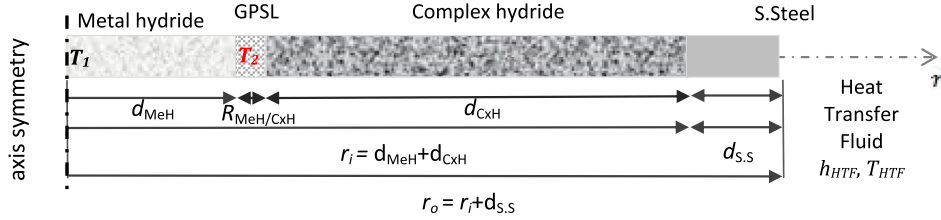


Fig. 1 – Scheme of the modelled 1D geometry of an axisymmetric tubular reactor.

pressure given in s^{-1} . The corresponding equations are summarized in the following Equations (3)–(5). More details can be found in Refs. [10,11,16].

Desorption of the CxH material (Li–Mg–N–H), 1st step, $0 < X_I < 0.67$:

$$r_{R,des,CxH,I} = \frac{\partial X_I}{\partial t} = 2.35 \cdot 10^{12} [s^{-1}] \cdot \exp\left(\frac{-131800 [Jmol^{-1}K^{-1}]}{\mathcal{R}T}\right) \cdot 1.5(1 - X_I) [-\ln(1 - X_I)]^{0.33} \cdot \ln\left(\frac{P_{eq}}{P}\right) \quad (3a)$$

Desorption of the CxH material (Li–Mg–N–H), 2nd step, $0.67 < X_{II} < 1$:

$$r_{R,des,CxH,II} = \frac{\partial X_{II}}{\partial t} = 3.044 \cdot 10^{15} [s^{-1}] \cdot \exp\left(\frac{-161400 [Jmol^{-1}K^{-1}]}{\mathcal{R}T}\right) \cdot \left(1 - \frac{0.001515}{wt_{max} \cdot 0.33} (P - 1.1 [\text{bar}])\right) \quad (3b)$$

Desorption of the MeH material:

$$r_{R,des,MeH} = \frac{\partial X}{\partial t} = 20 [s^{-1}] \cdot \exp\left(\frac{-16500 [Jmol^{-1}K^{-1}]}{\mathcal{R}T}\right) \cdot (1 - X) \cdot \ln\left(\frac{P_{eq}}{P}\right) \quad (4)$$

Absorption of the MeH material:

$$r_{R,abs,MeH} = \frac{\partial X}{\partial t} = 100 [s^{-1}] \cdot \exp\left(\frac{-21000 [Jmol^{-1}K^{-1}]}{\mathcal{R}T}\right) \cdot (1 - X) \cdot \left(\frac{P - P_{eq}}{P_{eq}}\right) \quad (5)$$

In case of “reabsorption” conditions during the desorption reaction (see Section Simulations with varying loads), r_R is described by an IF condition: IF the system pressure is below the desorption equilibrium pressure, the equations for $r_{R,des,MeH}$ are valid. IF the system is above the absorption equilibrium pressure

and IF already more than 1% of the transformed fraction has been desorbed, r_R is characterized by the equations for $r_{R,abs,MeH}$.

When Darcy’s law, $\nabla P_g = -\frac{\mu}{K} \cdot \vec{v}_g$, is applied for the description of the gas velocity, \vec{v}_g , the equation of the mass balance of the gas phase in terms of gas pressure P_g is given by

$$\varepsilon \frac{M}{T} \frac{\partial P_g}{\partial t} - \varepsilon \frac{P_g M}{\mathcal{R}T^2} \frac{\partial T}{\partial t} - \nabla \cdot \left(\rho_g \frac{K}{\mu} \nabla P_g \right) = -(1 - \varepsilon) r_R w_{t,max} \rho_s - \dot{m}_{des} \quad (6)$$

where M is the molar mass of H_2 , \mathcal{R} is the real gas constant, T the temperature, ρ_g the density of the gas, K the permeability of the powder bed, μ the viscosity of H_2 , ε the porosity of the bed, $w_{t,max}$ the maximum hydrogen storage capacity of the material and ρ_s the solid density. \dot{m}_{des} refers to the mass of hydrogen that is removed from the reactor, see Section Initial and boundary conditions.

For the energy balance of the system, local thermal equilibrium (LTE), $T = T_g = T_s$, is assumed leading to

$$\left[(1 - \varepsilon) c_{p,s} \rho_s + \varepsilon c_{p,g} \rho_g \right] \frac{\partial T}{\partial t} = c_{p,g} \rho_g \frac{K}{\mu} \nabla P_g \cdot \nabla T - \nabla \cdot (-\lambda_{eff} \nabla T) - (1 - \varepsilon) r_R w_{t,max} \rho_s \Delta_R H \quad (7)$$

The expression on the left hand side of Equation (7) refers to the accumulation of enthalpy in the gas as well as in the solid phase with the heat capacity of the gas and solid $c_{p,s/g}$. On the right hand side, convective heat transfer of the gas phase, heat transfer by thermal conduction in the powder and a heat source due to the reaction are accounted for, where $\Delta_R H$ is the enthalpy of the desorption reaction. In case of “reabsorption”, in analogy to the IF condition for the effective reaction rate mentioned above, another IF condition has been applied on the enthalpy of reaction.

Initial and boundary conditions

The initial condition for the temperature of the tank is given by the constraints of a HT-PEM fuel cell, $T_i = T_{steel,i} = 170$ °C, and the initial pressure is set to $P_i = 20$ bar. This pressure is

Table 1 – Overview of the simulated geometries/scenarios.

	Scenario	d_{MeH} in mm	$d_{S,S}$ in mm	ξ	ε_{CxH}	t_{dis} in h	m_{MeH} in g per m length	m_{CxH} in g per m length
basic geometry	A	10	2.0	1.25	0.80	3	10.5	12.6
	B	10	2.0	1.25	0.80	2	10.5	10.1
	C	10	2.0	1.25	0.80	5	10.5	16.4
variation in ξ	D	10	1.4	0.50	0.56	3	10.5	13.6
	E	10	2.7	2.00	0.89	3	10.5	11.3
	F	10	4.5	4.00	0.96	3	10.5	7.5
variation in d_{MeH}	G	5	1.6	2.50	0.92	3	2.6	8.2
	H	15	2.5	0.83	0.70	3	23.5	16.5

below the fuelling pressure of 70 bar, however, as in the first seconds H_2 is only released from the void space of the reactor, this behaviour is not relevant for the present considerations. Furthermore, in the initial state, both materials are fully in the absorbed state.

For the energy equation, the boundary condition at the center is a symmetry condition. At the outer surface, a heat flux from the steel wall to the heat transfer fluid has been assumed that is characterized by a heat transfer coefficient of $h_{HTF} = 600 \text{ Wm}^{-2}\text{K}^{-1}$, compare [11]. The most important boundary condition during desorption experiments, however, is given by the mass flow rate of H_2 that is removed from the system and consumed by the fuel cell. This flow rate is implemented as a (negative) source term in the gas balance of the system (see Equation (6)), and it causes the characteristic decrease in system pressure that results in the endothermal desorption reaction and the corresponding temperature decrease. Thus, this mass flow rate is a very important variable for the simulations and has to be chosen in a reasonable way. For the present simulations, the storage capacity of the reactor has been related to the storage discharging time in order to be able to compare different scenarios and different reactor designs. E.g., in the present basic case it has been assumed that the storage capacity of the MeH and the CxH in a reactor with a length of 1 m is deployed in 3 h. Thus, the required desorption H_2 flow rate r_{des} is given in s^{-1} as $1/10800 \text{ s} = 9.26 \cdot 10^{-5} \text{ s}^{-1}$, and the resulting mass flow rate is calculated as

$$\dot{m}_{des} = \rho_s w t_{max} (1 - \varepsilon) \cdot r_{des} \cdot A_{tube} \cdot H, \quad (8)$$

where A_{tube} refers to the perpendicular cut of tube axis that corresponds to the geometry of the model and the height of the reactor is defined as $H = 1 \text{ m}$. For the termination of the simulation, the following condition has been applied: as soon as the pressure reaches a value below 1.7 bar – the minimum working pressure to supply the fuel cell – the simulation is terminated. Besides simulations with a constant desorption H_2 flow rate, also simulations with periodic H_2 flow rates (thus, varying values of the source term) have been performed, see Section Simulations with varying loads.

Results and discussion

The general effect of the addition of a MeH material to a CxH material in a combination reactor has already been discussed in a previous publication [11] and can be summarized as follows:

- The addition of the MeH to the CxH material stabilizes the pressure in the system: As the reaction rate of the MeH is several orders of magnitude higher than the rate of the CxH, the pressure in the system will not fall below the equilibrium pressure of the MeH material as long as the MeH can desorb hydrogen.
- The efficiency of the hydrogen storage in the CxH material is improved since, as long as the MeH is stabilizing the pressure, the CxH material can desorb at its own

desorption rate. Thus, the MeH is only desorbing as much H_2 as to meet the demand of hydrogen for the fuel cell.

- The temperatures in the reactor decrease due to the endothermic reaction. As the MeH is placed at the center of the tube, where the lowest temperatures appear, this region of the reactor is efficiently used as the MeH still shows sufficient kinetics even at low temperatures. ($<150 \text{ }^\circ\text{C}$).

The goal of the present publication is to study these effects in more detail and derive suggestions for future tank design of similar reactors. First, the effect of varying geometries is studied in Section Optimum reactor design for desorption, and the optimum reactor design for absorption determined in a previous publication is evaluated with respect to desorption constraints. Then, in Section Discussion of minimum module size for desorption process, the minimum module size for a satisfying desorption performance is discussed, when the effective reaction rates of the materials are known. This minimum module size is important for applications requiring a substantial thermal management, e.g. sufficient heat transfer at a specific temperature level, when a tank is coupled to a HT-PEM fuel cell. Finally, the dynamic performance of a combination reactor is studied when the H_2 flow rate shows a dynamic behaviour, and the observed effects are explained by the effective desorption rates of the different materials, see Section Simulations with varying loads.

Optimum reactor design for desorption

In a previously published study, an optimum geometry for a combination reactor has been determined with respect to a short filling time leading to a reactor with a geometry of $d_{MeH} = 10 \text{ mm}$ and $\xi = 1.25$ [12]. In this section, it is now studied whether this radial geometry determined for absorption is also useful for the constraints that apply during desorption operation. Therefore, starting from the optimum absorption geometry, different geometric parameters are varied in the following, where always a scenario with a complete desorption in 3 h is considered.

Variation of the ratio ξ

First of all, the effect of varied values for ξ on the desorption performance is studied in analogy to the absorption study [12]. Fig. 2 shows the corresponding transformed fraction plot for ξ values of 0.5–4, for a discharging time of 3 h. Additionally, the values for volumetric ratio ($\varepsilon_{CxH} = V_{CxH}/V_{total}$), storage capacity and stored H_2 per m length of reactor are summarized in Table 1 for the different cases (A, D, E, F). In case of absorption there exists a clear optimum regarding the minimum fuelling time as it has been shown in a previous publication [12]. In contrast, for the desorption process the decision on an optimum is not clearly defined as there is not only one single criterium that has to be met. For the combination reactor, the optimal value is rather a trade-off between discharging efficiency and CxH volumetric ratio. For a value of $\xi = 0.5$ (green), the discharging efficiency is very high, however, with $\varepsilon_{CxH} = 0.56$, the tank mainly consists of MeH material. On the other hand, for $\xi = 4$ (turquoise), the discharging efficiency is very low as the desorption is interrupted early. Therefore, a value of 1.25 (black), which has been the optimum for

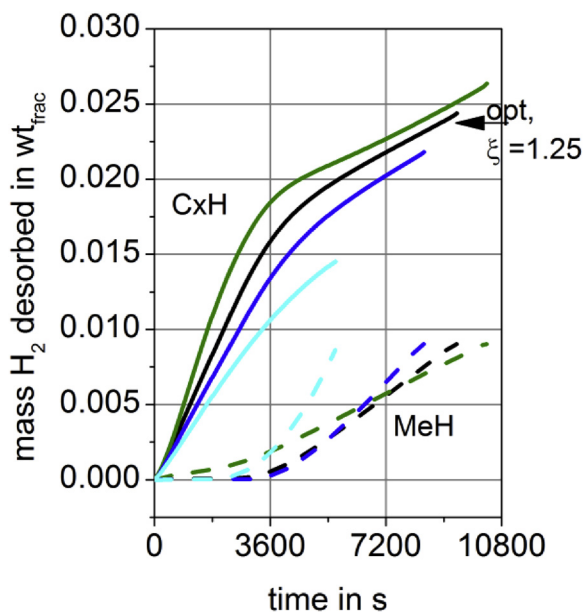


Fig. 2 – Mass of H₂ desorbed by the MeH material (dashes) and the CxH material (solid line) for a desorption scenario at 170 °C using a complete desorption in 3 h, (compare Table 1, scenario: A, D, E, F). ξ varies from 0.5 (green) to 1.25 (opt, black), 2 (blue) and 4 (turquoise). (For interpretation of the references to colour in this figure legend, the reader is referred to the web version of this article.)

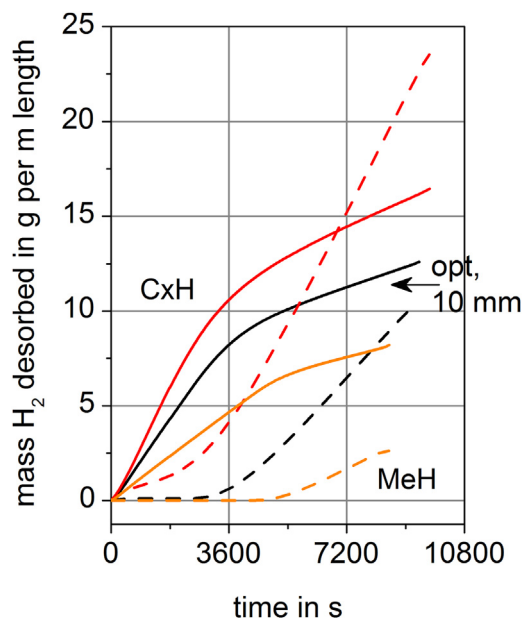


Fig. 3 – Desorption scenario at 170 °C with $\xi = 1.25$ and d_{MeH} varies from 5 mm (orange) to 10 mm (black) and 15 mm (red), (compare Table 1, scenario: A, G, H). Mass of hydrogen desorbed by the MeH (dashes) and the CxH (solid) in kg per m length of reactor. (For interpretation of the references to colour in this figure legend, the reader is referred to the web version of this article.)

absorption is also suitable for the discharging process leading to a CxH fraction of $\epsilon_{\text{CxH}} = 0.8$.

Variation in d_{MeH}

Next to a variation of ξ , also the radius of the MeH material d_{MeH} at the center has been varied from 10 to 5 and 15 mm, and the optimum values for each ξ have been adapted from the analogous absorption simulations. Fig. 3 shows the corresponding absolute mass of hydrogen that is desorbed in each case per m length of reactor (compare also Table 1 A, G, H). From this plot it is obvious that in case of the reactor with $d_{\text{MeH}} = 15$ mm (red), the MeH dominates the combination reactor as more hydrogen is actually stored in the MeH (23.5 g, dashes) than in the CxH (16.5 g, solid). In case of the 5 mm reactor (orange) this ratio is much better with 2.6–8.2 g. However, the total mass of H₂ stored per m length of reactor is very small. Thus, it can be concluded that for desorption a geometry using $d_{\text{MeH}} = 10$ mm (black), shows a good trade off between performance and stored H₂ per m.

Summarizing the parameter study on the optimum reactor geometry, it is obvious that the optimum geometry for absorption is also applicable for the desorption process.

Discussion of minimum module size for desorption process

As it has been concluded in the previous section, a reactor design that is optimal with regards to the absorption process - filling time - is also suitable for a general desorption scenario. However, for the desorption process also the module size of

the overall tank can be crucial, as it will be shown in the following.

In this section, the correlation between the effective reaction rates of the materials as well as the discharging time of the storage reactor and the minimum possible reactor module size is discussed. Furthermore, it is introduced how this module size can influence the thermal management of a reactor during desorption operation. As mentioned before, the module size always refers to the mass of hydride that desorbs hydrogen at the same time, thus it is independent of any geometric assumption.

First, two basic scenarios are depicted in Fig. 4, in order to explain the effects of different module sizes on the operation procedure. In both cases, a total mass of 5 kg_{H₂} is stored in 10 elements of the same dimensions and the reactor is operated for 10 h until it is completely discharged:

- I. In the 1st case, 5 (out of 10) elements are connected to one module. They are heated up to the nominal operation temperature and operated for the first 5 h. Each element is desorbing hydrogen with a rate of 0.1 kg_{H₂} per h resulting in an overall H₂ discharging rate of 0.5 kg_{H₂}h⁻¹ of the whole module. After 5 h, the second module has to be in operation. Therefore, the next 5 identical elements are heated up and the same H₂ flow rate is desorbed by the material in this module. So, hydrogen has been delivered at a discharging rate of 0.5 kg_{H₂} h⁻¹ to the fuel cell during 10 h of operation. In this case, it is possible to use hydride materials with very low effective (desorption) reaction rates, as the size of the two modules is rather big, and the material

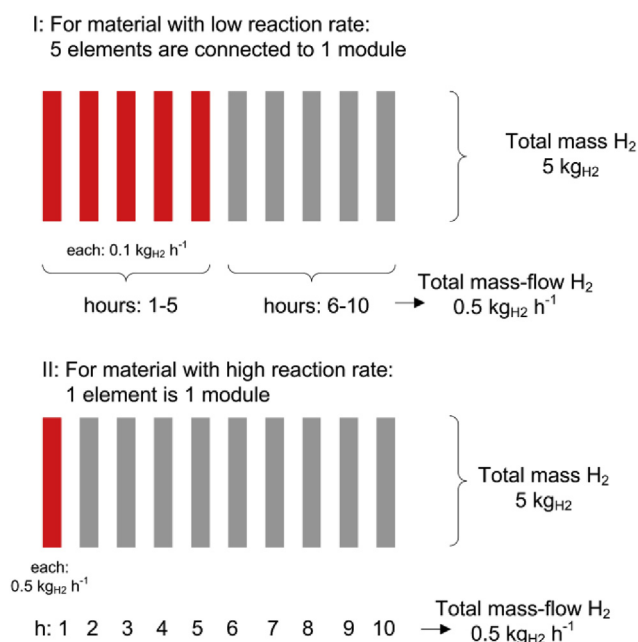


Fig. 4 – Effect of different module sizes on the flexibility of an overall hydride tank system during desorption.

in the single elements has to desorb H_2 at a rather low rate. However, this system is not very flexible concerning cold start ability and/or heat losses, as a very big part of the overall tank has to be heated up and kept at operation temperature at the same time.

II. In the 2nd case, only 1 element is heated up to operation temperature at the same time, so in this case one element refers to one module. Thus, in this module the effective desorption reaction rate of the materials has to be sufficiently high to discharge $0.5 \text{ kg}_{\text{H}_2} \text{ h}^{-1}$ for one hour. Then, the next module is heated up and desorbs the same amount of H_2 and so on. Therefore, also in this case a constant H_2 discharging rate of $0.5 \text{ kg}_{\text{H}_2} \text{ h}^{-1}$ can be realized while only 1 module is kept at operation temperature at the same time. This kind of configuration is advantageous when a more flexible operation behaviour is desired, especially considering the start-up of the system.

From these two cases it is clear that it is desirable to use the smallest possible module size for an enhanced thermal management allowing for a flexible operation of the tank. In the following section, it will be discussed how the minimum module size for a H_2 storage reactor can be determined analytically by the effective desorption reaction rate of the material. The considered boundary conditions for these analytical considerations are given by a HT-PEM fuel cell with an assumed temperature of the heat transfer fluid $T_{\text{HTF}} = 165\text{--}170 \text{ }^\circ\text{C}$ and a minimum H_2 supply pressure of 0.5–1 bar and for the material properties of the two reference materials.

Analytical considerations

For a first guess on the minimum modules size, it is sufficient to consider only the effective reaction rates of the materials.

The corresponding procedure can be seen in a plot showing the reaction rate versus the transformed fraction for the considered temperatures and pressures (170 $^\circ\text{C}$ and 0.5–1 bar). For the reference materials considered in this study, this kind of plot is shown in Fig. 5 A and B. First of all, from this plot it is clear that the reaction rates of the MeH material (B) are 2–3 orders of magnitude higher than the reaction rates of the considered CxH material (A), see different scales. The straight lines indicate the required rates for a complete desorption in $t_{\text{des}} = 2, 3$ or 5 h. As the effective rate of the MeH is higher than these rates even up to a fully discharged state, it is obvious that the MeH material can continuously desorb H_2 at a high rate. In contrast, the effective reaction rates for the CxH material are much lower. In this case the material requires at least 5 h for a complete discharging process, as only in this case the reaction rate is higher than the theoretical rate for a full conversion in 5 h (a rate of $1/(5 \cdot 3600 \text{ s}) = 5.56 \cdot 10^{-5} \text{ s}^{-1}$). Therefore, for this material, a desorption time of 2 or 3 h will only lead to a H_2 release from the 1st desorption step.

Thus, it can be concluded that for the MeH material, there does not exist a minimum module size from the point of view of reaction rates, as even the total capacity can be released in few seconds. However, for the CxH material, the size of the modules should be chosen in a way that each module can

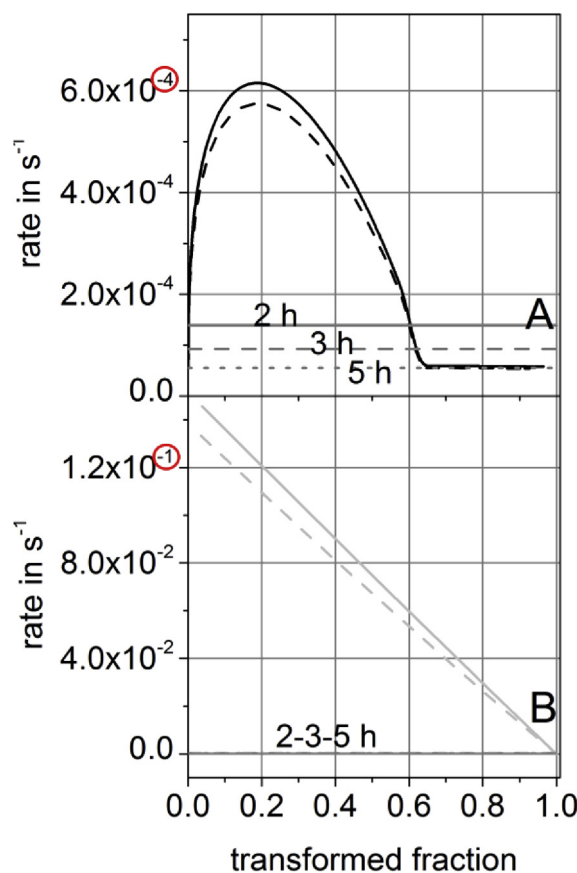


Fig. 5 – Effective reaction rates versus transformed fraction for 165 $^\circ\text{C}$ and 0.5 bar (solid) or 1 bar (dashed line). A: Reference CxH material: $2 \text{ LiNH}_2\text{--}1.1\text{MgH}_2\text{--}0.1 \text{ LiBH}_4\text{--}3\text{wt.}\% \text{ ZrCoH}_3$ B: Reference MeH material: $\text{LaNi}_{4.3}\text{Al}_{0.4}\text{Mn}_{0.3}$.

desorb H_2 for at least 5 h in order to be able to utilize the total capacity of the material. So, comparing Case I and II, each module has to consist of several elements.

Besides the effective reaction rates of the materials at isothermal and isobaric conditions, in a second step it is useful to include more information on the actual reactor design (tube diameters) in the considerations for the minimum module size. As the reactor design will influence the temperature profile appearing in the reactor, this will also influence the overall reactor performance and the assumption of isothermal conditions. E.g., for larger tube diameters the temperature at the center will decrease due to the endothermic reaction, thus, the temperature of the heat transfer fluid will not represent the temperature of the material, consequently the assumption of constant T and P is not valid any more. For the case of an annular ring filled with CxH material, the temperature decrease between the heat transfer fluid and the temperature T_2 at the GPSL, can be calculated analytically according to the following equation [17], assuming a constant heat flux due to the endothermal desorption reaction of a constant H_2 flow rate from the CxH material,

$$T_{HTF} - T_2 = -\frac{(\Delta_R H \rho)_{CxH}(1-\varepsilon)}{4\lambda_{eff}t_{dis}}(r_i^2 - d_{MeH}^2) + \frac{(\Delta_R H \rho)_{CxH}(1-\varepsilon)}{2\lambda_{eff}t_{dis}}d_{MeH}^2 \ln\left(\frac{r_i}{d_{MeH}}\right), \quad (9)$$

where T_{HTF} and T_2 are the temperatures of the heat transfer fluid and the GPSL, $\Delta_R H$, ρ_s , wt_{CxH} , ε and λ_{eff} are the reaction enthalpy, the density, the storage capacity, the porosity and the effective thermal conductivity, and r_{HTF} and d_{MeH} are the radii of the annulus corresponding to Fig. 1. Furthermore, t_{dis} is the given discharging time. The calculated temperature decreases for the optimum design determined in the absorption scenario [12] (compare Table 1, A, B, C), are 7.1 K, 4.7 K and 3.5 K for the complete desorption in 2 h, 3 h and 5 h, respectively.

Thus, for the 3 h and 5 h desorption the temperature decrease is not very prominent (<5 K) and it can be assumed that the first estimation of the minimum module size using only the effective reaction rate information at constant temperature is correct.

Simulation results

The previously introduced analytical considerations showed the challenges during desorption processes for materials with very low effective desorption reaction rates, e.g. CxH materials. Furthermore, they showed how a first estimate on the minimum possible module size for a combination reactor can be obtained, based on the assumption that the CxH material is dominating the overall performance. In this section, this initial analytical estimate is analysed in detail by a discussion of the time dependent desorption simulations of both materials in the combination reactor as well as by a discussion of the final mass of H_2 that could be desorbed in the different cases.

Fig. 6A shows the transformed fraction of MeH and CxH versus time profiles for the simulated cases, where the total stored H_2 capacity is desorbed in 2 h, 3 h and 5 h (compare

Table 1, A, B, C). Regarding the geometry, the optimum geometry obtained from the 1D simulations for absorption is considered with $d_{CxH} = 10$ mm and $\xi = 1.25$, and the length of one module is defined as 1 m.

The time dependent behaviour is in all three cases quite similar and can be described as follows: in the beginning the straight lines which indicate the mass H_2 desorbed by the CxH material increase, while the dashed lines referring to the MeH material stay at a very low level. Thus, the majority of H_2 is desorbed by the CxH material. Then, towards the end of each scenario, the effective reaction rate of the CxH is slowing down and the MeH material starts to desorb H_2 filling the gap to the required H_2 flow rate for the fuel cell. The same effect can be seen from Fig. 6B where the temperature at the GPSL, T_2 (dashes), as well as the temperature at the center, T_1 (solid), are plotted versus time for the same three cases. First, the temperature in the center follows the equilibrium of the CxH indicating that mainly CxH material is desorbing hydrogen. Then, more H_2 has to be desorbed by the MeH material

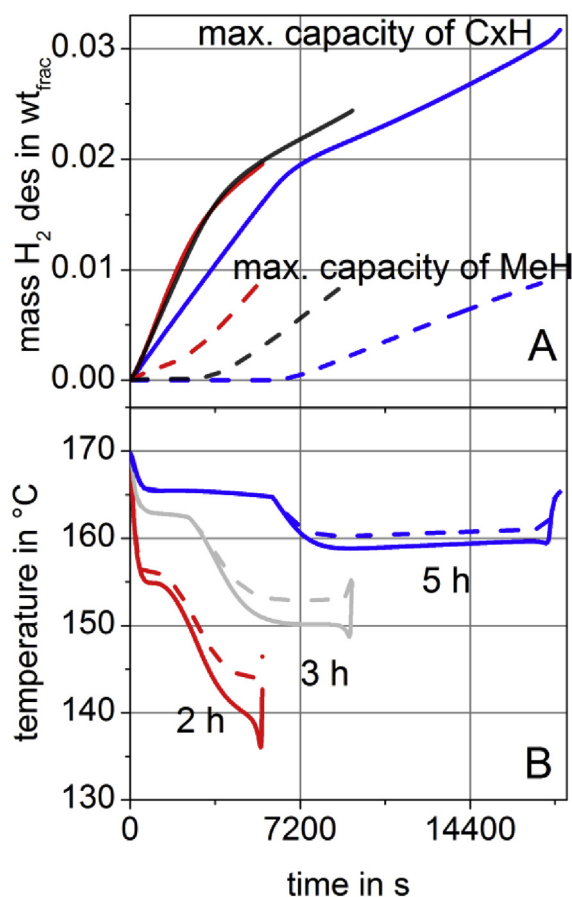


Fig. 6 – Desorption scenario at 170 °C using the optimal absorption geometry and r_{des} for a complete desorption in 2 h (red), 3 h (black) and 5 h (blue), (compare Table 1, scenario: A, B, C). A: Mass of H_2 desorbed by the CxH (solid) and MeH (dashes). B: Temperature T_1 (solid) and T_2 (dashes). (For interpretation of the references to colour in this figure legend, the reader is referred to the web version of this article.)

resulting in a temperature decrease to the equilibrium temperature of the MeH material, and the temperature T_1 in the center starts to vary significantly from the temperature at the GPSL, T_2 .

This behaviour of the three different desorption cases is in accordance with Fig. 5, that has been discussed above: in all three cases, towards the termination of the simulation the MeH is completely discharged with a $w_{t,frac}$ of 0.009 at 165 °C (dashed lines), as the effective reaction rate of this material is very high even at the applied pressures and temperature. However, for the discharge of the CxH material different values are obtained: in case of a discharging within 2 h and 3 h, just 2 wt.% and 2.4 wt.% can be desorbed corresponding mainly to the 1st desorption step. Only for the case of a desorption for 5 h the full H₂ capacity of 3.2 wt.% can be reached. Linking these findings to the general exemplary cases in Section Analytical considerations, it is obvious that for a discharging of the reaction in 2 or 3 h, the currently used module size is too small to completely discharge the reactor for the effective reaction rate of the reference materials. Therefore, if a complete discharging is desired, either the module size should be increased or the discharging rate reduced (to e.g. 5 h).

Concluding this section it can be stated that the analytical considerations and the simulated results agree very well: The minimum discharging rate from 3 h for the complete 1st desorption step and 5 h for a full 2nd step desorption that have been predicted by the analytical considerations have been confirmed in detail by the 1D simulations. For a discharging process within 2 h, significantly less H₂ could be desorbed. Here a clear deviation from the analytical estimation is obtained since it predicted a very similar behaviour to the discharging within 3 h. However, in this case, the more prominent temperature decrease - that has already been predicted analytically - deteriorates the performance, as it can be clearly seen from Fig. 6B.

Thus, the analytical considerations presented before can be useful to understand the correlations between the module size of a reactor and its desorption performance at a given discharging rate for materials with given desorption rates. This fact can especially be interesting for tank applications requiring a substantial thermal management, as it is the case for coupling a solid state hydrogen storage tank to a HT-PEM fuel cell.

Simulations with varying loads

In the previous section, it has been introduced why small module sizes can be an important issue for technically relevant storage tanks. This was done based on the assumption of constant discharging rates. In this section, more realistic boundary conditions, for e.g. a scenario where the tank is coupled to a HT-PEM fuel cell, will be considered. Therefore, besides scenarios with constant discharging rates simulating a constant power output of the fuel cell, the behaviour of a tank during varying loads is of high practical importance, e.g., in a driving scenario this can correspond to going uphill or going downhill [18].

In order to understand the performance of a combination reactor during dynamic loads and especially the effect of

the additional MeH, 3 different scenarios are simulated using the basic geometry with $d_{MeH} = 10$ mm and $\xi = 1.25$ (see Table 1, A):

- The first scenario (I) is the basic case for the optimum geometry with a discharging time of 3 h, as it has been used in the previous sections.
- The second scenario (II) refers to the same discharging time, however, in this case the rate is not constant but it is varied: for 30 s, 6 times the base load is discharged and for the following 450 s, the load is reduced by a factor of 10 to 0.67 times the base load.
- The third scenario (III) refers again to the same discharging time, but now the rate is varied between 30 s and 450 s from 0.53 to 8, so by a factor of 15.

Fig. 7 shows the discharging rates for the three different cases together with the rates versus transformed fraction plot of the CxH material at given temperature and pressure ($T_{HTF} = 170$ °C and $P > 1.7$ bar, compare Fig. 5A). From this plot it becomes obvious that using the constant discharging rate of Scenario I (blue straight line), the 1st desorption step of the CxH material can in principle be fully discharged as the required flow rate is below the possible desorption flow rate up to 60% transformed fraction. In Scenario II, the peak rates should be acceptable up to a transformed fraction of approx. 30%, thus in this case approx. half of the 1st desorption step should be available for this varying load case. Finally, for Scenario III, the peak loads exceed the possible desorption rates of the CxH material even at very low transformed fractions. Thus, in a pure CxH reactor with the present geometry and module size, the material would not be able to keep up the required discharging flow rate from the fuel cell even from the beginning – even for ideal (isothermal and isobaric) conditions.

For scenarios with varying discharging rates, the analytical considerations reflecting mainly the CxH material desorption rates are insufficient to capture the final behaviour. Therefore, detailed simulations are required that take the simultaneous reactions of both materials into account. Fig. 8 shows the results of the time dependent simulations of the three scenarios using the optimum geometry of the combination reactor (see Table 1, A). In Fig. 8A, the system pressure is plotted versus time for the three scenarios. Obviously, in Scenarios II and III, the pressure is varying periodically due to the periodic discharging rate. The intensity of this fluctuation depends on the intensity of the different discharging rates, thus for Scenario III (green, dots) the variations are more significant than for Scenario II (red, dashes). Furthermore, it is obvious that in all three scenarios the time until the experiment is interrupted is very similar. This is surprising as the rate during peak loads in Scenario III clearly exceeds the possible effective desorption rate of the CxH material, see discussion above. This behaviour is due to the additional MeH material in the combination reactor and it clearly shows the advantages on the dynamic behaviour of such a combination reactor: even when in a scenario the peak loads exceed the maximum desorption rates of the CxH material, the MeH material can additionally desorb and thus stabilize the system pressure. Furthermore, as the system

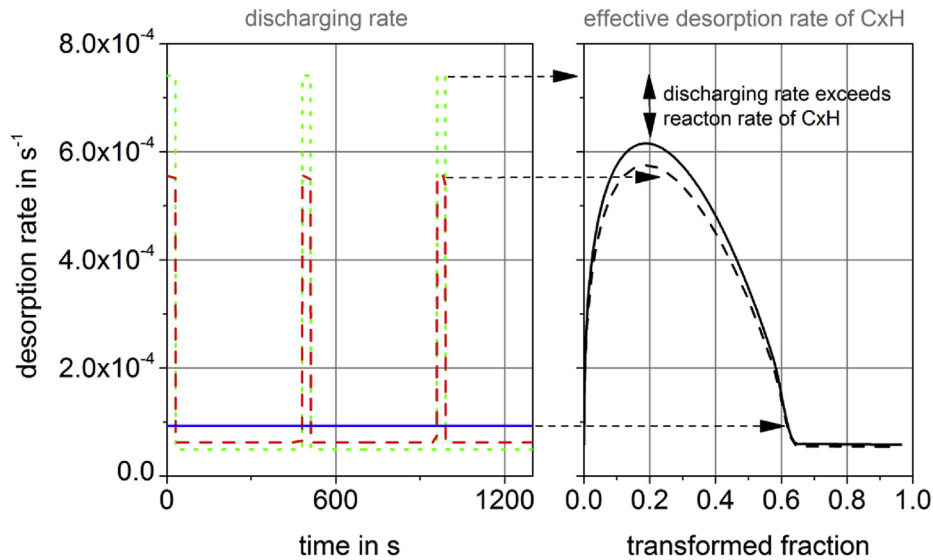


Fig. 7 – Discharging rates for the three different scenarios together with the desorption rate versus the transformed fraction of the reference CxH material. Complete desorption in 3 h (solid, blue), varying load varying by a factor of 10 between low and high load (dash, red) and varying load varying by factor of 15 (dot, green). Arrows indicate max. possible transformed fraction for each maximum rate. (For interpretation of the references to colour in this figure legend, the reader is referred to the web version of this article.)

pressure is stabilized, it is possible that in all three cases the same amount of H₂ is desorbed from both materials as it is shown in Fig. 8B, where the mass of desorbed H₂ is plotted: in all three cases not only the MeH but also the CxH material desorbs H₂ up to the same value.

In the following, the two parallel reactions are discussed in more detail. It will be shown that the MeH material is not only desorbing extra hydrogen during peak loads, but it is also able to “reabsorb” hydrogen during low loads. Thus, the “buffering” function of the MeH material is not only available once, but it can be recharged. Fig. 9 shows a detail of the system pressure (red) as well as the equilibrium pressures for desorption of the CxH (black dots) and the MeH (grey dots) and for absorption for the MeH (grey dashes) for Scenario III. From this graph it is obvious that the system pressure never falls below the desorption pressure of the MeH material as this is desorbing sufficiently fast to keep a constant system pressure. Furthermore, during low load conditions the system pressure never exceeds the absorption equilibrium pressure of the MeH material indicating that the material “reabsorbs” hydrogen. Since the system pressure is constantly below the desorption equilibrium pressure of the CxH material, the CxH desorbs continuously thereby also supplying hydrogen for the “reabsorption” in the MeH. The “reabsorption” is possible until approx. 3600 s, then the system pressure does not reach the required absorption pressure of the MeH anymore. The same fact is shown in Fig. 10, where a detail of the desorbed mass H₂ is plotted versus time only for the MeH material. Here, it can be clearly seen that the desorbed mass of H₂ in the MeH material is decreasing during low loads and – during the first part – increasing during peak loads.

In summary it can be concluded that especially Scenarios II and III clearly show the advantages of the combination reactor concept during a dynamic desorption

scenario: even when the required peak discharging rate exceeds the possible effective desorption rate of the CxH material, it is possible to show a satisfying performance on a reactor level. Thus, as long as the required discharging hydrogen rate can be on average supplied by the CxH material in a given geometry and module size, even much higher peak discharging rates can be tolerated in a combination reactor as the MeH material can desorb and reabsorb sufficiently fast.

Coming back to the discussion on the minimum module size, it is obvious that the addition of some MeH to the CxH material can decrease the required module size for a pure CxH tank and thus increase the flexibility of the tank. Especially for the start-up phase or during mode changes in the operation, that require a substantial thermal management, a reactor with a suitable combination of materials can improve the overall performance.

Conclusions

In the present publication, the desorption performance of different configurations of a combination reactor based on a reference metal hydride and a reference complex hydride have been studied using analytical methods and simulations of a 1D model using the software COMSOL.

First, a sensitivity study of the desorption performance has been performed by varying the ratio between the MeH and the CxH as well as the radius of the inner MeH tube starting from the previously determined optimal absorption geometry. Both studies indicated, that the optimal absorption geometry is also suitable for the given desorption conditions.

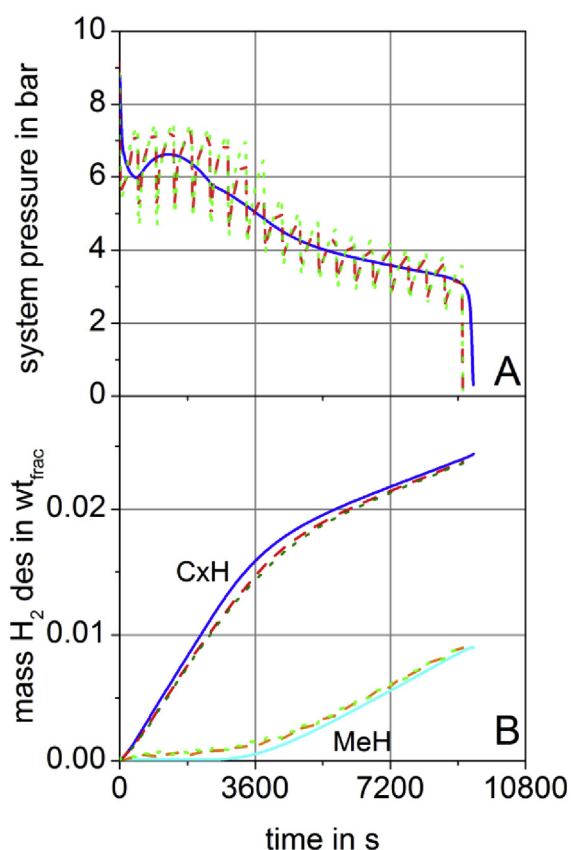


Fig. 8 – Desorption scenario for the three different scenarios: Complete desorption in 3 h (solid, blue), varying load by a factor of 10 between low and high load (dash, red) and varying load by a factor of 15 (dot, green). A: system pressure. B: mass H₂ desorbed by MeH material (turquoise, orange, light green) and mass H₂ desorbed by CxH material (blue, red and green). (For interpretation of the references to colour in this figure legend, the reader is referred to the web version of this article.)

Second, based on generic operation conditions, the influence of the module size of a reactor on the required thermal management during operation was analysed. Then, the minimal module size of a reactor has been discussed when a certain discharging time is required and the effective desorption reaction rates characterizing the CxH material are known. As the rates of the present reference material at 165 °C and 1 bar are quite low, very large modules are required in order to be able to deliver sufficient hydrogen. Thus, for these materials, the thermal management of the overall tank will be challenging.

Finally, the desorption process has also been studied for varying loads, e.g. for a load variation by a factor of 10 and 15. In this case it was shown that the combination reactor is advantageous as the MeH material was able to buffer and reabsorb hydrogen during peak and low loads, respectively, leading to smaller possible module sizes than analytically expected. Therefore, based on the combination principle the desorption performance on a reactor level can be better than indicated by the effective desorption rates of the respective CxH material.

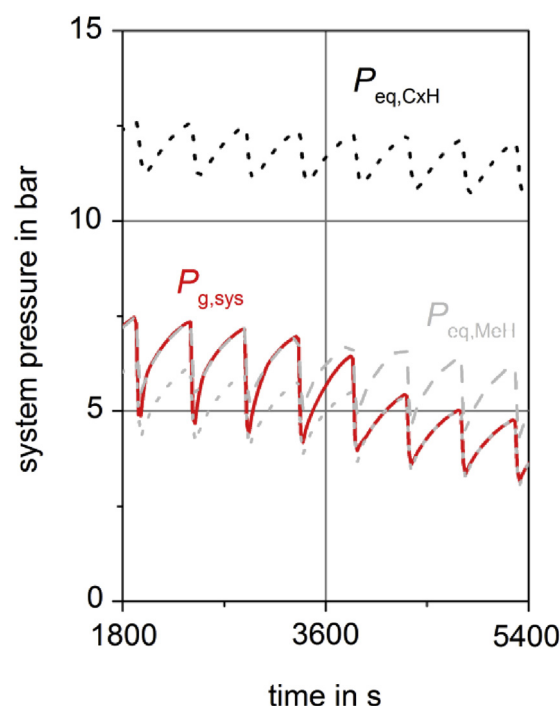


Fig. 9 – Detail of Scenario II. System pressure (red, solid), desorption equilibrium pressure of the CxH (black, dot), desorption equilibrium pressure of the MeH (grey, dot) and absorption equilibrium pressure of the MeH (grey, dash). (For interpretation of the references to colour in this figure legend, the reader is referred to the web version of this article.)

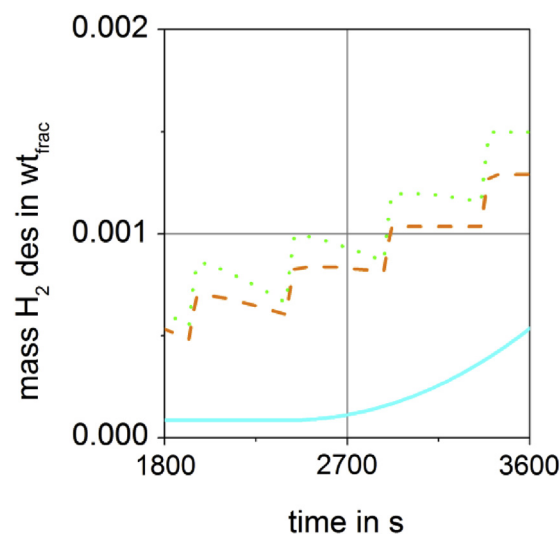


Fig. 10 – Detail of mass H₂ desorbed by MeH material for the desorption scenarios shown in Fig. 8. Turquoise, solid: Scenario I, orange, dash: Scenario II, light green, dot: Scenario III. (For interpretation of the references to colour in this figure legend, the reader is referred to the web version of this article.)

Acknowledgements

The research leading to these results has received funding from the European Union's Seventh Framework Programme (FP7/2007-2013) for the Fuel Cells and Hydrogen Joint Technology Initiative under grant agreement no. 256653 (SSH2S).

M.B. would like to thank the German Academic Exchange Service (DAAD) for the DLR-DAAD Research Fellowship.

REFERENCES

- [1] Eberle U, Felderhoff M, Schüth F. Chemical and physical solutions for hydrogen storage. *Angew Chem* 2009;48(36):6608–30.
- [2] Züttel A, Remhof A, Borgschulte A, Friedrichs O. Hydrogen: the future energy carrier. *Philos Trans A Math Phys Eng Sci* 2010;368(1923):3329–42.
- [3] Weidenthaler C, Felderhoff M. Solid-state hydrogen storage for mobile applications: Quo Vadis? *Energy Environ Sci* 2011;4(7):2495.
- [4] Kurtz J, Ainscough C, Simpson L, Caton M. Hydrogen storage needs for early motive fuel cell markets. 2012.
- [5] Klebanoff L, Pratt J, Johnson T, Arienti M, Shaw L, Moreno M. Analysis of H₂ storage needs for early market non-motive fuel cell applications. 2012.
- [6] Sakintuna B, Lamari-Darkrim F, Hirscher M, Lamaridarkrim F. Metal hydride materials for solid hydrogen storage: a review. *Int J Hydrogen Energy* 2007;32(9):1121–40.
- [7] Jain IPP, Jain P, Jain A. Novel hydrogen storage materials: a review of lightweight complex hydrides. *J Alloys Compd* 2010;503(2):303–39.
- [8] Klebanoff LE, Keller JO. 5 Years of hydrogen storage research in the U.S. DOE Metal Hydride Center of Excellence (MHCoe). *Int J Hydrogen Energy* 2013;38(11):4533–76.
- [9] Fichtner M. Conversion materials for hydrogen storage and electrochemical applications—concepts and similarities. *J Alloys Compd* 2011;509:S529–34.
- [10] Bürger I, Komogowski L, Linder M. Advanced reactor concept for complex hydrides: hydrogen absorption from room temperature. *Int J Hydrogen Energy* 2014;39:7030–41.
- [11] Bürger I, Luetto C, Linder M. Advanced reactor concept for complex hydrides: hydrogen desorption at fuel cell relevant boundary conditions. *Int J Hydrogen Energy* 2014;39:7346–55.
- [12] Bhourri M, Bürger I, Linder M. Optimization of hydrogen charging process parameters for an advanced complex hydride reactor concept. *Int J Hydrogen Energy* 2014;39(31):17726–39.
- [13] Pfeifer P, Wall C, Jensen O, Hahn H, Fichtner M. Thermal coupling of a high temperature PEM fuel cell with a complex hydride tank. *Int J Hydrogen Energy* 2009;34(8):3457–66.
- [14] Urbanczyk R, Peil S, Bathen D, Heßke C, Burfeind J, Hauschild K, et al. HT-PEM fuel cell system with integrated complex metal hydride storage tank. *Fuel Cells* 2011;11(6):911–20.
- [15] Weiß-Ungethüm J, Bürger I, Schmidt N, Linder M, Kallo J. Experimental investigation of a liquid cooled high temperature proton exchange membrane (HT-PEM) fuel cell coupled to a sodium-alanate tank. *Int J Hydrogen Energy* 2014;39:5931–41.
- [16] Bürger I, Hu JJ, Vitillo JG, Kalantzopoulos GN, Deledda S, Fichtner M, et al. Material properties and empirical rate equations for hydrogen sorption reactions in 2 LiNH₂-1.1 MgH₂-0.1 LiBH₂-3 wt.% ZrCoH₃. *Int J Hydrogen Energy* 2014;39:8283–92.
- [17] Corgnale C, Hardy BJ, Tamburello DA, Garrison SL, Anton DL. Acceptability envelope for metal hydride-based hydrogen storage systems. *Int J Hydrogen Energy* 2012;37(3):2812–24.
- [18] MacDonald BD, Rowe AM. Experimental and numerical analysis of dynamic metal hydride hydrogen storage systems. *J Power Sources* 2007;174(1):282–93.



ELSEVIER

Available online at www.sciencedirect.com

ScienceDirect

journal homepage: www.elsevier.com/locate/he

Feasibility analysis of a novel solid-state H₂ storage reactor concept based on thermochemical heat storage: MgH₂ and Mg(OH)₂ as reference materials

M. Bhourri ^{a,*}, I. Bürger ^b, M. Linder ^b

^a Mechanical Engineering, Dalhousie University, B3H 4R2, Halifax, Nova Scotia, Canada

^b Institute of Engineering Thermodynamics, German Aerospace Center (DLR), D-70569, Stuttgart, Germany

ARTICLE INFO

Article history:

Received 21 March 2016

Received in revised form

7 September 2016

Accepted 18 September 2016

Available online 13 October 2016

Keywords:

Hydrogen storage

Thermochemical heat storage

Magnesium hydride

Magnesium hydroxide

Hydrogen absorption time

Analytical study

ABSTRACT

This paper discusses the feasibility of a novel adiabatic magnesium hydride (MgH₂) reactor concept based on thermochemical heat storage. In such a concept, the heat of reaction released during the absorption of hydrogen is stored by a thermochemical material in order to be reused in a subsequent desorption stage. Magnesium hydroxide (Mg(OH)₂) has been selected as the suitable material for integration into the MgH₂ storage system due to its thermodynamic properties. An analytical formulation of hydrogen absorption time is used to determine the range of the geometrical characteristics of the two storage media, their properties and their operating conditions. The advantage of the proposed new concept is the possibility to reduce the mass of the heat storage media by a factor of 4 compared to phase change material, improving then the gravimetric system capacity as well as its total cost. The second advantage is an improved flexibility of the operating pressure conditions for MgH₂ absorption reaction and Mg(OH)₂ dehydration reaction that enables shorter hydrogen absorption times by ensuring larger temperature gradients between the two storage media.

© 2016 Hydrogen Energy Publications LLC. Published by Elsevier Ltd. All rights reserved.

Introduction

After decades of intensive research on metal hydrides, today, there is a tremendous volume of data covering their properties and application areas [1–5]. One of the traditional applications of these materials is the storage of hydrogen for fuel cell operation as they offer compact systems at rather low pressures. However, due to their high weight, current applications focus on heavy-duty vehicles or stationary devices.

One material that has been proposed in several publications for stationary hydrogen storage is magnesium hydride

(MgH₂). This material is inexpensive and offers still high gravimetric capacities of up to 7.6 wt.% [6]. However, the main drawback of this material is the low system efficiency, as it can only be operated at temperatures in the range of 300–400 °C due to thermodynamic and kinetic limitations. Thus, in contrast to most metal hydride systems where the focus is on a reactor design with improved heat transfer [7], for magnesium hydride, heat integration is the main challenge.

Furthermore, the MgH₂ enthalpy of reaction corresponds to up to 31% of the lower heating value of the absorbed hydrogen [8]. Thus, solutions have to be found to avoid a decrease of the system efficiency. One option is through systems where the

* Corresponding author. Fax: +1 902 423 6711.

E-mail addresses: bhourri_maha@yahoo.fr, maha.bhourri@dal.ca (M. Bhourri).

<http://dx.doi.org/10.1016/j.ijhydene.2016.09.125>

0360-3199/© 2016 Hydrogen Energy Publications LLC. Published by Elsevier Ltd. All rights reserved.

magnesium hydride storage tank is coupled with a high temperature solid oxide fuel cell (SOFC) using a diathermic heat transfer fluid that has to be pumped [9]. Thus, the heat is provided using the waste heat of the fuel cell by a system integration.

In order to simplify the system complexity, previously, a magnesium hydride reactor concept has been proposed by Garrier et al. [8] that stores the reaction enthalpy during absorption for the subsequent desorption process in a phase-change material (PCM). The selection criteria were based on a stable PCM with high melting enthalpy, high thermal conductivity, and a melting temperature in between the equilibrium temperatures of absorption and desorption, so that the heat of reaction is conducted from one media to another due to the presence of temperature gradient. An optimization study has shown that the eutectic $\text{Mg}_{69}\text{Zn}_{28}\text{Al}_3$ is a suitable PCM to be integrated into the MgH_2 storage system and a large-scale magnesium hydride tank with a total hydrogen storage capacity of 7050 NI has been successfully built and tested with main use for stationary applications.

In this paper, an alternative to such a PCM is presented that stores the heat released during the hydrogen uptake in a thermochemical material for the subsequent desorption. Similarly to the storage of hydrogen, the thermochemical heat storage involves reversible chemical reactions between solid and gas, mostly water vapor. The synthesis of the solid is exothermic, while its decomposition requires heat input [10]. In comparison to the sensible and latent heat storage methods, thermochemical energy storage technologies offer higher energy densities and longer-term preservation ability for thermal energy [11]. They have gained a lot of interest for heat pumping, heat storage, e.g. solar energy and waste heat recovery in industrial processes [12–16].

In case of hydrogen storage based applications and to the best of our knowledge, there has been no research performed so far to investigate the hydrogen loading process in an adiabatic hydrogen storage system based on the combination of a metal hydride and a thermochemical heat storage material. The proposed reactor design consists of an adiabatic system where heat is exchanged internally/reversibly between magnesium hydride and a suitable thermochemical material. Thus, the aim of this paper is (i) to discuss the feasibility of such a new reactor concept through the identification of the suitable thermochemical storage material to be combined with magnesium hydride, (ii) to present an analytical formulation of the hydrogen loading time, which would be used as preliminary calculation tool to identify the range of parameters for the two combined media in order to optimize the hydrogen loading process, and finally (iii) to discuss the competitiveness of this concept compared to the existing technology.

Basic concept

For such a new hydrogen storage system based on the combination of magnesium hydride and a thermochemical material, the heat of reaction released by the metal hydride during the absorption of hydrogen will be stored by the thermochemical material, and it will be given back during the

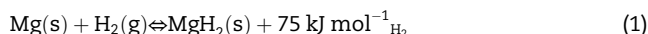
desorption stage (similar to the system with PCM). The choice of the heat storage material to be combined with the MgH_2 is based on the two materials reaction temperatures, their energy storage densities and their reaction rates. In addition, the two materials should have good reaction reversibility and durability, and good mass and heat transfer properties. No toxicity, corrosion resistance, availability and low cost are also among the criteria to be considered when selecting the material to be combined with the magnesium hydride.

Identification of the suitable thermochemical material

Hydrogen storage media

As outlined in the introduction, magnesium hydride has been proposed as a suitable candidate for hydrogen-based stationary applications owing to its high gravimetric capacity of 7.6 wt.%, low cost, and light weight. In addition, considerable improvements of its kinetics and thermal properties have been achieved in the past, so that today it is commercially available in form of pellets with stable sorption properties and efficient thermal conductivity [17]. Moreover, the same material has been selected for the development of hydrogen storage system using phase-change material to store the heat of reaction [8]. Thus, by referring to the related study, it is possible to compare the performance of the magnesium hydride reactor based on latent heat storage and the one using thermochemical heat storage in order to conclude about the relevance of the new reactor concept investigated in this study.

Magnesium hydride absorbs and desorbs hydrogen following the reversible reaction



The hydrogen uptake is an exothermic process and the heat of reaction should be removed, otherwise the temperature of MgH_2 media reaches the corresponding equilibrium temperature and the absorption of hydrogen is either slowed down or stopped. During the endothermic reaction of hydrogen release, heat supply is required.

Thermochemical heat storage media

For thermochemical systems, the thermal energy can be reversibly stored and released based on the following chemical reaction [10]:

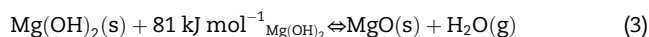


During the forward reaction, A and B are combined together to form the product C while releasing heat. In principle various gas–solid reactions are possible, e.g. reactions with water vapor, CO_2 , ammonia or hydrogen. With heat supply, the thermochemical material C is dissociated into components A and B.

Salt hydrates, ammonia, hydroxides, carbonates and metals can potentially be used for thermochemical storage applications. Kuravi et al. [14] presented a list of these most promising candidates with the range of their operating temperatures and reaction enthalpies. As first attempt to determine the thermochemical material suitable for integration into MgH_2 storage system, our focus has been directed to

identifying one of those heat storage media with the same range of reaction temperature as magnesium hydride (250 °C–400 °C) [18]. Such a selection criteria has restricted our choice to magnesium hydroxide, $\text{Mg}(\text{OH})_2$ as possible candidate to be combined with magnesium hydride.

The decomposition/synthesis of the $\text{Mg}(\text{OH})_2$ system is based on the following reversible chemical reaction



The charging process corresponds to the forward endothermic dehydration reaction where heat is stored and magnesium hydroxide is dissociated to magnesium oxide and water vapor. The reverse exothermic hydration reaction constitutes the thermal discharging process where heat is released and magnesium oxide reacts with water vapor to form magnesium hydroxide.

The “ $\text{MgO}/\text{H}_2\text{O}/\text{Mg}(\text{OH})_2$ ” system has mainly been investigated by Kato et al. [19–23] for medium temperature chemical heat pump applications. Their research has focused first on the development of a new magnesium oxide material using ultra fine oxide powder as precursor in order to improve its durability [20]. Subsequently, the same developed material has been used to test the performance of different packed bed reactor configurations of $\text{MgO}/\text{Mg}(\text{OH})_2$ chemical heat pumps [22,23], to study the reaction mechanism of the material mixed with different additives such as LiCl [24], LiBr [25–27] and CaCl_2 [28,29], and to improve its thermal properties by addition of expanded graphite [30–32]. The related results have shown the potential of the studied material to meet the requirements of the chemical heat storage/chemical heat pump technology.

In the current study, the same thermodynamic and thermal properties of the $\text{Mg}(\text{OH})_2$ investigated by Kato and co-workers are used (i) to discuss the feasibility of a MgH_2 reactor using $\text{Mg}(\text{OH})_2$ as thermochemical material to store the heat of reaction and (ii) to describe in detail the operational principle of this new reactor concept.

To avoid any confusion between the description of hydrogen and thermochemical systems, in the following text the designations of absorption and desorption reactions are used to describe hydrogen uptake and release for MgH_2 system, respectively; whereas the designations of hydration and dehydration reactions are used to describe discharging and charging processes for $\text{MgO}/\text{Mg}(\text{OH})_2$ system, respectively.

Thermodynamic considerations

The feasibility of the new MgH_2 reactor concept investigated in this study depends on the thermodynamic properties of used hydrogen and thermochemical heat storage materials. Based on the studies elaborated by Chaise et al. [18] and Kato et al. [19], the equilibrium diagrams of the two studied systems are shown in Fig. 1 within the range of their operating temperatures and pressures.

For Mg/MgH_2 system, the selection of the applied pressures during hydrogen uptake and release determines the equilibrium absorption and desorption temperatures to be reached by the hydrogen storage media. Based on the experience gained in practical operational conditions of MgH_2 tanks, the absorption and desorption pressures, P_{abs} and P_{des} are set at 1 MPa and 0.2 MPa, respectively. This corresponds to equilibrium absorption and desorption temperatures, $T_{\text{eq,abs}}$ and $T_{\text{eq,des}}$, of 370 and 305 °C as can be seen from Fig. 1.

As described earlier, the heat of reaction released by MgH_2 during its exothermic absorption reaction should be consumed during the endothermic dehydration of $\text{Mg}(\text{OH})_2$. To ensure the transfer of heat between the two media, a temperature gradient between Mg/MgH_2 and $\text{MgO}/\text{Mg}(\text{OH})_2$ systems is required. Specifically, the dehydration of $\text{Mg}(\text{OH})_2$ should occur at a temperature, $T_{\text{eq,dehy}}$, lower than the absorption temperature of the magnesium hydride at 1 MPa ($T_{\text{eq,dehy}} < T_{\text{eq,abs}} = 370$ °C). As first step to assess the feasibility of this new reactor concept, $T_{\text{eq,dehy}}$ is set to 340 °C, corresponding to the melting temperature of the PCM used in Ref.

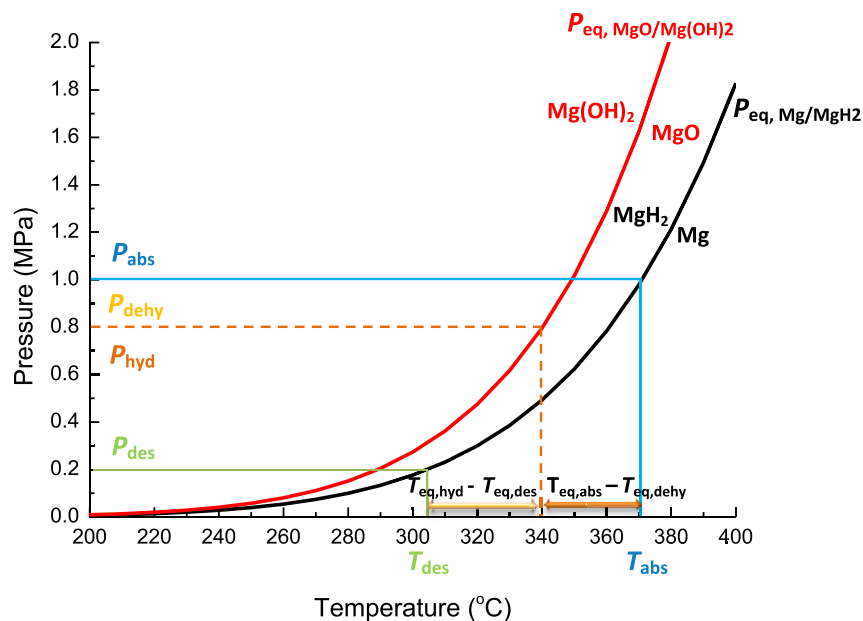


Fig. 1 – Pressure–Temperature phase diagrams for Mg/MgH_2 and $\text{MgO}/\text{Mg}(\text{OH})_2$ systems.

[8]. Referring to the equilibrium diagram of $\text{MgO}/\text{Mg}(\text{OH})_2$ system plotted in Fig. 1, this is equivalent to $\text{Mg}(\text{OH})_2$ dehydration pressure, $P_{\text{dehy,eq}}$ of 0.8 MPa. This means that in order to drive the thermochemical system towards the dissociation reaction of $\text{Mg}(\text{OH})_2$ at this temperature level, the pressure P_{dehy} should be lower than 0.8 MPa.

Indeed, referring to Kato and coworkers studies [26,28], the $\text{Mg}/\text{Mg}(\text{OH})_2$ system can store heat at around 300 °C (lower than the PCM melting temperature) under vacuum while achieving reasonable dehydration reaction rates.

In analogy, to transfer the heat released during the exothermic hydration of MgO towards MgH_2 media desorbing hydrogen, the hydration temperature, $T_{\text{eq,hyd}}$ should be higher than the desorption temperature, $T_{\text{eq,des}}$ to be reached at 0.2 MPa ($T_{\text{hyd}} > T_{\text{des}} = 305$ °C). Again, by setting $T_{\text{eq,hyd}} = 340$ °C, this means that a hydration pressure, P_{hyd} higher than 0.8 MPa is required to drive the thermochemical system towards the hydration reaction of MgO at this temperature level.

So far, the hydration reaction has only been investigated up to a pressure of 0.4 MPa [23]. However, since reported reaction rates are sufficiently high, the $\text{Mg}/\text{Mg}(\text{OH})_2$ system is an appropriate reference system for the purpose of this study.

Operating principle

The operating principle of the adiabatic MgH_2 reactor based on thermochemical heat storage is shown in Fig. 2. The proposed new system consists of a reactor combining both, (Mg/MgH_2) and $(\text{Mg}(\text{OH})_2/\text{MgO})$ systems separated by a wall, and a water reservoir. It has two operation modes: “Absorption of H_2 /Dehydration/Condensation of $\text{H}_2\text{O}_{(\text{g})}$ ” and “Desorption of H_2 /Hydration/Evaporation of $\text{H}_2\text{O}_{(\text{l})}$ ”.

In “Absorption of H_2 /Dehydration/Condensation of $\text{H}_2\text{O}_{(\text{g})}$ ” mode (Fig. 2(a)), the absorption and dehydration reactions of the two storage media occur simultaneously at two different temperature levels: hydrogen is absorbed at $T_{\text{eq,abs}}$ and magnesium hydroxide is dehydrated by consuming the hydride reaction heat, Q_{abs} at lower temperature, $T_{\text{eq,deh}}$. The generated water vapor is condensed at the water reservoir at T_c while releasing condensation heat, Q_c .

In “Desorption of H_2 /Hydration/Evaporation of $\text{H}_2\text{O}_{(\text{l})}$ ” mode (Fig. 2(b)), the system consists initially of magnesium hydride and magnesium oxide. The condensed water in the reservoir is heated up by consuming evaporation heat, Q_v of 40 kJ/mol H_2O . The produced vapor at T_v reacts with magnesium oxide and the thermochemical heat storage media

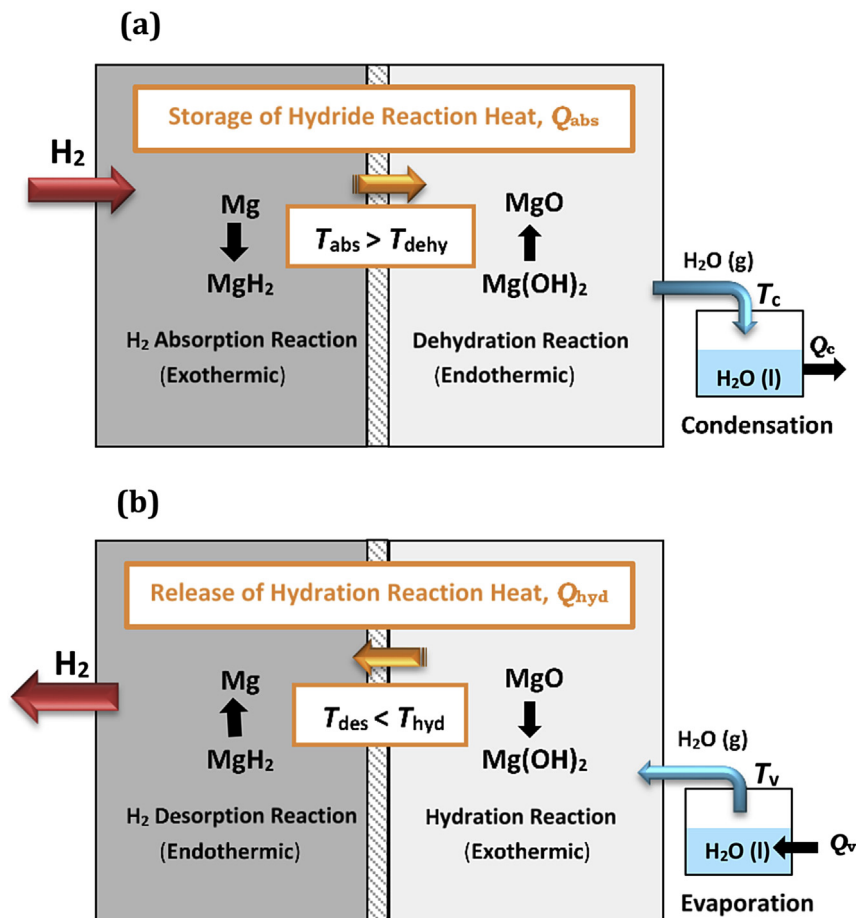


Fig. 2 – Operating principle of magnesium hydride reactor using magnesium hydroxide as heat storage media: (a) Absorption of H_2 /Dehydration of $\text{Mg}(\text{OH})_2$ /Condensation of H_2O and (b) Desorption of H_2 /Hydration of MgO /Evaporation of H_2O .

reaches temperature, $T_{\text{eq,hyd}}$, while releasing the hydration heat, Q_{hyd} . Due to the temperature gradient between the thermochemical heat storage media and hydrogen storage media, the hydration reaction heat is conducted towards magnesium hydride bed and the desorption of hydrogen occurs at temperature, $T_{\text{eq,des}}$, lower than the one reached by the MgO bed ($T_{\text{eq,hyd}}$).

In our reference case, the required heat to evaporate water has to be provided at T_v of 170 °C–180 °C due to the heat pump effect of the thermochemical storage [23]. Indeed, for this temperature range, the corresponding water vapor pressure is between 0.824 MPa and 1.05 MPa. This will result in an equilibrium hydration temperature, $T_{\text{eq,hyd}}$ greater than or equal to 340 °C (see the van't Hoff diagram in Fig. 1) which is much higher than 305 °C, the equilibrium desorption temperature of the MgH₂ bed desorbing hydrogen at 0.2 MPa (see discussion in the previous subsection). For the required T_v in this system, the temperature level of the exhaust heat of a High temperature (HT) polymer electrolyte membrane fuel cells (PEMFCs) is sufficient in contrast to systems with direct heat integration based on SOFCs. Furthermore, depending on the choice of reaction system, it is also possible to directly integrate the water vapor leaving the HT-PEMFC into the thermochemical storage.

Analytical formulation

After the selection of the suitable thermochemical material to be combined with the magnesium hydride, a first estimate of the charging performance is presented in this section. As for stationary applications, a hydrogen loading time of 5 h is acceptable [8], it is assessed if the new MgH₂ reactor concept investigated in this study, could be filled with hydrogen in a time interval of 5 h or less. This is closely related to the efficient thermal management of the reaction heat released during the hydrogen uptake: this heat should be quickly conducted to the thermochemical heat storage media to ensure that the temperature of the MgH₂ bed does not reach the equilibrium, resulting then in the slowdown of the hydrogen storage process. The efficient heat transfer between the hydrogen and heat storage media depends on these materials properties as well as the reactor design parameters.

Before performing numerical and experimental studies to investigate the hydrogen loading process in this MgH₂ reactor based on thermochemical heat storage, the development of an analytical expression of hydrogen absorption time is a good approach for evaluating the performance of the selected materials and directing research efforts for possible improvement of their properties. At the same time, it serves as preliminary calculation tool to optimize hydride and thermochemical materials thicknesses recognized as key design parameters [33–35].

Marty et al. [35] developed analytical expressions of loading times for various geometries of MgH₂ reactor based on latent heat storage and a good agreement was obtained by comparing the calculated values to numerical and experimental results. Here, the same calculation approach is adapted to the MgH₂ system based on thermochemical heat storage in order to evaluate its related hydrogen absorption time. The investigated reactor can be represented as a series

of rectangular cells or cylindrical tubes where MgH₂ and Mg(OH)₂ beds are combined and a separation layer is used to ensure the indirect contact between the two media. Fig. 3(a), (b) illustrates a single cell of one rectangular and cylindrical MgH₂ and Mg(OH)₂ shaped bed.

In order to describe such an adiabatic hydrogen storage reactor based on a thermochemical system, a new analytical equation has been formulated based on the following assumptions:

- The heat transfer process in H₂ storage media and heat storage media is one dimensional and due only to conduction.
- The H₂ absorption reaction and the Mg(OH)₂ dehydration reaction are controlled only by heat transfer (the kinetics is not the limiting step for the two systems, Mg/MgH₂ and MgO/Mg(OH)₂).
- The hydrogen absorption front and the Mg(OH)₂ dehydration front are moving into opposite directions.
- The heat released during the absorption of hydrogen in the magnesium hydride domain at the time interval, dt and in the elementary volume, dv_{MgH_2} is used to dehydrate the magnesium hydroxide at the same time interval in the elementary volume, $dv_{\text{Mg(OH)}_2}$.
- A perfect thermal contact between H₂ storage media and heat storage media is assumed.

Rectangular geometry of Mg/MgH₂ and MgO/Mg(OH)₂ beds

Fig. 3(a) shows a schematic drawing of the computational domains of Mg/MgH₂ and MgO/Mg(OH)₂ beds in case of one rectangular single cell where symmetry or insulation boundary conditions can be applied on both media sides.

The H₂ absorption front and the Mg(OH)₂ dehydration front are moving into opposite directions. Due to the presence of a temperature gradient between the two media, the heat of reaction released during the absorption of hydrogen, Q_{abs} is conducted towards the magnesium hydroxide media and it is stored during the Mg(OH)₂ dehydration reaction. Hence, magnesium hydride media and magnesium hydroxide media are respectively, cooled and heated faster in the contact zones characterized by lengths x_{Mg} and $x_{\text{Mg(OH)}_2}$ as shown in Fig. 3(a). As a result, these two zones saturate earlier than the rest of magnesium hydride and magnesium hydroxide beds where the respective equilibrium temperatures, $T_{\text{eq,abs}}$ and $T_{\text{eq,dehy}}$ are reached. Once the storage of absorption heat, Q_{abs} is completed, the hydrogen storage media and heat storage media are characterized by their thicknesses, L_{Mg} and $L_{\text{Mg(OH)}_2}$ and the hydrogen absorption time can be expressed as [35]

$$t_{\text{abs}} = L_{\text{Mg}}^2 / (2A) \cdot (1 + \lambda/K) \quad (4)$$

where $A = \lambda_{\text{Mg}} \cdot M_{\text{H}_2} (T_{\text{eq,abs}} - T_{\text{eq,dehy}}) / ((1 - \epsilon) \rho_{\text{Mg}} w_t \Delta H_{\text{Mg}})$ is the ratio of the sensible heat transferred between the MgH₂ and Mg(OH)₂ beds and the reaction heat released during the absorption of hydrogen and $\lambda = \lambda_{\text{Mg}} / \lambda_{\text{Mg(OH)}_2}$ is the ratio of the thermal conductivities of the two storage media, MgH₂ and Mg(OH)₂. $K = \Delta x_{\text{deh}} r_{\text{mix}} \rho_{\text{Mg(OH)}_2} \Delta H_{\text{Mg(OH)}_2} \times M_{\text{H}_2} / ((1 - \epsilon) w_t \rho_{\text{Mg}} \Delta H_{\text{Mg}} \times M_{\text{Mg(OH)}_2})$ is the ratio of the heat stored by the thermochemical

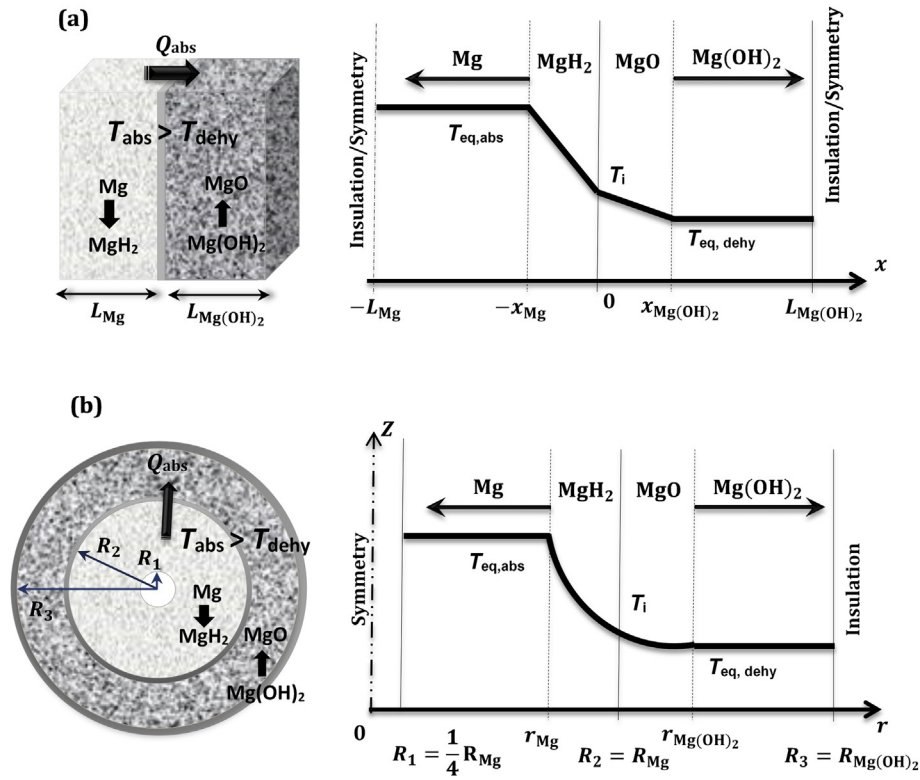


Fig. 3 – Schematic of the used geometry in the analytical study showing the hydrogen absorption front and the Mg(OH)_2 dehydration front in (a) rectangular and (b) cylindrical coordinates.

material and the heat released during the absorption of hydrogen. It is also equal to the ratio of the two bed thicknesses when the storage of the reaction heat is completed ($K=L_{\text{Mg}}/L_{\text{Mg(OH)}_2}$).

In these expressions, $T_{\text{eq,abs}}$, λ_{Mg} , ε , ρ_{Mg} , w_t and ΔH_{Mg} are the equilibrium absorption temperature, the thermal conductivity, the porosity, the density, the gravimetric capacity and the reaction enthalpy of magnesium hydride, respectively. $T_{\text{eq,dehy}}$, $\lambda_{\text{Mg(OH)}_2}$, $\rho_{\text{Mg(OH)}_2}$ and $\Delta H_{\text{Mg(OH)}_2}$ are the equilibrium dehydration temperature, the thermal conductivity, the density and the reaction enthalpy of magnesium hydroxide, respectively. The dehydrated fraction of water vapor is denoted as Δx_{deh} . In case where Mg(OH)_2 is mixed with expanded graphite (EG) to improve its thermal conductivity, the mixing mass ratio, r_{mix} is defined as $m_{\text{Mg(OH)}_2}/(m_{\text{Mg(OH)}_2} + m_{\text{EG}})$ [28].

Cylindrical geometry of Mg/MgH_2 and MgO/Mg(OH)_2 beds

In cylindrical geometry, magnesium hydride is introduced in the annular region between R_1 and R_2 and surrounded by magnesium hydroxide in the region between R_2 and R_3 , as illustrated in Fig. 3(b). The external surface of the cylindrical tube is adiabatic. Using the same assumptions and heat transfer description given above, the hydrogen absorption time is [35]

$$t_{\text{abs}} = \frac{R_2^2}{(4A)} \{ \chi (\ln \chi - 1) + \lambda (1 + K - \chi) [\ln((1 + K - \chi)/K) - 1] + 1 + \lambda K \} \quad (5)$$

χ is defined as $(R_1/R_2)^2$. The expressions of A , λ and K are the same defined in case of rectangular geometry; however for the expression of K , the complete storage of the reaction heat, Q_{abs} imposes the following relationship between MgH_2 and Mg(OH)_2 volume: $K = (R_2^2 - R_1^2)/(R_3^2 - R_2^2)$ [35].

Results of the analytical formulation

In order to evaluate the hydrogen storage performance of the new MgH_2 reactor based on thermochemical heat storage, the hydrogen absorption time is calculated for different MgH_2 and Mg(OH)_2 beds geometries and thicknesses, different Mg(OH)_2 properties and under different operational conditions of pressure and temperature for both materials. The properties of MgH_2 and Mg(OH)_2 used for calculations are listed in Tables 1 and 2. For magnesium hydride, calculations are performed based on the properties of pelletized material mixed with 5%

Table 1 – Properties of MgH_2 used in analytical analysis [36].

Parameter	Symbol	Value
Equilibrium absorption temperature ($^{\circ}\text{C}$)	$T_{\text{eq,abs}}$	370
Reaction enthalpy (kJ/mol)	ΔH_{Mg}	75
Density (kg/m^3)	ρ_{Mg}	1945
Porosity (1)	ε	0.44
H_2 storage capacity (%)	w_t	5.94
Thermal conductivity (W/(m K))	λ_{Mg}	10
Molecular weight of H_2 (kg/mol)	M_{H_2}	0.002

Table 2 – Properties of Mg(OH)₂ used in analytical analysis [16,32].

Parameter	Symbol	Value		
		EM8 Pellets	EM8 Block	Mg(OH) ₂ + Al foam
Equilibrium dehydration temperature (°C)	$T_{eq,dehy}$		340	
Reaction enthalpy (kJ/mol)	$\Delta H_{Mg(OH)_2}$		81	
Density (kg/m ³)	$\rho_{Mg(OH)_2}$	714	1022	209.32, 425.88, 638.82
Porosity	$\epsilon_{Mg(OH)_2}$	–	–	90%, 80%, 70%
Dehydrated fraction of water vapor (%)	Δx_{deh}		50–100	
Mixing ratio	r_{mix}	8/9	8/9	–
Thermal conductivity (W/(m.K))	$\lambda_{Mg(OH)_2}$	0.55	1.2	11
Molecular weight of Mg(OH) ₂ (kg/mol)	$M_{Mg(OH)_2}$		0.058	

of expanded natural graphite [36]. For magnesium hydroxide, three options are considered including composite materials made of Mg(OH)₂ and expanded graphite (EG) with an optimized mixing ratio, r_{mix} of 8/9, called EM8 and compressed either into (1) pellet shape [31], (2) as a block to match the dimensions of the container [32], or (3) as loose powder of pure Mg(OH)₂ filled into an aluminum matrix foam.

Dependence of the H₂ absorption time on MgH₂ and Mg(OH)₂ beds thicknesses

The relationship between the hydrogen absorption time and the MgH₂ and Mg(OH)₂ bed thicknesses given by Equations (4) and (5) are used to determine the range of geometrical characteristics of hydrogen storage media and heat storage media so that an absorption time of 5 h, comparable to the one reached in the case of MgH₂ based on latent heat storage, could be achieved [8]. For these calculations, the temperatures of MgH₂ and Mg(OH)₂ media are set equal to the equilibrium temperature of MgH₂ at 1 MPa and the melting temperature of Mg₆₉Zn₂₈Al₃, 370 °C and 340 °C, respectively. The properties of Mg(OH)₂ as EM8 pellets are used (see Table 2) and the dehydrated fraction of water vapor, Δx_{deh} is varied from 50% to 100%, since different values can be achieved depending on the operational conditions of MgO/Mg(OH)₂ system as well as its dehydration reaction time [26].

Case of rectangular geometry of Mg/MgH₂ and MgO/Mg(OH)₂ beds -magnesium hydroxide as EM8 pellets

Fig. 4(a), (b) shows the evolution of the hydrogen absorption time, t_{abs} and the thickness of Mg(OH)₂ media, $L_{Mg(OH)_2}$ as function of the dehydrated fraction of water vapor, Δx_{deh} ranging from 50% to 100% for three selected thicknesses of magnesium hydride bed, $L_{Mg} = 0.5$ cm, 0.75 cm and 1 cm. For a given value of Δx_{deh} , the increase of MgH₂ bed thickness is accompanied by a significant increase of Mg(OH)₂ bed thickness and H₂ absorption time. This is due to the fact that more reaction heat, Q_{abs} is released when thicker MgH₂ media is used. As a result, more Mg(OH)₂ material is required to store this reaction heat, and due to its low thermal conductivity of 0.55 W/(m.K), the conduction of Q_{abs} towards the magnesium hydroxide bed is very slow, inhibiting then the fast absorption of hydrogen.

It should also be noted that for a same thickness of MgH₂ bed, higher dehydrated fractions of water vapor, Δx_{deh} result in shorter hydrogen absorption times and thinner Mg(OH)₂

thicknesses. Indeed, due to the endothermic nature of Mg(OH)₂ dehydration reaction, more heat is required to reach higher dehydrated fractions of water vapor. Therefore, when Δx_{deh} increases and for the same amount of reaction heat, Q_{abs} released by magnesium hydride, less Mg(OH)₂ material is needed. As a result, a faster extraction of this reaction heat from MgH₂ media is obtained, which explains the profiles of t_{abs} and $L_{Mg(OH)_2}$ when Δx_{deh} increases.

By recalling that the hydrogen absorption time should be competitive with the one achieved in case of MgH₂ reactor based on latent heat storage, t_{abs} should not exceed in any case 5 h [8]. For instance, by selecting $L_{Mg} = 0.75$ cm as reference case, this suggests that a *minimum* dehydrated fraction,

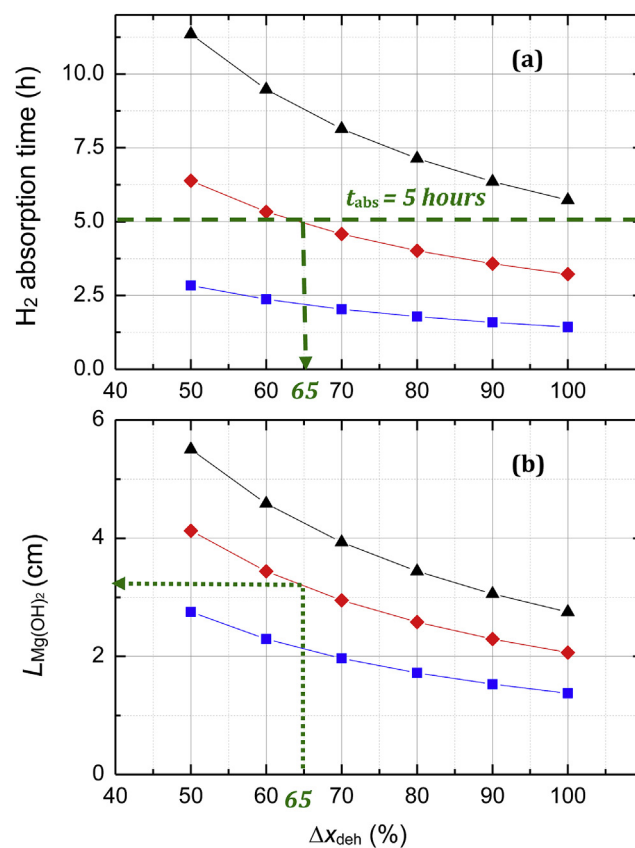


Fig. 4 – Dependence of (a) the H₂ absorption time and (b) the thickness of Mg(OH)₂ media on the dehydrated fraction of water vapor, Δx_{deh} for three selected thicknesses of MgH₂ bed – Case of rectangular geometry.

Δx_{deh} of 65% is required to reach such a goal (see the green dashed line (in the web version) in Fig. 4(a)), and the resulting $\text{Mg}(\text{OH})_2$ bed thickness is equal to 3.25 cm as shown in Fig. 4(b) (green dotted line). Shorter hydrogen absorption times can be expected for higher Δx_{deh} and thinner $\text{Mg}(\text{OH})_2$ bed thicknesses.

Case of cylindrical geometry of Mg/MgH_2 and $\text{MgO}/\text{Mg}(\text{OH})_2$ beds -magnesium hydroxide as EM8 pellets

In cylindrical geometry, the hydrogen absorption time, t_{abs} and the radius of $\text{Mg}(\text{OH})_2$ media, $R_{\text{Mg}(\text{OH})_2}$ are calculated as function of the dehydrated fraction of water vapor, Δx_{deh} ranging from 50% to 100% for three selected magnesium hydride radius, $R_{\text{Mg}} = 1$ cm, 2 cm and 3 cm while assuming a radius of the inner tube, R_1 equal to $1/4 R_{\text{Mg}}$ (see Fig. 3(b)). As can be seen from Fig. 5(a), (b), the evolution of t_{abs} and $R_{\text{Mg}(\text{OH})_2}$ are qualitatively similar to those in case of rectangular geometry (Fig. 4(a), (b)). However, for this cylindrical configuration, calculation results show that the selection of a radius, R_{Mg} of 2 cm or less can ensure the filling of the hydrogen storage media in a time interval less than 5 h (see the green dashed line (in the web version) in Fig. 5(a)). For example, by setting R_{Mg} equal to 2 cm, t_{abs} and $R_{\text{Mg}(\text{OH})_2}$ can vary from 3 to 5 h and from 3.75 cm to 5 cm, respectively, depending on the dehydrated fraction of water vapor, Δx_{deh} .

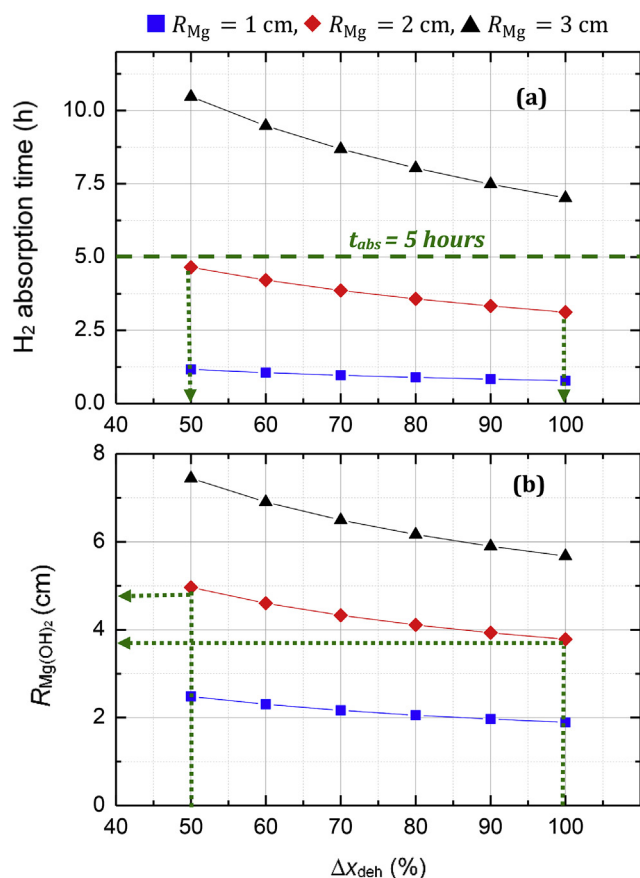


Fig. 5 – Dependence of the H₂ absorption time (a) and the thickness of Mg(OH)₂ media (b) on the dehydrated fraction of water vapor, Δx_{deh} for three selected thicknesses of MgH₂ bed – Case of cylindrical geometry.

Discussion and requirement for the optimization of thermochemical storage

For both, rectangular and cylindrical geometries, hydrogen absorption times much less than 5 h could be achieved for very thin thicknesses of MgH_2 and $\text{Mg}(\text{OH})_2$ media as can be seen from Figs. 4(a) and 5(a). However, the design of MgH_2 reactor based on such geometrical characteristics would require a large number of either, rectangular cells or cylindrical tubes to store the amount of hydrogen required by the targeted application. This would make the MgH_2 storage system based on $\text{Mg}(\text{OH})_2$ heavier and bulkier and increase its total cost. One way to address this issue is to improve the thermal conductivity of the magnesium hydroxide bed so that better heat exchange between the hydrogen and heat storage media could be achieved. This aspect is investigated in the next section while focusing on the cylindrical geometry. The choice of this reactor configuration allows the use of MgH_2 and $\text{Mg}(\text{OH})_2$ in pelletized form while benefiting from their high thermal conductivities in radial direction, as well as a uniform distribution of their operating pressures.

Dependence of the H₂ absorption time on Mg(OH)₂ properties

Three different types of magnesium hydroxide material are selected here to analyze and compare the effect of their densities and thermal conductivities on the performance of hydrogen absorption process. Kato et al. [32] developed a composite material, named EM by drying a mixture of $\text{Mg}(\text{OH})_2$ powder, expanded graphite (EG) and water, and took advantage of its mold-ability property to propose its use as small pellets or a block matching the dimensions of the container. With an optimized mixing mass ratio, r_{mix} of 8/9, this two shaped materials are referred here as EM8 pellets and EM8 block. Despite the high thermal conductivity of EG, their measured thermal conductivities are still low compared to the one of MgH_2 used for calculations (see Tables 1 and 2). Thus, a third alternative is considered where loose powder of pure $\text{Mg}(\text{OH})_2$ material is filled into a metal matrix foam (e.g. based on aluminum). The properties of the considered media are calculated based on the following expressions

$$\rho_{\text{Mg}(\text{OH})_2, \text{eqv}} = \epsilon_{\text{Al.foam}} (1 - \epsilon_{\text{Mg}(\text{OH})_2}) \rho_{\text{Mg}(\text{OH})_2} \quad (6)$$

$$\lambda_{\text{Mg}(\text{OH})_2, \text{eqv}} = \lambda_{\text{Al.foam}} + \epsilon_{\text{Al.foam}} \lambda_{\text{Mg}(\text{OH})_2} \quad (7)$$

while assuming a true density, porosity and thermal conductivity of the $\text{Mg}(\text{OH})_2$ powder of 2340 kg/m³, 90% and 0.1 W/(m.K), respectively [16]. The same properties of aluminum matrix foam presented in Ref. [37] are used for the present calculations and an effective thermal conductivity, $\lambda_{\text{Mg}(\text{OH})_2, \text{eqv}}$ of 11 W/(m.K) is achieved (see Table 2), comparable to that of magnesium hydride.

The H₂ absorption times and $\text{Mg}(\text{OH})_2$ radius of the selected cases are calculated for a minimum dehydrated fraction of water vapor, Δx_{deh} equal to 50% while setting the radius of MgH_2 tube, R_{Mg} at 2 cm. Results are illustrated in Fig. 6.

From these histograms, it is obvious that a significant reduction of H₂ absorption time is obtained with the improvement of $\text{Mg}(\text{OH})_2$ thermal conductivity. By increasing $\lambda_{\text{Mg}(\text{OH})_2}$ by a factor of 2 and 20, it would be possible to store

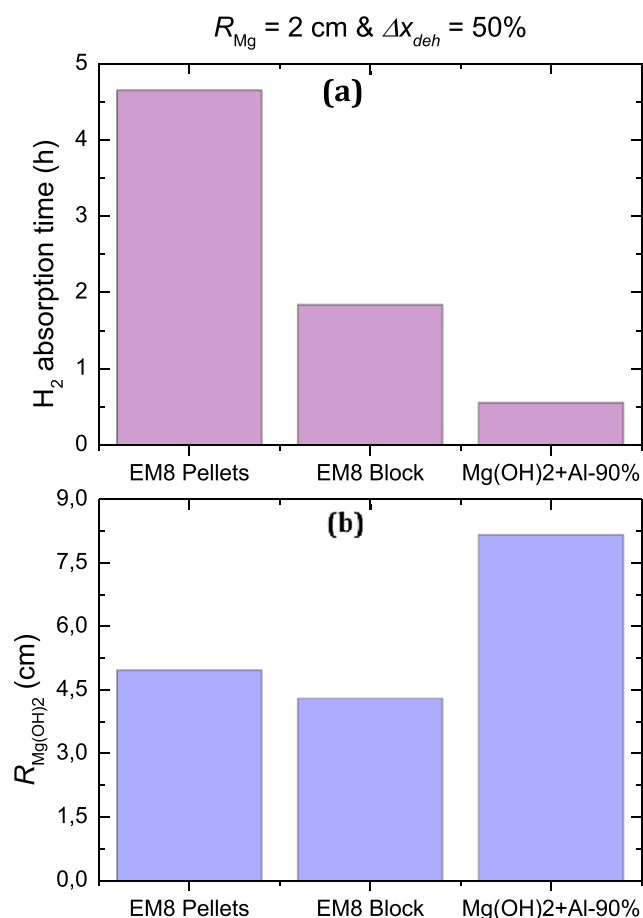


Fig. 6 – H₂ absorption time (a) and Mg(OH)₂ thickness (b) as a function of Mg(OH)₂ material properties (Mg(OH)₂ as EM8 pellets, Mg(OH)₂ as EM8 Block and Mg(OH)₂ as loose powder with a porosity of 90% filled in an Al matrix foam), calculated for a dehydrated fraction of water vapor, Δx_{deh} of 50% and a MgH₂ bed thickness of 2 cm, in case of cylindrical geometry.

hydrogen in time intervals of about 2 h and half an hour, respectively. Better results could be even obtained for higher dehydrated fractions, Δx_{deh}. Regarding the thickness of Mg(OH)₂ media, a slight decrease of R_{Mg(OH)₂} is obtained when the material density is increased by 30% in case of EM8 pellets and EM8 block (compare materials densities in Table 2). However, the use of Mg(OH)₂ as loose powder with a porosity of 90% lowers its density to 209 kg/m³. Thus, more amount of Mg(OH)₂ material is required and its radius is almost the double of R_{Mg(OH)₂} in case of EM8 block and eight times R_{Mg}. It follows from these results that there is a trade-off between the improvement of hydrogen absorption time and the size of the MgH₂/Mg(OH)₂ combination tube if Mg(OH)₂ material is filled into an aluminum matrix foam.

Dependence on the operational conditions

In addition to the geometric characteristics and material properties, the hydrogen absorption time also depends on the operational conditions of pressure and temperature. For magnesium hydride, the storage of hydrogen at a given

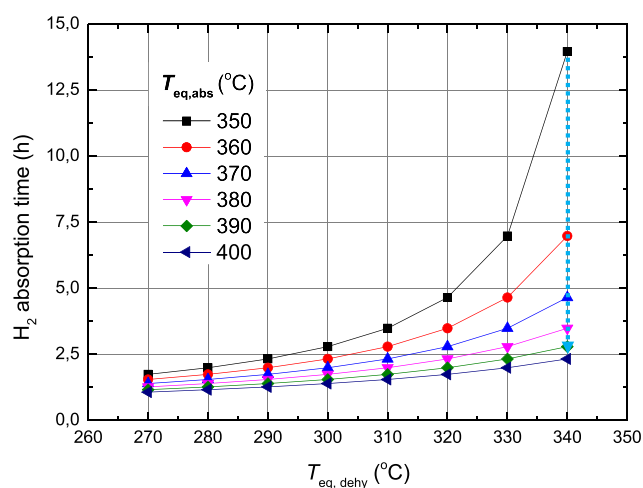


Fig. 7 – Dependence of the H₂ absorption time on the equilibrium H₂ absorption temperature, T_{eq,abs} of MgH₂ system and the equilibrium dehydration temperature, T_{eq,dehy} of Mg(OH)₂ system.

pressure, P_{H₂,abs} is accompanied by a heat release (Q_{abs}) due to the exothermic nature of the reaction. As a result, the hydride bed temperature increases and reaches the equilibrium, T_{eq,abs}. Similarly, during the endothermic dissociation of magnesium hydroxide, the dehydration temperature of the packed Mg(OH)₂ bed, T_{eq,dehy} depends on the water vapor pressure, P_{H₂O,dehy} [19]. Thus, by manipulating the hydrogen absorption pressure and the water vapor pressure, different temperature gradients between the hydride and hydroxide media could be obtained. Here, the hydrogen absorption time is calculated for T_{eq,abs} and T_{eq,dehy} ranging from 350 °C to 400 °C and from 270 °C to 340 °C, respectively (see Eqs. (4) and (5)). The properties of magnesium hydroxide as EM8 pellets with a dehydrated fraction of water vapor, Δx_{deh} of 50% are used for this calculation. The radius of magnesium hydride tube is set at 2 cm, corresponding to a magnesium hydroxide tube radius of 4.96 cm.

Fig. 7 shows the evolution of the hydrogen absorption time as function of the temperature gradient (T_{eq,abs} – T_{eq,dehy}). As expected, it follows that larger temperature gradients between the hydrogen storage media and the heat storage media result in shorter hydrogen absorption times. For example, by setting T_{eq,dehy} at 340 °C and increasing T_{eq,abs} from 350 °C to 400 °C, the hydrogen absorption time is reduced from about 14 h to two hours and a half (see blue dotted line (in the web version) in Fig. 7). This MgH₂ equilibrium temperature range corresponds to an absorption pressure, P_{H₂,abs} varying from 6.2 bar to 18 bar. However, as discussed earlier, the practical absorption pressure, P_{H₂,abs} for the magnesium hydride tank is 10 bar. Thus, it is more suitable to set the hydride temperature at 370 °C and vary T_{eq,dehy} (Curve with blue triangle symbol (in the web version) in Fig. 7). Kato et al. [26,28] showed that reasonable dehydration rates and good cyclic ability at medium-temperatures ranging from 270 °C to 300 °C and dehydration pressures, P_{H₂O,dehy} less than 1 bar, can be achieved when Mg(OH)₂ is mixed with optimized ratios of lithium bromide (LiBr) and expanded graphite (EG). For this same

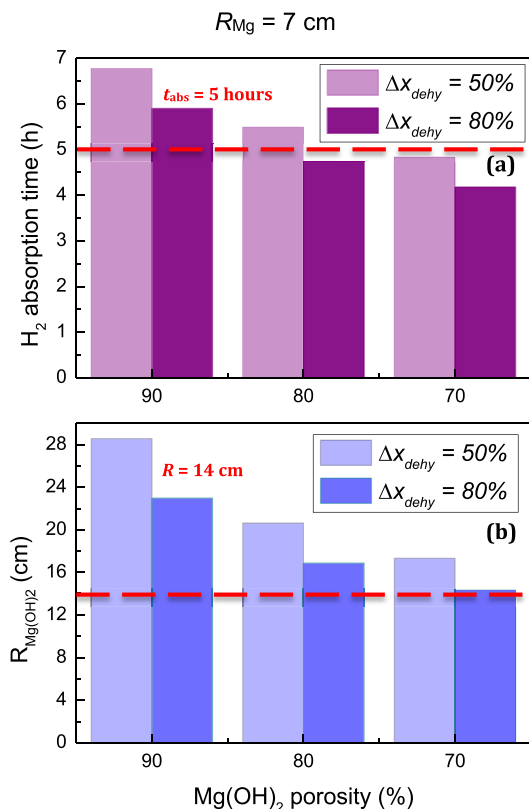


Fig. 8 – H₂ absorption time (a) and Mg(OH)₂ thickness (b) as function of Mg(OH)₂ porosity, calculated for a dehydrated fractions of water vapor, Δx_{deh} of 50% and 80%, and a MgH₂ bed thickness of 7 cm, in case of cylindrical geometry.

range of $T_{eq,dehy}$, a hydrogen absorption time of less than 2 h can be achieved, which is comparable to the case of using EM8 block (compare to Fig. 6).

Considerations for hydrogen desorption process

The same analytical formulation described above for hydrogen absorption can be used for the evaluation of hydrogen desorption time. In this case, the desorption pressure, $P_{H_2,des}$ dictates the minimum temperature to be reached in the magnesium hydride bed. For fuel cell supply applications, hydrogen should be released at pressure greater than or equal to 1 bar, which corresponds to equilibrium desorption temperature close to 300 °C (see MgH₂ van't Hoff diagram in Fig. 1). Accordingly, the hydration of magnesium oxide should occur at higher temperature to ensure the transfer of its reaction heat from the heat storage media to the hydrogen storage media as explained in Section **Thermodynamic considerations**. In other words, a water vapor pressure, $P_{H_2O,hyd}$ above 3.6 bar is required for the hydration of magnesium oxide as it can be seen from the theoretical Mg(OH)₂ van't Hoff diagram presented in Fig. 1. This pressure can, e.g., be ensured by the heat loss of a HT-PEMFCs or even the use of water vapor released during its operation, leading then to a closed system.

Experiments of Kato et al. [32] on MgO hydration reaction in EM8 block showed that at 3.61 bar, hydration was

completed within one hour and the reaction was controlled by heat transfer. However, the measured temperature of the packed bed was approximately 220–230 °C, which is much lower than the one calculated from the theoretical van't Hoff diagram at the same hydration pressure (310 °C at 3.61 bar). Such a result suggests the presence of a hysteresis between the hydration and dehydration reactions and further experimental studies for the MgO/Mg(OH)₂ material are required to indicate which hydration pressure will be needed for the desorption of hydrogen in an application.

Comparison with existing technology

After the general feasibility of the adiabatic hydride storage reactor based on Magnesium hydride/Magnesium hydroxide as well as first geometric studies have been shown, in this section, the new system is compared to state of the art systems with regard to general system properties as well as to H₂ uptake performance. As reference system, the magnesium hydride storage reactor in combination with a PCM has been used [8].

System characteristics

System weight

For the reference study by Garrier et al. [8], Mg₆₉Zn₂₈Al₃ has been used as PCM to store the heat of reaction in the MgH₂ reactor developed. The choice of this eutectic metal alloy is based on its attractive thermodynamic and thermal properties allowing better thermal exchange with MgH₂ media, so that acceptable time intervals for hydrogen absorption and desorption have been achieved in case of stationary applications. However, the use of Mg₆₉Zn₂₈Al₃ results in a drastic decrease of the gravimetric capacity of MgH₂ system. Indeed, starting with a gravimetric capacity of 6.3 wt.% for the MgH₂ pellets, it is lowered to 0.315 wt.% for the whole storage system since a mass of 126 kg of PCM is required to store/release the heat of reaction of 9.9 kg of MgH₂ pellets [8].

For the new reactor concept investigated in this study, Mg(OH)₂ is used as thermochemical heat storage media to store the heat of reaction released during the absorption of hydrogen. The amount of heat to be stored in Mg(OH)₂ dehydration reaction is given by $Q_{abs} = \Delta x \cdot m_{Mg(OH)_2} \cdot \Delta H_{Mg(OH)_2} / M_{Mg(OH)_2}$, where Δx, $m_{Mg(OH)_2}$, $M_{Mg(OH)_2}$ and $\Delta H_{Mg(OH)_2}$ are the reacted fraction of water vapor in 1, the mass in kg, the molecular weight of Mg(OH)₂ in kg mol⁻¹ and the enthalpy of reaction in J mol⁻¹, respectively. Based on the same mass of MgH₂ contained in the H₂ storage system using latent heat storage and its corresponding gravimetric capacity, the mass of Mg(OH)₂ required to remove the reaction heat generated during hydrogen absorption is

$$m_{Mg(OH)_2} = (w_t \cdot m_{MgH_2} \cdot \Delta H_{MgH_2} / M_{H_2}) / (\Delta x \cdot \Delta H_{Mg(OH)_2} / M_{Mg(OH)_2}) \quad (8)$$

where w_t , m_{MgH_2} and ΔH_{MgH_2} are the gravimetric capacity in wt.%, the mass in kg and the enthalpy of MgH₂ in J mol⁻¹ respectively and M_{H_2} is the molecular weight of hydrogen in kg mol⁻¹.

Even in a worst case scenario, where only $\Delta x = 50\%$ of the water vapor reacts, this results in a mass, $m_{\text{Mg(OH)}_2}$ of 31.6 kg using data listed in Tables 1 and 2. This represents a quarter of $\text{Mg}_{69}\text{Zn}_{28}\text{Al}_3$ mass used in Ref. [8] and it refers to a gravimetric capacity of still approx. 1.5 wt.%. Even though magnesium hydride is mainly used for stationary applications where achieving low system weight is not considered as high priority, it is obvious that the development of MgH_2 reactor using Mg(OH)_2 as thermochemical storage media would result in a considerable improvement of the gravimetric capacity of the whole storage system.

Furthermore, it can also be noted that the overall gravimetric capacity of the $\text{MgH}_2 + \text{Mg(OH)}_2$ with 1.5 wt.% is still in the range or even better than the capacity of classical metal hydride materials like LaNi_5 with approx. 1.3 wt.% [38].

System cost

For the Mg(OH)_2 material, the required mass is not only reduced to one quarter of the mass for the PCM, but also the cost per kg is significantly lower than for the PCM. Therefore, it is obvious that the system cost of the presented storage reactor is much lower. For instance, with a commercial price of 0.2–1 \$/kg [39], the storage reactor based on the Mg(OH)_2 will have extra material costs of approx. 20 to 30 \$. In contrast, as the price of magnesium (Mg), Zinc (Zn) and aluminum (Al) materials is approximately between 2 and 3 \$/kg [40], the material cost for the PCM storage are 250–375 \$! Thus, even though the reactor design for the Mg(OH)_2 material might be more complex, there exists a significant potential benefit of the new adiabatic MgH_2 reactor concept based on thermochemical heat storage.

System reliability and complexity

When looking at the system complexity, it is obvious that the combination of a MgH_2 with the Mg(OH)_2 system is more complex than the combination with a PCM. This is mainly due to the required water management for the Mg(OH)_2 material. However, as suggested in the operating principle, the integration with a HT-PEMFC can be sufficient to provide the required water for hydrogen desorption.

Furthermore, it is clear that the suggested concept is on a very low technology readiness level at the moment; however, it could also offer an advantage in system complexity: For the PCM, special care has to be taken to avoid cooling down below the melting temperature when storing the heat. In contrast, the Mg(OH)_2 system can still operate, even if it was cooled down to room temperature as the heat is stored in the chemical reaction (with a heat capacity that is reduced by the temperature decrease).

Flexibility of the system

Another advantage of the proposed concept is the flexibility of the operational conditions for both, magnesium hydride and magnesium hydroxide reactions. Indeed, for the H_2 storage system based on latent heat storage, the operation temperature of the phase change material is fixed and the driving temperature gradient between the MgH_2 and the PCM needs to be generated by the hydrogen storage material itself by imposing a higher hydrogen absorption pressure than the desorption. In case of MgH_2 reactor based on thermochemical

heat storage, the thermochemical material can contribute to the generation of different temperature gradients by varying the condensation and evaporation temperatures, T_c and T_v , respectively. Thus, larger driving temperature gradients between the hydrogen and heat storage media can be achieved and more efficient use of the reaction heat is expected.

System performance

Complementing the comparison of some general characteristics of the storage reactor, in this section the performance of this new adiabatic hydride reactor with Mg(OH)_2 is compared to the PCM-based system from the literature using the identical geometry.

The MgH_2 reactor based on latent heat storage [8] consists of two concentric tubes filled with MgH_2 and PCM and having radius of 7 cm and 14 cm, respectively. It was filled with hydrogen in a time interval of 5 h. Thus, the same radius of magnesium hydride tube, R_{Mg} equal to 7 cm is selected to recalculate the hydrogen absorption time using the equations presented before. As with this thick inner diameter the heat conductivity of the Mg(OH)_2 material gets more and more important, the radius of Mg(OH)_2 tube has been calculated for a case where the material is filled into an aluminum matrix foam. Due to the low density of the Mg(OH)_2 with 90% of porosity (see Eq. (6)), this results also in a very thick radius for this material. In order to address this problem, the Mg(OH)_2 porosity, $\epsilon_{\text{Mg(OH)}_2}$ is improved from 90% to 70% in the present calculations resulting in Mg(OH)_2 densities ranging from 209 kg/m³ to 638 kg/m³ for the same value of thermal conductivity, $\lambda_{\text{Mg(OH)}_2, \text{eqv}}$ equal to 11 W/(m.K).

Fig. 8 shows the resulting absorption time and Mg(OH)_2 radius for two values of the dehydrated fraction of water vapor, Δx_{deh} (50% and 80%). From these histograms, it can be seen that a comparable performance of the developed MgH_2 reactor based on latent heat storage could be achieved when magnesium hydroxide has a thermal conductivity of 11 W/(m.K) and a porosity of 70%. The corresponding density is equivalent to that of pelletized pure Mg(OH)_2 studied by Kato et al. [32]. With such properties and for Δx_{deh} of 80%, the radius of the Mg(OH)_2 tube is equal to 14 cm, same as the radius of PCM tube for the MgH_2 tank developed by Garrier et al. [8].

From a practical perspective, it is tricky to achieve such a density by filling the Mg(OH)_2 material into an aluminum matrix foam. However, the obtained results are useful since they allow to determine the optimum range of density and thermal conductivity of Mg(OH)_2 media so that comparable hydrogen storage performance to the case of MgH_2 based on latent heat storage could be achieved while using a less weight and cost thermochemical material, as discussed before.

Conclusions

In this paper, the feasibility of a new adiabatic metal hydride reactor concept using a thermochemical heat storage material to store the absorption reaction heat has been studied. Magnesium hydride and magnesium hydroxide have been identified as suitable reference materials to be combined based on their operating temperatures range. In addition, both of them

are promising materials in terms of cost, availability and storage capacity.

The performance of the hydrogen loading process for this new reactor concept has been evaluated based on an analytical formulation of the hydrogen absorption time as function of the geometrical characteristics of the two storage media, their properties and their operating conditions. The analytical formulation was applied for a pelletized magnesium hydride media and three types of magnesium hydroxide material: EM8 pellets, EM8 block and pure $\text{Mg}(\text{OH})_2$ filled in an aluminum matrix foam, to determine materials and systems parameters for different geometries and material parameters.

The main results arising from these calculations are that short hydrogen absorption times (less than 5 h) could be achieved for a reference MgH_2 pellet and thin $\text{Mg}(\text{OH})_2$ media thickness, and the improvement of the thermal conductivity of magnesium hydroxide bed enables the use of thicker hydrogen and heat storage media for the same absorption time intervals.

The comparison with state of the art MgH_2 tank using PCM showed that a comparable hydrogen absorption time and geometric characteristics could also be achieved if the effective $\text{Mg}(\text{OH})_2$ thermal conductivity is equal to the one of pelletized MgH_2 (~10 W/(m.K)) with a density of 638 kg/m³. Moreover, the possibility to adjust the gas pressures independently allows for more flexible operations. By adjusting the water vapor pressure and the hydrogen ab- and desorption pressures, faster dynamics of the system could be reached since higher gradient between the equilibrium temperatures of the two hydrogen and thermochemical heat storage media can be achieved.

Furthermore, with such a reactor design, the required mass of $\text{Mg}(\text{OH})_2$ is reduced by a factor of 4 in comparison to the mass of phase change material used in MgH_2 reactor based on latent heat storage. This will result in an adiabatic hydrogen storage system of lower cost (factor 10) and higher gravimetric capacity compared to the one using phase change material, potentially opening then the way to its integration in applications other than stationary sector.

Acknowledgements

M.B. would like to thank the German Academic Exchange Service (DAAD) for the DLR-DAAD Research Fellowship.

REFERENCES

- [1] Lototsky M, Satya Sekhar B, Muthukumar P, Linkov V, Pollet BG. Niche applications of metal hydrides and related thermal management issues. *J Alloys Compd* 2015;645:10–5. <http://dx.doi.org/10.1016/j.jallcom.2014.12.271>.
- [2] Lototsky MV, Yartys VA, Pollet BG, Bowman RC. Metal hydride hydrogen compressors: a review. *Int J Hydrogen Energy* 2014;39:5818–51. <http://dx.doi.org/10.1016/j.ijhydene.2014.01.158>.
- [3] Bhuiya MMH, Kumar A, Kim KJ. Metal hydrides in engineering systems, processes, and devices: a review of non-storage applications. *Int J Hydrogen Energy* 2015;40:2231–47. <http://dx.doi.org/10.1016/j.ijhydene.2014.12.009>.
- [4] Paskevicius M, Sheppard DA, Williamson K, Buckley CE. Metal hydride thermal heat storage prototype for concentrating solar thermal power. *Energy* 2015;88:469–77. <http://dx.doi.org/10.1016/j.energy.2015.05.068>.
- [5] Fiori C, Dell'Era A, Zuccari F, Santiangeli A, D'Orazio A, Orecchini F. Hydrides for submarine applications: overview and identification of optimal alloys for air independent propulsion maximization. *Int J Hydrogen Energy* 2015;40:11879–89. <http://dx.doi.org/10.1016/j.ijhydene.2015.02.105>.
- [6] Sakintuna B, Lamari-Darkrim F, Hirscher M. Metal hydride materials for solid hydrogen storage: a review. *Int J Hydrogen Energy* 2007;32:1121–40. <http://dx.doi.org/10.1016/j.ijhydene.2006.11.022>.
- [7] Mazzucco A, Dornheim M, Sloth M, Jensen TR, Jensen JO, Rokni M. Bed geometries, fueling strategies and optimization of heat exchanger designs in metal hydride storage systems for automotive applications: a review. *Int J Hydrogen Energy* 2014;39:17054–74. <http://dx.doi.org/10.1016/j.ijhydene.2014.08.047>.
- [8] Garrier S, Delhomme B, de Rango P, Marty P, Fruchart D, Miraglia S. A new MgH_2 tank concept using a phase-change material to store the heat of reaction. *Int J Hydrogen Energy* 2013;38:9766–71. <http://dx.doi.org/10.1016/j.ijhydene.2013.05.026>.
- [9] Delhomme B, Lanzini A, Ortigoza-Villalba GA, Nachev S, de Rango P, Santarelli M, et al. Coupling and thermal integration of a solid oxide fuel cell with a magnesium hydride tank. *Int J Hydrogen Energy* 2013;38:4740–7. <http://dx.doi.org/10.1016/j.ijhydene.2013.01.140>.
- [10] Abedin AH, Rosen MA. A critical review of thermochemical energy storage systems. *Open Renew Energy J* 2011;4:42–6. <http://dx.doi.org/10.2174/1876387101004010042>.
- [11] Aydin D, Casey SP, Riffat S. The latest advancements on thermochemical heat storage systems. *Renew Sustain Energy Rev* 2015;41:356–67. <http://dx.doi.org/10.1016/j.rser.2014.08.054>.
- [12] Myagmarjav O, Zamengo M, Ryu J, Kato Y. Energy density enhancement of chemical heat storage material for magnesium oxide/water chemical heat pump. *Appl Therm Eng* 2015. <http://dx.doi.org/10.1016/j.applthermaleng.2015.08.008>.
- [13] Schmidt M, Szczukowski C, Roßkopf C, Linder M, Wörner A. Experimental results of a 10 kW high temperature thermochemical storage reactor based on calcium hydroxide. *Appl Therm Eng* 2014;62:553–9. <http://dx.doi.org/10.1016/j.applthermaleng.2013.09.020>.
- [14] Kuravi S, Trahan J, Goswami DY, Rahman MM, Stefanakos EK. Thermal energy storage technologies and systems for concentrating solar power plants. *Prog Energy Combust Sci* 2013;39:285–319. <http://dx.doi.org/10.1016/j.pecs.2013.02.001>.
- [15] Pardo P, Deydier A, Anxionnaz-Minvielle Z, Rougé S, Cabassud M, Cognet P. A review on high temperature thermochemical heat energy storage. *Renew Sustain Energy Rev* 2014;32:591–610. <http://dx.doi.org/10.1016/j.rser.2013.12.014>.
- [16] Zamengo M, Ryu J, Kato Y. Numerical analysis of chemical heat storage units for waste heat recovery in steel making processes. *ISIJ Int* 2015;55:473–82. <http://dx.doi.org/10.2355/isijinternational.55.473>.
- [17] Jehan M, Fruchart D. McPhy-Energy's proposal for solid state hydrogen storage materials and systems. *J Alloys Compd* 2013;580:S343–8. <http://dx.doi.org/10.1016/j.jallcom.2013.03.266>.

- [18] Chaise A, de Rango P, Marty P, Fruchart D. Experimental and numerical study of a magnesium hydride tank. *Int J Hydrogen Energy* 2010;35:6311–22. <http://dx.doi.org/10.1016/j.ijhydene.2010.03.057>.
- [19] Kato Y, Yamashita N, Kobayashi K, Yoshizawa Y. Kinetic study of the hydration of magnesium oxide for a chemical heat pump. *Appl Therm Eng* 1996;16:853–62. [http://dx.doi.org/10.1016/1359-4311\(96\)00009-9](http://dx.doi.org/10.1016/1359-4311(96)00009-9).
- [20] Kato Y, Kobayashi K, Yoshizawa Y. Durability to repetitive reaction of magnesium oxide/water reaction system for a heat pump. *Appl Therm Eng* 1998;18:85–92. [http://dx.doi.org/10.1016/S1359-4311\(97\)00058-6](http://dx.doi.org/10.1016/S1359-4311(97)00058-6).
- [21] Kato Y, Nakahata J, Yoshizawa Y. Durability characteristics of the hydration of magnesium oxide under repetitive reaction. *J Mater Sci* 1999;4:475–80. <http://dx.doi.org/10.1023/A:1004530309298>.
- [22] Kato Y, Takahashi F, Watanabe A, Yoshizawa Y. Thermal analysis of a magnesium oxide/water chemical heat pump for cogeneration. *Appl Therm Eng* 2001;21:1067–81. [http://dx.doi.org/10.1016/S1359-4311\(00\)00103-4](http://dx.doi.org/10.1016/S1359-4311(00)00103-4).
- [23] Kato Y. Development of a magnesium oxide/water chemical heat pump for efficient energy storage and utilization. In: *V Minsk International Seminar “Heat Pipes, Heat Pumps, Refrigerators”*; 2003. p. 129–40.
- [24] Ishitobi H, Uruma K, Takeuchi M, Ryu J, Kato Y. Dehydration and hydration behavior of metal-salt-modified materials for chemical heat pumps. *Appl Therm Eng* 2013;50:1639–44. <http://dx.doi.org/10.1016/j.applthermaleng.2011.07.020>.
- [25] Myagmarjav O, Ryu J, Kato Y. Kinetic analysis of the effects of mixing mole ratios of LiBr-to-Mg(OH)₂ on dehydration and hydration. *J Chem Eng Jpn* 2014;47:595–601. <http://dx.doi.org/10.1252/jcej.13we301>.
- [26] Myagmarjav O, Ryu J, Kato Y. Dehydration kinetic study of a chemical heat storage material with lithium bromide for a magnesium oxide/water chemical heat pump. *Prog Nucl Energy* 2015;82:153–8. <http://dx.doi.org/10.1016/j.pnucene.2014.07.026>.
- [27] Myagmarjav O, Ryu J, Kato Y. Lithium bromide-mediated reaction performance enhancement of a chemical heat-storage material for magnesium oxide/water chemical heat pumps. *Appl Therm Eng* 2014;63:170–6. <http://dx.doi.org/10.1016/j.applthermaleng.2013.10.045>.
- [28] Kim ST, Ryu J, Kato Y. Optimization of magnesium hydroxide composite material mixed with expanded graphite and calcium chloride for chemical heat pumps. *Appl Therm Eng* 2013;50:485–90. <http://dx.doi.org/10.1016/j.applthermaleng.2012.07.005>.
- [29] Kim ST, Ryu J, Kato Y. The optimization of mixing ratio of expanded graphite mixed chemical heat storage material for magnesium oxide/water chemical heat pump. *Appl Therm Eng* 2014;66:274–81. <http://dx.doi.org/10.1016/j.applthermaleng.2014.02.024>.
- [30] Zamengo M, Ryu J, Kato Y. Magnesium hydroxide – expanded graphite composite pellets for a packed bed reactor chemical heat pump. *Appl Therm Eng* 2013;61:853–8. <http://dx.doi.org/10.1016/j.applthermaleng.2013.04.045>.
- [31] Zamengo M, Ryu J, Kato Y. Thermochemical performance of magnesium hydroxide–expanded graphite pellets for chemical heat pump. *Appl Therm Eng* 2014;64:339–47. <http://dx.doi.org/10.1016/j.applthermaleng.2013.12.036>.
- [32] Zamengo M, Ryu J, Kato Y. Composite block of magnesium hydroxide – expanded graphite for chemical heat storage and heat pump. *Appl Therm Eng* 2014;69:29–38. <http://dx.doi.org/10.1016/j.applthermaleng.2014.04.037>.
- [33] Visaria M, Mudawar I, Pourpoint T, Kumar S. Study of heat transfer and kinetics parameters influencing the design of heat exchangers for hydrogen storage in high-pressure metal hydrides. *Int J Heat Mass Transf* 2010;53:2229–39. <http://dx.doi.org/10.1016/j.ijheatmasstransfer.2009.12.010>.
- [34] Corgnale C, Hardy BJ, Tamburello DA, Garrison SL, Anton DL. Acceptability envelope for metal hydride-based hydrogen storage systems. *Int J Hydrogen Energy* 2012;37:2812–24. <http://dx.doi.org/10.1016/j.ijhydene.2011.07.037>.
- [35] Marty Ph, de Rango P, Delhomme B, Garrier S. Various tools for optimizing large scale magnesium hydride storage. *J Alloys Compd* 2013;580:S324–8. <http://dx.doi.org/10.1016/j.jallcom.2013.02.169>.
- [36] Chaise A. Etude expérimentale et numérique de réservoirs d’hydrure de magnésium. 2010. <https://tel.archives-ouvertes.fr/tel-00351465/document> [viewed 07.09.2016].
- [37] Laurencelle F, Goyette J. Simulation of heat transfer in a metal hydride reactor with aluminium foam. *Int J Hydrogen Energy* 2007;32:2957–64. <http://dx.doi.org/10.1016/j.ijhydene.2006.12.007>.
- [38] van Mal HH. A LaNi₅-hydride thermal absorption compressor for a hydrogen refrigerator. *Chem Ing Tech CIT* 1973;45:80–3. <http://dx.doi.org/10.1002/cite.330450207>.
- [39] Magnesium Hydroxide Pricing. <http://magnesiumhydroxide.com> [viewed 07.09.2016].
- [40] METALPRICES.COM. <http://www.metalprices.com> [viewed 07.09.2016].

Nomenclature

Materials

Al: aluminum
 EG: expanded graphite
 Mg/MgH₂: magnesium/magnesium hydride
 MgO/Mg(OH)₂: magnesium oxide/magnesium hydroxide
 Mg₆₉Zn₂₈Al₃: metallic PCM

Parameters

L: thickness of layer, m
 m: mass, kg
 M: molecular weight, kg mol⁻¹
 P: pressure, MPa
 Q: heat, kJ
 r_{mix}: mixing ratio of graphite and MgO
 R: radius, m
 t: time, hour
 T: temperature, °C
 w_t: transformed weight fraction of metal hydride, %
 Δx: reacted fraction of water vapor
 ΔH: reaction enthalpy, kJ mol⁻¹ K⁻¹
 λ_i: thermal conductivity of component i
 ε: porosity
 ρ: density, kg m⁻³

Subscripts

abs: absorption
 c: condensation
 dehy: dehydration
 des: desorption
 eq: equilibrium
 eqv: equivalent
 e: evaporation
 hy: hydration



ELSEVIER

Available online at www.sciencedirect.com

ScienceDirect

journal homepage: www.elsevier.com/locate/he

Novel reactor design for metal hydride cooling systems

C. Weckerle*, I. Bürger, M. Linder

Institute of Engineering Thermodynamics, German Aerospace Center (DLR), Pfaffenwaldring 38-40, D-70569 Stuttgart, Germany

ARTICLE INFO

Article history:

Received 4 November 2016

Received in revised form

9 January 2017

Accepted 10 January 2017

Available online 28 February 2017

Keywords:

Metal hydride

Reactor design

Plate reactor

Metal hydride cooling system

Air-conditioning in fuel cell vehicle

ABSTRACT

In this paper a plate reactor for metal hydride applications is presented and experimentally characterized. Through an optimized heat transfer characteristic the concept is suitable for all metal hydride high performance systems, where short reaction times are required. The experimental characterization using metal hydride Hydralloy® C5 reveals that very short half-cycle times ($t < 60$ s) are feasible enabling small and compact systems. With regard to the application of an open metal hydride cooling system for fuel cell vehicles and a cooling temperature of 10 °C, single reactor experiments lead to a high specific cooling power of 1.31 kW kg_{MeH}⁻¹. In a continuous working system where thermal losses are considered, still 690 W kg_{MeH}⁻¹ can be reached.

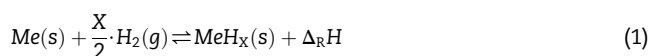
© 2017 Hydrogen Energy Publications LLC. Published by Elsevier Ltd. All rights reserved.

Introduction and operation principle

Electrical and fuel cell (FC) driven vehicles are considered as promising solutions to reduce the dependency on fossil fuels. In these vehicles, state of the art conventional compressor driven air-conditioning systems are the largest auxiliary power load with a significant impact on the vehicle range [1]. For FC vehicles, Pino et al. [2] have shown an increase of hydrogen consumption of up to 12.1% when the air-conditioning system is in operation. Additionally, current refrigerants for these systems show a high GWP or are flammable [3].

For this reason, innovative solutions for air-conditioning systems that are able to minimize the discrepancy between increased driving range and interior comfort have to be

developed. One possible approach for future air-conditioning systems are metal hydride based cooling systems (MHCS). In these systems the reversible reaction between metal hydrides and hydrogen is utilized. According to the reaction equation



the absorption and desorption of hydrogen is accompanied with a heat of formation $\Delta_R H$ that supplies – depending on the direction of the reaction – cold and heat for a cooling system or a heat pump, respectively.

In Fig. 1 the operation principle of a so called open MHCS (abbreviations according to Table 1) system is illustrated. In this system, a metal hydride reactor is integrated between the pressure tank and the fuel cell of a FC vehicle [4]. For an advanced driving range of FC cars, state of the art pressure

* Corresponding author. Fax: +49 711 6862 632.

E-mail address: Christoph.Weckerle@dlr.de (C. Weckerle).

<http://dx.doi.org/10.1016/j.ijhydene.2017.01.066>

0360-3199/© 2017 Hydrogen Energy Publications LLC. Published by Elsevier Ltd. All rights reserved.

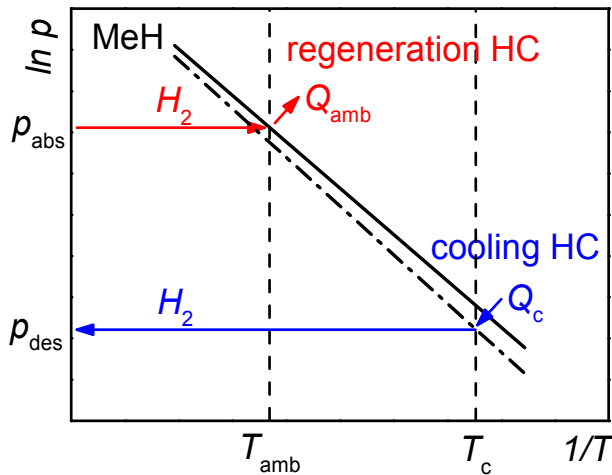


Fig. 1 – Operation principle of the open metal hydride based cooling system.

tanks are used where hydrogen is compressed up to 700 bar. For this compression process up to 15.5% [5] of the heating value of hydrogen is needed that is so far wasted, as during operation the pressure is simply throttled down to the pressure level of the fuel cell. With the open system it is possible to reuse part of this potential energy by generating cold. Thereby, the system operates at two pressure levels – the absorption pressure p_{abs} with hydrogen from the pressure tank and the fuel cell pressure p_{des} . In the regeneration half-cycle (HC), the metal hydride is initially charged with hydrogen from the pressure tank. Since the absorption of hydrogen is an exothermic reaction, the heat of formation is released to the ambient (cf. conventional heat pumps) or can be used for heating in winter months. Then, the desired cooling effect results from the subsequent desorption of hydrogen at the fuel cell supply pressure by absorbing heat at low temperature in the endothermic cooling half-cycle. In order to realise a “quasi-continuous” system, at least two identical alternating metal hydrides reactors have to be used, while the hydrogen from the pressure tank just passes the reactors before it is converted in the fuel cell. Thus, the open MHCS does not consume any hydrogen, but it simply uses part of the potential energy that is intrinsically available on-board in the 700 bar pressure tank.

In addition to the aforementioned open MHCS, there are so called closed MHCS where the released hydrogen of the cooling-half cycle is absorbed by a second metal hydride with a lower equilibrium characteristic. The hydrogen cycle is closed in the regeneration by a thermal compression using a heat source. MHCS – especially thermally driven closed MHCSs based on a coupled pair of MeHs – have been known and explored for more than thirty years. In review papers, Muthukumar et al. [6] and Bhuiya et al. [7] summarize the research progress and the current state of technology. A variety of systems are listed that mostly show low specific cooling powers and large half-cycle times. E.g. Qin et al. [8] developed an exhaust gas-driven automobile air conditioner system using cylindrical tube reactors. Related to metal hydride mass of one desorbing reactor, for the operating conditions of 150 °C/30 °C/0 °C an average specific cooling power of

Table 1 – Abbreviations and nomenclature.

Abbreviations:	
COP	Coefficient of performance
HC	Half-cycle
HTF	Heat transfer fluid
MHCS	Metal hydride cooling system
NPDM	Norm. pressure dependence method
PCI	Pressure-concentrations-isotherms
SCP	Specific cooling power
Nomenclature:	
A	Arrhenius coefficient, s^{-1}
c_p	Specific heat capacity, $J kg^{-1} K^{-1}$
E_a	Activation energy, $J K^{-1}$
ΔH	Heat of formation, $J mol^{-1}$
k	Reaction rate constant, s^{-1}
m	Mass, kg
n_{H_2}	Desorbed hydrogen, mol
p	Pressure, Pa
q	Specific heat, $J kg_{MeH}^{-1}$
\dot{q}	Specific power, $W kg_{MeH}^{-1}$
R	Universal gas constant, $J mol^{-1} K^{-1}$
r	Mass ratio, –
ΔS	Entropy of reaction, $J mol^{-1} K^{-1}$
T	Temperature, °C
t	Time, s
\dot{V}	Volume flow rate, $m^3 s^{-1}$
w	Hydrogen capacity, wt.%
X	Transformed fraction, –
Greek letters:	
ρ	Density, $kg m^{-3}$
τ_{TC}	Time constant, s
τ_{HC}	Half-cycle time, s
Subscripts:	
abs	Absorption
amb	Ambient
c	Cool
des	Desorption
eq	Equilibrium
i	Intrinsic
in	Inlet
max	Maximum
out	Outlet
PR	Plate reactor
r	Mass ratio
rb	Reaction bed
sys	System
TB	Thermostatic bath
TC	Time constant

30.7 $W kg_{MeH}^{-1}$, with a refrigeration half-cycle time of 1300 s was obtained. Also using cylindrical tube reactors with a central tube for the heat transfer fluid, Ni et al. [9] investigated the influence of the heat source temperature (115 °C, 130 °C and 150 °C) on the performance of a closed MHCS. As a result, both the average cooling power and the coefficient of performance (COP) increase with growing temperature. For a heat source temperature of 150 °C an average specific cooling power of 89 $W kg_{MeH}^{-1}$ was realized.

However, two more promising approaches are the following: In 1984 at the department of Materials Engineering, Technion – Israel Institute of Technology [10], a single stage MHCS driven by the exhaust gas of a bus was

developed. Upon cycling operation, a specific cooling power of 200–250 W kg_{MeH}⁻¹ and a half-cycle time for complete transformed fraction of 6 min for the material pair MmNi_{4.15}Fe_{0.85} (porous MeH compact) and LaNi_{4.7}Al_{0.3} (powder) was observed. Using two optimized capillary tube bundle reactors and a system with Ti_{0.99}Zr_{0.01}V_{0.43}Fe_{0.09}Cr_{0.05}Mn_{1.5}/Lm_{4.91}Sn_{0.15}, in 2010, Linder [11] realised a specific cooling power of 640 W kg_{MeH}⁻¹ at operating conditions of 130 °C/28 °C/15 °C.

These specific cooling power values are promising, however, for compact and lightweight systems in automotive applications the specific cooling power (SCP) of MHCS have to be further improved. Indeed, with regard to the intrinsic material properties of metal hydrides, much larger values of the SCP are possible due to the high reaction rates and enthalpies [12]. The observed gap between theoretically intrinsic feasible thermal powers and experimentally proven thermal powers is mainly due to heat transfer limitations in the reaction bed. Thus, the challenge is to transfer the heat/cold as fast as possible with small gradients to the desired heat transfer fluid.

This paper investigates a novel reactor design based on a plate heat exchanger that enables high systems performances and reduced hydrogen uptake or release times by an improved heat transfer characteristic. Since metal hydrides are used in a variety of engineering fields, this plate reactor concept will also be suitable for all applications where short reaction times are required. Beside the aforementioned MHCS, this is particular the case for metal hydride based heat pumps including heat transformers and thermally driven hydrogen compressors. In all these applications, the specific and volumetric power density mainly depends on the reactor design [13,14].

The organization of the paper is the following: First, the requirements for a high performance metal hydride reactor and the realized design of the plate reactor are presented in detail. Based on this introduction, the plate reactor is experimentally characterized in single reactor measurements and the performance is compared to intrinsic kinetic data. Finally, the plate reactor performance is evaluated with regard to constraints applying in an open MHCS.

Reactor design and choice of metal hydride

In the following section, general restraints and requirements of the reactor design for metal hydride high performance systems are presented. Based on this, the plate reactor is shown in detail and a suitable metal hydride is selected.

Reactor design

With regard to a suitable reactor design the mechanical stability as well as specified performance criteria have to be considered. In principle, criteria that limit the performance can be divided into four main aspects that have to be included in the reactor design and the material selection:

- The intrinsic reaction kinetics of the selected metal hydride.
- Hydrogen mass transfer in the reaction bed.
- Heat transfer characteristics of the reaction bed.
- Sensible mass of the overall reactor (especially for MHCS).

In Fig. 2, the impact of these potential limitations on the transformed fraction of a metal hydride reactor and the challenge of the reactor design for high performance systems is exemplary illustrated for a decomposition reaction. Thereby, the transformed fraction is defined as the ratio of the hydrogen capacity $w(t)$ at a time t and the maximum hydrogen capacity w_{\max} depending on the metal hydride. Starting from a completely hydrogenated state, the system pressure (black curve) as step input is reduced below the equilibrium pressure causing a desorption of the material. The transformed fraction $X(t)$ of the hydride using the intrinsic material properties (red) and the reaction bed dynamics (blue) are shown in the graph. As system response for both curves, a first order reaction can be assumed that is expressed by:

$$X(t) = 1 - \exp\left(-\frac{t}{\tau_{TC}}\right) \quad (2)$$

The time constant τ_{TC} corresponding the required time to reach 63.2% of the complete transformed fraction is used to characterize the response of such a linear time-invariant, first order system. After a time interval of $t = 5 \tau_{TC}$ and a transformed fraction of 99.3% the process is assumed to be completed. This time τ_{HC} is defined as half-cycle time for a complete transformed fraction. Comparing the schematic transformed fraction of the intrinsic kinetic and reaction bed dynamic in Fig. 2, both, the time constant and the half-cycle time for a complete transformed fraction are extended through the limitations in the reaction bed leading to a reduced system performance.

On a material basis, literature intrinsic kinetic measurements prove that very high-reaction rates and a full transformed fraction can be reached within seconds. E.g., for titanium manganese alloys, as used in this approach, a half-cycle time of 10 s for the desorption into vacuum with a

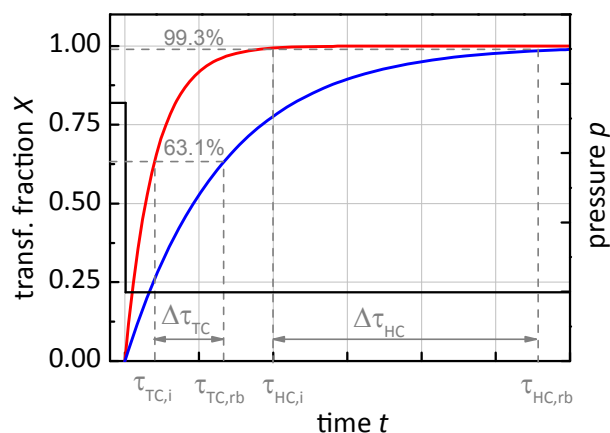


Fig. 2 – Schematic comparison of intrinsic kinetics (red) and reaction bed dynamics (blue) with hydrogen pressure (black). $\tau_{TC,i}$: Time constant of intrinsic kinetics, $\tau_{TC,rb}$: Time constant of reaction bed dynamics, $\tau_{HC,i}$: Half-cycle time for a complete transformed fraction of intrinsic kinetics, $\tau_{HC,rb}$: Half-cycle time for a complete transformed fraction of reaction bed dynamics. (For interpretation of the references to colour in this figure legend, the reader is referred to the web version of this article.)

hydride temperature of 20 °C is proven [15]. Thereby a specific cooling power for MHCS of around $20 \div 25 \text{ kW kg}_{\text{MeH}}^{-1}$ is theoretically obtainable when thermal losses are neglected. As a result intrinsic material limitations can be excluded when an appropriate MeH is selected. Furthermore, mass transfer limitations due to insufficient hydrogen transport can be avoided when a sintered metal filter is used. By integrating such a filter into the gas supply of the reactor, a uniform distribution of hydrogen in the entire hydride reaction bed can be achieved [16].

Consequently, previously published work pointed out that the system performance of the aforementioned MeH applications is mainly limited by heat transfer [16–18]. This includes in particular the internal heat transfer in the metal hydride bed and the external heat transfer to the heat transfer fluid. When the heat flow supplied (desorption) or dissipated (absorption) is lower than the respective heat flux due to the chemical reaction, the hydride formation or decomposition stops and the material reaches equilibrium.

As a result the discrepancy between intrinsic kinetics and reaction bed dynamics (see Fig. 2) is in this case mainly due to these heat transfer limitations. According to Fourier's law the internal heat transfer can be improved by either increasing the thermal conductivity of the metal hydride bed (using metal hydride compacts/inserting heat transfer enhancement matrices) or reducing the heat transfer distance. Since metal hydrides have a low effective heat conductivity in the range of $1.5 \text{ W m}^{-1} \text{ K}^{-1}$ [19], a small heat transfer distance in the reaction bed leads to a reduced heat transfer resistance and an increased system performance. However, especially with regard to the application of a MHCS where short half-cycle times are required, the sensible reactor mass is also a crucial parameter for the overall system performance: A part of the actual cooling effect of the endothermic reaction has to be used to cool down the reactor and the metal hydride while switching from the regeneration (temperature level T_{amb}) to the cooling half-cycle (temperature level T_c). Thus, the mass of the metal hydride reactor should be reduced to a minimum while at the same time short heat transfer distances need to be realized.

In addition to these performance limiting aspects, a further challenge in the reactor design is the mechanical stability of the reactor that is partially in conflict with the aforementioned performance limiting criteria. Mechanical strains caused by the metal hydride lead to mechanical stresses on the reactor wall up to 90 bar [20], beside the hydrogen pressure and the thermomechanical strains. The mechanical stresses in the reactor depend on a variety of aspects, e.g. porosity, cycle number and hydrogen supply and are a result of different mechanism in the reaction bed [20–22]. Through the phase change during absorption and desorption a cyclic swelling and shrinking of the material occurs that is called the breathing of the material [23]. In addition, during the activation procedure in the first hydrogenation cycles the material fragments into fine powder. This decrepitation is associated with a densification and a segregation effect with local higher stresses at the bottom of the reactor caused through a larger number of small grains in this section [24,25]. Thus, a decreasing variation of hydride bed volume during hydrogenation and dehydrogenation occurs with increased number of

cycles. For a Ti-Cr-V + Zr-Ni alloy as an example the bed volume variation reaches a constant level after around 30 cycles [26].

Summarizing, the aim of an optimized reactor design for high performance system is to achieve a maximum volumetric and specific power density with simultaneous exclusion of reactor failure through the expansion of the metal hydride. This implies two aspects: Short half-cycle times through high heat transfer coefficients and the maximum permissible amount of metal hydride in the reactor while taking into account the mechanical strains caused by the hydride expansion. Additionally, with respect to the thermal losses the reactor mass should be kept to the minimum required.

Final design

To reach short half-cycle times and to gain high performances, in this novel approach a soldered plate heat exchanger from VAU Thermotech GmbH & Co. KG with a one-way flow pattern is applied. In Table 2 all reactor design parameters of the series VM15/20 are summarised. The reactor consists of a primary and secondary side with 20 stacked plates and a gap width of approx. $1.5 \times 10^{-3} \text{ m}$ (see Fig. 3).

Thereby, the metal hydride and the heat transfer fluid (HTF) are arranged alternately in the primary and secondary side. The small gap width enables a low thermal resistance on the metal hydride side of the reactor. On the HTF side stamped plates permit optimized external heat transfer and a high heat transfer coefficient from the reactor wall to the fluid. The connections for the HTF are S3 (inlet) and S4 (outlet), respectively. The soldered plate heat exchanger is modified for the application as metal hydride reactor by the integration of a sintered metal filter element of $3 \times 10^{-6} \text{ m}$ mesh in the primary metal hydride side (connection S1). Thus, a uniform mass transport can be realised to each metal hydride plate. While connection S1 is applied for the hydrogen supply (absorption) and removal (desorption), connection S2 that is closed during operation, is used for the filling of the reactor with metal hydride. The reactor is designed up to a pressure of

Table 2 – Plate reactor design parameters and material properties of Hydralloy® C5.

Parameter	Symbol	Value
Number of plates	Z_{plate}	20
Number of channels	Z_{channel}	19 ($Z_{\text{MeH}} = 9$; $Z_{\text{HTF}} = 10$)
Reactor dimensions	$l \cdot b \cdot h$	$0.202 \text{ m} \cdot 0.073 \text{ m} \cdot 0.066 \text{ m}$
Reactor mass without connections	m_{R}	1.6 kg
Gap width	s	$\sim 1.5 \times 10^{-3} \text{ m}$
Plate thickness	f	$\sim 1 \times 10^{-3} \text{ m}$
Max. permitted temperature	T_{max}	195 °C
Max. permitted pressure	p_{max}	3 MPa
Metal hydride mass	m_{MeH}	0.353 kg
Enthalpy	$\Delta H_{\text{abs}}/\Delta H_{\text{des}}$	$-22.3 \text{ kJ mol}^{-1}/28.4 \text{ kJ mol}^{-1}$ [12]
Entropy	$\Delta S_{\text{abs}}/\Delta S_{\text{des}}$	$-95.3 \text{ kJ mol}^{-1} \text{ K}^{-1}/112 \text{ kJ mol}^{-1} \text{ K}^{-1}$ [12]
Hydrogen capacity	w_{max}	1.7 wt.% [27]

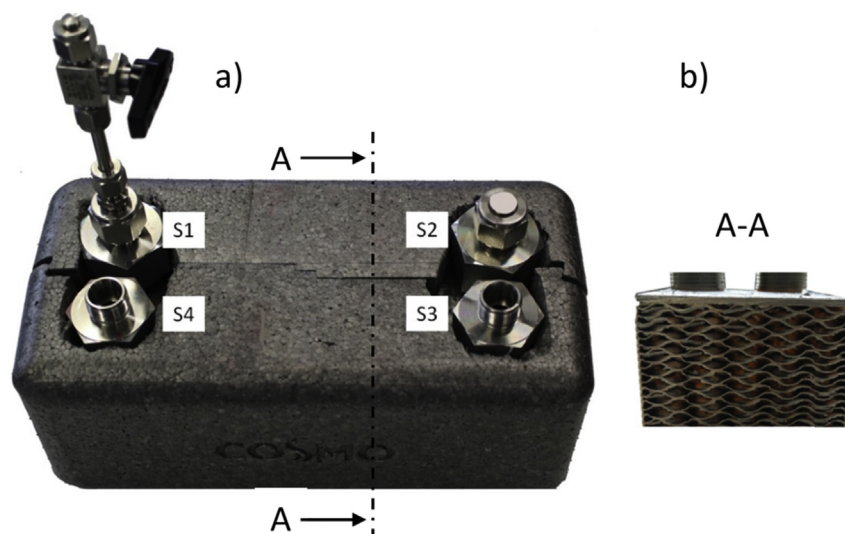


Fig. 3 – Design of the soldered plate reactor. a) Converted state with connections and insulation b) Unfilled cross-sectional view.

30 bar and a maximum temperature of 195 °C. Apart from the small acquisition cost and the good volume to surface ratio of the plate reactor, a major advantage of the concept is its scalability. As long as the dimensions of the plates are constant, heat and mass transfer remain unchanged. Therefore, the results, e.g. half-cycle time and specific transferred power can be scaled for bigger systems by increasing the number of plates and the HTF flow. Besides that, by up-scaling of the plate reactor the ratio of passive to active mass ($m_{\text{Reactor}} \cdot m_{\text{MeH}}^{-1}$) will decline. For an up-scaled identical reactor (series VM25/60) with a total hydride bed volume of $1.2 \times 10^{-3} \text{ m}^3$ and a not compacted bulk density of 2300 kg m^{-3} the ratio $m_{\text{Reactor}} \cdot m_{\text{MeH}}^{-1}$ would be 1.9. This ratio could be even decreased to 1.5 in case of compacting the metal hydride and enhancing the bulk density to 3500 kg m^{-3} . In this case the metal hydride expansion and stresses have to be accurately considered. For exclusion of reactor failure, the present small scale plate reactor is filled with a bulk density of 2300 kg m^{-3} and a safety factor of 30% is additionally included. Thus, the reactor is filled with a total metal hydride mass of 0.353 kg resulting in a ratio $m_{\text{Reactor}} \cdot m_{\text{MeH}}^{-1}$ of approx. 4.5.

Choice of metal hydride

Since the plate reactor as a component of the open MHCS is in the focus of this paper, the material selection is based on this application. However, in general, the selection criteria mentioned in the following can be applied for all aforementioned metal hydride high performance applications.

First, with regard to the intrinsic kinetics of the material short half-cycle times (for MHCS below 60 s) have to be feasible at the operating conditions. Second, the thermodynamic or equilibrium characteristics have to suit the boundary conditions of the system. Additionally, the metal hydride should, inter alia, show a flat plateau, low hysteresis, minimum degradation and a high thermal conductivity [6].

In view of an open MHCS for a sufficient cooling temperature (cf. Fig. 1) the equilibrium temperature of the metal

hydride at the desorption pressure p_{des} has to be clearly below the ambient temperature. Since the ambient is used as heat sink in the regeneration, the equilibrium temperature at the pressure p_{abs} has to be above the permitted ambient temperature. Furthermore, for reasons of mechanical stability this maximum operation pressure p_{abs} is limited by the design of the reactor. Finally, the metal hydride should have a high heat of formation ($\Delta H_{\text{des}} > 28 \text{ kJ mol}^{-1}$) and exhibit a high hydrogen absorption capacity ($w_{\text{max}} > 1.5 \text{ wt.}\%$) for an efficient system with a high volumetric and specific power density.

Due to its appropriate thermodynamic behaviour and excellent intrinsic kinetics [12], Hydralloy® C5 (51 wt.% Mn, 27 wt.% Ti, 15 wt.% V, 3 wt.% Fe, 3 wt.% Zr) is chosen as hydride material. The results of experimentally determined pressure-concentration-isotherms (PCI) are in good agreement with the fit of Herbrig et al. [27] that are not shown here in detail. The equilibrium pressure of Hydralloy® C5 at 35 °C and 15 °C are $p_{\text{abs}} = 1.61 \text{ MPa}$ and $p_{\text{des}} = 0.45 \text{ MPa}$, respectively. The material properties are summarised in Table 2.

Activation and filling procedure

The Hydralloy® C5 was purchased from GfE (Gesellschaft für Elektrometallurgie mbH), Germany. In the received condition the material has an average particle size of 0.01–0.015 μm [28]. The material is activated and pre-cycled in a Swagelok sample cylinder (304L-HDF4-1000 – proof tested at 11.7 MPa) with an inner diameter of 0.075 m that is inserted in the test bench of Fig. 4. The cylinder is positioned and temperature controlled (T_{TB}) in a thermostatic bath. A total number of 30 pre-cycles were conducted with a duration of 90 min for each half-cycle. While the boundary conditions for the absorption were $p_{\text{abs}} = 4 \text{ MPa}$ and $T_{\text{TB}} = 0 \text{ °C}$, the desorption was performed at $T_{\text{TB}} = 100 \text{ °C}$ against vacuum. The pre-cycling procedure of the material leads to a fragmentation, an increased specific surface area and a clearly reduced particle size in the range of $1\text{--}2 \cdot 10^{-5} \text{ m}$ [12]. This enables a filling of the plate reactor. Furthermore, by pre-cycling, the mechanical stress peaks during the activation and fragmentation are reduced in

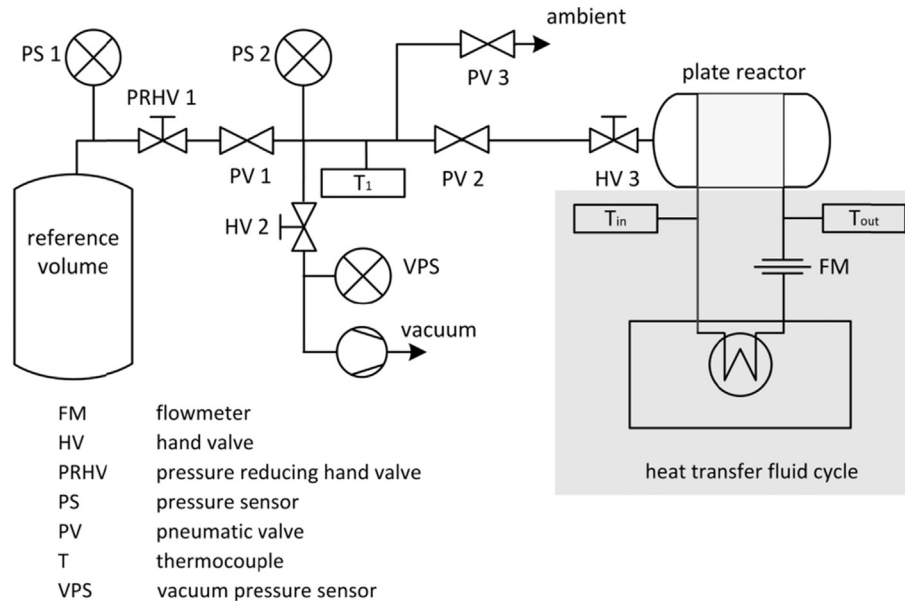


Fig. 4 – Schematic layout of the test bench.

the pressure proofed Swagelok sample cylinder. After 30 cycles the change of volume of the MeH is assumed to reach a constant value caused only by the breathing of the material.

Under Argon atmosphere the pre-cycled material was filled into the plate reactor. In all nine gaps of the metal hydride side, a consistent distribution of around 0.04 kg MeH is obtained. This results in a porosity of around 80% in each plate. Material accumulation and migration from one plate to another is excluded by sealing of the gaps using teflon slices. During the operation the reactor is positioned vertically and hydrogen is supplied from the bottom. Thereby densification and segregation at the bottom of the reactor are counteracted. Under exclusion of a reactor failure, with the plate reactor so far over 300 cycles have been performed.

Test bench and experimental procedure

Test bench

For the experimental validation of the novel reactor concept in various absorption and desorption experiments, the plate reactor is integrated into the setup shown in Fig. 4. In principle, the setup is separated in a hydrogen part and a heat transfer fluid cycle (grey shaded) on the right hand side of the test bench scheme. The hydrogen part consist of a reference volume (hydrogen gas bottle with a volume of 0.05 m³), a pressure reducing hand valve PRHV 1, a thermocouple T₁ and three pneumatic valves PV 1–3, hand valves HV 1–3 and pressure sensors PS 1–2/VPS each.

In the heat transfer fluid cycle the reactor inlet temperature is controlled via a thermostatic bath that supplies the required heat and cold, respectively to keep the inlet temperature constant during the absorption as well as desorption experiments. For the application as open MHGS, the heat transfer fluid cycle simulates the ambient and cooling temperature level of the regeneration and cooling half-cycle. To

determine the transferred thermal power to/from the HTF (Huber SilOil M40.165/220.10), the volume flow rate $\dot{V}_{\text{HTF}}(t)$ and the HTF inlet and outlet temperature (T_{in} and T_{out}) of the reactor are measured with a turbine flow metre FM (type: KEM HMP 06-SC, $\pm 2.5\%$) and two thermocouples of Type K (± 1.5 K, temperature difference calibrated). The instantaneously transferred specific power is referred to the metal hydride mass m_{MeH} and is calculated by the following equation:

$$\dot{q}_{\text{HTF}}(t) = \frac{\dot{V}_{\text{HTF}}(t) \cdot \bar{\rho}_{\text{HTF}} \cdot \bar{c}_{p,\text{HTF}} \cdot (T_{\text{in}}(t) - T_{\text{out}}(t))}{m_{\text{MeH}}} \quad (3)$$

According to a sign convention, negative values of the specific power represent the absorption and positive values the desorption.

Experimental procedure

Before each absorption experiment is initiated, the reactor is completely discharged by a vacuum pump (valves HV 2/3 and PV 2 open) down to a system pressure of 5×10^3 Pa at room temperature. The desired HTF inlet temperature is set via the thermostatic bath until steady state conditions between the HTF inlet and outlet temperature of the reactor is obtained.

After closing PV 2, the system pressure p_{abs} is adjusted with hydrogen from the reference volume and the pressure reducing valve PRHV 1. In all presented absorption experiments the charging pressure p_{abs} is 3 MPa. By opening PV C8, hydrogen flows from the reference volume into the hydrogen part of the plate reactor, the exothermic reaction is initiated and heat is transferred to the HTF depending on the boundary conditions of the reaction. The absorbed amount of hydrogen in the metal hydride is directly correlated to a pressure drop in the reference volume that is detected for each instant of time with the pressure sensor PS 1 (type: Keller LEO3, $\pm 0.2\%$). According to this Sieverts system [29] and considering the gas expansion in the free volume, the transformed fraction $X(t)$ is

calculated using real gas behaviour with, for instance, a real gas factor of 1.092 at a reference volume pressure of 15 MPa. Thereby, the free volume including tubing and reactor void volume was measured using inert gas. Due to the pressure reducing valve PRHV 1, the Sieverts type measurement can be combined with a constant supply pressure to the reactor. Therefore, the complete transformed fraction was done at constant pressure.

With the resulting transformed fraction profile, the time constant τ_{TC} and the half-cycle time for a complete transformed fraction τ_{HC} are determined for the plate reactor according to Fig. 2. At the end of each absorption experiment the valves PV 1/2 are closed and residual pressure p_{abs} is released to the ambient by opening PV 3.

As soon as steady state HTF temperature conditions at the desired temperature are reached, PV 2 is opened and the desorption is initiated. These dehydrogenation experiments are performed against atmospheric pressure ($p_{des} = 1.013 \times 10^5$ Pa) and hydrogen is released to the ambient. Since no reference volume is inserted in the release path, for the desorption experiments the transformed fraction $X(t)$ is not measured. In analogy to the absorption experiments before, the instant transferred specific cooling power is calculated by using Eq. (3). For conducting the experiments, a nominal experimental time of 180 s is chosen for both absorption and desorption experiments.

Experimental results

In this section, the experimental results for the plate reactor measurements are presented. First, representative experiments are shown for absorption and desorption, respectively. Furthermore the influence of a variation of the HTF flow rate is shown. The presented reactor design is subsequently evaluated with regard to literature intrinsic kinetic measurements. Finally, experimental data focussing on the application of the reactor in an open MHCS are presented and recommendations for the application are given.

Representative experiments

One representative absorption and one desorption experiment is hereinafter shown for a typical inlet temperature of $T_{in} = 20$ °C and a HTF flow rate of $\dot{V}_{HTF} = 7.5 \times 10^{-5}$ m³ s⁻¹. For both experiments the temperature characteristic as well as the calculated values of the transferred thermal power are presented. Moreover, the average transferred power for a nominal half-cycle time of 60 s is calculated and the values of the time constant and half-cycle time are given.

Absorption experiment

In Fig. 5, the results of the representative absorption experiment for an absorption pressure of 3 MPa are shown. The specific transferred power (blue line, left y-axis) and the HTF temperature characteristic (green and red, right y-axis) are illustrated in the upper diagram, whereas the course of transformed fraction is presented in the lower graph.

At $t = 0$, the reaction is initiated and due to the exothermic reaction, the HTF outlet temperature T_{out} increases.

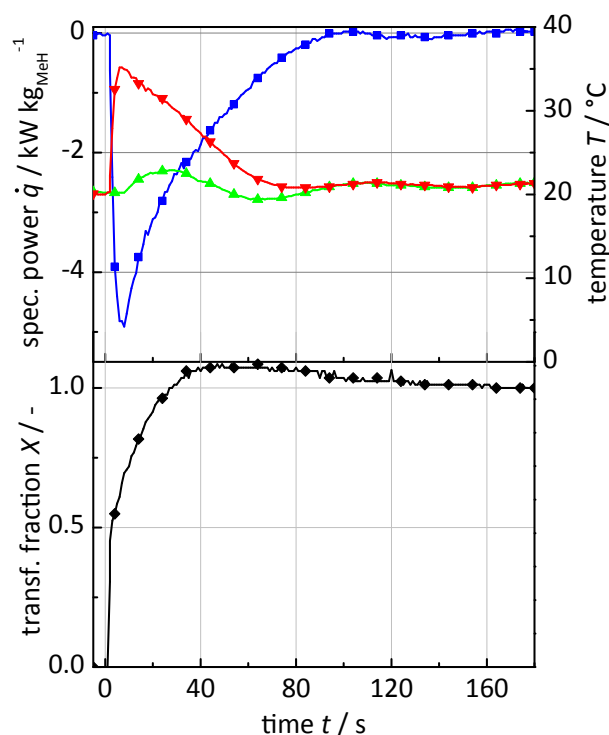


Fig. 5 – Results of the reference absorption experiments for $p_{abs} = 3$ MPa with $T_{in} = 20$ °C (green, \blacktriangle), T_{out} (red, \blacktriangledown), spec. power (blue, \blacksquare) and transformed fraction (black, \blacklozenge). (For interpretation of the references to colour in this figure legend, the reader is referred to the web version of this article.)

Furthermore, the transformed fraction of hydrogen (0.006 kg_{H2} total absorbed amount of hydrogen) also increases and shows a behaviour that corresponds to the assumed first-order system response in Fig. 2. Then, after approx. 100 s, all measured values are again in steady state. The oscillation in the inlet temperature of ± 2 K around the set value results from the insufficient regulation of the HTF cycle. Additionally, the slight overshoot in transformed fraction is due to the temperature change of the gas in the reference volume. The initial gas temperature is reached again after around 120–180 s.

Using the values for the transformed fraction, for this experiment, a time constant of $\tau_{TC} = 8$ s and a half-cycle time of around $\tau_{HC} = 40$ s for a complete transformed fraction can be determined. Thus, with the current design the reactor is able to transfer the heat from the material to the HTF in the desired time of $t < 60$ s.

Next to the cycle time it is also important to determine the experimentally transferred thermal power using this reactor. Therefore, the peak power as well as the average power is calculated using Eq. (3). The observed maximum temperature difference in the HTF of -15 K, results in a specific peak heat power of $\dot{q}_{HTF} = -4.9$ kW kg_{MeH}⁻¹. Furthermore, assuming a nominal half-cycle time of 60 s, the average to the HTF transferred specific power is calculated to $\bar{q}_{60s} = 2.42$ kW kg_{MeH}⁻¹. When the curves for the transformed fraction and specific power are compared, it is obvious that

heat is still transferred to the HTF although the reaction is completed after about 40 s. The reason for this observation is the sensible heating of the reactor and the metal hydride caused by the reaction. This heat is transferred to the HTF until steady state conditions are reached after approx. 100 s and the reactor as well as all hydride material is again at reference temperature.

Desorption experiment

The results for the reference desorption experiment at the same temperature and against ambient pressure (1.013×10^5 Pa) are shown in Fig. 6. The endothermic reaction is started by opening PV C2, causing a decline of the outlet temperature T_{out} due to the removal of heat. After a time interval of around 140 s no more heat is transferred from the HTF to the metal hydride.

As mentioned before, for the desorption experiment it was not possible to install a suitable flow metre or a reference volume, thus the half-cycle time is determined using the HTF temperature profiles. In analogy to the absorption reference experiment (see Fig. 5), it is assumed that the sensible mass leads to an extended heat transfer of around 60 s after a complete transformed fraction is reached. Therefore, for this desorption experiment a half-cycle time for complete transformed fraction τ_{HC} of approx. 80 s can be determined. This value is slightly longer than for the absorption reaction, as the operation conditions are closer to the equilibrium of the material. Using the experimentally measured maximum temperature difference of $\Delta T = 7.1$ K, the maximum specific cooling power can be calculated to $2.2 \text{ kW kg}_{\text{MeH}}^{-1}$. Furthermore, assuming a nominal fixed half-cycle time of 60 s, the average transferred specific cooling power removed from the HTF is calculated to $\bar{q}_{60\text{s}} = 1.7 \text{ kW kg}_{\text{MeH}}^{-1}$. Comparing these values with the representative absorption experiment, it can be noted that an extended half-cycle time leads to a reduced transferred specific power although the heat of formation for the desorption is larger than the heat of formation for the absorption.

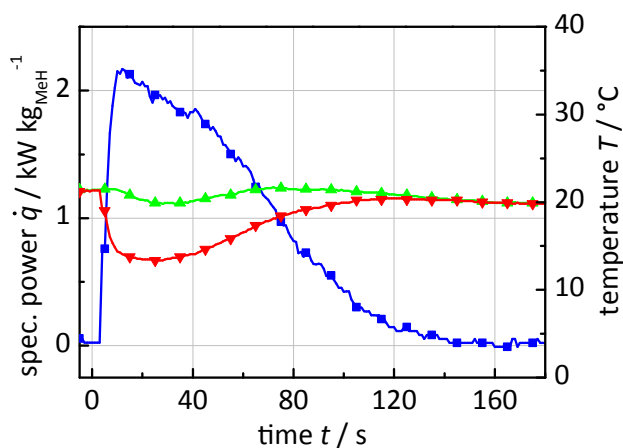


Fig. 6 – Results of the reference desorption experiment for $p_{\text{des}} = 1.013 \cdot 10^5$ Pa with $T_{\text{in}} = 20$ °C (green, ▲), T_{out} (red, ▼) and spec. power (blue, ■). (For interpretation of the references to colour in this figure legend, the reader is referred to the web version of this article.)

With regard to the aforementioned metal hydride high performance systems, the representative experiments show that high specific power densities can be realized through short half-cycle times by applying the plate reactor concept. Moreover, these experiments illustrated that a complete transformed fraction is not reasonable for metal hydride high performance applications, since the instant power and thus the transferred average power clearly decreases with time. Consequently, for a later application, the specific optimum of the half-cycle time needs to be determined. For this reason, in the following, the average transferred power is calculated for a nominal half-cycle time of 60 s.

Variation of the HTF flow rate

The impact of the HTF flow rate on the performance of the plate reactor is shown in Fig. 7. In all experiments the absorption pressure ($p_{\text{abs}} = 3$ MPa) and the inlet temperature ($T_{\text{in}} = 30$ °C) are kept constant and the HTF flow rate is varied.

The graphs show that there exists a significant influence of the HTF flow rate on the specific peak power. While for the reference flow rate of $7.5 \times 10^{-5} \text{ m}^3 \text{ s}^{-1}$ (red) the specific peak power is $-4.2 \text{ kW kg}_{\text{MeH}}^{-1}$, for an increased flow rate of $5.17 \times 10^{-5} \text{ m}^3 \text{ s}^{-1}$ (blue) and a reduced flow rate of $1.55 \times 10^{-4} \text{ m}^3 \text{ s}^{-1}$ (black), this value changes by approx. $\pm 30\%$. Furthermore, the calculated average specific power $\bar{q}_{60\text{s}}$ for the nominal half-cycle time of 60 s varies from $-1.96 \text{ kW kg}_{\text{MeH}}^{-1}$ to $-2.36 \text{ kW kg}_{\text{MeH}}^{-1}$. These results show that for the present reactor design there exists a limitation in the external heat transfer from the fluid to the reaction bed. This implies that in case the mass flow rate can be further increased, even lower cycling times and higher specific powers can be reached.

Steady state calculations with an average metal hydride temperature of $T_{\text{MeH}} = 40$ °C during the absorption correspond to these experimental results. Using the correlation of a

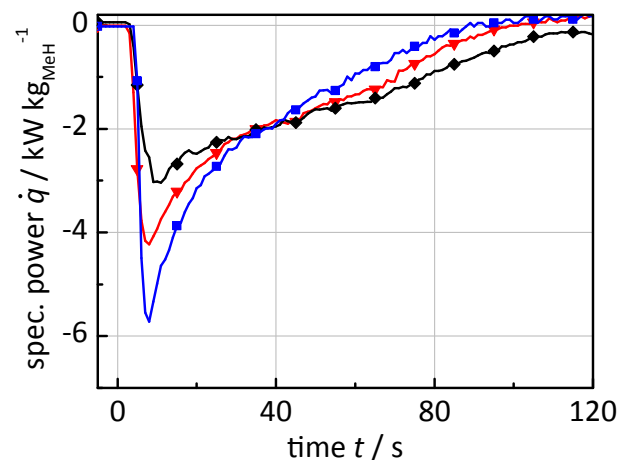


Fig. 7 – Results of the HTF flow rate variation for $T_{\text{in}} = 30$ °C and $p_{\text{abs}} = 3$ MPa with $\dot{V}_1 = 5.17 \times 10^{-5} \text{ m}^3 \text{ s}^{-1}$ (black, ◆), $\dot{V}_2 = 7.5 \times 10^{-5} \text{ m}^3 \text{ s}^{-1}$ (red, ▼) and $\dot{V}_3 = 1.55 \times 10^{-4} \text{ m}^3 \text{ s}^{-1}$ (blue, ■). (For interpretation of the references to colour in this figure legend, the reader is referred to the web version of this article.)

parallel plate duct without pattern [30] as an estimate, the overall heat transfer coefficient is enhanced by 15% by increasing the HTF flow rate from $7.5 \times 10^{-5} \text{ m}^3 \text{ s}^{-1}$ to $1.55 \times 10^{-4} \text{ m}^3 \text{ s}^{-1}$. Since the HTF flow is in the laminar range and the metal hydride bed thickness is very small, the reactor performance is still limited by the heat transfer to the HTF. Additionally, the calculations show that the thermal resistance of the separating wall is insignificant, since the temperature decrease in the plate with the thickness of $1 \times 10^{-3} \text{ m}$ is below $\Delta T < 0.5 \text{ K}$. For the calculation, the geometrical dimensions of the plate reactor are taken from Table 2.

Consequently, there exist two options for future applications. First, in case the highest possible rates are required, the flow rate should be increased by implementing more powerful pumps or reducing the pressure drop of the complete system. Second, in case the specific power of the present system is sufficient for the desired application, the system can be optimized in a different way: The thickness of each metal hydride layer can be slightly increased which will lead to a lower system weight and thus to an improved specific power values on the system level.

Evaluation of the reactor concept

For the evaluation of the presented reactor concept, the plate reactor dynamic is compared with literature intrinsic kinetic measurements. According to Fig. 2, the limitations in the reaction bed lead to an extended half-cycle time and reduced specific power. In the following section a method to assess the performance of the metal hydride reactor in comparison to the theoretical values based on material properties is shown. The objective is to rate the plate reactor concept and to identify further technical potential in the reactor development compared to the pure material properties that represent the theoretical possible maximum reaction rate and thermal power.

In order to do so, the performance of the plate reactor dynamic based on experimental results is compared with intrinsic kinetic measurements of C5₁ from Skripnyuk et al. [12]. This material matches the equilibrium characteristics as well as the material composition filled into the plate reactor. The literature kinetic experiments were carried out by applying the thermal ballast method with material to fine Ni powder ratios of up to 1:33 guaranteeing isothermal conditions ($\Delta T = \pm 1 \text{ }^\circ\text{C}$). In order to compare the measurements of the plate reactor with these intrinsic measurements, the normalized pressure dependence method (NPDM) has been used [12]. As an assumption for the reaction rate in the plate reactor the same general equation has been adapted known from intrinsic measurements:

$$\frac{dX}{dt} = k(T) \cdot f(p) \cdot f(x) \quad (4)$$

The first factor on the right side, the reaction rate constant $k(T)$, represents the temperature dependency of the reaction rate according to the Arrhenius equation. In particular through heat transfer limitations this rate constant is reduced for the plate reactor measurements (k_{PR}) in contrast to the intrinsic rate constant (k_i). The distance of the operating pressure to the equilibrium is considered by a pressure

dependence function $f(p)$. Thereby, the equilibrium pressure p_{eq} as a function of the transformed fraction and the temperature are essential to know. A first order reaction is assumed for the factor $f(x)$ and thus the reaction rate is expressed by Ref. [31]:

$$\frac{dX}{dt} = -A \cdot \exp\left(-\frac{E_a}{RT}\right) \cdot \frac{|p - p_{eq}|}{p_{eq}} \cdot (1 - x) \quad (5)$$

The integration of eq. (4) yields:

$$k(T) = \frac{\ln(1 - x) \cdot p_{eq}}{|p - p_{eq}| \cdot t} \quad (6)$$

Using experimental results in the temperature range of 0–60 °C, for seven different inlet temperatures the relationship between $-\ln(1-x)/f(p)$ vs. time t ($t > 0$) is determined for the plate reactor. From the slope of this plot, for each inlet temperature the effective rate constant $k_{PR}(T)$ is calculated at $t = 10 \text{ s}$. Since no course of transformed fraction is obtained for the desorption, the estimation is conducted for the absorption experiments only. The absorption pressure and the HTF flow are kept as in the reference experiment (3 MPa and $7.5 \times 10^{-5} \text{ m}^3 \text{ s}^{-1}$, respectively).

For this evaluation according to the NPDM, it is initially assumed that the metal hydride temperature corresponds to the HTF inlet temperature. The equilibrium pressure $p_{eq}(X, T)$ is estimated for this HTF inlet temperature as a function of transformed fraction by applying the fourth order PCI correlation of Herbrig et al. [27]. As a result, the actual existing performance limitations are considered by a reduced effective rate constant k_{PR} compared to intrinsic measurements. In the Arrhenius plot of Fig. 8, the literature intrinsic results (blue) of

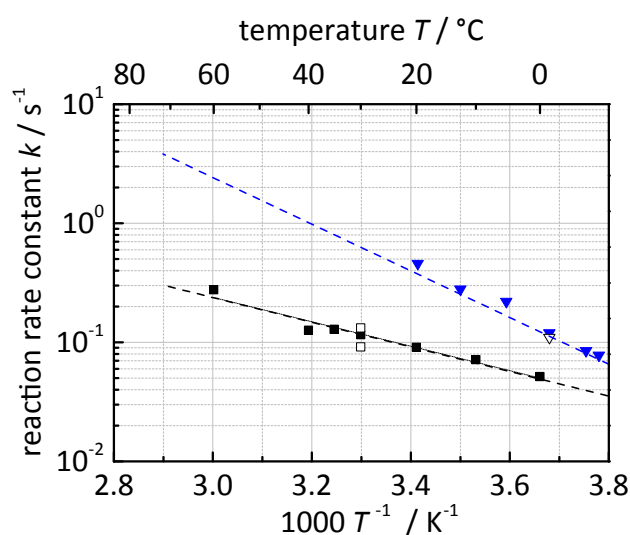


Fig. 8 – Comparison of intrinsic kinetics and plate reactor dynamics measurements with C5 intrinsic desorption kinetics (blue, ▼) [12], C5 intrinsic absorption kinetics (blue, ▽) [12], plate reactor absorption dynamics (black, ■) and variation of the HTF flow rate for the plate reactor absorption dynamics (black, □). (For interpretation of the references to colour in this figure legend, the reader is referred to the web version of this article.)

Skrypnik et al. are compared with those measured with the present plate reactor (black). Additionally, the values for a variation of the HTF flow rate according to Section 4.2 are illustrated.

It can be noted that the effective rate constant $k_{PR}(T)$ shows a linear behaviour and the values are below the intrinsic rate $k_i(T)$. However, the results are promising compared to literature MHCS mentioned in the introduction. For the complete system of Ron et al. [10], for instance the rate constant can be estimated to $k = 0.014$ for a half-cycle time of 6 min and an air inlet temperature of 19 °C. This value is 6.5 times less compared to the results of the present plate reactor at the same inlet temperature. The distance of the plate reactor values to the intrinsic reaction rates of the material illustrate that for this material and this reactor design, it still exists a possibility to improve the cycling time. However, this possible improvement might be very challenging when taking into account that the reactor needs to transfer thermal energy to a HTF whereas the intrinsic results are obtained by means of large quantities of thermal ballast. From Fig. 8, it is also obvious that the ratio $k_i \cdot k_{PR}^{-1}$ that describes the theoretical potential declines with temperature. Whereas for a hydride temperature of 60 °C the ratio is around ten, it is only a factor of four for a temperature of 10 °C. This indicates that at lower temperatures the reaction rate constant of the material becomes dominant.

Furthermore, based on the measurements of Section 4.2, an increase of the HFT flow rate leads to an enhanced effective rate constant and vice versa to a reduced rate for a reduction of the HTF flow rate (squared symbols). However, the influence is low since in all considered cases the flow is laminar and the change of reynolds number is comparatively small.

Additionally to the evaluation of the plate reactor concept, the normalized pressure dependence method that is used to evaluate plate reactor concept can be used to confirm the half-cycle time as well as the time constant of the reference desorption experiment. By using Eq. (6) and the resulting reaction rates of the plate reactor according to Fig. 8, the time constant and half-cycle time for a complete transformed fraction can subsequently be calculated to $\tau_{TC} = 14$ s and $\tau_{HC} = 71$ s, respectively. Thereby, it is assumed that next to the intrinsic reaction rate constants $k_i(T)$ of the applied Hydralloy® C5 [12], the heat transfer characteristic of the reactor are equal for absorption and desorption. In a sufficient approximation the pressure dependence function $f(p)$ is estimated with the equilibrium pressure in the middle of the plateau. This result is in good accordance with the value of approx. 80 s determined by using the temperature profiles.

Evaluation of the average specific power under MHCS relevant conditions

In this section, the plate reactor is characterized with respect to boundary conditions that appear when it is used as reactor of an open MHCS. Corresponding to Fig. 1, in an open MHCS the regeneration is performed at ambient temperature that is around 25–40 °C during the operation. Additionally, for a sufficient cooling effect the HTF inlet temperature should be in the range of 5–15 °C. Therefore, single experimental results with varying inlet temperature are presented and the specific

cooling power is calculated. Six experiments for both absorption and desorption were conducted, according to the described experimental procedure in Section 3. While the inlet temperature was varied in the range of $T_{in} = 0$ –40 °C, the absorption and desorption pressure ($p_{abs} = 3$ MPa and $p_{des} = 1.013 \cdot 10^5$ Pa) as well as the HTF flow rate ($7.5 \cdot 10^{-5}$ m³ s⁻¹) are kept as in the representative experiments. These experiments (compare Figs. 5 and 6) illustrated that a complete transformed fraction is not reasonable for an open MHCS with a high performance, since the instant power and thus the transferred average cooling power clearly decreases with time. Otherwise, a too short half-cycle time between switching from the cooling to the regeneration half-cycle time would result in a more considerable influence of thermal losses and an incomplete regeneration. For this reason, the average specific power is calculated for a fixed half-cycle time of 60 s that is assumed to be reasonable.

The corresponding results for the absorption (black) and desorption (red) are shown in Fig. 9 using closed symbols. In the chosen temperature range, a linear relationship between the inlet temperature and the average specific power is obtained. Considering the plate reactor as a component of a MHCS, for a desired cooling temperature of $T_{in} = 10$ °C an average specific cooling power of $\bar{q}_{60s} = 1.31$ kW kg_{MeH}⁻¹ is obtained in the single plate reactor experiments. However, the performance of the MHCS is strongly dependent on the inlet temperature. In the measured temperature range from $T_{in} = 0$ to 40 °C, the specific average cooling power increases by a factor of three. This is due to the fact that with increasing inlet temperature both the pressure function $f(p)$ that describes the distance to the equilibrium and the effective reaction rate constant k_{PR} increase. Thus, the half-cycle time is reduced resulting in a raise of specific average cooling power. This temperature dependency has a smaller impact on the absorption performance. The reason is that for the absorption

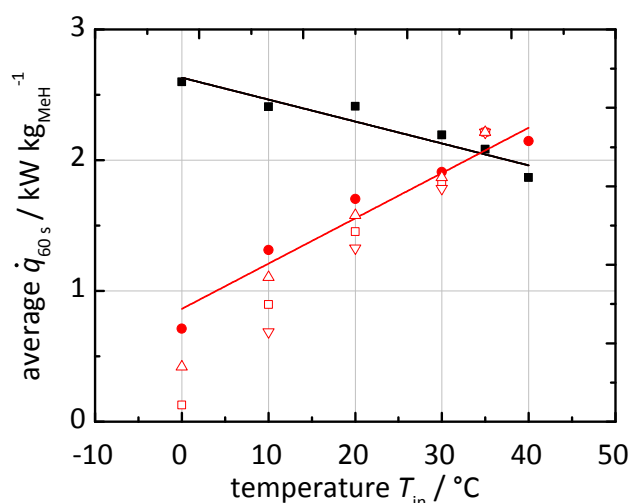


Fig. 9 – Measured absolute average specific power for absorption (black, ■) and desorption (red, ●). Thermal losses are considered with $r = 2$ (red, △), $r = 2.5$ (red, □) and $r = 3$ (red, ▽). (For interpretation of the references to colour in this figure legend, the reader is referred to the web version of this article.)

the pressure function decreases while the effective reaction rate rises with growing temperature. This inverse effect leads to a decline of the specific average power by just 30% in the temperature range from 0 to 40 °C.

From the negative slope of the reaction rates vs. reciprocal temperature (cf. Fig. 8) it can be finally identified that the cooling half-cycle at low temperatures is defining the required half-cycle time of an open MHCS system. For the same pressure dependence function values $f(p)$, the regeneration rate constant k_{PR} at an ambient temperature of 35 °C is almost doubled compared to the desorption rate k_{PR} at 10 °C ($k_{abs} = 0.013$ to $k_{des} = 0.072$).

For the coupling of the plate reactor with a fuel cell that requires a higher working pressure than the ambient pressure applied in the present experiments, it can be suitable to choose a metal hydride with higher equilibrium characteristics. For instance the metal hydrides C1 [18] or C2 [32] can be mentioned that exhibit similar material composition and intrinsic reaction kinetics, but higher equilibrium characteristics compared to Hydralloy[®] C5.

Discussion of the sensible reactor mass

The performed plate reactor experiments represent the analysis of a single half-cycle of the MHCS. Thus, the values shown in Fig. 9 as closed symbols represent the average specific cooling power that is achieved without changing the inlet temperature of the reactor. However, in real applications, the absorption (regeneration) will take place at temperatures above 30 °C and the desorption (cooling) at temperatures of around 10 °C. Therefore, part of the thermal power has to be used for these temperature changes that occur in the continuous operation. In this section the influence of the reactor design on these thermal losses is discussed.

The average specific cooling power \bar{q}_c for a continuous working MHCS is determined by the specific absorbed heat $q_{reaction}$ during the duration t reduced by the thermal specific energy losses q_{loss} and can be calculated with the following equation [10]:

$$\bar{q}_c = \frac{\bar{n}_{H_2} \cdot \Delta H_{des} - m_{sys} \cdot \bar{c}_{p,sys} (T_{amb} - T_c)}{m_{MeH} \cdot t} \quad (7)$$

Here \bar{n}_{H_2} , ΔH_{des} , m_{sys} and $c_{p,sys}$ are the complete desorbed hydrogen, the reaction enthalpy of desorption, the system mass as the sum of the metal hydride and reactor mass and the average specific heat capacity of the system also considering the reactor and metal hydride mass. In Fig. 9, for three different mass ratios $r = m_{sys} \cdot m_{MeH}^{-1}$ thermal losses are considered in the single plate reactor measurements shown with open symbols. For the plate reactor series VM25/60 and a not compacted bulk density of 2300 kg m⁻³ a system mass to material mass ratio of $r = 3$ can be achieved.

Thus, at an ambient temperature of 35 °C and a cooling temperature of 10 °C the thermal energy losses reduce the specific cooling power to $\bar{q}_{60s} = 690$ W kg_{MeH}⁻¹. This value is higher than the value of 640 W kg_{MeH}⁻¹ published by Linder [11] that was obtained at more moderate boundary conditions of $T_{amb} = 28$ °C and $T_c = 15$ °C.

It can be noted that a significant improvement can be gained by reducing the sensible mass of the plate reactor or using

thermal recovery measures. For the same conditions and a ratio of $r = 2$ the specific cooling performance of the plate reactor can be increased by 60% to around 1100 W kg_{MeH}⁻¹. Furthermore, Fig. 9 shows that the dependency of the MHCS performance on the thermal losses improves with increasing cooling temperature. This is obvious as a higher cooling temperature results in a small temperature difference during switching.

Conclusions

In the temperature range of 0–40 °C an experimental characterization of a novel plate reactor applying the metal hydride Hydralloy[®] C5 was carried out. Representative reference experiments for an inlet temperature of 20 °C lead to very short half-cycle time for a complete transformed fraction of around 40 s and 80 s for absorption and desorption, respectively.

To evaluate the reactor concept, the intrinsic reaction rate constant of literature data are compared with the experimentally determined effective rate constant of the plate reactor using the normalized pressure dependence method. For a HTF inlet temperature of 10 °C, the half-cycle time and thus the specific power of the reactor approaches intrinsic material properties up to a factor of four.

Under boundary conditions of an open MHCS and a cooling temperature of 10 °C, single reactor experiments resulted in an average specific cooling power of $\bar{q}_{60s} = 1.31$ kW kg_{MeH}⁻¹ for a nominal half-cycle time of 60 s. With regard to a continuous operating system thermal losses while switching from the regeneration to the cooling half-cycle reduce this cooling power. For a mass ratio of $r = 3$, feasible with the existing plate reactor concept, the average specific cooling power is $\bar{q}_{60s} = 690$ W kg_{MeH}⁻¹ that is higher than published values.

By the small heat transfer distance in the metal hydride bed and the low system mass, the plate reactor concept is finally feasible for all high performance metal hydride applications. Improvement can be realized by further reducing the parasitic sensible reactor mass and by increasing the external heat transfer.

REFERENCES

- [1] Kambly K, Bradley TH. Geographical and temporal differences in electric vehicle range due to cabin conditioning energy consumption. *J Power Sources* 2014;275:468–75. <http://dx.doi.org/10.1016/j.jpowsour.2014.10.142>.
- [2] Pino FJ, Marcos D, Bordons C, Rosa F. Car air-conditioning considerations on hydrogen consumption in fuel cell and driving limitations. *Int J Hydrogen Energy* 2015;40:11696–703. <http://dx.doi.org/10.1016/j.ijhydene.2015.04.079>.
- [3] Magnetto D, Mola S. A metal hydride mobile air conditioning system. *J Chem Inf Model* 2006;53:1689–99. <http://dx.doi.org/10.4271/2006-01-1235>.
- [4] Linder M, Kulenovic R. An energy-efficient air-conditioning system for hydrogen driven cars. *Int J Hydrogen Energy* 2011;36:3215–21. <http://dx.doi.org/10.1016/j.ijhydene.2010.11.101>.

- [5] Jensen JO, Vestbø AP, Li Q, Bjerrum NJ. The energy efficiency of onboard hydrogen storage. *J Alloys Compd* 2007;446–447:723–8. <http://dx.doi.org/10.1016/j.jallcom.2007.04.051>.
- [6] Muthukumar P, Groll M. Metal hydride based heating and cooling systems: a review. *Int J Hydrogen Energy* 2010;35:3817–31. <http://dx.doi.org/10.1016/j.ijhydene.2010.01.115>.
- [7] Bhuiya MMH, Kumar A, Kim KJ. Metal hydrides in engineering systems, processes, and devices: a review of non-storage applications. *Int J Hydrogen Energy* 2015;40:2231–47. <http://dx.doi.org/10.1016/j.ijhydene.2014.12.009>.
- [8] Qin F, Chen J, Lu M, Zhijiu C, Zhou Y, Yang K. Development of a metal hydride refrigeration system as an exhaust gas-driven automobile air conditioner. *Renew Energy* 2007;32:2034–52. <http://dx.doi.org/10.1016/j.renene.2006.10.014>.
- [9] Ni J, Liu H. Experimental research on refrigeration characteristics of a metal hydride heat pump in auto air-conditioning. *Int J Hydrogen Energy* 2007;32:2567–72. <http://dx.doi.org/10.1016/j.ijhydene.2006.09.038>.
- [10] Ron M. A hydrogen heat pump as a bus air conditioner. *J Less Common Met* 1984;104:259–78. [http://dx.doi.org/10.1016/0022-5088\(84\)90411-9](http://dx.doi.org/10.1016/0022-5088(84)90411-9).
- [11] Linder M. Automotive cooling systems based on metal hydrides. University of Stuttgart; 2010. <http://dx.doi.org/10.18419/opus-1882>.
- [12] Skripnyuk VM, Ron M. Evaluation of kinetics by utilizing the normalized pressure dependence method for the alloy Ti0.95Zr0.05Mn1.48V0.43Fe0.08Al0.01. *J Alloys Compd* 1999;293–295:385–90. [http://dx.doi.org/10.1016/S0925-8388\(99\)00375-8](http://dx.doi.org/10.1016/S0925-8388(99)00375-8).
- [13] Lototskyy MV, Yartys VA, Pollet BG, Bowman RC. Metal hydride hydrogen compressors: a review. *Int J Hydrogen Energy* 2014;39:5818–51. <http://dx.doi.org/10.1016/j.ijhydene.2014.01.158>.
- [14] Satya Sekhar B, Pailwan SP, Muthukumar P. Studies on metal hydride based single-stage heat transformer. *Int J Hydrogen Energy* 2013;38:7178–87. <http://dx.doi.org/10.1016/j.ijhydene.2013.03.135>.
- [15] Skripnyuk V, Ron M. Hydrogen desorption kinetics in intermetallic compounds C2, C51 and C52 with Laves phase structure. *Int J Hydrogen Energy* 2003;28:303–9. [http://dx.doi.org/10.1016/S0360-3199\(02\)00081-2](http://dx.doi.org/10.1016/S0360-3199(02)00081-2).
- [16] Linder M, Mertz R, Laurien E. Experimental analysis of fast metal hydride reaction bed dynamics. *Int J Hydrogen Energy* 2010;35:8755–61. <http://dx.doi.org/10.1016/j.ijhydene.2010.05.023>.
- [17] Lototskyy M, Satya Sekhar B, Muthukumar P, Linkov V, Pollet BG. Niche applications of metal hydrides and related thermal management issues. *J Alloys Compd* 2015;645:117–22. <http://dx.doi.org/10.1016/j.jallcom.2014.12.271>.
- [18] Payá J, Linder M, Mertz R, Corberán JM. Analysis and optimization of a metal hydride cooling system. *Int J Hydrogen Energy* 2011;36:920–30. <http://dx.doi.org/10.1016/j.ijhydene.2010.08.112>.
- [19] Satheesh A, Muthukumar P, Dewan A. Computational study of metal hydride cooling system. *Int J Hydrogen Energy* 2009;34:3164–72. <http://dx.doi.org/10.1016/j.ijhydene.2009.01.083>.
- [20] Heubner F, Pohlmann C, Mauermann S, Kieback B, Röntzsch L. Mechanical stresses originating from metal hydride composites during cyclic hydrogenation. *Int J Hydrogen Energy* 2015;40:10123–30. <http://dx.doi.org/10.1016/j.ijhydene.2015.06.053>.
- [21] Saito T, Suwa K, Kawamura T. Influence of expansion of metal hydride during hydriding–dehydriding cycles. *J Alloys Compd* 1997;253–254:682–5. [http://dx.doi.org/10.1016/S0925-8388\(96\)02893-9](http://dx.doi.org/10.1016/S0925-8388(96)02893-9).
- [22] Nasako K, Ito Y, Hiro N, Osumi M. Stress on a reaction vessel by the swelling of a hydrogen absorbing alloy. *J Alloys Compd* 1998;264:271–6. [http://dx.doi.org/10.1016/S0925-8388\(97\)00246-6](http://dx.doi.org/10.1016/S0925-8388(97)00246-6).
- [23] Charlas B, Kneib F, Gillia O, Imbault D, Doremus P. A tool for modelling the breathing of hydride powder in its container while cyclically absorbing and desorbing hydrogen. *Int J Hydrogen Energy* 2014;1–12. <http://dx.doi.org/10.1016/j.ijhydene.2014.11.077>.
- [24] Salque B, Chaise A, Iosub V, Gillia O, Charlas B, Dupuis C, et al. Measure of the hydride breathing while cyclically absorbing and desorbing hydrogen. *J Alloys Compd* 2015;645. <http://dx.doi.org/10.1016/j.jallcom.2014.12.112>.
- [25] Qin F, Guo LH, Chen JP, Chen ZJ. Pulverization, expansion of La0.6Y0.4Ni4.8Mn0.2 during hydrogen absorption-desorption cycles and their influences in thin-wall reactors. *Int J Hydrogen Energy* 2008;33:709–17. <http://dx.doi.org/10.1016/j.ijhydene.2007.10.029>.
- [26] Charlas B, Gillia O, Doremus P, Imbault D. Experimental investigation of the swelling/shrinkage of a hydride bed in a cell during hydrogen absorption/desorption cycles. *Int J Hydrogen Energy* 2012;37:16031–41. <http://dx.doi.org/10.1016/j.ijhydene.2012.07.091>.
- [27] Herbrig K, Röntzsch L, Pohlmann C, Weißgärber T, Kieback B. Hydrogen storage systems based on hydride-graphite composites: computer simulation and experimental validation. *Int J Hydrogen Energy* 2013;38:7026–36. <http://dx.doi.org/10.1016/j.ijhydene.2013.03.104>.
- [28] Capurso G, Schiavo B, Jepsen J, Lozano G, Metz O, Saccone A, et al. Development of a modular room-temperature hydride storage system for vehicular applications. *Appl Phys A* 2016;122(236). <http://dx.doi.org/10.1007/s00339-016-9771-x>.
- [29] Broom DP. The accuracy of hydrogen sorption measurements on potential storage materials. *Int J Hydrogen Energy* 2007;32:4871–88. <http://dx.doi.org/10.1016/j.ijhydene.2007.07.056>.
- [30] VDI-Gesellschaft. VDI heat atlas vol. 1; 2015. <http://dx.doi.org/10.1007/978-3-540-77877-6>.
- [31] Bürger I, Hu JJ, Vitillo JG, Kalantzopoulos GN, Deledda S, Fichtner M, et al. Material properties and empirical rate equations for hydrogen sorption reactions in 2 LiNH₂-1.1 MgH₂-0.1 LiBH₄-3 wt.% ZrCoH₃. *Int J Hydrogen Energy* 2014;39:8283–92. <http://dx.doi.org/10.1016/j.ijhydene.2014.02.120>.
- [32] Sandrock G. Panoramic overview of hydrogen storage alloys from a gas reaction point of view. *J Alloys Compd* 1999;293:877–88. [http://dx.doi.org/10.1016/S0925-8388\(99\)00384-9](http://dx.doi.org/10.1016/S0925-8388(99)00384-9).



Research Paper

Heat transformation based on $\text{CaCl}_2/\text{H}_2\text{O}$ – Part A: Closed operation principle

Margarethe Richter, Martin Bouché, Marc Linder*

German Aerospace Center (DLR), Institute of Engineering Thermodynamics, Pfaffenwaldring 38-40, 70569 Stuttgart, Germany

HIGHLIGHTS

- Upgrade and storage of thermal energy using a thermochemical system is investigated.
- Calcium chloride is used as reference material.
- Thermal charging at 130 °C, discharging at 165 °C experimentally demonstrated.
- Limitations and changes during reaction are analyzed.
- An innovative process concept for thermochemical heat storage is suggested.

ARTICLE INFO

Article history:

Received 20 October 2015

Accepted 18 March 2016

Available online 24 March 2016

Keywords:

Thermochemical energy storage

Heat transformation

Calcium chloride

Waste heat

Thermal upgrade

ABSTRACT

Thermochemical systems based on gas–solid-reactions enable both storage of thermal energy and its thermal upgrade by heat transformation. Thus, they are an interesting and promising option in order to reutilize industrial waste heat and reduce primary energy consumption. In this publication an experimental analysis of the reaction system calcium chloride and water vapor is presented. The endothermic dehydration reaction is used in order to charge the storage at 130 °C while the reverse reaction leads to a discharging at 165 °C. Thus, a thermal upgrade by 35 K could be demonstrated and main limitations by heat and mass transfer were analyzed. Whereas this part focusses on a closed operation principle, the associated part B deals with the open operation utilizing air as purge gas.

© 2016 Elsevier Ltd. All rights reserved.

1. Introduction

In Germany more than 50% of the primary energy is used for thermal purposes [1]. Besides space heating and warm water, the biggest amount of heat is needed as process heat. Especially the chemical industry is important in this context since it is one of the most energy consuming industrial sectors [1]. In order to further reduce energy consumption and CO_2 -emissions thermal energy could in principle be integrated into the processes. However, approx. $4.76 \cdot 10^{17}$ J waste heat (not used thermal energy) is released from industrial processes every year [2]. There are mainly two process related reasons for the limited re-utilization of waste heat:

- Fluctuation in heat source and demand.
- Low temperature level of waste heat [2,3].

In general, in order to tackle both aspects, two different technologies are needed. On the one hand the time dependent fluctuation has to be buffered by thermal energy storage. On the other hand a heat pump is needed to perform a thermal upgrade so reintegration of the waste heat is possible at the required temperature.

Thermochemical systems based on gas–solid-reactions exhibit the potential to do both, thermal storage and upgrade within one single process. Hereby, a reversible reaction



is used. During the endothermic reaction the storage is charged, whereas discharging takes place through the exothermic reaction. This storage function has been demonstrated in a 10 kW scale by Schmidt et al. with the reaction system $\text{CaO}/\text{H}_2\text{O}$ [4]. In order to perform the chemical heat pump function the gas pressure has to be changed between charging and discharging process. Several materials are discussed as chemical heat pump systems, e.g. metal hydrides or ammoniates, hydroxides and hydrates [5,6]. If hydrogen or ammonia is used as gaseous reactant a second solid is needed to

* Corresponding author. Tel.: +49 711 6862 8034; fax: +49 711 6862 632.

E-mail address: marc.linder@dlr.de (M. Linder).

Nomenclature

Abbreviations

HI	1st hydration step anhydrous CaCl_2 to $\text{CaCl}_2 \cdot 0.3\text{H}_2\text{O}$
HII	2nd hydration step $\text{CaCl}_2 \cdot 0.3\text{H}_2\text{O}$ to $\text{CaCl}_2 \cdot 1\text{H}_2\text{O}$
HIII	3rd hydration step $\text{CaCl}_2 \cdot 1\text{H}_2\text{O}$ to $\text{CaCl}_2 \cdot 2\text{H}_2\text{O}$
HTF	heat transfer fluid
tot	total, over all

Symbols

$c_{p,\text{HTF}}$	specific heat capacity ($\text{J kg}^{-1} \text{K}^{-1}$)
h	step of hydration (mol H_2O /mol CaCl_2)
$\Delta_R H$	enthalpy of reaction

\dot{M}	mass flow (kg s^{-1})
p	pressure (kPa)
\dot{Q}	heat flux (W)
ρ_E	energetic storage density (kW h m^{-3})
s	distance (mm)
T	temperature (K)
t	time (h)
X	conversion (-)
z	vertical position in reaction tube (m)
ϑ	temperature, thermocouple ($^{\circ}\text{C}$)

store it. Water vapor, in contrast, can easily be condensed at moderate pressures. Kato et al. analyzed a chemical heat pump with $\text{MgO}/\text{H}_2\text{O}$ as reaction system [7]. Due to kinetic limitations an application of this reaction requires further material improvements. Alternative reactions with water vapor are salts which form hydrates. These materials are suggested for seasonal storage in domestic applications [8]. The reaction of calcium chloride with water vapor



is also suitable for application at higher temperatures as it exhibits complete reversibility, thermal and cycling stability and reasonable kinetics at temperatures up to $200\text{ }^{\circ}\text{C}$ [9,10]. Therefore, this material was chosen for further analysis in a lab scale reactor in order to demonstrate the principle of thermal storage and upgrade in one single unit.

2. Experimental

The schematic sketch of the test bench is shown in Fig. 1. Since the process concept is based on a closed system the reactor (1) is connected with a condenser/evaporator (2). Therefore, the gaseous reactant water is condensed or evaporated depending on the operation mode. Thus, the conversion can be easily determined from the liquid level in the heat exchanger (2). The whole set-up is evacuated before operation, decreasing the absolute pressure to about 2 kPa.

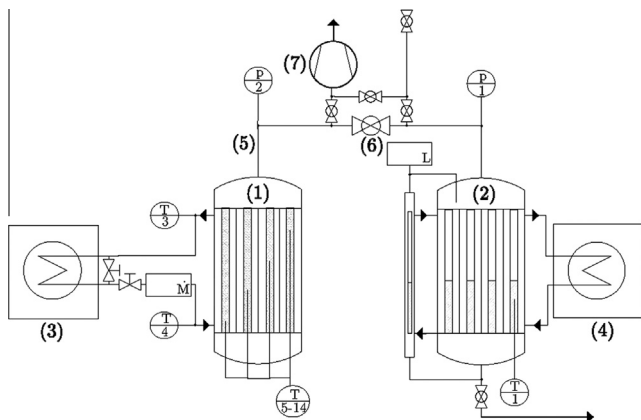


Fig. 1. Schematic sketch of the test bench in lab scale including (1) the reactor, (2) the condenser/evaporator, (3) thermostatic bath for the reactor, (4) thermostatic bath for the condenser/evaporator, (5) connecting tube, (6) valve and (7) vacuum pump.

2.1. Reactor

The permeability of the material with regard to the gaseous reactant is one important parameter and needs to be analyzed. To do so, a temperature measurement in different positions inside the reaction bed can be used to derive a rough estimate about the local reaction conditions. Therefore, a tube bundle heat exchanger is used as reactor enabling a long and thin reaction bed. The reaction material is filled into the upright tubes and tempered inside the shell. Here, a heat exchanger with 31 tubes with a diameter of 9 mm and a length of 400 mm is used (see Fig. 2, left). At the bottom of the tubes a lid including thermocouples is placed which closes the reactor and the whole system. On top of the tubes a filter is placed and the connection to the evaporator/condenser unit is mounted. Thus, the reaction gas is removed and supplied from the top of the reactor. Heat transfer oil (Petro Canada, Purity FG) is flowing through the shell of the reactor tempering the reaction bed through a thermostatic bath (Unistat 430, Huber Kältemaschinen GmbH).

The reaction bed can be modified by introducing fixed gas channels (see Fig. 2, right). These are made of a wire mesh filter material with a mesh size of $100\text{ }\mu\text{m}$. It is rolled to a thin tube with a diameter of 1 mm. These fixed gas channels enable a good gas transport along the tube.

2.2. Material

Calciumchloride dihydrate from Macco Organique/Magnesia (4155) is used in all experiments. The purity is specified with 97%. The particle size distribution has been determined by a Mastersizer 3000 (Malvern Instruments) as a dry dispersion in air. The intermediate particle size of the material is about $200\text{ }\mu\text{m}$.

2.3. Gas supply

To supply the reaction bed with the reaction gas water vapor a second tube bundle heat exchanger is used ((2) in Fig. 1). The apparatus is identical to the reactor but water is condensed and evaporated in the tubes. Again, the shell is tempered using heat transfer oil (Mobiltherm 600, Mobil) and a thermostatic bath (Lauda TW 220). With this set-up gas pressures between 0.8 kPa and 101.3 kPa are possible.

2.4. Measurement instrumentation

Through the bottom lid of the reactor ten thermocouples (type K) with a tolerance of $\pm 1.5\text{ K}$ are inserted into the reaction bed. They are placed in the radial center of ten different tubes at different vertical positions (see Fig. 3).



Fig. 2. Tube bundle heat exchanger, used as reactor (left) and its modification with fixed gas channels made of thin wire mesh (right).

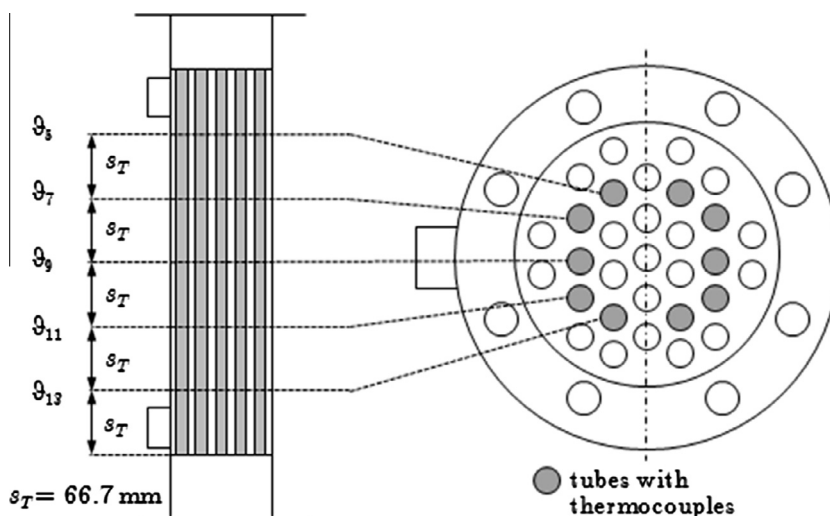


Fig. 3. Positions of thermocouples in the reaction bed. The thermocouples $\vartheta_6, \vartheta_8, \vartheta_{10}, \vartheta_{12}, \vartheta_{14}$ are at analog positions (mirrored at the symmetry plane).

The in- and the outlet temperature of the thermal oil in the reactor as well as the water temperature in the condenser/evaporator is determined by thermocouples, too.

The water level in the condenser/evaporator is determined with an accuracy of $\pm 1.5 \text{ mm}$ (Vegaflex 61, VEGA Grieshaber KG). From this the conversion of the reaction is calculated.

The gas pressure in the system is measured by a pressure sensor (PAA-35XHTT, Keller Ges. für Druckmesstechnik mbH) with an accuracy of $\pm 0.8 \text{ kPa}$. There are two pressure sensors placed in the set-up: one on top of the reactor and one on top of the condenser/evaporator. The mass flow of the thermal oil tempering the reactor is measured by a mass flow meter (Coriolis, F-Series, Emerson Process Management GmbH) with an accuracy of $\pm 0.0697 \text{ kg min}^{-1}$.

2.5. Experimental procedure

The reactor is filled with approx. 700 g calcium chloride dihydrate. Before starting the experiments, the whole set-up is evacuated to approx. $2 \text{ kPa} \pm 1 \text{ kPa}$ using the vacuum pump (Hena 25, Pfeiffer Vacuum GmbH, (7) in Fig. 1). The evaporator/condenser (2) is tempered in order to reach the requested vapor pressure. The starting temperature of the reactor is set by the heat transfer oil with a mass flow of 2 kg min^{-1} . As soon as thermal equilibrium is reached the valve (6) is opened to initiate the reaction. The experiment ends when thermal equilibrium is reached again.

The experimental conditions are summarized in Fig. 4. Here, the gas pressure and the inlet temperature of the heat transfer oil tempering the reactor are indicated by the squares and triangles. For

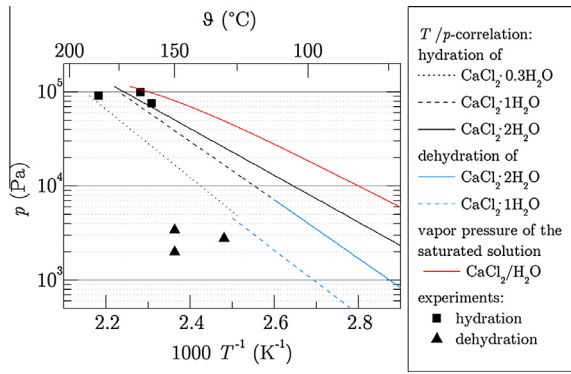


Fig. 4. Reaction lines for the hydration and dehydration of calcium chloride and its hydration steps [9]. Squares and triangles indicate the reaction conditions of the experiments in the reactor.

dehydration low vapor pressures (2–3 kPa) are chosen in order to decrease the charging temperature of the thermochemical storage. Thus, the water vapor generated by the reaction is condensed at these pressures. The reactor is tempered to 150 °C and 130 °C. In order to discharge the storage at higher temperatures the reverse reaction is performed at higher pressures (approx. 100 kPa). The temperature of the reactor is varied in these experiments between 160 °C and 185 °C. Lower temperatures than this result in deliquescence of the hydrate. This is indicated by the red¹ line in Fig. 4. Therefore, the feasible temperature and pressure range is very small. This is why accurate tempering of the reaction material is necessary in order to preclude the salt from dissolving in its own crystal water.

As the first reaction cycle might significantly differ from the following [9], only the second cycles are analyzed in this publication.

3. Results and discussion

3.1. Thermal charging

The dehydration reaction of calcium chloride dihydrate was performed at 150 °C. Fig. 5 shows the experimental results. The indicated gas pressure was measured at the top of the reaction bed. As soon as the valve to the condenser is opened ($t = 0$ h) the pressure drops to about 2 kPa. This initiates the endothermic dehydration reaction and the temperatures in the reaction bed drop. The trends of the temperatures indicate the multiple steps of the dehydration reaction. This is in good agreement with the thermodynamic characterization of the material, that has been published before [9]. The first minimum indicates the dehydration from dihydrate to monohydrate, the second one from monohydrate to the anhydrous calcium chloride.

But the temperatures in the reaction bed do not change simultaneously. The thermocouple ϑ_5 (black curve) is positioned at a height of $z = 0.33$ m. Therefore, it is only covered by a little amount of material. At this position the lowest temperature of 120 °C is reached. After about 45 min the temperature rises to 150 °C indicating the end of the reaction in this region of the reaction bed. Thus, the top part of the packed bed reacts faster and at lower temperatures than in the lower regions. This happens due to the low gas permeability of the packed bed of solid material. During dehydration, water vapor is generated which needs to be removed from the packed bed. At the top of the tubes the pressure is approx. constant, mainly influenced by the temperature in the condenser. Thus, the lower regions in the packed bed exhibit a higher gas pres-

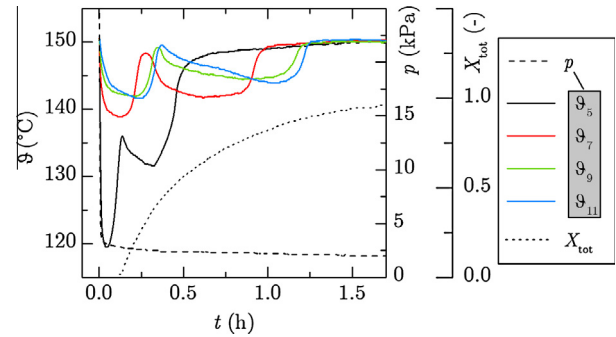


Fig. 5. Dehydration reaction of calcium chloride dihydrate at 150 °C without a modification of the reaction bed.

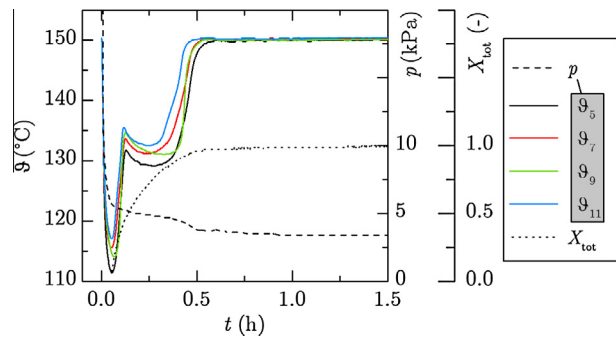


Fig. 6. Dehydration reaction of calcium chloride dihydrate at 150 °C with fixed gas channels as a modification of the packed bed.

sure due to the pressure drop produced through the gas flow through the bed. This can be confirmed by an experiment performed with a modified bed. Here, fixed gas channels are introduced into the fixed bed. Fig. 6 shows the experimental results of a dehydration reaction at the same conditions but with a modified reaction bed. The inserted thin tubes of wire mesh function as fixed gas channels, enabling a good axial gas flow in the reactor tubes. The second right ordinate refers to the conversion that has been calculated from the amount of water collected in the condenser. The conversion curve indicates the end of reaction after approx. 0.5 h. Thus, the reaction time is decreased to one third of the reaction time of the unmodified bed. The temperature at all heights of the fixed changes simultaneously. Thus, a simultaneous reaction can be observed.

The aim of heat transformation with gas–solid-reactions is to maximize the temperature difference between charging and discharging. In previous experiments (not shown here), it was analyzed that the low gas permeability of the solid material prohibits a lower charging temperature than 150 °C. However, this strong limitation can be overcome by using these fixed gas channels. Thus, a lower charging temperature is possible. Fig. 7 shows the experimental temperature curves during dehydration at 130 °C. Complete conversion can be observed after approx. 1 h. Compared to dehydration at 150 °C the reaction time doubles. Due to the temperature dependence described by Arrhenius the reaction rate decreases at lower temperatures. But this kinetic effect couples with a thermodynamic one: the reaction generates lower gas pressures at lower reaction temperatures. Therefore, the driving force for the gas transport through the fixed bed is reduced. This results in another raise of overall dehydration time. Nevertheless, a charging of the thermochemical energy storage is technically demonstrated at a temperature of 130 °C with reasonable effective reaction rates.

¹ For interpretation of color in Fig. 4, the reader is referred to the web version of this article.

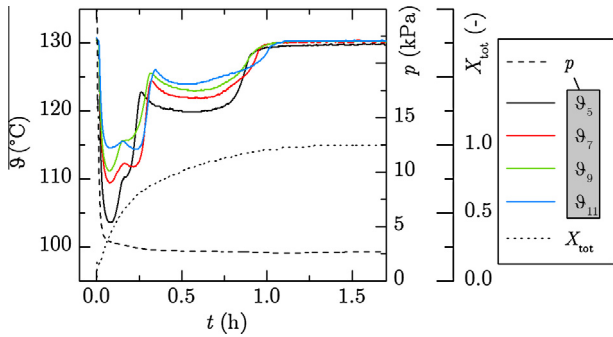


Fig. 7. Dehydration reaction of calcium chloride dihydrate at 130 °C with fixed gas channels.

The temperatures in the reactor show the characteristics discussed before. Although fixed gas channels were introduced into the reaction bed, a small axial gradient is visible. In contrast to dehydration at 150 °C the thermocouple ϑ_{11} shows a higher temperature than ϑ_5 . The deeper the position of the thermocouple the higher is the measured temperature. This effect can be explained by the van't Hoff dependence of the reaction. The temperature and gas pressure of the reaction are coupled through the relation $\ln(p) \propto T^{-1}$. Through this logarithmic dependence at smaller gas pressures a small change in pressure has a higher influence on the reaction temperature than at higher pressures. This effect becomes apparent comparing Figs. 6 and 7.

In closed mode lower charging temperatures are hard to reach. This would require a sufficient pressure difference between the reaction bed and the condenser leading to a lower temperature of condensation and a lower overall pressure. However, these boundary conditions are not interesting for the addressed application as a cooling of the condenser below ambient temperature would be required. Therefore, the lowest temperature for the thermal charging process is 130 °C in a closed mode operation. Therefore, in the associated paper of Bouche et al. an open operation mode was investigated. The open operation mode utilizes air as purge gas in order to decrease the mass transfer limitations discussed above.

3.2. Thermal discharging

In order to release the thermal energy from the storage at higher temperatures the hydration reaction is performed at higher vapor pressures. Fig. 8 shows the experimental results at a vapor pressure of 75 kPa. The reactor was tempered to 160 °C before reaction. If the reaction gas is introduced into the reaction bed,

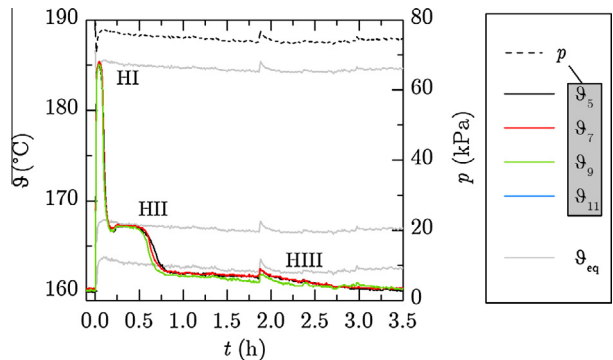


Fig. 8. Hydration of calcium chloride at a temperature of 160 °C and a vapor pressure of 75 kPa.

the temperatures rise up to 185 °C due to exothermal reaction. This temperature relates to the equilibrium of the first step in hydration reaction (HI), the formation of $\text{CaCl}_2 \cdot 0.3\text{H}_2\text{O}$ [9]. This corresponds to 15% of the overall conversion. After this reaction step is completed the temperatures drop to about 167 °C. At the present gas pressure this relates to the equilibrium temperature of the reaction from $\text{CaCl}_2 \cdot 0.3\text{H}_2\text{O}$ to monohydrate (HII). In this reaction step 35% of the overall reaction is converted. Thus, the second step corresponds to a bigger part of the overall reaction. Furthermore, it takes place at a lower temperature resulting in a smaller difference to the temperature of the heat transfer fluid. This leads to a lower heat transfer and the reaction time of step HIII is longer than the one of HI. A third temperature level is reached after 50% of the conversion is reached. The temperature of approx. 163 °C corresponds to the equilibrium temperature of the hydration from monohydrate to dihydrate (HIII) at 75 kPa. During this last reaction step the temperature difference between the reaction bed and the heat transfer fluid adds up to 3 K. Therefore, the overall reaction takes more than 3.3 h until full conversion is reached.

Although no fixed gas channels were introduced into the solid material, the whole material reacts simultaneously. At any time the same temperatures were detected at every measuring point. Therefore, the pressure loss of the incoming gas does not influence the reaction at higher pressures. Thus, the gas permeability is not a limiting factor for hydration reaction. The conversion rate is mostly limited by the heat transfer.

In order to reach higher conversion rates the gas pressure is increased to approx. 100 kPa. As can be seen in Fig. 4 at this pressure deliquescence might occur. Thus, the reaction temperature needs to be adapted. Choosing 165 °C the hydration can take place without dissolving. Fig. 9 shows the results of this experiment. The temperature of solid follows the three steps of the reaction (HI, HII and HIII) as described before. In this case, these temperature levels have a higher difference to the temperature of the heat transfer fluid. Thus, the heat of reaction is removed faster and the overall reaction consequently requires only approx. 1.5 h. The gas pressure during this experiment is highly influenced by the fast reaction. It drops as the reaction starts and reaches the set value of 100 kPa after about 60% of the reaction is completed.

In all experiments for the hydration of CaCl_2 the maximal temperatures directly relate to the multiple steps of reaction. For a maximal temperature difference between charging and discharging of the thermochemical storage a limitation to only one reaction step (HI) is necessary. At a vapor pressure of 100 kPa an equilibrium temperature of 190 °C can be expected. If the solid is tempered to 180 °C this reaction can take place completely without further reaction to monohydrate and dihydrate (see Fig. 10). Assuming a charging temperature of 130 °C this leads to a thermal

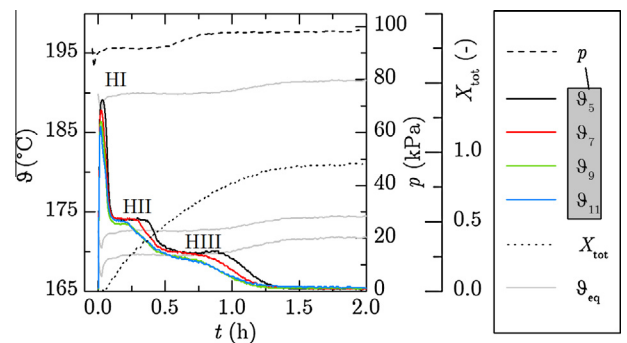


Fig. 9. Hydration of calcium chloride at a temperature of 165 °C and a vapor pressure of 100 kPa.

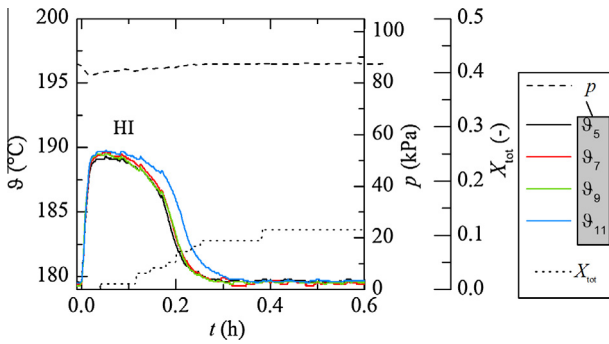


Fig. 10. Hydration of calcium chloride at a temperature of 180 °C and a vapor pressure of 100 kPa.

upgrade of 50 K. In this case the conversion is reduced to 15% at most, though.

3.3. Changes with cycling

Although cycling stability over 20 cycles was demonstrated before [9], the fixed bed changes considerably after several hydration and dehydration reactions. Fig. 11 shows the cycled material. On the one hand the particles agglomerate into highly porous solid structures. On the other hand bridges and channels are formed. The mean particle size of 200 μm does not change significantly during dehydration. But after three cycles of de- and rehydration a very broad particle size distribution is obtained. As can be seen in Fig. 11 big agglomerates in the size of few cm are formed, that easily decompose into smaller particles. This may lead to a change of the local thermophysical properties, e.g. the effective thermal conductivity and permeability of the reaction bed. These changes are highly anisotropic and depend on stochastic effects. Therefore, a homogeneous distribution of the reaction enthalpy is limited.

As a consequence not only the chemical properties considering thermodynamics and reaction kinetics should be addressed in cycling experiments but also the potentially changing macroscopic properties of packed beds.

Fig. 12 shows the overall conversion calculated by the water level in the evaporator and the heat flux transferred by the thermal oil for four hydration experiments with the same filling. The heat flux has been calculated by

$$\dot{Q}_{\text{HTF}} = \dot{M}_{\text{HTF}} \cdot c_{p,\text{HTF}} \cdot \Delta T_{\text{HTF}} \quad (3)$$

with the mass flow of the thermal oil $\dot{M}_{\text{HTF}} = 2 \text{ kg min}^{-1}$, the specific heat capacity $c_{p,\text{HTF}} = 2364.75 \text{ J kg}^{-1} \text{ K}^{-1}$ and the temperature differ-

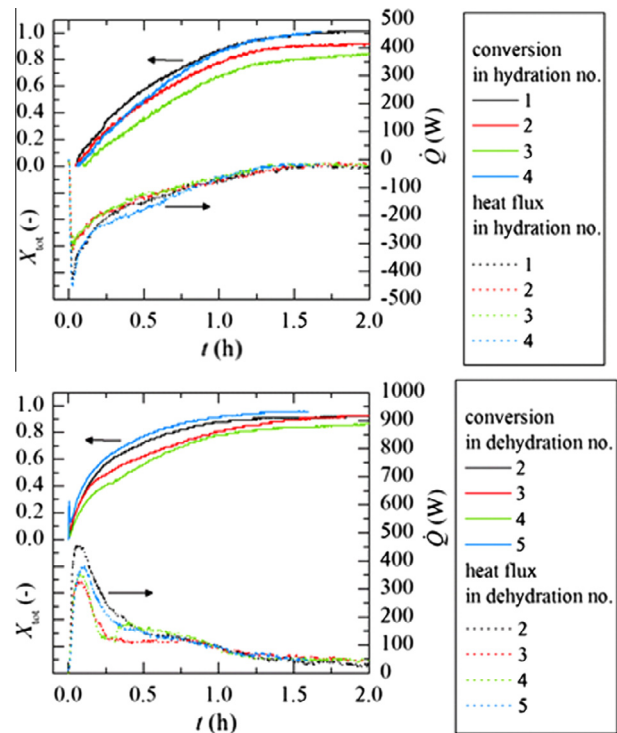


Fig. 12. Overall conversion and transferred heat flux during hydration cycles at a vapor pressure of 96 kPa and a starting temperature of 165 °C (above) and during dehydration cycles at a starting temperature of 130 °C.

ence ΔT_{HTF} between the inlet and the outlet of the reactor (maximum 8 K). Considering the error of measurement the heat flux is given with an accuracy of $\pm 101 \text{ W}$.

All experiments were performed at the same conditions (hydration: $\vartheta_{\text{HTF}} = 165 \text{ °C}$, $p_{\text{H}_2\text{O}} = 100 \text{ kPa}$; dehydration: $\vartheta_{\text{HTF}} = 130 \text{ °C}$). Comparing the different cycles, differences in the conversion and heat flux curves can be observed. But no clear trend for a de- or increase of the rate of reaction or thermal power can be identified. Consequently, the changes in the reaction bed may decline or improve the performance of such a system. But a degradation of the thermal power of the thermochemical system is not observed comparing the first cycles.

3.4. The potential of thermal upgrade using $\text{CaCl}_2/\text{H}_2\text{O}$

The energetic storage density of the thermochemical storage material CaCl_2 and $\text{H}_2\text{O}_{(\text{g})}$ is approx. 216 kW h m^{-3} , assuming a

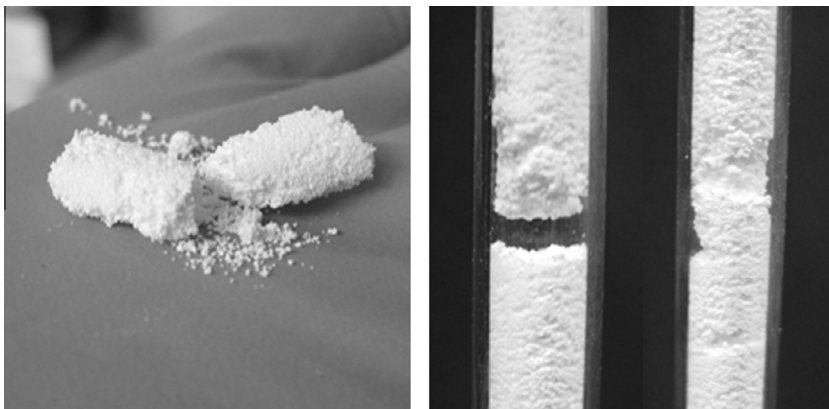


Fig. 11. Agglomerates, bridges and channels in the cycled calcium chloride reaction bed.

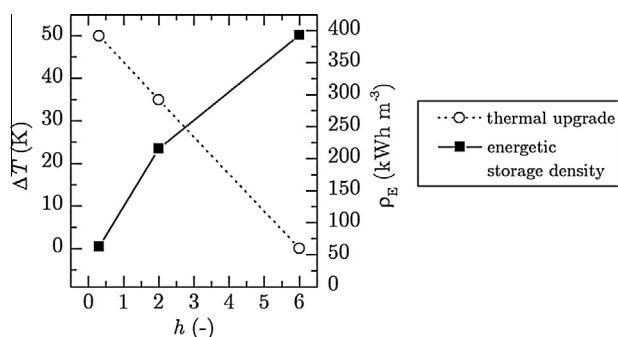


Fig. 13. Energetic storage density (ρ_E) and temperature lift (ΔT) of the heat transformation for different modes of operation of the reaction system $\text{CaCl}_2/\text{H}_2\text{O}$ with respect to different level of hydration (h).

void fraction of 0.5. Using water vapor with a pressure of 100 kPa the discharging can be performed at 165 °C, while charging can take place at 130 °C. Thus, a thermal upgrade of 35 K is possible using this system if full conversion from anhydrous CaCl_2 to dihydrate is realized. The multiple steps of the reaction limit the possible temperature lift between charging and discharging. If only one reaction step is used, e.g. the reversible hydration to $\text{CaCl}_2 \cdot 0.3\text{H}_2\text{O}$, discharging can be conducted at 180 °C. This increases the possible thermal upgrade to 50 K, but it reduces the storage density. Fig. 13 summarizes these possible modes of operation comparing temperature lift and storage density. Depending on the requirements of the thermochemical storage the reacting amount of water should be adapted. The higher the maximal level of hydration the higher the storage density on the one hand but the lower the temperature lift on the other hand. The theoretical limit is reached for the reaction to hexahydrate. In this case no thermal upgrade can be performed.

These values are upper limits for that material. If the whole setup (e.g. reactor and condenser) is taken into account, the storage density is obviously smaller. Compared to physical storage systems, e.g. sensible or PCM storage, the required system complexity is clearly higher and consequently the differences between material related and system related values might be higher. However, the possibility to combine thermal storage with a thermal upgrade that has been demonstrated in this paper might compensate the higher complexity.

To increase the thermal upgrade between charging and discharging of the system either hydration needs to take place at higher temperatures or dehydration at lower ones. Due to the low melting temperature of calcium chloride dihydrate the hydration temperature cannot be increased. Dehydration temperature could be decreased if mass transport limitations can be overcome. One approach to improve mass transfer is to conduct a constant flow of (dry) air through the fixed bed. Thus, an open operation mode should enable lower charging temperatures and consequently a higher temperature lift of the heat transformer. The results of the dehydration process in an open operation are described in the associated paper by Bouché et al.

4. Conclusions

The experimental results demonstrate the functionality of thermal energy storage and transformer using water vapor and calcium chloride. Different limitations occur during charging and discharging process: Macroscopic mass transport retards the dehydration reaction at low vapor pressures. Using gas-channels this limitation can be overcome. At higher gas pressures such as 100 kPa the permeability of the packed bed is not limiting. In this case, heat transport becomes the more important factor. Small temperature differences between reaction and tempering and the low thermal conductivity of the solid are the reasons for this limitation. A further analysis of these and other reaction effects is given by Molenda [11].

In general, it can be concluded that salt hydrates offer interesting options for the utilization of thermochemical systems in thermal processes. These systems are especially promising to reduce industrial waste heat due to thermal upgrade possibility. The reaction system $\text{CaCl}_2/\text{H}_2\text{O}$ is not optimal due to its multiple steps of reactions and deliquescence. But it is reasonable reference material to demonstrate the process and understand the limitations.

Acknowledgements

The authors highly appreciate the work of the former students Henning Jockenhöfer and Richard Günsch and the funding of the Federal Ministry of Education and Research of Germany.

References

- [1] Statistisches Bundesamt, Destatis, 2012. www.destatis.de.
- [2] M. Pehnt, J. Bödeker, M. Arens, E. Jochem, F. Idrissova, Nutzung industrieller Abwärme – technisch-wirtschaftliche Potenziale und energiepolitische Umsetzung, Karlsruhe, Heidelberg, 2010.
- [3] S. Spoelstra, W.G. Haije, J.W. Dijkstra, Techno-economic feasibility of high-temperature high-lift chemical heat pumps for upgrading industrial waste heat, *Appl. Therm. Eng.* 22 (2002) 1619–1630.
- [4] M. Schmidt, C. Szczukowski, C. Roßkopf, M. Linder, A. Wörner, Experimental results of a 10 kW high temperature thermochemical storage reactor based on calcium hydroxide, *Appl. Therm. Eng.* 62 (2014) 553–559, <http://dx.doi.org/10.1016/j.applthermaleng.2013.09.020>.
- [5] J. Cot-Gores, A. Castell, L.F. Cabeza, Thermochemical energy storage and conversion: a state-of-the-art review of the experimental research under practical conditions, *Renew. Sustain. Energy Rev.* 16 (2012) 5207–5224.
- [6] W. Wongsuwan, S. Kumar, P. Neveu, F. Meunier, A review of chemical heat pump technology and applications, *Appl. Therm. Eng.* 21 (2001) 1489–1519.
- [7] Y. Kato, T. Sekiguchi, J. Ryu, Packed bed reactor demonstration of magnesium oxide/water chemical heat pump, in: Proc. 11th Int. Conf. Therm. Energy Storage-Effstock, 2009.
- [8] M. van Essen, J. Cot Gores, L.P.J. Bleijendaal, H.A. Zondag, R. Schuitema, W.G.J. van Helden, Characterization of salt hydrates for compact seasonal thermochemical storage, in: Effstock 11th Int. Conf. Energy Storage, Goteborg, Sweden, 2009.
- [9] M. Molenda, J. Stengler, M. Linder, A. Wörner, Reversible hydration behavior of CaCl_2 at high H_2O partial pressures for thermochemical energy storage, *Thermochim. Acta* 560 (2013) 76–81.
- [10] K.E. N'Tsoukpoe, H.U. Rammelberg, A.F. Lele, K. Korhammer, B.A. Watts, T. Schmidt, et al., A review on the use of calcium chloride in applied thermal engineering, *Appl. Therm. Eng.* 75 (2015) 513–531, <http://dx.doi.org/10.1016/j.applthermaleng.2014.09.047>.
- [11] M. Molenda, Chemische Speicherung und Transformation thermischer Energie mit Calciumchlorid und Wasserdampf, Universität Stuttgart, 2015.



Research Paper

Heat transformation based on $\text{CaCl}_2/\text{H}_2\text{O}$ – Part B: Open operation principle

Martin Bouché, Margarethe Richter, Marc Linder*

German Aerospace Center (DLR), Institute of Engineering Thermodynamics, Pfaffenwaldring 38-40, 70569 Stuttgart, Germany

HIGHLIGHTS

- Thermal upgrade of waste heat using a thermochemical system.
- Dehydration of calcium chloride dihydrate using air represents charging process.
- Open operation principle in a fixed bed.
- Parametric experimental study regarding charging temperature and air flow rate.
- Thermal charging at 100 °C with long duration of reaction.

ARTICLE INFO

Article history:

Received 20 October 2015

Accepted 21 March 2016

Available online 29 March 2016

Keywords:

Thermochemical energy storage

Heat transformation

Calcium chloride

Waste heat

Thermal upgrade

Pressure drop

ABSTRACT

In order to increase the efficiency of industrial processes by means of thermal energy storage and upgrade of waste heat in a temperature range of 100–200 °C thermochemical systems are a promising option. The working pair $\text{CaCl}_2/\text{H}_2\text{O}$ has been identified as suitable reference system due to the possibility to store thermal energy and perform an upgrade of thermal energy at the same time. As working principle an open mode with air as purge gas is investigated in this work. Thus, an operation at ambient pressure level as well as a less complex experimental setup can be realized. Therefore, a test facility has been set up for experimental investigation of the thermochemical system focusing on dehydration reaction. First, various reactor modifications are examined with respect to influence the pressure drop of the reactor containing the CaCl_2 . It was shown that by the insertion of gas channels made of fine metal mesh a reduction of the pressure drop by factor 6 is possible in comparison to the unmodified fixed bed. Additionally, parametric studies have been carried out regarding the variation of charging temperature and volume rate of air. In order to obtain a high temperature lift in the heat transformation process, low thermal charging temperatures are targeted.

© 2016 Elsevier Ltd. All rights reserved.

1. Introduction

In order to decrease CO_2 emissions in the industrial sector, an efficient use of energy is necessary. Comparing the total energy consumption of Germany, a percentage of 29% is used for industrial purposes, while 64% of this are used for thermal process heat supply [1]. Studies have shown that there are huge amounts of industrial waste heat with a temperature level up to 150 °C [2]. Thus, a big potential for reducing costs and increasing efficiencies exists in this sector. However, there are different process related reasons why a reutilization of industrial waste heat seems currently not economical: Firstly, the temperature level of waste heat doesn't satisfy process requirements for further utilization.

Secondly, heat supply and demand are poorly synchronized. To overcome these problems there are several opportunities available. One approach is to store the waste heat in thermal energy storages and release it at a time with higher heat demand. Furthermore, a continuous upgrade of waste heat to higher temperature levels can be performed using heat pumps.

In order to combine these options of thermal energy storage and upgrading waste heat, thermochemical systems are a promising approach. Thermochemical systems are based on reversible chemical reactions between two components. The charging process takes place by thermal separation of the two components (endothermic). Release of heat occurs during the reverse (exothermic) recombination reaction of the components. In general, the reaction equation can be written as:



* Corresponding author. Tel.: +49 711 6862 8034; fax: +49 711 6862 632.

E-mail address: marc.linder@dlr.de (M. Linder).

Nomenclature

Symbols

ΔH_R	enthalpy of reaction (J mol^{-1})
m	mass (g)
M	molar weight (g mol^{-1})
p	pressure (kPa)
p^0	Standard pressure (1 kPa)
Δp	pressure drop (kPa)
R	universal gas constant ($\text{J mol}^{-1} \text{K}^{-1}$)
t	time (min)
$t_{X=90}$	time to 90% overall conversion (min)

T	temperature ($^{\circ}\text{C}$)
T^0	standard temperature (298 K)
\dot{V}	volume flow ($\text{m}^3 \text{h}^{-1}$)
x	water vapor concentration (-)
X	conversion (-)

Abbreviations

dehyd	dehydration
tot	total

Thermochemical energy storage with gas–solid-reactions theoretically exhibit the advantage of high volumetric energy storage densities and reduced heat losses during storage period. Additionally, thermochemical systems offer the option to upgrade low temperature heat to higher temperatures which is the main aspect of this paper.

The working principle of this kind of heat transformation can be described by the van't Hoff chart displayed in Fig. 1b. The equilibrium line represents the correlation of vapor pressure with given reaction temperature. In thermodynamic equilibrium, the gas pressure rises with increasing temperature. According to the van't Hoff chart, thermal charging at low temperatures is possible if the gas pressure is kept at a low level as well. The reverse process, thermal discharging, occurs at a higher pressure resulting in high output temperatures. Therefore, the thermal upgrade is performed between endothermic and exothermic reaction by change of gas pressure. This can refer to the absolute as well as to partial gas pressure. If the reaction is conducted in a gas mixture, e.g. air, the fraction of the reactive gas can be changed. Thus, the overall pressure could be equal to ambient which simplifies the construction of the technical components (see Fig. 2).

For the purpose of performing a heat transformation with thermochemical systems an open operation mode is a promising option. In this case, an inert gas (e.g. air) flows through the reactor removing the reaction gas and releasing it to environment (see schematic in Fig. 1a). The gaseous reaction component needs to be environmentally friendly, e.g. water vapor. Due to the reduced requirements (no vacuum, no additional storage container, no cold sink) the open system is rather simple and consequently high storage densities on a system level can be expected.

2. State of art and aim of work

In this chapter the state-of-the-art of thermochemical systems regarding heat transformation of industrial waste heat is presented. Various systems are proposed able to upgrade waste heat in a temperature range between $100\text{ }^{\circ}\text{C}$ and $200\text{ }^{\circ}\text{C}$.

Water/sorption. Well known physical sorption systems are zeolites or silica gels using water as reaction gas. Based on zeolite, a mobile thermal heat storage was built up by Krönauer et al. for waste heat utilization from a incineration plant [4]. As operating principle an open system is used with air as purge gas. Thermal charging takes place at a temperature level up to $130\text{ }^{\circ}\text{C}$ by means of dry air releasing the water steam to the environment. Extraction of thermal energy occurs by the use of humid air generating output temperatures up to $150\text{ }^{\circ}\text{C}$.

Ammonia. Neveau et al. reported on different ammonia based working pairs suitable for a wide range of temperatures [5]. Based on these data, Wongsuwan et al. suggested several ammonia-salt systems as promising working pairs for upgrading waste heat with an appropriate temperature lift [6]. Experimental studies were carried out by Haije et al. investigating the performance of the ammonia-salt system $\text{LiCl-MgCl}_2/\text{NH}_3$ for purposes of heat transformation [7]. Li et al. proposing an improved sorption cycle and a theoretical analysis with the ammonia-salt system $\text{MnCl}_2\text{-CaCl}_2/\text{NH}_3$ for upgrading low thermal energy up to $171\text{ }^{\circ}\text{C}$ [8]. However, due to strong toxicity of ammonia these reactions are only applicable in closed systems without any contact to ambient atmosphere.

Metal hydrides. Dantzer et al. proposed a selection of various metal-hydrides capable to react reversible with hydrogen as reaction gas [9]. A two stage metal hydride heat transformer was

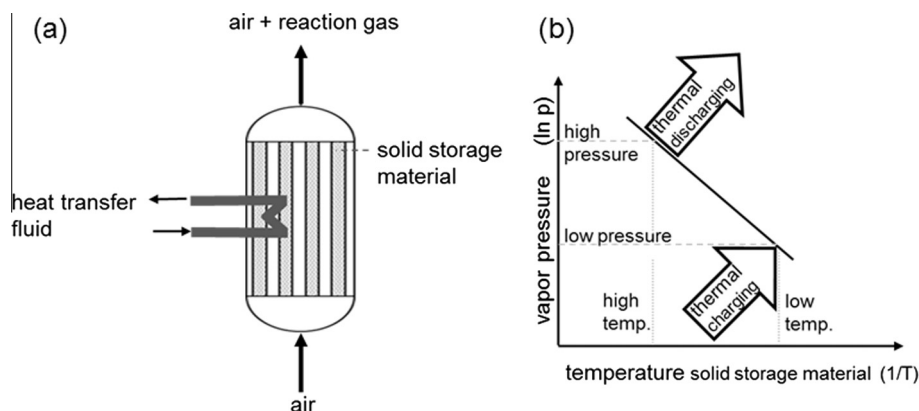


Fig. 1. (a) Schematic of open system (b) T/p -correlation (van't Hoff) - dependency of vapor pressure (reaction gas) and equilibrium temperature (solid storage material).

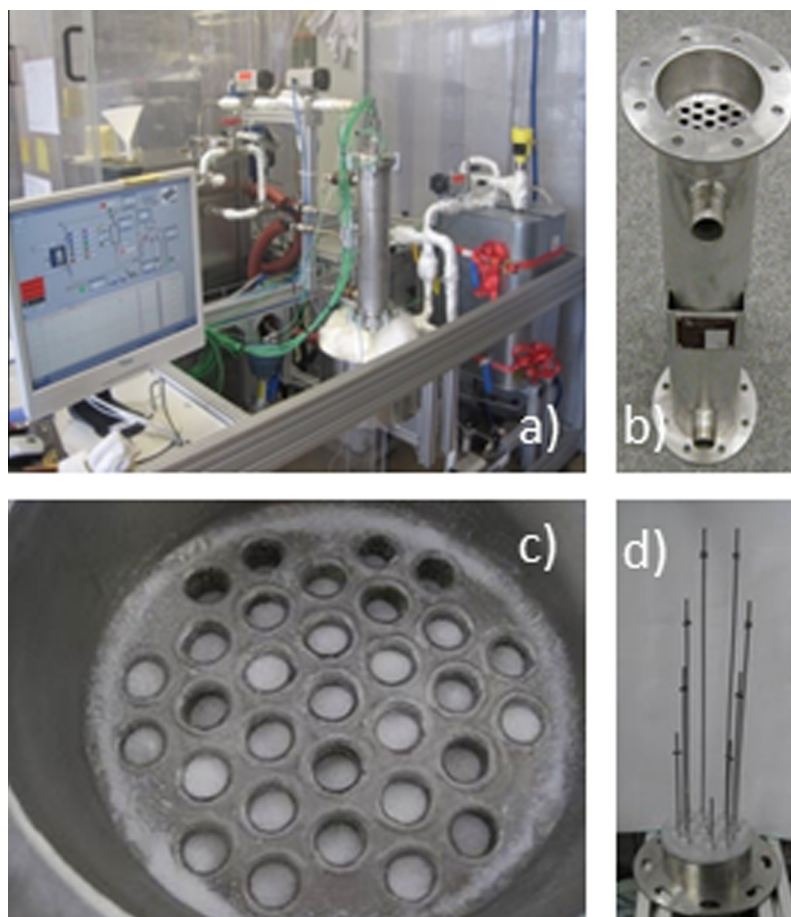
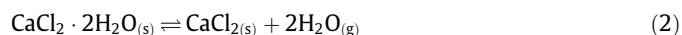


Fig. 2. (a) Test facility, reactor (b) tube bundle heat exchanger as reactor (c) CaCl_2 packed bed in tubes. (d) Thermocouples for temperature measurements at different heights of packed bed.

developed by Willers et al. upgrading thermal heat from a temperature level of 130 °C up to 200 °C [10]. Another system based on different metal hydrides is set up by Suda et al. [11]. In order to perform a heat transformation a low grade thermal energy source of 80 °C is used to generate a high output temperature of about 120 °C for steam generating applications.

Water/salt-hydrates. In order to realize a thermal heat storage or in combination with the possibility to transform heat in the target temperature range of 100–200 °C water based thermochemical systems seem to be promising candidates. Water steam used as heat transfer fluid is widely spread in thermal industrial processes for heating purposes in various technical applications. Additionally, using water vapor as nontoxic medium, also an open system as operation principle (as proposed in this paper) is feasible since the reaction gas can be released to the environment. Up to now there are only a couple of water based salt hydrates experimental investigated regarding suitability for thermal upgrade of industrial waste heat. Studies about the working pair $\text{Na}_2\text{S}-\text{H}_2\text{O}$ with respect to structure, thermodynamic and phase properties have been carried out by De Boer et al. [12]. In order to avoid the deliquescence of the solid material during regeneration, temperatures above 83 °C may not be exceeded. Thus suitability for higher temperatures within industrial processes was not given. For the utilization in a chemical heat pump the reaction pair $\text{MnCl}_2/\text{H}_2\text{O}$ is examined by Stitou et al. focusing on the reverse reaction between the anhydrate and the monohydrate [13]. Experimental results showed that a thermal upgrade from 95 °C to 160 °C during thermal discharging is achievable. However, thermal charging of the reaction systems needs around 320 °C.

In order to investigate the upgrade of industrial waste heat by means of an open process in the temperature range of 100–200 °C, the thermochemical system $\text{CaCl}_2/\text{H}_2\text{O}$ was chosen as reference material. The generic reaction equation is given in Eq. (2). However, the overall reaction is more complex since it occurs with intermediate steps. Details are reported by Molenda et al. [3].



The present paper includes an experimental part with examinations using different reactor modifications for charging process analyzing their influence on the pressure drop. Additionally, parametric studies are conducted regarding charging temperatures and flow rate of purge gas. The results are analyzed with respect to pressure drop, conversion time and progress of fixed bed temperatures. The aim is to increase the potential thermal upgrade of the heat transformer by decreasing the charging temperature. The respective discharging experiments at different water vapor pressures are not part of this study but are being reported in the associated paper of Richter et al.

3. Experimental

3.1. Setup

For experimental investigations of the open operation of the thermochemical system a test facility was built up. The main component of the test bench represents the reactor designed as tube

bundle heat exchanger. It consists of 31 tubes with a diameter of 9 mm each and a height of 400 mm surrounded by a shell. Within the tubes the solid granular CaCl_2 dihydrate is placed. Filters with a mesh size of $13 \mu\text{m}$ are installed at the in- and outlet of the tubes. The supply of air as purge gas is provided by the internal compressed air network. By means of an electric preheater, the air can be heated up to 200°C . In order to measure the temperature within the packed bed, 10 thermocouples at different heights of the tubes are installed. Inserted through the bottom of the reactor, the thermocouples are placed every 66 mm. For the supply of thermal energy during dehydration process thermo-oil is used streaming through the shell-side of the reactor. The temperature of the thermo-oil can be adjusted by a thermostatic bath up to the maximum temperature of 200°C . Due to the reactor design an indirect heat transfer via thermo-oil as well as a direct heat transfer by the heated air flow occurs. In order to receive information about the conversion of the reaction, a gas analyzer is installed. The gas analyzer measures the concentration of water vapor at the in- and outlet of the reactor. Additionally, pressure sensors are attached at the in- and outlet detecting the pressure drop of the reactor. To prevent condensation electric heating lines are installed at the piping of the test-bench as well as at the in- and outlet of the reactor.

3.2. Procedure

Fresh material of calcium chloride dihydrate $\text{CaCl}_2 \cdot 2\text{H}_2\text{O}$ (Macco Organiques s.r.o) for every dehydration experiment is used. Two different operation modes are taken into account. The unmodified reaction bed and subsequently the modified reaction bed with gas channels were investigated. Before starting, the reactor is heated by the thermo-oil to experimental conditions. The air is heated by the electric preheater to charging temperature and streaming through a bypass. In order to initiate dehydration reaction, the dry and hot air flow is led through the reaction bed. Due to the dehydration reaction water vapor is released increasing the partial vapor pressure in the air. At the outlet of the reactor the gas mixture is analyzed. By the use of the pressure sensors the pressure drop of the reaction bed is detected. A parametric study of charging temperature and air volume flow is conducted, as shown in Table 1.

4. Experimental results and discussion

4.1. Unmodified reaction bed

First experiments were performed using the tube bundle heat exchanger as reactor with an unmodified fixed bed of reaction material within the tubes. The experiment is carried out with a mass of 720 g of CaCl_2 dihydrate distributed equally within the reactor tubes.

First experimental investigation of decomposition reaction of CaCl_2 dihydrate in the open system is carried out under following boundary conditions: charging temperature is set to 150°C (thermo-oil + air) and air flow is adjusted to $4 \text{ m}^3 \text{ h}^{-1}$. The dehydration reaction is initiated by opening the valves at the in- and outlet of the reactor, whereby preheated air flows through the packed bed of reaction material. According to the van't Hoff chart of $\text{CaCl}_2 \cdot 2\text{H}_2\text{O}$ [3], the equilibrium pressure at a temperature of 150°C is around 40 kPa. The water content (partial pressure) of the incoming air can be assumed as zero. As a consequence, the CaCl_2 dihydrate is dissociated and the dry air dilutes the released water vapor. Due to the endothermic dissociation the temperature of the fixed bed decreases.

As displayed in Fig. 3, at the inlet of the packed bed a temperature minimum is reached very quickly since at this position the

Table 1

Parameter variation of experiments (um: unmodified reaction bed; m: modified reaction bed).

		Volume flow	
		$4 \text{ m}^3 \text{ h}^{-1}$	$8 \text{ m}^3 \text{ h}^{-1}$
Charging temperature	150°C	um; m	m
	130°C	m	m
	100°C		m

lowest water vapor pressure is available. Along the fixed bed, the partial pressure of water vapor increases due to the dissociation reaction of the material. As a result of the decreased local temperature, a large temperature gradient to the tempered reactor wall occurs causing a high heat flux from the shell side of the reactor into the fixed bed. Due to these good reaction conditions (low water vapor pressure, large temperature difference) at the inlet a fast conversion is observed indicated by a fast return of local temperature to initial conditions of 150°C . At sections of the fixed bed positioned along the axial axes the completion of dehydration reaction takes consequently longer due to the above mentioned continuous enrichment of the air stream with water vapor. According to Molenda et al. [3], the decomposition of CaCl_2 dihydrate to anhydrous salt occurs in consecutive separate reactions steps. This reaction process explains the temperature evolution with two local minima representative for discrete reaction steps. First, the decomposition of CaCl_2 dihydrate to monohydrate takes place indicated by the temperature decrease to the first minimum of each temperature profile. After a short increase of the temperature, the second reaction step, the dissociation of monohydrate occurs and leads to the second local minimum. As soon as the anhydrous state is reached, the endothermic reaction is terminated which can be seen by the sharp increase of the respective temperature curve to its initial conditions. The completion of the dehydration process occurs with a plug flow behavior represented by the successive finalization of the reaction in local sections.

The concentration of water vapor released by the reaction is measured by a gas analyzer at the outlet of the reactor. At the beginning of the dehydration a peak of the water vapor concentration up to 20 vol-% is measured (see Fig. 3). Afterwards a continuous drop is detected that occurs due to the termination of the decomposition reaction along with the formation of anhydrous CaCl_2 at sections close to the inlet. The slope of vapor concentration decreases at around $t = 12$ min. This behavior can be related to a completed conversion of the dihydrate phase, consequently from this point on only the monohydrate phase releases water vapor. Due to a lower equilibrium pressure of CaCl_2 monohydrate the driving force of the reaction is reduced. Therefore, the decomposition is slow for the given boundary conditions. As soon as the entire decomposition is completed, the water vapor concentration at the outlet reaches again its original value of zero. In order to determine the overall conversion the measured water vapor concentration is used:

$$X_{\text{Conv.}} = \frac{m_{\text{H}_2\text{O, out, exp}}}{m_{\text{H}_2\text{O, tot, theo}}} = \dot{V}_{\text{air}} \cdot \int \frac{x_{\text{H}_2\text{O, out}}}{1 - x_{\text{H}_2\text{O, out}}} dt \cdot \frac{p^0}{R \cdot T^0} \cdot \frac{M_{\text{CaCl}_2 \cdot 2\text{H}_2\text{O}}}{2 \cdot m_{\text{CaCl}_2 \cdot 2\text{H}_2\text{O}}} \quad (3)$$

As shown in Fig. 3, the dehydration process reaches full conversion after around 30–35 min. During the experiment also the pressure drop of the purge gas through the entire reactor is measured by sensors attached at the in- and outlet of the reactor. In the unmodified fixed bed a very high pressure drop of $\Delta p = 62$ kPa is measured at a volume flow of $4 \text{ m}^3/\text{h}$. This pressure drop is related to the flow resistances of the particles as well as the filters at the

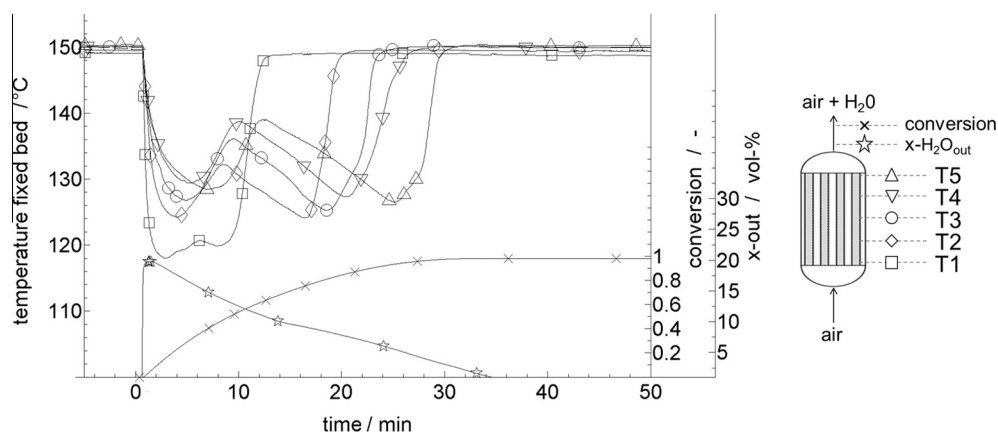


Fig. 3. Temperatures in the unmodified fixed bed, conversion, water vapor concentration at the outlet during dehydration reaction ($T_{\text{dehyd}} = 150\text{ }^{\circ}\text{C}$, $\dot{V} = 4\text{ m}^3/\text{h}$).

in- and outlet of the reactor. In this context, especially the filter at the outlet is important since it prevents a discharge of reaction material by the gas flow. Due to the already high pressure drop and the limitations of the pressure sensors an increase of the air flow rate is not possible.

4.2. Modified reaction bed with gas channels

In order to reduce the pressure drop along the channels as well as to examine the influence of the air flow rate and charging temperature on the dehydration process, the set-up has been slightly modified. For this purpose gas channels made of fine metal mesh were designed (see Fig. 4a) and placed into the tubes of the reactor. The solid reaction material was inserted around the filter tubes (see Fig. 4b). Due to the gas channels the main part of the air volume flow does not flow through the whole cross-section of the fixed bed. Consequently, the pressure drop along the reaction bed should be clearly reduced. Although an exchange of water steam into the purge gas is possible, a penetration of single particles into gas channels can be prevented. The effect on the decomposition reaction is analyzed by subsequent experiments.

Several experiments were carried out with charging temperatures to $150\text{ }^{\circ}\text{C}$, $130\text{ }^{\circ}\text{C}$ and $100\text{ }^{\circ}\text{C}$ and air flow rates of $4\text{ m}^3/\text{h}$ and $8\text{ m}^3/\text{h}$, respectively. Due to the additional volume of the gas channels less space is available for the reaction material, thus for these experiments only approx. 630 g of $\text{CaCl}_2 \cdot 2\text{H}_2\text{O}$ were filled into the reactor.

During the experiments a significant improvement of the specific pressure drop in consequence of the installed gas channels was observed. As shown in Table 2 at a given charging temperature of $150\text{ }^{\circ}\text{C}$ and a constant gas flow of $4\text{ m}^3/\text{h}$, a reduction of the pressure drop by nearly a factor of 6 was reached. Thus, using

the modification of the reaction bed, experiments with higher volume flow of purge air ($8\text{ m}^3/\text{h}$) are possible.

In the following the dehydration experiment with gas channels ($T_{\text{dehyd}} = 150\text{ }^{\circ}\text{C}$, $\dot{V} = 8\text{ m}^3/\text{h}$) is presented in detail. In principle, the results displayed in Fig. 5 show a similar behavior compared to the experiments carried out with the unmodified fixed bed. According to the temperature evolution within the fixed bed, the completion of decomposition reaction also takes place by a plug flow behavior. Thereby, a reaction front moves from the inlet of the reactor to the outlet, indicated by the successive return of the respective local temperatures to external conditions of $150\text{ }^{\circ}\text{C}$. However, in comparison to the unmodified fixed bed, the temperature profiles are less defined. The differentiation of the two decomposition reaction steps is possible but less clear. Since the same effect occurs with a reduced gas flow of $4\text{ m}^3\text{ h}^{-1}$ (not shown), the influence of the higher gas flow can be excluded. One possible explanation could be based on the additionally required mass transfer process in radial direction – from the actual point of reaction to the channel. This would lead to an additional resistance and consequently to a less pronounced temperature drop due to the endothermic reaction.

Table 2

Pressure drop of fixed bed influenced by reactor configuration and volume rate of purge gas.

		Volume flow	
		$4\text{ m}^3\text{ h}^{-1}$	$8\text{ m}^3\text{ h}^{-1}$
Charging temp. $150\text{ }^{\circ}\text{C}$	Unmodified reaction bed	$\text{dp} = 62\text{ kPa}$	
	Modified reaction bed	$\text{dp} = 11\text{ kPa}$	$\text{dp} = 34\text{ kPa}$

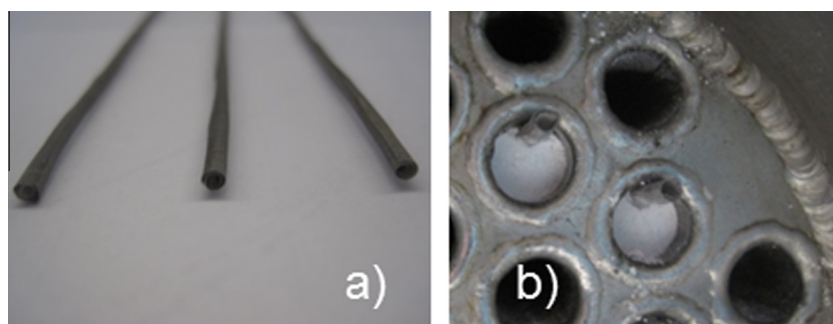


Fig. 4. (a) Gas channels made of fine metal mesh ($\varnothing \approx 1\text{ mm}$) (b) gas channels inside the packed bed of $\text{CaCl}_2 \cdot 2\text{H}_2\text{O}$.

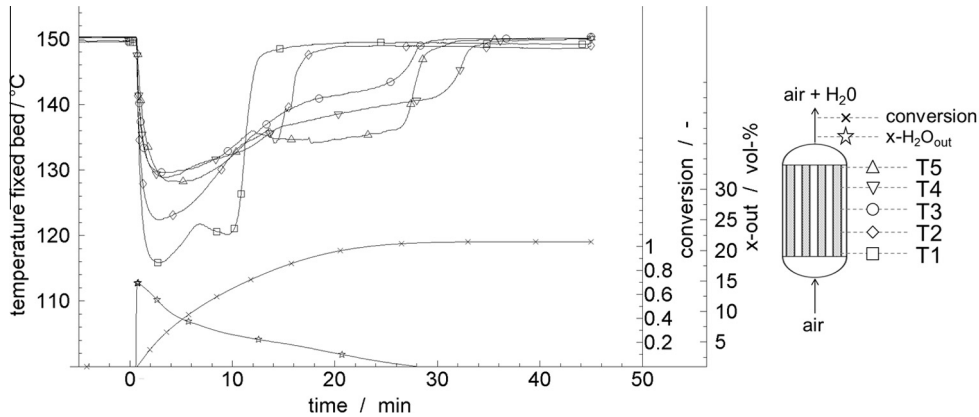


Fig. 5. Temperatures in the modified fixed bed (with gas channels), conversion, water steam concentration at the outlet during dehydration reaction ($T_{\text{dehyd}} = 150\text{ }^{\circ}\text{C}$, $\dot{V} = 8\text{ m}^3/\text{h}$).

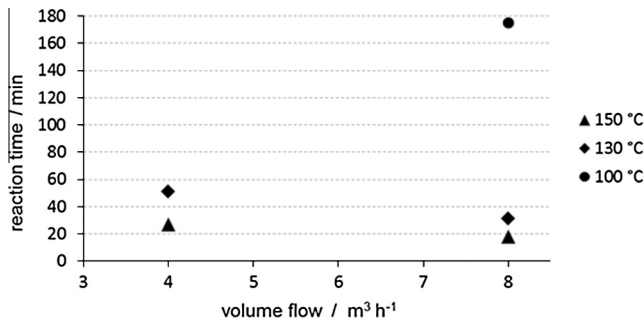


Fig. 6. Conversion time ($t_{x=90}$) of dehydration in dependency of volume flow (air) at different charging temperatures.

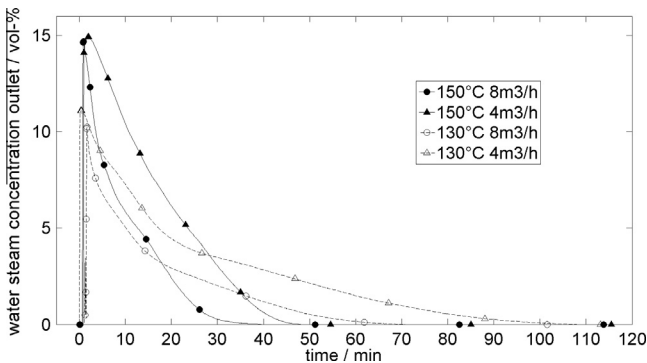


Fig. 7. Water vapor concentration at reactor outlet during dehydration at different experimental conditions.

For the assessment of the dehydration performance, the time for 90% of conversion is used ($t_{x=90}$). Fig. 6 shows the comparison of the dehydration performance for different temperatures and flow rates, respectively. A clear dependency between conversion time and charging temperature as well as air volume flow can be observed. The higher the charging temperature and the higher the volume flow the faster the reaction occurs. The rapid reaction can be explained by the high mass and heat transfer gradient between the reaction and the local boundaries during the reaction process. Additionally, due to the higher flow rates, a better dilution of the water vapor in the gaseous phase occurs, resulting in lower partial pressures. Therefore, with a flow rate of $8\text{ m}^3/\text{h}$, a dissociation of the reaction material is possible at an inlet temperature of

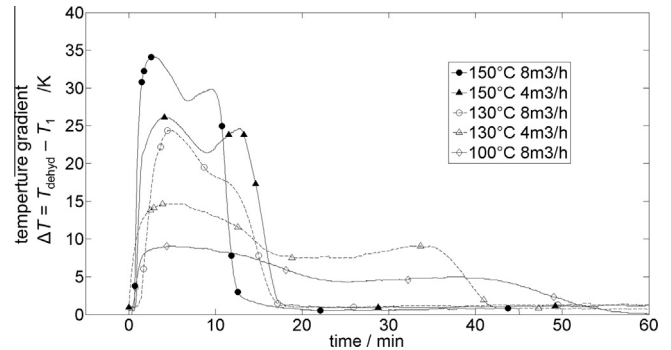


Fig. 8. Temperature gradient between inlet of packed bed and tempered reactor wall (charging temp.) during dehydration at different experimental conditions.

$100\text{ }^{\circ}\text{C}$. Even though, this reaction is comparatively slow, it demonstrates that a charging of the reaction system is possible even at low temperatures.

The influence of the charging temperature and the flow rate on the water vapor concentration measured at the outlet is shown in Fig. 7. For a given charging temperature the peak concentration at the beginning of the experiment is unaffected by the flow rate of the purge gas. However, with increasing reaction time, a higher flow rate leads to a faster decrease of the outlet concentration and consequently to a faster conversion.

The impact of the temperature gradient between the reaction material (inlet of fixed bed) and the reactor wall is shown in Fig. 8. The charging temperature T_{dehyd} is a boundary condition (heated reactor wall) whereas the temperature of the reaction material at the inlet of the reactor T_1 is a consequence of the reaction conditions. It is obvious that the largest gradient occurs at the beginning of each experiment leading to a fast release of water vapor (compare Fig. 8). Comparing the different charging temperatures, a correlation to the resulting temperature gradient can be observed: the lower the charging temperature the smaller the temperature gradient. This can be explained by the decrease in the rate of conversion for lower charging temperatures.

With respect to the intended application of a thermal upgrade, one important purpose of the reaction is to reach high temperature lifts between the recovery of thermal energy and the thermal charging of the system. According to the associated paper of Richter et al., the discharging of the reaction system is possible at temperatures up to $165\text{ }^{\circ}\text{C}$ using water vapor at atmospheric pressure. However, a trade-off between the power density of the

reactor and the possible temperature lift of the heat transformer has to be faced.

5. Conclusions

Regarding waste heat recovery the reported open operation principle of a thermochemical system is very promising. It enables the utilization of waste heat at 100 °C. Waste heat at this temperature level is generally hard to integrate into industrial processes. However, applying the here presented open operation mode, this thermal energy could be used to charge a thermochemical storage. While the charging process is performed using dry air, discharging takes place at a vapor pressure of 100 kPa, as reported in the associated paper by Richter et al. Thus, in an industrial application the thermochemical heat transformer is interesting especially if waste steam or waste heat at 100 °C (to generate steam) is available. Using the reference reaction system $\text{CaCl}_2/\text{H}_2\text{O}$ a thermal upgrade of approximately 65 K can be reached. If a maximum temperature lift is desired a long duration for the discharging needs to be accepted. From a technological point of view this might be questionable. Therefore, further work should focus on the effect of the intrinsic reaction kinetics on the reaction rate, new reaction materials as well as on possibilities to improve the heat transfer within the fixed bed.

Acknowledgements

The authors highly appreciate the work of the former students Henning Jockenhöfer and Richard Günsch and the funding of the Federal Ministry of Education and Research of Germany.

References

- [1] A.G. Energiebilanzen e.V. Anwendungsbilanzen für die Endenergiesektoren in Deutschland in den Jahren 2011 und 2012 mit Zeitreihen von 2008 bis 2012, 2013, 2013, p. 31.
- [2] S. Spoelstra, W.G. Haije, J.W. Dijkstra, P.W. Bach, and P.T. Alderliesten, Techno-economic feasibility of high-temperature high-lift chemical heat pumps for upgrading industrial waste heat, no. July, 2002.
- [3] M. Molenda, J. Stengler, M. Linder, A. Wörner, Reversible hydration behavior of CaCl_2 at high H_2O partial pressures for thermochemical energy storage, *Thermochim. Acta* 560 (2013) 76–81.
- [4] A. Krönauer, Mobile thermische Energiespeicher zur Nutzung industrieller Abwärme, Conference: "Berliner Energietage", 2013.
- [5] P. Neveu, J. Castaing, Solid-gas chemical heat pumps: field of application and performance of the internal heat of reaction recovery process, *Heat Recovery Syst. CHP* 13 (3) (1993) 233–251.
- [6] W. Wongsuwan, S. Kumar, P. Neveu, F. Meunier, A review of chemical heat pump technology and applications, *Appl. Therm. Eng.* 21 (15) (2001) 1489–1519, [http://dx.doi.org/10.1016/S1359-4311\(01\)00022-9](http://dx.doi.org/10.1016/S1359-4311(01)00022-9).
- [7] W.G. Haije, J.B.J. Veldhuis, S.F. Smeding, R.J.H. Grisel, Solid/vapour sorption heat transformer: design and performance, *Appl. Therm. Eng.* 27 (8–9) (2007) 1371–1376.
- [8] T. Li, R. Wang, J.K. Kiplagat, Thermodynamic and molecular-scale phenomena: a target-oriented solid-gas thermochemical sorption heat transformer for integrated energy storage and energy upgrade 59 (4) (2013).
- [9] P. Dantzer, E. Orgaz, Thermodynamics of hydride chemical heat pump—II. How to select a pair of alloys, *Int. J. Hydrogen Energy* 11 (12) (1986) 797–806.
- [10] E. Willers, The two-stage metal hydride heat transformer, *Int. J. Hydrogen Energy* 24 (2–3) (1999) 269–276.
- [11] S. Suda, Y. Komazaki, H. Narasaki, M. Uchida, Development of a double-stage heat pump: experimental and analytical surveys, *J. Less Common Met.* 172–174 (1991) 1092–1110. P, no. 0.
- [12] R. De Boer, W.G. Haije, J.B.J. Veldhuis, Determination of structural, thermodynamic and phase properties in the $\text{Na}_2\text{S}-\text{H}_2\text{O}$ system for application in a chemical heat pump, *Thermochim. Acta* 395 (2002) 3–19.
- [13] D. Stitou, N. Mazet, M. Bonnissel, Performance of a high temperature hydrate solid/gas sorption heat pump used as topping cycle for cascaded sorption chillers, *Energy* 29 (2) (2004) 267–285.



A systematic screening of salt hydrates as materials for a thermochemical heat transformer

Margarethe Richter*, Eva-Maria Habermann, Eleonore Siebecke, Marc Linder

German Aerospace Center (DLR), Institute of Engineering Thermodynamics, Pfaffenwaldring 38-40, 70569 Stuttgart, Germany



ARTICLE INFO

Keywords:

Material screening
Thermochemical storage
Heat transformer
Chemical heat pump
Salt hydrates
Reaction hysteresis

ABSTRACT

The selection of suitable reaction systems for thermochemical processes, e.g. thermal storage, chemical heat pumps or heat transformers, is challenging. Not only harmlessness of chemicals, theoretical energy storage density and thermodynamics play an important role, but also reversibility, reaction kinetics and cycling stability need to be considered. In this paper a systematic methodology for screening salt hydrates as thermochemical reaction material is suggested and applied to 308 different inorganic salts. It consists of a theoretical analysis of thermodynamic data as well as an extensive experimental analysis of the reversibility, reaction hysteresis and cycling stability. The target application is the heat transformation and reintegration of process waste heat up to 300 °C. SrBr₂ meets all requirements for this application and is a promising material.

1. Introduction

The utilization of currently unused process waste heat has an immense potential to save primary energy and to decrease carbon dioxide emissions. Different technologies, ranging from storage solutions to heat pumps and converters, have been developed in order to make this possible [1–7]. In this context, thermochemical energy storage has drawn attention in the last decades. This technology offers significant advantages over other storage concepts, e.g. high storage density and the possibility of heat transformation [8]. The working principle of a chemical heat pump or heat transformer is shown in Fig. 1. Hereby, a chemical reaction between a solid A and a gas B is used in order to store and release heat. The temperature level depends on the gas pressure p_B following the van't Hoff equation (Eq. (1)).

$$\ln\left(\frac{p_B}{p^+}\right) = \frac{\Delta_R S^\ominus}{R\nu} - \frac{\Delta_R H^\ominus}{R\nu T} \quad (1)$$

Here, p^+ is the reference pressure (100 kPa), $\Delta_R S^\ominus$ and $\Delta_R H^\ominus$ the standard entropy and enthalpy of reaction, respectively. R represents the universal gas constant, ν the stoichiometric factor for the respective reaction and T the temperature in K. The equilibrium of the reaction is indicated by a line in the $\ln(p_B/p^+)$ vs. T^{-1} plot. As a consequence, the

reaction temperature of the storage can be increased with an increased reaction gas pressure. In Fig. 1 a second (dashed) line is plotted representing the vapor pressure of the coupled component B. At point 1 the storage is charged at the temperature T_{in} by performing the decomposition reaction. The gas B is produced at the pressure p_1 which can be condensed at point 2 releasing low-temperature heat, e.g. at ambient temperature T_a . The evaporation of B at T_{in} can be considered as a thermal compression of the gas, which is the underlying “driving force” of the process. This step (3) initiates the discharging reaction of the thermal storage (formation of AB_ν) at the elevated pressure p_2 . Thus, the enthalpy of reaction is released as heat at T_{out} , a higher temperature than the one used for the charging process (T_{in}). Consequently, this process allows a thermal upgrade and a reintegration of industrial waste heat [9,10].

Many different reaction systems have been used and analyzed for heat transformation. Hydrogen, ammonia, oxygen or carbon dioxide are common gaseous components [4,11,12]. Focusing on water vapor as gaseous reactant offers several advantages: On the one hand, in comparison to hydrogen water vapor can be easily condensed, offering the advantage of no additional storage material for the absorption of the gas. On the other hand, the process can be run in open mode as water (vapor) is a harmless, nonhazardous and well available component.

* Corresponding author.

E-mail address: m.a.richter@outlook.de (M. Richter).

Nomenclature

Symbols

h	Level of hydration (mol mol^{-1})
$\Delta_f H^\ominus$	Standard enthalpy of formation (kJ mol^{-1})
$\Delta_R H$	Enthalpy of reaction (kJ mol^{-1})
$\Delta_R H^\ominus$	Standard enthalpy of reaction (kJ mol^{-1})
$\Delta_v H$	Enthalpy of vaporization (kJ mol^{-1})
ν	Stoichiometric factor
p^+	Reference gas pressure (100 kPa)
p_B	Partial gas pressure (kPa)
$p_{\text{H}_2\text{O}}$	Partial vapor pressure in N_2 (kPa)
R	Universal gas constant ($8.3145 \text{ J mol}^{-1} \text{ K}^{-1}$)

S^\ominus	Standard entropy ($\text{J mol}^{-1} \text{ K}^{-1}$)
$\Delta_R S^\ominus$	Standard entropy of reaction ($\text{J mol}^{-1} \text{ K}^{-1}$)
ϑ	Temperature ($^\circ\text{C}$)
T	Temperature (K)

Abbreviations/indices

D	Dehydration
eq	Equilibrium (calculated)
H	Hydration
onset	Extrapolated starting point of reaction (experimentally determined)
STA	Simultaneous thermal analysis

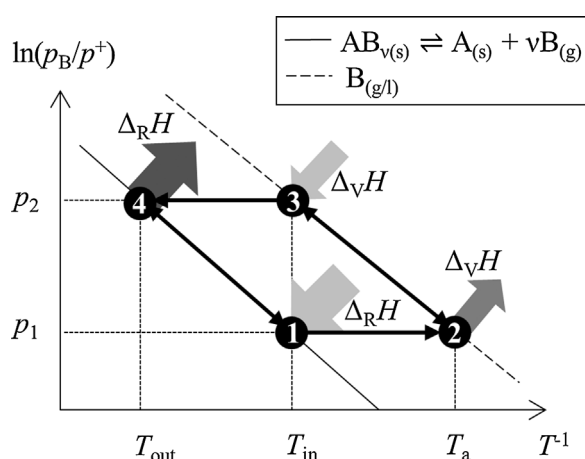


Fig. 1. Principle of heat transformer, reaction enthalpy.

Thus, the gas does not necessarily have to be stored which decreases the complexity of the process apparatus, reduces costs and increases over all energy storage density.

A relevant use case and analysis of such a heat transformer using the system $\text{CaCl}_2/\text{H}_2\text{O}$ has been published before [9,13]. In these studies, the temperature level of hydration and dehydration reaction was adjusted so charging of the thermal storage could be performed at a lower temperature than discharging. Comparable analysis has been done for hydride and ammonia systems [12,14–16] but to our knowledge the investigation of water driven heat transformers is rare.

To choose a suitable reaction system for thermochemical storage and transformation is generally challenging due to various aspects and characteristics that need to be considered. Previous screenings focused on the energy storage density [17–21]. N^oTsoukpoie et al. published a systematic screening of salt hydrates for low temperature thermochemical storage [19]. This screening follows a good straight forward methodology. However, the authors conclude that the application of these materials in domestic hot water supply is limited due to the high complexity of the system and low resulting energy storage density.

Material screenings like this mainly focus on energy density of thermal storage materials. However, many materials have shown other more relevant limiting effects [9,13,18,22–25]. Especially the assumption that charging of the storage can be performed at the same temperature as discharging turns out to be wrong in many cases.

There are several material related reasons that need to be taken into account for thermochemical storage and/or transformation systems: Firstly, some reactions exhibit multiple steps [22,23]. To reach the maximum energy storage density all reaction steps have to be overcome. In this case, there are multiple van't Hoff lines instead of only a single one as indicated in Fig. 1. The higher the level of hydration the closer is the equilibrium line to the vapor pressure line of water. A complete discharge of the thermal storage requires a full hydration but also a complete dehydration. Thus, all equilibrium lines need to be overcome and the difference between T_{out} and T_{in} is decreased compared to a one-step reaction at the same pressure difference ($\Delta p = p_2 - p_1$).

Secondly, some reaction systems exhibit deliquescence at high levels of hydration. This leads to a phase change—the materials “melt in their own crystal water”. To maintain respective material properties (e.g. permeability for the reaction gas) this has to be prevented. Thus, the storage has to be tempered above the temperature where deliquescence occurs. This requires a very narrow temperature range for the operation of the thermochemical storage: keeping the temperature far from the phase change means operating very close to the equilibrium temperature of the chemical reaction. It is doubtful if this temperature stability can be realized in a technical storage at all. But at least such an operation limits the heat exchange between the reacting material and the heat transfer fluid [9,13].

Thirdly, many reactions are very slow or reaction kinetics decrease with cycling [25–27]. This can have many different reasons, e.g. heat and mass transfer limitation within the material, the bulk or the reactor. But also the nature of the chemical reaction itself can be limiting which can be seen by the temperature dependence of the dehydration of salt hydrates or hydroxides [28]. In a systematic approach for finding suitable materials this aspect has to be considered as well.

Last but not least, a strong limitation is given by large reaction hysteresis. From a thermodynamic point of view the reaction has to take place as soon as process conditions next to the equilibrium line are reached. In reality many reactions are kinetically inhibited. Thus,

process conditions have to be set far from equilibrium in order to overcome these inhibitions. But not only kinetic inhibition can be the reason for a large hysteresis between hydration and dehydration reaction. The thermodynamic nature of the reaction system can lead to a hysteresis, too. The system MgO/H₂O shows such a behavior (especially at low vapor pressures) [29]. An intense development of MgO for thermochemical energy storage material has been performed by Kato et al. [25]. However, the still comparably large reaction hysteresis of MgO/H₂O limits its potential for heat transformation application.

Considering these issues, special requirements for thermochemical reactions as heat transformers have been set in this screening in order to find materials without these limitations. The target application is the reintegration of industrial waste heat by thermal upgrade to temperatures between 150 °C and 300 °C. Low temperature waste heat from chemical processes could be one application. According to a study about unused potential of waste heat from German industry most waste heat occurs at below 150 °C [30]. Thus, a thermal upgrade to temperature above that leads to an increased potential for the reintegration of heat. Furthermore, the material has to allow an open heat transformation process. This leads to the target temperatures and pressures for the desired reaction system: Pure water vapor at the atmospheric pressure should allow a reaction equilibrium temperature higher than 150 °C. The dehydration with air (assuming a maximum partial vapor pressure $p_1 = 5$ kPa in humid summer) has to be performed at lower temperatures than 150 °C. With this set of requirements a systematic theoretic and experimental screening has been performed to find suitable materials for a thermochemical heat transformer.

2. Methodology

308 salts have been chosen for the screening, based on the twenty most frequently occurring metals in the geosphere [31] to ensure high availability. Table 1 summarizes the material matrix. On the left-hand side the cations are shown ranked by the availability in the geosphere. On the right eleven common anions were chosen for the screening.

Table 1
Material matrix as starting point for the screening.

	Cations		Cations	Anions
1	Al ³⁺	11	Cr ⁶⁺	F ⁻
2	Fe ^{2+/3+}	12	Ni ^{2+/4+}	Cl ⁻
3	Ca ²⁺	13	Sr ²⁺	Br ⁻
4	Na ⁺	14	V ^{2+/3+/4+/5+}	I ⁻
5	K ⁺	15	Zn ²⁺	O ²⁻
6	Mg ²⁺	16	Cu ²⁺	S ²⁻
7	Ti ^{3+/4+}	17	W ⁶⁺	OH ⁻
8	Mn ²⁺	18	Li ⁺	SO ₄ ²⁻
9	Ba ²⁺	19	Ce ^{3+/4+}	NO ₃ ⁻
10	Zr ⁴⁺	20	Co ^{2+/3+}	PO ₄ ³⁻
				CO ₃ ²⁻

Fig. 2 summarizes the methodology developed for the screening of salt hydrates as thermochemical heat transformer materials. In the first four steps of the screening a theoretical analysis was performed. In general, materials that are carcinogen or hazardous (category 1 or 2, see [32]) have been excluded. As representative compounds the carbonates, oxides and hydroxides of each metal have been chosen (first

step).

If the salts form hydrates (second step) a thermodynamic calculation was performed in the third step. Based on literature data (standard enthalpies of formation $\Delta_f H^\ominus$ and standard entropies S^\ominus) the standard enthalpy and entropy of reaction $\Delta_R H^\ominus$ and $\Delta_R S^\ominus$ were calculated for every hydration reaction. If there is no data available for S^\ominus the entropy of reaction was estimated in this study. This is based on the known values of entropies of dehydration reactions of salt hydrates and hydroxides (see Table A1) with an average value of the entropy of reaction of approx. $150 \text{ J mol}^{-1} \text{ K}^{-1}$ and a standard deviation of 10. This range has been widened to $\Delta_R S^\ominus \approx 120 \text{ J mol}^{-1} \text{ K}^{-1}$ – $160 \text{ J mol}^{-1} \text{ K}^{-1}$ in order to be sure to keep suitable candidate materials in the screening. Using the Van't Hoff equation (see Eq. (1) with $p_B = p_{\text{H}_2\text{O}}$) the equilibrium temperature T_{eq} at ambient pressure was determined. For a chemical heat pump application thermal discharging at temperatures above 150 °C is needed. As a reference pressure the mean ambient pressure in Stuttgart (96 kPa), where the experimental analysis was performed, has been chosen. A equilibrium temperature T_{eq} (96 kPa) lower than 150 °C results in exclusion of the reaction from further analysis.

For the remaining materials a literature survey regarding the thermal stability of the salt hydrate was performed in the fourth step. The following criteria need to be fulfilled: The salts must not dissolve in their own crystal water in the relevant temperature and pressure range ($T < 300$ °C, $p < 96$ kPa). There must not be a side reaction with water or oxygen or thermal decomposition up to 300 °C.

After the theoretical analysis the remaining materials were tested in thermal analysis using three experiments. Experiment I was the test on reversibility of reaction, thermal stability and hydration temperature ($\vartheta_{\text{onset,H}}$) in 96 kPa water vapor. A lower but stable conversion (compared to the expected one) can be accepted if the reaction meets all the other requirements. In experiment II the hysteresis of the reaction at a constant partial vapor pressure of $p_{\text{H}_2\text{O}} = 5$ kPa was investigated. The reaction should take place at temperatures close to theoretical equilibrium. As criterion for exclusion the dehydration temperature at $p_{\text{H}_2\text{O}} = 5$ kPa is compared to the hydration temperature at $p_{\text{H}_2\text{O}} = 96$ kPa. In the heat transformer the discharging process (hydration) should take place at higher temperatures than the charging (dehydration) process. If this was the case experiment III was conducted. Here, ten isothermal reaction cycles were performed changing the atmosphere from pure nitrogen for dehydration to pure water vapor for hydration. The conversion should be constant over these cycles. Otherwise the materials were excluded.

3. Experimental

The experiments were carried out using a simultaneous thermal analysis (NETZSCH STA 449C Jupiter[®], see Fig. 3). The set-up was equipped with a water vapor generator (aDROP, Bronkhorst[®]) and a water vapor furnace. A thermogravimetric sample carrier with a thermocouple type S and an accuracy of ± 1 K was used. The accuracy of the balance was ± 0.1 μg . The used STA system exhibits a noticeable mass drift due to buoyance effects, water adsorption to the sample holder at high vapor pressures and balance drift. This needs to be corrected using a baseline measurement. Thus, every experiment has been repeated with an empty crucible. The resulting change in mass has been subtracted from the sample measurement. Thus, all resulting mass changes can be dedicated to the sample only.

As protective gas a nitrogen volume flow of 50 N-ml min^{-1} was used. The sample was surrounded by a constant gas flow of 100 N-ml

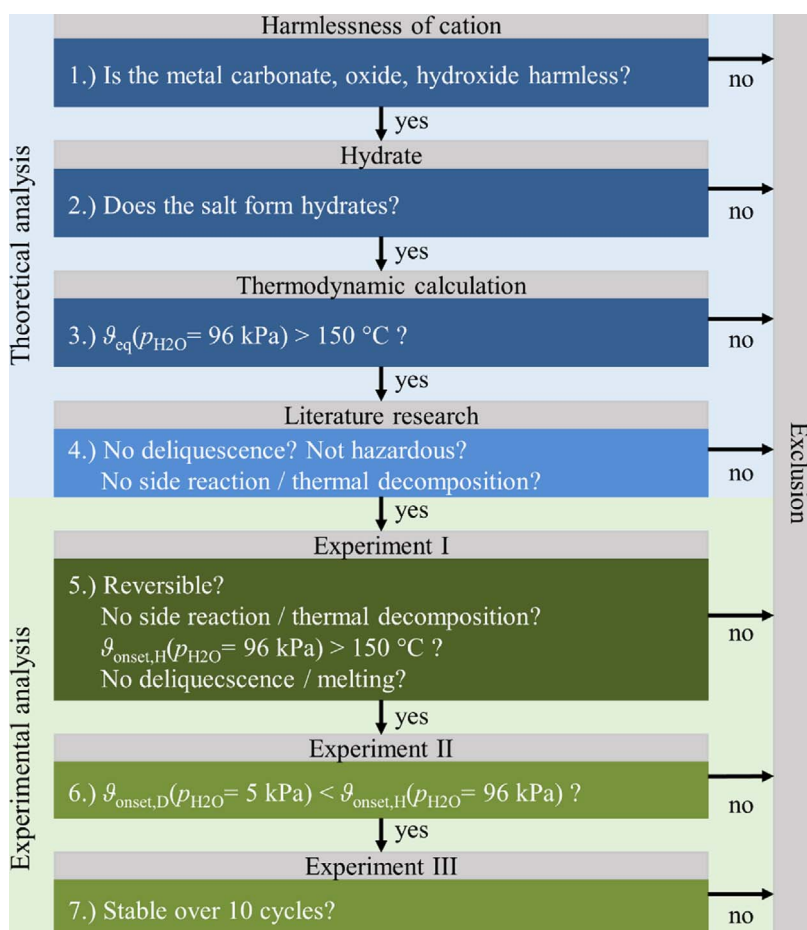


Fig. 2. Methodology of the materials screening.

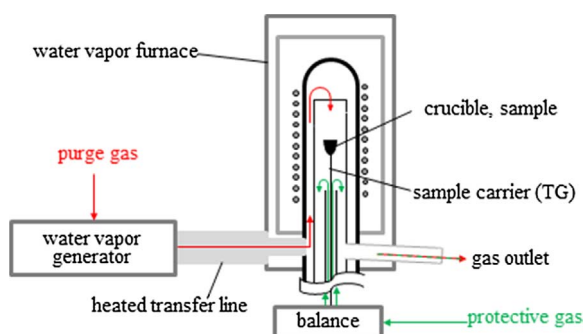


Fig. 3. Schematic of the thermal analysis (STA).

min^{-1} nitrogen and/or water vapor. Either pure nitrogen was used or partial vapor pressures of 5 kPa or 96 kPa \pm 1 kPa was set.

Dynamic experiments were performed with heating rates of 5 K min^{-1} and 1 K min^{-1} . As relatively low temperatures are necessary in

order to initiate hydration reaction of some salts, the temperature was set to a minimum of 20 K above the dew point of the gas mixture. The cycling tests were performed isothermally by changing the atmosphere from pure nitrogen to pure water vapor.

All tested materials obtained a purity of at least 98 %. The initial mass of the samples was set to 15 mg.

4. Results and discussion

4.1. Theoretical analysis

In the first step of the screening the harmlessness of the materials was analyzed. Here, the cations Cr^{6+} , $\text{Co}^{2+/3+}$ and $\text{Ni}^{2+/4+}$ have been excluded from further screening, as their carbonates, hydroxides and oxides are carcinogen or toxic (cat. 1 or 2).

For the application of a hydration reaction only salts that form hydrates are relevant (second step). Table 2 summarizes the matrix of the analyzed materials as a combination of cations and anions. The numbers indicate the level of hydration in mol water per mol salt. If no number is given no hydrates of the salt are reported. Out of these 253 salts 113 form hydrates, most of them in different levels of hydration.

Table 2

Matrix of inorganic salts analyzed in the present screening: The numbers indicate the level of hydration (mol mol^{-1}). [33,37–40,43–61]. The colors indicate the results of the theoretical part of the screening. Yellow: not suitable thermodynamics; Blue: deliquescence/melting; Red: side reactions with air/water or thermal decomposition; Violet: toxic; Green: (hydrates) commercially not available. (For interpretation of the references to colour in the Table, the reader is referred to the web version of this article.)

	F ⁻	Cl ⁻	Br ⁻	I ⁻	O ²⁻	S ²⁻	OH ⁻	SO ₄ ²⁻	NO ₃ ⁻	PO ₄ ³⁻	CO ₃ ²⁻
Li ⁺		1; 2; 3	1; 2	1; 2; 3			1	1	3	0.5	
Na ⁺			2	2		2; 4.5; 5; 9	1; 2; 3.5; 4; 5; 7	7; 10		12; 10; 8; 7; 6	1; 7; 10
K ⁺	2					2; 5	1; 2			3; 7; 9	0.5; 1.5
Mg ²⁺		1; 2; 4; 6	6					1; 2; 4; 5; 6; 7	2; 6	5; 8; 22	3; 5
Ca ²⁺		1; 2; 4; 6	6	6; 8				0.5; 2	2; 3; 4		
Sr ²⁺		1; 2; 6	1; 6	1; 2; 6			1; 8		4		
Ba ²⁺		1; 2	1; 2	1; 2; 2.5; 7			1; 3; 8				
Ce ³⁺	1; 3	1; 2; 3; 7	6					1; 4; 5; 8; 10; 14	3; 4; 6	2	8
Ce ⁴⁺	1				2			1; 2; 4; 5; 14			
Ti ³⁺		6	6	1							
Ti ⁴⁺	2				1; 2			3; 4; 9			
Zr ⁴⁺	1; 3				2			1; 4; 5; 7	2; 5; 6		
V ²⁺	1; 4	2; 4	2; 4; 6	4; 6				6; 7			
V ³⁺	2; 3	4; 6	4; 6	6				3; 4; 9; 10; 11		1	
V ⁴⁺					1						
V ⁵⁺					1						
W ⁶⁺					1; 2						
Mn ²⁺	4	1; 2; 4	1; 4; 6	2; 4				1; 4; 5; 7	6	3; 6; 7	
Fe ²⁺	4; 8	1; 2; 4; 6	1; 2; 4; 6; 9	1; 2; 4; 6; 9				1; 1.5; 2; 3; 4; 5; 6; 7	6; 9; 15; 18	1; 5; 8	
Fe ³⁺	3; 4.5	2; 2.5; 3.5; 5; 6; 7; 12	6		1; 3			2; 3; 6; 7; 7.5; 9; 10; 12	1; 2; 3; 6; 9	2; 3; 4	
Cu ²⁺	2	2	4					1; 3; 5	3; 6	2; 3	
Zn ²⁺	4	1; 2; 3; 4	2		2			1; 2; 6; 7	1; 2; 4; 6	1; 2; 4	1
Al ³⁺		6					1; 3	6; 16; 18	6; 9	2; 3; 3.5	

In the third step of the screening the equilibrium temperature of the single hydration reactions has been calculated based on literature data. The enthalpies and entropies of reaction and the calculated equilibrium temperature are summarized in the [Appendix A](#) in [Table A1](#). The values

are given for the lowest hydrates, as those generally obtain higher equilibrium temperatures than the reaction to higher hydrates. Alternatively, the relevant step of hydration is chosen in order to reach the relevant temperature range of 150 °C to 300 °C. For many reactions

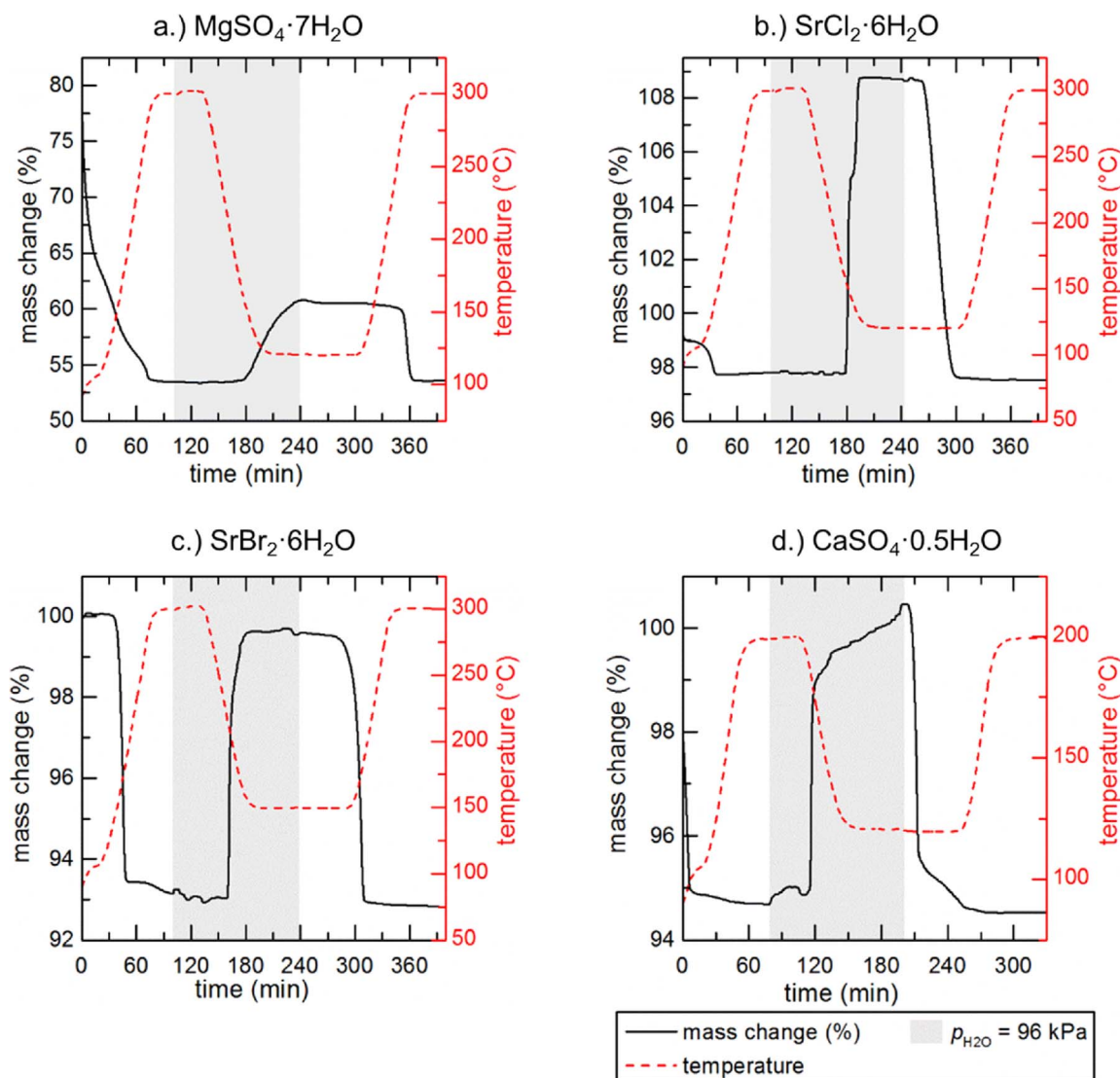


Fig. 4. Exemplary results: Experiment I with a.) $\text{MgSO}_4 \cdot 7\text{H}_2\text{O}$ and b.) $\text{SrCl}_2 \cdot 6\text{H}_2\text{O}$ (dehydrated before). Adapted experiment I with c.) $\text{SrBr}_2 \cdot 6\text{H}_2\text{O}$ (dehydrated before) and d.) $\text{CaSO}_4 \cdot 0.5\text{H}_2\text{O}$.

thermodynamic data is missing. If at least the enthalpy of reaction is available an estimation of the equilibrium temperature has been done assuming an entropy of reaction between $120 \text{ J mol}^{-1} \text{ K}^{-1}$ and $160 \text{ J mol}^{-1} \text{ K}^{-1}$. For the hydrates of K_2S e.g. no entropies of formation could be found. With the above given assumption the equilibrium temperature could be estimated between $73 \text{ }^\circ\text{C}$ and $188 \text{ }^\circ\text{C}$. As the reaction might take place in the relevant temperature range, this material is analyzed in the next step of the screening.

All materials that show suitable thermodynamics and those with unknown reaction equilibrium were investigated regarding their thermal stability based on literature data [22,33–43]. Side reactions (with air or water) or thermal decomposition in the relevant temperature range are reported for $\text{Al}(\text{NO}_3)_3$, BaBr_2 , BaI_2 , CaBr_2 , CaI_2 , $\text{Ce}(\text{NO}_3)_3$, $\text{Ce}(\text{CO}_3)_3$, CeBr_3 , CeCl_3 , CeF_4 , $\text{Cu}(\text{NO}_3)_2$, CuF_2 , FeBr_2 , FeCl_3 , FeF_2 , FeF_3 , FeI_2 , K_2S , LiI , $\text{Mg}(\text{NO}_3)_2$, MgCl_2 , $\text{Mn}(\text{NO}_3)_2$, MnI_2 , Na_2S , NaOH , $\text{Ti}(\text{SO}_4)_2$, TiBr_3 , TiCl_3 , TiF_4 , TiI_3 , VBr_2 , VBr_3 , VCl_2 , VCl_3 , VI_2 , VI_3 , VO_2 , VSO_4 , ZnCO_3 , ZnO_2 , $\text{Zr}(\text{NO}_3)_4$, ZrF_4 . The following materials were

excluded from further analysis due to deliquescence or melting in the relevant temperature range: CaBr_2 , CaCl_2 , CaI_2 , $\text{Ce}(\text{NO}_3)_3$, $\text{Fe}(\text{NO}_3)_2$, $\text{Fe}(\text{NO}_3)_3$, FeBr_2 , FeBr_3 , FeI_2 , K_2S , KOH , LiI , MgBr_2 , MgCl_2 , $\text{Mn}(\text{NO}_3)_2$, NaOH , TiBr_3 , TiCl_3 , VCl_2 , VCl_3 and $\text{Zn}(\text{NO}_3)_2$. VF_3 was excluded due to its toxicity. As hydrated TiO_2 , $\text{V}_2(\text{SO}_4)_3$, VF_2 and VPO_4 are not commercially available, no experimental analysis has been done with these materials.

4.2. Experimental analysis

4.2.1. Reversibility of reaction

Based on the theoretical analysis 32 materials were selected for the experimental tests. In the first experiment the reversibility of the reaction was analyzed. In Fig. 4a the typical temperature profile of experiment I is given. Segments with water containing atmosphere are marked with a grey area. The material was heated with 5 K min^{-1} to $300 \text{ }^\circ\text{C}$ in nitrogen atmosphere. Then, the purge gas was changed to

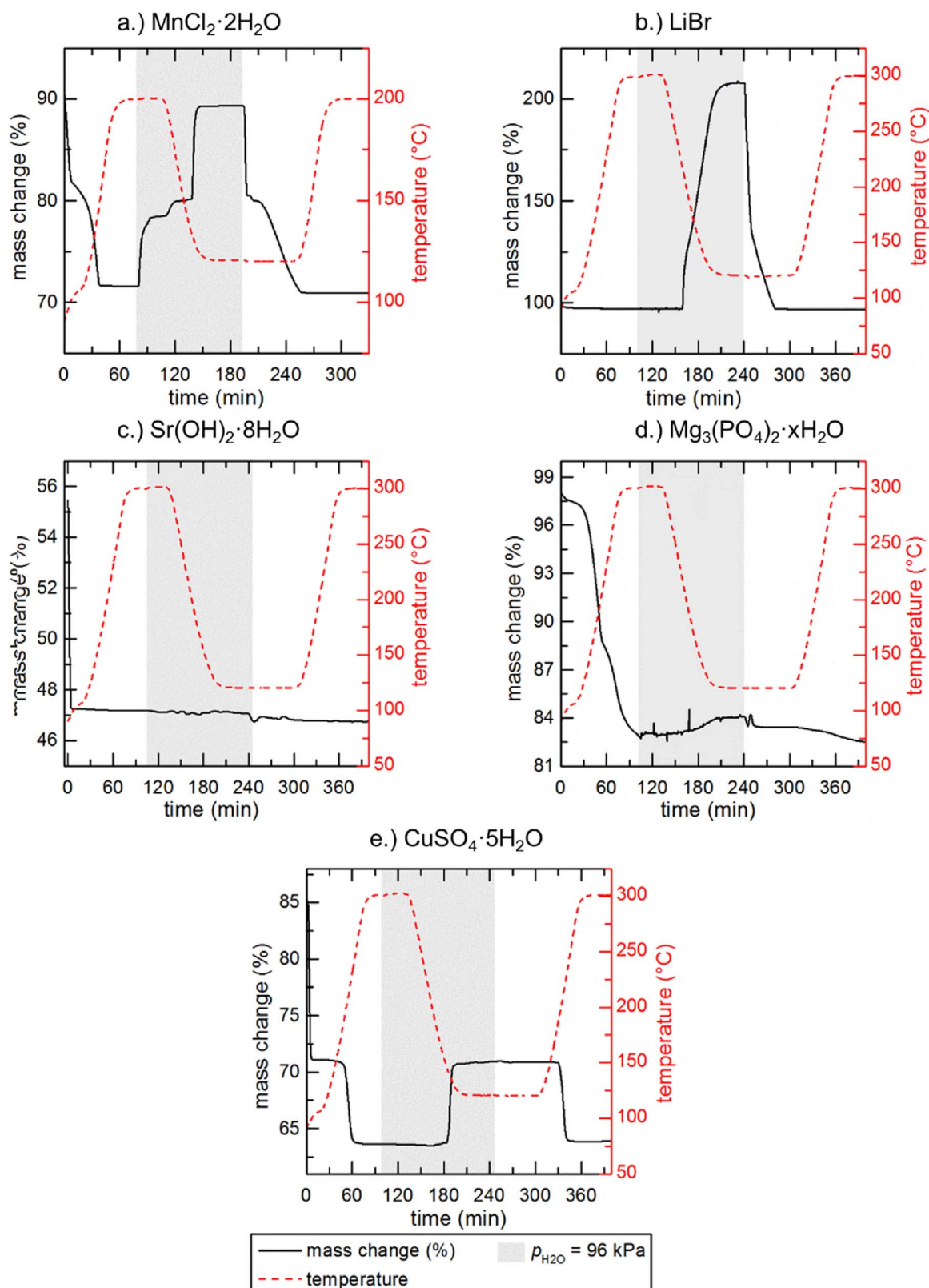


Fig. 5. Exemplary results for thermal decomposition, observed deliquescence, no or incomplete hydration and low hydration temperature: Adapted experiment I with a.) $\text{MnCl}_2 \cdot 2\text{H}_2\text{O}$, experiment I with b.) LiBr, c.) $\text{Sr}(\text{OH})_2 \cdot 8\text{H}_2\text{O}$, d.) $\text{Mg}_3(\text{PO}_4)_2 \cdot x\text{H}_2\text{O}$ and e.) $\text{CuSO}_4 \cdot 5\text{H}_2\text{O}$.

pure water vapor ($p_{\text{H}_2\text{O}} = 96 \text{ kPa}$) and cooling with -5 K min^{-1} to a minimum temperature of $120 \text{ }^\circ\text{C}$ was performed. In this segment rehydration was expected. After a 1 h isotherm the purge gas was changed back to nitrogen and a heating segment (5 K min^{-1} to $300 \text{ }^\circ\text{C}$) followed. In Fig. 4a the mass change from TG-signal of $\text{MgSO}_4 \cdot 7\text{H}_2\text{O}$ is

given. As the experiment started at approx. $100 \text{ }^\circ\text{C}$ the dehydration started before the measurement was initiated. Therefore, the mass dropped right at the beginning to about 75 % of the starting mass. After the first heating segment the mass changed to 53 % of the starting mass. This corresponds to the anhydrous MgSO_4 . During the cooling segment

rehydration with an onset temperature of 154 °C occurred. The mass difference indicates the formation of $\text{MgSO}_4 \cdot \text{H}_2\text{O}$. In the next heating segment this hydrate released its water at about 282 °C. From this data a reversible dehydration of $\text{MgSO}_4 \cdot \text{H}_2\text{O}$ in the relevant temperature range (150 °C–300 °C) can be derived.

$\text{SrCl}_2 \cdot 6\text{H}_2\text{O}$ melts at 61.3 °C [19]. To prevent a phase change, this material was pretreated by a slow heating to a temperature below the melting point and then further to 110 °C. Thus, the material had been dehydrated before experiment I was conducted. Fig. 4b shows the results from experiment I. A reversible hydration to $\text{SrCl}_2 \cdot \text{H}_2\text{O}$ can be observed. An onset temperature of 154 °C for the hydration was determined whereas the dehydration occurred in the isothermal segment at 120 °C. Thus, no onset temperature can be given for the dehydration reaction in nitrogen.

Similar to the chloride, strontium bromide forms a hexahydrate that melts at 88.6 °C [19]. Therefore, $\text{SrBr}_2 \cdot 6\text{H}_2\text{O}$ has been dehydrated in advance at a low heating rate below the melting point and stored at 110 °C. In this screening the reaction to the monohydrate is interesting. The theoretical equilibrium temperature of the further hydration reaction (to hexahydrate) at $p_{\text{H}_2\text{O}} = 96$ kPa is 130.85 °C. To prevent further reaction to hexahydrate and deliquescence of the material the minimum temperature for the hydration in experiment I was set to 150 °C. Thus, a reversible reaction from monohydrate to anhydrous SrBr_2 was expected. Fig. 4c shows the results of this adapted experiment I. The reaction occurred reversibly with an onset temperature of hydration of 213 °C. The dehydration in nitrogen obtained an onset temperature of 156 °C.

Regarding gypsum the reaction of the anhydrous CaSO_4 to the hemihydrate is interesting for this screening. As different anhydrous phases exist, the theoretical equilibrium of the reaction at $p_{\text{H}_2\text{O}} = 96$ kPa is in between 149 °C and 206 °C. Abriel et al. report a formation of a stable, less reactive phase of anhydrous CaSO_4 at 250 °C [62]. Therefore, experiment I has been adapted to a maximum temperature of 200 °C. Fig. 4d shows the reversible reaction of $\text{CaSO}_4 \cdot 0.5\text{H}_2\text{O}$. Assuming the anhydrous phase at the end of the experiment a maximum level of hydration of 0.47 was reached in this experiment with an onset temperature of 184 °C. Dehydration occurred instantly when the atmosphere was changed to nitrogen in the isothermal segment at 120 °C.

The materials presented in Fig. 4 showed a reversible hydration reaction in the relevant temperature range. Similar results could be observed from experiment I with $\text{MnBr}_2 \cdot \text{H}_2\text{O}$ and $\text{ZnSO}_4 \cdot \text{H}_2\text{O}$. For MnBr_2 a hydration at 184 °C to monohydrate was observed whereas the dehydration took place in the isothermal segment at 120 °C. ZnSO_4 was hydrated to the monohydrate at an onset temperature of 157 °C. Dehydration in nitrogen atmosphere occurred at 203 °C.

The materials that have been described so far meet the requirements for the reversibility of the reaction. In the following some experiments are described, that led finally to the exclusion of the materials in the present screening based on the above given methodology.

4.2.2. Thermal decomposition

Thermal decomposition of MnCl_2 in the presence of water to MnO and HCl is reported in the temperature range of 250 °C to 400 °C [63]. Therefore, 15 mg of $\text{MnCl}_2 \cdot 2\text{H}_2\text{O}$ were tested in experiment I with a maximum temperature of 200 °C. In the case of complete dehydration, a mass change to 77 % of the starting mass was expected. As can be seen in Fig. 5a the mass dropped to the lower value of 72 %. A rehydration took place but after the second dehydration an even higher mass loss to approx. 71 % occurred. Thus, the resulting mass loss is too high to be only explained by dehydration. After rehydration an even lower mass is reached. Consequently, even below 200 °C a decomposition of the material was observed.

A similar conclusion can be drawn from the experiment I with SrI_2 , $\text{Mn}_3(\text{PO}_4)_2$, FeSO_4 , $\text{Fe}_3(\text{PO}_4)_2$ and ZnCl_2 , (not shown here). SrI_2 was pretreated (dehydrated at low heating rate up to 110 °C) before experiment I. Oxidation (by traces of oxygen in the apparatus) was indicated by a change to brown color. $\text{Mn}_3(\text{PO}_4)_2$ showed a decrease of mass starting at about 158 °C. No hydration could be observed. On the one hand FeSO_4 indicated a reversible hydration to a level of hydration of 0.7. On the other hand thermal decomposition was indicated by a change of color of the sample from green (hydrate) to brown. For the anhydrous FeSO_4 a colorless sample is expected. Starting the experiment I with anhydrous $\text{Fe}_3(\text{PO}_4)_2$ and ZnCl_2 the mass of the samples decreased constantly. In the case of ZnCl_2 a rehydration took place, but the mass at the end of the experiment decreased to 82 % of the starting mass. Therefore, these materials have been excluded from further screening due to thermal decomposition.

4.2.3. Deliquescence or phase change

LiCl , LiBr , $\text{Zr}(\text{SO}_4)_2 \cdot 4\text{H}_2\text{O}$, $\text{Fe}_2(\text{SO}_4)_3 \cdot x\text{H}_2\text{O}$ showed deliquescence during experiment I. The (re)hydration took place within one step and instantly higher hydrates were formed. Exemplary the results for LiBr are shown in Fig. 5b. The reaction to monohydrate is interesting for the present screening. However, during cool down in water vapor atmosphere the mass increased to more than 200 % of the initial mass. This corresponds to a level of hydration of about 5.7. The material dissolved in its own crystal water. The powdery sample was one solid piece after the experiment.

4.2.4. No or incomplete hydration

Although dehydration was observed, many materials did not show rehydration in experiment I. In Fig. 5c the results for $\text{Sr}(\text{OH})_2 \cdot 8\text{H}_2\text{O}$ are given. The material dehydrated instantly when the sample was put in the STA. The mass loss to 47 % of the starting mass corresponds to the anhydrous $\text{Sr}(\text{OH})_2$. A rehydration could not be observed. Similar results were obtained from the experiments with Li_3PO_4 , $\text{CeO}_2 \cdot x\text{H}_2\text{O}$, WO_3 , $\text{Zn}_3(\text{PO}_4)_2 \cdot x\text{H}_2\text{O}$.

$\text{Mg}_3(\text{PO}_4)_2 \cdot x\text{H}_2\text{O}$ dehydrates in experiment I but the rehydration was very slow (see Fig. 5d). Thus, the reaction to monohydrate was incomplete and the maximum level of hydration reached in this experiment was 0.28. Similar results were obtained for $\text{Ce}_2(\text{SO}_4)_3 \cdot 8\text{H}_2\text{O}$, $\text{Ce}(\text{SO}_4)_2 \cdot x\text{H}_2\text{O}$, $\text{ZrO}_2 \cdot 2\text{H}_2\text{O}$ ($\text{Zr}(\text{OH})_4$), $2\text{Cu}_3(\text{PO}_4)_2$ and $\text{Al}_2\text{O}_3 \cdot \text{H}_2\text{O}$. Even though it is not absolutely sure that these materials are not suitable, the very slow reaction rate clearly hinders a later application. Consequently, these materials could be further analyzed according to above described methodology if an improved re-hydration rate can be realized. The aspect of potential material modifications was not included in this study.

4.2.5. Low hydration temperature

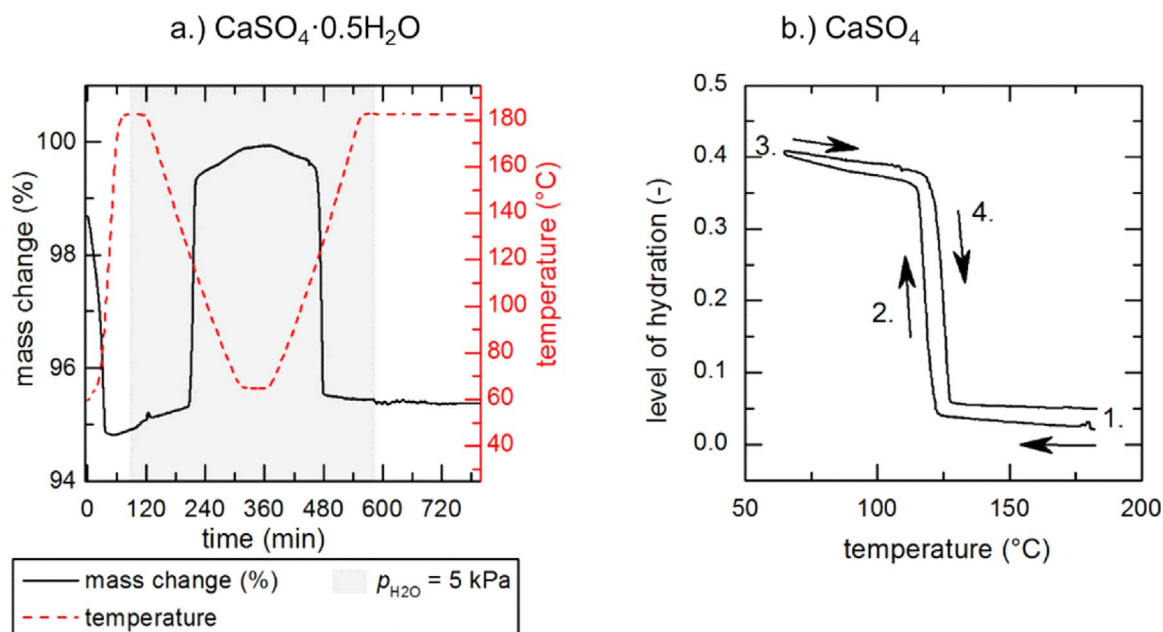
Although reversible reaction was observed some materials were excluded from further analysis due to low hydration temperature. CuSO_4 dehydrated and rehydrated reversibly in experiment I (see Fig. 5e). But the onset temperature for hydration was 142 °C and thus it is below the required temperature of 150 °C. Regarding other applications this material might be interesting but for the desired heat transformation higher reaction temperatures are required. Furthermore, the dehydration in nitrogen demands more than 196 °C, which indicates a big reaction hysteresis for that material.

The same conclusion can be drawn for the materials K_2CO_3 , $\text{MnSO}_4 \cdot \text{H}_2\text{O}$ and $\text{Al}_2(\text{SO}_4)_3 \cdot 18\text{H}_2\text{O}$ that also have been tested in experiment I (not shown here).

The results from experiment I are summarized in Table 3. Only materials that obtain a reversible reaction have been tested in the next step of the screening.

Table 3Results from experiment I (reversibility of reaction): Values marked with * are estimates using $\Delta_R S^\ominus \approx 120 \text{ J mol}^{-1} \text{ K}^{-1}$ to $160 \text{ J mol}^{-1} \text{ K}^{-1}$.

Reaction	$p_{\text{H}_2\text{O}} = 0 \text{ kPa } \vartheta_{\text{onset,D}}(^{\circ}\text{C})$	$p_{\text{H}_2\text{O}} = 96 \text{ kPa } \vartheta_{\text{onset,H}}(^{\circ}\text{C})$	$p_{\text{H}_2\text{O}} = 96 \text{ kPa } \vartheta_{\text{eq}}(^{\circ}\text{C})$	Observation in Exp. I
$\text{LiCl} \cdot \text{H}_2\text{O} \rightleftharpoons \text{LiCl} + \text{H}_2\text{O}$	n/a	162	153.56	deliquescence
$\text{LiBr} \cdot \text{H}_2\text{O} \rightleftharpoons \text{LiBr} + \text{H}_2\text{O}$	n/a	216	178.95	deliquescence
$2\text{Li}_3\text{PO}_4 \cdot 0.5\text{H}_2\text{O} \rightleftharpoons 2\text{Li}_3\text{PO}_4 + \text{H}_2\text{O}$	n/a	n/a	n/a	no hydration
$2\text{K}_2\text{CO}_3 \cdot 0.5\text{H}_2\text{O} \rightleftharpoons 2\text{K}_2\text{CO}_3 + \text{H}_2\text{O}$	n/a	134	251.06	low hydration temperature
$\text{MgSO}_4 \cdot \text{H}_2\text{O} \rightleftharpoons \text{MgSO}_4 + \text{H}_2\text{O}$	282	154	215.19	reversible reaction
$1/5\text{Mg}_3(\text{PO}_4)_2 \cdot 5\text{H}_2\text{O} \rightleftharpoons 1/5\text{Mg}_3(\text{PO}_4)_2 + \text{H}_2\text{O}$	n/a	n/a	n/a	incomplete hydration
$2\text{CaSO}_4 \cdot 0.5\text{H}_2\text{O} \rightleftharpoons 2\text{CaSO}_4 + \text{H}_2\text{O}$	n/a	184	149–206	reversible reaction
$\text{SrCl}_2 \cdot \text{H}_2\text{O} \rightleftharpoons \text{SrCl}_2 + \text{H}_2\text{O}$	n/a	154	227.42	reversible reaction
$\text{SrBr}_2 \cdot \text{H}_2\text{O} \rightleftharpoons \text{SrBr}_2 + \text{H}_2\text{O}$	156	213	225.81	reversible reaction
$\text{SrI}_2 \cdot \text{H}_2\text{O} \rightleftharpoons \text{SrI}_2 + \text{H}_2\text{O}$	n/a	n/a	267–447*	thermal decomposition
$\text{Sr}(\text{OH})_2 \cdot \text{H}_2\text{O} \rightleftharpoons \text{Sr}(\text{OH})_2 + \text{H}_2\text{O}$	n/a	n/a	126–259*	no hydration
$1/2\text{CeO}_2 \cdot 2\text{H}_2\text{O} \rightleftharpoons 1/2\text{CeO}_2 + \text{H}_2\text{O}$	n/a	n/a	n/a	no hydration
$1/x\text{Ce}_2(\text{SO}_4)_3 \cdot x\text{H}_2\text{O} \rightleftharpoons 1/x\text{Ce}_2(\text{SO}_4)_3 + \text{H}_2\text{O}$	n/a	n/a	n/a	incomplete hydration
$1/2\text{Ce}(\text{SO}_4)_2 \cdot 2\text{H}_2\text{O} \rightleftharpoons 1/2\text{Ce}(\text{SO}_4)_2 + \text{H}_2\text{O}$	161	129	145–284*	incomplete hydration
$1/2\text{ZrO}_2 \cdot 2\text{H}_2\text{O} \rightleftharpoons 1/2\text{ZrO}_2 + \text{H}_2\text{O}$	n/a	n/a	186.69	incomplete hydration
$\text{Zr}(\text{SO}_4)_2 \cdot \text{H}_2\text{O} \rightleftharpoons \text{Zr}(\text{SO}_4)_2 + \text{H}_2\text{O}$	120	147	155–297*	deliquescence
$\text{WO}_3 \cdot \text{H}_2\text{O} \rightleftharpoons \text{WO}_3 + \text{H}_2\text{O}$	n/a	n/a	316.29	no hydration
$\text{MnCl}_2 \cdot \text{H}_2\text{O} \rightleftharpoons \text{MnCl}_2 + \text{H}_2\text{O}$	n/a	n/a	227.90	thermal decomposition
$\text{MnBr}_2 \cdot \text{H}_2\text{O} \rightleftharpoons \text{MnBr}_2 + \text{H}_2\text{O}$	n/a	184	215–377*	reversible reaction
$\text{MnSO}_4 \cdot \text{H}_2\text{O} \rightleftharpoons \text{MnSO}_4 + \text{H}_2\text{O}$	190	130	200.93	low hydration temperature
$1/3\text{Mn}_3(\text{PO}_4)_2 \cdot 3\text{H}_2\text{O} \rightleftharpoons 1/3\text{Mn}_3(\text{PO}_4)_2 + \text{H}_2\text{O}$	n/a	n/a	95–217*	thermal decomposition
$\text{FeSO}_4 \cdot \text{H}_2\text{O} \rightleftharpoons \text{FeSO}_4 + \text{H}_2\text{O}$	200	153	208.99	thermal decomposition
$1/2\text{Fe}_3(\text{PO}_4)_2 \cdot 2\text{H}_2\text{O} \rightleftharpoons 1/2\text{Fe}_3(\text{PO}_4)_2 + \text{H}_2\text{O}$	n/a	n/a	n/a	thermal decomposition
$1/x\text{Fe}_2(\text{SO}_4)_3 \cdot x\text{H}_2\text{O} \rightleftharpoons 1/x\text{Fe}_2(\text{SO}_4)_3 + \text{H}_2\text{O}$	121	126	n/a	deliquescence
$\text{CuSO}_4 \cdot \text{H}_2\text{O} \rightleftharpoons \text{CuSO}_4 + \text{H}_2\text{O}$	196	142	204.31	low hydration temperature
$1/2\text{Cu}_3(\text{PO}_4)_2 \cdot 2\text{H}_2\text{O} \rightleftharpoons 1/2\text{Cu}_3(\text{PO}_4)_2 + \text{H}_2\text{O}$	n/a	n/a	123–255*	incomplete hydration
$1/x\text{ZnCl}_2 \cdot x\text{H}_2\text{O} \rightleftharpoons 1/x\text{ZnCl}_2 + \text{H}_2\text{O}$	n/a	n/a	n/a	thermal decomposition
$\text{ZnSO}_4 \cdot \text{H}_2\text{O} \rightleftharpoons \text{ZnSO}_4 + \text{H}_2\text{O}$	203	157	239.70	reversible reaction
$\text{Zn}_3(\text{PO}_4)_2 \cdot \text{H}_2\text{O} \rightleftharpoons \text{Zn}_3(\text{PO}_4)_2 + \text{H}_2\text{O}$	n/a	n/a	184–336*	no hydration
$\text{Al}_2\text{O}_3 \cdot \text{H}_2\text{O} \rightleftharpoons \text{Al}_2\text{O}_3 + \text{H}_2\text{O}$	n/a	n/a	168–207	incomplete hydration
$1/6\text{Al}_2(\text{SO}_4)_3 \cdot 6\text{H}_2\text{O} \rightleftharpoons 1/6\text{Al}_2(\text{SO}_4)_3 + \text{H}_2\text{O}$	n/a	140	190.75	low hydration temperature
$1/2\text{AlPO}_4 \cdot 2\text{H}_2\text{O} \rightleftharpoons 1/2\text{AlPO}_4 + \text{H}_2\text{O}$	n/a	n/a	180.03	no hydration

**Fig. 6.** a.) Experiment II with $\text{CaSO}_4 \cdot 0.5\text{H}_2\text{O}$ and b.) Hysteresis plot of the reversible hydration of CaSO_4 .

4.2.6. Reaction hysteresis

The hysteresis of the reaction was analyzed in experiment II. Here, the material was heated to $185 \text{ }^{\circ}\text{C}$ and cooled down to $65 \text{ }^{\circ}\text{C}$. The cool-down took place with -1 K min^{-1} at a partial vapor pressure of 5 kPa . These conditions were chosen in order to determine the dehydration temperature in a humid atmosphere such as charging the thermal storage with humid air in summer. Furthermore, the sample was heated

with 1 K min^{-1} to $185 \text{ }^{\circ}\text{C}$ in humid atmosphere so the difference between hydration and dehydration could be analyzed. **Fig. 6** shows the results of this experiment with $\text{CaSO}_4 \cdot 0.5\text{H}_2\text{O}$ where an almost complete reaction was reached. The reaction hysteresis can be seen in a clearer way, if the level of hydration is plotted versus the temperature for the segments of the experiments with water containing atmosphere (grey area). **Fig. 6b** shows this graph. Starting with anhydrous CaSO_4

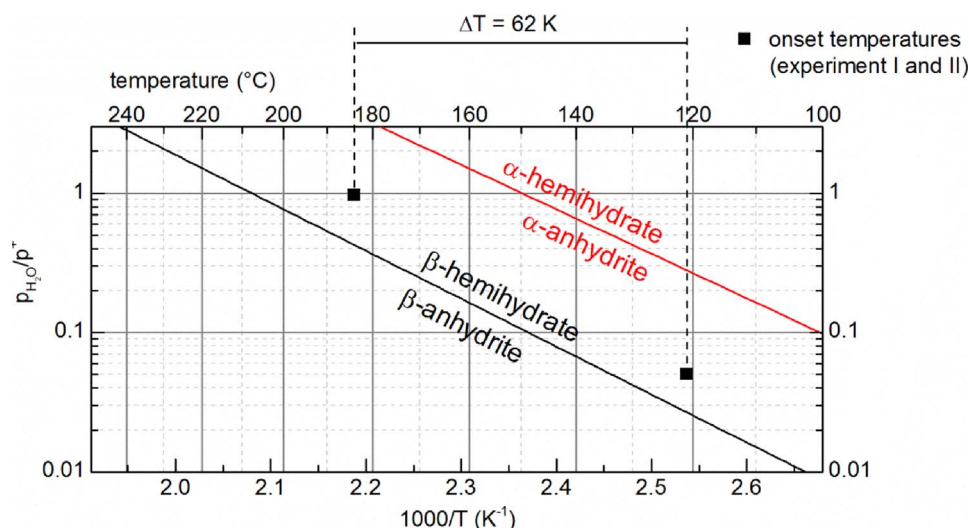


Fig. 7. Van't Hoff Diagram of the hydration reaction of CaSO_4 .

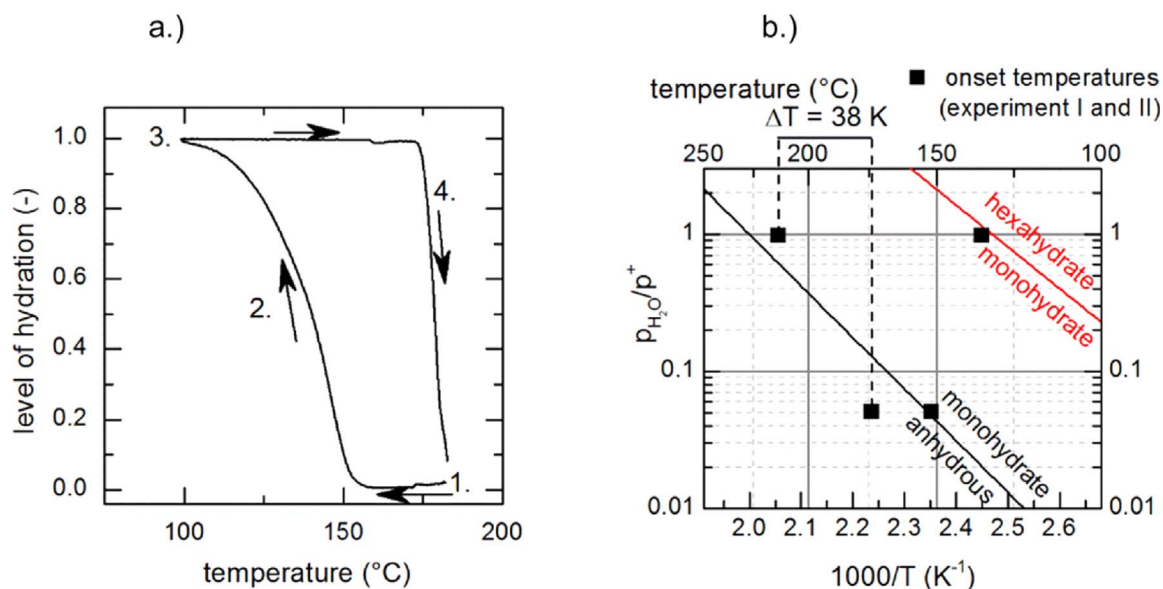


Fig. 8. a.) Hysteresis of reversible hydration of SrBr_2 from experiment II and b.) Van't Hoff Diagram of the hydration reaction of SrBr_2 .

(1.) the level of hydration stayed approx. constant when the temperature decreased. At 121 °C hydration started and a level of hydration of about 0.4 was reached (3.). In the heating segment the hydrate was stable up to 122 °C where dehydration took place (4.). At the end of the experiment the anhydrous phase was obtained. This reaction showed a very small hysteresis as the temperature for hydration and dehydration only differed by around 1 K.

The results of the onset temperatures are summarized in the van't Hoff diagram in Fig. 7. For the dehydration at a partial vapor pressure of 5 kPa the onset temperature of 122 °C has been determined. The hydration at 96 kPa could be conducted at 184 °C (in experiment I). Therefore, at these boundary conditions the material could perform a thermal upgrade of 62 K.

The hysteresis of the hydration reaction of SrBr_2 from experiment II is shown in Fig. 8a. In comparison to CaSO_4 a bigger hysteresis was observed. Hydration reaction started at 152 °C whereas the dehydration required at least 174 °C. Summarized in the van't Hoff plot in Fig. 8b a thermal upgrade between dehydration and rehydration of 38 K would be possible (dashed lines).

The other materials tested in experiment II showed a bigger hysteresis. MnBr_2 , e.g., obtained a two-step hydration reaction that clearly limits thermal upgrade. Fig. 9a shows the hysteresis of the hydration reaction. The anhydrous MnBr_2 (1.) hydrated at 114 °C to the monohydrate. The second step started at 76 °C and the dihydrate was formed (3.). The dehydration obtained the same intermediate step with clearly shifted temperatures to 96 °C and 140 °C, respectively. Fig. 9b shows the onset temperatures plotted in the Van't Hoff diagram. The dehydration of the monohydrate at $p_{\text{H}_2\text{O}} = 5$ kPa requires a minimum temperature of 140 °C. According to experiment I, the formation of the dihydrate at a partial vapor pressure of 96 kPa starts below 141 °C. This is indicated by the dashed line in Fig. 9b. Therefore, no thermal upgrade can be performed if both reaction steps are used. Since the reaction temperatures are clearly below the temperature limits for the intended application, this material was excluded from further analysis.

All onset temperatures determined in experiment II are summarized in Table 4. MgSO_4 showed no hydration in this experiment. This indicates that the hysteresis is very big or the reaction is very slow at low temperatures and partial vapor pressures. SrCl_2 obtained an

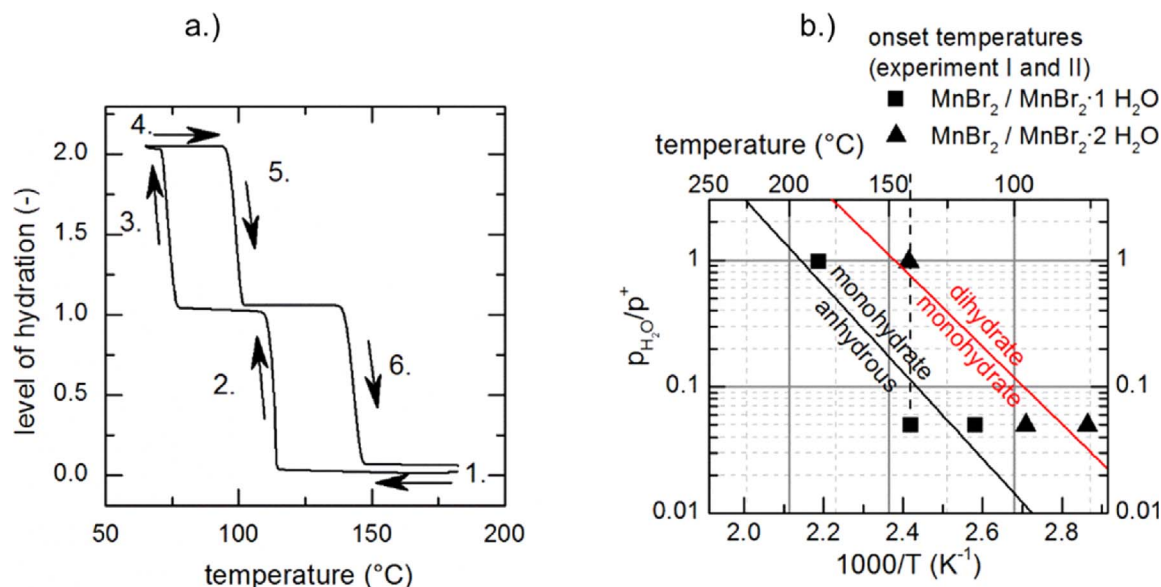


Fig. 9. a.) Hysteresis of reversible hydration of MnBr₂ and b.) Van't Hoff Diagram of the hydration reaction of MnBr₂.

intermediate step during dehydration reaction at $h = 0.66$. Therefore, two onset temperatures are given for the dehydration reaction. For the dehydration at $p_{H_2O} = 5$ kPa (see Table 4) and the rehydration at $p_{H_2O} = 96$ kPa (see Table 3) the same temperature of 154 °C has been determined. Therefore, no thermal upgrade is possible with this material unless a higher pressure difference is given. ZnSO₄ hydrated in pure water vapor at ambient pressure at 157 °C (see Table 3). For a dehydration in $p_{H_2O} = 5$ kPa at least the same temperature is necessary. Therefore, this material is also not suitable for the application addressed in this screening.

Table 4

Results from experiment II (reaction hysteresis); # indicates that two different phases have been considered (α , β). Values marked with * are estimates using $\Delta_R S^0 \approx 120$ J mol⁻¹ K⁻¹ to 160 J mol⁻¹ K⁻¹.

Reaction	$p_{H_2O} = 5$ kPa $\vartheta_{onset,D}$ (°C)	$p_{H_2O} = 5$ kPa $\vartheta_{onset,H}$ (°C)	$p_{H_2O} = 5$ kPa ϑ_{eq} (°C)
MgSO ₄ ·H ₂ O ⇌ MgSO ₄ + H ₂ O	n/a	n/a	148.14
2CaSO ₄ ·0.5H ₂ O ⇌ 2CaSO ₄ + H ₂ O	122	121	88; 134 [#]
SrCl ₂ ·H ₂ O ⇌ SrCl ₂ + H ₂ O	127; 154	89	148.88
SrBr ₂ ·H ₂ O ⇌ SrBr ₂ + H ₂ O	174	152	153.20
MnBr ₂ ·H ₂ O ⇌ MnBr ₂ + H ₂ O	140	114	150–267*
MnBr ₂ ·2H ₂ O ⇌ MnBr ₂ ·H ₂ O + H ₂ O	96	76	n/a
ZnSO ₄ ·H ₂ O ⇌ ZnSO ₄ + H ₂ O	203	157	171.86

4.2.7. Cycling stability

The materials SrBr₂ and CaSO₄ obtain appropriate temperature levels for the reversible hydration reaction and a small reaction hysteresis that enables heat transformation. In the next step of the screening the materials were analyzed regarding the cycling stability over 10 hydration and dehydration cycles. These were performed isothermally at temperatures of at least 20 K below the respective hydration temperatures at $p_{H_2O} = 96$ kPa. In experiment III hydration has been performed in water vapor atmosphere, dehydration in dry nitrogen.

As can be seen in Fig. 10a the level of hydration of CaSO₄ decreased over 10 cycles. From XRD-analysis (not shown here) this decrease can

be connected with the formation of a less reactive AII-phase of the anhydrous CaSO₄ [62].

The hydration reaction of SrBr₂ was stable over 10 cycles Fig. 10b. After each hydration and dehydration the same mass difference was achieved in thermal analysis. The time for each hydration was constant so no kinetically relevant change of the material could be observed. Dehydration accelerated slightly after each cycle (from approx. 70 min to 60 min).

5. Conclusions

From a systematic screening of 308 salts SrBr₂ meets all requirements for a thermochemical heat transformer. The gravimetric and volumetric storage density for an open SrBr₂/H₂O system are 73 kWh t⁻¹ and 140 kWh m⁻³, respectively, assuming the formation of a monohydrate and a bulk density of 1.9 g cm⁻³. As the addressed application of this material is not only thermal storage but heat transformation, other criteria are more important: SrBr₂ is not toxic and forms a monohydrate with appropriate thermodynamics to thermally upgrade heat from 174 °C to 213 °C in an open process mode. The reaction is fully reversible with an acceptable reaction hysteresis, i.e. a ΔT of 22 K between hydration and dehydration at the same partial vapor pressure (5 kPa). Furthermore, the reaction is stable over 10 cycles.

Other materials analyzed in this screening showed also very promising results and might be interesting for other applications. The strong focus on hydration temperatures above 150 °C in water vapor at ambient pressure resulted in an exclusion of many salt hydrates that may perform very well at lower temperatures. Focusing on commercially available materials, some salts were not analyzed experimentally. A synthesis of the right phases may increase the amount of suitable materials. The calculated thermodynamic data of all materials is summarized in the Appendix A (Table A1), giving a good starting point for other screenings.

The large amount of comparable experimental data is a good basis for further thermodynamic and kinetic investigation of these materials, especially because many of them are already used or foreseen in thermochemical storage or chemical heat pumps.

From the obtained data further development of the thermochemical reaction materials should follow. Some limitations, e.g. slow reaction kinetics, can be overcome by material development. The collected data summarizes materials with similar effects. Reaction kinetics and especially big reaction hysteresis lead to an exclusion of many salts.

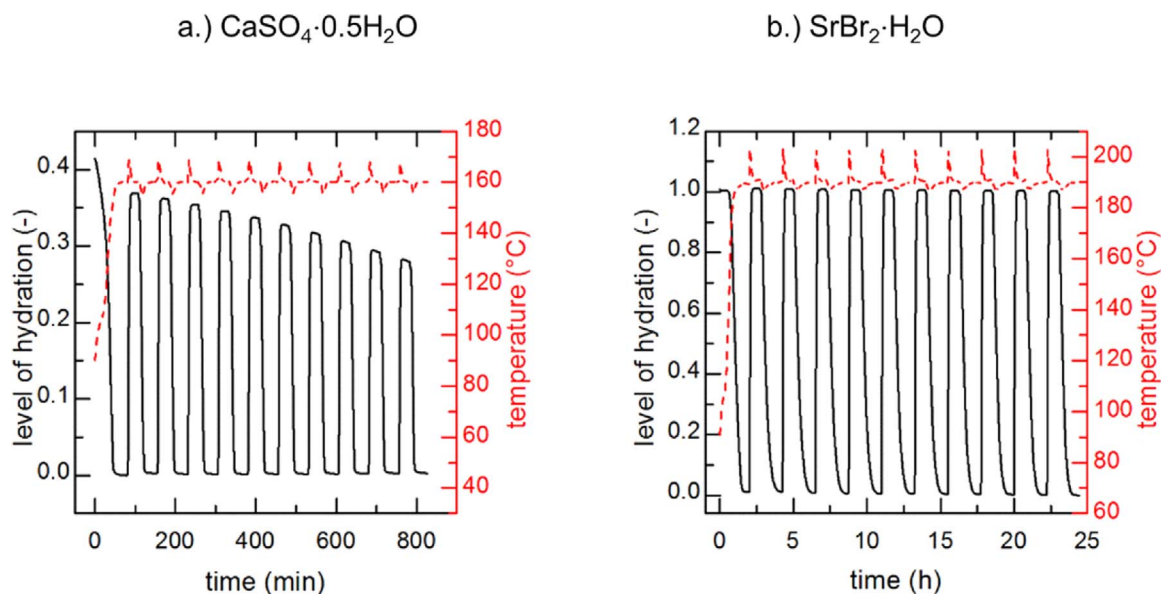


Fig. 10. Experiment III with a.) $\text{CaSO}_4 \cdot 0.5\text{H}_2\text{O}$ and b.) $\text{SrBr}_2 \cdot \text{H}_2\text{O}$.

Therefore, development of new materials or material improvements could focus on these points.

Furthermore, the here suggested methodology can be adapted and

applied to other screenings as it is a straightforward approach to systematically screen a large amount of materials.

Appendix A

Table A1

Results from thermodynamic calculation: Only the relevant hydration steps are indicated, i.e. either the lowest or the one matching with the relevant temperature range. Values marked with * are estimated using $\Delta_{\text{R}}S^{\ominus} \approx 120 \text{ J mol}^{-1} \text{ K}^{-1}$ to $160 \text{ J mol}^{-1} \text{ K}^{-1}$ [42,45,52,60,64–67].

Reaction	$\Delta_{\text{R}}H^{\ominus}$ (kJ mol ⁻¹)	$\Delta_{\text{R}}S^{\ominus}$ (J mol ⁻¹ K ⁻¹)	ϑ_{eq} (96 kPa) (°C)
Li			
$\text{LiCl} \cdot \text{H}_2\text{O} \rightleftharpoons \text{LiCl} + \text{H}_2\text{O}$	62.15	145.32	153.56
$\text{LiBr} \cdot \text{H}_2\text{O} \rightleftharpoons \text{LiBr} + \text{H}_2\text{O}$	69.55	153.50	178.95
$\text{LiI} \cdot \text{H}_2\text{O} \rightleftharpoons \text{LiI} + \text{H}_2\text{O}$	78.09	152.61	237.44
$\text{LiOH} \cdot \text{H}_2\text{O} \rightleftharpoons \text{LiOH} + \text{H}_2\text{O}$	61.26	160.42	107.94
$\text{Li}_2\text{SO}_4 \cdot \text{H}_2\text{O} \rightleftharpoons \text{Li}_2\text{SO}_4 + \text{H}_2\text{O}$	57.19	140.33	133.43
$\text{LiNO}_2 \cdot \text{H}_2\text{O} \rightleftharpoons \text{LiNO}_2 + \text{H}_2\text{O}$	61.88	163.83	103.80
Na			
$1/2\text{NaBr} \cdot 2\text{H}_2\text{O} \rightleftharpoons 1/2\text{NaBr} + \text{H}_2\text{O}$	53.62	142.69	101.76
$1/2\text{NaI} \cdot 2\text{H}_2\text{O} \rightleftharpoons 1/2\text{NaI} + \text{H}_2\text{O}$	55.84	139.99	124.77
$1/2\text{Na}_2\text{S} \cdot 2\text{H}_2\text{O} \rightleftharpoons 1/2\text{Na}_2\text{S} + \text{H}_2\text{O}$	74.00	177.00	144.13
$\text{NaOH} \cdot \text{H}_2\text{O} \rightleftharpoons \text{NaOH} + \text{H}_2\text{O}$	67.12	153.78	162.33
$1/7\text{Na}_2\text{SO}_4 \cdot 7\text{H}_2\text{O} \rightleftharpoons 1/7\text{Na}_2\text{SO}_4 + \text{H}_2\text{O}$	53.86	151.38	81.82
$1/12\text{Na}_3\text{PO}_4 \cdot 12\text{H}_2\text{O} \rightleftharpoons 1/12\text{Na}_3\text{PO}_4 + \text{H}_2\text{O}$	55.13	148.22	97.93
$\text{Na}_2\text{CO}_3 \cdot \text{H}_2\text{O} \rightleftharpoons \text{Na}_2\text{CO}_3 + \text{H}_2\text{O}$	58.76	155.70	103.45
K			
$1/2\text{KF} \cdot 2\text{H}_2\text{O} \rightleftharpoons 1/2\text{KF} + \text{H}_2\text{O}$	56.36	144.51	115.93
$1/2 \text{K}_2\text{S} \cdot 2\text{H}_2\text{O} \rightleftharpoons 1/2 \text{K}_2\text{S} + \text{H}_2\text{O}$	55.48		73–188*
$\text{KOH} \cdot \text{H}_2\text{O} \rightleftharpoons \text{KOH} + \text{H}_2\text{O}$	82.32	150.53	272.49
$1/7 \text{K}_3\text{PO}_4 \cdot 7\text{H}_2\text{O} \rightleftharpoons 1/7 \text{K}_3\text{PO}_4 + \text{H}_2\text{O}$	49.92	147.95	63.48
$2 \text{K}_2\text{CO}_3 \cdot 0.5\text{H}_2\text{O} \rightleftharpoons 2 \text{K}_2\text{CO}_3 + \text{H}_2\text{O}$	82.36	156.78	251.06
Mg			
$1/2\text{MgCl}_2 \cdot 4\text{H}_2\text{O} \rightleftharpoons 1/2\text{MgCl}_2 \cdot 2\text{H}_2\text{O} + \text{H}_2\text{O}$	67.82	146.78	187.83
$\text{MgCl}_2 \cdot 2\text{H}_2\text{O} \rightleftharpoons \text{MgCl}_2 \cdot \text{H}_2\text{O} + \text{H}_2\text{O}$	71.27	146.13	213.47
$1/6\text{MgBr}_2 \cdot 6\text{H}_2\text{O} \rightleftharpoons 1/6\text{MgBr}_2 + \text{H}_2\text{O}$	72.47	142.19	235.27
$\text{MgSO}_4 \cdot \text{H}_2\text{O} \rightleftharpoons \text{MgSO}_4 + \text{H}_2\text{O}$	75.38	154.03	215.19
$1/2\text{Mg}(\text{NO}_3)_2 \cdot 2\text{H}_2\text{O} \rightleftharpoons 1/2\text{Mg}(\text{NO}_3)_2 + \text{H}_2\text{O}$	67.46	145.31	190.01
$1/3\text{MgCO}_3 \cdot 3\text{H}_2\text{O} \rightleftharpoons 1/3\text{MgCO}_3 + \text{H}_2\text{O}$	52.00	145.51	83.39
Ca			
$\text{CaCl}_2 \cdot \text{H}_2\text{O} \rightleftharpoons \text{CaCl}_2 + \text{H}_2\text{O}$	73.36	136.53	262.87
$1/6\text{CaBr}_2 \cdot 6\text{H}_2\text{O} \rightleftharpoons 1/6\text{CaBr}_2 + \text{H}_2\text{O}$	62.08	142.16	162.52
$1/8\text{CaI}_2 \cdot 8\text{H}_2\text{O} \rightleftharpoons 1/8\text{CaI}_2 + \text{H}_2\text{O}$	57.69		87–206*
$2\text{CaSO}_4 \cdot 0.5\text{H}_2\text{O} \rightleftharpoons 2\text{CaSO}_4 + \text{H}_2\text{O}$ (α)	61.18	144.63	148.87
$2\text{CaSO}_4 \cdot 0.5\text{H}_2\text{O} \rightleftharpoons 2\text{CaSO}_4 + \text{H}_2\text{O}$ (β)	65.88	137.03	206.43
$1/2\text{Ca}(\text{NO}_3)_2 \cdot 2\text{H}_2\text{O} \rightleftharpoons 1/2\text{Ca}(\text{NO}_3)_2 + \text{H}_2\text{O}$	59.37	150.78	119.71

(continued on next page)

Table A1 (continued)

Reaction	$\Delta_R H^\ominus$ (kJ mol ⁻¹)	$\Delta_R S^\ominus$ (J mol ⁻¹ K ⁻¹)	ϑ_{eq} (96 kPa) (°C)
Sr			
SrCl ₂ ·H ₂ O ⇌ SrCl ₂ + H ₂ O	66.08	131.68	227.42
1/5SrBr ₂ ·6H ₂ O ⇌ 1/5SrBr ₂ ·H ₂ O + H ₂ O	58.16	143.63	130.85
SrBr ₂ ·H ₂ O ⇌ SrBr ₂ + H ₂ O	71.98	143.93	225.81
SrI ₂ ·H ₂ O ⇌ SrI ₂ + H ₂ O	86.68		267–447*
Sr(OH) ₂ ·H ₂ O ⇌ Sr(OH) ₂ + H ₂ O	63.98		126–259*
1/4Sr(NO ₃) ₂ ·4H ₂ O ⇌ 1/4Sr(NO ₃) ₂ + H ₂ O	52.33	145.21	86.35
Ba			
BaCl ₂ ·H ₂ O ⇌ BaCl ₂ + H ₂ O	60.18	145.61	139.21
BaBr ₂ ·H ₂ O ⇌ BaBr ₂ + H ₂ O	69.08	146.55	197.17
BaI ₂ ·H ₂ O ⇌ BaI ₂ + H ₂ O	75.28	148.95	231.11
Ba(OH) ₂ ·H ₂ O ⇌ Ba(OH) ₂ + H ₂ O	61.98	152.76	131.71
Ce			
CeF ₃ ·H ₂ O ⇌ CeF ₃ + H ₂ O	45.77		12–107
1/7CeCl ₃ ·7H ₂ O ⇌ 1/7CeCl ₃ + H ₂ O	61.02	150.02	132.70
1/2Ce(SO ₄) ₂ ·2H ₂ O ⇌ 1/2Ce(SO ₄) ₂ + H ₂ O	67.05		145–284*
1/3Ce(NO ₃) ₃ ·3H ₂ O ⇌ 1/3Ce(NO ₃) ₃ + H ₂ O	69.22		159–302*
1/2CePO ₄ ·2H ₂ O ⇌ 1/2CePO ₄ + H ₂ O	50.53	151.27	60.15
Zr			
ZrF ₄ ·H ₂ O ⇌ ZrF ₄ + H ₂ O	76.18	144.06	254.45
1/2ZrO ₂ ·2H ₂ O ⇌ 1/2 ZrO ₂ + H ₂ O	68.68	149.02	186.69
Zr(SO ₄) ₂ ·H ₂ O ⇌ Zr(SO ₄) ₂ + H ₂ O	68.65		155–297*
V			
V ₂ O ₅ ·H ₂ O ⇌ V ₂ O ₅ + H ₂ O	52.18	147.33	80.23
W			
WO ₃ ·H ₂ O ⇌ WO ₃ + H ₂ O	87.27	147.72	316.29
Mn			
1/4MnF ₂ ·4H ₂ O ⇌ 1/4MnF ₂ + H ₂ O	50.25	146.73	68.55
MnCl ₂ ·H ₂ O ⇌ MnCl ₂ + H ₂ O	66.79	132.97	227.90
MnBr ₂ ·H ₂ O ⇌ MnBr ₂ + H ₂ O	78.28		215–377*
1/2MnI ₂ ·2H ₂ O ⇌ 1/2MnI ₂ + H ₂ O	58.28		89–210*
1/6Mn(NO ₃) ₂ ·6H ₂ O ⇌ 1/6Mn(NO ₃) ₂ + H ₂ O	57.46		85–204*
MnSO ₄ ·H ₂ O ⇌ MnSO ₄ + H ₂ O	69.43	146.12	200.93
1/3Mn ₃ (PO ₄) ₂ ·3H ₂ O ⇌ 1/3Mn ₃ (PO ₄) ₂ + H ₂ O	59.01		95–217*
Fe			
1/2FeCl ₂ ·2H ₂ O ⇌ 1/2FeCl ₂ + H ₂ O	63.84	165.30	112.24
1/6FeCl ₃ ·6H ₂ O ⇌ 1/6FeCl ₃ + H ₂ O	62.23	153.81	130.56
Fe ₂ O ₃ ·H ₂ O ⇌ Fe ₂ O ₃ + H ₂ O	51.36	157.40	52.48
FeSO ₄ ·H ₂ O ⇌ FeSO ₄ + H ₂ O	73.47	152.05	208.99
1/2FePO ₄ ·2H ₂ O ⇌ 1/2FePO ₄ + H ₂ O	53.78	150.06	84.46
Cu			
1/2CuF ₂ ·2H ₂ O ⇌ 1/2CuF ₂ + H ₂ O	71.33	151.99	195.11
1/2CuCl ₂ ·2H ₂ O ⇌ 1/2CuCl ₂ + H ₂ O	58.78	159.36	94.93
1/4CuBr ₂ ·4H ₂ O ⇌ 1/4CuBr ₂ + H ₂ O	54.31	147.90	93.21
CuSO ₄ ·H ₂ O ⇌ CuSO ₄ + H ₂ O	72.65	151.83	204.31
1/3Cu(NO ₃) ₂ ·3H ₂ O ⇌ 1/3Cu(NO ₃) ₂ + H ₂ O	62.92		119–250*
1/2Cu ₃ (PO ₄) ₂ ·2H ₂ O ⇌ 1/2Cu ₃ (PO ₄) ₂ + H ₂ O	63.58		123–255*
Zn			
1/4ZnF ₂ ·4H ₂ O ⇌ 1/4ZnF ₂ + H ₂ O	55.71	151.12	94.67
1/2ZnBr ₂ ·2H ₂ O ⇌ 1/2ZnBr ₂ + H ₂ O	62.29	158.70	118.51
ZnSO ₄ ·H ₂ O ⇌ ZnSO ₄ + H ₂ O	82.65	160.83	239.70
1/2Zn(NO ₃) ₂ ·4H ₂ O ⇌ 1/2Zn(NO ₃) ₂ ·2H ₂ O + H ₂ O	52.61	110.78	200.30
Zn ₃ (PO ₄) ₂ ·H ₂ O ⇌ Zn ₃ (PO ₄) ₂ + H ₂ O	73.28		184–336*
Al			
1/6AlCl ₃ ·6H ₂ O ⇌ 1/6AlCl ₃ + H ₂ O	89.42	154.27	305.18
Al ₂ O ₃ ·H ₂ O ⇌ Al ₂ O ₃ + H ₂ O (boehmite, corundum)	63.18	142.89	167.96
Al ₂ O ₃ ·H ₂ O ⇌ Al ₂ O ₃ + H ₂ O (diaspore, corundum)	81.39	169.08	207.26
1/6Al ₂ (SO ₄) ₃ ·6H ₂ O ⇌ 1/6Al ₂ (SO ₄) ₃ + H ₂ O	69.99	150.54	190.75
1/6Al(NO ₃) ₃ ·6H ₂ O ⇌ 1/6Al(NO ₃) ₃ + H ₂ O	40.76	169.08	207.28
1/2AlPO ₄ ·2H ₂ O ⇌ 1/2AlPO ₄ + H ₂ O	67.91	149.50	180.03

References

- [1] Eckhard Rebhan, *Energiehandbuch: Gewinnung, Wandlung und Nutzung von Energie* [in German], Springer, 2002.
- [2] A. Sharma, V.V. Tyagi, C.R. Chen, D. Buddhi, Review on thermal energy storage with phase change materials and applications, *Renew. Sustain. Energy Rev.* 13 (2009) 318–345.
- [3] M.M. Farid, A.M. Khudhair, S.A. Razack, S. Al-Hallaj, A review on phase change energy storage: materials and applications, *Energy Convers. Manag.* 45 (2004) 1597–1615.
- [4] J. Cot-Gores, A. Castell, L.F. Cabeza, Thermochemical energy storage and conversion: a state-of-the-art review of the experimental research under practical conditions, *Renew. Sustain. Energy Rev.* 16 (2012) 5207–5224.
- [5] K. Bakken, System Trepidus, high capacity thermochemical storage/heat pump, *Int. Conf. Energy Storage*, Brighton, UK, 1981.
- [6] A. Hauer, Evaluation of adsorbent materials for heat pump and thermal energy storage applications in open systems, *Adsorption* 13 (2007) 399–405.
- [7] Y. Kato, T. Sekiguchi, J. Ryu, Packed bed reactor demonstration of magnesium oxide/water chemical heat pump, *Proc. 11th Int. Conf. Therm. Energy Storage-Efstock* (2009).
- [8] M. Molenda, *Chemische Speicherung und Transformation thermischer Energie mit Calciumchlorid und Wasserdampf* [in German], Universität Stuttgart, 2015, <http://www.dr.hut-verlag.de/9783843921152.html>.
- [9] M. Richter, M. Bouché, M. Linder, Heat transformation based on CaCl₂/H₂O – part A: closed operation principle, *Appl. Therm. Eng.* 102 (2016) 615–621, <http://dx.doi.org/10.1016/j.applthermaleng.2016.03.076>.
- [10] M. Bouché, M. Richter, M. Linder, Heat transformation based on CaCl₂/H₂O – Part B: open operation principle, *Appl. Therm. Eng.* inreview (2016).
- [11] W. Wongsuwan, S. Kumar, P. Neveu, F. Meunier, A review of chemical heat pump technology and applications, *Appl. Therm. Eng.* 21 (2001) 1489–1519.
- [12] E. Willers, M. Groll, The two-stage metal hydride heat transformer, *Int. J. Hydrogen Energy*. 24 (1999) 269–276.
- [13] M. Bouché, M. Richter, M. Linder, Heat transformation based on CaCl₂/H₂O – Part B: open operation principle, *Appl. Therm. Eng.* 102 (2016) 641–647, <http://dx.doi.org/10.1016/j.applthermaleng.2016.03.102>.
- [14] V.K. Sharma, E.A. Kumar, Thermodynamic analysis of novel multi stage multi effect metal hydride based thermodynamic system for simultaneous cooling, heat pumping and heat transformation, *Int. J. Hydrogen Energy* 42 (2016) 437–447, <http://dx.doi.org/10.1016/j.ijhydene.2016.09.154>.
- [15] W.G. Haije, J.B.J. Veldhuis, S.F. Smeding, R.J.H. Grisel, Solid/vapour sorption heat transformer: design and performance, *Appl. Therm. Eng.* 27 (2007) 1371–1376, <http://dx.doi.org/10.1016/j.applthermaleng.2006.10.022>.
- [16] S. Spoelstra, W.G. Haije, J.W. Dijkstra, Techno-economic feasibility of high-temperature high-lift chemical heat pumps for upgrading industrial waste heat, *Appl. Therm. Eng.* 22 (2002) 1619–1630.
- [17] K. Visscher, J.B.J. Veldhuis, Comparison of candidate materials for seasonal storage of solar heat through dynamic simulation of building and renewable energy system, *Build Simul., Ninth International Building Performance Simulation Association*, Montreal, Canada, 2005.
- [18] F. Bertsch, B. Mette, S. Asenbeck, H. Kerskes, H. Müller-Steinhagen, Low temperature chemical heat storage – an investigation of hydration reactions, *EFFSTOCK 11th Int. Conf. Energy Storage*, Stockholm, 2009.
- [19] K.E. N'Tsoukpo, T. Schmidt, H.U. Rammelberg, B.A. Watts, W.K.L. Ruck, A systematic multi-step screening of numerous salt hydrates for low temperature thermochemical energy storage, *Appl. Energy* 124 (2014) 1–16.
- [20] A. Abedin, M. Rosen, A critical review of thermochemical energy storage systems, open renew, *Energy J.* 4 (2011) 42–46, <http://dx.doi.org/10.2174/1876387101004010042>.
- [21] F. Trausel, A.J. De Jong, R. Cuypers, A review on the properties of salt hydrates for thermochemical storage, *Energy Procedia* 48 (2014) 447–452, <http://dx.doi.org/10.1016/j.egypro.2014.02.053>.
- [22] M. Molenda, J. Stengler, M. Linder, A. Wörner, Reversible hydration behavior of CaCl₂ at high H₂O partial pressures for thermochemical energy storage, *Thermochim. Acta* 560 (2013) 76–81.
- [23] H. Zondag, B. Kikkert, S. Smeding, R. de Boer, M. Bakker, Prototype thermochemical heat storage with open reactor system, *Appl. Energy* 109 (2013) 360–365, <http://dx.doi.org/10.1016/j.apenergy.2013.01.082>.
- [24] V.M. van Essen, H. a. Zondag, J.C. Gores, L.P. Bleijendaal, M. Bakker, R. Schuitema, W.G. van Helden, Z. He, C.C. Rindt, Characterization of MgSO₄ hydrate for thermochemical seasonal heat storage, *J. Sol. Energy Eng.* 131 (2009).
- [25] Y. Kato, R. Takahashi, T. Sekiguchi, J. Ryu, Study on medium-temperature chemical heat storage using mixed hydroxides, *Int. J. Refrig.* 32 (2009) 661–666, <http://dx.doi.org/10.1016/j.ijrefrig.2009.01.032>.
- [26] H. Zondag, M. van Essen, Z. He, R. Schuitema, W. van Helden, Characterisation of MgSO₄ for thermochemical storage, *Second Int. Renew. Energy Storage Conf. (IRES II)* (2007).
- [27] L.F. Cabeza, A. Sole, C. Barreneche, Review on sorption materials and technologies for heat pumps and thermal energy storage, *Renew. Energy* (2016), <http://dx.doi.org/10.1016/j.renene.2016.09.059>.
- [28] A. Galway, M. Brown, *Thermal Decomposition of Ionic Solids*, 1st ed., Elsevier Science B.V., Amsterdam, 1999.
- [29] Y. Kato, N. Yamashita, K. Kobayashi, Y. Yoshizawa, Kinetic study of the hydration of magnesium oxide for a chemical heat pump, *Appl. Therm. Eng.* 16 (1996) 853–862.
- [30] M. Peht, J. Bödeker, M. Arens, E. Jochem, F. Idrissova, Nutzung industrieller Abwärme – technisch-wirtschaftliche Potenziale und energiepolitische Umsetzung [in German], Heidelberg, Karlsruhe, 2010.
- [31] H.H. Binder, *Lexikon der chemischen Elemente* [in German], Hirzel, 1999.
- [32] UNECE Transport Division, *Globally Harmonized System of Classification and Labelling of Chemicals (GHS)*, New York and Geneva, 2015.
- [33] Institut für Arbeitsschutz der Deutschen Gesetzlichen Unfallversicherung, *Gestis-Stoffdatenbank* [in German], IFA, 2013. <http://gestis.itrust.de>.
- [34] L. Kolditz, A. Feltz, Über fluorhaltige Komplexe III. Über Zirkontetrafluoridhydrate, Zirkonhydroxofluoride und ihre Kondensationsprodukte [in German], *Zeitschrift für Anorg. Und Allg. Chemie.* 310 (1961) 217–224, <http://dx.doi.org/10.1002/zaac.19613100405>.
- [35] A.K.K. Lee, E.F. Johnson, Stoichiometry and kinetics of the thermal decomposition of molten anhydrous lithium nitrite, *Inorg. Chem.* 11 (1972) 782–787, <http://dx.doi.org/10.1021/ic50110a025>.
- [36] R.J. Meyer, Barium [in German], in: *Deutsche Chemische Gesellschaft (Ed.), Gmelins Handb. Der Anorg. Chemie*, 8th ed., Verlag Chemie GmbH, Berlin, 1932.
- [37] R.J. Meyer, E. Pietsch, Titan [in German], *Gmelins Handb. Der Anorg. Chemie*, 8th ed., Verlag Chemie GmbH, 1951.
- [38] R.J. Meyer, E. Pietsch, Vanadium Teil A – Lieferung 2 [in German], *Gmelins Handb. Der Anorg. Chemie*, 8th ed., Verlag Chemie GmbH, Weinheim, 1968.
- [39] R.J. Meyer, E. Pietsch, Wolfram [in German], *Gmelins Handb. Der Anorg. Chemie*, 8th ed., Verlag Chemie GmbH, Weinheim, 1933.
- [40] R.J. Meyer, E. Pietsch, Eisen [in German], *Gmelins Handb. Der Anorg. Chemie*, 8th ed., Verlag Chemie GmbH, Weinheim, 1931.
- [41] R.J. Meyer, E. Pietsch, Lithium [in German], *Gmelins Handb. Der Anorg. Chemie*, 8th ed., Verlag Chemie GmbH, Berlin, 1927.
- [42] P. Patnaik, *Handbook of Inorganic Chemicals*, McGraw-Hill, New York, 2003.
- [43] Römpp, *Römpp Lexikon Chemie* [in German], Calciumchlorid, Georg Thieme Verlag, 2013.
- [44] W.J. Asker, A.W. Wylie, Cerium tetrafluoride. I. Preparation and reactions, *Aust. J. Chem.* 18 (1965) 959–968.
- [45] R. De Boer, W.G. Haije, J.B.J. Veldhuis, Determination of structural, thermodynamic and phase properties in the Na₂S – H₂O system for application in a chemical heat pump, *Thermochim. Acta* 395 (2002) 3–19.
- [46] M.C. Caracoe, M.T. Dova, A.R. López García, Stabilization and hyperfine characterization of metastable tetragonal ZrO₂, *J. Mater. Res.* 5 (1990) 1940–1947, <http://dx.doi.org/10.1557/JMR.1990.1940>.
- [47] P. Masset, J.Y. Poinso, J.C. Poinnet, TG/DTA/MS Study of the thermal decomposition of FeSO₄ 6H₂O, *J. Therm. Anal. Calorim.* 83 (2006) 457–462, <http://dx.doi.org/10.1007/s10973-005-7267-6>.
- [48] I. Mayer, S. Zolotov, The thermal decomposition of rare earth and yttrium bromide hydrates, *J. Inorganics Nucl. Chem.* 27 (1965) 1905–1909.
- [49] R.J. Meyer, E. Pietsch, Vanadium Teil B – Lieferung 1 [in German], *Gmelins Handb. Der Anorg. Chemie*, 8th ed., Verlag Chemie GmbH, Weinheim, 1976.
- [50] R.J. Meyer, E. Pietsch, Zirkonium [in German], *Gmelins Handb. Der Anorg. Chemie*, 8th ed., Verlag Chemie GmbH, 1958.
- [51] S.S. Moosath, Studies on hydrated ceric oxide, *J. Inorg. Nucl. Chem.* 11 (1959) 286–289, [http://dx.doi.org/10.1016/0022-1902\(59\)80042-7](http://dx.doi.org/10.1016/0022-1902(59)80042-7).
- [52] Outotec, *HSC Chemistry 8.0*, 2014. <http://www.outotec.com>.
- [53] P. Patnaik, *Handbook of Inorganic Chemicals*, McGraw-Hill, 2003.
- [54] O. Pawlig, R. Trettin, Synthesis and characterization of α-hopeite, Zn₃(PO₄)₂·4H₂O, *Mater. Res. Bull.* 34 (1999) 1959–1966, [http://dx.doi.org/10.1016/S0025-5408\(99\)00206-8](http://dx.doi.org/10.1016/S0025-5408(99)00206-8).
- [55] D.L. Perry, L. Tsao, H.G. Brittain, X-ray photoelectron and infrared spectroscopic studies of the decarboxylation/oxidation of cerium(III) carbonate octahydrate, *J. Mater. Sci. Lett.* 3 (1984) 1017–1019.
- [56] J.A. Poston, R.V. Siriwardane, E.P. Fisher, A.L. Miltz, Thermal decomposition of the rare earth sulfates of cerium(III), cerium(IV), lanthanum(III) and samarium(III), *Appl. Surf. Sci.* 214 (2003) 83–102, [http://dx.doi.org/10.1016/S0169-4332\(03\)00358-1](http://dx.doi.org/10.1016/S0169-4332(03)00358-1).
- [57] E. Spundflasche, H. Fink, H.J. Seifert, Erste Abbauprodukte von Hexahydraten MCl₃·6H₂O (M = V, Ti, Cr, Al) mit einer Verfeinerung der Struktur von [Cr(H₂O)₆]Cl₃ [in German], *Zeitschrift Für Anorg. Und Allg. Chemie* 579 (1989) 143–150, <http://dx.doi.org/10.1002/zaac.19895790118>.
- [58] M.R. Udupa, Thermal decomposition of cerium(IV), cerium(III), chromium(III) and titanium(IV) sulphates, *Thermochim. Acta* 57 (1982) 377–381, [http://dx.doi.org/10.1016/0040-6031\(82\)80048-8](http://dx.doi.org/10.1016/0040-6031(82)80048-8).
- [59] J.T. Vaughy, W.T.A. Harrison, A.J. Jacobson, D.P. Goshorn, J.W. Johnson, Synthesis, structure, and properties of two new Vanadium(III) phosphates: VPO₄·H₂O and V(PO₄)(OH)_{0.69}(H₂O)_{0.31}·0.33H₂O, *Inorg. Chem.* 33 (1994) 2481–2487, <http://dx.doi.org/10.1021/ic00089a027>.
- [60] D.D. Wagmen, W.H. Evans, The NBS tables of chemical thermodynamic properties, *J. Phys. Chem. Ref. Data* 11 (1982).
- [61] S. Suri, K.K. Bamzai, V. Singh, Growth and thermal kinetics of pure and cadmium doped barium phosphate single crystal, *J. Therm. Anal. Calorim.* 105 (2011) 229–238, <http://dx.doi.org/10.1007/s10973-011-1365-4>.

- [62] W. Abriel, K. Reisdorf, J. Pannetier, Dehydration reactions of gypsum: a neutron and X-ray diffraction study, *J. Solid State Chem.* 85 (1990) 23–30, [http://dx.doi.org/10.1016/S0022-4596\(05\)80055-6](http://dx.doi.org/10.1016/S0022-4596(05)80055-6).
- [63] R.J. Meyer, E. Pietsch, A. Kotowski, Mangan Teil C5 – Verbindungen des Mangans mit Chlor, Brom und Jod [in German], *Gmelins Handb. Der Anorg. Chemie*, 8th ed., Springer Berlin Heidelberg, 1978.
- [64] I. Barin, *Thermochemical Data of Pure Substances*, VCH verlagsgesellschaft mbH, Weinheim, 1993.
- [65] B. Boonchom, C. Danvirutai, Thermal decomposition kinetics of FePO₄·3H₂O precursor to synthesize spherical nanoparticles FePO₄, *Ind. Eng. Chem. Res.* 46 (2007) 9071–9076, <http://dx.doi.org/10.1021/ie071107z>.
- [66] A. La Iglesia, Estimating the thermodynamic properties of phosphate minerals at high and low temperature from the sum of constituent units, *Estud. Geológicos*. 65 (2009) 109–119, <http://dx.doi.org/10.3989/egeol.39849.060>.
- [67] P. Vieillard, Y. Tardy, J.O. Nriagu, P.B. Moore (Eds.), *Phosphate Minerals*, Springer Berlin Heidelberg, Berlin, Heidelberg, 1984, pp. 171–198, http://dx.doi.org/10.1007/978-3-642-61736-2_4.

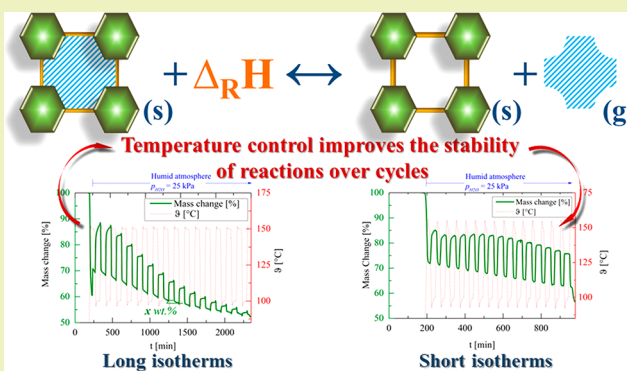
High Carnallite-Bearing Material for Thermochemical Energy Storage: Thermophysical Characterization

Andrea Gutierrez,^{*,†} Svetlana Ushak,[‡] and Marc Linder[†][†]German Aerospace Center – DLR e. V., Institute of Engineering Thermodynamics, Pfaffenwaldring 38, 70569 Stuttgart, Germany[‡]Department of Chemical Engineering and Mineral Processing and Center for Advanced Study of Lithium and Industrial Minerals (CELiMIN), Universidad de Antofagasta, Campus Coloso, Av. Universidad de Antofagasta, 02800 Antofagasta, Chile

S Supporting Information

ABSTRACT: Thermochemical energy storage has a high material-related energy density and low energy losses over time compared to sensible and latent energy storage. Considering economic and ecological aspects, there is a great opportunity in using low cost or even waste materials from the mining industry, as thermochemical energy storage medium. In this study, a systematic analysis of a high carnallite-bearing material, comparable to the natural waste, for thermochemical energy storage was performed. The material displays gradual decomposition and poor reversibility of hydration reaction at temperatures above 150 °C. However, the reversibility is significantly higher and the decomposition is slower between 100 and 150 °C under $p_{H_2O} = 25$ kPa. The reversible behavior of the hydration reaction of carnallite, between 100 and 150 °C, is stable for 15 cycles when the material is exposed at 150 °C for short periods of time ($t < 20$ min). Following this path, any potential application of this material is definitely limited to low temperature thermal storage or thermal upgrade. Taking the low material cost into account, one of the potential applications of this material could be in the context of long-term heat storage. For this purpose, the temperatures of dehydration can be below 150 °C and the temperatures of rehydration close to 40 °C.

KEYWORDS: Thermochemical energy storage, Low-cost material, Salt hydrates, Potassium carnallite, Magnesium chloride hexahydrate, Solid–gas reaction



INTRODUCTION

Thermal energy storage (TES) has been identified as one of the key technologies for a sustainable and continuous supply of renewable energy. Thermal energy can be stored whenever the source is available, for example during the day or in summer. The heat can then be released when it is required, for example during the night or in winter.

There are three well-known mechanisms for storing thermal energy that are briefly described below. For each of these concepts, there is a wide variety of materials applied as medium of storage, such as paraffins, fatty acids, rocks, water, nitrate salts, and salt hydrates, among others.^{1,2} The inorganic salts addressed in this paper could be applied as storage materials for all three concepts. Regarding this, several studies have been published showing a high potential of use of byproducts or wastes from inorganic mining as TES materials.^{3–6} By utilizing currently unexploited inorganic wastes as a storage material, critical aspects such as the energy burden of storage materials, economic aspects as well as ecological aspects, e.g. due to mining, can be tackled at the same time. Recent approaches and results concerning thermal energy storage based on inorganic waste materials can be found in the given references:

- Sensible heat storage (SHS): the amount of energy stored/released while the temperature of the inorganic salt is increased/decreased,^{1,7}
- Latent heat storage (LHS): the amount of energy stored/released when the inorganic salt changes phase,^{2,7}
- Thermochemical storage: the amount of energy stored/released when a reversible reaction takes place, e.g. hydration/dehydration of inorganic salts.

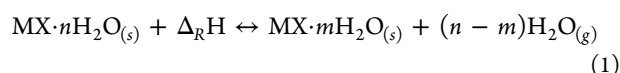
The main advantages of thermochemical storage materials (TCM) compared to sensible ($0.033–0.4$ GJ/m³) and latent heat storage ($0.15–0.37$ GJ/m³)^{1,8} are their high material-related energy densities ($0.92–3.56$ GJ/m³)^{8,9} and low energy losses over time.^{1,10–12} Additionally, TCM exhibit a wide versatility of applications: one example is heat transformation, in which thermal energy (forward reaction) can be stored at low temperatures and released at higher temperatures (reversible reaction) by changing the pressure of the reaction system.^{12–15} However, as this mechanism involves a chemical

Received: December 19, 2017

Revised: February 28, 2018

Published: March 23, 2018

reaction, some additional challenges have to be faced, e.g. the complexity of components and especially material-related aspects such as cycling stability.^{15,16} A typical gas–solid reaction system using salt hydrates is shown in eq 1. (Modified from¹⁷)



In this reaction $\text{MX}\cdot n\text{H}_2\text{O}_{(s)}$ would be a salt hydrate which consists of $\text{MX}\cdot m\text{H}_2\text{O}_{(s)}$ and $(n - m)$ mol of reactive water vapor. In order to deploy these technologies successfully, it is important that they satisfy specific technical and economic requirements. Considering economic and ecological aspects, there is a great opportunity in using low cost or even waste materials from the mining industry. In doing so, the accumulation of wastes in mining sites can also be reduced and potential long-term, harmful environmental impacts can be avoided. Several salt hydrates are currently obtained as by-products or wastes from the mining industry, which are natural materials already available in the mining sites. These materials correspond mainly to double salts such as carnallite, bischofite, kainite, astrakanite, darapskite, and schoenite. They contain from two to six mol water of crystallization per mol of anhydrous salt and are therefore theoretically suitable for thermochemical storage with water vapor as a gaseous reactant. The most critical point for a potential application of these salts is the reversible reaction of hydration/dehydration. Gutierrez et al. 2017 have already studied the thermal stability of three of these materials: potassium carnallite, lithium carnallite, and astrakanite. Results showed that potassium carnallite and astrakanite could have potential as thermochemical storage materials, based only on their studies of thermal stability below 350 °C.⁶

In this study, a systematic analysis of a high potassium carnallite-bearing material as thermochemical energy storage medium was performed. In order to minimize the influence of low-bearing impurities contained in the natural potassium carnallite, such as calcium sulfate dihydrate, lithium chloride monohydrate, among others,^{18,19} the experimental study was performed with a synthetic material. The reversibility of the reaction was studied, and the limiting conditions of operation were evaluated, in order to investigate its suitability as a TCM. Finally, based on its thermophysical properties some potential applications were discussed.

EXPERIMENTAL METHOD

Materials. The compounds used to prepare the synthetic material were KCl (potassium chloride, anhydrous powder, 99.5%, Merck) and $\text{MgCl}_2\cdot 6\text{H}_2\text{O}$ (magnesium chloride hexahydrate, hygroscopic crystals, 99%, Merck). The sample was prepared by crystallization from a ternary equilibrium solution $\text{KCl}\text{--}\text{MgCl}_2\text{--}\text{H}_2\text{O}$ at 35 °C. The precipitated crystals were separate from the stock solution by vacuum filtration.

Chemical and Morphological Characterization. Chemical analyses of the synthetic material were performed in order to calculate its chemical composition. Potassium and magnesium concentrations were determined by atomic absorption spectrometry. Chloride was determined by volumetric titration with AgNO_3 , and moisture was determined by drying until constant weight at 40 °C.

The mineral composition and morphology of crystals were analyzed using X-ray diffraction (XRD) and scanning electron microscopy (SEM). Patterns of XRD (Bruker AXS - D8 Discover Bruker GADDS with a VANTEC-2000 detector) were recorded on a diffractometer (using $\text{Cu K}\alpha$ radiation) operating at 45 kV/0.650 mA. A scanning

rate of 0.5°/s was applied to record the patterns in the 2θ angle range from 15° to 60°. XRD analyses for fresh sample of carnallite and products after 5 cycles of hydration and dehydration were carried out. The morphology and particle size of the crystals were examined by SEM (Zeiss ULTRA Plus). To perform this experiment, a fresh sample of material was dehydrated overnight in a furnace at 120 °C surrounded by air and cooled in a desiccator to ambient temperature.

Thermal Properties. *Thermogravimetric–Mass Spectroscopy (TG-MS).* The thermal decomposition or reaction steps of the material were recorded by thermogravimetric analysis (NETZSCH STA 449 C Jupiter). A thermogravimetric sample carrier with a thermocouple type S and an accuracy of ± 1 K was used. The accuracy of the balance was ± 0.1 μg . The measurements were performed from room temperature (25 °C) to 1100 °C performing dynamic experiments with a heating rate of 5 K/min using nitrogen as protective gas with a volumetric flow of 50 N·mL/min. The atmosphere surrounding the sample was kept inert using 100 N·mL/min of nitrogen flow. In order to analyze the generated gases, a mass spectrometer (NETZSCH QMS 403 C Aeolos) was coupled to the TG analyzer. Sample sizes of about ~50 mg were measured in open Al_2O_3 crucibles.

STA–MHG Reversibility of Reactions. The reversibility of reaction and potential operating conditions were studied using a Simultaneous thermal analyzer (NETZSCH STA-449 F3 Jupiter, see Figure 1). The

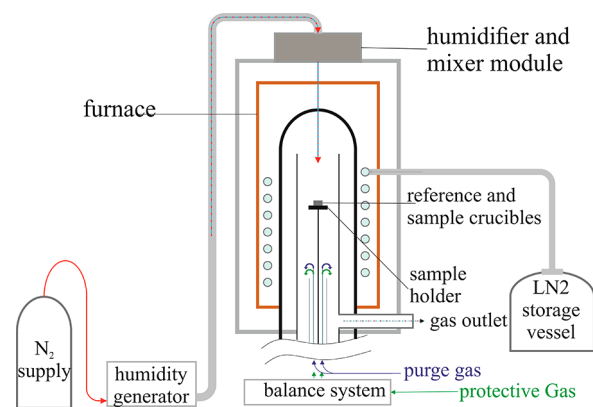


Figure 1. Schematic diagram of the simultaneous thermal analyzer (STA).

setup was equipped with a Modular Humidity Generator (ProUmid MHG-32). A differential scanning calorimetric and thermogravimetric (DSC-TG) sample holder with a thermocouple Type P and an accuracy of ± 1 K was used. The accuracy of the balance was ± 0.1 μg . Nitrogen was used as protective and purges gas with a volume flow for both of 20 N·mL/min. The atmosphere surrounding the sample was kept inert using 100 N·mL/min of nitrogen flow and water vapor. Either pure nitrogen was used or a mix of nitrogen and water vapor. Liquid nitrogen was used to support the controlled cooling process. Partial vapor pressures of 15 kPa (15.9% RH), 25 kPa (30% RH), or 30 kPa (38% RH) were set as is shown in Figure 2, named Experiment 1. According to the literature the critical relative humidity (CRH) of potassium carnallite (the main component of the synthetic material) is within the range of 50–55% at 30 °C.²⁰ However, the phase diagram of the $\text{KCl}\text{--}\text{MgCl}_2$ (anhydrous compound from potassium carnallite) in equilibrium with water is not available. This means that there is no evidence that accurately shows how the CRH will vary with temperature. Under these circumstances the maximum partial water vapor pressure was set to 30 kPa (38% RH). Sample sizes of about ~15 mg were measured in open platinum crucibles (85 μL).

Dynamic experiments were carried out with heating/cooling rates of 5 K/min. The temperatures of hydration were set to a minimum of 100 °C, due to the hygroscopic/deliquescent behavior of samples previously mentioned.

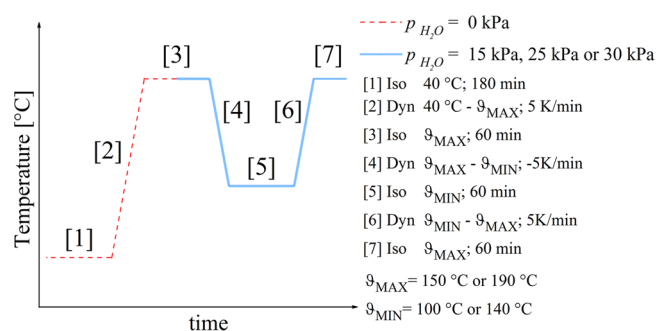


Figure 2. Experiment 1: Temperature and humidity program to study the reversibility of reactions.

RESULTS AND DISCUSSION

Chemical and Morphological Characterization. Considering the composition of the product on a dry basis, the results of chemical analyses for ions and water of crystallization (in wt %) of the synthesized material are shown in Table 1.

Table 1. Synthetic Material Composition (wt %)

Element	Mg ²⁺	K ⁺	Cl ⁻	H ₂ O
Composition	9.28	11.76	37.73	41.22

Figure 3 shows the XRD diffractogram of the synthetic material (fresh sample) where two phases were identified,

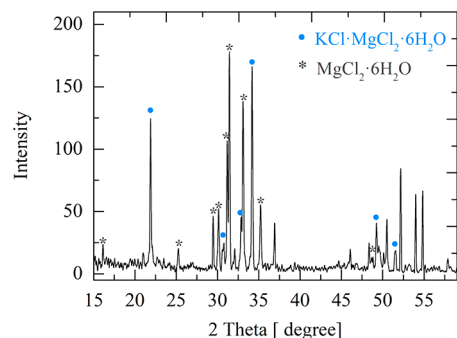


Figure 3. XRD diffractogram of fresh sample used for this study.

potassium carnallite (hereinafter called “carnallite”; $\text{KCl}\cdot\text{MgCl}_2\cdot 6\text{H}_2\text{O}$) and magnesium chloride hexahydrate ($\text{MgCl}_2\cdot 6\text{H}_2\text{O}$).

Taking into account the phases identified by XRD and the chemical analysis results, the calculation of the mineralization was carried out. The weight percentage (wt %) composition of the sample is shown in Figure 4, where it can be seen that the content of carnallite is 76.53 wt %, magnesium chloride hexahydrate 15.05 wt %, and the content of stock solution is

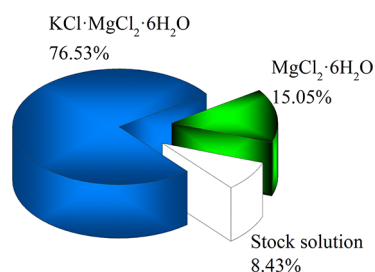


Figure 4. Weight composition of fresh synthetic material.

8.43 wt %; the latter was presumably soaked into the sample crystals. The amount of carnallite contained in the material is in agreement with the natural waste obtained from Salar de Atacama in Chile, that contains from 60 wt % to 73.77 wt % of $\text{KCl}\cdot\text{MgCl}_2\cdot 6\text{H}_2\text{O}$ plus impurities such as NaCl, KCl, and CaSO_4 .^{18,19} This waste precipitates in the solar evaporation ponds during the processes to obtain lithium carbonate and potassium chloride. Additionally, if the water contained in the stock solution of the synthetic material evaporates completely, then magnesium chloride hexahydrate would precipitate. If this is the case, the new theoretical composition of the synthetic material would be carnallite 83.6 wt % and magnesium chloride hexahydrate 16.4 wt %.

Using SEM, the morphology of the dehydrated product obtained from the synthetic material was determined (Figure 5). It can be seen that the dried crystals have an undefined and irregular form, presenting a porous surface and also some surface cracks obtained as a result of the dehydration of carnallite and magnesium chloride hexahydrate in atmosphere of air.

Thermal Properties. *Thermogravimetric–Mass Spectroscopy (TG-MS).* The investigation of the reaction steps of dehydration, resulting from the TG experiments (Figure 6), shows a weight loss in two steps below 260 °C (green curve). As the sample is composed by two different salt hydrates, it is not possible to determine, only with the TG results, if both salts are reacting or what the ratio of dehydration reaction between them is.

However, useful information regarding the decomposition of the synthetic material can be obtained from the MS results. The first step of mass loss was identified by MS as mainly water vapor (blue curve), with a small amount of HCl close to 180 °C (orange curve). The second step corresponds to a partial mass loss of 19.00 wt % (5.00 wt % + 14.00 wt %, up to ~260 °C), which was identified by MS as water vapor and HCl. In contrast to the first step, the second step presents a significant increase of HCl release starting at 204 °C. This step of dehydration takes place from 167 to 260 °C. Some authors report that a lower hydrate of magnesium chloride hexahydrate as well as of carnallite release HCl as a result of partial hydrolysis starting at 120 and 200 °C, respectively.^{22–24} Thus the mass losses shown in Figure 6 correspond to the dehydration reaction of both salt hydrates present in the synthetic material. However, the mass balance based on the stoichiometric calculation indicates that in the case of complete dehydration reaction of both materials plus the evaporation of water present in the stock solution, the mass loss should be 46.2 wt %. As the mass loss at 260 °C is only 42.5 wt %, it can be assumed that the water available in the fresh material is not completely released. This could be due to partial dehydration of both salt hydrates and/or partial evaporation of the water contained in the stock solution.

Due to the hazardousness of HCl and the irreversibility of this reaction in humid atmospheres, the temperature range of this study was limited to temperatures below 200 °C to take potential applications into consideration.

Reversibility of Reactions. Experiment 1 to evaluate the reversibility of reactions followed the temperature and humidity program shown in Figure 2. The first results obtained are summarized in Figure 7: (a) rehydration reaction (segments 3–5 of experiment 1) and Figure 7 (b) (segments 5–7 of experiment 1). To carry out the calculations of the level of hydration, it was assumed that only potassium carnallite was reacting. This is due to the thermophysical properties of

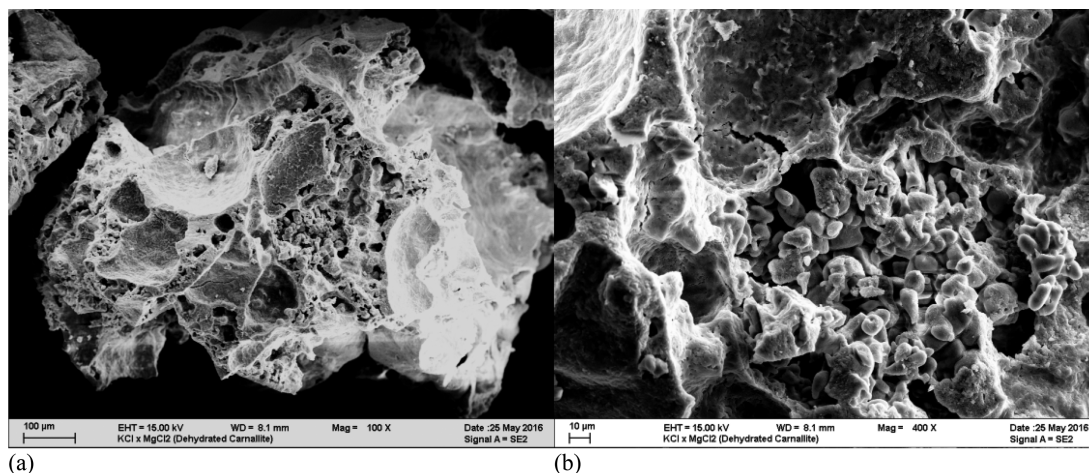


Figure 5. SEM images of dehydrated material at (a) $\times 100$ and (b) $\times 400$.

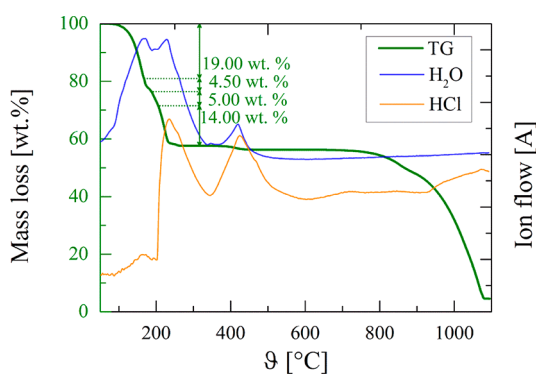


Figure 6. Thermal decomposition of carnallite, TG-MS curves. Heating rate of 5 K/min.

magnesium chloride hexahydrate such as melting point at 117 °C and solidification point at 75 °C,³ besides the fact that magnesium chloride in equilibrium with water at temperatures above 100 °C and RH above 15% is either magnesium chloride hexahydrate or is in the liquid state.¹⁷ Thus, the increase of mass, according to our assumption, corresponds only to the rehydration of $\text{KCl}\cdot\text{MgCl}_2$, and the level of hydration and dehydration are shown in Figure 7. It can be seen that the three experiments present two steps of hydration (Figure 7(a)) as well as two steps of dehydration (Figure 7(b)) and they are clearly identifiable. This two-step dehydration/hydration behavior is also similar to that reported by Molenda et al. for $\text{CaCl}_2\cdot 2\text{H}_2\text{O}$.²¹ Even though the operating conditions were quite different, the two-step hydration behavior remains

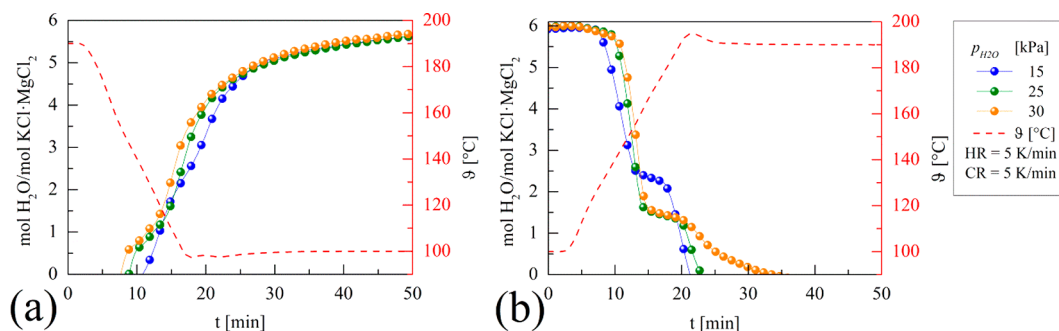


Figure 7. Level of (a) hydration and (b) dehydration of anhydrous carnallite

constant under different water vapor partial pressures. However, the two-step dehydration was slightly different at lower water vapor partial pressures. In this study, it is observed that of the three samples showing complete hydration/dehydration reactions, only the sample under 30 kPa shows slower dehydration in the second step. Based on this the intermediate value of 25 kPa was chosen to continue with further experiments.

Figure 8 is a closer look at the level of hydration of experiment 1 using 25 kPa of partial vapor pressure in terms of

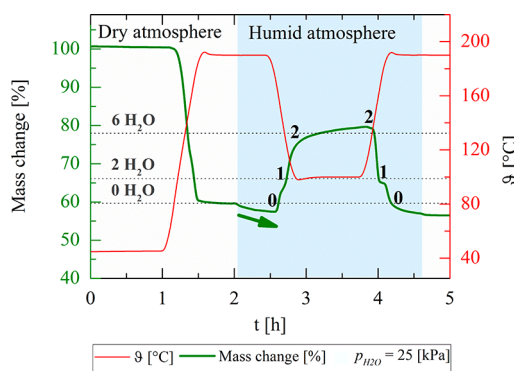


Figure 8. Percentage mass changes due to dehydration–hydration reactions of potassium carnallite and subproducts ($p_{\text{H}_2\text{O}} = 25$ kPa).

mass percentage. Additionally, the first dehydration step (dynamic phase) performed under dry atmosphere of nitrogen is shown. According to the results obtained from experiment 1,

a combination of high temperature and humid atmosphere leads to a continuous mass loss of sample (see the arrow starting at two hours) that might be due to the formation of gaseous HCl from magnesium chloride hexahydrate or a lower hydrate from this salt. With decreasing temperature (dynamic phase), the mass of the sample starts to increase due to the rehydration of the anhydrous phase, that, as was mentioned before, would correspond only to the hydration of $\text{KCl}\cdot\text{MgCl}_2$.

The temperatures of hydration/dehydration depend on the gas pressure ($p_{\text{H}_2\text{O}}$) according to the van't Hoff equation (eq 2).

$$\ln\left(\frac{p_{\text{H}_2\text{O}}}{p^+}\right) = \frac{\Delta_R S^\theta}{R\nu} - \frac{\Delta_R H^\theta}{R\nu T} \quad (2)$$

where $p_{\text{H}_2\text{O}}$ is the water vapor partial pressure (kPa), p^+ the reference pressure (100 kPa), and $\Delta_R S^\theta$ (J/(mol K)) and $\Delta_R H^\theta$ (kJ/(mol K)) the standard entropy and enthalpy of reaction, respectively. R is the universal gas constant (8.314 J/(mol K)), ν the stoichiometric factor for each reaction, and T the temperature (K). The estimated values of entropy of reactions from 150 ± 5 J/(mol K) reported by Richter et al.¹⁵ were used. The enthalpy of reaction was calculated based on literature data available for the standard enthalpy of formation ($\Delta_f H^\theta$). Replacing all these values in eq 2, the van't Hoff diagram for carnallite and $\text{MgCl}_2\cdot 6\text{H}_2\text{O}$ was built and is shown in Figure 9.

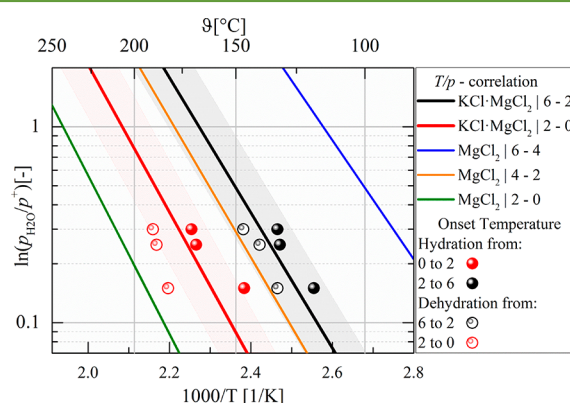


Figure 9. Van't Hoff diagram of carnallite and magnesium chloride hexahydrate. Equilibrium lines calculated for $S = 150$ J/K mol.

It can be seen that the experimental results shown in Figure 7 are in agreement with the theoretical equilibrium temperatures of carnallite. The empty markers correspond to the dehydration temperatures of reactions from Figure 7, and the filled markers correspond to the hydration temperatures of reaction from the same figure. This preliminarily confirms that the measured mass change during the reversible reaction could not be related to the whole sample mass but only to the content of carnallite, (76.53 wt %) of fresh material, which corresponds to the “active” material of the sample. However, there are still two issues to solve. The first is that the hydration curve (mass

increase at low temperature) does not reach the equilibrium; this can be deduced from the continuous increase of mass at low isothermal temperature. And second, the equilibrium temperature of MgCl_2 from 4 to 2 is very close to the equilibrium temperature of $\text{KCl}\cdot\text{MgCl}_2$ from 2 to 0. This could explain why the mass is continuously increasing without reaching the equilibrium, because the MgCl_2 must still be active. Despite this, carnallite seems to be promising because the reaction is detected close to the theoretical equilibrium and, measured with relatively fast heating and cooling rates of 5 K/min, only a small hysteresis can be observed. However, since a combination of water vapor and high temperature leads to a complete or partial hydrolysis reaction of magnesium chloride hexahydrate, this effect on the storage capability of the synthetic sample has been further analyzed.

Therefore, three more experiments were performed in order to study the cycling stability of the synthetic sample under different operating conditions, based on the steps of reaction shown in Figure 8. These conditions are described in Table 2.

The results of these experiments using the synthetic sample are shown in Figure 10. The mass change during the hydration/

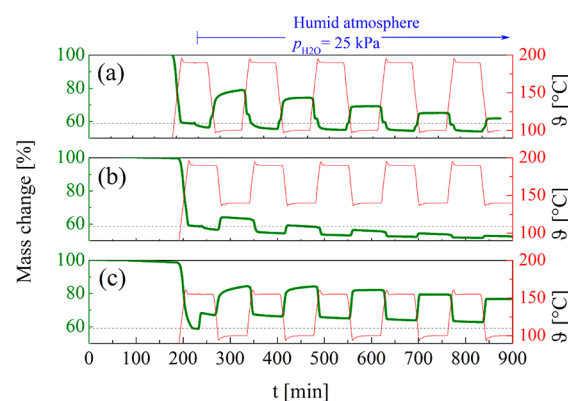


Figure 10. Level of dehydration/hydration of carnallite for five cycles (continuous green curves). (a) Experiment 2, (b) Experiment 3, and (c) Experiment 4.

dehydration of the sample obtained for the experiment 2 can be seen in Figure 10(a). The first dehydration step ($t < 230$ min) corresponds to the dehydration of the fresh material that has been performed under dry atmosphere of nitrogen. It can also be seen that the maximum mass increase is lowered for every subsequent cycle. Figure 10(b) shows the results obtained for experiment 3 in Table 2. In this case, the mass increase due to the reversible reaction of hydration over the cycles is lower than in Figure 10(a), which indicates a faster decomposition of the sample compared to the results of experiment 2. Finally, Figure 10(c) shows the results obtained from experiment 3 described in Table 2. The results show a more stable behavior over the cycles, indicating either that there is no decomposition of the sample or that the decomposition is slower under these

Table 2. Operating Conditions of Cycle Stability Experiments Performed for 5 Cycles

Experiment	Reaction steps		Temp range [°C]	$p_{\text{H}_2\text{O}}$ [kPa]	T/p correlation plotted in Figure 9
	Hydration	Dehydration			
2	2	2	100–190	25	Black and red lines
3	1	1	140–190	25	Red line (2–0)
4	1	1	100–150	25	Black line (6–2)

operating conditions. Additionally, in the results of experiment 4 (Figure 10(c)) the continuous increase of mass is also observed, in this case in the first two cycles. Since only the temperature conditions were changed, it can be concluded that the temperature level has a direct effect on the cycling stability of the material as well as on the conversion of reaction of the sample.

In order to understand the effect of magnesium chloride hexahydrate on the cycling stability of the synthetic sample, experiment 2 and experiment 4 were performed using only synthetic magnesium chloride hexahydrate (See Figure S1 and Figure S2 in the Supporting Information). The results show that this salt is active under these operating conditions. However, after the second cycle the material is completely decomposed (see Figure 11) or is not significantly active anymore (see Figure S3 in the supporting information).

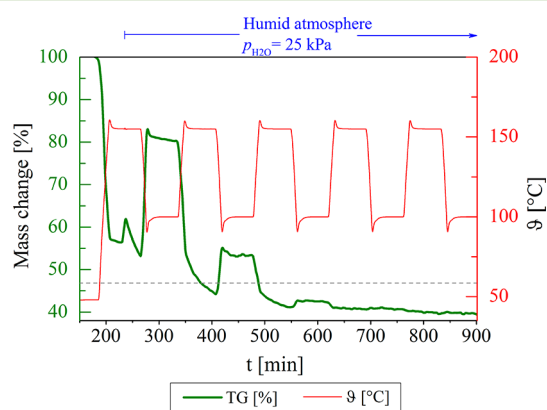


Figure 11. Level of dehydration/hydration of $\text{MgCl}_2 \cdot 6\text{H}_2\text{O}$ for five cycles (experiment 4); Continuous green curves.

This also explains why the hydration of the synthetic sample containing carnallite does not reach equilibrium in the first two cycles, but it does from the third cycle onward, where magnesium chloride hexahydrate is not active anymore.

In addition, further investigation on the cycling stability in the long term of the synthetic sample containing carnallite was carried out. To do this, a new experiment (experiment 4.1) was performed. This new experiment was based on experiment 4, but instead of 5 cycles consisted of 15 cycles. The results of experiment 4.1 are shown in Figure 12. In line with the results of experiment 4, the first cycles show the highest increase of mass during the hydration reactions, plus the first two cycles do

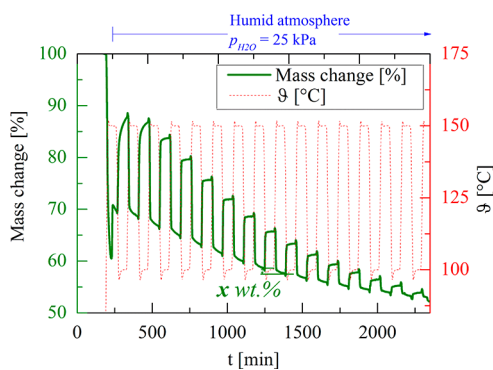


Figure 12. Measurement of the mass change in the sample of experiment 4.1.

not reach the equilibrium due to the reaction of magnesium chloride hexahydrate. However, the maximum increase of mass is gradually reduced as the cycles are performed. Furthermore, in every cycle a constant percentage of sample mass is lost (x wt %), corresponding to approximately 1.1 wt %. This explains the negative slope of the TG-signal baseline. In other words, not only do the temperature and the presence of the magnesium chloride hexahydrate influence the conversion of carnallite but they also affect the gradual increase of inactive material, e.g. due to irreversible decomposition caused by hydrolysis. A visualization of this behavior and the relation between active and inactive material is shown in Figure 13.

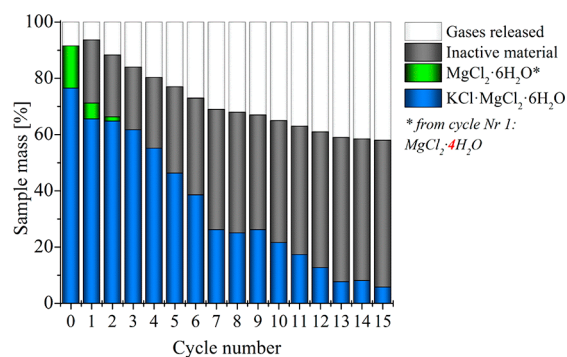


Figure 13. Amount of active and inactive material through cycles based on results from experiment 4.

These results lead us to the conclusion that after 15 cycles the gradual decomposition of high carnallite-bearing material jeopardizes the feasibility of carnallite for thermochemical storage applications.

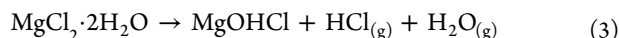
One hypothesis for this behavior is related to the presence of molten magnesium chloride hexahydrate or lower hydrates from it. This molten material dissolves or contributes to the decompositions of a small amount of carnallite in every cycle, thus reducing the amount of active material. In addition, this molten material and/or lower hydrates evidence partial hydrolysis which explains the decrease of mass “ x wt %” with every cycle.

Following this hypothesis, factors that could have an influence on the decomposition of magnesium chloride hexahydrate contained in the material were evaluated separately. These are described below:

Influence of Crucible Material. Experiment 4.1 was repeated twice more using different crucible materials, aluminum (Al) crucibles and aluminum oxide (Al_2O_3) crucibles. The results showed that the decomposition of synthetic material, specifically of the magnesium chloride hexahydrate, followed the same path of decomposition already shown in Figure 12 when platinum crucibles were used. That means that the material of the crucible had no influence on the decomposition of magnesium chloride hexahydrate.

Influence of Temperature. It is possible that the temperature has both a direct and indirect influence on the decomposition of the sample. The indirect influence could be due to the dissociation of carnallite driven by the molten material present in the sample within the operating conditions range. This dissociation could take place either due to the melting process or due to the overhydration of magnesium chloride hexahydrate. This salt hydrate has a melting point of 117 °C according to available data and also shows a

deliquescent behavior at 22% RH (100 °C).^{17,25} As a consequence, less carnallite is available; thus, the efficiency of the reaction is reduced with each cycle. On the other hand, the direct cause could be associated with the hydrolysis reaction of lower hydrates of magnesium chloride hexahydrate ($\text{MgCl}_2 \cdot 2\text{H}_2\text{O}$; eq 3).^{6,23} Although it is extensively reported that this reaction takes place significantly above 180 °C, some authors also report that partial hydrolysis of these lower hydrates can take place even from 120 °C.^{24,28–30} Additionally, it has also been reported that hydrolysis is more likely to take place in the liquid phase compared to the solid phase,³¹ behavior that, according to the results obtained in this study, can also be accelerated by the influence of temperature.



In order to investigate if these two factors are responsible for the gradual decomposition of carnallite, the samples resulting from experiments 2, 3, and 4 (from Figure 10) were analyzed by XRD. The diffractograms are plotted in Figure 14, besides

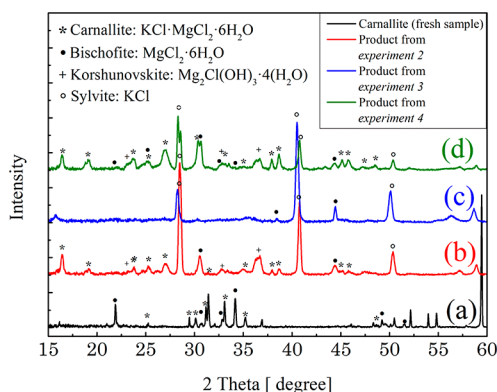


Figure 14. XRD patterns of carnallite (fresh sample) (pattern a) and products after 5 cycle stability experiments 2, 3, and 4 (patterns b, c, and d, respectively).

the diffractogram of fresh synthetic material (black diffractogram), in order to compare the change of the pattern before and after the experiments. The diffractograms of experiments 2 and 3 (red and blue, respectively) show intense peaks that fit with the pattern of potassium chloride. This could confirm not only that the hydrolysis took place during the experiments, since peaks corresponding to magnesium chloride hexahydrate are less intense, but also that carnallite is being gradually dissolved by the molten material, increasing the amount of potassium chloride that is a product of the dissolution of carnallite, and reducing at the same time the amount of “active material”. In addition, on the diffractograms of experiment 2 and experiment 4, the Korshunovskite ($\text{Mg}_2\text{Cl}(\text{OH})_3 \cdot 4(\text{H}_2\text{O})$) was identified. Korshunovskite is comparable to some intermediate products of hydrolysis of magnesium chloride hexahydrate previously reported.³² Moreover, the product from experiment 3 is the one that showed the highest degree of dissolution of carnallite and decomposition of magnesium chloride hexahydrate, since almost only KCl is identified by XRD.

This indicates that the temperature is the main parameter responsible for accelerating the reduction of active material. Based on this, “experiment 4.1” was repeated reducing the times of isothermal intervals; this experiment was named “experiment 4.2”. That means that experiment 4.2 was

performed using intervals of isothermal conditions at 150 and 100 °C of 10 and 20 min, respectively, instead of 60 min.

The results of experiment 4.2 for synthetic material containing carnallite seem to be more stable compared to the behavior during experiment 4.1, as is shown in Figure 15.

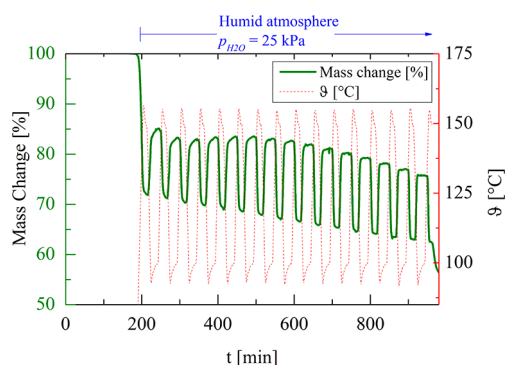


Figure 15. Measurement of the mass change in the sample of experiment 4.2.

However, in the first 4 cycles, part of the carnallite contained in the synthetic material seems to be inactive, seeing that fewer molecules of water are involved in the reactions of hydration and dehydration (~ 3 mol H_2O).

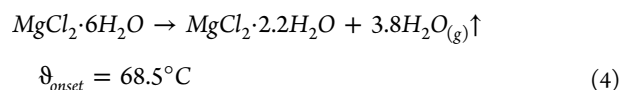
Similarly, a small gradual decomposition can be observed from cycle 8, but the degree of decomposition is significantly smaller and slower compared to the results of experiment 4.1 (Figure 12). This indicates that if the time at which the material is exposed to high temperatures is controlled, the potential to apply carnallite as TCM increases significantly. Also, dehydration (i.e., thermal charging) should be performed at the lowest possible temperatures.

It is still unclear why not all of the reactive material is undergoing a reaction. Nevertheless, it can be influenced by the behavior of $\text{MgCl}_2 \cdot 6\text{H}_2\text{O}$ contained in the sample, which is reacting in the first 6 cycles of this experiment (see Figure 16). This reaction can be identified in the DSC curves of synthetic sample at approximately 117 °C, even though this temperature has been extensively reported as the melting point of magnesium chloride hexahydrate by other authors.^{1,2,32–38}

In order to understand if this temperature corresponds to a melting or a chemical reaction under the operating conditions used in this study, experiment 4.2 was also performed using only synthetic magnesium chloride hexahydrate.

The results show that this material is in fact reacting under these operating conditions over the cycles (see Figure 17), on the contrary to the results obtained from experiment 4, where this material was reacting only in the first two cycles. However, based on the molten appearance of the sample at the end of the experiment (See Figure S4 in the Supporting Information), this reaction is occurring in the liquid phase.

Moreover, the reactions of dehydration and hydration of magnesium chloride hexahydrate are not complete. In the first cycle, only 3.8 mol of water was released (see eq 4), and 3.3 mol of water reacted during the first hydration step (see eq 5). From the second dehydration onward, only one mole of water reacts (see eq 6)



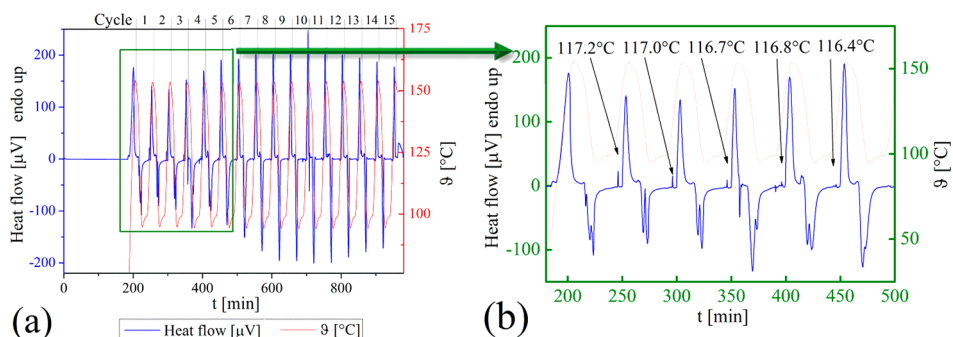


Figure 16. DSC curves obtained from experiment 4.2. Results of the complete experiment (a) and of the first 6 cycles (b).

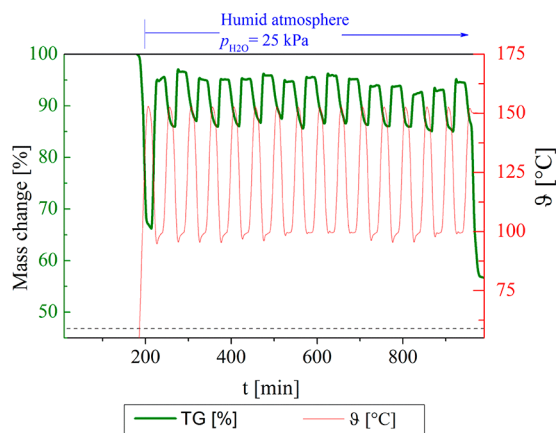
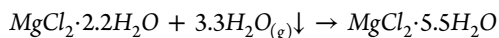


Figure 17. Measurement of the mass change in the synthetic $\text{MgCl}_2 \cdot 6\text{H}_2\text{O}$ of experiment 4.2.



$$\vartheta_{\text{onset}} = 138.1^\circ\text{C} \quad (5)$$



$$\vartheta_{\text{onset}} = 114.7^\circ\text{C} \quad (6)$$

Based on results from experiment 4.2 performed for $\text{MgCl}_2 \cdot 6\text{H}_2\text{O}$, it could be assumed that the improvement in the behavior shown in Figure 15 is because more MgCl_2 is available in the sample, and this is the material that is actually reacting. Nevertheless, the average onset temperatures were obtained from the thermogravimetric results, as is shown in Table 3. Furthermore, these temperatures were also added to the van't Hoff diagram as is shown in Figure 18. The semitransparent bars correspond to the error of each onset temperature. It can be seen that the temperatures at which the reactions start (ϑ_{ONSET}) are different when the experiments were carried out with synthetic sample in comparison with those with “only synthetic $\text{MgCl}_2 \cdot 6\text{H}_2\text{O}$ ”. In the first case, the onset temperatures are significantly close to the $\text{KCl} \cdot \text{MgCl}_2$ equilibrium temperatures (6–2). While in the second case, the onset

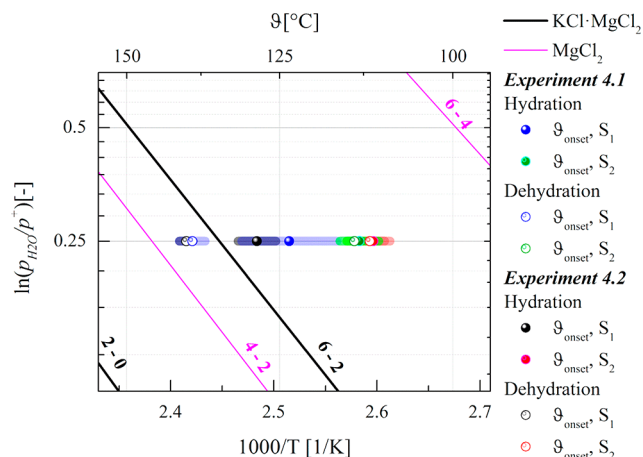


Figure 18. Van't Hoff diagram of $\text{KCl} \cdot \text{MgCl}_2 \cdot 6\text{H}_2\text{O}$ (carnallite) and $\text{MgCl}_2 \cdot 6\text{H}_2\text{O}$, and their experimental onset temperatures of hydration and dehydration from experiments 4.1 and 4.2.

temperatures are between the $\text{KCl} \cdot \text{MgCl}_2$ equilibrium temperatures (6–2) and MgCl_2 equilibrium temperatures (6–4).

Under these circumstances it can be concluded that both materials, carnallite and $\text{MgCl}_2 \cdot 6\text{H}_2\text{O}$, are active. However, the mechanism of the effect of $\text{MgCl}_2 \cdot 6\text{H}_2\text{O}$ on the reaction of carnallite is yet unclear.

Considering that the reactions of $\text{MgCl}_2 \cdot 6\text{H}_2\text{O}$ and carnallite are undergone simultaneously in experiment 4.2, the calculation of active and inactive material in the synthetic sample was also carried out (see Figure 19). It can be seen that the amount of active material over cycles of this experiment is significantly higher compared to the results obtained from experiment 4.1, shown in Figure 13.

Finally, the effect of temperature and isothermal time on the enthalpies of reaction was analyzed. Figure 20 shows the enthalpies of hydration and dehydration obtained from experiments performed for synthetic samples. Figure 20(a) shows the results of experiment 4.1, which, as expected shows a decrease of the enthalpies over cycles, from a maximum absolute value of 168.5 [kJ/mol] to 4.0 [kJ/mol], due to the decomposition of the sample. The results of experiment 4.2

Table 3. Average Onset Temperatures of Synthetic Sample and Synthetic $\text{MgCl}_2 \cdot 6\text{H}_2\text{O}$ Obtained from Experiments 4.1 and 4.2

In Figure 18	Sample	Experiment 4.1		Experiment 4.2	
		Hydration ϑ_{ONSET} ($^\circ\text{C}$)	Dehydration ϑ_{ONSET} ($^\circ\text{C}$)	Hydration ϑ_{ONSET} ($^\circ\text{C}$)	Dehydration ϑ_{ONSET} ($^\circ\text{C}$)
S ₁	Synthetic sample	124.4 ± 7.3	139.9 ± 2.1	129.5 ± 3.0	140.9 ± 1.1
S ₂	Only synthetic $\text{MgCl}_2 \cdot 6\text{H}_2\text{O}$	114.0 ± 2.8	114.8 ± 1.1	112.0 ± 2.4	112.5 ± 2.2

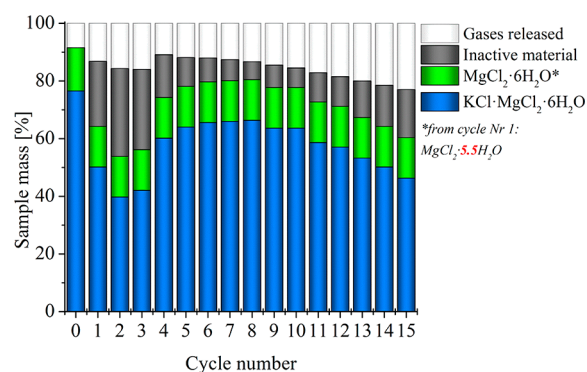


Figure 19. Amount of active and inactive material through cycles based on results of experiment 4.2.

(Figure 20(b)) show lower yet more constant behavior over cycles with an average absolute value of 99.9 ± 13 kJ/mol.

Using these values, the energy storage density of carnallite was calculated and compared with values reported for other systems of reaction that operate under similar conditions. The results are shown in Table 4.

Following this path, any potential application of this material is definitely limited to low temperature thermal storage or thermal upgrade. Taking the low material cost into account, one of the potential applications of this material could also be in the context of long-term heat storage. For this purpose, the temperatures of dehydration can be below 150 °C and the temperatures of rehydration close to 40 °C under lower water vapor partial pressures ($p_{H_2O} < 1.5$ kPa).^{26,27} Additionally, even though this work gives the first ideas on how to improve the cycling stability of carnallite containing materials as TCM, still further improvements and a better understanding of the decomposition mechanisms are necessary.

Apart from the temperature control presented in this study, previous works report different methods in order to prevent the hydrolysis reaction of magnesium salts, during their dehydration. The most popular of all is the dehydration of magnesium chloride hexahydrate or carnallite in an atmosphere of HCl in order to increase the amount of $MgCl_2$ for different applications.^{28,31,38–41} Due to the hazardousness of HCl, this method has not been tested in this study. Another method suggested is the use of additives in order to improve the cycling stability of the reaction of magnesium chloride hexahydrate.⁴² The case of carnallite derived from waste material offers interesting characteristics of a specific application, and further

studies could evaluate if this method can have the same effect on the investigated material in this study.

Future work will concentrate on the investigation of waste material and its comparison with the synthetic one used for this study. Since the amount of carnallite is around 75% comparable but the presence of bischofite can be excluded, a reduced tendency for hydrolysis can be expected—at least if material impurities contained in the waste material do not have a comparable impact.

CONCLUSIONS

The thermal stability of a high carnallite-bearing material, its possibility to rehydrate, and consequently its potential operating conditions as a thermochemical energy storage material were identified. That is, the maximum charging temperature (dehydration) was identified at 150 °C, for 10 min, and the discharging temperature (rehydration) at 100 °C, for both processes using 25 kPa of partial vapor pressure in nitrogen.

Furthermore, hydrolysis of magnesium chloride hexahydrate contained in the synthetic material at temperatures below 200 °C was observed. Also the decomposition and/or melting of the magnesium chloride hexahydrate present in the sample was confirmed as an inactive material as well as a low reactive material. This has a strong impact on the cycling stability of carnallite when applied as a thermochemical material. In the first case, the amount of active material (reactive carnallite) is also reduced under the operating conditions used in this study. As a consequence, the specific capacity of the thermochemical storage of carnallite is reduced. And in the second case, even when the reduction of active material was observed, the magnesium chloride hexahydrate seems to have a positive effect on the carnallite, stabilizing it over cycles.

Additionally, further experiments to understand the progressive decomposition of carnallite as TCM have been performed. It was shown that the dehydration of carnallite occurs quickly which allows a limit in the time of high temperature exposure. By doing so, a remarkable improvement of the cycling stability of the synthetic material could be observed. However, further improvements on cycling stability are necessary if carnallite should be used in thermochemical storage.

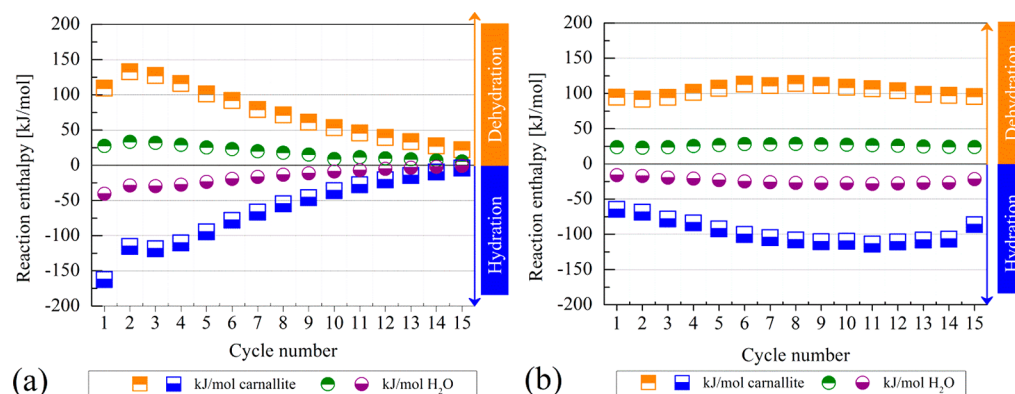


Figure 20. Enthalpies of hydration and dehydration from experiments 4.1 and 4.2 for synthetic samples.

Table 4. Enthalpy of Reaction and Energy Storage Density for Different Salt Hydrate Reaction Systems

$MX \cdot nH_2O_{(s)}$	$MX \cdot mH_2O_{(s)}$	$(n - m)$	$\Delta_R H$ [kJ/mol]	$\Delta_R H / (n - m)$ [kJ/mol]	Price ^a [Euro/MJ]	esd ^c [kWh/m ³]
KCl·MgCl ₂ ·6H ₂ O	KCl·MgCl ₂	6	191.1	31.9	0.05 ^b	303.94
CaCl ₂ ·2H ₂ O	CaCl ₂ ·0.3H ₂ O	1.7	114.0	67.1	0.21	341.63
Al ₂ (SO ₄) ₃ ·18H ₂ O	Al ₂ (SO ₄) ₃ ·8H ₂ O	10	554.5	55.4	0.21	366.57
LiCl·H ₂ O	LiCl	1	62.2	62.2	11.81	453.64
LaCl ₃ ·7H ₂ O	LaCl ₃ ·H ₂ O	6	355.5	59.3	24.57	421.72
K ₂ CO ₃ ·1.5H ₂ O	K ₂ CO ₃	1.5	95.5	63.7	2.10	254.64

^aConsidering only the price of medium of storage. Price obtained from Alibaba for industrial quality of materials (www.alibaba.com February 2018).

^bThe price of low quality bischofite 40US\$/ton (31.1 Euro/ton, February 2018), obtained from Salar de Atacama was used as a reference to calculate costs of investment for using carnallite. ^c $\rho = 1586 \pm 94$ [kg/m³].

■ ASSOCIATED CONTENT

Supporting Information

The Supporting Information is available free of charge on the ACS Publications website at DOI: [10.1021/acssuschemeng.7b04803](https://doi.org/10.1021/acssuschemeng.7b04803).

The operating conditions of experiment 2 and experiment 4 using MgCl₂·6H₂O, the van't Hoff plot of KCl·MgCl₂ and MgCl₂ with the respective operating conditions of both experiments, and results of experiment 2 using MgCl₂·6H₂O and molten sample after experiment 4.2. (PDF)

■ AUTHOR INFORMATION

Corresponding Author

*E-mail: andrea.gutierrezrojas@dlr.de. Tel: +49-(0)711-6862-8236.

ORCID

Andrea Gutierrez: 0000-0002-6313-8264

Notes

The authors declare no competing financial interest.

■ ACKNOWLEDGMENTS

The work at the University of Antofagasta was supported by CONICYT/FONDAP N° 15110019 and CONICYT/FONDECYT/REGULAR/N°1170675. Andrea Gutierrez would like to thank CONICYT - PROGRAMA EN ENERGÍAS Convocatoria 2015, Green Talents (BMBF-FONA2), and DAAD for her fellowships.

■ REFERENCES

- Hasnain, S. M. review on sustainable thermal energy storage technologies, part I: Heat storage materials and techniques. *Energy Convers. Manage.* **1998**, *39* (11), 1127–1138.
- Sharma, A.; Tyagi, V. V.; Chen, C. R.; Buddhi, D. Review on thermal energy storage with phase change materials and applications. *Renewable Sustainable Energy Rev.* **2009**, *13* (2), 318–345.
- Miró, L.; Navarro, M. E.; Suresh, P.; Gil, A.; Fernandez, A. I.; Cabeza, L. F. Experimental characterization of a solid industrial by-product as material for high temperature sensible thermal energy storage (TES). *Appl. Energy* **2014**, *113*, 1261–1268.
- Ushak, S.; Gutierrez, A.; Galleguillos, H.; Fernandez, A. G.; Cabeza, L. F.; Grágeda, M. Thermophysical characterization of a by-product from the non-metallic industry as inorganic PCM. *Sol. Energy Mater. Sol. Cells* **2015**, *132*, 385–391.
- Gutierrez, A.; Miró, L.; Gil, A.; Rodríguez-Aseguinolaza, J.; Barreneche, C.; Calvet, N.; Py, X.; Fernández, A. I.; Grágeda, M.; Ushak, S.; Cabeza, L. F. Advances in the valorization of waste and by-product materials as thermal energy storage (TES) materials. *Renewable Sustainable Energy Rev.* **2016**, *59*, 763–783.
- Gutierrez, A.; Ushak, S.; Mamani, V.; Vargas, P.; Barreneche, P.; Cabeza, L. F.; Grágeda, M. Characterization of wastes based on inorganic double salt hydrates as potential thermal energy storage materials. *Sol. Energy Mater. Sol. Cells* **2017**, *170*, 149–159.
- Letcher, T. M. In *Storing Energy: with Special Reference to Renewable Energy Sources*, 1st ed.; Elsevier: Oxford, 2016.
- Hadorn, J. C. Advanced storage concepts for active solar energy. In *Proceedings of EUROSUN 2008*; 1st International congress on heating, cooling and Buildings, October 7th to 10th, Lisbon, Portugal.
- Abedin, A. H.; Rosen, M. A. A critical review of thermochemical energy storage systems. *Open Renewable Energy J.* **2011**, *4*, 42–46.
- Weck, P. F.; Kim, E. Solar energy storage in phase change materials: First-Principles thermodynamic modeling of magnesium chloride hydrates. *J. Phys. Chem. C* **2014**, *118* (9), 4618–4625.
- Lizana, J.; Chacartegui, R.; Barrios-Padura, A.; Valverde, J. M. Advances in thermal energy storage materials and their applications towards zero energy buildings: A critical review. *Appl. Energy* **2017**, *203*, 219–239.
- Solé, A.; Fontanet, X.; Barreneche, C.; Fernández, A. I.; Martorell, I.; Cabeza, L. F. Requirements to consider when choosing a thermochemical material for solar energy storage. *Sol. Energy* **2013**, *97*, 398–404.
- Richter, M.; Bouché, M.; Linder, M. Heat transformation based on CaCl₂/H₂O – Part A: Closed operation principle. *Appl. Therm. Eng.* **2016**, *102*, 615–621.
- Bouché, M.; Richter, M.; Linder, M. Heat transformation based on CaCl₂/H₂O – Part B: Open operation principle. *Appl. Therm. Eng.* **2016**, *102*, 641–647.
- Richter, M.; Habermann, E. M.; Siebecke, L.; Linder, M. A systematic screening of salt hydrates as materials for a thermochemical heat transformer. *Thermochim. Acta* **2018**, *659*, 136–150.
- Cabeza, L. F., Ed. *Advances in thermal energy storage systems: Methods and applications*, 1st ed.; Elsevier, 2014.
- Donkers, P. A. J. Experimental study on thermochemical heat storage materials. Ph.D. Dissertation, Eindhoven University of Technology, Eindhoven, Netherlands, 2015.
- Mamani, V.; Gutierrez, A.; Li20nder, M.; Ushak, S. Characterization of an industrial waste based on double salt hydrate with potential use as thermochemical material. In *Proceedings: SDEWES - 1st Latin American conference on sustainable development of energy, water and environment systems*, 2018, January 28th to 31th, Rio de Janeiro, Brazil.
- Mamani, V.; Gutierrez, A.; Ushak, A. Inorganic Industrial Wastes used as Thermochemical Energy Storage Materials. In *Proceedings of SWC 2017/SHC 2017 2017*, October 29–November 02, Abu Dhabi, United Arab Emirates, 2017.
- Korotkov, J. A.; Mikhkailov, E. F.; Andreevm, G. A.; Eltsov, B. I.; Plyakov, J. A.; Shestakov, B. G.; Kechina, G. D. Method of dehydrating carnallite. United States Patent Nr. 4,224,291, 1980.
- Molenda, M.; Stengler, J.; Linder, M.; Wörner, A. Reversible hydration behavior of CaCl₂ at high H₂O partial pressures for thermochemical energy storage. *Thermochim. Acta* **2013**, *560*, 76–81.
- Emons, H.-H.; Naumann, R.; Pohl, T.; Voigt, H. Thermoanalytical investigations on the decomposition of double salts: I. the decomposition of carnallite. *J. Therm. Anal.* **1984**, *29* (3), 571–579.

(23) Friedrich, H. E.; Mordike, B. L. *Magnesium Technology, Metallurgy, Design Data, Applications*, 1st ed.; Springer: Berlin Heidelberg, 2006.

(24) Zondag, H. A.; van Essen, V. M.; Bleijendaal, L. P. J.; Kikkert, B. W. J.; Bakker, M. Application of $\text{MgCl}_2 \cdot 6\text{H}_2\text{O}$ for thermochemical seasonal solar heat storage. Presented at the the 5th International Renewable Energy Storage Conference IRES 2010, Berlin, Germany, 2010.

(25) Ferchaud, C. J.; Zondag, H. A.; Veldhuis, J. B.; de Boer, R. Study of the reversible water vapour sorption process of $\text{MgSO}_4 \cdot 7\text{H}_2\text{O}$ and $\text{MgCl}_2 \cdot 6\text{H}_2\text{O}$ under the conditions of seasonal solar heat storage. *J. Phys.: Conf. Ser.* **2012**, 395, 012069.

(26) Gutierrez, A.; Ushak, S.; Linder, M. Carnallite as potential thermochemical energy storage material for seasonal heat storage applications. In *Proceedings: IWLiME 2017—4th International Workshop on Lithium, Industrial Minerals and Energy*, 2017, September 25th – 27th, Cochabamba, Bolivia.

(27) Donkers, P. A. J.; Sögütöglü, L. C.; Huinink, H. P.; Fischer, H. R.; Adan, O. C. G. A review of salt hydrates for seasonal heat storage in domestic applications. *Appl. Energy* **2017**, 199, 45–68.

(28) Kelley, K. K. *Energy requirements and equilibria in the dehydration, hydrolysis, and decomposition of magnesium chloride*; United States Government Printing Office: WA, 1945.

(29) Mamani, V.; Gutierrez, A.; Ushak, S. Development of low-cost inorganic salt hydrate as a thermochemical energy storage material. *Sol. Energy Mater. Sol. Cells* **2018**, 176, 346–356.

(30) Ferchaud, C. Experimental study of salt hydrates for thermochemical seasonal heat storage. Ph.D. Dissertation, Eindhoven University of Technology, Eindhoven, Netherlands, 2016.

(31) Smeets, B.; Iype, E.; Nedea, S. V.; Zondag, H. A.; Rindt, C. C. M. A DFT based equilibrium study on the hydrolysis and the dehydration reactions of MgCl_2 hydrates. *J. Chem. Phys.* **2013**, 139 (12), 124312.

(32) Huang, Q.; Lu, G.; Wang, J.; Yu, J. Thermal decomposition mechanisms of $\text{MgCl}_2 \cdot 6\text{H}_2\text{O}$ and $\text{MgCl}_2 \cdot \text{H}_2\text{O}$. *J. Anal. Appl. Pyrolysis* **2011**, 91 (1), 159–164.

(33) Zalba, B.; Marín, J. M.; Cabeza, L. F.; Mehling, H. Review on thermal energy storage with phase change: materials, heat transfer analysis and applications. *Appl. Therm. Eng.* **2003**, 23 (3), 251–283.

(34) Cabeza, L. F.; Castell, A.; Barreneche, C.; de Gracia, A.; Fernández, A. I. Materials used as PCM in thermal energy storage in buildings: a review. *Renewable Sustainable Energy Rev.* **2011**, 15 (3), 1675–1695.

(35) Abhat, A. Low temperature latent heat thermal energy storage: heat storage materials. *Sol. Energy* **1983**, 30 (4), 313–332.

(36) Dincer, I.; Rosen, M. A. *Thermal energy storage, systems and applications*, 2nd ed.; John Wiley & Sons, Ltd, Press: Chichester, 2002.

(37) Naumann, R.; Emons, H. H. Results of thermal analysis for investigation of salt hydrates as latent heat-storage materials. *J. Therm. Anal.* **1989**, 35 (3), 1009–1031.

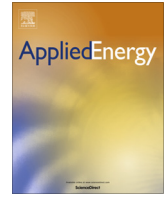
(38) Mehling, H.; Cabeza, L. F. *Heat and cold storage with PCM. An up to Date introduction into basics and applications*, 1st ed.; Springer Press: Berlin Heidelberg, 2008.

(39) Kipouros, G. J.; Sadoway, D. R. A thermochemical analysis of the production of anhydrous MgCl_2 . *J. Light Met* **2001**, 1 (2), 111–117.

(40) Moscowitz, H.; Lando, D.; Cohen, H.; Wolf, D. Bishophite Chlorination. *Ind. Eng. Chem. Prod. Res. Dev.* **1978**, 17 (2), 156–160.

(41) Liu, X.; Cui, X. Research progress in dehydration technology of bischofite for preparing anhydrous magnesium chloride. *5th International Conference on Civil Architectural and Hydraulic Engineering (ICCAHE 2016)*; 2016; pp 261–267.

(42) Rammelberg, H. U.; Osterland, T.; Priehs, B.; Opel, O.; Ruck, W. K. L. Thermochemical heat storage materials – Performance of mixed salt hydrates. *Sol. Energy* **2016**, 136, 571–589.



Thermochemical energy storage with CaO/Ca(OH)₂ – Experimental investigation of the thermal capability at low vapor pressures in a lab scale reactor



Matthias Schmidt^{a,*}, Andrea Gutierrez^b, Marc Linder^b

^a German Aerospace Center – DLR e.V., Institute of Technical Thermodynamics, Linder Höhe, 51147 Köln, Germany

^b German Aerospace Center – DLR e.V., Institute of Technical Thermodynamics, Pfaffenwaldring 38, 70569 Stuttgart, Germany

HIGHLIGHTS

- Development of a novel indirectly heated reaction bed for thermochemical energy storage.
- Experimental demonstration of thermal charging and discharging at low vapor pressures (1.4–20 kPa).
- Experimental study of the reaction at various heating and cooling loads of the heat transfer fluid.
- Identification of operational limits under some technically relevant boundary conditions.

ARTICLE INFO

Article history:

Received 24 August 2016

Received in revised form 18 October 2016

Accepted 7 November 2016

Available online 21 December 2016

Keywords:

Thermochemical energy storage

Calcium hydroxide

Calcium oxide

Operation modes

Low vapor pressures

Thermal charging and discharging

ABSTRACT

The reversible reaction of calcium hydroxide (Ca(OH)₂) to calcium oxide (CaO) and water vapor is well known in the context of thermochemical energy storage. Cheap material costs, a theoretically very high energy density and the potentially wide temperature range of the reaction imply that the storage system could be beneficial for many high temperature processes. For example the system could be applied to store and reutilize industrial waste heat or as an alternative storage solution in future concentrated solar power plants.

In this publication the reaction is experimentally investigated in an indirectly operated fixed bed reactor at different technically relevant but so far not investigated operating conditions. This in particular means the thermal charging and discharging of the storage at low water vapor pressures under different heating and cooling loads induced by a heat transfer fluid. The experiments revealed that the reaction gas handling not only affects the operating range of the storage but has also a significant influence on its thermal capability. Especially at low vapor pressures operational limits of the system have been identified and could be contributed to the effective reaction rate of the reaction material which is in the relevant operating range very sensitive to small changes of the local reaction conditions.

© 2016 Elsevier Ltd. All rights reserved.

1. Introduction

Thermochemical energy storage by means of the reversible gas solid reaction of calcium hydroxide (Ca(OH)₂) to calcium oxide (CaO) and water vapor offers several advantages. Firstly, calcium hydroxide is a cheap industrial mass product abundantly available all over the world. Secondly, the enthalpy of reaction is high which leads to high possible energy storage densities. Thirdly, the charge and discharge temperature of the reaction can theoretically be

adapted in a wide range (approx. 300–650 °C). Thus the application of the system could potentially be beneficial for many high temperature processes such as the storage and reutilization of industrial waste heat [1] or as an alternative storage solution in future concentrated solar power plants [2–5].

The reaction system has been examined in many studies but the majority of the studies focus on the thermal analysis of small sample masses. Already in 1979 Rosemary and his colleagues demonstrated cycle stability of the reaction for 1171 cycles [6]. Until today different research groups derive kinetic equations from de-and rehydration experiments carried out in thermogravimetric devices [7–9]. Beyond that other groups focus on the modification

* Corresponding author.

E-mail address: Matthias.schmidt@dlr.de (M. Schmidt).

Nomenclature

HEX	heat exchanger	t	time
TGA	thermogravimetric analysis	ϑ	temperature measurement point, thermocouple
P	pressure	\dot{V}	volume flow
T	temperature	X_{tot}	conversion
F	filling level	d_{50}	median diameter of the particle size distribution

of the material in order to adapt the reaction temperature [10], enhance the reaction rate [11], improve powder bed properties [12], or to achieve mechanically stable pellets [13]. Simulation models based on the kinetic equations and the theory of porous media have also been established [14,15].

Besides these investigations on the material level, reports on experiments with lab scale reactors are scarce. Schaubé et al. demonstrated the operation of a fixed bed reactor where the material is in direct contact with a gas mixture of air and water vapor [16]. Pardo et al. carried out the reaction in a fluidized bed reactor using a mixture of $\text{Ca}(\text{OH})_2$ and 70 wt% inert easy to fluidize particles [17]. Yan et al. recently reported experiments with 400 g of material in a fixed bed set up. They analyzed the hydration reaction at different vapor pressures but the reactor concept did not allow the recovery of the released heat. Furthermore the dehydration reaction was driven by an electrical heating jacket [18].

All of these concepts have their special advantages and are worth investigating since at the current state of development an optimal reactor design is not available. However, some process applications require an indirectly heated concept. For example, if the heat transfer fluid of the process is liquid or a direct contact of the flue gas and the storage material could cause impurities. In both cases thermal energy has to be transferred via a heat exchanging surface that separates the reaction from the heat transfer fluid – a so called indirect concept. An additional advantage of this concept is that the reaction temperature can be adapted independently from the power output of the reactor. This in conclusion leads to more flexible operating modes and thus could extend process integration possibilities.

However for indirectly heated reactor concepts there is even less experimental data available. Ogura et al. were the first who demonstrated a concept where the heat released during the exothermic reaction was transferred via a heat exchanger to an air flow at ambient temperature [19]. The dehydration step though was still performed in a furnace. The first concept in which not only the discharging but also the charging step was driven by an indirect coupling of the reaction bed with a heat transfer fluid was presented from our group in a previous publication [20]. On one hand the reactor showed good performance especially for the discharge at reaction gas pressures of 100 kPa and higher. On the other hand the design of the reaction bed limited the operating range of the reactor. Particularly at low vapor pressures (e. g. 10 kPa) the performance during charging and discharging was significantly limited. We mainly contributed this limitation to the mass transfer of the reaction gas due to the low permeable reaction bed and its height of 200 mm.

Nevertheless, as soon as energy efficient process integration is considered, the operation of the storage system at low vapor pressures is of high technical relevance. There are two main reasons for that. Firstly, the dehydration at lower vapor pressures results in a lower reaction temperature. As a consequence we can use lower grade heat to charge the storage. Secondly, the hydration at lower vapor pressures requires only a reduced evaporation temperature. Therefore the enthalpy of evaporation can more likely be supplied by waste heat available from the process. On the other hand, operating the system at low

vapor pressures makes the reactor design more challenging and requires larger pipe diameters for the vapor connections. Thus it finally depends on the specific process if an operation at lower or higher pressure levels is more promising.

Fig. 1 shows the experimentally obtained equilibrium lines of the reaction system $\text{Ca}(\text{OH})_2/\text{CaO}$ from Schaubé [8] and Samms [21] as well as the theoretical equilibrium line based on thermochemical values from Barin [22]. In addition reported onset temperatures, determined in thermogravimetric measurements from Schaubé [8] and Matsuda [23] are displayed as well as the results of equilibrium measurements performed by Halstead [24] in an appropriate test bench. It is obvious that within the important operating range for indirect concepts at low vapor pressure (marked as grey area), the results vary significantly. This may be on one side contributed to differences in the used material but on the other side also the measurement principle itself (e.g. dynamic or static) might have an influence.

In order to investigate the reaction for thermochemical storage under technically relevant operating conditions, we designed a novel reaction bed with minimized mass transfer limitations but a sufficient mass of reactive material to investigate thermal capabilities. With this reactor we performed several charging and discharging experiments at low vapor pressures and analyzed the influence of different heating and cooling loads induced by a heat transfer fluid. The operating conditions for the kg-scale experiments presented in this study are marked in Fig. 1 by the red triangles for the dehydration and the red squares for the hydration. For the analysis of the results, the experiments in lab-scale were complemented by thermogravimetric measurements in mg-scale with the same material.

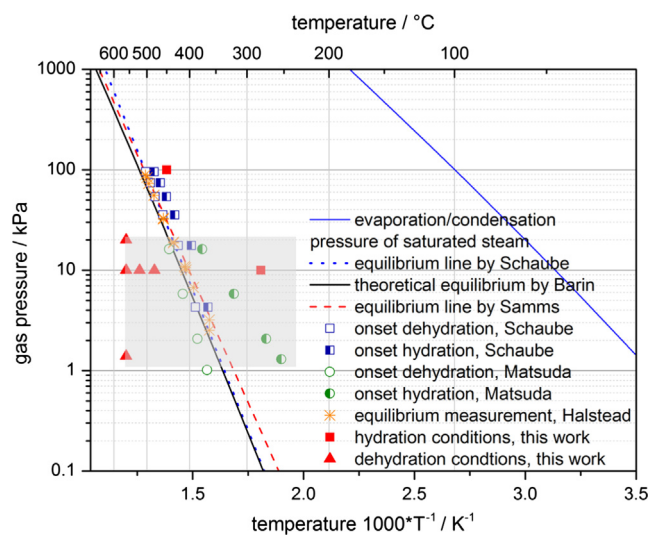


Fig. 1. Thermodynamic equilibrium lines for the $\text{Ca}(\text{OH})_2/\text{CaO}$ reaction system and operating conditions of the performed experiments; evaporation/condensation pressure of saturated steam.

2. Experimental set up

2.1. Reactor

The aim of the reaction bed development was to analyze the performance of the storage material for a wide operating range. The main limitations that are generally contributed to the reactor (not to the material) are mainly caused by the low permeability and the poor thermal conductivity of the bulk material. Bearing in mind to minimize these limitations without affecting the material properties we derived two important design constraints for the novel reactor. First of all, the reaction gas should only pass through a very thin layer of storage material. Secondly, the furthest distance between a single particle and the heat exchange surface should be short. Both design constraints would in principle lead to a very small mass of reaction material. In contrast a representative mass of reaction material is mandatory, in order to be able to operate the material according to the later application as thermochemical storage and to allow for both: a proper analysis of the thermal capability of the reaction and the analysis of the impact of the indirect heating or cooling.

Taken all design constraints into account it is obvious that the reactor has to offer a reasonable compromise between a reactor for investigations and a reactor for thermochemical energy storage. For this purpose, we choose a single heat exchanger plate as the basis for our reaction bed (see Fig. 1, top). In this concept, the heat transfer fluid, air, flows inside the plate while the storage material lies on the plate. The plate is on both sides surrounded by a metallic frame of 10 mm height. The inner sides of the frame measure 150 mm in width and 1600 mm in length giving us 0.48 m² heat exchange surface. Consequently the reactor offers a cubic volume of 4.8 L (2.4 L on each side of the plate) for the storage material (see Fig. 2, bottom left). A gas permeable metallic filter (pore size is 5 μm) placed over the powder material and screwed to the frame encases the reaction bed (see Fig. 1, bottom right). The large filter area allows for a negligible pressure drop between the powder material and the reaction gas supply.

The heat exchanger plate with the encased bed on both sides is mounted into a pressure resistant casing pipe. Fig. 3 shows a sectional view of the whole set up including important dimensions and positions of the measurement instruments. To observe the reaction progress seven thermocouples ϑ_{1-7} (type K, $\pm 0.4\%$ X T) are located in the middle of the beds height, at a vertical distance

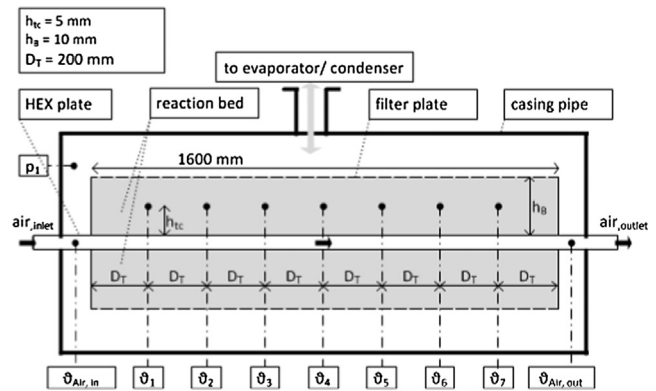


Fig. 3. Sectional view of the reaction bed in the casing pipe including important dimension and positions of thermocouples and the pressure sensor.

of 5 mm to the heat exchange surface. In the horizontal direction of air flow the distance between each measurement point is 200 mm with the first point 200 mm away from the beginning of the reaction bed. Additional thermocouples measure the air temperature directly at the air in- ($\vartheta_{Air,in}$) and outlet ($\vartheta_{Air,out}$) of the plate. Due to the design of the heat exchanger it was not possible to measure the air temperature directly at the position opposite of the thermocouples in the reaction bed. Furthermore a pressure sensor p_1 (PPA-35XHTT, Keller Ges. für Druckmesstechnik mbH, ± 0.8 kPa) measures the gas pressure in the reaction chamber.

2.2. Material

All experiments presented in this paper we performed with Ca(OH)₂, product type “Sorbacal®H”, supplied by Rheinkalk GmbH/Lhoist group. Based on the products data sheet the purity of the material is approximately 98% the specific surface area is 19 m²/g and the d_{50} is 5.5 μm.

2.3. Test bench

Fig. 4 shows the schematic process flow diagram of the test bench. The test bench was designed to operate the reactor under different thermal load conditions and at a wide range of vapor



Fig. 2. Top: heat exchanger plate used as reactor; bottom left: storage material filled into the frame; bottom right: filter plate to encase the reaction bed.

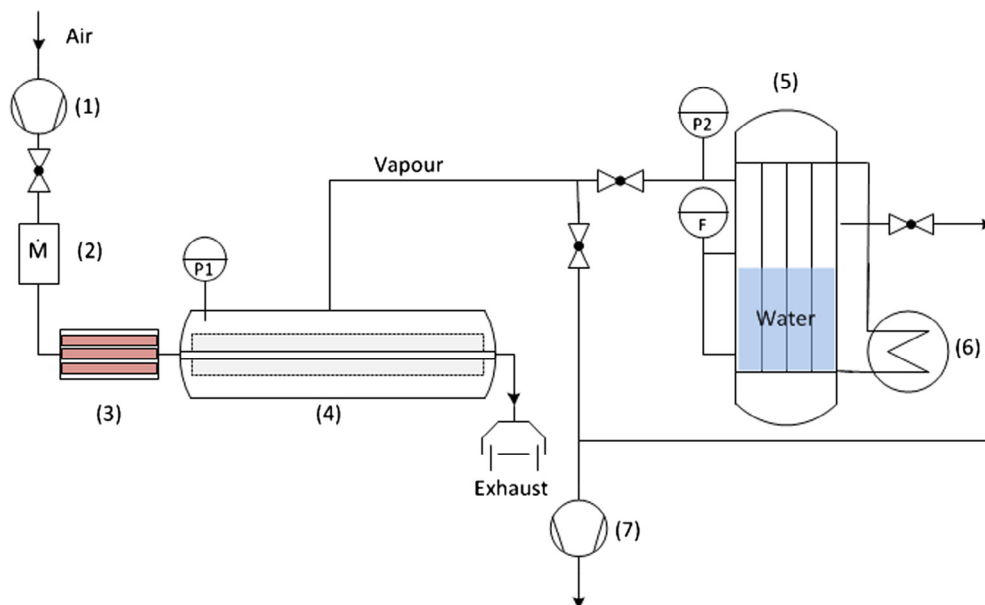


Fig. 4. Layout of the test bench.

pressures. Therefore it was most important to be able to adjust the thermal power of the heat transfer fluid and the vapor pressure in the reaction chamber independently of each other.

2.3.1. Heat transfer fluid supply

Due to the required temperatures, ambient air is used as heat transfer fluid in the experiments and is supplied by a compressor (1). The air volume flow can be adjusted with a mass flow controller (2) (Bronkhorst, digital flow controller, $\pm 0.4\%$) before it splits up and enters three parallel electrical heating units (3). Each heating unit has an electrical power of 2 kW and preheats the air to a maximum temperature of 600 °C. After these heating units the air flows merge again in a diminishing pipe. This diminishing pipe is equipped with a controllable auxiliary heating to ensure a homogenous air temperature at the reactor inlet.

2.3.2. Reaction gas handling

During an ongoing reaction we must either remove water vapor from or supply it to the reaction bed. To realize this, a tube bundle heat exchanger (5) and a vacuum pump (7) are connected to the reactor. With the vacuum pump inert gases are removed from the system ensuring a pure vapor atmosphere. The tube bundle heat exchanger operates as condenser or evaporator depending on the direction of reaction. A thermal oil flows inside the tubes of the bundle. The oils inlet temperature can be tempered between 3 and 160 °C by a thermostatic bath (6). On the shell side is liquid water (for condensation or evaporation) and the water temperature can be kept constant during experiments because the thermal oil takes up the heat of condensation or supplies the heat of evaporation. Accordingly the evaporation/condensation pressure in the system can be varied between 0.7–618 kPa and be kept constant during an ongoing reaction. A pressure sensor at the outlet flange measures the pressure in the evaporator/condenser and the change of the water level is measured with a filling level meter (Vegaflex 65, ± 2 mm). By means of this value we can monitor the reaction and calculate its conversion.

2.4. Experimental procedure

For all experiments presented in this paper only one batch of the material described in 2.2 is used. In total 2.4 kg are filled in

the reactor, equally distributed on each side of the heat exchanger plate. Overall 33 cycles were performed with the same batch of material. Before every experiment the whole set up is evacuated to 0.5 kPa \pm 0.3 kPa and afterwards all valves are closed. The reactor is preheated to a set starting temperature with the air volume flow and additional auxiliary heating cables attached to the casing pipe. Simultaneously we adjust the vapor pressure for the experiment in the condenser/evaporator by the thermostatic bath. As soon as the pressure in the condenser/evaporator and the temperatures in the reaction bed stay constant an experiment can be started.

The different operating conditions were shown above (compare Fig. 1). From the equilibrium line for water and saturated steam (blue solid line in Fig. 1) the operating temperature of the condenser/evaporator at the required pressure can be determined. Besides the different temperatures, in some experiments the volume flow of the heat transfer fluid has also been varied. The volume flows as well as an overview of all parameters of each presented experiment is given in Table 1.

2.4.1. Thermal charging procedure (Dehydration)

At the beginning of each dehydration only $\text{Ca}(\text{OH})_2$ is in the reactor and the set up is preheated to a temperature below the equilibrium temperature of the reaction at the adjusted vapor pressure. To start the experiment the valve between condenser and reactor is opened and simultaneously the air inlet temperature is increased to the set dehydration temperature (marked with red triangles in Fig. 1). The induced heat load drives the dehydration reaction. Accordingly water vapor comes out of the reaction bed and condenses in the condenser. When no further increase of the water level is observed the dehydration is finished.

2.4.2. Thermal discharging procedure (Hydration)

At the beginning of every hydration experiment only CaO is in the reactor and the set up is preheated to a set starting temperature (marked with red squares in Fig. 1) below the equilibrium temperature of the adjusted evaporation pressure. To start the experiment the valve between reactor and evaporator is opened. In that moment water vapor streams into the reaction chamber and initiates the exothermic hydration reaction. The air flow takes up the heat of reaction as long as the reaction proceeds.

Table 1
Parameters of all experiments presented in this study.

Experiment	$T_{\text{air, initial}}/^{\circ}\text{C}$	$\dot{V}/\frac{\text{Nm}}{\text{h}}$	$T_{\text{air, inlet}}/^{\circ}\text{C}$	$P_{\text{condenser/evaporator}}/\text{kPa}$	$T_{\text{water}}/^{\circ}\text{C}$
<i>Dehydration</i>					
A	400	20	560	10	45
B	400	12	560	10	45
C	400	12	520	10	45
D	400	12	480	10	45
E	400	12	560	19.9	60
F	400	12	560	1.4	12
<i>Hydration</i>					
G	280	12	-	8.7	43
H	280	16	-	8.7	43
J	280	20	-	8.7	43
M	450	12	-	100	100

The experiment is finished as soon as the temperature in every region of the reaction bed has reached its starting value.

2.5. Thermogravimetric analysis

To compare some results observed in the reactor a small sample mass (10 mg) of the same batch has additionally been analyzed in the thermogravimetric analysis (TGA). For these experiments a NETZSCH simultaneous thermal analysis (STA 449 F3 Jupiter[®]) was used, equipped with a molar humidity generator (MHG32). The atmosphere during the measurements was inert using nitrogen, or a mixture of nitrogen and water vapor as purge gas (surrounds the sample) and pure nitrogen as the protective gas. The pressure inside the furnace was ambient pressure at ~ 97 kPa and a volume flow of 100 ml/min of purge gas was used. The bottom of the furnace was heated to 120 $^{\circ}\text{C}$ and a protection gas volume flow of 20 ml/min nitrogen was supplied, in order to protect the thermo-balance of condensation drops. The furnace design does not allow the mixing between the purge and protective gases, thus the protective gas flow does not affect the concentration of humidity inside of the furnace. The conversion is calculated by the ratio of the measured mass change of each cycle to the measured mass change of the first complete dehydration cycle. With this set up we were able to conduct isothermal hydration and dehydration experiments in the TGA at vapor pressures comparable to the conditions in the reactor.

3. Results and discussions

3.1. Set in operation

In order to prove the correct function of the reactor and the measurement equipment a hydration experiment at an evaporation pressure of 100 kPa according to the procedure as described in 2.4 was performed.

Fig. 5 shows the results of the experiment. The air inlet temperature $\vartheta_{\text{Air, in}}$ (red solid line) was kept constant at 450 $^{\circ}\text{C}$ during the experiment. At $t = 0$ min we open the valve between evaporator and reactor thus the pressure in the reactor rises to 100 kPa (black dash dotted line). Consequently the temperatures in the reaction bed ϑ_1 (green solid line) and ϑ_7 (blue solid line) jump up to a maximum of 507 $^{\circ}\text{C}$. This temperature accords to the theoretical equilibrium temperature (grey dashed line) which was calculated by the measured pressure and the respective correlation given by Samms et al. [21] (compare Fig. 1). The slight difference between the equilibrium temperature and the bed temperatures during the first 10 min is related to small pressure differences between the measured pressure in the casing pipe and the local pressure in

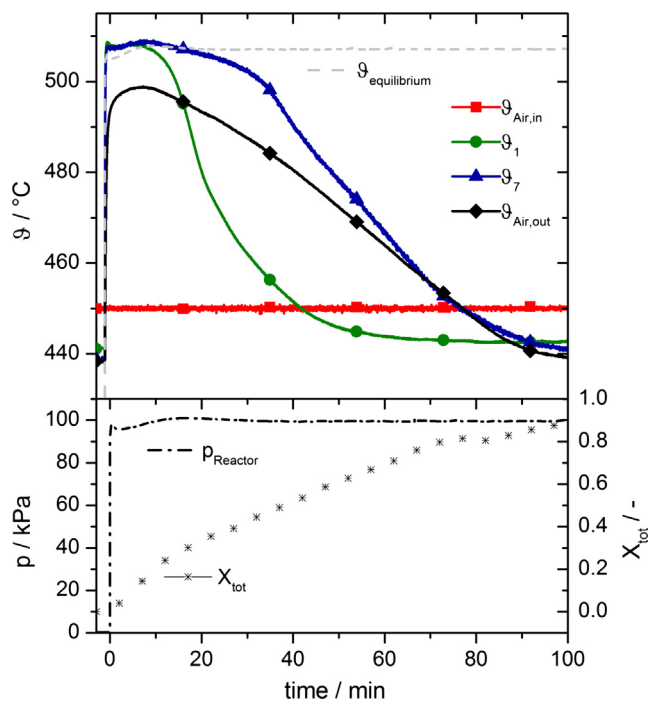


Fig. 5. Hydration experiment at 100 kPa and a starting temperature of 450 $^{\circ}\text{C}$.

the reaction bed. These differences are only significant during the initial period where dynamic changes occur in the system. We also observe a reaction front along the flow direction of the air. Close to the air inlet the cooling of the reaction bed is maximal due to the largest temperature difference between the bed and the air. Thus the reaction proceeds quickly and 10 min after the initiation the temperature ϑ_1 drops again. This indicates that a major part of the material is already converted in this region and the heat released by the reaction decreases. In contrast in the rear region of the reactor the temperature between the bed and the air flow is small in the beginning. As a consequence the reaction proceeds slower indicated by the constant temperature plateau which is hold for 25 min. As more and more material has reacted in this part also the temperature ϑ_7 starts to drop. After 100 min the bed reaches its initial temperature again indicating that no more heat is released. Accordingly, a conversion of 95% (black cross dots) is measured at this time. The difference before and after the reaction between air inlet temperature and temperatures inside the reaction bed are contributed to radiative heat losses inside the reaction chamber, that have been minimized but cannot be completely removed.

3.2. Thermal charging

A reference dehydration experiment has been performed with a preheating temperature of 400 °C and a condensation pressure of 10 kPa (condensation temperature 45 °C). Fig. 6 shows the temperature, pressure and conversion trends. At $t = 0$ min the air inlet temperature starts to rise up to the set dehydration temperature of 560 °C (red solid line). Exemplarily the temperatures ϑ_1 (green solid line) ϑ_3 (blue solid line) and ϑ_7 (orange solid line) positioned in the front, middle, and rear region (compare Fig. 2) of the bed are plotted. Within the first 30 min the material temperatures increase to 445 °C due to the incoming heat flux. At a temperature of 445 °C a significant change occurs in the slope of the temperature trend. In particular in the middle (ϑ_3) and rear region (ϑ_7) of the bed a temperature plateau can be observed. The temperature plateau indicates that the heat input from the heat transfer fluid is completely absorbed by the endothermic reaction. Accordingly during this time we also observe that the conversion trend (black cross dots) shows a constant rate indicating the ongoing reaction with a constant thermal charging power. After 120 min almost 80% of the material is converted thus the heat input in the rear region slowly becomes larger than the amount of heat which is still absorbed by the endothermal reaction. Consequently the material temperature rise again until after 200 min a conversion of 96% is reached and all bed temperatures reach their constant maximum. What might seem controversy is that the temperature plateau lies at 445 °C while the equilibrium temperature at the condensation pressure of 10 kPa is 400 °C (grey dash dotted line). This significant distance to the theoretical equilibrium temperature was further analyzed with a variation of thermal power of the heat transfer fluid.

3.2.1. Variation of heat load of the heat transfer fluid

In order to analyze the influence of the thermal power of the heat transfer fluid on the dehydration reaction, we performed the dehydration experiments at a condensation pressure of 10 kPa with 4 different thermal heat fluxes into the reaction bed. The

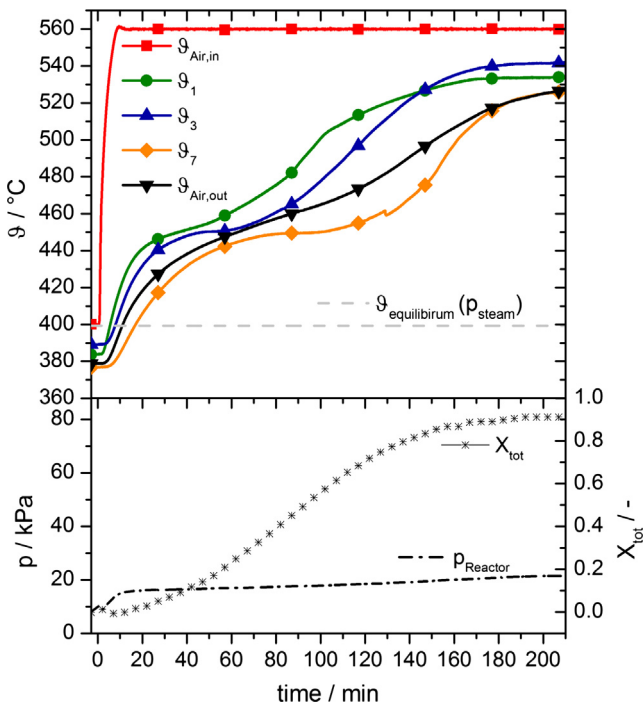


Fig. 6. Dehydration experiment at 10 kPa and an air inlet temperature of 560 °C.

results are shown in Fig. 7. Experiment A (red curves) runs with a 60% higher volume flow than the reference experiment B (green curves) but with the same air inlet temperature of 560 °C. Experiment C (blue curves) and D (orange curves) run with the nominal volume flow but at reduced air inlet temperatures of 520 °C respectively 480 °C (compare Table 1. for all parameters). The conversion curves show that the influence of the heat flux into the bed directly correlates with the speed of conversion. With the largest heat flux we receive the shortest dehydration time (red squares – experiment A), whereas smaller heat fluxes prolong the dehydration times (B, C, D).

Fig. 7 also shows the temperature trend of ϑ_7 for every experiment. We can see that independently from the heat flux into the bed, the material temperatures increase within the first 30 min. This indicates that initially the reaction speed is so slow that the incoming heat flux is larger than the thermal energy absorbed by the reaction. However a constant temperature plateau develops at temperatures above 440 °C for all experiments. In general, a temperature plateau region during dehydration is characterized by an equilibrium state between the thermal energy absorbed by the endothermic reaction and the heat flux delivered by the heat transfer fluid. It is remarkable that during the experiments A, B and C the plateau develops at the same temperature of 445 °C independently of the heat flux into the reaction bed. Only in experiment D the plateau temperature is slightly lower at 440 °C – but at the same time the charging power seems not anymore of technical relevance due to its long dehydration time.

The results support the hypothesis that a significant change in the rate of reaction occurs at temperatures above 440 °C. The rate of the reaction is then fast enough that the heat transfer becomes the limiting factor in the conducted experiments. However at low

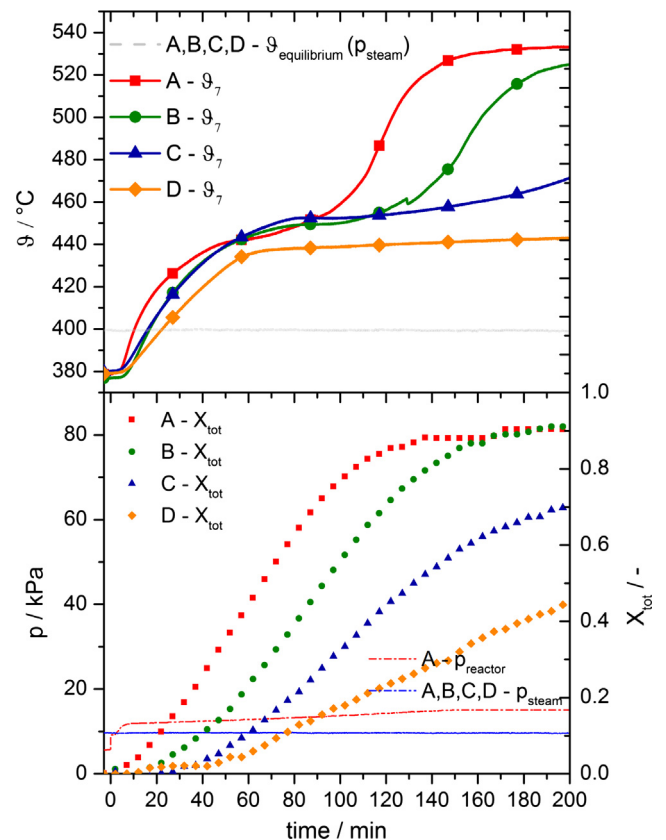


Fig. 7. Dehydration experiments at 10 kPa at different heat loads of the heat transfer fluid.

pressures (in this case ~ 10 kPa) and temperatures below 440 °C the slow effective reaction rate of the material lead to a serious limitation of the operating range of this thermochemical storage: The experiments reveal that if a certain thermal charging power density is required at the respective pressure conditions, the charging temperature has to be around 45 K higher than the value predicted by the equilibrium line.

In order to further analyze this important aspect for the operation flexibility of a thermochemical energy storage based on $\text{Ca}(\text{OH})_2$, we performed additional experiments by thermogravimetric analysis.

3.2.2. Dehydration at 10 kPa in the TGA

The experiments in the TGA were performed according to the procedure described in 2.5 and conditions comparable to the reactor experiments. The main differences to generally reported TGA data for $\text{Ca}(\text{OH})_2$ are isothermal measurement conditions at very low gas pressures. Six different dehydration experiments at a humid atmosphere inside the furnace of 10 kPa and isothermal temperatures between 410 °C and 450 °C were conducted. Each temperature was remained constant for 1 h while the mass change was measured.

Fig. 8 shows the conversion trend of $\text{Ca}(\text{OH})_2$ to CaO at different isothermal measurements. It can be observed that at 410 °C no mass change occurs within 1 h. At 420 °C a small mass change was measured, while at 430 °C the rate of conversion changes significantly but conversion is still incomplete after 1 h. At 435 °C we reach full conversion after 30 min - but with only a slight increase of 5 K to 440 °C the dehydration time is reduced to less than 10 min. A further increase to 450 °C does not result in a significantly faster conversion.

The results from the thermogravimetric analysis accord to what was observed in the reactor. Below a temperature of 440 °C the reaction rate is rather slow thus the heat flux into the reaction bed is always higher than the thermal energy absorbed by the reaction. As a consequence the reaction bed heats up sensible. When we exceed 440 °C the reaction becomes so fast that the heat flux into the reaction bed is completely absorbed by the endothermic reaction. Consequently a constant temperature plateau forms. With regard to a later application of $\text{Ca}(\text{OH})_2$ as thermochemical storage, it can be concluded that the unmodified material possesses a kind of tipping point: at a condensation pressure of 10 kPa (corresponding to a condensation temperature of 45 °C) a charging temperature of at least 445 °C is required to achieve high charging power densities.

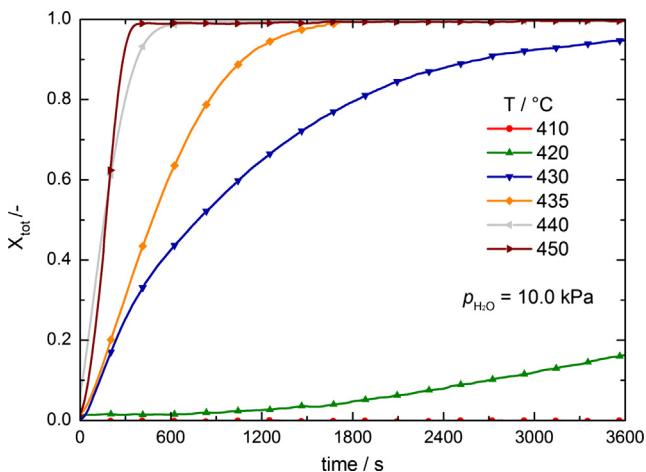


Fig. 8. Effect of the temperature on the dehydration reaction of $\text{Ca}(\text{OH})_2$ at a vapor pressure of 10 kPa.

3.2.3. Variation of condensation pressure

In order to examine the influence of the condensation pressure on the dehydration time and the charging temperature we performed experiments at three different condensation pressures but at the same heat load induced by the heat transfer fluid. Fig. 9 shows the results. Experiment B (green line) is the reference dehydration experiment at 10 kPa while experiment E (red line) is performed at 20 kPa and experiment F (blue line) is performed at 1.4 kPa. Each experiment was run with the nominal volume flow and the air inlet temperature was increased to 560 °C. From the conversion curves we can clearly see, that the lower the condensation pressure the faster we reach full conversion. For example for experiment F 80% is converted after 80 min while for experiment B 80% conversion is achieved 100 min after the equilibrium temperature is exceeded, respectively after 150 min for experiment E.

Even more interesting are the plotted temperature trends for the rear region of the bed. We can see that for the experiments at 10 kPa and 20 kPa the temperature trends are qualitatively similar. The material heats up sensible in the beginning until the reaction becomes as fast that we reach an equilibrium state between heat influx into the reaction bed and the thermal energy absorbed by the reaction (indicated by the constant temperature plateaus). For experiment F no plateau arises indicating that the heat flux into the reaction bed is always higher than the energy absorbed by the reaction. In all cases we observe that the above discussed temperature difference to the theoretical equilibrium temperature (red, green and blue dashed line) is required. However the difference tends to be smaller for higher dehydration pressures: the difference is 35 K at 20 kPa, 45 K at 10 kPa and more than 50 K for 1.4 kPa (compare Fig. 9). But even though a smaller temperature difference to the equilibrium is required at 20 kPa the dehydration

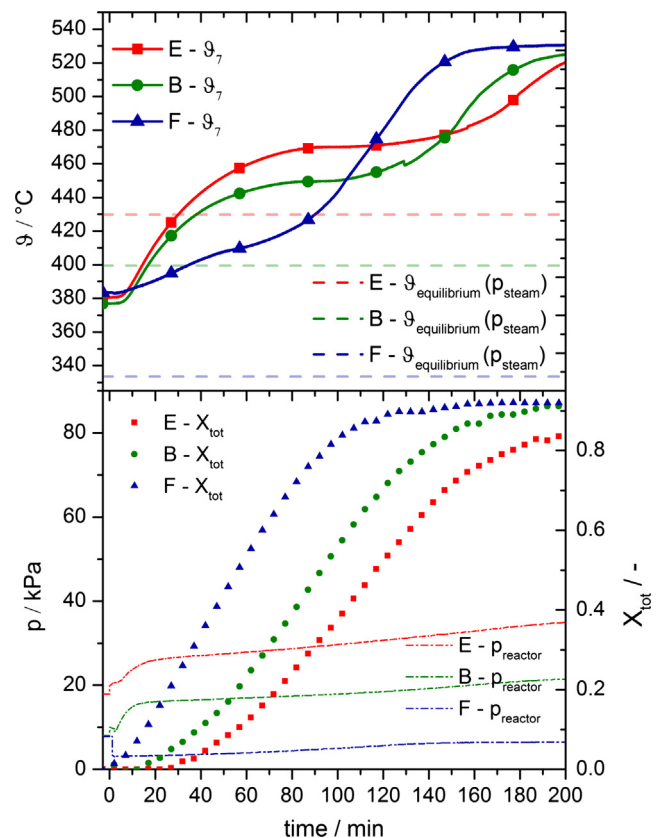


Fig. 9. Dehydration experiments at 1.4 , 10 and 20 kPa and an air inlet temperature of 560 °C.

temperature at which reasonable reaction rates can be realized is already 465 °C. From a process integration point of view this means energy at a higher temperature is required to charge the storage. If the condensation pressure is lower the dehydration can be performed faster and at lower temperatures which would be favorable for the integration of the storage system (lower charging temperatures are required). However it must be taken into account that a lower condensation pressure might require an additional cooling load for the condenser.

3.3. Thermal discharge

Fig. 10 shows a reference experiment for the thermal discharging. The initial temperature was set to 280 °C and the evaporator was tempered at 43 °C. At min 0 the valve between evaporator and reactor is opened and the pressure in the reactor increases to ~8.7 kPa (compare black dash dotted line in Fig. 10). In the moment when the vapor enters the reactor the bed temperatures escalate (compare ϑ_1 , ϑ_3 and ϑ_7 in Fig. 10) due to the heat released by the exothermic reaction. It seems that in the front (ϑ_1) and middle region (ϑ_3) of the bed the temperatures reach slightly lower maxima than in the rear region (ϑ_7). This can be ascribed to the higher cooling load of the reaction bed closer to the air inlet where the temperature difference between bed and the incoming air is maximal.

In the rear region the temperature in the bed reaches a maximum of ~383 °C and stays constant for approximately 20 min. In contradiction to the discharging experiment at 100 kPa (compare Fig. 5), in this case, at lower vapor pressures, a deviation of the plateau temperature from the equilibrium line of 15 K is observed. Since it is lower than the theoretical equilibrium temperature of the reaction (grey dashed line) one could dedicate this observation again to the reaction rate at given conditions: Initially, at the beginning of the experiment, the rate of reaction is high since the temperature difference between the start temperature of 280 °C and the theoretical equilibrium temperature of 398 °C is large. As a consequence more heat is released by the exothermic

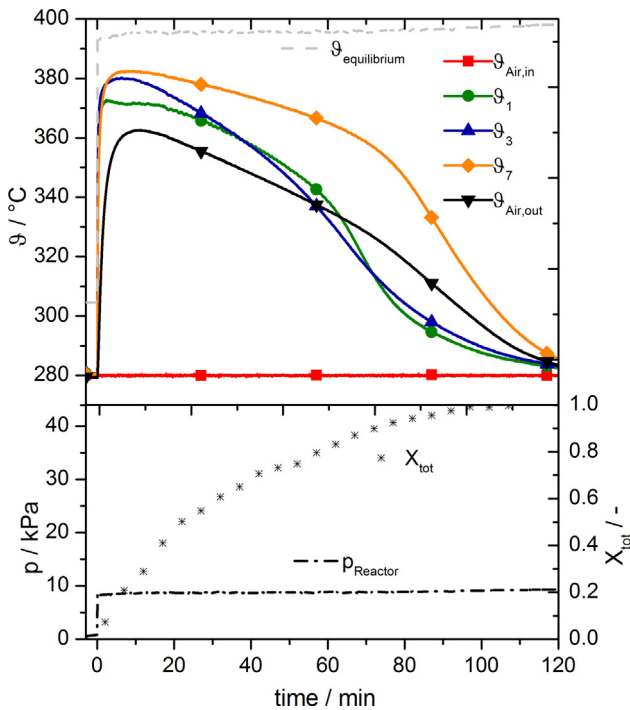


Fig. 10. Hydration experiment at 8.7 kPa and a starting temperature of 280 °C.

reaction than removed by the heat transfer fluid which leads in turn to increasing temperatures. The increasing temperature directly leads to a deceleration of the reaction rate. The deceleration of the heat release at the respective low vapor pressures seems to be so pronounced that the temperature predicted by the theoretical equilibrium line cannot be reached for the given experimental boundary conditions.

3.3.1. Variation of cooling load of the heat transfer fluid

To analyze the influence of different cooling loads on the discharge temperature experiments at three different volume flows of the heat transfer fluid have been conducted. The results are shown in Fig. 11. Experiment G (red solid lines) was run with the nominal volume flow of 12 N m³/h while in the experiments H (green solid line) and J (blue solid line) the volume flow was increased to 16 N m³/h and 20 N m³/h. In all cases the air inlet temperature was set to 280 °C and the exothermic reaction was induced by a gas pressure of 8.7 kPa. The temperature trends in the front (ϑ_1), middle (ϑ_3) and rear region (ϑ_7) of the bed are plotted.

In particular in the front region of the reaction bed (compare ϑ_1 , first diagram of Fig. 11) the reached temperatures directly correlate

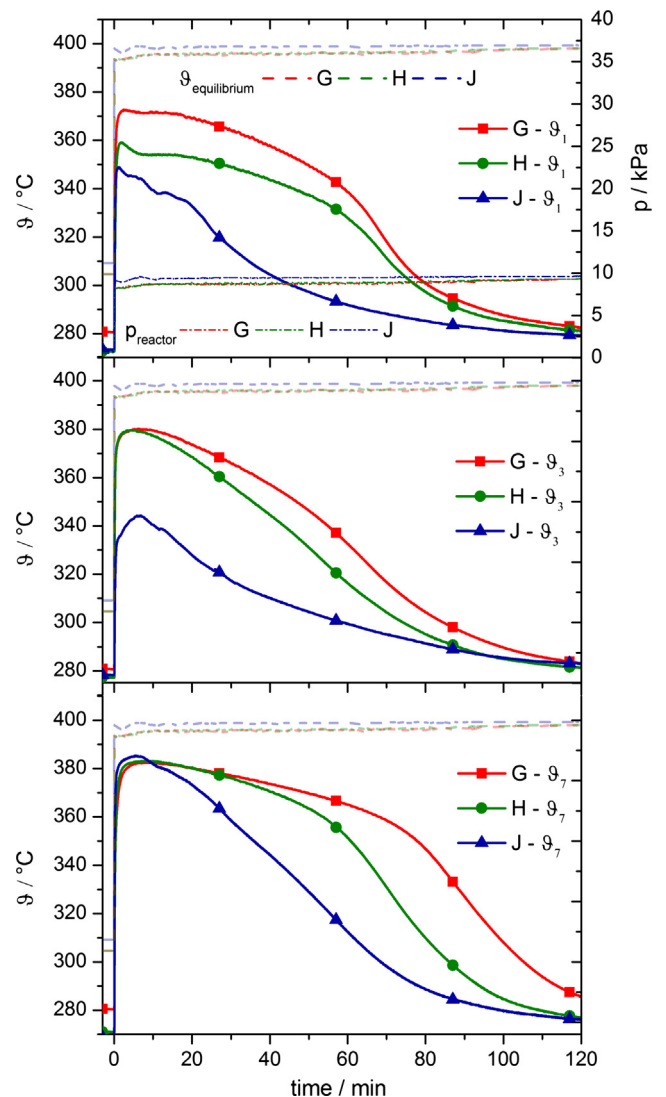


Fig. 11. Hydration experiments at 8.7 kPa under different cooling loads of the heat transfer fluid.

with the volume flow of the heat transfer fluid, respectively the cooling load of the reaction bed. The experiment with the highest cooling load shows the lowest temperature maximum of $\sim 350^\circ\text{C}$ (blue curve). Whereas the experiment with the medium cooling load (green curve) shows a kind of plateau at $\sim 355^\circ\text{C}$ and a clear temperature plateau lies at 370°C for the experiment with the lowest cooling load (red curve). Again, temperature plateaus indicate an equilibrium state between the heat released due to the exothermic reaction and the heat taken up by the heat transfer fluid. Closer to the equilibrium temperature the reaction decelerates thus less heat is released. Accordingly the plateau for lower cooling loads is at higher temperatures. If the cooling load increases, the temperature plateau arises at lower temperatures, since at temperatures further away from the equilibrium temperature, the reaction rate accelerates. This trend can be observed in the first diagram of Fig. 11 even though the experiment with the highest cooling load (blue) reaches rather a peak than a plateau.

In the middle region of the reactor (ϑ_3 , second diagram Fig. 11) we observe that the material temperature for the experiment with the highest cooling load still remains below 350°C while for the other two experiments the same maximum temperature of 380°C is reached. In the rear region of the reactor (ϑ_7) the same maximum temperature of around $380\text{--}383^\circ\text{C}$ is reached for all experiments. At this position the temperature difference between the reaction and the heat transfer fluid is rather small since the heat exchange takes first place in the front and later in the middle region of the reactor. However, still the maximum temperature is approximately 15 K below the thermal equilibrium.

Since for these experiments, the inlet temperature was kept constant, the temperature difference between the reaction and heat transfer fluid was generated by the exothermic reaction itself. In contrast to physical storages, in this case a high local heat flux is characterized by a reaction at a lower temperature level (compare values for highest heat flux at the front region). Consequently, one can conclude that this leads in turn to an optimization question for the later application of the thermochemical storage: for low vapor pressures, high power densities directly reduce the quality (temperature level) of the discharged thermal energy. To investigate this hypothesis additional isothermal hydration experiments have been conducted by TGA.

3.3.2. Hydration at 8.7 kPa in the TGA

To support the findings observed in the reactor we examined the rate of reaction under comparable operating conditions in the thermogravimetric analysis. Before every hydration cycle, $\text{Ca}(\text{OH})_2$ was dehydrated under nitrogen atmosphere. The hydration experiments were performed at a water vapor pressure of 8.7 kPa and at different isothermal temperatures between 390°C and 110°C . The hydration temperature was reduced about 10 K in each following cycle.

Fig. 12 shows the conversion trends for the experiments. We can see that for temperatures between 391°C (theoretical equilibrium is 398°C) and 367°C almost no material has reacted after one hour. At 357°C approximately 30% of the material is hydrated after 1 h while at 347°C almost 80% is hydrated within the first 20 min. At a temperature of 337°C we achieve 80% of conversion within 10 min while at temperatures below 300°C the conversion accelerates only slightly.

One can conclude that at temperatures above 360°C the rate of reaction is rather slow while at temperatures below 350°C the rate of reaction quickly accelerates. Consequently, one can state that the tipping point for a technically relevant discharge reaction of the $\text{Ca}(\text{OH})_2$ with a vapor pressure of 8.7 kPa (corresponding to an evaporation temperature of 43°C) is at around 350°C . This value is around 48 K below the theoretical discharge temperature according to the equilibrium line.

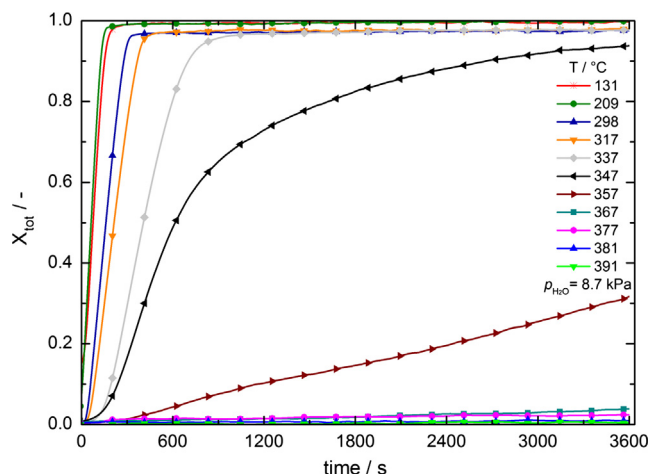


Fig. 12. Effect of the temperature on the hydration reaction of CaO at a gas pressure of 8.7 kPa.

4. Conclusions

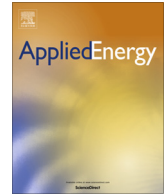
This study presents a newly designed indirectly heated reaction bed for 2.4 kg of calcium hydroxide storage material. The reactor design was especially dedicated to investigate the reaction at low vapor pressures and under different thermal loads induced by the heat transfer fluid.

Thermal charging and discharging at technically relevant operating conditions were experimentally demonstrated at vapor pressures between 1.4 kPa and 20 kPa. It can be stated that the operation of the storage system at low vapor pressures is possible. This not only enhances process integration possibilities (gas handling) but could also increase the overall storage efficiency of the thermochemical system. However, the experiments revealed that the operating range of the calcium hydroxide system is partially limited due to the effective reaction rate of the storage material at low vapor pressure. For example for the thermal charging at 10 kPa (condensation at 45°C) a technically relevant minimum temperature of 445°C was identified which is around 45 K higher compared to the theoretical values. For the discharge at 8.7 kPa (evaporation at 43°C) a maximum temperature of only 383°C could be reached which is 15 K below the theoretical value. However for high discharge powers a reaction temperature below 350°C should be maintained during the discharge process. For process integration studies as well as evaluations of $\text{Ca}(\text{OH})_2$ as thermochemical energy storage, this limited operating range at low water pressures has to be taken into account. Further studies will complement the technically relevant operation range of $\text{Ca}(\text{OH})_2$ for higher vapor pressures.

References

- [1] Zhang H, Wang H, Zhu X, Qiu Y-J, Li K, Chen R, et al. A review of waste heat recovery technologies towards molten slag in steel industry. *Appl Energy* 2013;112:956–66. <http://dx.doi.org/10.1016/j.apenergy.2013.02.019>.
- [2] Schaub F, Wörner A, Tamme R. High temperature thermochemical heat storage for concentrated solar power using gas–solid reactions. *J Sol Energy Eng* 2011;133. <http://dx.doi.org/10.1115/1.400424>.
- [3] Prieto C, Cooper P, Fernández AI, Cabeza LF. Review of technology: thermochemical energy storage for concentrated solar power plants. *Renew Sustain Energy Rev* 2016;60:909–29. <http://dx.doi.org/10.1016/j.rser.2015.12.364>.
- [4] Pardo P, Deydier a, Anxionnaz-Minville Z, Rougé S, Cabassud M, Cognet P. A review on high temperature thermochemical heat energy storage. *Renew Sustain Energy Rev* 2014;32:591–610. <http://dx.doi.org/10.1016/j.rser.2013.12.01>.
- [5] Zhang H, Baeyens J, Cáceres G, Degreè J, Lv Y. Thermal energy storage: recent developments and practical aspects. *Prog Energy Combust Sci* 2016;53:1–40. <http://dx.doi.org/10.1016/j.pecs.2015.10.003>.

- [6] Rosemary JK, Bauerle GL, Springer TH. Solar energy storage using reversible hydration-dehydration of CaO-Ca(OH)_2 . *J Energy* 1979;3:321–2.
- [7] Galwey AK, Lavery GM. A kinetic and mechanistic study of the dehydroxylation of calcium hydroxide. *Thermochim Acta* 1993;228:359–78. [http://dx.doi.org/10.1016/0040-6031\(93\)80304-S](http://dx.doi.org/10.1016/0040-6031(93)80304-S).
- [8] Schaube F, Koch L, Wörner A, Müller-Steinhagen H. A thermodynamic and kinetic study of the de- and rehydration of Ca(OH)_2 at high H_2O partial pressures for thermo-chemical heat storage. *Thermochim Acta* 2012;538:9–20. <http://dx.doi.org/10.1016/j.tca.2012.03.003>.
- [9] Criado YA, Alonso M, Abanades JC. Kinetics of the CaO/Ca(OH)_2 hydration/dehydration reaction for thermochemical energy storage applications. *Ind Eng Chem Res* 2014;53:12594–601. <http://dx.doi.org/10.1021/ie404246p>.
- [10] Shkatulov A, Aristov Y. Modification of magnesium and calcium hydroxides with salts: An efficient way to advanced materials for storage of middle-temperature heat. *Energy* 2015. <http://dx.doi.org/10.1016/j.energy.2015.04.004>.
- [11] Kariya J, Ryu J, Kato Y. Development of thermal storage material using vermiculite and calcium hydroxide. *Appl Therm Eng* 2016;94:186–92. <http://dx.doi.org/10.1016/j.applthermaleng.2015.10.090>.
- [12] Roßkopf C, Afflerbach S, Schmidt M, Görtz B, Kowald T, Linder M, et al. Investigations of nano coated calcium hydroxide cycled in a thermochemical heat storage. *Energy Convers Manage* 2015;97:94–102. <http://dx.doi.org/10.1016/j.enconman.2015.03.034>.
- [13] Criado YA, Alonso M, Abanades JC. Enhancement of a CaO/Ca(OH)_2 based material for thermochemical energy storage. *Sol Energy* 2016;135:800–9. <http://dx.doi.org/10.1016/j.solener.2016.06.056>.
- [14] Nagel T, Shao H, Roßkopf C, Linder M, Wörner A, Kolditz O. The influence of gas–solid reaction kinetics in models of thermochemical heat storage under monotonic and cyclic loading. *Appl Energy* 2014;136:289–302. <http://dx.doi.org/10.1016/j.apenergy.2014.08.104>.
- [15] Wang W, Kolditz O, Nagel T. Parallel finite element modelling of multi-physical processes in thermochemical energy storage devices. *Appl Energy* 2017;185:1954–64.
- [16] Schaube F, Kohzer A, Schütz J, Wörner a, Müller-Steinhagen H. De- and rehydration of Ca(OH)_2 in a reactor with direct heat transfer for thermochemical heat storage. Part A: experimental results. *Chem Eng Res Des* 2013;91:856–64. <http://dx.doi.org/10.1016/j.cherd.2012.09.02>.
- [17] Pardo P, Anxionnaz-Minvielle Z, Rougé S, Cognet P, Cabassud M. $\text{Ca(OH)}_2/\text{CaO}$ reversible reaction in a fluidized bed reactor for thermochemical heat storage. *Sol Energy* 2014;107:605–16. <http://dx.doi.org/10.1016/j.solener.2014.06.010>.
- [18] Yan J, Zhao CY. Experimental study of CaO/Ca(OH)_2 in a fixed-bed reactor for thermochemical heat storage. *Appl Energy* 2016;175:277–84. <http://dx.doi.org/10.1016/j.apenergy.2016.05.038>.
- [19] Ogura H, Yamamoto T, Kage H. Effects of heat exchange condition on hot air production by a chemical heat pump dryer using $\text{CaO/H}_2\text{O/Ca(OH)}_2$ reaction. *Chem Eng* 2002;86:3–10.
- [20] Schmidt M, Szczukowski C, Roßkopf C, Linder M, Wörner A. Experimental results of a 10 kW high temperature thermochemical storage reactor based on calcium hydroxide. *Appl Therm Eng* 2014;62:553–9. <http://dx.doi.org/10.1016/j.applthermaleng.2013.09.020>.
- [21] Samms AC, Evans BE. Thermal dissociation of Ca(OH)_2 . *At Elevated Pressures* 1968;18.
- [22] Barin I. *Thermochemical data of pure substances*. Weinheim: VCH Verlagsgesellschaft; 1993.
- [23] Matsuda H, Ishizu T, Lee SK, Hasatani M. Kinetic study of $\text{Ca(OH)}_2/\text{CaO}$ reversible thermochemical reaction for thermal energy storage by means of chemical reaction. *Kagaku Kogaku Ronbunshu* 1985;11:542–8.
- [24] Halstead PE, Moore AE. 769. The thermal dissociation of calcium hydroxide. *J Chem Soc (Resumed)* 1957:3873. <http://dx.doi.org/10.1039/jr957000387>.



Power generation based on the $\text{Ca}(\text{OH})_2/\text{CaO}$ thermochemical storage system – Experimental investigation of discharge operation modes in lab scale and corresponding conceptual process design



Matthias Schmidt*, Marc Linder

German Aerospace Center – DLR e.V., Institute of Engineering Thermodynamics, Linder Höhe, 51147 Köln, Germany

HIGHLIGHTS

- Experimental investigation of thermal discharging in a lab scale reactor.
- Operation of storage system at 4–470 kPa and temperatures of 280–600 °C.
- Demonstration of operation modes at boundary conditions to drive a Rankine cycle.
- Analysis of power generation with CaO and water and assessment of storage efficiency.

ARTICLE INFO

Article history:

Received 6 March 2017

Received in revised form 16 June 2017

Accepted 17 June 2017

Keywords:

Thermochemical energy storage
Calcium hydroxide/ oxide
Thermal discharge operation modes
High vapour pressures
Power generation
Storage efficiency

ABSTRACT

Thermochemical storage systems offer in theory promising advantages for a wide range of applications. In particular the reversible reaction of calcium hydroxide to calcium oxide and water vapour is intensively discussed as an alternative storage solution for concentrated solar power plants. The material is cheap, environmentally friendly and discharge temperatures of the reaction of 600 °C and above fit to the operating range of today's power plants. However, experimental data on the operation of the system in lab scale and at load conditions comparable to the real application is rarely reported.

Therefore the thermal discharge of the reaction system at vapour pressures between 4 and 470 kPa and temperatures between 280 and 600 °C is experimentally investigated in this study. In particular the influence of the cooling load at various vapour pressures on the achievable discharge temperatures is analysed. The presented data complements the experimental characterisation of the reaction system in the complete temperature and pressure range which is relevant for real process applications. Based on this knowledge the applicability of the storage for various processes can now be assessed more accurate. By means of the experimental results a first integration option of the thermochemical system in a CSP plant is proposed in this work and thermodynamically analysed. The analysis revealed that, when the required steam production during discharge is thermally integrated into the Rankine steam cycle, a high storage efficiency of up to 87% can be reached compared to only 60% in the reference case.

© 2017 Elsevier Ltd. All rights reserved.

1. Introduction

Concentrating solar power (CSP) plants can produce electricity completely renewable and free of carbon dioxide emissions. Since this technology converts solar irradiation into thermal energy in the first step a combination with large scale thermal energy storage system allows the decoupling of the availability of solar energy from the electricity production.

Until today, the parabolic through technology is the most advanced, with the greatest number of commercial plants in operation [1]. However the central receiver tower technology with molten salt as heat transfer fluid is gaining importance because they operate at higher maximum temperatures of currently 565 °C and the molten salt can directly be stored in large tanks with minimal losses [2,3]. Large molten salt tower plants like the Gemasolar (20 MWe and 15 h storage) in Spain or the Crescent Dunes plant (110 MWe and 10 h storage) in the US have been recently set into operation and more plants based on this technology are currently under development.

* Corresponding author.

E-mail address: Matthias.schmidt@dlr.de (M. Schmidt).

Nomenclature

CSP	concentrated solar power	V	valve
cp	specific heat capacity	ϑ	temperature measurement point, thermocouple
EV	evaporator	X_{tot}	conversion
EX	extraction point	%w	weight percentage
F	filling level	d_{50}	median diameter of the particle size distribution
HEX	heat exchanger	\dot{V}	volume flow
HTF	heat transfer fluid	\dot{Q}	thermal power output
LP	low pressure	\dot{n}	molar rate of reaction
PH	preheater	\dot{m}	mass flow rate
P	electrical power output	η	efficiency
p	pressure	ΔH	enthalpy change
TCS	thermochemical system	$M_{\text{H}_2\text{O}}$	molar mass
T	temperature		

The direct two tank molten salt system is the state of the art storage system for today's CSP plants. Nevertheless in a typical configuration the salt itself accounts for around 50% of the cost of the storage system [4]. In order to reduce the costs researchers investigate alternative thermal storage solutions [5]. In the thermochemical concept for example the expensive salt is partly replaced with inexpensive filler materials and only one storage tank is used [6]. Besides these approaches for cost reduction in sensible storage systems also latent [7–9] and thermochemical systems are gaining importance. Recently published review articles give a comprehensive overview of high temperature thermal storage technologies, their state of development and potential applications [10–14].

Among the thermal energy storage methods thermochemical systems offer in theory a very promising potential [15,16]. Some of the reaction systems have high energy densities, the storage principal itself is free of losses and especially the temperature at which the heat is released can be adjusted in a certain range [17,18]. A recent survey of thermochemical storage technologies and their level of maturity is given by Pardo et al. [19] and Prieto et al. [20].

One reaction system suggested for CSP applications is the reversible reaction of calcium hydroxide to calcium oxide and water vapour. First of all, the material is very cheap and abundantly available in industrial scale. Combined with the high enthalpy of reaction the material offers in principle a very cheap storage capacity. Secondly the theoretical temperature range of the reaction between 300 °C and up to 600 °C fits to the operating range of the plant. Thirdly, the gaseous reactant, water vapour, can safely be handled and stored volume efficient as liquid water.

Despite these advantages the technology development is still in an early research state. The majority of the works focus on investigations with small sample masses in thermogravimetric apparatus. Cycle stability has first been proven by Rosemary for 1171 cycles [21]. Kinetic equations for the de- and rehydration have been derived by several authors [22–24] and the development of simulation models is still ongoing [25,26]. Other groups focus on the modification of the material in order to enhance the reaction rate [27], adapt the reaction temperatures [28], or to encapsulate the storage material in a permeable shell [29]. These investigations on the material level are important to improve the fundamental understanding of the reaction system. But for the development of a thermochemical storage systems additional experimental research in larger reactors and under process relevant boundary conditions is essential.

In lab and pilot scale set-ups two different type of reactor concepts are currently realized. One is the so called directly heated concept where the heat transfer fluid is in direct contact with the reacting particles. Pardo et al. carried out the reaction in a fluidized

bed for 1.9 kg of material composed of 30 %w $\text{Ca}(\text{OH})_2$ and 70 %w inert easy to fluidize particles [30]. Criado et al. presented a theoretical study on a fluidized bed concept for large CSP plants [31] while recently the group proofed the concept experimentally in a newly constructed lab scale set up [32].

The second concept is the so called indirectly heated reactor where the heat transfer fluid is physically separated from the storage material and the thermal energy is transferred via a heat exchanging surface. Experimental data on the operation of indirectly heated reactors is rather scarce. Ogura et al. firstly presented a reactor where heat from the exothermal reaction was transferred to an air flow at ambient temperature [33] and Yan et al. performed the exothermal reaction at different vapour pressures but the reactor did not allow the recovery of the released heat [34]. Even though these investigations are helpful to understand the reaction in larger scale, the experiments do not sufficiently represent the required operation modes of an indirectly heated storage system in the real application. In case of thermal energy storage both the endo- and exothermal reaction will be thermally driven by the heat transfer fluid and the reaction system has to be operated in a pressure and temperature range which depends on the boundary conditions of the process only.

Fig. 1 shows the theoretical equilibrium line of the reaction calculated by values from Barin [35] as well as the upper and lower

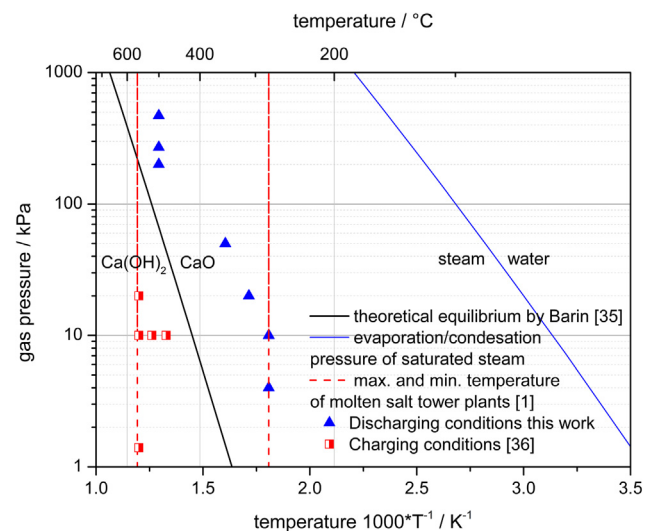


Fig. 1. Equilibrium line of the reaction system $\text{Ca}(\text{OH})_2/\text{CaO}$ and operating temperature range of molten salt; experimental conditions of the presented experiments in this work.

temperature limit of current molten salt tower plants (red dashed lines). The relevant operating range for the indirectly heated storage system is marked as grey area. In a recent publication of our group we analysed the thermal charging of the system at different low vapour pressures in detail [36] (dehydration conditions marked with partly filled red squares). The present study therefore focuses in the first part on the discharge reaction at different pressures between 4 and up to 470 kPa at different cooling loads (operating conditions marked with blue triangles). The presented data complements our experimental characterisation of the reaction system in the complete temperature and pressure range which is relevant for real process applications. Based on the experimental results a first integration concept of the storage system into a CSP plant has been analysed theoretically in the second part of the paper with a special focus on the operation of the power block with the storage system as the only energy source. For this application case we analysed how the use of different low grade heat sources from the Rankine cycle to evaporate steam for the discharge reaction affects the overall storage efficiency. The charging performance has been assessed taking the available condensation temperature at the plant location as well as the experimentally determined operation characteristic into account.

2. Experimental set up

2.1. Reactor

The reactor used in this study was especially designed to analyse the thermal capability of the reaction system in operation

modes and boundary conditions comparable to the operation in the real application. This on one hand means that the reaction is driven by indirect heating or cooling loads induced by the heat transfer fluid and on the other hand the reaction gas is supplied or removed through a comparable system and within the respective pressure range. An additional approach was to minimize heat and mass transport limitations which in general are contributed to the reactor design, in order to characterise the operational performance of the commercial calcium hydroxide material. For more details on the reactor please refer to our previous publication [36].

Fig. 2 left shows the reactor which consists of one single heat exchanger plate. Air serves as the heat transfer fluid in the experimental set up and flows inside the plate while a bulk of reactive material (white powder in Fig. 2 left) is placed on both sides of the plate. The inside area of the plate is 1600 mm long, 150 mm wide and surrounded by a frame of 10 mm height. In this volume of 2.4 L on each side of the plate the storage material can be placed. The total heat exchange surface is 0.48 m². The reaction bed is encased with a gas permeable metallic filter (pore size 5 μm) to hold the reaction bed in position (Fig. 2 right).

The heat exchanger plate with the encased reaction bed is placed into a casing pipe of 200 mm in diameter. The casing pipe is made of stainless steel (alloy 1.4571) with a wall thickness of 3 mm in order to operate at pressures of up to 1000 kPa and 550 °C. Fig. 3 right shows a sectional view of the reaction bed in the casing pipe including important dimensions and positions of measurement instruments. To record the air inlet ($\vartheta_{\text{Air,in}}$) and outlet temperature ($\vartheta_{\text{Air,out}}$) a thermocouple is placed directly before and after the reaction bed. Seven thermocouples ϑ_{1-7}

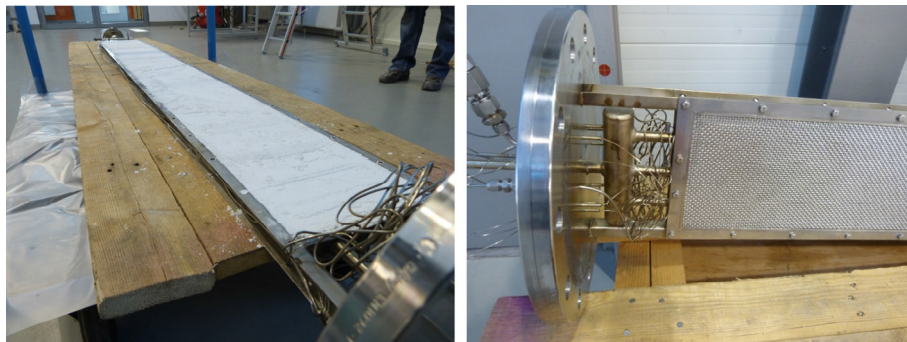


Fig. 2. Left: heat exchanger plate filled with calcium hydroxide; right: reaction bed encased with gas permeable metal filter plate.

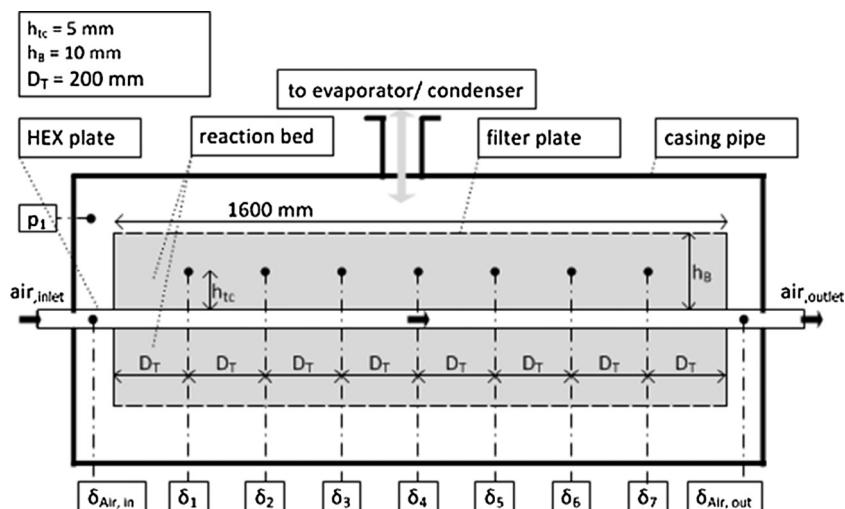


Fig. 3. Sectional view of the reaction bed in the casing pipe including important dimensions and position of measurement instruments.

(type K, $\pm 0.4\% \times T$) measure the material temperature in the reaction bed. These are positioned 5 mm in vertical distance from the heat exchange surface and every 200 mm along the horizontal direction of the air flow. An additional pressure sensor (p_1) (PPA-35XHTT, Keller Ges. für Druckmesstechnik mbH, ± 0.8 kPa) mounted into the casing, records the vapour pressure in the reaction chamber.

2.2. Material

In total 2.4 kg of $\text{Ca}(\text{OH})_2$, supplied by Rheinkalk GmbH/Lhoist group (product type “Sorbacal©H”), has been filled into the reactor. According to the companies data sheet the d_{50} is $5.5 \mu\text{m}$ and the purity of the material is 97–98%.

2.3. Experimental procedure

The reactor is integrated into an infrastructure which supplies the heat transfer fluid and handles the reaction gas. A flow sheet and a more detailed description of the test bench can also be found in a previous publication on this set up [36]. Air, supplied by a compressor, serves as the heat transfer fluid. The air volume flow is adjusted by a mass flow controller (Bronkhorst, digital flow controller, $\pm 0.4\%$) before it gets heated up with an electrical preheater and enters the reactor. To supply the reaction gas, the central outlet of the casing pipe (compare Fig. 3) is connected to the evaporator. The evaporator consists of a tube bundle heat exchanger where the shell side is partly filled with liquid water (for evaporation) and thermal oil runs on the tube side. By tempering the inlet temperature of the thermal oil with a thermostatic bath an evaporation pressure between 0.7 and 618 kPa can be adjusted. A filling level meter (Vegaflex 65, ± 2 mm) records the change of the water level in the evaporator. By means of this value the conversion of the storage material is determined.

Before every discharge experiment the material present in the reaction bed is completely dehydrated and the whole set up is evacuated with the vacuum pump ensuring a pure water vapour atmosphere during the experiment. Afterwards the valve to the evaporator is closed. The air flow is started and set to a certain preheating temperature. Additionally the auxiliary heating cables attached to the casing pipe to minimize thermal losses are set to the same preheating temperature. Simultaneously the evaporation pressure for the experiment is adjusted. When the vapour pressure and the temperatures in the reaction bed become constant the experiment can be started by opening the valve between evaporator and reactor. Consequently the pressure in the reactor increases and the exothermal reaction takes place. The heat released by the reaction is taken up from the heat transfer fluid. When the heat of reaction is completely released and the temperatures in the bed reach their initial values again the experiment is finished. The operation parameters of all experiments are given in Table 1.

We already published a detailed investigation of the charging procedure with the same reactor [36]. Therefore dehydration experiments are not presented in this study. However, the dehydration reaction after every discharge experiment of this study was performed at identical conditions (air temperature of 500°C and a condensation pressure of 10 kPa in the condenser). The experiments A to E are part of a measurement series where one batch of the material (described in Section 2.2) was cycled for 10 times in total. The experiments F to I are part of a second measurement series (35 cycles in total) performed with another batch of the same starting material. The respective cycle number for each experiment is given in Table 1.

3. Experimental results and discussion

3.1. Thermal discharging at 200–470 kPa

In a real application the storage system should ideally supply thermal energy at an as high as possible temperature level in order to reach for example high efficiencies in the power block. Therefore we performed the discharging procedure at high vapour pressures and evaluated the capability of the reaction system to supply thermal energy at temperatures between 500 and 600°C .

Fig. 4 shows the reference discharge experiment A. The reaction bed is preheated to a temperature of 500°C while in the evaporator a temperature of 150°C is adjusted (for all parameters refer to experiment A in Table 1). At minute 0 the valve between evaporator and reactor is opened thus the pressure in the reactor increases up to 470 kPa (red dash dotted line). Triggered by the pressure increase the exothermal reaction set in and the material temperatures in the front (ϑ_1), middle (ϑ_3) and rear (ϑ_7) of the reaction bed jump to a maximum of 600°C . The reached temperature corresponds to the equilibrium temperature (grey dashed line) which was calculated with the measured pressure in the reactor and the correlation given by Samms et al. [37]. Furthermore, we observe a clear reaction front in the horizontal direction of the air flow. At all three measurement points the reaction proceeds very close to the equilibrium temperature which is indicated by the constant temperatures plateaus and the simultaneously measured constant increase in conversion. The temperature (ϑ_1) drops after 8 min which indicates that a major part of the material in the front region is already completely converted. The reactive area then moves along the reaction bed until also the material in the rear region has completely reacted and (ϑ_7) starts to decrease after 35 min. Accordingly 80% of the total mass is converted after 35 min (black cross dots) while a total conversion of 92% is measured after 60 min.

3.1.1. Variation of cooling load at 470 kPa

In order to analyse the thermal capability of the reaction system at 470 kPa, experiments with three different cooling loads have

Table 1
Parameters of all experiments presented in this study.

Experiment	$T_{\text{air, initial}}/^\circ\text{C}$	$\dot{V}/\frac{\text{N}_m}{\text{h}}$	$p_{\text{evaporator}}/\text{kPa}$	$T_{\text{water}}/^\circ\text{C}$	Cycle no.
<i>Hydration</i>					
A	500	16	470	150	5
B	500	20	470	150	4
C	500	28	470	150	7
D	500	20	200	45	2
E	500	20	270	60	3
F	280	12	4	32	21
G	280	12	10	45	32
H	310	12	20	60	9
I	350	12	50	81	10

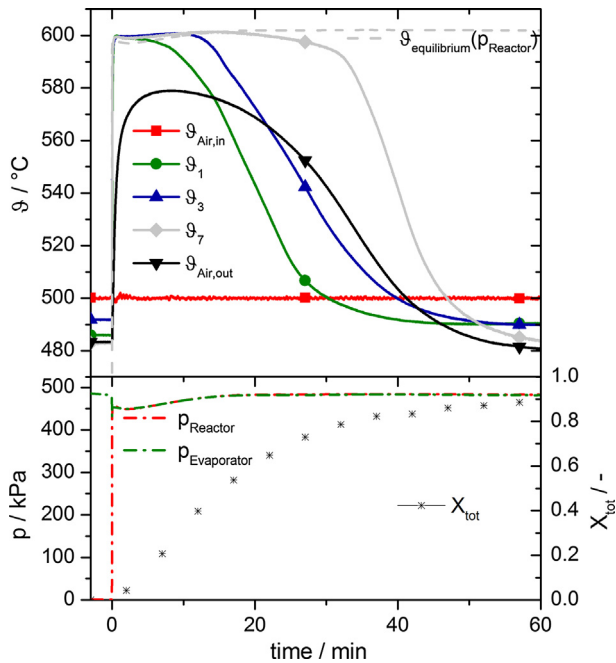


Fig. 4. Hydration experiment at 470 kPa and a starting temperature of 500 °C.

been performed. Experiment A was conducted with an air volume flow of 16 N m³/h while the volume flow was increased to 20 and 28 N m³/h for the experiments B and C respectively. For all cases a constant air inlet temperature of 500 °C and an evaporation temperature of 150 °C was adjusted (refer to Table 1 for details of the experimental conditions). Fig. 5 shows the temperature trends in the front (ϑ_2) and rear (ϑ_6) region of the reaction bed as well as the air outlet temperature. We can observe that the reaction proceeds at a constant temperature which corresponds to the theoretical equilibrium temperature (dashed lines). The lengths of the

plateaus directly correlate to the applied cooling loads. With an increasing cooling load (experiment A to B to C) the plateaus become shorter which can be attributed to a faster conversion. It is remarkable that even at a more than 40% higher cooling load (compare A to C) no deviation of the plateau temperature from the equilibrium temperature can be observed. This indicates that the heat released by the exothermal reaction keeps up with the heat removed out of the reaction bed for all applied cooling loads. In other words the reaction rate is controlled by the heat transport out of the reaction bed. It can be concluded that at a pressure of 470 kPa the reaction is very fast even at (very close to) the equilibrium temperature.

3.1.2. Variation of discharge pressure

Even though the discharge of the storage system at 470 kPa showed good performance, it might be reasonable to operate the system at slightly lower vapour pressures depending on the boundary conditions of the process. For example if the available heat source for evaporation has a lower temperature level than 150 °C. Therefore and to complete the operating range between 500 and 600 °C we conducted additional discharge procedures at 200 and 270 kPa (experiment D and E). The reactor again was operated at a constant air flow rate of 20 N m³/h and an air inlet temperature of 500 °C.

Fig. 6 shows the temperature trends of ϑ_1 (beginning of the reaction bed), ϑ_3 (middle of the reaction bed) and ϑ_7 (end of the reaction bed) for the experiments D and E as well as for comparison the experiment B with a pressure of 470 kPa. We can see that in all cases the reached maximum temperature corresponds to the predicted temperature by the equilibrium line. The small differences within the first minutes can be contributed to pressure differences between the global measured pressure in the casing pipe and the pressure in the reaction bed (compare position of pressure sensor in Fig. 3) which occur during the initial dynamic changes. Consistently in all experiments a reaction front moves along the direction of the air flow. Close to the air inlet where initially the cooling load is the highest, the material temperatures (ϑ_1) drop at first due to a decreasing amount of reacting material. The plateaus in the middle region (ϑ_3) are longer while the temperatures in the rear region drop at last.

The cooling loads of the experiments also vary due to the different temperature differences between the air inlet temperature and the plateau temperatures. Accordingly the experiment with the highest plateau temperature (case B) is the first where the heat released by the reaction is completely absorbed and all reaction bed temperatures reach their initial values again (after 60 min at ϑ_7). With lower cooling loads (induced due to lower vapour pressures), in the cases D and E, the duration of the discharge procedure prolongs (timeline is not plotted until the end of the experiments D and E).

3.2. Thermal discharging at 4–50 kPa

3.2.1. Discharge at 4 kPa

Fig. 7 shows the temperature and conversion trend within the first 30 min of the discharge experiment at a vapour pressure of 4 kPa. The reaction bed is preheated with an air flow rate of 12 N m³/h at an inlet temperature of 280 °C (red solid line). The reaction chamber is evacuated while the evaporator is adjusted to a temperature of 30 °C. At minute zero the valve between reactor and evaporator is opened indicated by the pressure increase in the reactor (red¹ dash dotted line). Correspondingly the material

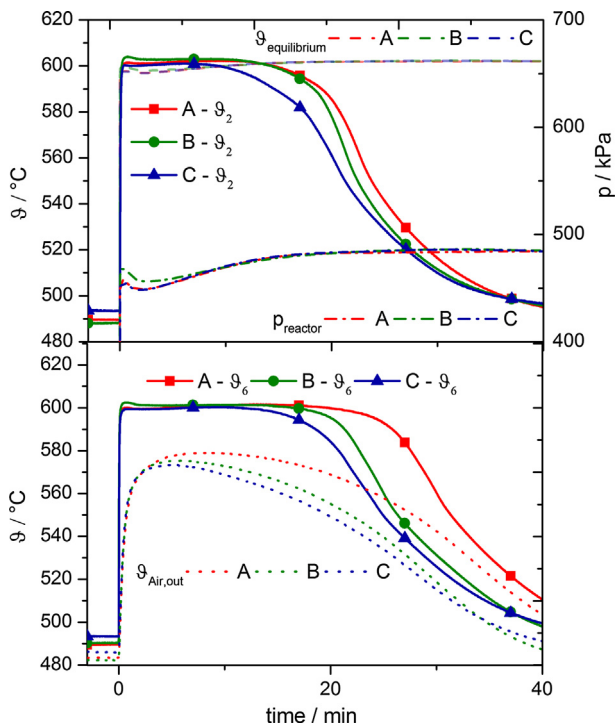


Fig. 5. Hydration at 470 kPa and a starting temperature of 500 °C under different cooling loads.

¹ For interpretation of color in 'Fig. 7', the reader is referred to the web version of this article.

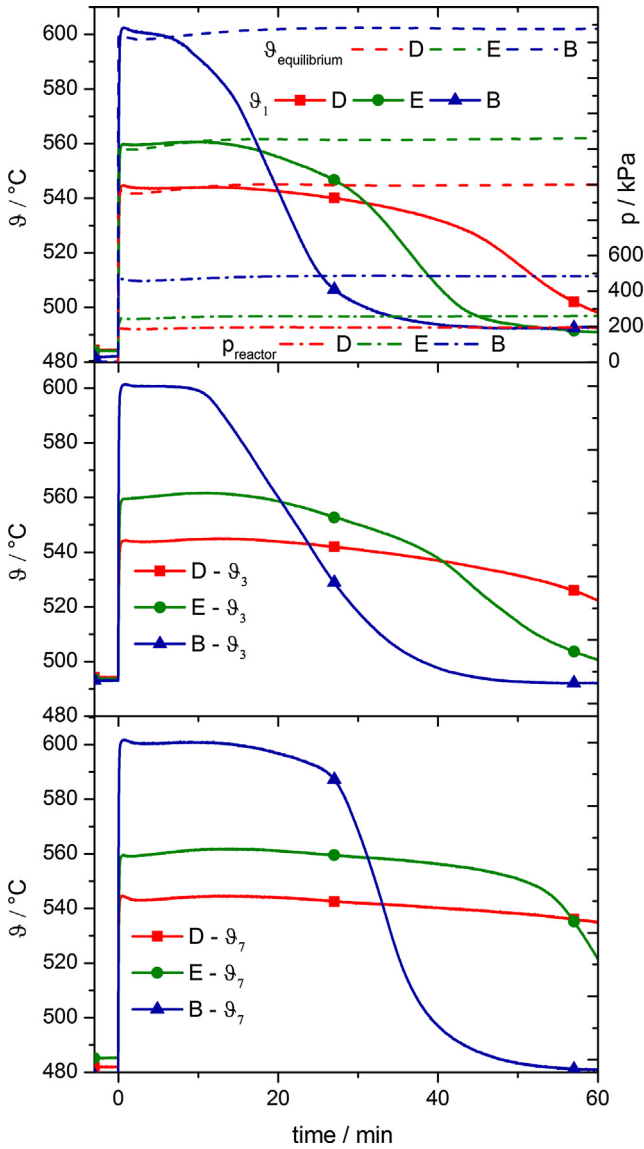


Fig. 6. Hydration experiment at 200, 270 and 470 kPa and a starting temperature of 500 $^{\circ}\text{C}$.

temperatures rise quickly due to the heat released by the exothermal reaction. A particular important observation is that temperature plateaus arise at different levels according to the positions in the reactor. The temperature plateaus indicate an equilibrium state between the heat released by the reaction and the heat absorbed by the heat transfer fluid. Coherently we observe the lowest plateau temperature of 340 $^{\circ}\text{C}$ in the front region (ϑ_1) of the reactor, where the cooling load is maximal due to the proximity to the air inlet. Smaller cooling loads in the middle (ϑ_5) and rear (ϑ_7) region of the reactor lead to higher plateau temperatures of approximately 350 $^{\circ}\text{C}$ (ϑ_5) and 360 $^{\circ}\text{C}$ (ϑ_7). This correlation can directly be ascribed to the dependency of the reaction rate from the temperature gap to the equilibrium. With an increasing distance between reaction temperature and equilibrium temperature the rate of reaction increases. The temperature plateaus of the experiment reveal that at a pressure of 4 kPa a certain gap to the equilibrium needs to be maintained in order to operate at high cooling loads. This is in contrast to the reference experiment at 470 kPa where the storage system could be operated at the equilibrium temperature even at drastically increased cooling loads. However it can be stated that the discharging with a vapour pressure of 4 kPa is possible and an outlet temper-

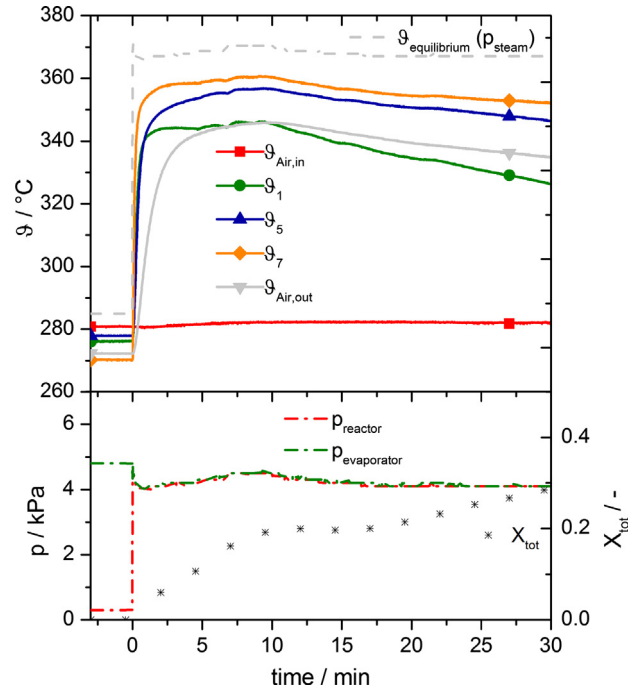


Fig. 7. Hydration at 4 kPa and a starting temperature of 280 $^{\circ}\text{C}$.

ature of 340 $^{\circ}\text{C}$, 25 K lower than the equilibrium temperature, can be expected with reasonable cooling rates. It has to be mentioned that the trend lines in Fig. 7 are not presented until the end of the experiment in order to focus on the temperature plateaus. The reaction was completed after 140 min.

3.2.2. Discharge at 10 kPa

The discharge of the storage system at a pressure of 10 kPa is of particular interest since in many process applications low grade heat at a temperature level of 45 $^{\circ}\text{C}$, which can be used to generate steam at 10 kPa, is available. The hydration experiment is performed at a volume flow of 12 $\text{N m}^3/\text{h}$, a starting temperature of 280 $^{\circ}\text{C}$ and an evaporation temperature of 45 $^{\circ}\text{C}$. Fig. 8 shows the temperature and conversion trend for the first 30 min after the exothermal reaction is triggered by the pressure increase in the reactor. Complete conversion was reached after 100 min in this experiment (timeline in Fig. 8 is shortened in order to focus the display on the temperature plateaus). A qualitatively similar temperature trend compared to the experiment at 4 kPa can be observed. Temperature plateaus arise at different levels according to the different cooling loads in the front (ϑ_1), middle (ϑ_5) and rear (ϑ_7) part of the reaction bed. The temperature plateau in the front region where the highest cooling load applies arises at 360 $^{\circ}\text{C}$ for these experimental conditions. Consequently for the real application it can be derived that at a discharge pressure of 10 kPa an additional temperature distance to the theoretical equilibrium temperature must be maintained to allow the operation with high cooling loads.

3.2.3. Variation of discharge pressure

Since the temperature level of the available heat source for evaporation depends on the process of the real application we additionally analysed the discharge operation at vapour pressures of 10, 20 and 50 kPa, respectively at evaporation temperatures of 45 $^{\circ}\text{C}$, 60 $^{\circ}\text{C}$ and 81 $^{\circ}\text{C}$. The air volume flow was 12 $\text{N m}^3/\text{h}$ for all experiments while the air inlet temperature is constant but different for each case in order to achieve comparable cooling loads. The air inlet temperature and starting temperature in each experiment

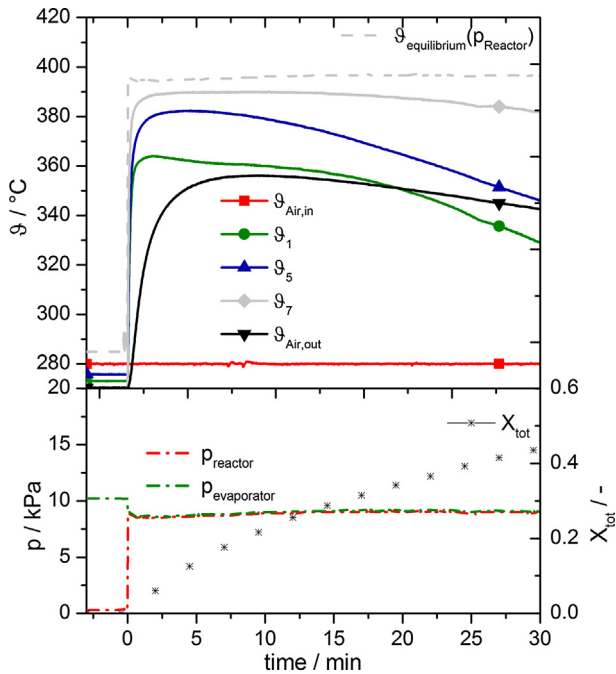


Fig. 8. Hydration at 10 kPa and a starting temperature of 280 °C.

is set 120 K lower than the theoretical equilibrium temperature at the applied vapour pressure. For example, experiment F was operated at a water vapour pressure of 50 kPa which correspond to an equilibrium temperature of 470 °C. Therefore the air inlet temperature was set to 350 °C. For comparison of the experimental parameters please refer to Table 1.

As already explained the cooling load is initially maximal in the front region of the reactor. Fig. 9 therefore only represents the temperature θ_1 (beginning of reaction bed) and the equilibrium temperature based on the measured pressure for each experiment. It can clearly be observed that in all cases plateaus arises while a certain gap to the equilibrium temperature is maintained. The gap is about 15 K for case H and I (50 and 20 kPa respectively) while it is approximately 30 K for the cases F and G (4 and 10 kPa).

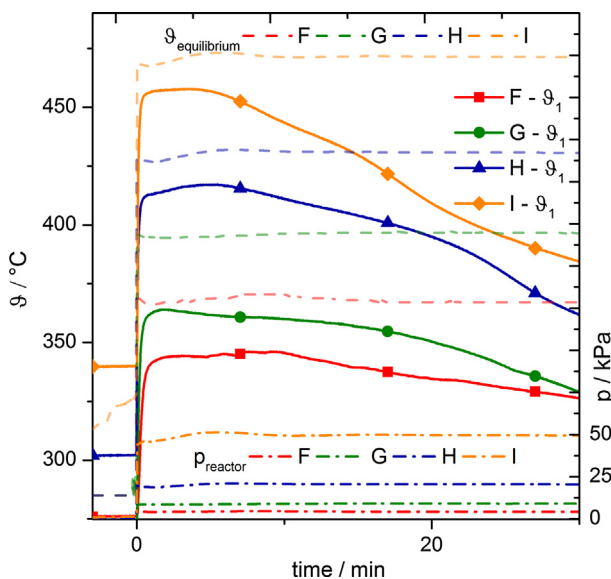


Fig. 9. Hydration at 4, 10, 20 and 50 kPa under comparable cooling loads.

3.3. Cycle stability and changes of the reaction bed

Cycle stability of the reaction system has already been demonstrated in several works by means of TGA as well as reactor experiments. Therefore the analysis of the cycle stability was not a main focus of this study. Nevertheless we can confirm that for the performed experiments in general a conversion of 90–95% (compare Fig. 4 and the experiments presented in [36]) was achieved and no decreasing tendency over the number of cycles could be observed. As already mentioned the conversion of the experiments in Figs. 7 and 8 do not show complete conversion because the timeline is not presented until the end of the experiment (to improve the display of the discussed temperature plateaus). That the conversion reaches only 90–95% in the lab scale reactor can be attributed to two reasons. First is, that the purity of the basic raw material is only 97–98% $\text{Ca}(\text{OH})_2$. The second reason is that the last 5–10% of conversion during the dehydration demands a very long time. Since full conversion of the material does not have any influence on the phenomena's discussed in this paper, experiments were finished when a conversion between 90 and 95% was reached. Overall we can confirm that the reaction is cycle stable and 90% of the theoretical full conversion is exploitable in technically relevant times.

The right picture in Fig. 10 shows the reaction bed of $\text{Ca}(\text{OH})_2$ when it was removed from the casing pipe after 35 cycles. It can be observed that the reaction bed is slightly compressed and the bulk density increased compared to the initially loose filling (compare Fig. 2) of the storage material. Roughly 20% of the heat exchange surface is not covered with material anymore due to the compression of the bed. The compression might enhance the thermal conductivity of the bulk on the one hand but could also worsen the gas permeability on the other hand. We assume that these changes occur within the first cycles and subsequently do not significantly change anymore. In addition no effect dedicated to these changes of the reaction bed could be observed in our experiments. However the reaction bed design (very thin layer) also was explicitly dedicated to minimize these transport resistances. Nevertheless the findings indicate that in larger reactors the changes which occur in large reactive bulks might have a significant influence on the performance. The heat and mass transport phenomena's in a changing reactive bulk should therefore be investigated in an experimental set up especially designed to address these questions. A more detailed description of these transactions in the models will improve simulation results. The picture in Fig. 10 left shows the agglomerates after loosening of the bulk but even though the agglomerates look very hard, they fall apart into smaller particles with only slight mechanical strains. This formation of agglomerates has consistently been reported in lab scale reactors, even in the directly heated fixed bed.

3.4. Summary of experimental results and implications for the process application

The superheated steam cycle is a well-established thermodynamic cycle for power generation. Different configurations and power sizes are readily available on the market. From today's perspective the maximum process temperature is in general limited to 600 °C due to economic reasons: The operation at higher temperatures demands more expensive alloys for the plant components and the higher costs are not compensated by the higher cycle efficiency. Market availability and scalability of the power cycle, the suitable temperature range as well as the working fluid water vapour (which is also required for the operation of the storage) lead to the conclusion that Rankine cycles powered by calcium oxide and water as the only energy source is one promising application.



Fig. 10. Right: reaction bed after 35 cycles; left: larger agglomerates after loosening of the bed.

Particular relevant operating condition is the discharge at pressures of 200–470 kPa in order to meet the upper temperature level of the current cycles of 545–600 °C. However the operation at these high pressures also requires a heat source with a temperature level of 120–150 °C to supply the discharge steam. In general thermal energy at this temperature level can usefully be incorporated into the process while at the same time thermal energy at a lower temperature level needs to be rejected from the Rankine cycle (e. g. condensation to the ambient). For the overall storage efficiency it could be highly valuable to make use of this low grade thermal energy to supply steam for the discharge procedure. For this reason the thermal discharge of the reaction system at pressures between 4 and 50 kPa, corresponding to evaporation temperatures between 30 and 81.3 °C has been additionally examined in the experimental section.

The experiments A–C showed that the discharge at pressures between 200 and 470 kPa achieved very good performances. For the first time a discharge temperature of 600 °C and 565 °C under significant cooling loads of the heat transfer fluid was demonstrated. In all experiments even with drastically increased cooling loads the reaction proceeded close to the theoretical equilibrium temperature. It can be summarized that in this operating range reactors with high power densities can be designed to operate with discharge temperatures very close to the theoretical equilibrium temperature. Finally it was demonstrated that if the reaction system is operated at 470 kPa it is capable to supply thermal energy at a temperature of 600 °C, the current maximum temperature of superheated steam cycles.

The thermal discharge at a pressure of 10 kPa was investigated due to its high relevance for a more efficient operation of a Rankine steam cycle (10 kPa is a common condensation pressure for dry cooling power plants). The experiments revealed that at this low pressure the equilibrium temperature was not reached in a technically relevant time. In the reactor a discharge temperature of 360 °C (in contrast to 400 °C equilibrium temperature) was determined for high cooling loads. Comparable limitations could be observed for all other investigated discharge pressures below 50 kPa. Overall it could be demonstrated that it is possible to discharge the storage reactor at reasonable reaction rates and vapour pressures between 4 and 50 kPa. However, in this operating range it is particular important that depending on the required thermal power an additional gap to the equilibrium temperature needs to be taken into account which reduces the achievable discharge temperature. Nevertheless even for the relatively low vapour pressures of 4 and 10 kPa outlet temperatures of 340 and 360 °C have been demonstrated (Figs. 7 and 8). These findings open the possibility of interesting interconnections between the steam cycle and the storage which will be thermodynamically analysed in Section 4.3.

4. Evaluation of process integration based on molten salt CSP

For the study we consider the boundary conditions of a current molten salt tower plant [10]. The heat transfer fluid is a molten salt mixture (60% NaNO₃ + 40% KNO₃) operating in a temperature range from 290 °C to 565 °C. Even though the molten salt cycle is not the most innovative CSP concept discussed in the literature it has been chosen for a first reference integration scenario. The analysis should therefore be seen as one exemplarily process integration study to identify the general challenges related to the process integration of the calcium hydroxide system. Molten salt has been chosen due to the following reasons: The technology is commercially available and the community seeks for solutions to replace the expensive salt as the storage material. Additionally the coupling of the calcium hydroxide system with a superheated steam cycle offers potential synergies since water vapour is the working fluid in the cycle as well as the required reaction gas of the storage system. For the charging procedure we used available data for a central receiver power plant provided by DLR Institute of Solar Research. For the discharge procedure a state of the art power block configuration is considered.

Special focus in this chapter lies on the analysis of the discharge period of the storage where the power block should run only with thermal energy supplied by the storage system. During this discharging process it is particular important to consider the source of thermal energy required for evaporation since it represents a large share of the energy released by the reaction. Therefore different configurations, including the extraction of low grade heat from the steam cycle, and their effect on the overall storage efficiency have been analysed.

During the charging period the temperature of the available heat sink for condensation of the reaction gas has huge influence on the amount of potentially stored thermal energy. Therefore the charging performance is evaluated against a commercial CPS plant technology based on a direct molten salt storage system.

4.1. Integration concept for CSP plant

For an application in CSP plants large storage capacities of up to 15 h of nominal thermal power are desirable in order to ensure a continuous operation of the plant during most of the year. For a typical configuration with a nominal thermal power of 300 MW_{thermal} this leads to a required storage capacity of 4500 MW h which corresponds to 11,250 tons of calcium hydroxide. Taking these numbers into account it becomes obvious that for such large storage capacities the only economically viable way to realize indirectly heated reactors is the separation of power and capacity. In such a concept the heat exchanger is detached from the mass of the storage material. This allows to design the

energy can be stored. Or, expressed in alternative values: whereas in a direct molten salt system 10 h of nominal thermal load are stored the investigated thermochemical storage system can theoretically only be charged with 5.9 h of nominal thermal load and 4.2 h for the more realistic case of an outlet temperature of 445 °C.

This can be contributed to two reasons: one is that the minimal condensation temperature of the plants location limits the temperature difference between the maximum temperature of the heat transfer fluid and the temperature level of the reaction. The second is that kinetic limitations at such low vapour pressure enforce an additional temperature difference of approximately 45 K to the theoretical reaction temperature (which has been experimentally identified in [19]). This drastic difference makes it obvious that a thermochemical storage cannot simply substitute a conventional storage method without changing at least some parts of the overall concept.

However, if the configuration of the plant will be adapted to the storage system the pointed out problems can be overcome. One proposal with minimal adaptation of the CSP technology would be to have two different central receivers. One receiver would still operate in the nominal temperature range of the power block from 290 to 565 °C to supply the power block during on sun operation. The second receiver cycle would be especially designed to charge the storage system during daytime and operate at temperatures between 565 °C and 445 °C. Of course the higher return temperature of the heat transfer fluid provokes higher losses in the central receiver. Nevertheless a detailed simulation of such a configuration could be worth investigating.

4.3. Power generation driven by the storage system – Operation modes

The steam cycle for power generation considered in this work is based on a standard Rankine cycle configuration for molten salt solar tower plants. The configuration consists of two high pressure turbine stages, one reheater, and 5 low pressure turbine stages. Live steam is generated at 136,000 kPa and 552 °C Steam is extracted at 6 turbine stages to preheat the feed water. The cycle is designed for a nominal output of 125 MW_{el} and reaches a gross efficiency of 0.419 at a condensation pressure of 10 kPa. Table 2 summarizes the main nominal parameters of the power block.

Four different operation strategies where the steam cycle is only powered by the thermochemical storage system are analysed. The operation modes differ in the quality and flow rate of steam which is extracted at different turbine stages to supply vapour for the discharge reaction. For each operation mode the required flow rate at the extraction point is calculated by general mass and energy balances. The power block is simulated with the commercial software tool Ebsilon©. By means of the simulation the electrical output in part load mode for the different steam extraction flow rates is determined.

Fig. 13 shows the process flow diagram of the steam cycle and the operation of the thermochemical reactor(s) during the discharge procedure. We at first describe the different configurations while in the subsequent section the overall storage efficiencies are compared.

4.3.1. Reference case

In the reference case only the high pressure TCS-Reactor (TCS1) and the evaporator (EV1) are in operation. Discharge steam is generated in evaporator (EV1) which is driven by thermal energy supplied by the heat transfer fluid. The molten salt is directed to evaporator (EV1) after it leaves the preheater with an outlet temperature of 290 °C. The steam is generated at a pressure of 470 kPa and directed into the reactor (TCS1). As we demonstrated in the experimental section (compare Fig. 4) with the operation at 470 kPa a reaction temperature of 600 °C can be expected.

Table 2
Nominal values for power block cycle.

<i>HTF parameters</i>	
Nominal thermal input/MW _{th}	298.35
Flowrate of HTF/(kg/s)	713.373
HTF inlet temperature/°C	565
HTF return temperature/°C	290
<i>Steam parameters</i>	
Live steam flowrate/(kg/s)	384.451
Live/reheat steam pressure/kPa	13600/3200
Live/reheat steam temperature/°C	334/552
<i>Turbine parameters</i>	
Gross turbine power/MW _{electric}	125
Turbine isentropic efficiency/%	86
Generator efficiency/%	96
Power block gross efficiency/%	41.9
<i>Condenser</i>	
Condensation pressure/kPa	10
<i>Steam extraction</i>	
(EXP1) – pressure/kPa/flowrate/(kg/s)	5000/2.8
(EXP2) – pressure/kPa/flowrate/(kg/s)	3400/10.9
(EXP3) – pressure/kPa/flowrate/(kg/s)	1000/5
(EXP4) – pressure/kPa/flowrate/(kg/s)	450/5.3
(EXP5) – pressure/kPa/flowrate/(kg/s)	150/4.9
(EXP6) – pressure/kPa/flowrate/(kg/s)	40/3.7
<i>Thermal power</i>	
Superheater/MW	89.796
Reheater/MW	41.202
Steam generator/MW	114.47
Preheater/MW	52.89

Therefore the power block can continue to operate at nominal conditions of 552 °C superheated steam.

In this operation mode the reactor not only has to supply the nominal thermal power of the steam cycle but also the thermal power for the evaporation of the required discharge steam (compare Fig. 13). The required discharge power can thus be calculated by the equations:

$$\dot{Q}_{TCS-discharging-A} = \dot{Q}_{PB,nominal} + \dot{Q}_{evaporation} \quad (2)$$

$$\dot{n} * \Delta H_{reaction} = \dot{Q}_{PB,nominal} + \dot{n} * \Delta H_{evaporation(149.5\text{ °C}, 470\text{ kPa})} \quad (3)$$

With the enthalpy values given in Table 3, the required thermal power that has to be delivered by the thermochemical reactor $\dot{Q}_{TCS-discharging-A}$ accounts to 470.16 MW in this operation mode.

4.3.2. Steam extraction at LP-Turbine

In operation mode B steam is extracted at the second stage of the low pressure turbine at extraction point 4 (EX4). The extracted steam is directed into evaporator (EV2) where steam at 450 kPa is generated for the thermochemical discharge reaction. Again according to our experimental demonstration in Section 3.1 the reaction temperature at this pressure will be close to the equilibrium temperature (597 °C). For this simplified examination, losses related to the heat exchanger (EV2) are neglected. In contrast to operation mode A the thermal power required in this configuration is only the nominal thermal power of the power block (298.35 MW). Thus the molar rate of reaction can be calculated by the equation:

$$\dot{Q}_{TCS-discharging-B} = \dot{Q}_{PB,nominal} = \dot{n} * \Delta H_{reaction} \quad (4)$$

With the molar rate of reaction the flow rate of required water vapour for the discharge reaction can be calculated by Eq. (5):

$$\dot{m}_{vapour} = \dot{n} * M_{H2O} \quad (5)$$

and accounts 51.68 kg/s. Consequently, this amount of steam is not available for power generation. Therefore, the operation of the

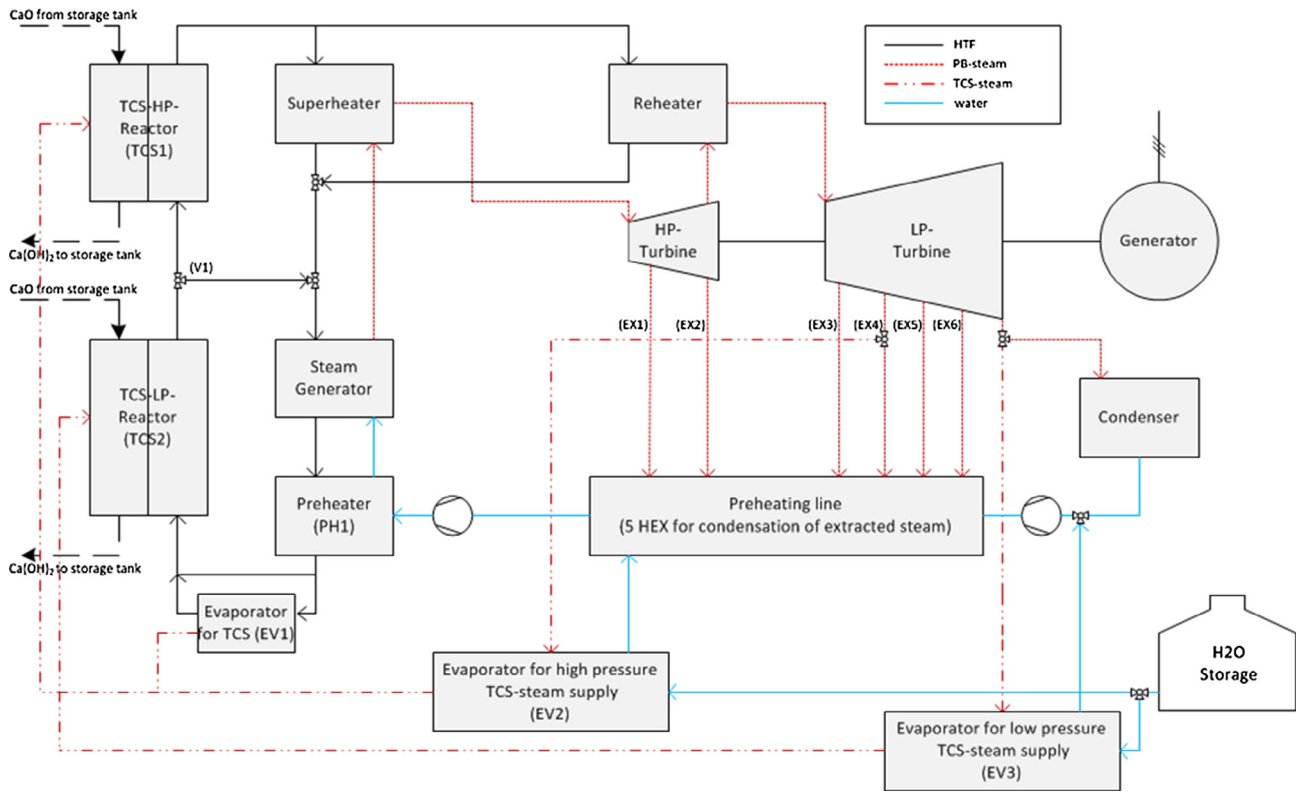


Fig. 13. Flow sheet of power block operation with the thermochemical storage system.

Table 3
General values for the calculations.

General values	
$\dot{Q}_{PB_{nominal}} / \text{MW}$	298.35
$\eta_{PB_{nominal}}$	0.419
$\Delta H_{reaction} / (\text{kJ/mol})$	104
$\Delta H_{evaporation(149.5^\circ\text{C}, 470\text{ kPa})} / (\text{kJ/mol})$	38
$M_{\text{H}_2\text{O}} / (\text{kg/mol})$	0.018

power block is simulated with a steam extraction of 51.68 kg/s at (EX4) which results in a reduced electrical output of 92.1 MW compared to the nominal output of 125 MW (no steam is extracted for the TCS operation).

4.3.3. Steam extraction at LP-Turbine and use of exhaust steam

In order to further increase the efficiency it seems reasonable to make use of the condensation enthalpy of the exhaust steam at the outlet of the low pressure turbine. Nevertheless this operation mode results in a more complex integration. To incorporate the steam at the condensation pressure of 10 kPa the outlet flow of the low pressure turbine is partially directed to evaporator (EV3). There steam is generated at a pressure of 10 kPa and directed into a second reactor (TCS2) for low pressure operation. Losses of the heat exchanger (EV3) are again neglected. In this operation mode two reactors are necessary because the temperature level which is reached in TCS2 is limited. Taking the experimental results for the discharge at 10 kPa into account (compare Fig. 8) a temperature of around 360 °C can be expected. Since the steam generator of the plant operates at 334 °C, the low pressure reactor TCS2 is in principle able to supply the thermal energy for the steam generator and the preheater. Consequently, only the superheater and the reheater need to be driven by TCS1. Therefore the mass flow of the HTF is separated after TCS2 at valve (V1). One part is directed to

supply the steam generator and the preheater whereas a smaller mass flow is directed into TCS1. The reactor TCS1 again operates at 450 kPa while, like in operation mode B, the required steam comes from evaporator EV2 which in turn is driven by condensation of steam from extraction point 4 (EX4). Since TCS1 now only provides the thermal power required by the superheater and the reheater the necessary thermal power is clearly reduced:

$$\dot{Q}_{TCS1-discharging-C} = \dot{Q}_{superheater} + \dot{Q}_{reheater} = \dot{n}_{TCS1-C} * \Delta H_{reaction} \quad (6)$$

Accordingly the necessary steam flow rate at (EX4) is calculated to 22.69 kg/s. The molar reaction rate required at TCS2 is calculated by:

$$\dot{Q}_{TCS2-discharging-C} = \dot{Q}_{evaporator} + \dot{Q}_{preheater} = \dot{n}_{TCS2-C} * \Delta H_{reaction} \quad (7)$$

According to Eq. (5) the flow rate of steam which needs to be generated by the enthalpy of condensation at 10 kPa is calculated to 28.99 kg/s. Since in this case, a huge fraction of the reaction gas could be derived from the condensation pressure of the power block, the calculated electrical output for this configuration is 109.91 MW.

4.3.4. Steam extraction at LP-Turbine and lowering of condensation temperature

In operation mode D it is assumed that the TCS2 reactor operates at a vapour pressure of 4 kPa, which in principle would allow to reduce the condensation temperature of the power block. However, it is obvious that operating the system at such low pressures requires huge efforts in gas handling and heat exchange. The experimental results presented in Fig. 7 show that a reaction temperature of 340 °C can be reached which is in principle high enough to supply the steam generator and the preheater (comparable to configuration C). Since evaporator (EV3) operates at a pressure of 4 kPa (instead of 10 kPa) the efficiency of the power block is increased which could partially compensate the reduced mass flow

of steam. However, this configuration would require an additional turbine stage in which 28.99 kg/s of steam can be condensed at 4 kPa while 24.7 kg/s are condensed at 10 kPa after the nominal fifth turbine stage (configuration is not illustrated in Fig. 13). Comparable to operation mode C an additional mass flow of 22.69 kg/s of steam must be extracted at 450 kPa at (EX4) to supply the TCS1 reactor. The calculated power output of this configuration is 112.48 MW which is only slightly higher than case C that could be realized with clearly minor changes of the power block.

4.4. Storage efficiency

Table 4 summarizes the results for the different operation modes. It becomes obvious that in the reference case A the power block operates at its nominal electric output but at the same time the thermal power required at the thermochemical reactor is much higher compared to the configurations where steam is extracted from the power block.

Therefore, in order to be able to compare the operation modes we defined an efficiency which relates the electric energy output during discharge of the storage to the potential electricity which has not been produced during the charging period of the storage system. The efficiency is represented by Eq. (8):

$$\eta_{\text{storage}} = \frac{P_{el \text{ discharging-case A-D}}}{\dot{Q}_{TCS\text{-charging-case A-D}} * \eta_{PB\text{nominal}}} \quad (8)$$

Further we assume that for all cases the thermal power required during discharge is equal to the thermal power supplied during the charging procedure:

$$\dot{Q}_{TCS\text{-charging-case A-D}} = \dot{Q}_{TCS1\text{-discharging-case A-D}} + \dot{Q}_{TCS2\text{-discharging-case A-D}} \quad (9)$$

Consequently since losses are neglected the ratio of charging power to discharging power is 1 and the storage can be discharged exactly for the time span as it was charged.

Fig. 14 shows the storage efficiency calculated by Eqs. (8) and (9) for the different configurations. The reference case A only reaches an efficiency of 63.4%. The low efficiency can be mainly attributed to the fact that the energy content of the steam released during the charging process is not used and the steam required for the discharge needs to be generated by thermal energy from the storage itself. Therefore we lose roughly 36% of the energy content which is related to the ratio of enthalpy of condensation to the enthalpy of reaction (38/104 (kJ/mol)).

In operation mode B a large steam mass flow needs to be extracted at 450 kPa from the low pressure turbine. This clearly reduces the electrical output of the power block. But on the other hand the thermal power required from the storage during the discharging process is also reduced compared to the reference case A. Overall we reach a clearly increased storage efficiency of 73%. Advantageous of this concept is that only one TCS reactor is required and it is operated at a relatively high pressure. The higher pressure in principal allows smaller pipe diameters and compact reactor designs. Additionally, as experimentally demonstrated (compare Section 3.1), a reaction pressure of > 200 kPa allows for

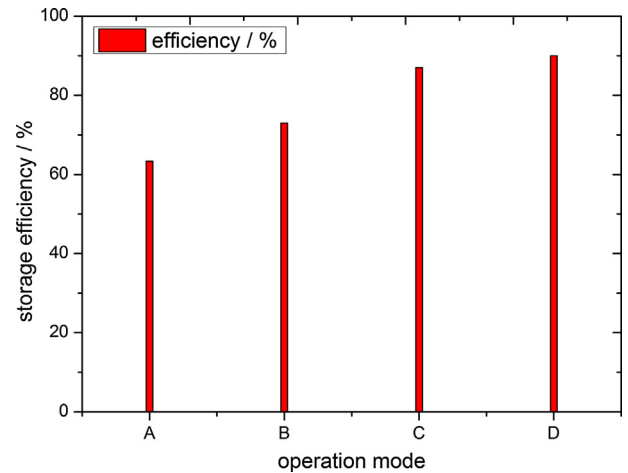


Fig. 14. Storage efficiency according to Eqs. (8) and (9) for the different operation modes.

outlet temperatures that are very close to the equilibrium even for high required reaction rates.

Operation mode C greatly improves the overall efficiency to 87%. In this operation mode only the amount of thermal power required at the higher temperature level of 565 °C is generated in TCS1. The remaining required thermal power is generated in TCS2 where steam which has no exergetic value in the steam cycle is used for the discharging reaction. Consequently a much smaller mass flow of steam has to be extracted at point 4 (EX4) which in turn increases the electricity output. The obvious disadvantage of this operation mode is that in total four devices are necessary: two TCS-reactors and two evaporators. The direct incorporation of the extracted steam from the turbines to the thermochemical reactors (to avoid the two evaporators) is to our knowledge not possible. The steam which was in contact with the storage material might not be clean enough anymore to operate the turbines. Additionally the operation of the thermochemical reactor at such a low vapour pressure of 10 kPa might be challenging due to: large pipe diameters that are required for the transport of the steam. Furthermore the reactor design becomes more complex since the reaction gas distribution within the reaction bed is easier for higher pressures. And finally, the reaction temperature which can be reached at this vapour pressures deviates clearly from the theoretical value if technical relevant reaction rates are required (compare Fig. 8).

Operation mode D reaches an efficiency of 90%. But since this increase of the electrical output of the power block would lead to even more challenging operating conditions of the power block and the storage, it is doubtful that the increase of 3 percentage points in storage efficiency will be economically reasonable.

To summarize: the experimental investigation of commercially available $\text{Ca}(\text{OH})_2$ shows that in principle the required heat sink of the power block (cooling tower) could be combined with the required low grade heat source of the thermochemical system (evaporator). This concept clearly improves the overall efficiency of the thermochemical storage but requires at the same time to a

Table 4

Calculated thermal power, flow rates of extracted steam and electrical output of the power block for the different operation modes.

Mode	$\dot{Q}_{TCS1}/\text{MW}_{th}$	$\dot{Q}_{TCS2}/\text{MW}_{th}$	$\dot{m}_{\text{vapour @}(EX4)}/(\text{kg/s})$	$\dot{m}_{\text{vapour @}(EV3)}/(\text{kg/s})$	P_{el}/MW_{el}
A	470.16	0	0	0	125
B	298.35	0	51.68	0	92.1
C	130.99	167.376	22.69	28.99	109.91
D	130.99	167.376	22.69	28.99	112.484

certain extent modifications of the power block. The simplest configuration reaches a storage efficiency of 73% (in comparison 63.4% for the baseline case) while with a more complex and technically challenging integration values of 87% and more could be reached. It has to be stated that for all operation modes with increased efficiency (mode B, C and D) a large fraction of the nominal steam mass flow has to be extracted at the low pressure turbine. Such a large steam extraction is thermodynamically possible but to the knowledge of the author's no turbine, which allows such an operation, is currently available on the market. The design of such a turbine is technically challenging and thus would demand extensive development work. One possibility to overcome this challenge might be to use two separated turbines especially designed for the required boundary conditions instead of extracting a large steam fraction from one low pressure turbine stage.

To which extend the released steam during the charging of the storage can be used to increase the efficiency of the power block and compensates for the reduced power output during the discharging process needs to be evaluated based on a more detailed simulation of the plant including economic aspects.

5. Conclusions

In this study the thermal discharging of the reaction of CaO and water vapour has been experimentally demonstrated in lab scale in the complete temperature (280–600 °C) and pressure (4–470 kPa) range which is relevant to operate a Rankine steam cycle with the thermochemical storage system. The experiments revealed that especially at pressures of 200 kPa and more the reaction is very fast even at the (or very close to the) equilibrium temperature. Therefore it can be concluded that for this pressure range reactors can be designed to operate with high power densities and at outlet temperatures close to the equilibrium temperature. The discharge procedure at pressures between 4 and 50 kPa has also been experimentally demonstrated and showed promising performance. Nevertheless at this low pressure operation an additional temperature difference to the equilibrium temperature occurs and has to be maintained if the reactor should be operated at high power densities. With the presented discharge experiments and our previously published charging experiments the complete relevant operating range of the thermochemical storage system has been experimentally characterised in lab scale. The experimental results now provide a more realistic understanding of the operation characteristic as well as the quantification of achievable charge and discharge temperatures. Based on this knowledge the applicability of the storage for many real processes can now be assessed more accurate from a technical as well as a thermodynamic point of view.

Besides the experimental investigations a first study on the integration of the thermochemical system in a conventional CSP plant has been thermodynamically analysed. It could be shown that, when the steam production required during discharge is thermally integrated into the Rankine steam cycle a high storage efficiency of 87% can be reached. However the charging procedure with molten salt as the heat transfer fluid is challenging: The minimal condensation pressure of 10 kPa available at most CSP locations (dry cooling in hot regions) as well as kinetic limitations at low pressure charging enforce reaction temperatures of 445 °C or higher. In conclusion the thermal power which can be incorporated is limited due to the small temperature difference between the reaction temperature and today's maximum operating temperature of the salt. On the other hand the experimentally demonstrated characteristic of the storage system indicate promising potential for a wide range of applications. The posed charging challenge can be overcome by using heat transfer fluids which allow a higher maximum temperature, for example liquid metal. Another

approach to charge the storage system would be direct solar irradiation in a particle receiver. The determined potentially achievable high storage efficiencies indicate that such applications should be investigated in future studies.

References

- [1] Zhang HL, Baeyens J, Degève J, Cáceres G. Concentrated solar power plants: review and design methodology. *Renew Sustain Energy Rev* 2013;22:466–81. <http://dx.doi.org/10.1016/j.rser.2013.01.032>.
- [2] Dunn RI, Hearps PJ, Wright MN. Molten-salt power towers: newly commercial concentrating solar storage. *Proc IEEE* 2012;100:504–15. <http://dx.doi.org/10.1109/JPROC.2011.2163739>.
- [3] Franchini G, Perdichizzi A, Ravelli S, Barigozzi G. A comparative study between parabolic trough and solar tower technologies in solar Rankine cycle and Integrated solar combined cycle plants. *Sol Energy* 2013;98:302–14. <http://dx.doi.org/10.1016/j.solener.2013.09.033>.
- [4] IRENA. Renewable energy technologies: cost analysis series concentrating solar power. IRENA work pap; 2012.
- [5] Kuravi S, Trahan J, Goswami DY, Rahman MM, Stefanakos EK. Thermal energy storage technologies and systems for concentrating solar power plants. *Prog Energy Combust Sci* 2013;39:285–319. <http://dx.doi.org/10.1016/j.pecs.2013.02.001>.
- [6] Flueckiger SM, Iverson BD, Garimella SV. Economic optimization of a concentrating solar power plant with molten-salt thermocline storage. *J Sol Energy Eng* 2013;136:1–8. <http://dx.doi.org/10.1115/1.4025516>.
- [7] Xu Y, Ren Q, Zheng Z-J, He Y-L. Evaluation and optimization of melting performance for a latent heat thermal energy storage unit partially filled with porous media. *Appl Energy* 2017;193:84–95. <http://dx.doi.org/10.1016/j.apenergy.2017.02.019>.
- [8] Zhou L, Xu G, Zhao S, Xu C, Yang Y. Parametric analysis and process optimization of steam cycle in double reheat ultra-supercritical power plants. *Appl Therm Eng* 2016;99:652–60. <http://dx.doi.org/10.1016/j.applthermaleng.2016.01.047>.
- [9] Meng ZN, Zhang P. Experimental and numerical investigation of a tube-in-tank latent thermal energy storage unit using composite PCM. *Appl Energy* 2017;190:524–39. <http://dx.doi.org/10.1016/j.apenergy.2016.12.163>.
- [10] Liu M, Steven Tay NH, Bell S, Belusko M, Jacob R, Will G, et al. Review on concentrating solar power plants and new developments in high temperature thermal energy storage technologies. *Renew Sustain Energy Rev* 2016;53:1411–32. <http://dx.doi.org/10.1016/j.rser.2015.09.026>.
- [11] Zhang H, Baeyens J, Cáceres G, Degève J, Lv Y. Thermal energy storage: recent developments and practical aspects. *Prog Energy Combust Sci* 2016;53:1–40. <http://dx.doi.org/10.1016/j.pecs.2015.10.003>.
- [12] Miró L, Gasia J, Cabeza LF. Thermal energy storage (TES) for industrial waste heat (IWH) recovery: a review. *Appl Energy* 2016;179:284–301. <http://dx.doi.org/10.1016/j.apenergy.2016.06.147>.
- [13] Gil A, Medrano M, Martorell I, Lázaro A, Dolado P, Zalba B, et al. State of the art on high temperature thermal energy storage for power generation. Part 1—Concepts, materials and modellization. *Renew Sustain Energy Rev* 2010;14:31–55.
- [14] Medrano M, Gil A, Martorell I, Potau X, Cabeza LF. State of the art on high-temperature thermal energy storage for power generation. Part 2—Case studies. *Renew Sustain Energy Rev* 2010;14:56–72.
- [15] Cabeza LF, Solé A, Fontanet X, Barreneche C, Jové A, Gallas M, et al. Thermochemical energy storage by consecutive reactions for higher efficient concentrated solar power plants (CSP): proof of concept. *Appl Energy* 2017;185:836–45. <http://dx.doi.org/10.1016/j.apenergy.2016.10.093>.
- [16] Chacartegui R, Alovio A, Ortiz C, Valverde JM, Verda V, Becerra JA. Thermochemical energy storage of concentrated solar power by integration of the calcium looping process and a CO₂ power cycle. *Appl Energy* 2016;173:589–605. <http://dx.doi.org/10.1016/j.apenergy.2016.04.053>.
- [17] Deutsch M, Müller D, Aumeyr C, Jordan C, Gierl-Mayer C, Weinberger P, et al. Systematic search algorithm for potential thermochemical energy storage systems. *Appl Energy* 2016;183:113–20. <http://dx.doi.org/10.1016/j.apenergy.2016.08.142>.
- [18] Aydin D, Casey SP, Riffat S. The latest advancements on thermochemical heat storage systems. *Renew Sustain Energy Rev* 2015;41:356–67. <http://dx.doi.org/10.1016/j.rser.2014.08.054>.
- [19] Pardo P, Deydier A, Anxionnaz-Minvielle Z, Rougé S, Cabassud M, Cognet P. A review on high temperature thermochemical heat energy storage. *Renew Sustain Energy Rev* 2014;32:591–610. <http://dx.doi.org/10.1016/j.rser.2013.12.014>.
- [20] Prieto C, Cooper P, Fernández AI, Cabeza LF. Review of technology: thermochemical energy storage for concentrated solar power plants. *Renew Sustain Energy Rev* 2016;60:909–29. <http://dx.doi.org/10.1016/j.rser.2015.12.364>.
- [21] Rosemary JK, Bauerle GL, Springer TH. Solar energy storage using reversible hydration-dehydration of CaO-Ca(OH)₂. *J Energy* 1979;3:321–2. <http://dx.doi.org/10.2514/3.62440>.
- [22] Schaub F, Koch L, Wörner A, Müller-Steinhagen H. A thermodynamic and kinetic study of the de- and rehydration of Ca(OH)₂ at high H₂O partial pressures for thermo-chemical heat storage. *Thermochim Acta* 2012;538:9–20. <http://dx.doi.org/10.1016/j.tca.2012.03.003>.

- [23] Criado YA, Alonso M, Abanades JC. Kinetics of the $\text{CaO}/\text{Ca}(\text{OH})_2$ hydration/dehydration reaction for thermochemical energy storage applications. *Ind Eng Chem Res* 2014;53:12594–601. <http://dx.doi.org/10.1021/ie404246p>.
- [24] Galwey AK, Laverty GM. A kinetic and mechanistic study of the dehydroxylation of calcium hydroxide. *Thermochim Acta* 1993;228:359–78. [http://dx.doi.org/10.1016/0040-6031\(93\)80304-S](http://dx.doi.org/10.1016/0040-6031(93)80304-S).
- [25] Nagel T, Shao H, Roßkopf C, Linder M, Wörner A, Kolditz O. The influence of gas–solid reaction kinetics in models of thermochemical heat storage under monotonic and cyclic loading. *Appl Energy* 2014;136:289–302. <http://dx.doi.org/10.1016/j.apenergy.2014.08.104>.
- [26] Wang W, Kolditz O, Nagel T. Parallel finite element modelling of multi-physical processes in thermochemical energy storage devices. *Appl Energy* 2016. <http://dx.doi.org/10.1016/j.apenergy.2016.03.053>.
- [27] Kariya J, Ryu J, Kato Y. Development of thermal storage material using vermiculite and calcium hydroxide. *Appl Therm Eng* 2016;94:186–92. <http://dx.doi.org/10.1016/j.applthermaleng.2015.10.090>.
- [28] Shkatulov A, Ryu J, Kato Y, Aristov Y. Composite material “ $\text{Mg}(\text{OH})_2$ /vermiculite”: a promising new candidate for storage of middle temperature heat. *Energy* 2012;44:1028–34. <http://dx.doi.org/10.1016/j.energy.2012.04.045>.
- [29] Afflerbach S, Kappes M, Gipperich A, Trettin R, Krumm W. Semipermeable encapsulation of calcium hydroxide for thermochemical heat storage solutions. *Sol Energy* 2017;148:1–11. <http://dx.doi.org/10.1016/j.solener.2017.03.074>.
- [30] Pardo P, Anxionnaz-Minvielle Z, Rougé S, Cognet P, Cabassud M. $\text{Ca}(\text{OH})_2/\text{CaO}$ reversible reaction in a fluidized bed reactor for thermochemical heat storage. *Sol Energy* 2014;107:605–16. <http://dx.doi.org/10.1016/j.solener.2014.06.010>.
- [31] Criado YA, Alonso M, Abanades JC, Anxionnaz-Minvielle Z. Conceptual process design of a $\text{CaO}/\text{Ca}(\text{OH})_2$ thermochemical energy storage system using fluidized bed reactors. *Appl Therm Eng* 2014;73:1085–92. <http://dx.doi.org/10.1016/j.applthermaleng.2014.08.065>.
- [32] Rougé S, A. Criado Y, Soriano O, Abanades JC. Continuous $\text{CaO}/\text{Ca}(\text{OH})_2$ fluidized bed reactor for energy storage: first experimental results and reactor model validation. *Ind Eng Chem Res* 2017;56:844–52. <http://dx.doi.org/10.1021/acs.iecr.6b04105>.
- [33] Ogura H, Yamamoto T, Kage H, Matsuno Y, Mujumdar AS. Effects of heat exchange condition on hot air production by a chemical heat pump dryer using $\text{CaO}/\text{H}_2\text{O}/\text{Ca}(\text{OH})_2$ reaction. *Chem Eng J* 2002;86:3–10. [http://dx.doi.org/10.1016/S1385-8947\(01\)00265-0](http://dx.doi.org/10.1016/S1385-8947(01)00265-0).
- [34] Yan J, Zhao CY. Experimental study of $\text{CaO}/\text{Ca}(\text{OH})_2$ in a fixed-bed reactor for thermochemical heat storage. *Appl Energy* 2016;175:277–84. <http://dx.doi.org/10.1016/j.apenergy.2016.05.038>.
- [35] Barin I. Thermochemical data of pure substances doi: Weinheim, Germany: Wiley-VCH Verlag GmbH; 1995. 10.1002/9783527619825.
- [36] Schmidt M, Gutierrez A, Linder M. Thermochemical energy storage with $\text{CaO}/\text{Ca}(\text{OH})_2$ – experimental investigation of the thermal capability at low vapor pressures in a lab scale reactor doi:10.1016/j.apenergy.2016.11.023. *Appl Energy* 2017;188:672–81.
- [37] Samms JAC, Evans BE. Thermal dissociation of $\text{Ca}(\text{OH})_2$ at elevated pressures. *J Appl Chem* 2007;18:5–8. <http://dx.doi.org/10.1002/jctb.5010180102>.
- [38] Schmidt M, Gollsch M, Giger F, Grün M, Linder M. Development of a moving bed pilot plant for thermochemical energy storage with $\text{CaO}/\text{Ca}(\text{OH})_2$. *SOLARPACES* 2015. In: *Int conf conc sol power chem energy syst*, vol. 1734. AIP Publishing; 2016, p. 50041. 10.1063/1.4949139.